







Optimalisatie van de lay-out van een  
park golfenergieconvertoren in de Noordzee  
Studie van beschikbaar golfvermogen, zogeeffecten, productie en kost

Optimization of the Lay-Out of a  
Farm of Wave Energy Converters in the North Sea  
Analysis of Wave Power Resources, Wake Effects, Production and Cost

Charlotte Beels

Promotoren: prof. dr. ir. J. De Rouck, prof. dr. ir. P. Troch  
Proefschrift ingediend tot het behalen van de graad van  
Doctor in de Ingenieurswetenschappen: Bouwkunde

Vakgroep Civiele Techniek  
Voorzitter: prof. dr. ir. J. De Rouck  
Faculteit Ingenieurswetenschappen  
Academiejaar 2009 - 2010



ISBN 978-90-8578-321-3  
NUR 956, 961  
Wettelijk depot: D/2009/10.500/79



Universiteit Gent  
Faculteit Ingenieurswetenschappen  
Vakgroep Civiele Techniek  
Afdeling Weg- en Waterbouwkunde

**Supervisors:**

Prof. dr. ir. J. De Rouck  
Prof. dr. ir. P. Troch

**Research institute:**

Ghent University  
Faculty of Engineering

Department of Civil Engineering  
Coastal Engineering Division  
Technologiepark 904  
B-9052 Zwijnaarde, Belgium

Tel.: +32-9-264.54.89  
Fax.: +32-9-264.58.37

Research funded by a PhD grant of the Institute for the Promotion of Innovation through Science and Technology in Flanders (IWT-Vlaanderen).

**Copyright © Charlotte Beels**

All rights reserved. No part of the material protected by this copyright notice may be reproduced or utilised in any form or by any means, without written permission of the author or publisher.



# Dankwoord

Ik ben blij, héél blij! Het (extra) harde werk gedurende de laatste maanden heeft zijn vruchten afgeworpen: mijn boek is af! Dit boek zou echter nooit geworden zijn tot wat het nu is zonder de bijdrage en de steun van mijn promotoren, collega's, vrienden en familie. Zij verdienen hier dan ook een speciaal woordje van dank.

Mijn promotor, prof. Julien De Rouck, wens ik te bedanken om mij de kans te geven om mijn onderzoek aan de afdeling Weg- en Waterbouwkunde uit te voeren en om mij de mogelijkheid te geven om mijn horizon te verruimen gedurende verschillende buitenlandse stages en congressen. Een bijzonder woordje van dank richt ik tot mijn co-promotor, prof. Peter Troch, voor het beantwoorden van mijn vele – grote en kleine – vraagjes gedurende de voorbije 4 jaar. Zijn gedrevenheid heeft mij enorm geïnspireerd! Verder wil ik mijn beide promotoren ook bedanken voor hun niet-technische capaciteiten; ze hebben verschillende keren de tijd genomen om me aan te moedigen als ik de golven door de storm niet meer zag.

Ik wil van de gelegenheid gebruik maken om Prof. Marc Vantorre te bedanken voor de nuttige discussies tijdens mijn doctoraat. Tina Mertens en Robby Caspeele hebben mij op de juiste weg gezet tijdens de opstart van mijn onderzoek, waarvoor dank. Het team van Guido Dumon (afdeling Kust) wil ik bedanken voor de nodige golfdata op het Belgisch Continentaal Plat. Voor de suggesties met betrekking tot het economische luik van mijn doctoraat dank ik tevens prof. Hendrik Van Landeghem.

Tijdens mijn studies was ik al door de buitenlandse microbe gebeten. In de voorbije 4 jaar heb ik dan ook meer dan eens de kans gegrepen om kennis en ervaring op te doen in het buitenland. Thanks to Dr. Teresa Pontes, Dr. João Henriques and my colleagues at INETI and IST for the nice instructive month in Portugal. For their support from Belgium during this period I would also like to thank Ruben Maddens and Prof. Jaak Monbaliu. Further, I am very grateful to Prof. Jens Peter Kofoed, Prof. Peter Frigaard, Prof. Michael Brorsen and Dr. James Tedd from Aalborg University for their useful suggestions and ideas. The several short visits at Aalborg University during my PhD got me going again.

They introduced me to Wave Dragon ApS., which I would like to acknowledge for providing data on the Wave Dragon wave energy converter. I would also like to thank DONG Energy and in particular Jon Vindahl Kringelum and Peter Carsten Kromann for the nice collaboration. Their interest and enthusiasm gave me a boost at the end of my PhD. Thanks to the whole wave energy team at DONG Energy for the nice stay in Copenhagen. Finally a word of thanks goes to Prof. Torgeir Moan for inviting me in Trondheim as part of the EU project SEEWEC. In those two weeks I mainly cooperated closely with Dr. Reza Taghipour. Reza, thanks for your valuable input. Within this framework the additional support of the EU is also gratefully acknowledged.

Ook mijn collega's mogen in dit dankwoord niet ontbreken. Mijn middagen werden steeds opgefleurd door uiteenlopende discussies over de 'dingen des levens'. In het eerste jaar waren de meer of minder succesvolle verbouwingen het gespreksonderwerp. Later werden alle details van zwanger zijn, bevallen en kleuters grootbrengen uit de doeken gedaan. Met de komst van een aantal jongere collega's ging onze aandacht terug naar het begin: de zoektocht naar de ware... dit zorgde uiteraard voor de nodige hilariteit... Amélie, Anny, Bart, Corneel, Dieter, Dogan, Dries, Ellen, Etienne, Florent, Giang, Hadewych, Hans, Jan, Jonas, Jesus, Jimmy, Ken, Koen, Lander, Lien, Ludo, Nathalie, Philippe, Pieter D.W., Pieter M., Tingqui, Vicky, Vincent, Willem, Wim, Wouter en Yvan, een welgemeende dank je wel! Een bijzonder woordje van dank gaat uiteraard naar mijn bureaugenootjes Leen en Griet. We hebben heel wat afgelachen in onze 'meisjes'-bureau. Griet, ook bedankt voor de vruchtbare samenwerking, voor de vele conferenties die we samen hebben bijgewoond en voor onze eilandhopping in Hawaï. De kennis en ervaring van het technisch personeel was onontbeerlijk in het fysische luik van mijn doctoraat: dank je wel Tom, Herman, Sam en Dave! In dit kader wil ik tevens Marc Willems en Frans Verstraeten van het Waterbouwkundig Laboratorium in Borgerhout bedanken. Ook de thesisstudenten die onder mijn begeleiding hebben bijgedragen tot dit werk ben ik zeer dankbaar: Amélie, Charlotte, Hannes, Ine, Jeroen, Kenneth, Sam, Vincent en Wim.

Mijn vrienden verdienen zeker en vast hun plaatsje in dit dankwoord! De gezellige etentjes of stresserende 'Mijn Restaurant'-toestanden, nachtelijke uitstapjes, avondjes Risk en sportieve ups and downs zorgden voor de nodige ontspanning!

Voor hun steun en vertrouwen bedank ik graag mijn familie. In het bijzonder mijn zus Laurence en haar vriend Sam om de voorbije zomer af en toe eens onverwacht binnen te springen en mij een hart onder de riem te steken en mijn ouders om mij een duwtje in de rug te geven als ik het moeilijk had. Ma, pa, ik sta steeds verbijsterd van jullie enthousiasme en doorzettingsvermogen. Jullie steun was van ontelbaar belang!

Tot slot wil ik mijn vriend Dries bedanken om mee te denken als ik ergens niet aan uitkon, om te helpen met allerlei technische (PC) probleempjes en om steeds vertrouwen te hebben in mijn kunnen, maar ook om mij de nodige afleiding en rust te geven, om te verhinderen dat ik in het weekend achter mijn bureau zat en om mijn 'To Do'-lijstjes in te korten. Je poging om mijn doctoraat volledig door te nemen, betekende heel veel voor mij (ook al was het niet altijd even gemakkelijk om je kritische opmerkingen te aanvaarden). Ik kijk enorm uit naar ons reisje samen: een nieuwe stap in ons 'avontuurtje' dat 9 jaar geleden begon!

*Gent, december 2009*  
*Charlotte Beels*





# Table of contents

<b>List of symbols</b>	<b>xi</b>
<b>List of acronyms</b>	<b>xv</b>
<b>Glossary</b>	<b>xvii</b>
<b>Nederlandse samenvatting</b>	<b>xxi</b>
<b>English summary</b>	<b>xxv</b>
<b>1 Introduction</b>	<b>1-1</b>
1.1 Current status of wave energy . . . . .	1-1
1.1.1 Concepts . . . . .	1-1
1.1.2 A farm of wave energy converters . . . . .	1-4
1.2 Objectives . . . . .	1-8
1.3 Outline . . . . .	1-10
References . . . . .	1-11
<b>I Resources and planning</b>	
<b>2 Wave power resources in the North Sea</b>	<b>2-1</b>
2.1 Introduction . . . . .	2-1
2.2 Wave energy on the Belgian Continental Shelf . . . . .	2-3
2.2.1 Activities on the Belgian Continental Shelf . . . . .	2-3
2.2.2 Wave power near shore . . . . .	2-5
2.2.3 Temporal and directional trend of the available wave power	2-9
2.2.4 Wave climate specification . . . . .	2-14
2.2.5 Characteristic sea states . . . . .	2-17
2.2.6 Possibilities for wave energy conversion on the Belgian Continental Shelf . . . . .	2-20
2.3 Wave energy in the North Sea . . . . .	2-21
2.3.1 Analysis of available data . . . . .	2-21
2.3.2 Spatial distribution of the available wave power . . . . .	2-31
2.4 Conclusions . . . . .	2-37

References . . . . .	2-39
<b>3 Geo-spatial multi-criteria decision analysis</b>	<b>3-1</b>
3.1 Introduction . . . . .	3-1
3.2 Determination of suitable locations for wave power conversion in the southern North Sea . . . . .	3-3
3.2.1 Constraints . . . . .	3-3
3.2.2 Weighted factors . . . . .	3-7
3.2.3 Scores . . . . .	3-15
3.2.4 Weights . . . . .	3-17
3.2.5 Suitable locations in the southern North Sea . . . . .	3-19
3.3 Sensitivity analysis . . . . .	3-21
3.3.1 Importance of factor <i>produced power</i> . . . . .	3-22
3.3.2 Importance of factor <i>distance to the grid</i> . . . . .	3-23
3.3.3 Importance of factor <i>extreme wave conditions</i> . . . . .	3-24
3.3.4 Installation in 12-mile zone . . . . .	3-25
3.4 Accuracy of the geo-spatial multi-criteria decision analysis . . . . .	3-26
3.5 Conclusions . . . . .	3-26
References . . . . .	3-27

## II Production of a farm of wave energy converters

<b>4 Wave farm modelling</b>	<b>4-1</b>
4.1 Introduction . . . . .	4-1
4.2 State of the art in wave farm modelling . . . . .	4-1
4.3 Discussion on the applicability of wave propagation models for wave farm modelling . . . . .	4-3
4.3.1 Implementation of a farm of WECs in wave propagation models . . . . .	4-3
4.3.2 Shortcomings . . . . .	4-5
4.3.3 Mild-slope wave propagation model MILDwave . . . . .	4-6
4.4 Conclusions . . . . .	4-7
References . . . . .	4-8
<b>5 Mild-slope wave propagation model MILDwave</b>	<b>5-1</b>
5.1 Introduction . . . . .	5-1
5.2 Mild-slope equations of Radder and Dingemans . . . . .	5-2
5.3 Wave generation . . . . .	5-4
5.3.1 Regular waves . . . . .	5-5
5.3.2 Irregular waves . . . . .	5-16
5.4 Domain boundaries . . . . .	5-25
5.4.1 Head-on waves . . . . .	5-25
5.4.2 Waves with $0^\circ < \theta < 90^\circ$ . . . . .	5-27
5.5 Code development . . . . .	5-31

---

5.6	Reflection on a vertical, surface-piercing wall . . . . .	5-31
5.6.1	Reflection on a vertical, impermeable, rigid surface-piercing wall . . . . .	5-32
5.6.2	Reflection on a vertical, permeable, surface-piercing wall . . . . .	5-33
5.7	Wave diffraction around the tip of a semi-infinite breakwater . . . . .	5-34
5.8	Conclusions . . . . .	5-36
	References . . . . .	5-38
<b>6</b>	<b>A farm of wave energy converters in MILDwave</b>	<b>6-1</b>
6.1	Introduction . . . . .	6-1
6.2	Implementation of wave power absorption in MILDwave . . . . .	6-2
6.2.1	Numerical set-up . . . . .	6-3
6.2.2	Influence of the value of the absorption coefficient on the absorption characteristics . . . . .	6-5
6.2.3	Uncoupling of reflection and transmission . . . . .	6-8
6.2.4	Influence of the length of the WEC on the absorption characteristics . . . . .	6-9
6.2.5	Frequency dependent absorption . . . . .	6-12
6.3	Application of wave power absorption in MILDwave . . . . .	6-18
6.3.1	Wake behind a single hypothetical WEC . . . . .	6-18
6.3.2	Wave power absorption of a farm of hypothetical WECs . . . . .	6-23
6.4	Validation of wave power absorption in MILDwave . . . . .	6-38
6.4.1	Wave pattern around a fully reflective obstacle . . . . .	6-38
6.4.2	Wave pattern around a single and multiple absorbing obstacles . . . . .	6-49
6.4.3	Calculation of wave power absorption in MILDwave . . . . .	6-69
6.5	Conclusions . . . . .	6-78
	References . . . . .	6-81
<b>7</b>	<b>Power absorption of a farm of Wave Dragon wave energy converters</b>	<b>7-1</b>
7.1	Introduction . . . . .	7-1
7.2	Implementation of a Wave Dragon WEC in MILDwave . . . . .	7-2
7.2.1	Implementation of the wave reflectors . . . . .	7-4
7.2.2	Implementation of the main body . . . . .	7-9
7.3	Wake behind a single Wave Dragon WEC . . . . .	7-11
7.4	A farm of 5 Wave Dragon WECs . . . . .	7-20
7.4.1	Irregular long-crested waves . . . . .	7-22
7.4.2	Irregular short-crested waves . . . . .	7-28
7.5	Conclusions . . . . .	7-36
	References . . . . .	7-38
<b>8</b>	<b>Power absorption of a farm of FO<sup>3</sup> wave energy converters</b>	<b>8-1</b>
8.1	Introduction . . . . .	8-1
8.2	Implementation of an FO <sup>3</sup> WEC in MILDwave . . . . .	8-3

8.2.1	Results of WAMIT for a regular wave with unit wave amplitude and wave period of 6 s . . . . .	8-4
8.2.2	Wave diffraction . . . . .	8-8
8.2.3	Wave radiation . . . . .	8-18
8.2.4	Diffraction and radiation . . . . .	8-26
8.3	A farm of 9 FO <sup>3</sup> WECs . . . . .	8-36
8.4	Conclusions . . . . .	8-42
	References . . . . .	8-44

### III Cost of a farm of wave energy converters

<b>9</b>	<b>Production and cost assessment of a farm of Wave Dragon wave energy converters</b>	<b>9-1</b>
9.1	Introduction . . . . .	9-1
9.2	Test conditions . . . . .	9-2
9.3	Power absorbed by a single Wave Dragon WEC . . . . .	9-4
9.3.1	Rated power of a Wave Dragon WEC . . . . .	9-4
9.3.2	Wake behind a Wave Dragon WEC . . . . .	9-5
9.4	Production of a farm of Wave Dragon WECs . . . . .	9-10
9.4.1	Lay-out A: a single line of WD-WECs . . . . .	9-13
9.4.2	Lay-out B: a staggered grid lay-out . . . . .	9-14
9.4.3	Lay-out C: all WD-WECs installed behind each other . . . . .	9-18
9.4.4	Comparison between lay-out A, B and C . . . . .	9-21
9.5	Cost of a farm of Wave Dragon WECs . . . . .	9-23
9.5.1	Cost of subsea cabling . . . . .	9-23
9.5.2	Cost Of Energy (COE) . . . . .	9-28
9.6	Wave height decrease behind a farm of Wave Dragon WECs . . . . .	9-30
9.7	Conclusions . . . . .	9-34
	References . . . . .	9-36
<b>10</b>	<b>Investment analysis</b>	<b>10-1</b>
10.1	Introduction . . . . .	10-1
10.2	Sites for the deployment of a farm of Pelamis WECs . . . . .	10-2
10.3	Investment analysis . . . . .	10-4
10.3.1	Bases for comparison . . . . .	10-5
10.3.2	Variables . . . . .	10-6
10.3.3	Worst case, base case and best case scenarios . . . . .	10-17
10.3.4	Sensitivity analysis . . . . .	10-19
10.3.5	Risk analysis . . . . .	10-21
10.4	Remarks . . . . .	10-26
10.5	Conclusions . . . . .	10-26
	References . . . . .	10-28
<b>11</b>	<b>General conclusions and recommendations</b>	<b>11-1</b>

---

11.1	General conclusions . . . . .	11-1
11.1.1	Wave power resources and spatial planning of a farm of WECs . . . . .	11-2
11.1.2	Production of a farm of WECs . . . . .	11-3
11.1.3	Cost of a farm of WECs . . . . .	11-5
11.2	Recommendations for further research . . . . .	11-6
<b>A</b>	<b>List of publications</b>	<b>A-1</b>
A.1	International journal publications . . . . .	A-1
A.2	National journal publications . . . . .	A-2
A.3	International conference publications . . . . .	A-2
A.4	National conference publications . . . . .	A-3
<b>B</b>	<b>Wave power</b>	<b>B-1</b>
B.1	Regular waves . . . . .	B-1
B.2	Irregular waves . . . . .	B-3
	References . . . . .	B-4
<b>C</b>	<b>Wave measurements at Westhinder and ZW-Akkaert from 1977 on</b>	<b>C-1</b>
	References . . . . .	C-3
<b>D</b>	<b>Mild-slope equations of Radder and Dingemans</b>	<b>D-1</b>
	References . . . . .	D-5
<b>E</b>	<b>Practical use of MILDwave</b>	<b>E-1</b>
E.1	Preprocessor . . . . .	E-1
E.1.1	Grid . . . . .	E-3
E.1.2	Wave . . . . .	E-4
E.1.3	Time step . . . . .	E-7
E.1.4	Bathymetry . . . . .	E-8
E.1.5	Obstacles . . . . .	E-10
E.1.6	Output . . . . .	E-11
E.2	Calculation of $\eta$ , $\varphi$ , $K_d$ , $p_x$ and $p_y$ across the domain . . . . .	E-12
E.3	Postprocessing of the results in Matlab . . . . .	E-12
<b>F</b>	<b>Results for an FO<sup>3</sup> WEC in regular waves with T = 4 s and 8 s</b>	<b>F-1</b>
F.1	Results for a regular wave with unit wave amplitude and wave period of 4 s . . . . .	F-1
F.1.1	Results of WAMIT . . . . .	F-1
F.1.2	Wave diffraction . . . . .	F-4
F.1.3	Wave radiation . . . . .	F-12
F.1.4	Diffraction and radiation . . . . .	F-18
F.2	Results for a regular wave with unit wave amplitude and wave period of 8 s . . . . .	F-26
F.2.1	Results of WAMIT . . . . .	F-26
F.2.2	Wave diffraction . . . . .	F-29

F.2.3	Wave radiation . . . . .	F-37
F.2.4	Diffraction and radiation . . . . .	F-44
<b>G</b>	<b>Cable network cost</b>	<b>G-1</b>
G.1	Lay-out A: a single line of WD-WECs . . . . .	G-1
G.2	Lay-out B: a staggered grid lay-out . . . . .	G-2
G.3	Lay-out C: all WD-WECs installed behind each other . . . . .	G-3
<b>H</b>	<b>Cost of Energy</b>	<b>H-1</b>

# List of symbols

$a$	=	wave amplitude [m]
$A'$	=	cross section of electricity cable [mm <sup>2</sup> /phase]
$b$	=	distance from the outside domain boundary in terms of number of grid cells [-]
$B_s$	=	length of the sponge layer in terms of number of grid cells [-]
$c$	=	score [-]
$c'$	=	cost of energy of lay-out A [€/kWh]
$C$	=	phase velocity [m/s]
	=	$\frac{L}{T}$
$C'$	=	cost of cable network of lay-out A [€]
$C'_{tot}$	=	total cost of lay-out A [€]
$C_e$	=	energy velocity [m/s]
	=	$\frac{\bar{C}\bar{C}_g}{C}$
$C_g$	=	group velocity [m/s]
	=	$\frac{C}{2} \left( 1 + \frac{2kh}{\sinh(2kh)} \right)$
$C'_m$	=	cost of m <sup>th</sup> WEC [€]
$d$	=	draft [m]
$D$	=	width of the deck of the FO <sup>3</sup> WEC [m]
$D_h$	=	width of the hypothetical WEC [m]
$D_R$	=	distance between the tips of the wave reflectors [m]
$D_s$	=	damping coefficient [-]
$D(f, \theta)$	=	directional spreading function [1/°]
$e$	=	error [-]
$E_{kin}$	=	kinetic energy density [J/m <sup>2</sup> ]
$E_{pot}$	=	potential energy density [J/m <sup>2</sup> ]
$f$	=	wave frequency [Hz]
$f(z, h)$	=	vertical structure of the wave motion [-]
$g$	=	gravitational acceleration (=9.81) [m/s <sup>2</sup> ]
$h$	=	water depth [m]
$H$	=	wave height [m]
$H_s$	=	significant wave height [m]
$H_{s,25y}$	=	significant wave height that occurs once in 25 years [m]
$H_{m0}$	=	estimate of significant wave height from spectral analysis [m]
	=	$4\sqrt{m_0}$
$H_{1/3}$	=	mean of the highest 1/3 <sup>th</sup> of the wave heights derived from time domain analysis [m]

$\mathcal{H}$	=	Hamiltonian [J/m <sup>2</sup> ]
$i$	=	discount rate [%]
$I$	=	current [A/phase]
$I_{100\%}$	=	current rating [A/phase]
$I_c$	=	charging current [A/km/phase]
$k$	=	wave number [rad/m]
	=	$\frac{2\pi}{L}$
$K'$	=	diffraction coefficient [-]
$K_d$	=	disturbance coefficient [-]
$K_r$	=	reflection coefficient [-]
$K_t$	=	transmission coefficient [-]
$l$	=	longitudinal spacing between WECs [m]
$l'$	=	length of the electricity cable [m]
$L$	=	wave length [m]
$m_n$	=	n <sup>th</sup> moment of spectral density [m <sup>2</sup> /s <sup>n</sup> ]
	=	$\int_0^\infty f^n S(f) df$
$M$	=	number of wave directions [-]
$n_{life}$	=	lifetime [year]
$n^*$	=	payback period without interest [year]
$N$	=	number of frequencies [-]
$N_x$	=	number of grid cells along the width of the computational domain [-]
$N_y$	=	number of grid cells along the length of the computational domain [-]
$p$	=	wave power per meter of wave crest [W/m]
$\mathbf{p}$	=	wave power vector [W/m]
$p_{BM}$	=	average available wave power of two successive months (bimonthly) [W/m]
$\wp$	=	pressure [N/m <sup>2</sup> ]
$P$	=	wave power [W]
$P_s$	=	power absorbed by a single WEC [W]
$q$	=	overtopping rate [m <sup>3</sup> /s/m]
$q_N$	=	non-dimensional overtopping rate [-]
$r$	=	Pearson's correlation coefficient [-]
$r_c$	=	radius of circle [m]
$R$	=	electrical resistance [ $\Omega$ /km]
$R^2$	=	determination coefficient [-]
$R_c$	=	crest freeboard [m]
$s$	=	directional spreading parameter [-]
$S$	=	absorption coefficient [-]
$Sc$	=	final score for each location [-]
$S(b)$	=	absorption function [-]
$S(f)$	=	frequency spectrum [m <sup>2</sup> s]
$S(f, \theta)$	=	directional wave spectrum [m <sup>2</sup> s/ $^\circ$ ]



---

$t$	=	time [s]
$T$	=	wave period [s]
$T_m$	=	mean wave period [s]
$T_e$	=	energy period [s]
	=	$T_{m-1,0}$
$T_{m0,1}$	=	mean wave period derived from spectral analysis [s]
	=	$\frac{m_0}{m_1}$
$T_{m0,2}$	=	mean wave period derived from spectral analysis [s]
	=	$\sqrt{\frac{m_0}{m_2}}$
$T_{m-1,0}$	=	mean wave period derived from spectral analysis [s]
	=	$\frac{m_{-1}}{m_0}$
$T_z$	=	mean zero-upcrossing period [s]
$U_A$	=	wind stress factor [m/s]
$\mathbf{v}$	=	fluid particle velocity vector [m/s]
$V$	=	voltage difference [volt]
$w$	=	lateral spacing between WECs [m]
$W$	=	weight [m]
$W_B$	=	width of the main body of the WD-WEC [m]
$W_m$	=	model width [m]
$x_c$	=	x-co-ordinate of centre of circle [m]
$y_c$	=	y-co-ordinate of centre of circle [m]
$z$	=	side of a square [m]
$\alpha$	=	scaling parameter [-]
$\gamma$	=	peak enhancement factor [-]
$\delta$	=	loss load factor [-]
$\epsilon$	=	angle between normal on wave generation arc and x-axis or y-axis [°]
$\eta$	=	surface elevation [m]
$\eta^*$	=	additional surface elevation [m]
$\eta_R$	=	efficiency of the wave reflectors of the WD-WEC [-]
$\theta$	=	angle of wave ray from x-axis [°]
$\theta_0$	=	mean wave angle from x-axis [°]
$\theta_{wave}$	=	direction of the high frequency waves [°]
$\theta_{wind}$	=	wind direction [°]
$\Theta$	=	phase angle [rad]
$\lambda_{dB}$	=	ratio between the time averaged amount of energy flux, integrated from the draft of the main body up to the surface, and the time averaged amount of incident energy flux, integrated from the seabed up to the surface [-]
$\lambda_{dR}$	=	ratio between the time averaged amount of energy flux, integrated from the draft of the wave reflector up to the surface, and the time averaged amount of incident energy flux, integrated from the seabed up to the surface [-]
$\varphi$	=	velocity potential at SWL [m <sup>2</sup> /s]
$\phi$	=	phase shift [rad]

$\Phi$	=	velocity potential [m <sup>2</sup> /s]
$\rho$	=	density of sea water (=1 026) [kg/m <sup>3</sup> ]
$\rho'$	=	electrical resistivity [ $\Omega$ cm]
$\sigma$	=	spectral width parameter [-]
$\sigma_\theta$	=	directional width parameter [-]
$\omega$	=	angular frequency [rad/s]
	=	$2\pi f$
$\Delta b$	=	angle interval [rad]
$\Delta t$	=	time step [s]
$\Delta x$	=	grid size in x-direction [m]
$\Delta y$	=	grid size in y-direction [m]
$\Delta\theta_{ww}$	=	difference between wind and wave direction [°]
	=	$\Delta\theta_{ww} = 180 -  180 -  \theta_{wind} - \theta_{wave}  $
$\nabla$	=	horizontal gradient operator
€	=	euro
M€	=	10 <sup>6</sup> euro
M\$	=	10 <sup>6</sup> dollar

## Subscripts

<i>a</i>	=	absorbed
<i>ab</i>	=	absolute
<i>B</i>	=	main body
<i>cs</i>	=	cross section
<i>d</i>	=	disturbed
<i>dyn</i>	=	dynamic
<i>i</i>	=	incident
<i>me</i>	=	measured
<i>max</i>	=	maximum
<i>min</i>	=	minimum
<i>n</i>	=	new
<i>o</i>	=	old
<i>p</i>	=	peak
<i>r</i>	=	reflected
<i>R</i>	=	reflector
<i>s</i>	=	absorbed by a single WEC
<i>stat</i>	=	static
<i>t</i>	=	transmitted
<i>tar</i>	=	target
<i>tot</i>	=	total
<i>x</i>	=	in x-direction
<i>y</i>	=	in y-direction

# List of acronyms

AC	Alternating Current
BCS	Belgian Continental Shelf
BGS	British Geological Survey
BSH	Bundesamt für Seeschifffahrt und Hydrographie
BV	Bimonthly Variability index
DC	Direct Current
DCS	Dutch Continental Shelf
$CF_0$	Initial Cash Flow
$CF_t$	Cash Flow in year t
COE	Cost Of Energy
DHI	Dansk Hydraulisk Institut
E	East
ECMWF	European Centre for Medium-Range Weather Forecasts
ELD	Eierlands Gat
EMEC	European Marine Energy Centre
ENE	East Northeast
ESE	East Southeast
ESPO	European Sea Ports Organisation
FO	Frequency of Occurrence
GCS	German Continental Shelf
GENI	Global Energy Network Institute
GIS	Geographic Information System
GW	Gigawatt
GWh	Gigawatt hour
HVDC	High Voltage Direct Current
IRR	Internal Rate of Return
JONSWAP	Joint North Sea Wave Project
kW	Kilowatt
kWh	Kilowatt hour
LCW	Long-Crested Waves
LR	Learning Rate
M	Maintenance
MAE	Mean Absolute Error
MCDA	Multi-Criteria Decision Analysis
MUMM	Management Unit of the North Sea Mathematical

	Models
MW	Megawatt
MWh	Megawatt hour
N	North
NE	Northeast
NNE	North Northeast
NNW	North Northwest
NPV	Net Present Value
NTNU	Norwegian University of Science and Technology
NW	Northwest
O&M	Operation and Maintenance
OP	Occurrence Probability
OWC	Oscillating Water Column
POT	Peak Over Threshold
PR	Progression Rate
PTO	Power Take-Off
PV	Present Value
R&D	Research and Development
RMSE	Root Mean Square Error
S	South
SCW	Short-Crested Waves
SE	Southeast
SEEWEC	Sustainable Economically Efficient Wave Energy Converter
SI	Scatter Index
SSE	South Southeast
SSW	South Southwest
SW	Southwest
SWAN	Simulating Waves Nearshore
SWL	Still Water Level
TW	Terawatt
TWh	Terawatt hour
UKMO	United Kingdom Meteorological Office
V	Volt
W	West/Watt
WAM	Wave Model
WD-WEC	Wave Dragon Wave Energy Converter
WEC	Wave Energy Converter
WGS 84	World Geodetic System 1984
WNW	West Northwest
WS	Wave Situation
WSW	West Southwest

# Glossary

This glossary is partly based on the Marine Energy Glossary (Carbon Trust, July 2005) and the Ocean Energy Glossary (Wave Energy Centre, December 2007).

Absorbed power	Power extracted from the waves, not taking any losses into account (a.o. conversion losses, transmission losses)
Bandwidth	The range of wave frequencies over which a WEC responds.
Bathymetry	The measurement of the water depth (and the shape of the seabed).
Capacity factor	The energy produced during a given period as a proportion of the energy that would have been produced had the device been running continually and at maximum output.
Capture ratio	The ratio between the absorbed power and the wave power incident on a wave-front width equal to the width of the WEC.
Cost of energy	Minimum price at which energy must be sold for the energy project to break even. The cost of energy (COE) is the ratio between the present value of the costs of a farm and the present value of its energy production.
Deep water	Water sufficiently deep that surface waves are little affected by the ocean bottom. Generally, water deeper than $\frac{L}{2}$ is considered as deep water.
Diffraction of waves	When water waves encounter an obstacle (e.g. WEC) during propagation, they pivot about the edge of the obstacle and move into the shadow zone of the obstacle. Wave diffraction is the apparent bending of waves around small obstacles and the spreading out of waves past small openings.
Eigenfrequency	The frequency of vibration of an oscillating system when vibrating freely.
Farm	A farm of WECs is an arrangement or geometric configuration of WECs.
Fixed premium	A fixed premium (in addition to the electricity price)

	guarantees return to producers of electricity from renewable energy, as the regional or national electricity utilities are obligated to buy renewable electricity at above-market rates set by the government.
Heave	Vertical motion of a floating body.
Installed capacity	Total power that the device can produce when operating correctly and at full power output (measured in kilowatts (kW) or megawatts (MW)).
Long-crested waves	Waves that are propagating in the same wave direction. Long-crested waves have straight and parallel crests.
Loss load factor	The ratio between the annual average power loss and the peak power loss.
Oscillating water column	An oscillating water column (OWC) is formed by a chamber which is filled with air above the water line. The waves cause the water level in the air chamber to oscillate. Consequently the air in the chamber is compressed and expanded generating an air flow through an air turbine.
Overtopping of waves	The amount of sea water transported over the crest of a structure.
Pitch	Rotary oscillatory motion of a WEC around a horizontal axis perpendicular to the direction of wave propagation.
Point absorber	An oscillating wave energy converter that is small compared to the incident wave length.
Power matrix	A power matrix describes the time averaged mean power production of a WEC in each sea state.
Power take-off (PTO)	Mean mechanisms to convert wave into mechanical and/or electrical energy.
Produced power	Electrical power generated by the WEC not taking transmission losses and losses due to planned and unplanned maintenance into account, unless expressly stated.
Radiation of waves	Radiation is the energy spread away from the WEC by its interaction with the water. It is the wave pattern that would be generated by the WEC when oscillating in calm water.
Rated power	Or installed capacity.
Reflection of waves	When waves are reflected by a WEC, the reflected waves cause increased agitation of the water in front of the WEC.
Refraction of waves	When waves are propagating at an angle to the depth contours one part of the wave front is at smaller depth than another and therefore moves with a smaller

---

	speed. This causes the waves to change direction and the crests to bend into the pattern of the depth contours of the sea bottom.
Roll	Rotary oscillatory motion of a WEC around a horizontal axis in the direction of wave propagation.
Scatter diagram	A scatter diagram shows the average frequency of occurrence (in %) of different sea states for one or more year(s) (or one specific month) and a given wind direction.
Sea state	A sea state is defined by a combination of significant wave height $H_s$ and mean wave period $T_m$ .
Shallow water	When the water depth is smaller than $\frac{L}{25}$ the term shallow water is used. Surface waves are noticeably affected by the bottom in shallow water.
Shoaling of waves	The change in wave height due to varying depth is called shoaling.
Short-crested waves	Many component waves propagating in various directions.
Surge	Linear oscillatory horizontal motion of a WEC in the direction of wave propagation.
Survivability	The ability of a WEC to remain intact and operational in storm conditions.
Sway	Linear oscillatory horizontal motion of a WEC perpendicular to the direction of wave propagation.
Transformer	Device that transfers energy from one electrical circuit to another via a magnetic coupling.
Transmission of waves	Waves propagating through and under the WEC.
Tuning	Adjusting the size and shape of a WEC and/or controlling a WEC to change its oscillation frequency.
Wave rose	The segments of a wave rose show the relative frequencies of mean wave directions in each wave sector.





# Nederlandse samenvatting

## –Summary in Dutch–

De Europese Unie wil tegen 2020 de emissie van broeikasgassen verminderen met 20 % (ten opzichte van 1990) om de opwarming van de aarde tegen te gaan. Bovendien wil de EU het aandeel van hernieuwbare energie in de energieconsumptie verhogen tot 20 % en zijn primaire energieverbruik met 20 % verminderen tegen 2020. De EU is immers sterk afhankelijk van de invoer van fossiele brandstoffen, maar de voorraad van deze fossiele brandstoffen is niet oneindig. Bovendien kan de continuïteit van de aanvoer van deze fossiele brandstoffen uit politiek minder stabiele regio's, bedreigd worden. Golfenergie, net als alle andere hernieuwbare energiebronnen, zal een bijdrage moeten leveren om deze 20/20/20 doelstellingen te bereiken.

Golfenergie biedt heel wat perspectieven. Oceanen zijn immers een oneindige bron van hernieuwbare energie. In het verleden werden vele concepten voor golfenergieconversie ontwikkeld en beproefd. Een golfenergieconvector (GEC) zet de kinetische en/of potentiële energie van golven om in elektrische energie. Golfenergieconvertoren (GECs) kunnen volgens hun conversieprincipe ingedeeld worden in twee categorieën: (i) GECs waar een lichaam of waterkolom oscilleert onder de invloed van zeegolven en (ii) GECs die overtoppende golven opvangen in een bassin dat hoger ligt dan het zeeniveau en op die manier een hydraulisch verval creëren. Tot op heden is echter geen enkel concept voor golfenergieconversie klaar voor commercialisatie op grote schaal door verschillende obstakels van zowel technische als niet-technische aard.

Aangezien het nominaal vermogen van een GEC beperkt is, zijn in de praktijk altijd meerdere GECs nodig. Zij worden in een geometrische configuratie of in een 'GEC-park' geplaatst. Het invallend golfvermogen wordt gedeeltelijk geabsorbeerd en gedeeltelijk verstrooid door de GECs in een park. Bijgevolg wordt het geproduceerde vermogen van elke GEC in het park beïnvloed door de aanwezigheid van de naburige GECs. De huidige kennis omtrent de herverdeling van energie in en achter een GEC-park is echter beperkt. Zowel de productie als de kost van een GEC-park zijn lay-out afhankelijk. In een eerste fase ligt de nadruk typisch op de optimalisatie van 1 convector, maar wil men echter een commercieel bruikbare technologie ontwikkelen, dan is het onderzoeken van een GEC-park onontbeerlijk. De optimalisatie van de lay-out van een park golfenergieconvertoren in de Noordzee was het hoofddoel van dit doctoraatsonderzoek. Er werd gezocht naar een optimale balans tussen de energieproductie en de kost van een

GEC-park.

De bepaling van **het beschikbaar golfvermogen en interessante locaties voor golfenergieconversie** in de Noordzee ligt aan de basis van de berekening van de productie en de kost van een GEC-park. Het beschikbaar golfvermogen en mogelijke locaties voor golfenergieconversie werden in een eerste deel van dit werk onderzocht. Het is de eerste keer dat het golfenergiepotentieel in de Noordzee in detail werd bestudeerd. Beschikbare data van golfmeetboeien en numerieke golfvoortplantingsmodellen werden verzameld en geanalyseerd. Het resulterende beschikbaar golfvermogen in de Noordzee werd in kaart gebracht. Het beschikbaar golfvermogen in de zuidelijke Noordzee is eerder klein door de afscherming van de Atlantische Oceaan door Groot-Brittannië. Een zeer energetisch golfklimaat maakt daarentegen installatie en onderhoud van GECs niet gemakkelijk. Bovendien zijn tot op heden meerdere problemen in verband met structurele sterkte en verankering in een energetisch golfklimaat nog niet opgelost (E: survival mode). Naast het beschikbaar golfvermogen dienen ook de eigenschappen van de GEC zelf (zoals minimale en/of maximale waterdiepte, golfperiode, golfhoogte) en de kost voor installatie, gridconnectie, werking en onderhoud beschouwd te worden bij het selecteren van een geschikte locatie voor de installatie van een GEC-park. Bovendien beïnvloeden ook andere activiteiten in de Noordzee de keuze van een geschikte locatie. Mogelijke locaties voor de installatie van een park Pelamis GECs in de zuidelijke Noordzee werden aan de hand van een ruimtelijke multi-criteria beslissingsanalyse bepaald (E: GIS-based multi-criteria decision analysis). De Pelamis GEC is een drijvende convertor van de eerste categorie. Deze GEC bestaat uit een aaneenschakeling van vier drijvende cilindersegmenten die scharnierend met elkaar verbonden zijn. De segmenten volgen de golfbeweging en de hoekverdraaiing in de scharnieren drijft een hydraulisch systeem aan. Uit deze analyse blijkt dat toegankelijke locaties nabij de kust met een relatief energetisch golfklimaat het meest geschikt zijn voor de installatie van een park Pelamis GECs.

In het tweede deel van dit doctoraatsonderzoek werd de **elektriciteitsproductie van een GEC-park** begroot in een numeriek golfvoortplantingsmodel MILDwave, ontwikkeld aan Universiteit Gent. De implementatie van een GEC-park in een numeriek golfvoortplantingsmodel is relatief nieuw. In sommige studies werd een park geïmplementeerd als één poreus samenhangend obstakel. In die modellering wordt de herverdeling van energie rond de GECs in het park niet in rekening gebracht. In andere studies werden de reflectie op de GEC en de transmissie onder en door de GEC samengebracht in één parameter: de porositeit van de structuur. Hierdoor kan de productie van de GEC in het park niet aangepast worden aan het omringend golfklimaat. In dit doctoraatsonderzoek werd een sponslaagtechniek ontwikkeld waarin GECs als individuele obstakels met onafhankelijke reflectie-, transmissie-, en bijgevolg absorptiekenmerken worden gemodelleerd. Deze techniek is enkel toepasbaar op overtoppingssystemen (GECs van de tweede categorie). De sponslaagtechniek werd echter uitgebreid

om eveneens GECs van de eerste categorie te implementeren in MILDwave. In deze uitbreiding werden golven, gegenereerd door de beweging van de GECs, in MILDwave gesimuleerd.

Een park werd in MILDwave gemodelleerd door de energieabsorptie van elke GEC af te stemmen op het omringend golfklimaat. De absorptie van een park hypothetische overtoppingssystemen bepaald met resultaten uit MILDwave, werd vergeleken met de absorptie van het park vereenvoudigd tot één poreus obstakel. Met de nieuwe sponslaagtechniek kan de absorptie van een GEC-park veel nauwkeuriger ingeschat worden. De herverdeling van energie in het park wordt immers in rekening gebracht. Uit de vergelijking blijkt dat de vereenvoudigde aanpak tot een aanzienlijke onder- of overschatting van het geabsorbeerd vermogen kan leiden (tot 40 %).

De validatie van de sponslaagtechniek is complex. Het golfpatroon rond één en drie absorberende obstakels werd experimenteel en numeriek bepaald. De overeenkomst tussen de experimentele en numerieke golfhoogtes is echter niet bevredigend (afwijking van de gemiddelde golfhoogte voor en achter de drie absorberende obstakels tot 20 %). Reflectie op de zijwanden van de fysische golfgoot (4 m) verstoortte het golfpatroon rond de GEC (0.72 m breed) in grote mate. Daarom werd de sponslaagtechniek geverifieerd door het berekenen van de vermogensabsorptie van een GEC in een tweedimensioneel domein in MILDwave. De resultaten tonen aan dat de sponslaagtechniek een betrouwbare methode is om zogeeffekten van overtoppingssystemen te modelleren.

Deze innovatieve sponslaagtechniek werd toegepast op een prototype GEC; de Wave Dragon GEC. De Wave Dragon GEC is een drijvend offshore overtoppingssysteem. Golven worden via lange golfreflectoren naar een centraal oplooppvlak geleid, overtoppen in een bassin en worden via turbines met een klein verval, aangesloten op een generator, terug in zee geloosd. In het zog van de Wave Dragon GEC werd een aanzienlijke golfhoogtedaling waargenomen. Voor deininggolven (met een grote voorkomingfrequentie in de Noordzee) daalt de absorptie van een tweede Wave Dragon GEC, die 3 km achter de eerste Wave Dragon GEC geplaatst is, met 30 %.

Een tweede prototype, de FO<sup>3</sup> GEC (eerste categorie), werd in MILDwave geïmplementeerd met de uitgebreide sponslaagtechniek. De FO<sup>3</sup> GEC is eveneens een drijvende offshore converter. Deze GEC bestaat een platform met verschillende (12 of 21) verticaal oscillerende vlotter. De verticale beweging van deze vlotter wordt omgezet naar een rotatiebeweging door een hydraulisch systeem. De zogzone achter een FO<sup>3</sup> GEC is over het algemeen eerder beperkt.

De vermogensabsorptie van verscheidene lay-outs van Wave Dragon GECs en FO<sup>3</sup> GECs met verschillende laterale en longitudinale tussenafstanden werd in MILDwave bepaald voor verschillende golfcondities. De bestaande golfgeneratietechniek in MILDwave werd, samen met de absorberende sponslagen aan de randen van het simulatiedomein in MILDwave, uitgebreid en gevalideerd om golven met verschillende golfinvalsrichting en directionele spreiding te genereren. Uit de resultaten blijkt dat de herverdeling van golfvermogen in het park, en bijgevolg de productie van het park, niet alleen bepaald wordt door de lay-out van

het park, maar ook door de afmetingen en de absorptie van de GEC, het type GEC en door het invallend golfklimaat (golfperiode, golfvalsrichting en directionele spreiding).

Naast de elektriciteitsproductie wordt ook de kost van een GEC-park beïnvloed door de lay-out van het park. De **kost van een GEC-park** werd in het derde en laatste deel van dit doctoraatsonderzoek geanalyseerd. De lay-out van het GEC-park bepaalt hoofdzakelijk de kost van de elektriciteitskabels tussen de GECs in het park. De installatie-, de werkings- en de onderhoudskosten zijn daarentegen minder lay-out afhankelijk. Door het minimaliseren van de kost van het kabelnetwerk zelf en de gekapitaliseerde kost van de verwachte energieverliezen in de kabels werd een optimaal kabelnetwerk ontworpen voor verschillende lay-outs van een park van Wave Dragon GECs. Uit de berekeningen volgt dat de investeringskost van het onderzees kabelnetwerk slechts een fractie is van de totale investeringskost van het GEC-park. Bijgevolg heeft het minimaliseren van deze kost enkel een kleine impact op de energiekost. Bij het ontwerpen van de lay-out van een GEC-park moet dus hoofdzakelijk een maximale productie nagestreefd worden. Eén enkele rij van Wave Dragon GECs resulteert in de grootste productie en de laagste energiekost. Daarentegen is een lange zone nodig om deze lay-out te realiseren.

De installatie van een kortere rij Wave Dragon GECs voor een windmolenpark lijkt interessant. Enerzijds kunnen deze Wave Dragon GECs verbonden worden met het transformator platform van het windmolenpark, waardoor de totale gridconnectiekost gereduceerd wordt. Anderzijds daalt de golfhoogte achter de Wave Dragon GECs. Hierdoor wordt onderhoud van het windmolenpark gemakkelijker en goedkoper.

Ten slotte werd een investeringsanalyse voor de installatie van een rij Pelamis GECs in de zuidelijke Noordzee uitgevoerd. Meestal zijn gegevens i.v.m. de kosten van GECs confidentieel. De beperkt publiek beschikbare gegevens werden in de investeringsanalyse van dit doctoraatsonderzoek gebruikt. Uit de analyse blijkt dat de installatie van een Pelamis GEC-park in de zuidelijke Noordzee momenteel niet haalbaar is zonder subsidies. De huidige subsidies voor offshore windenergie zijn over het algemeen niet voldoende voor golfenergie.

# English summary

In 2007 the EU has set a new target for the reduction of greenhouse gas emissions: 20 % reduction by 2020 compared to 1990. Furthermore, the EU aims to increase the share of renewables in its energy mix and to decrease its primary energy use with 20 % by 2020. These targets are needed to decrease the EU's dependency on fossil fuel imports and to cope with the increasing energy demand, the shrinking reserves of fossil fuels and the climate change. All renewable energy sources will have to contribute to achieve these 20/20/20 targets, including wave energy.

Wave energy holds a lot of possibilities, as oceans contain an infinite amount of energy. In the past many concepts for wave power conversion were invented and tested. A Wave Energy Converter (WEC) converts the kinetic and/or potential energy of waves into electricity. Two main principles of wave power conversion can be distinguished: (i) Wave Energy Converters (WECs) with a body or water column that is oscillating by the incident waves and (ii) WECs that capture the overtopping waves in a basin above sea level and consequently create a hydraulic head. Thus far, none of the concepts for wave power conversion has reached a maturity that makes it economic exploitable due to several technological and non-technological barriers.

As the rated power of a single WEC is rather small, several WECs need to be arranged in a geometric configuration or in a 'farm'. WECs in a farm are partly absorbing and partly redistributing the incident wave power. The power produced by each individual WEC in the farm is affected by the presence of its neighbouring WECs. The current knowledge about the redistribution of energy inside and behind a farm of WECs is rather limited. Both the power production and cost of a farm are dependent on the lay-out of the farm. So far, most studies concentrate on the optimization of a single WEC, rather than optimizing a complete farm. To develop a commercial technology, the impact of arranging WECs in a farm has to be investigated as well. The optimization of the lay-out of a farm of WECs in the North Sea is the focus of this PhD research. An optimal balance between power production and cost of a farm of WECs is aimed at.

To assess the power production and cost of a farm of WECs, the **wave power resources and possible locations for the deployment of a farm of WECs** in the North Sea are quantified in a first part. It is the first time that the wave power potential in the North Sea is studied in detail. Available wave data from buoy measurements and numerical wave propagation models are gathered and analysed, resulting in the production of a map of the available wave power in the North

Sea. The resource in the southern part of the North Sea is rather limited as large swells from the Atlantic Ocean are blocked by the UK. Since WECs still contend with problems regarding structural strength and mooring in a severe wave climate, the mild wave climate of the southern North Sea is more likely to assure the survivability of WECs. To select a good location to install a farm of WECs not only the wave power resource but also the technological requirements of the considered WEC, the cost of installation, grid connection, operation and maintenance (O&M) and other activities in the North Sea should be considered. A geo-spatial multi-criteria decision analysis is performed in this PhD dissertation to select possible locations for the installation of a farm of Pelamis WECs in the southern North Sea. The Pelamis WEC is a semi-submerged WEC of the first category. The WEC consists of four cylindrical sections linked together by hinged joints. The rotation of these hinged joints drive a hydraulic system. The results show that accessible areas with a relatively high energetic wave climate and situated rather close to shore are preferred.

In a second part of this PhD research the **production of a farm of WECs** is studied in a time-dependent mild-slope wave propagation model MILDwave, developed at Ghent University. The implementation of a farm of WECs in a numerical wave propagation model is relatively new. In some studies a farm is simplified to one transmitting obstacle. Consequently, the redistribution of wave energy around the WECs in the farm is not taken into account. In other studies the reflection from the WEC and transmission under and through the WEC are coupled through the degree of porosity assigned to the structure, which makes the adaptation of the production of the WEC to its surrounding wave climate in the farm impossible. In this PhD dissertation a sponge layer technique is developed to model WECs as individual obstacles with uncoupled reflection and transmission (and consequently absorption) characteristics. This technique is only applicable to WECs of the overtopping type (second category). To implement a WEC of the first category in MILDwave the sponge layer technique is extended. In this extension waves generated by the WEC motions are taken into account.

In MILDwave a farm is modelled by adapting the power absorption of each WEC to its surrounding wave climate. The power absorption of a farm of hypothetical WECs of the overtopping type obtained from MILDwave results, is compared to the power absorption when the farm is simplified to a single transmitting obstacle. A more accurate estimation of the power absorption is obtained with the method developed in MILDwave, as the redistribution of wave power inside the farm is taken into account. The comparison reveals that the simplified method may result in a high overestimation or underestimation of the absorbed power (up to 40 %).

The validation of the sponge layer technique is not straightforward. The agreement between the wave pattern around a single and three absorbing obstacles, assessed both numerically and experimentally is not satisfactory (differences in average wave height in front of and behind the three absorbing obstacles up till 20 %). Reflection on the side walls of the physical wave flume with limited width

(4 m) caused large disturbances of the wave pattern around the WEC (with a width of 0.72 m). Consequently the sponge layer technique is validated by calculating the power absorbed by a WEC in a two dimensional domain in MILDwave. The results demonstrate that the sponge layer technique is a reliable tool to study wake effects behind WECs of the overtopping type.

This innovative sponge layer technique is applied to a prototype; the Wave Dragon WEC. The Wave Dragon WEC is a floating offshore converter of the overtopping type (second category), which captures the water volume of overtopped waves in a basin above mean sea level and produces power when the water drains back to the sea through hydro turbines. In general, a large wake is observed behind the Wave Dragon WEC. For swell waves (with a high frequency of occurrence in the North Sea), the absorption of a second Wave Dragon WEC installed 3 km behind a first WEC is decreased with 30 %.

A second prototype, an FO<sup>3</sup> WEC (first category), is implemented in MILDwave by using the extended sponge layer technique. The FO<sup>3</sup> WEC is a floating offshore converter which consists of several (12 or 21) heaving buoys placed in a floating platform. The vertical motion of the heaving buoys is converted to a rotational motion by means of a hydraulic system. In general, the wake effect behind an FO<sup>3</sup> WEC is limited.

The power absorption of several lay-outs of Wave Dragon WECs and FO<sup>3</sup> WECs with varying lateral and longitudinal spacing is assessed in MILDwave for different wave situations. The existing wave generation technique, together with absorbing domain boundaries, is extended and validated in MILDwave to generate not only head-on waves but waves with varying mean wave directions and directional spreading. The results show that the redistribution of wave power in a farm, and consequently the production of a farm, is not only depending on the lay-out of the WECs, but also on the dimensions and absorption of the WEC, the type of WEC and the incident wave climate (wave period, wave direction and directional spreading).

Not only the power production but also the cost of a farm is lay-out dependent. The **cost of a farm** is discussed in a third part of this PhD work. Mainly the cost of the electrical cables between the WECs in a farm is affected by the farm lay-out. The costs of installation, operation and maintenance are to a lesser degree dependent on the farm lay-out. An optimal cable network is designed for different farm lay-outs of Wave Dragon WECs by minimizing the cost of the cable network itself and the capitalized cost of expected constrained energy from cable losses. The results indicate that the investment cost of the submarine cable network is only a fraction of the total investment cost of the farm. Consequently, minimizing the cost of the cable network has only a small effect on the cost of energy. Hence, when designing the lay-out of a farm of Wave Dragon WECs, mainly maximum power production should be aimed at. A single line of Wave Dragon WECs results in the highest power production and lowest cost of energy. On the other hand this lay-out requires a wide sea area.

The installation of a shorter line of Wave Dragon WECs in front of a farm of

wind turbines may be beneficial. In that case the Wave Dragon WECs may be connected to the transformer platform of the wind farm, which reduces the grid connection cost. Furthermore, the Wave Dragon WECs reduce the wave height in their lee, which makes maintenance of the farm of wind turbines easier and cheaper.

Finally an investment analysis of the deployment of a single line of Pelamis WECs in the southern North Sea is presented. So far, cost estimates of WECs are mostly kept confidential by the WEC developers. The limited publicly available data are used in the analysis in this PhD dissertation. Today, installation of a farm of Pelamis WECs in the southern part of the North Sea is not feasible without subsidies. The current subsidies for offshore wind energy are in general not sufficient for wave energy.







# 1

## Introduction

### 1.1 Current status of wave energy

#### 1.1.1 Concepts

The development of renewable energy technologies is pressing. Today, Europe is heavily dependent on imports of fossil fuels (54 % of the EU's primary energy demand [1]), often from areas which are potentially politically unstable. Without a change in direction, this reliance will be as high as 70 % by 2030 [2]. Furthermore, the supply of fossil fuels is limited. At the same time global energy demand is increasing rapidly and finally climate change requires urgent action. We are forced to use energy more economically and to develop renewable energy technologies to meet the European 20/20/20 targets by 2020: reduction of greenhouse gas emissions by 20 % compared to 1990, 20 % energy production from renewable energy sources and 20 % reduction of primary energy use by 2020. Note that actual trends still show a continuous growth of 1% CO<sub>2</sub> emissions per year (European Energy Outlook until 2030, European Commission, 2006).

It is widely accepted that wave energy has the potential to significantly contribute to the renewable energy supply. The overall wave power resources (2 terawatt) are of the same order of magnitude as the world's electricity consumption [3].

Many concepts for wave power conversion, with an installed capacity of a few kilowatts up to more than one megawatt, have been invented during the last three decades. This resulted in more than 1 000 patents. A Wave Energy Converter

(WEC) converts the kinetic and/or potential energy of waves into electricity. WECs can be divided into two major categories:

- (i) **Devices based on the oscillation principle**, where a body or water column is oscillating.
- (ii) **Devices based on the overtopping principle**, where waves are overtopping in a basin at a higher level than the surrounding sea.

The first category comprises different types of floating or submerged bodies and oscillating water columns (OWCs), while the second category consists of fixed or slack moored overtopping devices. An overview of the 16 leading technologies in 2009 is given in Table 1.1 [4].

*Table 1.1: Overview of 16 leading wave energy converters in 2009 [4]*

Device	Company	Country	Category	Prototype rating
Oyster	Aquamarine Power	UK	(i)	500 kW
WaveRoller	AW Energy Oy	Finland	(i)	15 kW
Wave Swing	AWS Ocean Energy	UK	(i)	2 MW
AquaBuOY	Finavera	Canada	(i)	250 kW
FO <sup>3</sup>	Fred Olsen	Norway	(i)	2.5 MW <sup>1</sup>
OE Buoy	Ocean Energy	Ireland	(i) OWC	2 MW
Oceanlinx	Oceanlinx	Australia	(i) OWC	2 MW
PowerBuoy	OPT	USA	(i)	150 kW
Pelamis	Pelamis Wave Power <sup>2</sup>	UK	(i)	750 kW
CETO	Seapower Pacific	Australia	(i)	180 kW
Wave Dragon	Wave Dragon	Denmark	(ii)	7 MW
Wavebob	Wavebob	Ireland	(i)	2 MW
Limpet	Wavegen	UK	(i) OWC	500 kW
SSG	WAVEnergy	Norway	(ii)	150 kW
WavePlane	WavePlane	Denmark	(ii)	500 kW
Wavestar	Wavestar	Denmark	(i)	5 MW

<sup>1</sup> Results from the EU project SEEWEC (Sustainable Economically Efficient Wave Energy Converter - contract n<sup>o</sup>: SES6-CT2005-019969) showed that the initial prototype rating was too optimistic. A prototype rating of 0.4 MW - 0.6 MW was found in [5]. This led directly to the requirement for an adapted concept.

<sup>2</sup> Ocean Power Delivery changed its name in Pelamis Wave Power in 2007.

The wind industry quite quickly converged on one model of air turbine; the horizontal axis type. Unlike the wind industry, there is not a single WEC (or even generic type of WEC) that is proving more successful than another. Not a

single WEC has reached an economically exploitable level due to several technological and non-technological barriers. Technological barriers are device specific and comprise design and development, construction, installation, operation and survivability issues. The most important non-technological barriers [6] can be divided into 6 groups :

- **Regulatory issues:** currently, it is still very difficult, expensive and time consuming to obtain licences for the deployment of a farm of WECs. It is hard to convince permitting authorities without field data. Furthermore, several administrative departments need to be consulted to obtain the necessary licences. The more departments involved, the more time is required to obtain those licences. Processing all permits through one department may accelerate the licensing process.

Several European countries (Portugal, Denmark, Ireland, UK, Spain and France) provide sea trial facilities to overcome this barrier, as the necessary licences are already obtained for these facilities. An overview of the existing sea trial facilities can be found in [4].

- **Financial incentives:** research on wave power conversion started in the 70s in response to the oil crisis. As in the 80s government support was removed, the progress was limited. The lack of early financial incentives have slowed down the development of wave power conversion. It is clear that substantial subsidies are needed as in the development phase costs are very high compared to the economic benefits. Indirect (solutions to discourage the use of fossil fuels) and direct (a.o. a guaranteed electricity purchase price) measures can be used. Furthermore, financial incentives should be clear and should be guaranteed during an adequate period to attract investors.
- **Infrastructure and logistics:** in general, only weak transmission lines are available in coastal regions. It is not always clear who will finance the grid expansion, the offshore and onshore cabling and who will determine the grid access for WECs. Moreover, specialised equipment is needed to install WECs, which is also used in the oil, gas and offshore wind industry. The limited availability of this equipment increases installation costs. Some European sea trial facilities also provide a grid connection, wave measurement buoys, a monitoring station and other facilities to limit the costs in the development phase.
- **Conflicts of use:** a thorough study of the existing use of the maritime space is needed before planning the deployment of WECs. Early communication with the groups that might be affected, can prevent possible opposition.

- **Environmental issues:** these issues comprise a.o. impact on fauna and flora by installation of WECs, underwater noise, electromagnetic fields around the WECs and the electrical cables, wake effects and leakage of working fluids. Currently, knowledge about potential environmental impact of a WEC is rather scarce. During early sea trials, these issues should be investigated. For example, since 2005 the artificial reef effect of WEC foundations at the Swedish west coast has been studied [7]. Not only the impact of the WEC on the marine environment but also the fouling impact on WECs have been investigated. So far, it has been observed that the dynamic behaviour of the WEC has not been affected by fouling.
- **Public perception:** involvement of the public is very important to prevent misunderstandings and opposition.

### 1.1.2 A farm of wave energy converters

To extract a substantial amount of wave power, wave energy converters are arranged in several arrays or ‘farm’. WECs in a farm are interacting and the overall power absorption<sup>1</sup> is affected. The first category of WECs, oscillating systems, absorb power by simultaneously generating a wave [8]. The incident wave is partly scattered and partly absorbed due to the destructive interference with the generated (also called radiated) wave. Furthermore the performance of neighbouring devices in a farm is influenced by the scattered incident wave and radiated wave from the oscillating device and vice versa. On the other hand, WECs based on the overtopping principle (second category) absorb power by capturing the water volume of overtopped waves in a basin and creating a hydraulic head. Consequently a wake is formed behind the WEC which affects the performance of WECs installed in the wake. The redistribution of wave power in the farm is different for both categories, as each category has its own specific way of absorbing power.

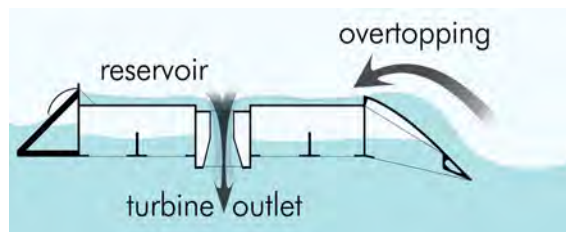
The current knowledge about the redistribution of wave power inside and behind a farm of WECs is rather limited. So far, most studies concentrate on the optimization of a single WEC, rather than optimizing a complete farm. To develop a commercial technology, the impact of arranging WECs in a farm should be investigated as well. In this PhD dissertation the lay-out of a farm is optimized to decrease the cost per produced kWh. In the farm study three leading technologies are used as an example: the Wave Dragon WEC, the FO<sup>3</sup> WEC and the Pelamis WEC.

---

<sup>1</sup>The power absorbed by the farm (or power absorption of the farm) is defined as the power extracted from the waves not taking any losses (a.o. conversion losses) into account. The power produced by the farm (or power production of the farm) is equal to the power absorption multiplied with a reduction factor to account for conversion losses. Transmission losses and losses due to planned and unplanned maintenance are generally not incorporated in the term ‘produced power’, unless explicitly stated.

- **The Wave Dragon WEC**

The Wave Dragon WEC is a floating converter of the overtopping type (Figure 1.1(b)). Two wave reflectors focus the incident wave power towards a ramp. The focussed waves run up the ramp and overtop in a water reservoir above mean sea level (Figure 1.1(a)). The created hydraulic head is converted into electricity when the stored water drains back to the sea through hydro turbines.



(a) Overtopping principle



(b) 1:4.5 prototype at Nissum Bredning (Denmark)

*Figure 1.1: Wave Dragon WEC (copyright Wave Dragon)*

Each Wave Dragon unit will have a rated power between 1.5 and 11 MW [9] depending on the local wave climate. Since 2003 an 1:4.5 prototype has been tested at Nissum Bredning, an inland sea, connected to the North Sea. The 1:4.5 prototype corresponds to a full scale prototype with a rated power of 4 MW in a 24 kW/m wave climate. The operation of the prototype is described in detail in [10]. The current focus for the Wave Dragon technology is to build and deploy a multi MW unit [9]. A European Commission project has started in May 2006 to develop this multi MW Wave Dragon WEC. Furthermore, a Wave Dragon pre-commercial demonstrator with a rated power of 4 to 7 MW is planned in Wales [11].

Recently, the project development company TecDragon focuses on the planning of a 50 MW farm of Wave Dragon WECs in Portuguese waters [12].

- **The FO<sup>3</sup> WEC**

The FO<sup>3</sup> WEC is a floating offshore converter (36 m x 36 m) which consists of several (12 or 21) heaving point absorbers placed in a floating platform [13]. This WEC is part of the first category.



(a) 1:3 laboratory rig in Norway



(b) Artist impression of a farm of FO<sup>3</sup> WECs

*Figure 1.2: FO<sup>3</sup> WEC*

The vertical motion of the point absorbers is converted to a rotational motion by means of a hydraulic system. The rated power of a full-scale FO<sup>3</sup> WEC is estimated to 0.4-0.6 MW [5]. A complete laboratory platform at scale 1:3 (Figure 1.2(a)) was constructed at the Brevik ship yard in Norway and



was launched in the sea in February 2005 off the southern coast of Norway. While the original FO<sup>3</sup> point absorber concept was platform-based, the results of the EU project SEEWEC (Sustainable Economically Efficient Wave Energy Converter - contract n<sup>o</sup>: SES6-CT2005-019969) showed that it was worthwhile to pursue an alternative based on a single point absorber moored directly to the seabed rather than attached to a platform [5]. In this PhD dissertation the original concept is used as an example. An artist impression of a farm of FO<sup>3</sup> WECs is given in Figure 1.2(b).

- **The Pelamis WEC**

The Pelamis WEC [14] is a semi-submerged WEC of the first category. The WEC consists of four cylindrical sections linked together by hinged joints. The wave-induced motion of these joints is resisted by hydraulic rams that pump high-pressure oil through hydraulic motors via smoothing accumulators. These hydraulic motors drive electrical generators to produce electricity. A full-scale prototype (120 m long, 3.5 m in diameter) with a rated power of 750 kW was tested at the European Marine Energy Centre (EMEC) [14] and is shown in Figure 1.3(a).



(a) Full scale prototype (EMEC - Scotland)



(b) Aguçadoura wave farm (Portugal)

Figure 1.3: Pelamis WEC (copyright Pelamis Wave Power)

Results from the prototype testing can be found in [15]. A farm of four Pelamis WECs and the testing of a next generation Pelamis WEC are planned at EMEC.

Currently the first farms of WECs are getting installed. In 2008, 3 Pelamis WECs, each with a rated power of 750 kW, were installed in Aguçadoura (Portugal). This first wave farm is shown in Figure 1.3(b). At present, a breakwater with 16 oscillating water columns (16 Wells turbines (Wavegen), each with a rated power of 18.5 kW) is getting installed in Mutriku (North of Spain). Moreover, three 250 kW Wells turbines (study of Massachusetts Institute of Technology and Instituto Superior Tecnico) are incorporated in a breakwater at the mouth of the Douro river (Portugal). Furthermore, most companies are planning to install a small farm in the near future.

## 1.2 Objectives

This PhD research focuses on the study of a farm of wave energy converters.

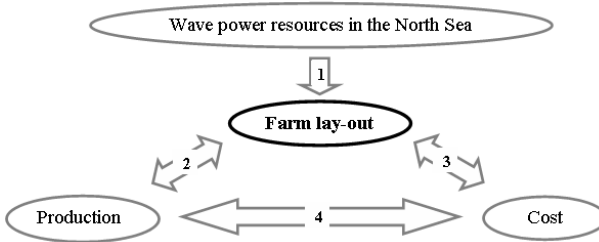


Figure 1.4: Objectives of this PhD research

The specific objectives of this PhD dissertation are shown in Figure 1.4:

### 1. Analysis of the wave power resources in the North Sea

Before calculating the possible production of a farm of WECs the available wave power at the location of the farm should be known. The resources in the North Sea, with main focus on the resources on the Belgian Continental Shelf, are calculated by using wave data from buoy measurements and numerical wave propagation models. Besides, suitable sites for the deployment of a farm of Pelamis WECs are identified by using a GIS-based (Geographical Information System) multi-criteria decision analysis. This first objective is dealt with in a first part of this PhD dissertation.

## *2. Impact of farm lay-out on power production*

A second objective of this PhD work is to study the impact of the farm lay-out on its power production. A numerical approach is developed to calculate the power production of several lay-outs, with varying lateral and longitudinal distances between the WECs. A distinction is made between both categories of WECs. The physical process of power absorption is implemented for both categories in a mild-slope wave propagation model. The wave power redistribution in and behind a farm is modelled for different wave conditions (long-crested and short-crested waves) and farm lay-outs. From the simulated wave power redistribution in and around a farm of WECs the power absorption of various farm lay-outs is derived. The numerical approach is validated through experimental tests and numerical calculations and is applied to real prototype WECs. The study of the power production of a farm is presented in a second part of this PhD dissertation.

## *3. Impact of farm lay-out on cost*

Not only the power production but also the cost of a farm of WECs is lay-out dependent. Mainly the cost of the electrical cables between the WECs in a farm is affected by the farm lay-out. The costs of installation, operation and maintenance are to a lesser degree dependent on the farm lay-out. An optimal cable network is designed for different farm lay-outs of Wave Dragon WECs by minimizing the cost of the cable network itself and the capitalized cost of expected constrained energy from cable losses. Furthermore, an investment analysis for the installation of a farm of Pelamis WECs in the southern North Sea is performed. The impact of the location and the number of WECs on the farm investment are investigated. Finally, the risk of the farm investment is determined. The cost of a farm of WECs is described in detail in a third part of this PhD dissertation.

## *4. Optimum between power production and cost*

Once the impact of the farm lay-out on the power production (second objective) and cost (third objective) of a farm were quantified, an optimal balance between the power production and cost of a farm is obtained. This is the main objective of this PhD research. Final results are formulated in the third part of this PhD dissertation.

### 1.3 Outline

This PhD dissertation is divided into three parts.

A first part deals with the wave power resources and the spatial planning of a farm of WECs. In chapter 2 the wave power resources in the North Sea are presented. A geo-spatial multi-criteria decision analysis is performed in chapter 3. The sensitivity of several factors on the site selection is discussed at the end of this chapter.

A second part elaborates on the production of a farm of WECs. In chapter 4 the applicability of wave propagation models to study wake effects behind a farm of WECs is discussed. In chapter 5, a mild-slope time domain model to study the power production of a farm of WECs is presented: the technique of wave generation, together with absorbing domain boundaries, is extended and validated. Furthermore the physical processes, wave reflection and diffraction, are validated with analytical solutions. In chapter 6, the implementation of a farm of WECs in the mild-slope model and its validation are described. Chapter 7 and 8 present each an application of the implementation of a farm of WECs: the study of wake effects behind a farm of Wave Dragon WECs and FO<sup>3</sup> WECs, respectively.

A third part of this PhD dissertation deals with the economic study of a farm of WECs. In chapter 9 the production and the cost of three lay-outs of a farm of Wave Dragon WECs are assessed. An investment analysis of five possibilities to install a farm of Pelamis WECs in the southern part of the North Sea is described in chapter 10. In chapter 11 general conclusions and recommendations for further research on a farm of WECs are formulated.

Eight appendices are included at the end of the dissertation. Appendix A provides an overview of the publications of the author of this dissertation. A derivation of the calculation of the wave power in regular and irregular waves can be found in appendix B. The wave power resources on two locations on the Belgian Continental Shelf are discussed in more detail in appendix C. The basic equations of the mild-slope wave propagation model, used in this PhD dissertation, are presented in appendix D. Appendix E gives an overview of the practical use of the mild-slope equation model. Results of the implementation of the FO<sup>3</sup> WEC in the mild-slope model for regular waves with a wave period of 4 s and 8 s are given in appendix F. Details of the cable network cost of the considered lay-outs of Wave Dragon WECs are presented in appendix G. A derivation of the Cost of Energy (COE) can be found in appendix H.

## References

- [1] S. Krohn, P.-E. Morthorst, and S. Awerbuch. *The Economics of Wind Energy. A report by the European Wind Energy Association*. Technical report, EWEA (European Wind Energy Association), 2009.
- [2] P. Capros and L. Mantzos. *The European energy outlook to 2010 and 2030*. Int. J. Global Energy Issues, 14:137–154, 2000.
- [3] J. Cruz. *Chapter 1: Introduction*. In J. Cruz, editor, *Ocean Wave Energy, Current Status and Perspectives*, pages 1–6. Springer, 2008.
- [4] Hydraulics and Maritime Research Centre. *State of the art analysis (Waveplam)*. Technical report, Hydraulics and Maritime Research Centre, 2009.
- [5] J. De Rouck and V. Meirshaert. *SEEWEC (Sustainable Economically Efficient Wave Energy Converter - contract n°: SES6-CT2005-019969) Publishable Final Activity Report*. Technical report, Ghent University, 2009.
- [6] F. Neumann. *Non-technological Barriers to Wave Energy Implementation (Waveplam)*. Technical report, Wave Energy Centre, 2009.
- [7] O. Langhamer, D. Wilhelmsson, and J. Engström. *Development of invertebrate assemblages and fish on offshore wave power*. In *Proceedings of the 28<sup>th</sup> International Conference on Ocean, Offshore and Arctic Engineering (OMAE)*, Honolulu, Hawaii, 2009.
- [8] J. Falnes and K. Budal. *Wave-power conversion by point absorbers*. Norwegian Maritime Research, 6:2–11, 1978.
- [9] Wave Dragon ApS. <http://www.wavedragon.net>, Accessed July 2009.
- [10] J. Tedd, J. P. Kofoed, E. Friis-Madsen, and L. Christensen. *7.5.5 Wave Dragon*. In J. Cruz, editor, *Ocean Wave Energy, Current Status and Perspectives*, pages 371–382. Springer, 2008.
- [11] Wave Dragon Wales Ltd. <http://www.wavedragon.co.uk>, Accessed July 2009.
- [12] TecDragon. <http://www.tecdragon.pt>, Accessed July 2009.
- [13] SEEWEC (Sustainable Economically Efficient Wave Energy Converter). <http://www.seewec.org>, Accessed July 2009.
- [14] Pelamis Wave Power. <http://www.pelamiswave.com>, Accessed July 2009.

- [15] J. Cruz, R. Henderson, and R. Yemm. *7.5.4 Pelamis*. In J. Cruz, editor, *Ocean Wave Energy, Current status and Perspectives*, pages 361–371. Springer, 2008.

## **Part I**

# **Resources and planning**





# 2

## Wave power resources in the North Sea

### 2.1 Introduction

Oceans are an enormous source of energy. The overall resources (approximately 2 TW) are of the same order of magnitude as the world's electricity consumption [1]. The highest wave power is encountered off the western coasts in the 40° to 60° latitude range in the northern and southern hemisphere (Figure 2.1). Along the West European coast the resources increase from approximately 30 to 40 kW per meter of wave crest in front of the Norwegian and Portuguese coast up till more than 70 kW/m along the Irish coast.

Till now the wave power resources are mainly studied in detail for regions with a high wave energy density [2, 3]. However, even for regions with a rather limited amount of available wave power (e.g. 10-20 kW/m) the global technical resource is estimated to range from 23 till 114 GW [4].

The amount of available wave power is often considered the most important characteristic to determine interesting locations for wave power conversion, whereas the survivability of the converter is actually as important and should be taken into account. In general a severe wave climate has a larger potential, but a lot of difficulties related to the structural strength and the mooring of the device are encountered. Therefore a milder wave climate is more convenient to produce electrical power, certainly in this stage of development.

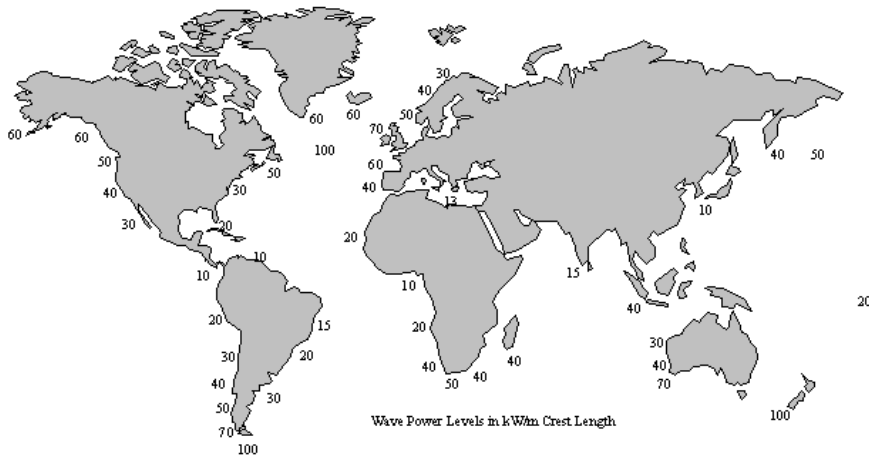


Figure 2.1: World-wide estimate of wave power in kilowatt per meter of wave crest (Tom Thorpe, 1999)

An overview of the wave power resources in sheltered and calmer European waters is given in Table 2.1.

Table 2.1: Wave power in kilowatt per meter of wave crest in calmer European waters

Name of location	Wave power [kW/m]
Baltic Sea [4, 5]	5
Swedish west coast [6]	2 to 6
Mediterranean sea [7]	1 to 6
North Sea [7]	11 to 60

The wave climate in the North Sea is less aggressive compared to open seas and therefore more likely to assure the survivability of WECs. So far, only a general overview of the wave power resources in the North Sea has been presented [2, 3, 7]. A detailed study of the available wave power in the North Sea is given in this chapter. The first section describes the wave climate and corresponding wave power resource in a rather sheltered area in the North Sea i.e., the Belgian Continental Shelf (southern part of the North Sea). In a second part the resources in the North Sea are described on 34 locations by using available wave data from buoy measurements or numerical wave propagation models. A more detailed spatial distribution of the wave power potential in the southern part of the North Sea is estimated with hindcasts of the WAM-PRO model [8] during 2003 and 2004. In

the next chapter possible locations for wave power conversion in the North Sea are selected. Not only the wave power resources, as studied in this chapter, are used as a criterion but also technological requirements of the considered WEC, the cost of installation, grid connection and Operation and Maintenance (O&M) and other activities in the North Sea are considered.

## **2.2 Wave energy on the Belgian Continental Shelf**

The Belgian Continental Shelf (BCS) is located in the southern part of the North Sea and borders on the Dutch, French, and UK Continental Shelf (Figure 2.2). The shelf is 3 600 km<sup>2</sup> in area and occupies only 0.5 % of the North Sea [9].

On average 12 TWh of wave power reaches yearly the BCS. This resource corresponds with the yearly demand for electricity in Belgium. One needs to bear in mind that not all available wave power can be converted to electricity. Several losses and restrictions reduce the resource; (i) available space on the BCS, (ii) loss of energy when waves are entering shallow waters, (iii) temporal and directional trend of the resource, (iv) operational and survival specifications of the device and (v) conversion losses, dependent on device and transmission specifications. These mentioned losses may be considered as the most important ones. The losses and restrictions related to the resource ((i), (ii), (iii) and (iv)) are briefly discussed in this section.

### **2.2.1 Activities on the Belgian Continental Shelf**

Considering the current activities (e.g. ports, navigation routes, military practice areas, extraction zones, pipelines, cables, offshore wind farm, . . .) on the Belgian Continental Shelf (Figure 2.2) it is clear that the space left for wave power conversion is rather scarce. To select an optimal location to install a farm of WECs in the remaining space, several criteria need to be considered: distances to shore, grid connection and harbour, available water depth, geology, dimensions of the selected locations, . . . Spatial and temporal conflicts need to be avoided through a multi-criteria analysis (chapter 3).

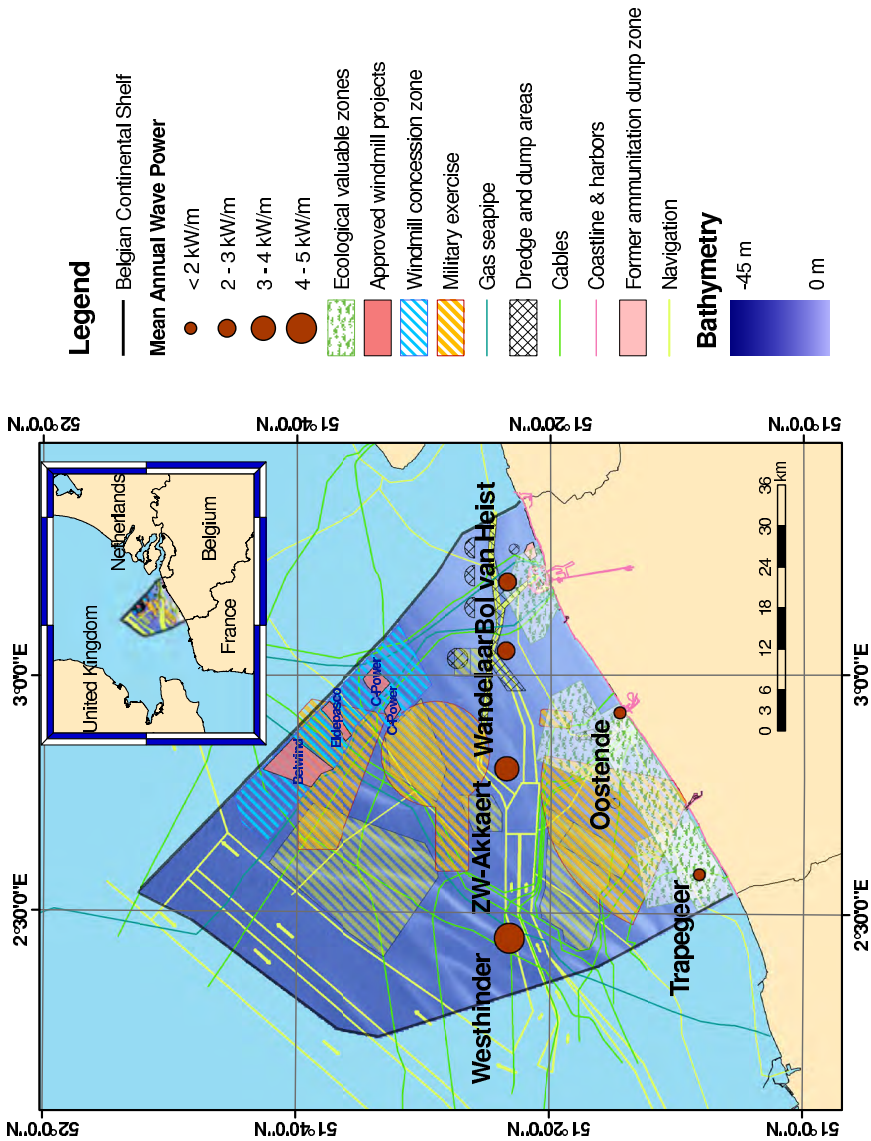


Figure 2.2: Average annual available wave power in kilowatt per meter of wave crest on six buoy locations and current activities, without fishery, on the Belgian Continental Shelf (Sources: MUMM, Kustatlas, Marebasse [10]).

## 2.2.2 Wave power near shore

### 2.2.2.1 Buoy locations

Waves are modified when they travel to the coast and enter in shallower waters. The direction of waves changes when approaching the coast at an angle to the depth contours. Furthermore, waves lose energy through bottom friction and depth-induced wave breaking. On the Belgian Continental shelf wave measurement buoys are installed in varying water depths on various distances from the coast. The wave power resource on the BCS is estimated with wave data from these wave measurement buoys. The properties of six wave measurement buoys (Westhinder, ZW-Akkaert, Trapegeer, Oostende, Wandelaar, and Bol van Heist), used in this study, are given in Table 2.2. The location of these buoys is shown on Figure 2.2. The co-ordinates are given in the geographical reference system (longitude and latitude) based on the World Geodetic System 1984 (WGS 84).

Table 2.2: Properties of wave measurement buoys on the Belgian Continental Shelf used in this study

Name of location	Type of buoy	Longitude (WGS 84)	Latitude (WGS 84)	Wave data interval
Westhinder	Wavec	2 ° 26 ' 52 "E	51 ° 23 ' 12 "N	1990-2004
ZW-Akkaert	Waverider	2 ° 48 ' 12 "E	51 ° 24 ' 29 "N	1984-2004
Trapegeer	Waverider	2 ° 34 ' 59 "E	51 ° 08 ' 15 "N	1994-2004
Oostende(1)	Waverider	2 ° 55 ' 14 "E	51 ° 14 ' 34 "N	1997-2002
Oostende(2)	Directional Waverider	2 ° 55 ' 14 "E	51 ° 14 ' 34 "N	2002-2005
Wandelaar	Waverider	3 ° 03 ' 02 "E	51 ° 23 ' 32 "N	1995-2004
Bol van Heist	Wavec	3 ° 11 ' 43 "E	51 ° 23 ' 25 "N	1985-2004

Three different types of buoys are installed: a Waverider, a Wavec and a Directional Waverider [11]. A **Waverider** (Datawell) is a buoy floating on the water surface that is measuring the vertical acceleration with an accelerometer on a gravity stabilised platform. Double integration of the acceleration yields the vertical displacement. The Waverider has a diameter of 0.9 m. The **Wavec** (Datawell) concerns a disc-shaped buoy with a diameter of 2.5 m, and was the first wave direction measuring buoy on the market. This buoy measures, besides the vertical movement, the pitch and roll motions. Those parameters are derived from the acceleration of the buoy, measured in three directions. To define the direction relative to the geographical north, a three-dimensional compass is built in the buoy. A **Directional Waverider** (Datawell) is a spherical buoy with a diameter

of 0.9 m. This buoy measures the heave, sway and surge motions rather than the heave, pitch and roll. This means that a more compact spherical hull could be used as a measurement platform. Measurements with a Wavec and Directional Waverider have an interval of 30 minutes, while a Waverider has only an interval of 15 minutes.

Scatter diagrams, for the total measurement period of each buoy, are provided by the Flemish Ministry of Transport and Public Works (Agency for Maritime and Coastal Services - Coastal Division) for different wind directions. The scatter diagrams show the average frequency of occurrence (in %) of different sea states for one or more year(s) (or one specific month) and a given wind direction. A sea state is defined by a combination of significant wave height  $H_s$  and mean wave period  $T_m$ .

The measurements of a Wavec and Directional Waverider are analyzed in the spectral domain. In the scatter diagrams derived from these measurements  $H_s = H_{m0}$  and  $T_m = T_{m0,2}$ . The significant wave height  $H_{m0}$  is derived using equation (2.1).

$$H_{m0} = 4\sqrt{m_0} \quad (2.1)$$

with  $m_0$  the zeroth moment of the wave spectrum.  $T_{m0,2}$  is obtained using the second moment of spectral density (equation (2.2)) and as a result may be sensitive to high-frequency low energy variations in the wave spectrum.

$$T_{m0,2} = \sqrt{\frac{m_0}{m_2}} \quad (2.2)$$

Therefore sometimes  $T_p$  or  $T_e$ , instead of  $T_{m0,2}$ , is given in a scatter diagram. The energy period  $T_e$  is defined as equation (2.3), and is equal to the spectral wave period  $T_{m-1,0}$ .

$$T_e = T_{m-1,0} = \frac{m_{-1}}{m_0} \quad (2.3)$$

where  $m_{-1}$  is the first negative spectral moment.  $T_e$  depends mainly on the lower frequency band of the spectrum (that contains most of the energy) and is therefore a more stable parameter than the traditional mean period  $T_{m0,2}$  (equation (2.2)). The peak period  $T_p$  is the inverse of the peak frequency that corresponds to the highest spectral density.

The analysis of the measurements with a Waverider are performed in the time domain. In the derived scatter diagrams  $H_s = H_{1/3}$  and  $T_m = T_z$ .  $H_{1/3}$  is the average wave height of the one-third largest waves in the record. The mean zero

up-crossing period  $T_z$  is the ratio of the wave sampling period and the number of zero up crosses in that period.

As an example the average annual scatter diagram for all wind directions at Westhinder is shown in Table 2.3.  $H_s$ -values are divided in intervals of 0.5 m and  $T_m$ -values in intervals of 1 s (except for the first interval).

Table 2.3: Average annual scatter diagram for all wind directions at Westhinder, based on measurements from 1-7-1990 until 30-6-2004 (Source: Flemish Ministry of Transport and Public Works (Agency for Maritime and Coastal Services - Coastal Division))

$T_m$ [s]	0- 2.5	2.5- 3.5	3.5- 4.5	4.5- 5.5	5.5- 6.5	6.5- 7.5	7.5- 8.5	>8.5	Sum
$H_s$ [m]									
<b>0.0-0.5</b>	0.05	4.52	12.33	4.07	0.55	0.06	0.01	-	21.58
<b>0.5-1.0</b>	0.01	6.12	20.51	8.38	1.91	0.3	0.02	-	37.25
<b>1.0-1.5</b>	-	0.29	11.63	8.98	1.83	0.27	0.02	-	22.02
<b>1.5-2.0</b>	-	-	1.89	6.46	2.02	0.27	0.01	-	10.65
<b>2.0-2.5</b>	-	-	0.04	2.67	2.00	0.42	0.01	-	5.14
<b>2.5-3.0</b>	-	-	-	0.57	1.17	0.5	0.02	-	2.26
<b>3.0-3.5</b>	-	-	-	0.04	0.46	0.26	0.04	-	0.8
<b>3.5-4.0</b>	-	-	-	-	0.09	0.07	0.05	-	0.21
<b>4.0-4.5</b>	-	-	-	-	0.02	0.03	0.02	-	0.07
<b>4.5-5.0</b>	-	-	-	-	-	0.01	-	-	0.01
<b>&gt;5.0</b>	-	-	-	-	-	-	-	-	-
Sum	0.06	10.93	45.4	31.17	10.05	2.19	0.2	-	100

Based on the given scatter diagrams, the average annual available wave power and its directional and temporal variation can be calculated.

### 2.2.2.2 Average annual available wave power

For each sea state in the scatter diagram<sup>1</sup> the energy transported per unit time through an envisaged vertical strip of unit width, parallel to the wave front, or the energy-flux or wave power  $p$  (W/m) is calculated with equation (B.16). The derivation of equation (B.16) can be found in appendix B.

$$p = \rho g \int_0^{\infty} C_g(f, h) S(f) df \quad (\text{B.16})$$

<sup>1</sup>A sea state is defined by a combination of the central value of a  $H_s$ -interval and the central value of a  $T_m$ -interval in the scatter diagram. The central value of the  $H_s$ -interval or  $T_m$ -interval is considered representative for the interval.

where  $\rho$  represents the sea water density ( $= 1\,026\text{ kg/m}^3$ ),  $g$  the acceleration due to gravity ( $= 9.81\text{ m/s}^2$ ),  $C_g(f, h)$  the group velocity,  $S(f)$  the spectral density,  $h$  the water depth and  $f$  the wave frequency. The spectral distribution of the energy at the Belgian Continental Shelf can be described by a parameterized JONSWAP spectrum (equation (2.4)) [12] with peak enhancement factor  $\gamma = 3.3$  and scaling parameter  $\alpha = 0.2044$ .

$$S(f) = \alpha H_s^2 f_p^4 f^{-5} \gamma^{\exp\left(-\frac{(f-f_p)^2}{2\sigma^2 f_p^2}\right)} \exp\left(\frac{-5}{4} \left(\frac{f_p}{f}\right)^4\right) \quad (2.4)$$

where  $f_p = \frac{1}{T_p}$  is the peak frequency. For a JONSWAP spectrum with  $\gamma = 3.3$ ,  $T_p = 1.29 T_m$ . The spectral width parameter  $\sigma$  equals 0.07 for  $f \leq f_p$  and 0.09 for  $f \geq f_p$ .

The group velocity  $C_g(f, h)$  is given by equation (B.15).

$$C_g(f, h) = \frac{1}{2} \left(\frac{g}{k} \tanh(kh)\right)^{\frac{1}{2}} \left(1 + \frac{2kh}{\sinh(2kh)}\right) \quad (B.15)$$

where  $k$  is the wave number. The wave power of each sea state  $p$  is multiplied with its frequency of occurrence FO given in the scatter diagram. Summation leads to the average available wave power (per meter of wave crest)  $\bar{p}$  (equation 2.5).

$$\bar{p} = \sum_{j=1}^n p_j FO_j \quad (2.5)$$

with  $n$  the number of sea states in the scatter diagram.

Table 2.4 shows the obtained average annual available wave power for the selected locations on the Belgian Continental Shelf together with the mean water depth and the shortest distance to shore.

Table 2.4: Average annual available wave power on the Belgian Continental Shelf

Name of location	Average annual available wave power [kW/m]	Mean water depth [m]	Shortest distance to shore [km]
Westhinder	4.64	29	32
ZW-Akkaert	3.64	23	20
Trapegeer	1.51	7	4
Oostende	1.66	6	1
Wandelaar	2.63	13	10
Bol van Heist	2.54	12	7



The resource increases from 1.51 kW/m near the coast till 4.64 kW/m 32 km offshore. The mean annual available wave power is also shown on Figure 2.2. Note that it would be better to use the measured spectra in equation (B.16) instead of assuming a parameterized JONSWAP spectrum. However, measured spectra were not available for this study.

Scatter diagrams in [13], based on measurements between 1977 and 1986 result in an average annual available wave power of 5.05 kW/m at ZW-Akkaert and 4.42 kW/m at Westhinder. The resource obtained with measurements between 1990 and 2004 is comparable to the resource calculated with measurements between 1977 and 1986 at Westhinder. On the other hand, at ZW-Akkaert, a larger wave power resource is observed with measurements between 1977 and 1986 compared to the resource based on measurements during 1984-2004. The measurements from 1977 on are analysed in appendix C to explain the observed difference.

The resource at the locations Westhinder (32 km offshore) and ZW-Akkaert (20 km offshore) is studied in more detail in the next sections.

## **2.2.3 Temporal and directional trend of the available wave power**

In order to estimate the possible contribution of wave energy to the overall energy supply the knowledge of the variation of the resource is of primordial interest. Therefore the annual, seasonal, monthly and directional variation of the available wave power is investigated.

### **2.2.3.1 Yearly variation**

The yearly variation of the measured available wave power is given in Figure 2.3. Also the average annual available wave power is indicated.

At Westhinder the minimum and maximum occur in 2003 (2.63 kW/m) and 1995 (6.76 kW/m). At ZW-Akkaert the minimum and the maximum wave power values are slightly lower (2.58 kW/m in 1989 and 6.23 kW/m in 1984). At both locations the maximum is more than the double of the minimum. A comparable variation was seen on the Danish Continental Shelf [14]. The large yearly variations in Figure 2.3 indicate that calculations of average available wave power have to be based on wave statistics covering several years. In Figure 2.4 the measurement period has been extended until 2008. By taking the measurements during the last four years into account, the average annual available wave power increases with only 1 %. Consequently the buoy measurements until 2004 give an accurate overview of the available wave power on the Belgian Continental Shelf. In further analysis wave data until 2004 are used.

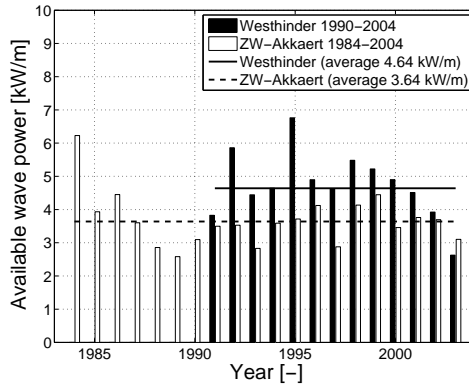


Figure 2.3: Yearly variation of the available wave power during the period 1990-2004 at Westhinder and 1984-2004 at ZW-Akkaert

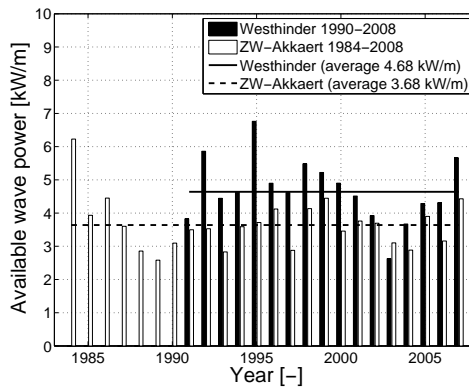


Figure 2.4: Yearly variation of the available wave power during the period 1990-2008 at Westhinder and 1984-2008 at ZW-Akkaert

### 2.2.3.2 Monthly variation

The variability of the wave power resource on daily, weekly, monthly and seasonal timescales is a very important factor when planning a farm of wave energy converters. Sites with a moderate and steady wave power resource may be more attractive than sites with a more energetic but less reliable wave power resource. Furthermore, some WECs can be tuned for maximum efficiency in predefined ranges of wave height and wave period. The efficiency of the WEC can decrease significantly in a highly variable wave climate. In Figure 2.5 the monthly variation of the average available wave power is presented.

At ZW-Akkaert, the available wave power from September till February is

higher than the average annual wave power. The average wave power during the latter period is approximately 4.76 kW/m. During the period March through August the average is approximately 2.60 kW/m. At Westhinder, the average available wave power from October till March equals approximately 6.14 kW/m, while only 3.22 kW/m is on average available from April till September.

To conclude, the resource in autumn and winter is approximately double the resource in spring and summer at both locations. Most wave power is available when the demand for energy is the largest, contrary to solar energy.

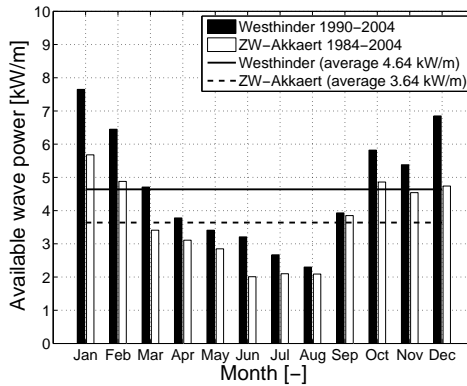


Figure 2.5: Monthly variation of the available wave power during the period 1990-2004 at Westhinder and 1984-2004 at ZW-Akkaert

The yearly variation of the measured wave power in February and August during the period 1990-2004 at Westhinder is given in Figure 2.6.

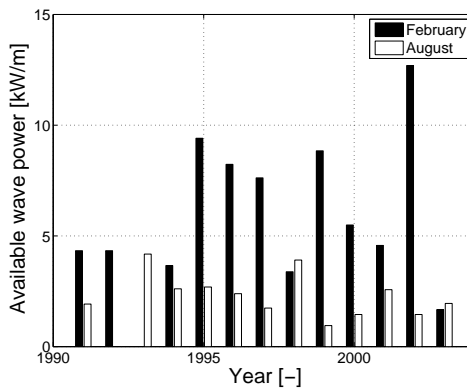


Figure 2.6: Yearly variation of the available wave power in February and August during the period 1990-2004 at Westhinder

No data were registered during August 1992 and February 1993. The ratio between the maximum wave power and minimum wave power in February and August is 12.69 and 4.40, respectively. The wave power is much more variable during winter, as large storms take place in winter. Note that measurement equipment is more likely to fail in winter. So even higher waves than the measured ones may occur.

**2.2.3.3 Directional variation**

For wave direction dependent WECs and farms of WECs also the directional variation of the average annual available wave power has to be taken into account. A direction dependent WEC and a farm of WECs will be orientated towards the wave direction which contributes the most to the yearly average available wave power. Wave direction dependent WECs are preferably installed on a location where waves are mainly propagating in one direction, as the power production will be higher. To estimate the power output of a farm the directional variation of the wave climate is needed, as for some wave directions several WECs will be located in the shadow of neighbouring WECs (chapter 6).

Wave roses are shown in Figure 2.7(a) and Figure 2.7(b). The segments of the wave roses show the relative frequencies of mean wave directions in each sector. Sixteen sectors (each 22.5°) are considered.<sup>2</sup> Each segment is divided into power ranges.

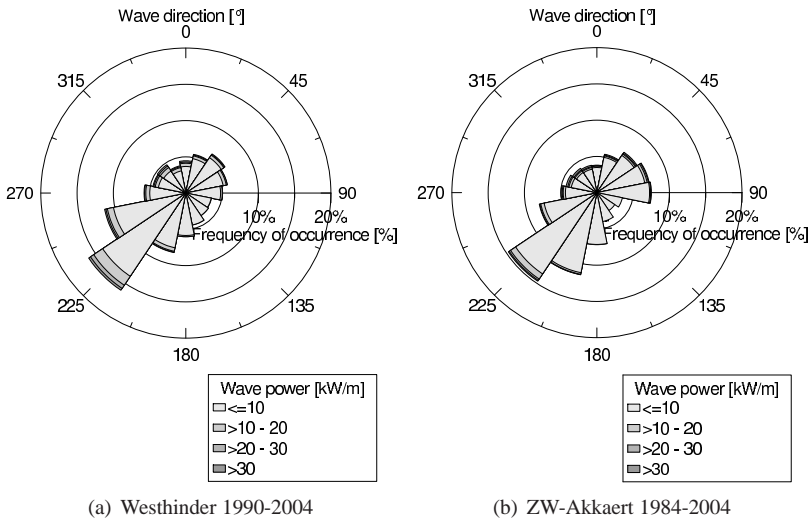


Figure 2.7: Wave rose at (a) Westhinder and (b) ZW-Akkaert

<sup>2</sup>For example, the sector north (N) contains waves with a mean wave direction in the interval [-11.25°, 11.25°].

In all directions the contribution of the low energetic ( $\leq 10$  kW/m) waves is dominant. From the sector east till south no high energetic ( $> 30$  kW/m) waves occur. For both locations the prevailing wave direction is southwest. Also the neighbouring sectors contain a large part of the total average annual available wave power as shown in Figure 2.8. The dominant direction contains approximately 20 % of the average available wave power. 40 % is coming from the dominant and neighbouring sectors.

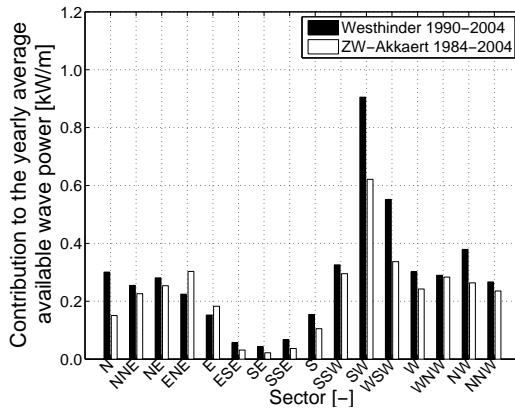


Figure 2.8: Contribution of the wave sectors to the average annual available wave power

The wave roses are based on the assumption that wind and wave direction coincide. Therefore the difference between the direction of the high frequency waves (wave period between 2 s and 5 s) and wind direction is studied with measurements between 07/07/1990 and 30/04/2008 at Westhinder (Figure 2.9).

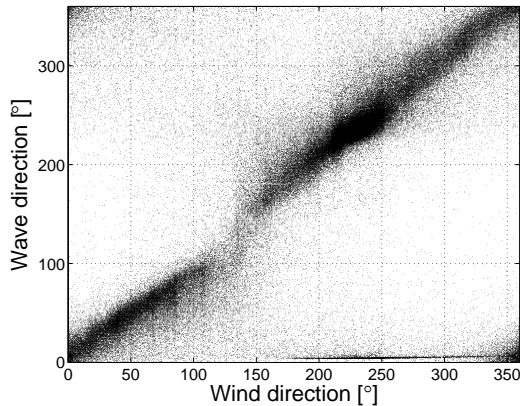


Figure 2.9: Comparison between the direction of the high frequency waves (wave period between 2 s and 5 s) and the wind direction

In general good agreement between both directions is observed. When wave and wind direction differ, swell dominated waves instead of wind dominated waves occur. The mean value of the difference between the direction of the high frequency waves  $\theta_{wave}$  and the wind direction  $\theta_{wind}$ ,  $\Delta\theta_{ww} = 180 - |180 - |\theta_{wind} - \theta_{wave}||$ , equals  $29^\circ$ . The wind direction is measured by two sensors near Westhinder. Both sensors give the same value of  $\Delta\theta_{ww}$ . The standard deviation of  $\Delta\theta_{ww}$  equals  $37^\circ$ .

In [15] the frequency of occurrence of wind and wave sectors at the location Westhinder have been compared (measurements between September 1995 and August 2005). The result is shown in Figure 2.10.

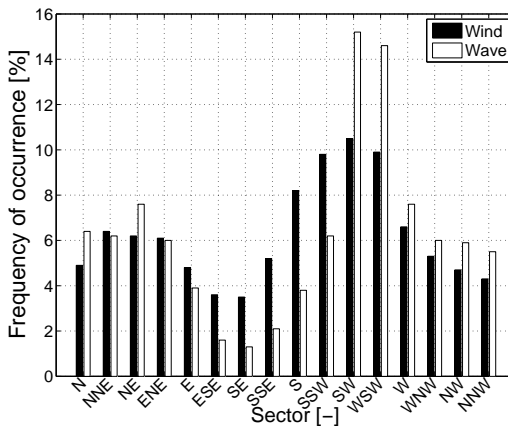


Figure 2.10: Frequency of occurrence of wind sectors and wave sectors at Westhinder

The wave sectors ESE till S occur less than half of the wind sectors ESE till S. The wave sectors SW and WSW occur more (factor 1.5) than expected from the wind sectors. For the other sectors smaller differences are observed. As wave directions have only been measured at Westhinder and not at ZW-Akkaert, wind directions have been used to compare both locations. The reader of this PhD manuscript should keep these differences between wind direction and wave direction in mind.

## 2.2.4 Wave climate specification

A wave energy converter is designed for a predefined wave climate and can produce power in a specific range of  $H_s$  and  $T_m$ . Moreover, the efficiency of the WEC depends on  $H_s$  and  $T_m$ . Some WECs do not produce power in small waves ( $H_s < 1$  m). On the other hand not all power in the higher waves will be captured depending on the design limit of the electro-mechanics. Consequently a part of the available wave power will not be converted to electricity. Furthermore,

a wave energy converter will have to withstand storm conditions. A detailed study of the operational and design wave conditions is necessary.

### 2.2.4.1 Operational wave conditions

The average annual distribution of the significant wave height  $H_s$  and the mean wave period  $T_m$  is shown in Figure 2.11 respectively Figure 2.12. The central value of each  $H_s$ - and  $T_m$ -class (Table 2.3) is indicated on the axes in Figure 2.11 and Figure 2.12.

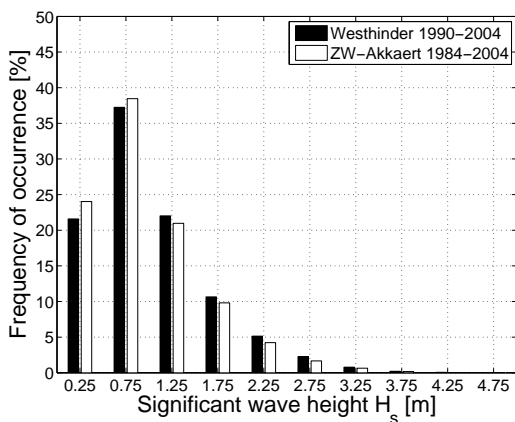


Figure 2.11: Distribution of significant wave height  $H_s$  at Westhinder and ZW-Akkaert

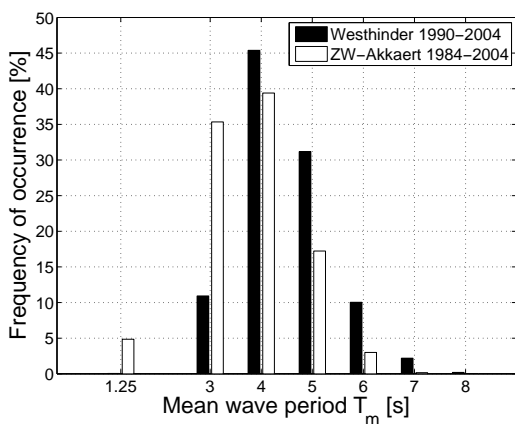


Figure 2.12: Distribution of mean wave period  $T_m$  at Westhinder and ZW-Akkaert

Significant wave heights between 0.5 m and 1 m occur most frequently at both

locations. Only WECs that produce power in these smaller waves are suitable for installation on the BCS. The contribution of waves higher than 3 m is negligible ( $< 1\%$ ). Significant wave heights higher than 5 m never occurred during the measurement period. The last two findings confirm the moderate wave climate on the BCS, as compared to the large oceans (e.g. near Scotland  $H_s$  till 11 m [7]). At Westhinder the most common wave periods vary between 3.5 s and 5.5 s whereas at ZW-Akkaert wave periods between 2.5 s and 4.5 s are dominating. At the two locations wave periods between 3.5 s and 4.5 s occur most frequently. The working range of the WEC should contain these periods in order to produce power on the BCS.

#### 2.2.4.2 Design wave conditions

So far the focus has been on operational (productive) wave conditions, but to assure the survivability of wave energy converters, also survival wave conditions should be studied.

Design wave conditions for those circumstances are obtained based on measured  $H_s$ -values by using a Peak Over Threshold (POT) analysis [16]. A Weibull distribution is used to calculate  $H_s$ -values for low probability of occurrence. The significant wave height corresponding to a return period of 100 years equals 6.5 m at ZW-Akkaert and 6.6 m at Westhinder. The corresponding peak period varies between 10 and 12 s. On the Danish Continental Shelf  $H_s$ - and  $T_p$ -values with a return period of 100 years up to 12 m and 14 s are found [14]. It is clear that the wave climate on the Belgian Continental Shelf is less severe which is, with regard to survivability, an advantage. On the other hand the mean annual available wave power is smaller compared to the Danish Continental Shelf (table 2.9).

It is also interesting to calculate the ratio between the extreme and mean significant wave height. This ratio is a rough measure for the feasibility of a wave energy project, as the extreme significant wave height determines the investment cost and a part of the operational costs while the mean significant wave height represents the resource and the income [1]. A high extreme wave height results in higher costs as the WEC needs to withstand large storms. A high mean wave height corresponds to a higher amount of available wave power and consequently higher power production and income. A low ratio (small difference between extreme and mean significant wave height) is preferred. In that case, the extreme significant wave height is relatively small compared to the mean significant wave height. So, the costs are relatively small compared to the income. The ratio between the extreme and mean significant wave height is calculated for the Belgian (Westhinder [16]), Dutch (ELD [17]) and Danish Continental Shelf (Point 3 [14]). These locations are given in Table 2.8 and indicated on Figure 2.15. The extreme significant wave height is defined as the wave height corresponding to a return period of 100 years. The mean significant wave height  $\bar{H}_s$  is the weighted average



of wave heights in the obtained scatter diagrams (equation 2.6).

$$\bar{H}_s = \sum_{j=1}^n H_{s,j} FO_j \quad (2.6)$$

with  $n$  the number of significant wave heights given in the scatter diagram.

*Table 2.5: Ratio between extreme and mean significant wave height*

Name of location	Ratio between extreme and mean significant wave height [-]
Westhinder	6.43
ELD	6.42
Point 3	6.03

From Table 2.5 it is observed that this ratio is comparable for the three locations. From this first rough measure a preferable area for the installation of a farm of WECs cannot be determined.

It is clear that not all offshore available wave power can be converted to electricity. Sections 2.2.1, 2.2.2, 2.2.3 and 2.2.4 illustrated the limited available space for wave power conversion on the BCS, the average annual available wave power near shore, the temporal and directional trend of the available wave power and the operational and design conditions on the BCS. Furthermore, conversion and transmission losses will even further reduce the possible electricity production.

In the next section characteristic sea states for design and testing of WECs are presented for the locations Westhinder and ZW-Akkaert.

### **2.2.5 Characteristic sea states**

Characteristic sea states are defined to limit the number of sea states given in a scatter diagram. The reduced number of sea states are derived as a weighted average of the total number of sea states and are therefore a good representation of the wave climate on the Belgian Continental Shelf. Characteristic sea states can be applied during the initial design of wave energy converters and preliminary power production calculations. The use of characteristic sea states results in a fast but still accurate manner for preliminary design. For detailed design more site specific measurements and data are needed. On the selected sites omni-directional characteristic sea states are defined. For each significant wave height with an average annual frequency of occurrence higher than 1 % a weighted average period  $\bar{T}_m$  is calculated (equation 2.7).

$$\bar{T}_m = \sum_{j=1}^n T_{m,j} F O_j \quad (2.7)$$

with  $n$  the number of wave periods  $T_m$  in the scatter diagram. A relation between  $\bar{T}_e$  and  $\bar{T}_m$  has been derived based on a parameterized JONSWAP frequency spectrum with  $\gamma=3.3$ ,  $\bar{T}_e=1.16 \bar{T}_m$ . All characteristic sea states with their wave power and frequency of occurrence are given in Table 2.6 and Table 2.7 for Westhinder and ZW-Akkaert, respectively.<sup>3</sup>

Table 2.6: Characteristic sea states at Westhinder

Location	Westhinder					
Mean water depth [m]	29					
Distance to shore [km]	32					
Average annual available wave power [kW/m]	4.64					
$H_s$ with a return period of 25 years [m]	5.29					
Sea State	1	2	3	4	5	6
$H_s$ [m]	0.25	0.75	1.25	1.75	2.25	2.75
$T_e$ [s]	4.69	4.87	5.35	5.89	6.45	6.93
Wave power $p$ [kW/m]	0.15	1.39	4.29	9.42	17.48	28.86
Frequency of occurrence FO [%]	21.58	37.25	22.02	10.65	5.14	2.27

Table 2.7: Characteristic sea states at ZW-Akkaert

Location	ZW-Akkaert					
Mean water depth [m]	23					
Distance to shore [km]	20					
Average annual available wave power [kW/m]	3.64					
$H_s$ with a return period of 25 years [m]	5.01					
Sea State	1	2	3	4	5	6
$H_s$ [m]	0.25	0.75	1.25	1.75	2.25	2.75
$T_e$ [s]	3.59	4.08	4.73	5.32	5.88	6.37
Wave power $p$ [kW/m]	0.11	1.16	3.80	8.59	16.02	26.73
Frequency of occurrence FO [%]	24.02	38.46	20.97	9.81	4.23	1.66

Also the mean water depth, distance to shore, average annual available wave power<sup>4</sup> and the significant wave height with a return period of 25 years are given.

<sup>3</sup>Note that the wave period  $T_e$  of the characteristic sea states is the weighted average period  $\bar{T}_e$ .

<sup>4</sup>Note that this value is based on the entire scatter diagram. The average annual available wave power based on the limited number of characteristic sea states will be smaller.

This wave height has been estimated by extrapolating a Weibull distribution of the exceeding probability of the observed data on each location.

More than 50 % of the time, the significant wave height on both locations is smaller than 1 m. Figure 2.13 shows the contribution ( $p$  FO) of the different sea states to the average annual available wave power at Westhinder and ZW-Akkaert.

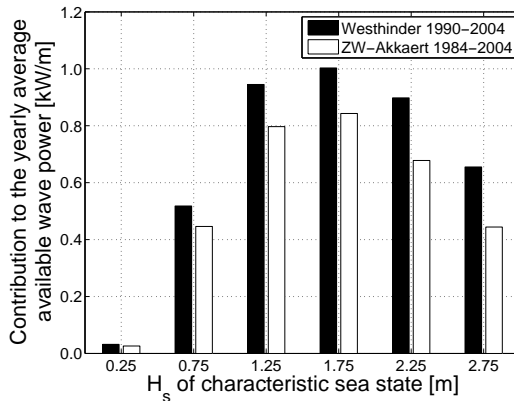


Figure 2.13: Contribution of the different sea states to the average annual available wave power

Although the lower sea states occur less frequently at Westhinder compared to ZW-Akkaert, the contribution of the lower sea states to the average annual available wave power is higher at Westhinder, due to the higher mean periods in the sea states (see Table 2.6 and 2.7). For Westhinder the frequency of occurrence of the sea states and the contribution, in terms of percentage, of each sea state to the average annual available wave power are presented in Figure 2.14. The contribution of the lower sea states to the average annual available wave power is, despite the high frequency of occurrence, rather low.

When planning wave power extraction on the BCS, a detailed study on the planned location is needed. The characteristic sea states, presented in this PhD dissertation, should only be used for first design. The final design should be based on measured spectra at the site.

The reader should be aware that only average statistics have been presented in this study, as no measured spectra were available. As discussed in [18], the measured spectrum is important to estimate the power output of a WEC. For example, when an energy trough exists between swell and wind components that coincides with the eigenfrequency of the device, the produced power is very small. The latter energy trough will not be present in the parameterized JONSWAP spectrum.

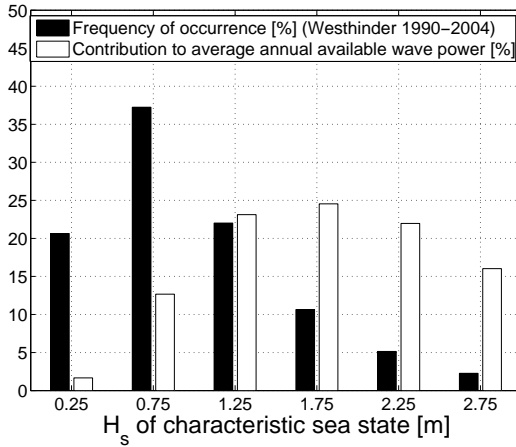


Figure 2.14: Occurrence frequency and contribution to the average annual available wave power of the defined sea states at Westhinder

## 2.2.6 Possibilities for wave energy conversion on the Belgian Continental Shelf

The wave power resource on the Belgian Continental Shelf is highly affected by the sheltering effect of the UK. The propagation of large swells from the Northern Atlantic in the North Sea is partly prevented by the UK. Only 4.64 kW/m (yearly average) is available at the most energetic buoy location. On the other hand the wave height corresponding to a return period of 100 years is estimated to be approximately 6.6 m, which is advantageous for solving the problem of assuring the survivability of WECs. With the current knowledge and technology the Belgian Continental Shelf is a suitable area for testing scale models and WECs designed for smaller  $H_s$  and  $T_p$ . The mild wave climate allows testing of scale models with a ‘scaled severe wave climate’. Furthermore, the relatively cheap scale model (compared to testing a prototype) can be installed without large vessels and can be easily accessed. When the technology of wave energy conversion improves, the efficiency of wave energy conversion in smaller waves will increase. Depending on the amount of improvement and on the cost of energy, wave energy conversion on the Belgian Continental Shelf can contribute to the renewable energy supply in Belgium.

In the next section the resource on the Belgian Continental Shelf will be compared to the resource on the other continental shelves in the North Sea.

## 2.3 Wave energy in the North Sea

### 2.3.1 Analysis of available data

The North Sea (Figure 2.15) is an inland sea of the Atlantic Ocean in Northwest Europe with an average water depth of 94 m. The North Sea is located between the European continent (Denmark, Germany, The Netherlands, Belgium and France), the Scandinavian peninsula (Norway) and the UK, with a surface of 575 000 km<sup>2</sup>. On Figure 2.15 different sites are indicated with numbers. On those sites wave measurement equipment is installed or wave data are available through numerical calculations. The data on those locations are used to quantify the wave power resource in the North Sea. A list of the available data, together with their geographical co-ordinates and data source is given in Table 2.8.

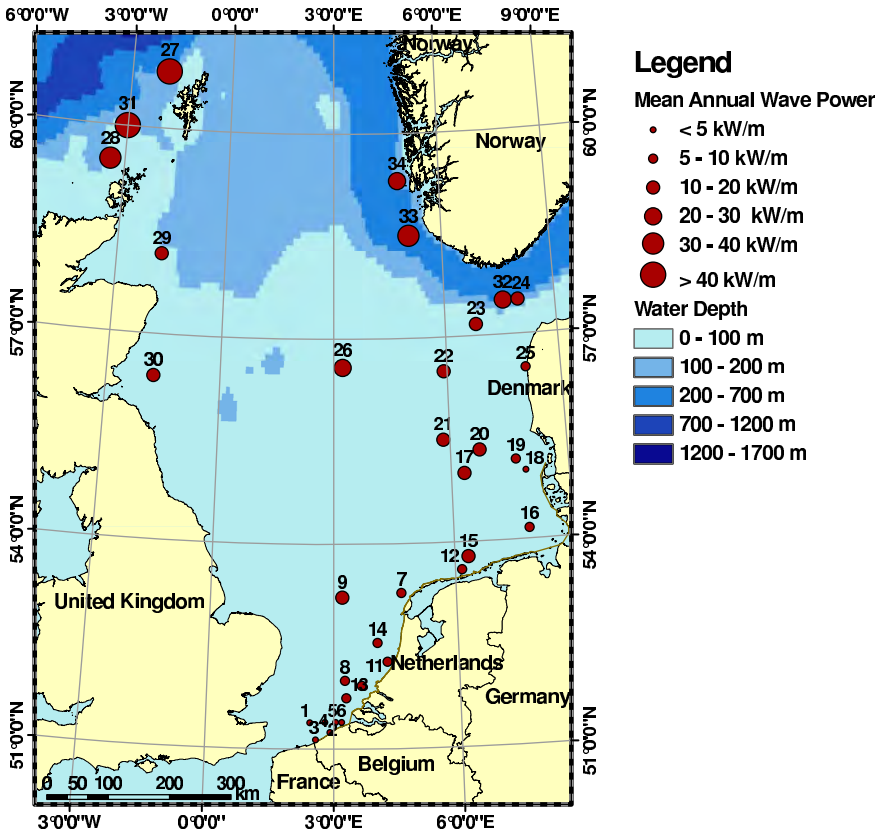


Figure 2.15: Average annual available wave power in kilowatt per meter of wave crest and water depth in the North Sea. The different sites are indicated with a number. More information on each site is given in Table 2.8 and Table 2.9.

Table 2.8: Available wave data in the North Sea

Name of location (N°)	Longitude (WGS 84)	Latitude (WGS 84)	Research on which data is based
<b>Belgian Continental Shelf</b>			
<b>Westhinder (1)</b>	<b>2 ° 26 ' 52 "E</b>	<b>51 ° 23 ' 12 "N</b>	<b>Physical data (1990-2004)</b>
ZW-Akkaert (2)	2 ° 48 ' 12 "E	51 ° 24 ' 29 "N	Physical data (1984-2004)
Trapegeer (3)	2 ° 34 ' 59 "E	51 ° 08 ' 15 "N	Physical data (1994-2004)
Oostende (4)	2 ° 55 ' 14 "E	51 ° 14 ' 34 "N	Physical data (1997-2005)
Wandelaar (5)	3 ° 03 ' 02 "E	51 ° 23 ' 32 "N	Physical data (1995-2004)
Bol van Heist (6)	3 ° 11 ' 43 "E	51 ° 23 ' 25 "N	Physical data (1985-2004)
<b>Dutch Continental Shelf</b>			
<b>ELD (7)</b>	<b>04 ° 39 ' 42 "E</b>	<b>53 ° 16 ' 37 "N</b>	<b>Physical data (1979-2002)</b>
EUR (8)	03 ° 16 ' 35 "E	51 ° 59 ' 55 "N	Physical data (1979-2002)
K13 (9)	03 ° 13 ' 13 "E	53 ° 13 ' 04 "N	Physical data (1979-2002)
LEG (10)	03 ° 40 ' 11 "E	51 ° 55 ' 33 "N	Physical data (1979-2002)
MPN (11)	04 ° 17 ' 46 "E	52 ° 16 ' 26 "N	Physical data (1979-2002)
SON (12)	06 ° 10 ' 00 "E	53 ° 35 ' 44 "N	Physical data (1979-2002)
SWB (13)	03 ° 18 ' 24 "E	51 ° 44 ' 48 "N	Physical data (1979-2002)
YM6 (14)	04 ° 03 ' 30 "E	52 ° 33 ' 00 "N	Physical data (1979-2002)
<b>German Continental Shelf</b>			
<b>Fino-Borkumriff (15)</b>	<b>6 ° 20 ' 06 "E</b>	<b>53 ° 46 ' 54 "N</b>	<b>Physical data (2003-2005)</b>
Helgoland (16)	7 ° 53 ' 39 "E	54 ° 09 ' 27 "N	Physical data (1990-2004)
NSB II (17)	6 ° 20 ' 00 "E	55 ° 00 ' 00 "N	Physical data (1994-2004)
Westerland (18)	7 ° 54 ' 12 "E	55 ° 00 ' 00 "N	Physical data (2002-2005)
<b>Danish Continental Shelf</b>			
Point 1 (19)	7 ° 40 ' 00 "E	55 ° 10 ' 00 "N	MIKE 21 OSW (1979-1993)
Point 2 (20)	6 ° 45 ' 00 "E	55 ° 20 ' 00 "N	MIKE 21 OSW (1979-1993)
<b>Point 3 (21)</b>	<b>5 ° 50 ' 00 "E</b>	<b>55 ° 30 ' 00 "N</b>	<b>MIKE 21 OSW (1979-1993)</b>
Point 4 (22)	5 ° 55 ' 00 "E	56 ° 30 ' 00 "N	MIKE 21 OSW (1979-1993)
Point 5 (23)	6 ° 50 ' 00 "E	57 ° 10 ' 00 "N	MIKE 21 OSW (1979-1993)
Point 6 (24)	8 ° 00 ' 00 "E	57 ° 30 ' 00 "N	MIKE 21 OSW (1979-1993)
Fjaltring (25)	8 ° 05 ' 00 "E	56 ° 30 ' 00 "N	Physical data (1979-1993)
<b>Norwegian Continental Shelf</b>			
Point1160 (32)	7 ° 36 ' 00 "E	57 ° 30 ' 00 "N	WINCH model (1971-2000)
Point1261 (33)	5 ° 06 ' 00 "E	58 ° 30 ' 00 "N	WINCH model (1971-2000)
<b>Utsira (34)</b>	<b>4 ° 49 ' 12 "E</b>	<b>59 ° 18 ' 00 "N</b>	<b>Physical data (1974-1986)</b>
Ekofisk (26)	3 ° 15 ' 00 "E	56 ° 35 ' 00 "N	Physical data (1979-1993)
<b>UK Continental Shelf</b>			
Shetland (27)	1 ° 54 ' 00 "W	60 ° 49 ' 48 "N	UK Wave Model (2000-2004)
Orkney (28)	3 ° 25 ' 12 "W	59 ° 30 ' 00 "N	UK Wave Model (2000-2004)
Moray Firth (29)	1 ° 45 ' 00 "W	58 ° 10 ' 12 "N	UK Wave Model (2000-2004)
<b>Marr Bank (30)</b>	<b>1 ° 45 ' 00 "W</b>	<b>56 ° 23 ' 24 "N</b>	<b>UK Wave Model (2000-2004)</b>
Fair Isle (31)	3 ° 00 ' 00 "W	60 ° 00 ' 00 "N	WAM (1987-1994)

The average annual available wave power on the indicated sites is calculated with the data provided through scatter diagrams. Table 2.9 shows the obtained average annual available wave power for the selected locations in the North Sea together with the mean water depth and the shortest distance to shore.

Table 2.9: Average annual available wave power in the North Sea

Name of location (N°)	Average annual available wave power [kW/m]	Mean water depth [m]	Shortest distance to shore [km]
<b>Belgian Continental Shelf</b>			
<b>Westhinder (1)</b>	<b>4.64</b>	<b>29</b>	<b>32</b>
ZW-Akkaert (2)	3.64	23	20
Trapegeer (3)	1.51	7	4
Oostende (4)	1.66	6	1
Wandelaar (5)	2.63	13	10
Bol van Heist (6)	2.54	12	7
<b>Dutch Continental Shelf</b>			
<b>ELD (7)</b>	<b>9.86</b>	<b>26</b>	<b>31</b>
EUR (8)	7.04	32	36
K13 (9)	10.80	30	88
LEG (10)	6.13	21	15
MPN (11)	5.42	18	8
SON (12)	7.44	19	16
SWB (13)	5.57	20	20
YM6 (14)	8.68	21	32
<b>German Continental Shelf</b>			
<b>Fino-Borkumriff (15)</b>	<b>11.60</b>	<b>27</b>	<b>35</b>
Helgoland (16)	5.91	20	43
NSB II (17)	17.55	42	118
Westerland (18)	4.47	18	44
<b>Danish Continental Shelf</b>			
Point 1 (19)	7	20	64
Point 2 (20)	12	31	100
<b>Point 3 (21)</b>	<b>16</b>	<b>39</b>	<b>150</b>
Point 4 (22)	17	40	150
Point 5 (23)	14	58	100
Point 6 (24)	11	166	68
Fjaltring (25)	7	20	4
<b>Norwegian Continental Shelf</b>			
Point1160 (32)	23.60	200	57
Point1261 (33)	32.52	270	43
<b>Utsira (34)</b>	<b>23.12</b>	<b>200</b>	<b>21</b>
Ekofisk (26)	24	71	300
<b>UK Continental Shelf</b>			
Shetland (27)	42	200	30
Orkney (28)	33	90	27
Moray Firth (29)	19	112	55
<b>Marr Bank (30)</b>	<b>11</b>	<b>57</b>	<b>52</b>
Fair Isle (31)	61.47	100	70

In sections 2.3.1.1, 2.3.1.2, 2.3.1.3, 2.3.1.4 and 2.3.1.5, the resource on the Dutch, German, Danish, Norwegian and UK Continental Shelf is discussed. Omni-directional characteristic sea states are defined for a location on the Dutch, German, Danish, Norwegian and UK Continental Shelf, approximately 30 km offshore with a water depth of approximately 30 m (indicated in bold in Table 2.8

and Table 2.9). The reader should keep in mind that the number of sea states depends on the number of  $H_s$ -intervals in the obtained scatter diagrams. Furthermore when available, a wave rose and the contribution of different wave sectors to the average annual available wave power are given for the characteristic locations (Dutch, German and Danish Continental Shelf).

### 2.3.1.1 The Dutch Continental Shelf

Table 2.9 shows the average annual available wave power on the Dutch Continental Shelf. The available wave power ranges from 5.4 kW/m, 8 km offshore, to approximately 10 kW/m, 30 km offshore (ignoring the location K13 which is situated far offshore). The wave power resource is approximately twice as high as on the Belgian Continental Shelf. Characteristic sea states are defined for the location Eierlands Gat (ELD) (Table 2.10). Significant wave heights smaller than 1 m occur 40 % of the time and higher significant wave heights occur, compared to the Belgian Continental Shelf. On the other hand  $H_s$  with a return period of 25 years is higher as well.

*Table 2.10: Characteristic sea states on the Dutch Continental Shelf*

Location	ELD				
Mean water depth [m]	26				
Distance to shore [km]	31				
Average annual available wave power [kW/m]	9.86				
$H_s$ with a return period of 25 years [m]	7.84				
Sea State	1	2	3	4	5
$H_s$ [m]	0.5	1.5	2.5	3.5	4.5
$T_e$ [s]	4.72	5.58	6.44	7.29	8.13
Wave power $p$ [kW/m]	0.60	6.56	21.85	50.47	95.87
Frequency of occurrence FO [%]	40.65	39.42	14.09	4.29	1.17

Figure 2.16(a) shows the dominant wave directions. Again it is assumed that wave and wind direction coincide. Eight sectors of  $45^\circ$  are taken into consideration. The waves are coming most frequently from the sectors west and southwest, while the sector west contributes the most to the yearly average available wave power (Figure 2.16(b)). More waves are coming from the west and the share of the high energetic waves is increased, compared to Westhinder. Table 2.9, Table 2.10 and Figure 2.16 are based on scatter diagrams provided by the National Institute for Coastal and Marine Management (Rijkswaterstaat).



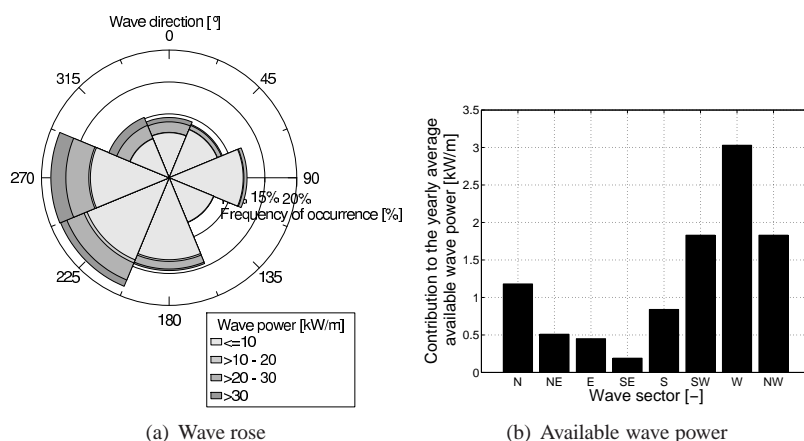


Figure 2.16: (a) Wave rose and (b) contribution of wave sectors to the average annual available wave power at ELD

### 2.3.1.2 The German Continental Shelf

The Federal Maritime and Hydrographic Agency (BSH) provided scatter diagrams on 4 locations of the German Continental Shelf. Table 2.9, Table 2.11 and Figure 2.17 are based on those scatter diagrams. Table 2.9 shows the average annual available wave power on the German Continental Shelf. The resource varies between approximately 4.5 and 12 kW/m (between 35 and 44 km offshore).

Table 2.11: Characteristic sea states on the German Continental Shelf

Location	Fino-Borkumriff							
Mean water depth [m]	27							
Distance to shore [km]	35							
Average annual available wave power [kW/m]	11.6							
$H_s$ with a return period of 25 years [m]	8.21							
Sea State	1	2	3	4	5	6	7	8
$H_s$ [m]	0.25	0.75	1.25	1.75	2.25	2.75	3.25	3.75
$T_e$ [s]	4.15	4.67	5.53	5.95	6.21	6.59	7.55	8.16
Wave power $p$ [kW/m]	0.13	1.35	4.50	9.57	16.77	27.73	45.39	66.54
Frequency of occurrence FO [%]	9.14	27.31	22.62	18.55	10.25	5.08	3.35	1.63

Fino-Borkumriff meets the conditions for characteristic location on the German Continental Shelf (Table 2.11). The wave power resource and the occurrence frequencies of the characteristic sea states are comparable to those on the Dutch Continental Shelf. Figure 2.17(a) shows a wave rose on the characteristic location.

Note that wave directions, and no wind directions, are provided in these scatter diagrams. Most waves are coming from the sectors west, northwest and north, while the yearly average available wave power in the sector northwest is the highest (Figure 2.17(b)). Note that the scatter diagrams at Fino-Borkumriff and Westerland are only based on measurements during 2 and 3 years, respectively. Consequently the wave power resource can be underestimated or overestimated. When available, a longer measurement period should be taken into account.

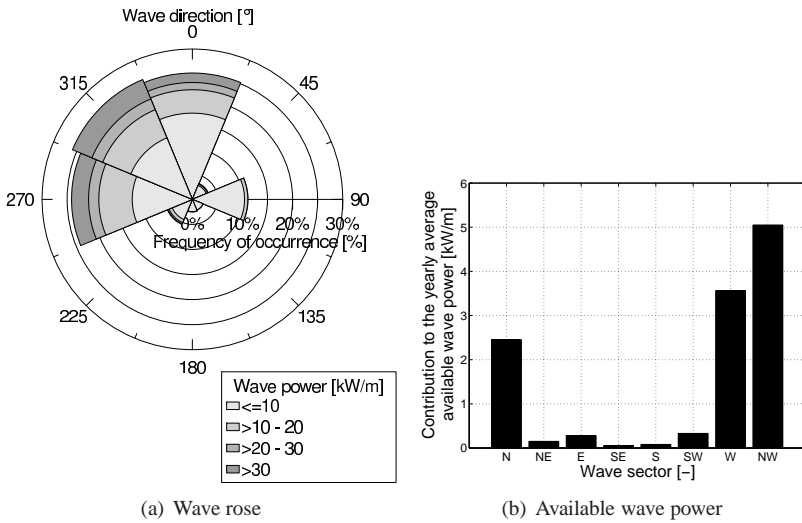


Figure 2.17: (a) Wave rose and (b) contribution of wave sectors to the average annual available wave power at Fino-Borkumriff

### 2.3.1.3 The Danish Continental Shelf

Table 2.9 shows the average annual available wave power [19] on the Danish Continental Shelf. On six locations (Point 1 till 6) the wave climate is calculated by DHI (Dansk Hydraulisk Institut) with the wave propagation model Mike 21 OSW (DHI), based on wind data from the European Centre for Medium-Range Weather Forecasting (ECMWF) for the period from 1/1/1979 till 31/12/1993. The model was calibrated with wave measurements at two locations: Ekofisk (Norwegian Continental Shelf) and Fjaltring [19]. On the Danish Continental Shelf the resource is varying from 7 kW/m near the coast to 17 kW/m far from shore (150 km). The resource near the coast is slightly higher than the near shore resource on the Dutch Continental Shelf. Generally it can be concluded that the average annual available wave power is comparable to the resource on the Dutch and German Continental Shelf.

Characteristic sea states are given in Table 2.12. The characteristic sea states

are defined for a location 150 km offshore, because this location is used as a standard in Denmark [20] and no data approximately 30 km offshore were available. The high distance to shore of this point should be taken into account when comparing the resource with other locations. The impact of the distance to shore on a farm investment is studied in chapter 10. Note that Point 1 is located closer to shore. On the other hand, the water depth at Point 1 is rather small.

Table 2.12: Characteristic sea states on the Danish Continental Shelf

Location	Point 3				
Mean water depth [m]	39				
Distance to shore [km]	150				
Average annual available wave power [kW/m]	16				
$H_s$ with a return period of 25 years [m]	10.21				
Sea State	1	2	3	4	5
$H_s$ [m]	1	2	3	4	5
$T_e$ [s]	4.84	5.99	7.11	8.02	8.76
Wave power $p$ [kW/m]	2.48	12.43	33.54	69.56	124.22
Frequency of occurrence FO [%]	46.8	22.6	10.8	5.1	2.4

Approximately 50 % of the time  $H_s$  is smaller than 1.5 m. The frequency of occurrence of the smaller waves is still very high.

The method to calculate the characteristic sea states used in [20] differs from the method used in this PhD dissertation. Instead of calculating a weighted average of  $T_m$  for each  $H_s$ , the average of the two neighbouring  $T_m$ -values with the highest frequencies of occurrence is determined for each  $H_s$ . For most sea states the difference in  $T_m$  is small.

Figure 2.18(a) shows the dominant wave directions at Point 3, based on the scatter tables in [19]. Wave directions, as calculated in the wave propagation model, are taken into account. Most of the waves are coming from the northwest. All sectors have a contribution of high energetic waves. The sector west has the highest contribution to the yearly average available wave power (Figure 2.18(b)).

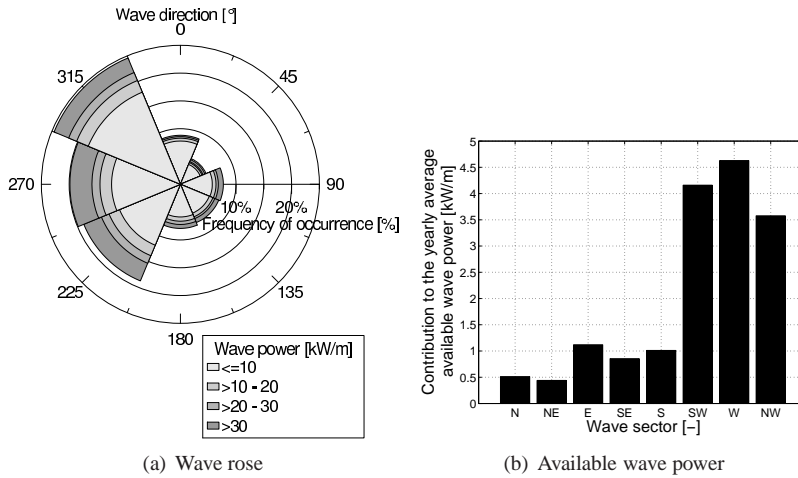


Figure 2.18: (a) Wave rose and (b) contribution of wave sectors to the average annual available wave power at Point 3

### 2.3.1.4 The Norwegian Continental Shelf

Scatter diagrams at four locations on the Norwegian Continental Shelf were available for this PhD research. Scatter diagrams in two hindcast data points on the Norwegian Continental Shelf are provided by the Norwegian Meteorological Institute. Air pressure fields for the period 1955-2005 are fed into a wind model and the resulting wind fields are used by a second generation wave prediction model (WINCH model - calibrated with buoy data from 1980). Until June 1987 the pressure fields were taken from digitized weather maps. From July 1987 on, the pressure fields have been obtained from the European Centre for Medium-Range Weather Forecasts (ECMWF). In one location (Utsira) on the Norwegian Continental Shelf a scatter diagram based on buoy measurements between 1974 and 1986 can be found in the WERATLAS [7]. Finally, a scatter diagram at the location Ekofisk, which was used to calibrate the wave propagation model Mike 21 OSW (see 2.3.1.3), could be used as well. Table 2.9 shows the average annual available wave power on those four locations on the Norwegian Continental Shelf. The resource in front of the Norwegian coast is very high (as compared to other parts of the North Sea), since the Norwegian Continental Shelf is hardly shaded by the UK. The mean annual available wave power varies between approximately 23 and 32.5 kW/m.

At the Norwegian coast the water depth 30 km offshore is higher than approximately 30 m. Utsira is chosen as characteristic location (Table 2.13). Only 20 % of the time the significant wave height is smaller than 1 m. Data on the distribution of the mean wave direction are available at the Norwegian

Meteorological Institute.

*Table 2.13: Characteristic sea states on the Norwegian Continental Shelf*

Location	Utsira				
Mean water depth [m]	200				
Distance to shore [km]	21				
Average annual available wave power [kW/m]	23.12				
$H_s$ with a return period of 25 years [m]	10.60				
Sea State	1	2	3	4	5
$H_s$ [m]	0.5	1.25	1.75	2.25	2.75
$T_e$ [s]	7.13	7.44	7.69	8.04	8.39
Wave power $p$ [kW/m]	0.88	5.76	11.69	20.20	31.49
Frequency of occurrence FO [%]	19.70	21.80	17.10	12.90	9.40
Sea State	6	7	8	9	10
$H_s$ [m]	3.25	3.75	4.25	4.75	5.25
$T_e$ [s]	8.80	9.01	9.09	9.51	9.96
Wave power $p$ [kW/m]	46.17	62.78	81.31	106.17	137.56
Frequency of occurrence FO [%]	6.40	4.20	2.70	1.60	1.20

### 2.3.1.5 The UK Continental Shelf

Through the UK Waters Wave Model [21], operated by Met Office, three-hourly wave data for the period from 29 March 2000 through 9 November 2004 for a total of 95 grid points around the UK were obtained. In [22] scatter diagrams and the average annual available wave power on 10 grid points from the UK Waters Wave Model are given. Only 4 of those 10 grid points are located in the North Sea. Note that the simulation period of 4.5 years is still relatively short. In one location (Fair Isle) a scatter diagram based on directional spectra from WAM (Third Generation Wave Model) between 1987 and 1994 can be found in the WERATLAS [7].

Table 2.9 shows the average annual available wave power on those 5 locations of the UK Continental Shelf. It is clear that the northern part of the North Sea has a larger wave power resource (Shetland, Orkney and Fair Isle). Only the resource at Marr Bank is comparable to the available wave power on the Dutch, German and Danish Continental Shelf.

Characteristic sea states are given in Table 2.14. Marr Bank satisfies the conditions for characteristic location. Significant wave heights smaller than 1 m occur approximately 30 % of the time. Data on the distribution of mean direction at Marr Bank can be found in [22].

Table 2.14: Characteristic sea states on the UK Continental Shelf

Location	Marr Bank				
Mean water depth [m]	57				
Distance to shore [km]	52				
Average annual available wave power [kW/m]	11				
$H_s$ with a return period of 25 years [m]	12.4				
Sea State	1	2	3	4	5
$H_s$ [m]	0.5	1.5	2.5	3.5	4.5
$T_e$ [s]	5.39	6.11	7.17	8.37	9.28
Wave power $p$ [kW/m]	0.67	6.91	22.78	53.71	101.09
Frequency of occurrence FO [%]	31.2	45.1	15.9	4.5	1.3

### 2.3.1.6 Comparison between the continental shelves

The near shore wave power resource on the Dutch, German, Danish and southern UK Continental Shelf is comparable (between approximately 4.5 and 12 kW/m) and in general higher than the resource on the Belgian Continental Shelf. The resource on the northern UK and Norwegian Continental Shelf is higher than the resource in the southern North Sea. A maximum of 61.47 kW/m is observed (Table 2.9).

In general there is a shift in frequency of occurrence to higher significant waves when going more northwards in the North Sea. On the other hand  $H_s$  with a return period of 25 years increases as well. The wave period corresponding to a specific significant wave height is comparable on the Belgian, Dutch, German and Danish Continental Shelf, whereas the wave period on the UK and Norwegian Continental Shelf is slightly higher. When comparing Figure 2.7(a), 2.16(a), 2.17(a) and 2.18(a) an increasing share of high energetic waves ( $> 30$  kW/m) and a shift in prevailing wave direction from southwest till north, northwest is observed.

### 2.3.1.7 Comparison with the resources of the West European coast

In general the wave power resource in the North Sea is rather small compared with the resource in front of the West European coast (40 - 70 kW/m). Near shore ( $< 30$  km), less than approximately 12 kW/m is available, not only on the Belgian Continental Shelf, but also on the Dutch, German, Danish and southern UK Continental Shelf. Only the resource in the northern part of the North Sea (maximum 61.47 kW/m) is comparable with the one of the West European coast. On the other hand the wave climate is less aggressive and this feature makes the North Sea attractive for wave power conversion.

So far only buoy measurements and limited numerical wave propagation results (Denmark, Norway and UK) were studied to characterize the wave climate

in the North Sea. In general, the analysis of buoys is more accurate than the results of numerical wave propagation models, but buoys are not always located on sites of interest. Therefore calculations with a numerical wave propagation model are needed.

### **2.3.2 Spatial distribution of the available wave power**

Numerical wave propagation models are used to define the wave characteristics in near shore locations when the characteristics in deep water are known. Wave propagation models are usually classified in two types, i.e. phase-averaged spectral models and phase-resolving time domain models. Spectral models describe the evolution of the wave energy spectrum (energy balance equation) in space and time while time domain models calculate the sea surface as a function of time (conservation of mass and momentum equations). Time domain models may be categorized into models based on (i) the linear mild-slope and (ii) the nonlinear Boussinesq equations. The mild-slope equations describe the transformation of linear water waves when propagating from deep to shallow water while the Boussinesq equations (e.g. MIKE 21) predict the propagation of nonlinear waves with high accuracy, especially in shallow water, but are computationally very demanding.

The calculation time of phase-averaged spectral models is limited compared to phase-resolving time domain models. Therefore results in a large area can be obtained in a relatively fast way with a phase-averaged spectral model. Furthermore the spectral wave energy distribution contains sufficient information to determine the most important wave parameters [8]. Third-generation spectral wave models (e.g. WAM) solve the energy balance equation, accounting in deep water for sink-source terms as the energy input by wind, transfer of energy input by wind at high frequencies to lower frequencies by non-linear wave-wave interactions and the dissipation due to wave breaking (white-capping) and bottom friction. In shallow water and in the presence of currents, wave energy is not conserved. Therefore in that case the balance equation is written in terms of the action density. In addition other sink mechanisms come into play as depth-induced breaking and triad wave-wave interactions (e.g. SWAN [23]). Triad wave-wave interactions are significant for steep waves in shallow water and involve the transfer of energy to higher frequency components, resulting in waves with sharper crests and flatter troughs. An overview of the evolution from first-generation till third generation spectral wave models is given in [24].

In this section hindcasts of the wave model WAM-PRO [8], a version of the WAM model [24] adapted to run efficiently with high resolution in near shore applications, have been used to estimate the wave power resource in the southern part of the North Sea during 2003-2004 [25].

The WAM-PRO model is driven by analyzed wind fields from the United Kingdom Meteorological Office (UKMO), delivered by The Management Unit of the North Sea Mathematical Models (MUMM). The wind fields have a resolution of  $1.25^\circ$  and a time step of 6 hours. The grid domain covers the entire North Sea and part of the Norwegian Sea in order to capture swell waves generated at the northern boundary. To reduce calculation time on the one hand and to obtain a detailed resolution grid in the southern North Sea on the other hand, two nested grids have been used [26]. The grids together with the bathymetry and UKMO wind fields grid are shown on Figure 2.19 and the grid characteristics are given in Table 2.15.

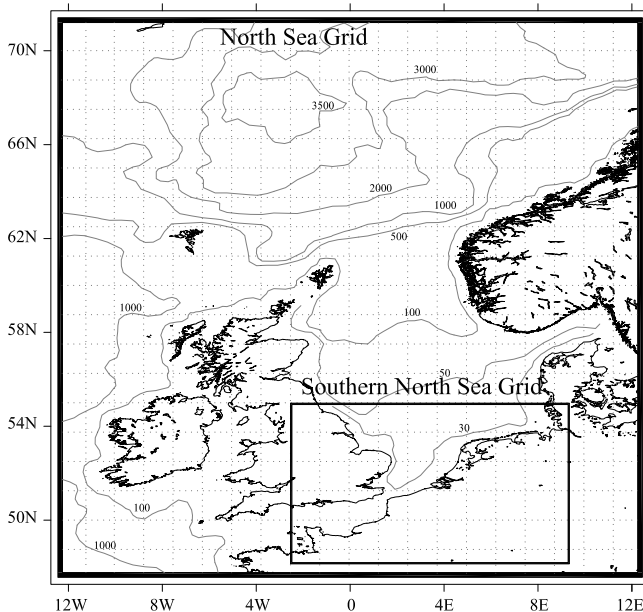


Figure 2.19: North Sea Grid and Southern North Sea Grid [26]. Gray continuous lines are bathymetric contour lines at the indicated depths given in meters. The dotted grid lines correspond to the UKMO wind fields grid.

The bathymetric data used correspond to the CSM Bathymetry derived from the digitalization of navigation charts [27]. The calculated wave data were stored in 12 826 grid points every 3 hours. The number of frequencies used to describe the wave spectrum is 25 and the number of directions is 12, with the lowest frequency equal to  $0.0418 \text{ Hz}^5$ . The propagation time step is 600 s for the coarse grid and 200 s for the fine grid and the source time step equals 600 s for both grids.

<sup>5</sup>Frequency resolution:  $f_{i+1}=1.1f_i$



Table 2.15: WAM nested grid characteristics

	North Sea		Southern North Sea	
<b>Resolution</b>	[°]	[km]	[°]	[km]
Latitude resolution	1/3	36.6	1/15	7.2
Longitude resolution	1/2	47.7	1/10	8.7
<b>Coordinates</b>	[°]		[°]	
Most northern latitude	71.17		55.50	
Most southern latitude	12.25		48.50	
Most eastern longitude	47.83		9.25	
Most western longitude	12.25		2.75	

Buoy data at Westhinder, Bol van Heist, K13 and Fino-Borkumriff (respectively location number 1, 6, 9 and 15 on Figure 2.15), have been used to validate the WAM-PRO calculations. Measured time series of  $H_{m0}$  and  $T_e$  have been compared to the calculated time series with WAM-PRO. At Fino-Borkumriff only measured time series of  $H_{m0}$  and  $T_p$  during 2004 were available.  $T_e$  has been calculated from  $T_p$  with  $T_e = \frac{T_p}{1.1}$  [11]. The comparisons are shown in the scatter plots of Figures 2.20, 2.21, 2.22 and 2.23.

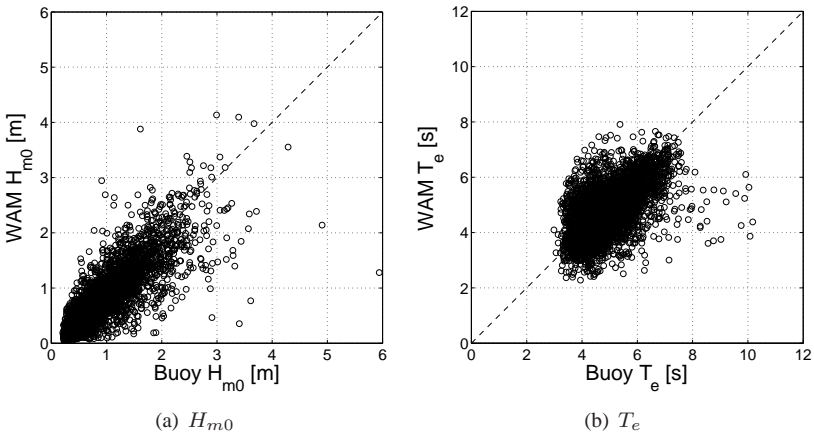


Figure 2.20: Scatter plot between measured and calculated significant wave height  $H_{m0}$  and mean wave period  $T_e$  at Westhinder during 2003-2004

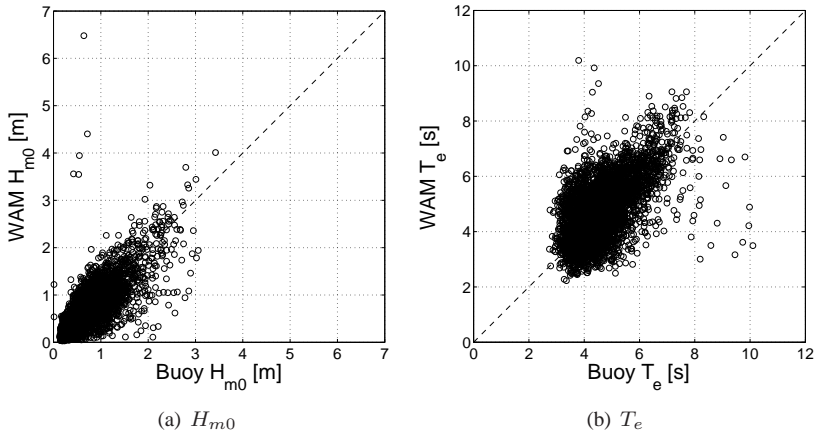


Figure 2.21: Scatter plot between measured and calculated significant wave height  $H_{m0}$  and mean wave period  $T_e$  at Bol van Heist during 2003-2004

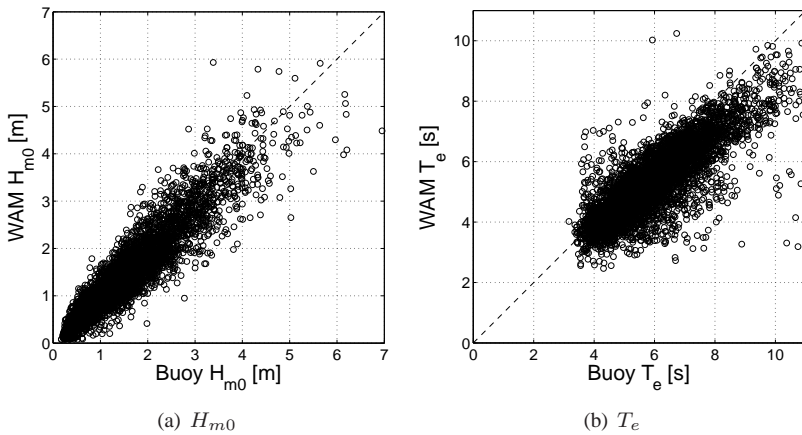


Figure 2.22: Scatter plot between measured and calculated significant wave height  $H_{m0}$  and mean wave period  $T_e$  at K13 during 2003-2004

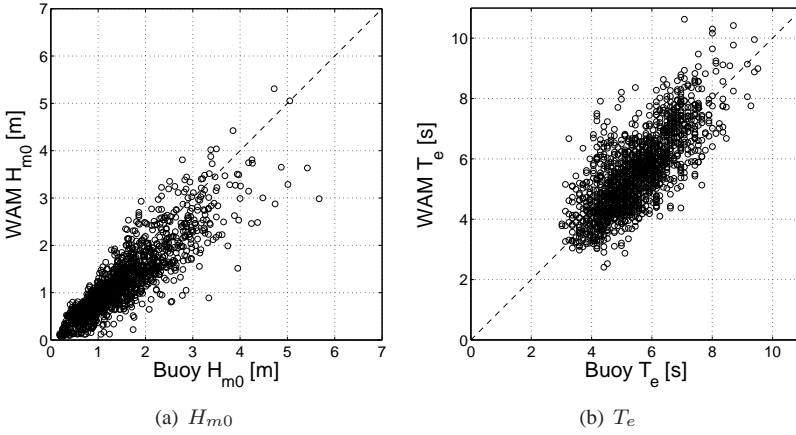


Figure 2.23: Scatter plot between measured and calculated significant wave height  $H_{m0}$  and mean wave period  $T_e$  at Fino-Borkumriff during 2004

The following statistical parameters are calculated to compare the WAM-PRO calculations and the buoy measurements: the average value of the simulated data and the buoy data, the bias, the Root Mean Square Error (RMSE), the Scatter Index (SI) and the Pearson’s correlation coefficient  $r$ . If  $x_i$  represent the measured values (buoy data),  $y_i$  the simulated values (WAM data) and  $n$  the number of observations, the mentioned statistics can be defined with [28]:

$$\bar{x} = \frac{\sum_{i=1}^n x_i}{n} \tag{2.8}$$

$$\bar{y} = \frac{\sum_{i=1}^n y_i}{n} \tag{2.9}$$

$$\text{Bias} = \frac{\sum_{i=1}^n (y_i - x_i)}{n} \tag{2.10}$$

$$\text{RMSE} = \sqrt{\frac{\sum_{i=1}^n (x_i - y_i)^2}{n}} \tag{2.11}$$

$$\text{SI} = \frac{\text{RMSE}}{\bar{x}} \tag{2.12}$$

$$r = \frac{\sum_{i=1}^n (x_i - \bar{x})(y_i - \bar{y})}{\sqrt{\sum_{i=1}^n (x_i - \bar{x})^2 \sum_{i=1}^n (y_i - \bar{y})^2}} \tag{2.13}$$

The values of these statistical parameters are given in Table 2.16

Table 2.16: Statistical parameters for  $H_{m0}$  and  $T_e$  for the locations Westhinder, Bol van Heist, K13 and Fino-Borkumriff.  $\bar{x}$ ,  $\bar{y}$ , Bias and RMSE are given in meters for  $H_{m,0}$  and seconds for  $T_e$ .

Name of location	$n$		$\bar{x}$ buoy	$\bar{y}$ WAM	Bias	RMSE	SI	$r$
			[m or s]	[m or s]	[m or s]	[m or s]	[-]	[-]
Westhinder	4193	$H_{m0}$	0.90	0.78	-0.09	0.30	0.33	0.83
	4410	$T_e$	4.94	4.72	-0.16	0.76	0.15	0.56
Bol van Heist	4973	$H_{m0}$	0.67	0.62	-0.04	0.29	0.42	0.78
	4947	$T_e$	4.58	4.66	0.07	0.84	0.18	0.59
K13	5565	$H_{m0}$	1.45	1.35	-0.10	0.39	0.27	0.91
	5565	$T_e$	6.06	5.39	-0.63	1.08	0.18	0.81
Fino-Borkumriff	1483	$H_{m0}$	1.47	1.20	-0.13	0.34	0.23	0.88
	1483	$T_e$	5.51	5.56	0.03	0.63	0.11	0.76

In general a good agreement between buoy and model data is seen (Figures 2.20, 2.21, 2.22 and 2.23). The correlation coefficient is relatively high, except for  $T_e$  at Westhinder and Bol van Heist. Scatter indices are about 40 % and lower for the significant wave height and lower than 20 % for the energy period. At each location the calculated wave height is a little smaller than the measured wave height (negative bias). At K13 the energy period is under predicted (bias = -0.63).

The available wave power at each grid point (Figure 2.24) is estimated by using the hindcasts of the WAM-PRO model (during 2003 and 2004) and a deep water approximation of equation (B.16), equation (B.18).<sup>6</sup> The derivation of equation (B.18) can be found in appendix B.

$$p = \frac{\rho g^2}{64\pi} H_s^2 T_e \quad (\text{B.18})$$

It should be mentioned that the resulting spatial variation of the average annual available wave power is only based on 2 years of hindcasts. In [29] a good spatial variation in wave power was obtained with data from only 2 years with a sampling rate of 5 days. Therefore when studying Figure 2.24 main attention should go to the spatial variation of the wave power and not to the absolute values themselves, as it was observed in Figure 2.4 that the available wave power during those two years was rather low at Westhinder and ZW-Akkaert.

<sup>6</sup>By using the deep water approximation of equation (B.16), the wave power resources in shallow water near the coast are a little underestimated.

It is clear that the average annual available amount of wave power increases further offshore and further north in the North Sea.

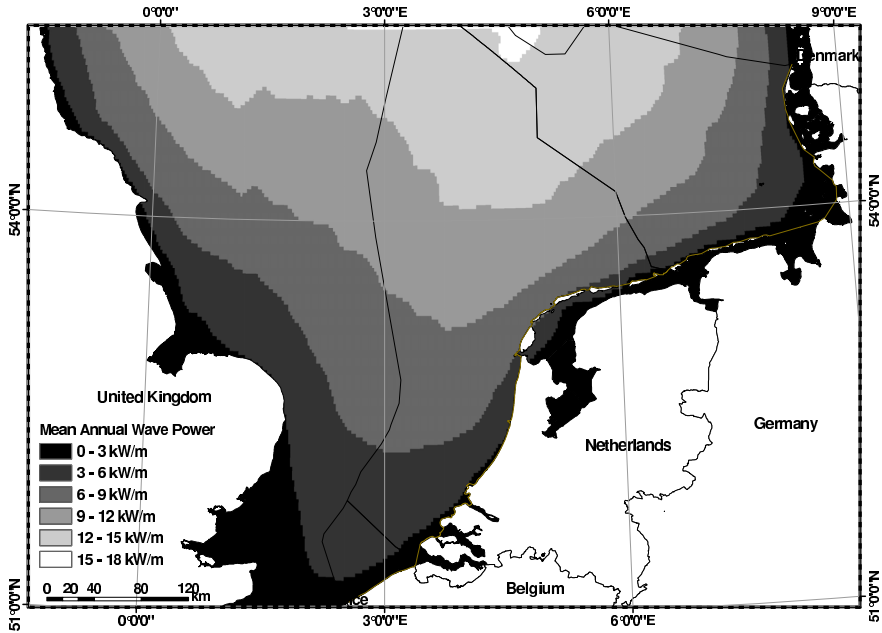


Figure 2.24: Average annual available wave power in kilowatt per meter of wave crest in the southern North Sea

## 2.4 Conclusions

The wave power resource in the North Sea has been studied in detail in this chapter. Available wave data from buoy measurements and numerical wave propagation models have been analysed on 34 locations. The available wave power ranges from less than 5 kW/m in the southern part of the North Sea till more than 60 kW/m in the northern part. The wave power resource in the southern part is highly affected by the sheltering effect of the UK. Only 4.64 kW/m is available at the most energetic buoy location on the Belgian Continental Shelf (Westhinder). On the other hand WECs installed in this less severe wave climate are more likely to survive storm conditions. A detailed spatial distribution of the available wave power in the southern North Sea has been obtained with hindcasts from the WAM-PRO model during 2003 and 2004.

An in-depth study of the wave power resource on the Belgian Continental Shelf has revealed its temporal and directional variation. A high yearly and seasonal variation has been observed. The resource in autumn and winter is approximately

twice the resource in spring and summer. The sectors west-southwest, southwest and south-southwest contain approximately 40 % of the average annual available wave power. Further, operational and design wave conditions have been specified. With the current knowledge and technology the Belgian Continental Shelf is a suitable area for testing scale models and WECs designed for smaller wave heights and wave periods. The mild wave climate allows testing of scale models with a 'scaled severe wave climate'. Furthermore, the relatively cheap scale model (compared to testing a prototype) can be installed without large vessels and can be easily accessed.

Finally omni-directional characteristic sea states have been defined for the Belgian, Dutch, German, Danish, Norwegian and UK Continental Shelf. This limited number of sea states can be considered during initial design of a WEC to get a fast and general picture of its power production in the North Sea. When planning to install a WEC or a farm of WECs in the North Sea, a more detailed study of the wave climate on the planned location is needed.

## References

- [1] S. Barstow, D. Mollison, and J. Cruz. *Chapter 4: The Wave Energy Resource*. In J. Cruz, editor, *Ocean Wave Energy, Current Status and Perspectives*, pages 93–132. Springer, 2008.
- [2] *WORLDWAVES*. <http://www.geos.com/services/consultancy/worldwaves.asp>. Accessed April 2009.
- [3] A.M. Cornett. *A global wave energy resource assessment*. In Proceedings of the 18<sup>th</sup> International Offshore and Polar Engineering Conference (ISOPE), Vancouver, Canada, 2008.
- [4] H. Bernhoff, E. Sjöstedt, and M. Leijon. *Wave energy resources in sheltered sea areas: a case study of the Baltic Sea*. In Proceedings of the 5<sup>th</sup> European Wave and Tidal Energy Conference (EWTEC), Cork, Ireland, 2003.
- [5] U. Henfridsson, V. Neimane, K. Strand, R. Kapper, H. Bernhoff, O. Danielsson, M. Leijon, J. Sundberg, K. Thorburn, E. Ericsson, and K. Bergman. *Wave energy potential in the Baltic Sea and the Danish part of the North Sea, with reflections on the Skagerrak*. *Renewable Energy*, 32:2069–2084, 2007.
- [6] R. Waters, J. Engström, J. Isberg, and M. Leijon. *Wave climate off the Swedish west coast*. *Renewable Energy*, 34:1600–1606, 2008.
- [7] M.T. Pontes. *Assessing the European Wave Energy Resource*. *Journal of Offshore Mechanics and Arctic Engineering*, 120:226–231, 1998.
- [8] J. Monbaliu, R. Padilla-Hernández, J.C. Hargreaves, J.C.C. Albiach, W.M. Luo, M. Sclavo, and H. Günther. *The spectral wave model WAM, adapted for application with high spatial resolution*. *Coastal Engineering*, 41:41–62, 2000.
- [9] T. Mertens. *Golfenergie op het Belgisch Continentaal Plat: droom of werkelijkheid? Analyse van het golfklimaat*. Master's thesis, Ghent University, 2005.
- [10] V. Van Lancker et al. *Management, research and budgeting of aggregates in shelf seas related to end-users (Marebasse)*. Final Scientific Report, Belgian Science Policy, 2007.
- [11] L.H. Holthuijsen. *Waves in oceanic and coastal waters*. Cambridge University Press, 2007.

- [12] Z. Liu and P. Frigaard. *Random Seas*. Technical report, Hydraulics and Coastal Engineering Laboratory, Aalborg University, 1997.
- [13] Haecon. *Atlas hydro-meteo waarnemingen voor de Vlaamse kust*. Technical report, Vlaamse Gemeenschap, Diensten van de Vlaamse executieve openbare werken en verkeer, Bestuur der waterwegen en van het zeezeven, Dienst der kust.
- [14] M. Rugbjerg, K. Nielsen, J.H. Christensen, and V. Jacobsen. *Wave energy in the Danish part of the North Sea*. In Proceedings of the 4<sup>th</sup> European Wave Energy Conference, Aalborg, Denmark, 2000.
- [15] IMDC. *Afstemming Vlaamse en Nederlandse voorspelling golfklimaat op ondiep water - Deelrapport 4: Technisch Wetenschappelijk Bijstand - Traject Golfklimaat*. Technical report, Vlaamse Overheid Departement Mobiliteit en Openbare Werken - Afdeling Waterbouwkundig Laboratorium, 2009.
- [16] Afdeling Waterwegen Kust, Haecon nv, and Probabilitas nv. *Hydro Meteo Atlas Meetnet Vlaamse Banken*. <http://www.vlaamsehydrografie.be>, Accessed April 2009.
- [17] Rijkswaterstaat. *Golfklimaat*. <http://www.golfklimaat.nl>, Accessed April 2009.
- [18] S. Barrett, B. Holmes, and T. Lewis. *Monitoring of Seaway Variability on WEC Performance*. In Proceedings of the 2<sup>nd</sup> International Conference on Ocean Energy (ICOE), Brest, France, 2008.
- [19] Dansk Hydraulisk Institut. *Raport50105\_DHI*. Technical report, DHI, 1999.
- [20] N.I. Meyer. *Bølgekræftprogram*. Technical report, Bølgekræftudvalgets Sekretariat RAMBØLL, 2002.
- [21] ABP Marine Environmental Research Ltd. *Atlas of UK Marine Renewable Energy Resources: Technical Report*. Technical report, Department of Trade and Industry, 2004.
- [22] T. Boehme. *Matching Renewable Electricity Generation with Demand in Scotland*. PhD thesis, University of Edinburgh, 2006.
- [23] N. Booij, I.J.G. Haagsma, L.H. Holthuijsen, A.T.M.M. Kieftenburg, R.C. Ris, A.J. van der Westhuysen, and M. Zijlema. *SWAN cycle III version 40.41 User Manual [online]*. Available from: <http://fluidmechanics.tudelft.nl/swan/default.htm>, [Accessed 7 April 2005], 2004.



- 
- [24] G. J. Komen, L. Cavaleri, M. Donelan, K. Hasselmann, S. Hasselmann, and P. A. E. M. Janssen. *Dynamics and Modelling of Ocean Waves*. Cambridge University Press, 1994.
- [25] J. Portilla. *Estimating wave power at the Southern North Sea using WAM model hindcasts*. Technical report, Department of Civil Engineering, Ghent University, 2009.
- [26] J. Portilla. *Buoy data assimilation in nearshore wave modelling*. PhD thesis, Laboratorium voor Hydraulica, Katholieke Universiteit Leuven, 2009.
- [27] R.A. Flather. *Results from a model of the North east Atlantic relating to the Norwegian Coastal current*. In Norwegian Coastal Current Symposium, Geilo, volume 2, pages 427–458, 1981.
- [28] P. Pilar, C. Guedes Soares, and J.C. Carretero. *44-year wave hindcast for the North East Atlantic European Coast*. *Coastal Engineering*, 55:861–871, 2008.
- [29] S. Barstow, O. Haug, and H. Krogstad. *Satellite Altimeter Data in Wave Energy Studies*. In *Waves 1997*, ASCE, volume 2, pages 339–354, 1998.



# 3

## Geo-spatial multi-criteria decision analysis

### 3.1 Introduction

Not all sites in the North Sea are suitable to deploy a farm of wave energy converters. As seen in the previous chapter, the wave power resource is highly depending on the location. In general, the resource increases from the southern to the northern part of the North Sea and locations further from the coast contain more energy compared to near shore locations. A steady, reliable and high wave power resource is preferred. Also the technological specifications and limitations of a wave energy converter affect the choice of a suitable site for deployment. Moreover, the cost of several aspects of a farm such as installation, grid connection and operation and maintenance are influenced by the location. Finally, environmental and social conflicts should be avoided when planning a farm of wave energy converters.

To select a good location to deploy a farm of wave energy converters a comparative assessment between minimal cost and maximal production of a farm should be made while avoiding spatial and temporal conflicts. A detailed life-cycle-cost analysis would indicate the optimal location for wave energy conversion. However, this analysis is too time demanding for a large spatial domain and experience from existing farms of WECs is too scarce. Therefore in this chapter a geo-spatial Multi-Criteria Decision Analysis (MCDA) is performed to identify possible locations for wave energy conversion in the southern part of

the North Sea. In this MCDA several factors are weighted against each other. A Geographic Information System (GIS) is used for the spatial data analysis and serves as a framework for the MCDA.

In [1] an overview of GIS-based MCDA approaches since 1990 is given. A GIS-based MCDA has intensively been used to select a good location for wind farms [2, 3] and more recently for farms of wave energy converters [4, 5]. Criteria used in such a MCDA consist of constraints and weighted factors (Figure 3.1). Constraints (a.o. marine protected areas) impose restrictions on the studied area and do not allow exploitation of a farm of wind turbines or wave energy converters. Factors (a.o. distance to the electricity grid) are evaluated for their impact on the installation of a farm (score  $c_i$ ) and are weighted according to their relevance (weight  $W_i$ ). As a result, a number indicating the suitability of a location is obtained for each location.

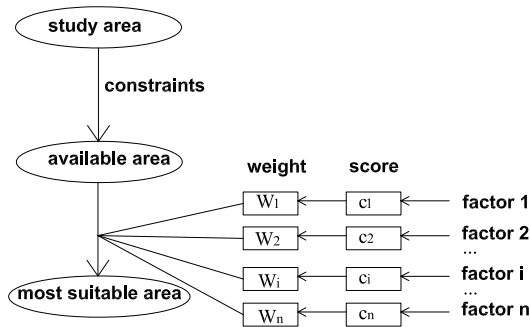


Figure 3.1: Methodology of GIS-based MCDA

In [5] the influence of a relaxation of the applied constraints on possible areas for wave energy conversion and on grid connection cost has been studied. The number of locations that could be connected to the electricity grid for less than M\$10 increased by 33 % and 50 % [5] when the cable could be installed in a national park or could traverse a cliff, respectively. In [2] a comparison has been made between the remaining suitable areas for a farm of wind turbines when applying equal weights to the selected factors and weights according to their relative importance (varying weights). The method with the varying weights resulted in a slightly higher geographical extent of the most suitable sites. In the MCDA in this chapter the relative importance of the selected factors is estimated and the impact of the weights is quantified through a sensitivity analysis.

In a first section of this chapter the methodology of the GIS-based MCDA is described in detail and applied to the deployment of a farm of Pelamis WECs in the southern North Sea, in particular on the Belgian, Dutch and German Continental Shelf (respectively BCS, DCS and GCS). The impact of the restrictions and the weights of several factors on the suitable locations is studied in section 3.3. Finally,

in section 3.4 the accuracy of the MCDA is discussed.

## 3.2 Determination of suitable locations for wave power conversion in the southern North Sea

In this PhD dissertation the GIS-based MCDA is performed in the ArcGIS (ArcInfo 9.2) software. The data used for the MCDA are shown in Table 3.1. All data are imported and analysed in ArcGIS in a vector structure (points, lines and polygons).

### 3.2.1 Constraints

First, the studied area is reduced by eliminating zones which have to be excluded because of their existing and restricting user functions. Only the constraints on the Belgian Continental Shelf were available in digital format (Table 3.1). The other constraints were acquired from paper charts. These paper charts were scanned, geo-referenced to WGS84 and digitized (vectorized) into points, lines and polygons.

The constraints implemented in the analysis are shown on Figure 3.2. The constraints on the Belgian Continental Shelf are given in more detail on Figure 2.2. The constraints include:

- **Navigation routes, anchorage areas, dredging zones and dumping zones:** the North Sea has one of the highest traffic circulations in the world. The dedicated zones have to be permanently accessible for vessels and cannot be used for other purposes. To decrease the risk of collision, a buffer of 500 m at both sides of the navigation routes and anchorage areas is taken into account. Dredging zones are located near harbours to increase the accessibility of the harbour. These zones coincide with navigation routes. As the influence of small dumping zones on the installation of a farm of WECs is not clear, these zones are excluded as well.
- **Marine protected areas:** these areas should not be considered in the analysis because they are restricted for the protection and maintenance of biodiversity.

Table 3.1: Summary of implemented data

Data use	Data description	Data source
Define study area	Borders BCS, DCS and GCS	MUMM <sup>1</sup> (BCS) Rijkswaterstaat (DCS) BSH <sup>2</sup> (GCS)
Define study area, constraint, factor	Borders surrounding countries	Automotive Navigation Data (Global Road Data)
Constraint	Navigation routes	MUMM (BCS) Rijkswaterstaat (DCS) BSH (GCS)
Constraint	Anchorage place	MUMM (BCS) Rijkswaterstaat (DCS)
Constraint	Dredging zones	MUMM (BCS) BSH (GCS)
Constraint	Dumping zones	MUMM (BCS) Rijkswaterstaat (DCS) BSH (GCS)
Constraint	Marine protected areas	MUMM (BCS) BSH (GCS)
Constraint	Extraction zones	MUMM (BCS) Rijkswaterstaat (DCS) BSH (GCS)
Constraint	Military practice zones	MUMM (BCS) Rijkswaterstaat (DCS) BSH (GCS)
Constraint	Ammunition zones	MUMM (BCS) Rijkswaterstaat (DCS) BSH (GCS)
Constraint	Platforms	Rijkswaterstaat (DCS) BSH (GCS)
Factor	Scatter diagrams	Chapter 2
Factor	Grid connections	[6] (BCS) TenneT (DCS) GENI <sup>3</sup> (GCS)
Factor	Bathymetry	British Geological Survey (BGS)
Factor	Geology	Admiralty charts
Factor	$H_{s,25y}$	Chapter 2
Factor	Ports	ESPO <sup>4</sup>

<sup>1</sup> Management Unit of the North Sea Mathematical Models

<sup>2</sup> Bundesamt für Seeschifffahrt und Hydrographie

<sup>3</sup> Global Energy Network Institute

<sup>4</sup> European Sea Ports Organisation

- Extraction zones for sand, gravel and sea shells:** these areas are mostly concentrated along the Dutch coast. Any exploitation of wave energy is excluded in these areas. In Belgium, specific areas allocated to sand or gravel extraction can be shifted to another zone based on a concession of the federal minister of economic affairs. In the following, these zones will be excluded completely. It could be interesting to study the suitability for wave energy conversion of these areas as well. If one of these zones turns out to be a good location, a request for moving an extraction zone can be made. One should note that the movement of an extraction zone requires a lot of administrative work before the possible installation of a farm can take place.

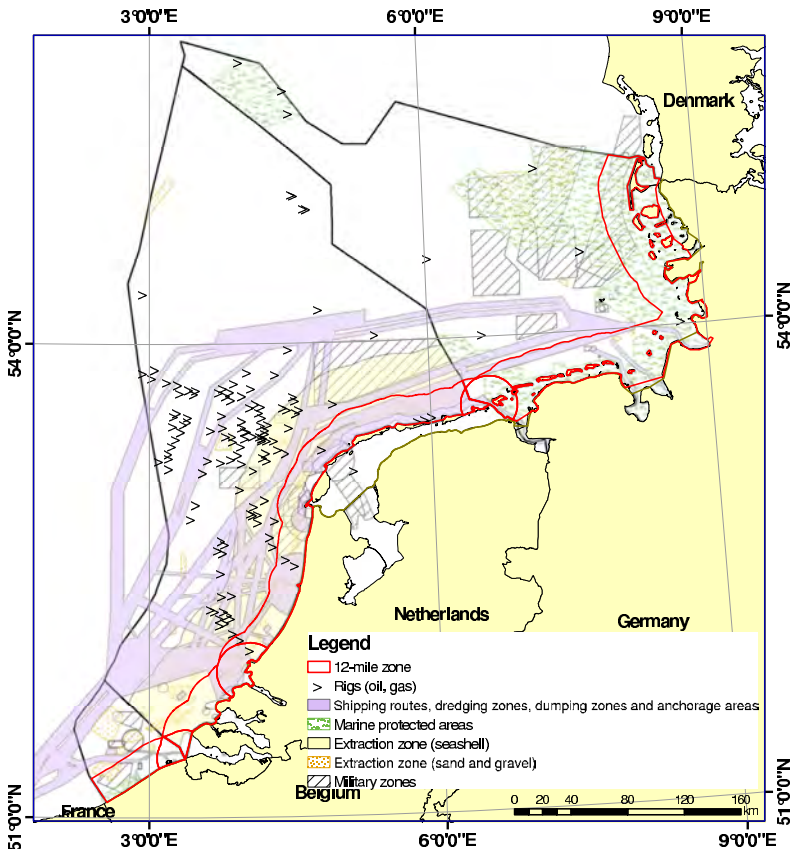


Figure 3.2: Overview of all constraints (excluded for further analysis)

- Military zones (military practice and ammunition areas):** military practice zones are regularly used for firing exercises. Because of the high

risk of accidents in the vicinity of military and ammunition zones, a buffer of 500 m is implemented around these zones.

- **Platforms (gas and oil rigs):** to avoid collisions between a wave energy converter and a platform and to guarantee the accessibility of a platform a buffer of 250 m around each platform is taken into account.
- **12-mile zone:** installation of a farm of WECs in a buffer of 12 miles off the shore depends on federal legislations. In Nobre et al. [4] this zone is excluded. Initially a buffer of 12 miles off the shore is excluded from further analysis in this study. According to Maes [7] the installation of a farm of WECs is allowed in the 12-mile zone. Therefore in section 3.3.4 the impact of permitting the installation of a farm of WECs in the 12-mile zone, on interesting locations for wave power conversion is discussed.

In [4, 5] zones with submarine cables and pipelines (and 500 m buffer) are avoided as well as these cables can be broken by anchoring or trawling. In the North Sea a lot of cables and pipelines are installed. Too many sites would be excluded by considering the zones with submarine cables and pipelines as a constraint. Therefore these zones have not been excluded in this work. Once optimal sites for the deployment of WECs have been selected, precautions against the damage of submarine cables and pipelines should be taken. Note that the crossing of cables and pipelines should be avoided when installing the electricity cable between the farm and the coastline as a crossing requires special precautions and causes a higher grid connection cost (chapter 10). The crossing of cables could be an extra factor in the MCDA. In this PhD dissertation this factor is not considered (section 3.2.2).

Zones with shipwrecks are also not taken into account in [5]. As a lot of shipwrecks are on the bottom of the North Sea, these zones are not excluded in this study. Again precautions need to be taken when shipwrecks occur in interesting locations for wave power conversion.

Further, zones with offshore wind farms are not excluded, as a combination of a farm of WECs and a farm of wind turbines could be possible. Combining both types of renewable energy may have several advantages [8]:

- Higher availability of produced power when swells continue after the wind has declined
- A more steady supply of power to the grid
- Lower grid connection cost by sharing the same transmission cable. A concession for the installation of the transmission cable to land is needed



when installing a farm of WECs. It is not known which areas are excluded in advance.

- Lower operation and maintenance costs (chapter 9)
- Smaller required area and environmental impact for the same power production

In the considered study area no ice accretion is observed. Consequently possible damage of wave energy converters due to ice should not be considered. When performing this analysis in other regions this constraint may be important.

All the considered constraints are finally merged in one map (Figure 3.2). An overview of all constraints is given in Figure 3.3. These locations will not be considered for further analysis.

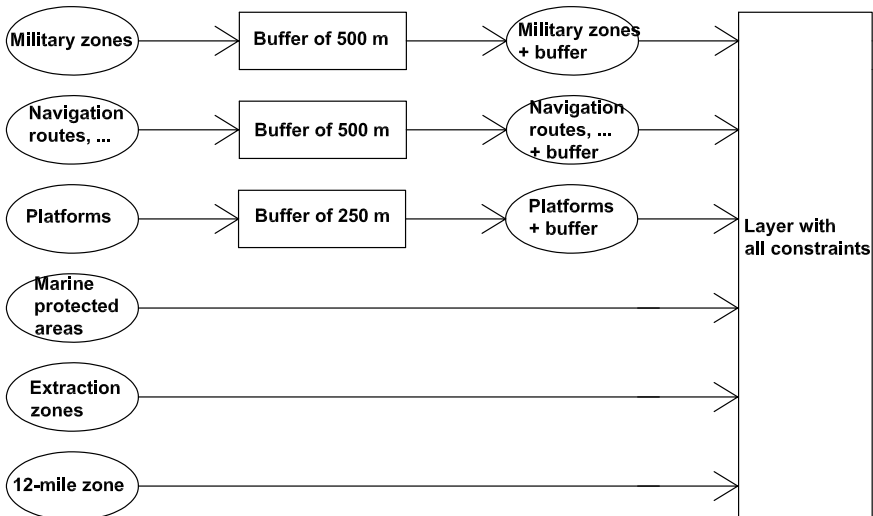


Figure 3.3: Methodology to obtain a layer with all constraints

### 3.2.2 Weighted factors

The remaining area is evaluated by use of factors. The significance of factors is quantified by means of scores and weights. The location of the shoreline, grid connections and harbours and the bottom type were acquired from paper charts for the considered area. The bathymetry was available in digital format. The following factors have been taken into account:

1. **Produced power:** the produced power is the most important feature as the ultimate goal is the production of a substantial amount of power at an

acceptable cost. The time averaged mean power produced by a WEC, as a function of the incident wave climate (sea state), is given in a power matrix. The mean annual produced power is obtained by multiplying the produced power in each sea state with its frequency of occurrence, given in a scatter diagram (chapter 2), and summing up the results. The Pelamis WEC has been taken as an example in this study, as it is the only WEC of which information on the cost components of a farm is publicly available [9, 10]. This information allows a better estimation of the relative weights of the considered factors (section 3.2.4). Furthermore, a power matrix of the Pelamis WEC, with a rated power of 750 kW, is available as well [9]. Note that the Pelamis WEC is not the most suitable WEC for the southern North Sea, as the production in smaller waves ( $\leq 1.5$  m) is rather low. The power produced by a single Pelamis WEC is considered as a factor. Note that losses due to planned and unplanned maintenance of the Pelamis WEC and transmission losses are not taken into account. The mean annual power produced by a single Pelamis WEC in the study area is shown on Figure 3.4. The *Create Thiessen Polygons* tool in ArcGIS has been used to transfer the results on discrete locations to a continuous surface. A Thiessen polygon is a polygon whose boundaries define the area that is closest to a buoy location relative to all other buoy locations. The value of the produced power on a buoy location is assigned to the whole area covered by the polygon.

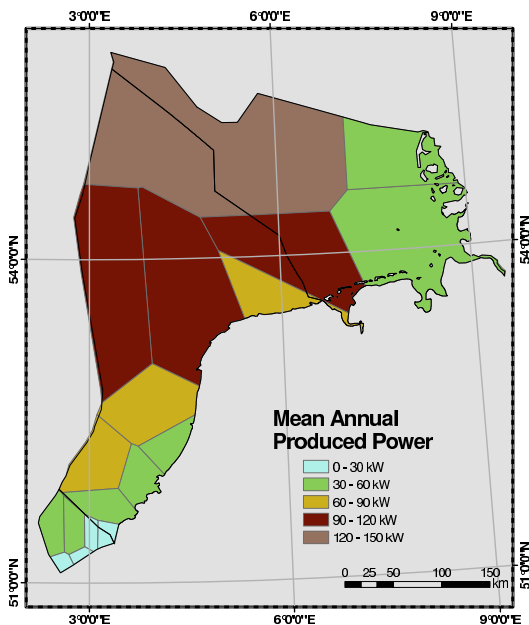


Figure 3.4: Mean annual produced power by a single Pelamis WEC

In Nobre et al. [4] the available wave power and the ranges of available wave heights and wave periods have been considered as three separate factors. The available wave power should be as high as possible while the available wave heights and wave periods should lie within the working limits of the device. These three factors are combined in the factor *produced power*, as considered in this PhD work. The higher the produced power the more the site is suitable for wave power conversion.

The production of a farm depends on the number of installed WECs and on the lay-out of the farm, which are both depending on the dimensions of the available area. The obtained interesting locations with this MCDA, should be studied in more detail to determine which location (and consequently farm) results in the smallest cost per produced kWh.

The estimation of the produced power, using scatter diagrams on a finer spatial grid, resulting from numerical wave simulations (chapter 2 - section 2.3.2), would be more accurate. As only hindcast data during 2003 and 2004 have been used to calculate the available wave power, as presented on Figure 2.24, it is chosen to use the widely spaced data from wave buoys and to create Thiessen polygons to cover the entire study area in this PhD dissertation.

2. **Distance to shore:** an important cost of a farm of WECs is the electrical cable connection to land (chapter 10). A location with a small distance to shore is preferred. The *Multiple Ring Buffer* tool has been used in ArcGIS to visualize the distance to the coast (Figure 3.5).
3. **Distance to grid connection:** once the installation of a submarine cable is executed, a land cable has to be installed towards the nearest and serviceable grid connection on land. The distance has to be minimized to keep installation and cable costs onshore as low as possible. Figure 3.6 shows the distance to the grid, again obtained with the *Multiple Ring Buffer* tool.

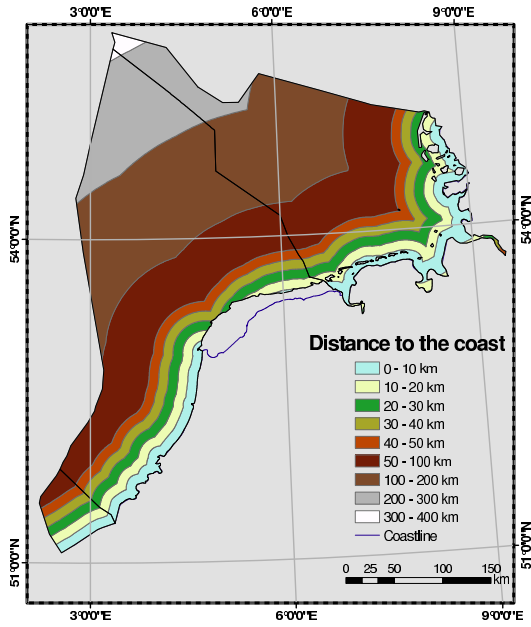


Figure 3.5: Distance to shore

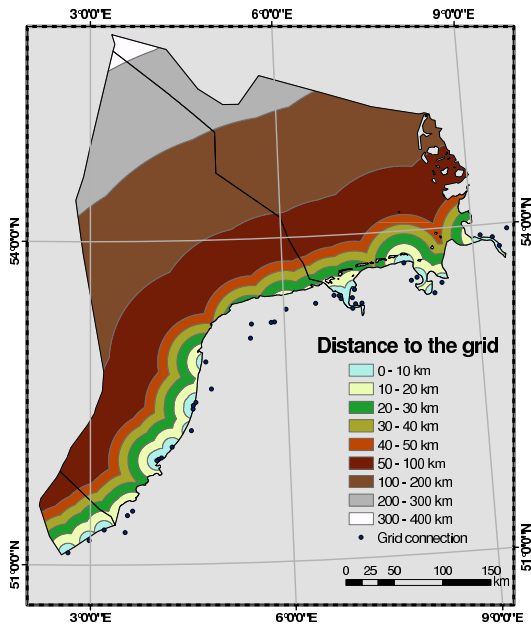


Figure 3.6: Distance to grid

4. **Distance to nearest harbour:** the distance to the nearest harbour takes partially the installation costs of the devices and the (un)scheduled maintenance and repair costs in consideration. A shorter distance is preferred. The harbours shown on Figure 3.7 have been considered. The *Multiple Ring Buffer* tool applied on the harbours results in Figure 3.7.

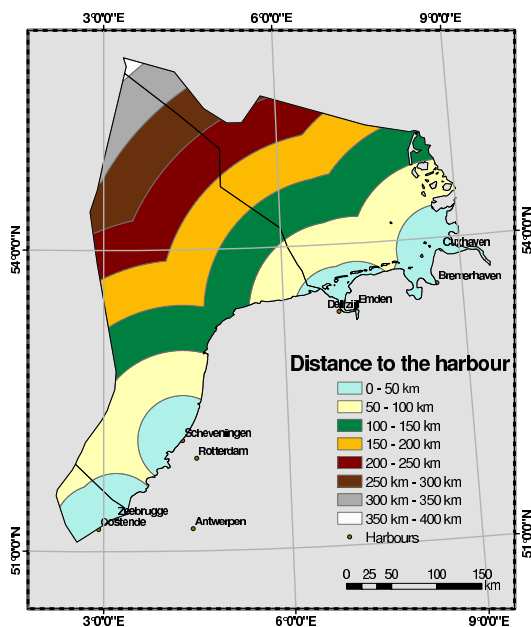


Figure 3.7: Distance to harbour

5. **Extreme wave conditions:** extreme conditions entail problems during installation, maintenance and repair, and can cause damage or failure during the operation of a WEC. The extreme wave condition is defined in this chapter as the significant wave height that occurs once in 25 years  $H_{s,25y}$ . This wave height has been estimated by extrapolating a Weibull distribution of the exceeding probability of the observed data on each location. A less severe wave climate is preferred. Figure 3.8 shows the extreme wave conditions after using the *Create Thiessen Polygons* in ArcGIS.
6. **Bimonthly variation of available wave power:** the bimonthly variation of available wave power indicates whether the wave climate is steady and reliable. A high variation in available wave power is not desired. On the DCS, the average available wave power during the months January-February, March-April, May-June, July-August, September-October, November-December is determined on all buoy locations. On the BCS the monthly

available wave power was calculated (Figure 2.5) at Westhinder and ZW-Akkaert. On the GCS no data were available.

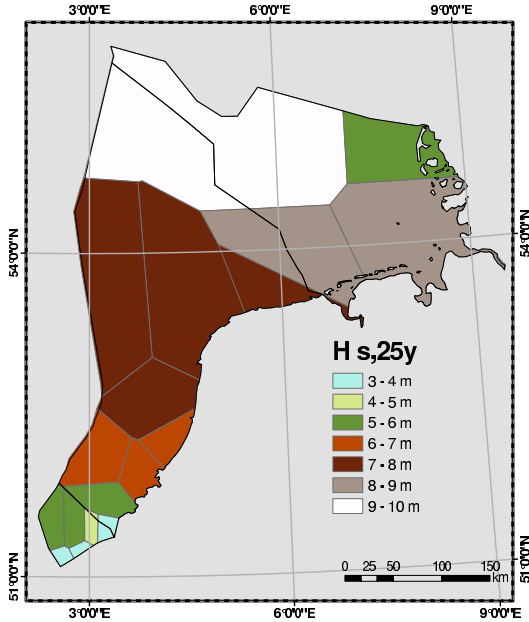


Figure 3.8: Extreme wave conditions ( $H_{s,25y}$ )

A bimonthly variability index ( $BV$ ) is defined, analogously with the seasonal and monthly variability index defined in [11].

$$BV = \frac{\bar{p}_{BM_{max}} - \bar{p}_{BM_{min}}}{\bar{p}} \quad (3.1)$$

with  $\bar{p}_{BM_{max}}$  the average available wave power of the two successive most energetic months,  $\bar{p}_{BM_{min}}$  the average available wave power of the two successive less energetic months and  $\bar{p}$ , the yearly average available wave power. With the *Create Thiessen Polygons* tool Figure 3.9 is obtained.

When  $BV$  is small the wave climate is less variable. When  $BV$  equals 1, the difference between available wave power in the most energetic months and in the least energetic months is equal to the yearly average available wave power. It is observed that the bimonthly variability index increases when the buoys are located further from shore and more northerly in the North Sea.

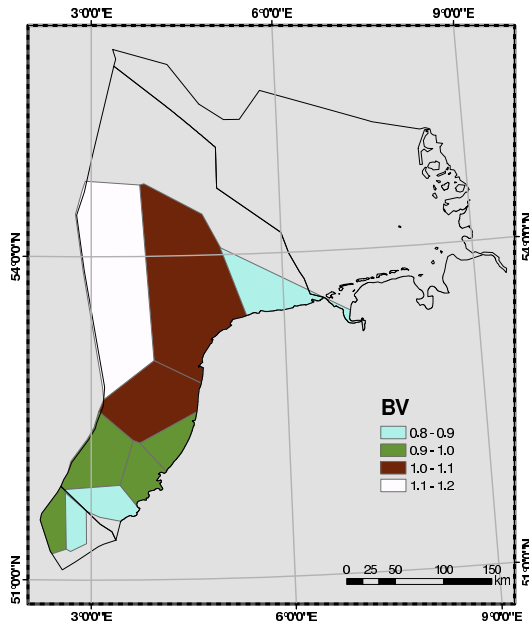


Figure 3.9: Bimonthly variability index (BV)

7. **Water depth:** the installation of a submarine cable and the type of anchorage system of a WEC depend on the available water depth. Furthermore some WECs require a minimal water depth for operation. The available water depth in the study area is shown in Figure 3.10.
8. **Geology / bottom type:** the bottom type (Figure 3.11) influences installation of submarine cables and the type of anchorage system for a wave energy converter. Installation in sand is easier compared to gravel.

The MCDA is restricted to the eight factors mentioned above. Additional factors, with a small impact, could be considered in future analysis:

- Crossing submarine cables: more crossings will increase the installation cost of the transmission cable.
- Guaranteed electricity purchase price in Belgium, Germany and the Netherlands.
- Directional variation of the wave climate: when designing the farm layout this aspect should be taken into account, as wake effects are direction dependent (part II). Wake effects may decrease the power production of several WECs in the farm.

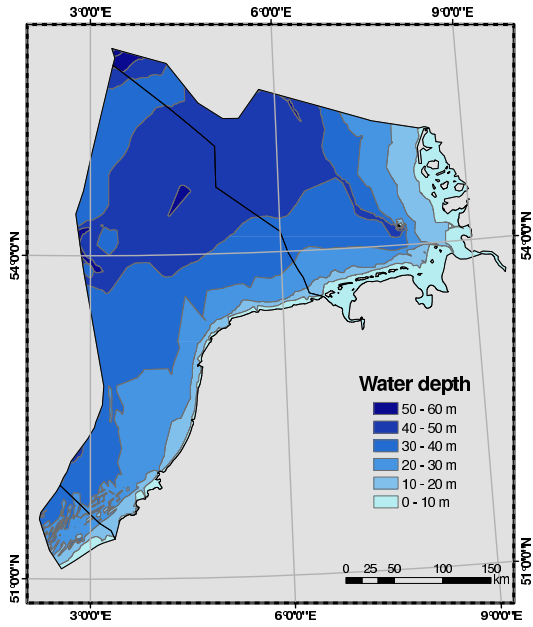


Figure 3.10: Water depth

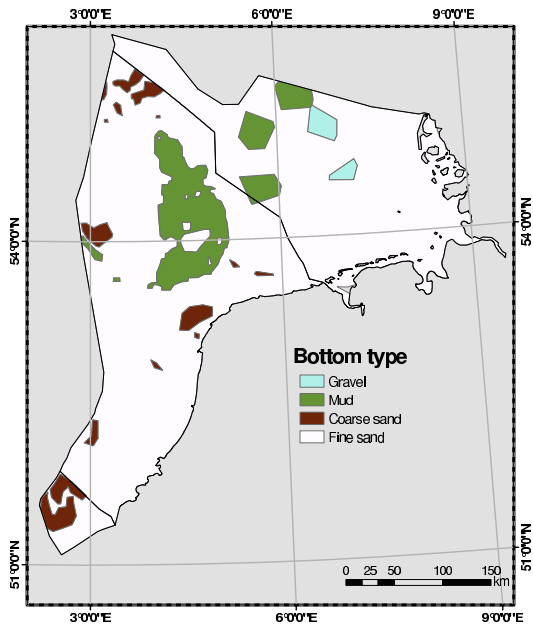


Figure 3.11: Bottom type



- Tides: some WECs perform worse in areas with high tides.
- Impact on other user groups: installation of a farm of WECs may have a visual impact, may create noise or may change the wave conditions (wake effects). For example, in [12] the conflict with the surfing community and industry caused by a possible wave height decrease through the installation of a 20 MW wave energy facility off the coast of Cornwall (UK), is discussed.
- Time to install and maintain a farm: high waves can prevent installation and maintenance.

### 3.2.3 Scores

Scores  $c_i$  describe the suitability of one single factor  $i$ . Values range between 0 (worst case) and 100 (best case). The scores  $c_i$  of some factors (a.o. water depth) depend on the type of converter.

The score for the factor *distance to the shore* varies between 100, if the distance is smaller than 10 km, and 0, if the distance equals 400 km (maximum distance from shore in the study area). A linear interpolation is made for the distances ranging from 10 km to 400 km. The closer the farm of WECs is installed to the coast, the smaller the installation, maintenance and grid connection costs. Since no detailed information is available of the variation of these costs with distance to coast, a linear correlation is assumed.

The same approach is used for the factors *produced power*, *distance to grid*, *distance to harbour*, *extreme wave conditions* and *bimonthly variation of available wave power*. The values of these factors, corresponding to  $c_i = 0$  and  $c_i = 100$  are given in Table 3.2. Note that a larger interval for *distance to harbour* is used as the costs affected by the distance to the harbour will differ less within 50 km, compared to the costs that are influenced by the factors *distance to the shore* and *distance to the grid*.

Table 3.2: Values of the factors 1 till 6 with score  $c_i = 0$  and  $c_i = 100$

Factor	$c_i = 0$	$c_i = 100$
(1) Produced power	9 kW	145 kW
(2) Distance to shore	400 km	$\leq 10$ km
(3) Distance to grid	400 km	$\leq 10$ km
(4) Distance to harbour	400 km	$\leq 50$ km
(5) Extreme wave conditions	9.5 m	$\leq 6.5$ m
(6) Bimonthly variation	1.125	0.875

The Pelamis WEC can produce power in waves with a  $H_s$  up to 6.5 m. Therefore it is assumed that the Pelamis WEC can withstand storms with  $H_s = 6.5$  m without special precautions. The factor *extreme wave conditions* is in this case equal to 100. Each location with  $H_{s,25y}$  which exceed this threshold (6.5 m) has a lower score as these significant wave heights impose higher loads on the WEC. The author wants to underline that the maintenance costs will increase with increasing wave height. Consequently a variation of the score for  $H_s$ -values smaller than 6.5 m should be considered as well. As the differences in maintenance costs in smaller and higher waves are not known, this aspect has not been taken into account in this work.

As in Nobre et al. [4], a discrete relation has been attributed to the factor *bottom type* (Table 3.3). The same scores as in the study of Nobre et al. [4] are used.

Table 3.3: Scores  $c_i$  for factor 8, bottom type

Geology	$c_i$ [-]
Fine sand	100
Coarse sand	80
Mud	20
Gravel	10

The ideal working depth of the Pelamis WEC is 50 m. A depth of 50 m or more is considered as the perfect working depth and has the maximum score of 100. The scores are given in Table 3.4.

Table 3.4: Scores  $c_i$  for factor 7, water depth

Water depth [m]	$c_i$ [-]
0	0
5	0
10	0
15	10
25	40
35	70
45	90
50	100
55	100
60	100

A low score has been ascribed to depths ranging from 0 m till 10 m, and the

highest scores have been assigned to depths ranging from 50 m to 60 m. The installation cost of the submarine cable and the type of anchorage system is also depth dependent. However, as the depth in the considered area is only varying between 0 m and 60 m, only very small differences in these costs will occur. When more detailed information about the minimal working depth of the Pelamis WEC becomes available, a score equal to zero should be attributed to areas with a smaller water depth.

### 3.2.4 Weights

A comparison between the different factors is quantified by means of weights  $W_i$ . Weights define the importance of one factor compared to another factor. The sum of all weights equals 100. The selection of weights attributed to each factor is one of the most contentious tasks in the planning process. Different decision groups, like investors and researchers, will attach great importance to different factors. Furthermore, the attribution of weights is device dependent. One WEC compared to another may be for example far more sensitive to extreme wave conditions. This means that a higher weight will have to be assigned to this factor.

The weights can be determined by using literature investigation [4], cost calculations or pairwise comparison. An average weight based on these three methods is calculated in this section to increase the reliability of the applied weights. The weights, used in Nobre et al. [4], are considered as a first set of values for  $W_i$ . Secondly, each factor is related to specific costs. The factor *extreme wave conditions* for example has an impact on the maintenance, repair, installation and insurance costs of a wave energy converter. The percentage of the latter costs in the total cost is defined as the weight for the factor *extreme wave conditions*. The costs analysed in chapter 10 have been used to estimate the weights. And finally, in a third method, the weights  $W_i$  have been estimated based on a pairwise comparison for the relative importance of both factors [13]. Ratings are provided on a 9 point continuous scale [14] (Table 3.5).

The ratings are entered in a pairwise comparison matrix (Table 3.6). Since the matrix is symmetrical only the lower triangular half actually needs to be filled. The remaining cells are the reciprocals of the lower triangular half. For example, factor 1 (*produced power*) is 3 times more important (or *moderately more important*) than factor 3, *distance to the grid connection* (Table 3.6). One should note that the estimation of the relative importance of the different factors is implicitly related to cost. The author wants to stress that the pairwise comparison, presented in this work, should be based on discussions with all involved parties when planning to install a farm of WECs.

Table 3.5: Continuous rating scale [14]

Scale of importance	
1/9	extremely less important
1/7	very strongly less important
1/5	strongly less important
1/3	moderately less important
1	equally important
3	moderately more important
5	strongly more important
7	very strongly more important
9	extremely more important

Table 3.6: Definition of weights by pairwise comparison (Factor 1: produced power, Factor 2: distance to shore, Factor 3: distance to grid connection, Factor 4: distance to nearest harbour, Factor 5: extreme wave conditions, Factor 6: bimonthly variation of available wave power, Factor 7: water depth, Factor 8: geology)

Factor	1	2	3	4	5	6	7	8
1	1							
2	1/7	1						
3	1/3	3	1					
4	1/9	1/5	1/7	1				
5	1/7	1/5	1/7	1	1			
6	1/5	1/3	1/3	1	3	1		
7	1/9	1/5	1/7	1/3	1	1/5	1	
8	1/9	1/5	1/7	1/3	1/3	1/3	5	1

Further, each value in Table 3.6 is divided by the sum of its column and multiplied by 100. Finally, the average value of each row determines the weight,  $W_i$ , of each factor. The weight for factor 1 with the pairwise comparison equals 39.5.

Finally an average weight has been calculated, based on the three methods (literature investigation, cost calculation, pairwise comparison). These weights are given in Table 3.7. It is clear that the factor *produced power* is the most important factor, followed by the factors *distance to the grid* and *distance to the coast*. These latter factors are related to the cost of the transmission cable. Also *distance to the harbour* has a relatively high weight, because of its relation with

the installation and maintenance costs. The factors *water depth* and *bimonthly variation of the available wave power* have a small weight, as the differences in depth and bimonthly variation in the North Sea are relatively small.

Table 3.7: Weights  $W_i$  for the basic scenario

Factor	$W_i$ [-]
Produced power	38
Distance to shore	12
Distance to grid	20
Distance to harbour	10
Extreme wave conditions	9
Bimonthly variation	3
Water depth	2
Geology	6

### 3.2.5 Suitable locations in the southern North Sea

Once every weight and score is determined a total final score  $Sc_k$ , indicating the suitability, of each location  $k$  can be calculated:

$$Sc_k = \sum_{i=1}^8 c_{k,i} W_i \quad (3.2)$$

where  $c_{k,i}$  is the score for factor  $i$  on location  $k$  and  $W_i$  is the weight for factor  $i$ . A high score indicates that the location is suitable for the deployment of a farm of Pelamis WECs.  $Sc_k$  cannot be higher than 10 000.<sup>1</sup>

Figure 3.12 shows the results for the weights represented in Table 3.7. The best locations are coloured brown, gray and white (highest total scores) and the worst zones are coloured blue and green. The minimum and maximum score is 5 317 and 8 194, respectively. The best location is situated near shore on the German Continental Shelf. The most suitable area on the Dutch Continental Shelf is located near shore, next to the border with the German Continental Shelf. Figure 3.12 shows that accessible areas with a relatively high energetic wave climate and situated rather close to the shore are preferred.

<sup>1</sup>When all factors have a score  $c_i$  equal to 100, a total score  $Sc$  of 10 000 is obtained.

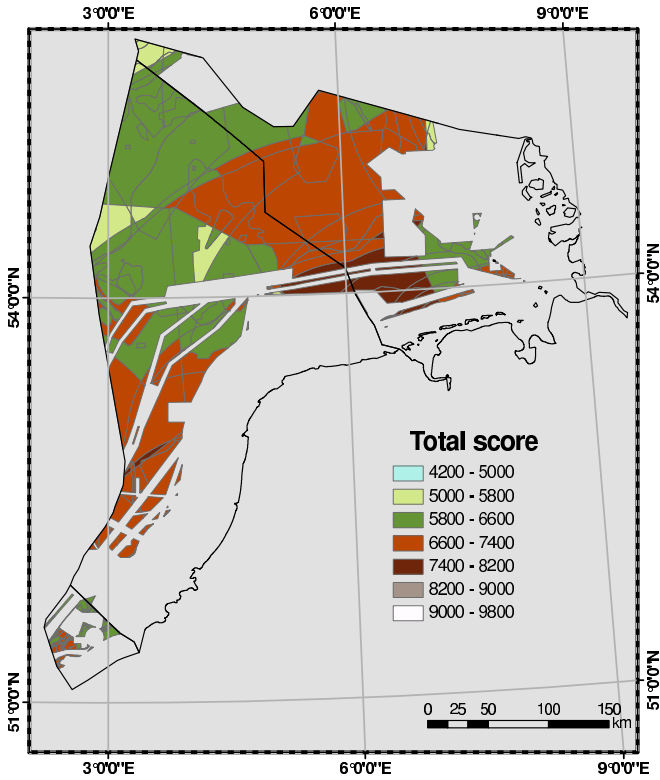


Figure 3.12: Total score for the basic scenario on the Belgian, Dutch and German Continental Shelf

In Figure 3.13 the Belgian Continental Shelf is shown in more detail. In general the scores of the locations on the BCS are comparable with the scores of most locations on the DCS and GCS. The difference between the scores on the BCS is rather small. In the following analysis this scenario is the basic scenario.

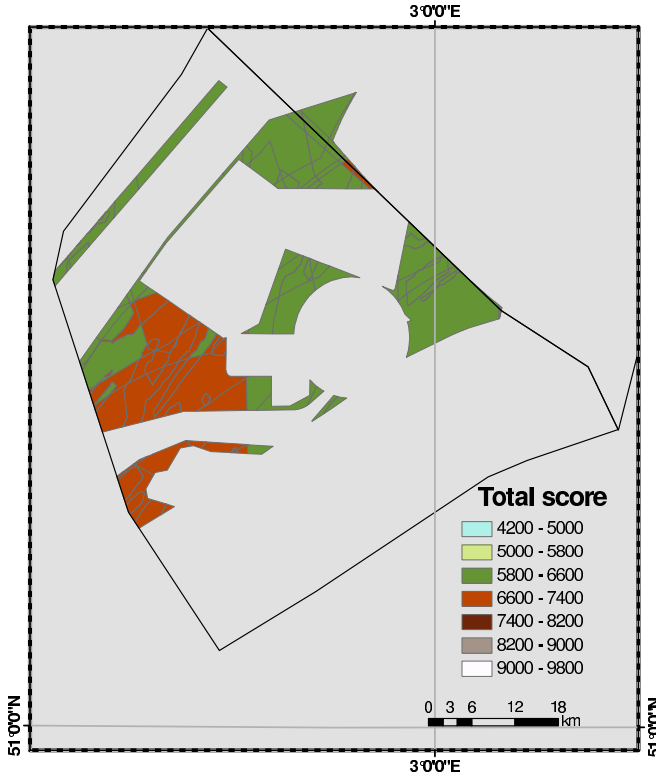


Figure 3.13: Total score for the basic scenario on the Belgian Continental Shelf

### 3.3 Sensitivity analysis

As estimating the relative importance (weight) of the selected factors is not an easy and straightforward task, a sensitivity analysis is performed by varying the weights of three factors (*produced power*, *distance to the grid* and *extreme wave conditions*). The impact of their weights on suitable locations for wave energy conversion is studied. In [2] it was seen that changing the weights of the factors had only a small influence on the selected areas for wind farm deployment.

Changing the weight of a factor will affect the weight of the other factors as the sum of all weights has to be equal to 100. All other factors will equally be scaled. If for example, a variation on the weight of *produced power* (factor 1) is considered, the new weights of the other factors can be determined with equation (3.3):

$$W_{i,n} = W_{i,o} \left( 1 - \frac{W_{1,n} - W_{1,o}}{100 - W_{1,o}} \right) \quad (3.3)$$

where  $W_{i,n}$  is the new weight of factor  $i$ ,  $W_{i,o}$  is the old weight of factor  $i$ ,

$W_{1,n}$  and  $W_{1,o}$  are respectively the new and old weight of the varying factor 1, *produced power*.

### 3.3.1 Importance of factor *produced power*

As the factor *produced power* has the maximum weight (Table 3.7), it is expected that varying the weight of this factor will have the largest impact on the most convenient locations for the deployment of a farm of Pelamis WECs. Figure 3.14 shows the best locations when the weight for the *produced power* is respectively 20 and 60. Weights between 20 and 60 have been considered in [15].

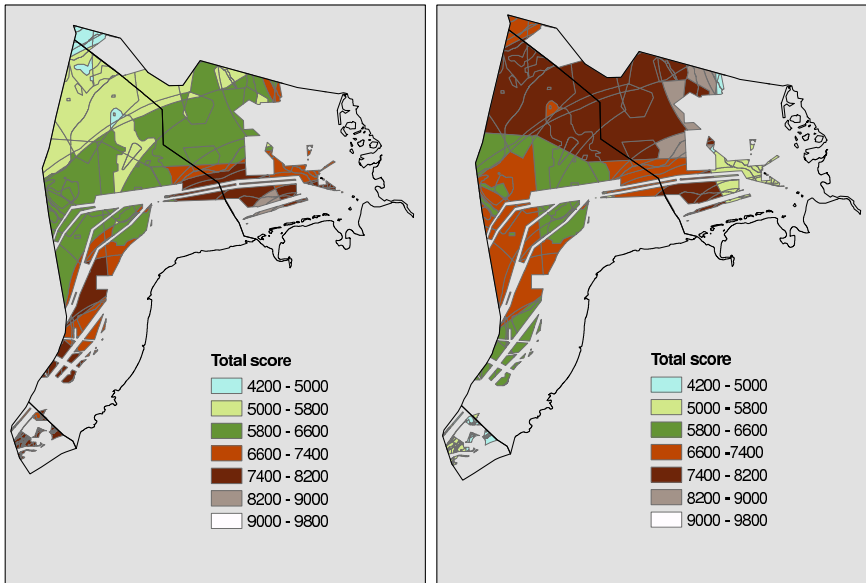


Figure 3.14: Total score for a weight of the produced power of 20 (left) and 60 (right)

The best locations do not change when the weight varies between 20 (Figure 3.14 - left) and 38 (basic scenario - Figure 3.12). When the weight equals 20 more near shore locations on the DCS and BCS become suitable for the installation of a farm of Pelamis WECs. When the weight is higher than 38 locations situated further off the coast are preferred (Figure 3.14 - right). Note that the locations on the BCS clearly have a lower score than locations on the DCS and GCS when the weight is equal to 60. Lowering the weight below 38 results in interesting locations closer to the shore which do not dispose of the maximum produced power.

When the weight is smaller than 38 the relative importance of the factors which give preference to a near shore location (*distance to the shore, grid and harbour,*



*extreme wave conditions* and *bimonthly variation of the available wave power*), rises. In that case the ratio between the factor *produced power* and the sum of the factors *distance to the shore*, *grid and harbour*, *extreme wave conditions* and *bimonthly variation of the available wave power* is smaller than 0.7. The score of the factor *water depth* is, like the factor *produced power*, higher for locations further from shore. As the weight of the factor *water depth* is very small compared to the weight of the factor *produced power*, the weight of the factor *water depth* is neglected when calculating this ratio. Note that the factor *geology* does not give preference to a far or near shore location.

The estimation of the weight of the factor *produced power* is very strong related to the estimation of the revenues of a farm of WECs. When the electricity price is high and support is available, a higher weight can be applied. On the other hand, in the case of a low electricity price and lack of support, the weight should be smaller.

### 3.3.2 Importance of factor *distance to the grid*

The second most important factor is the distance to the electricity grid (Table 3.7). When the weight of this factor equals 10 (Figure 3.15 - left) more locations further off shore become suitable for the installation of a farm of Pelamis WECs.

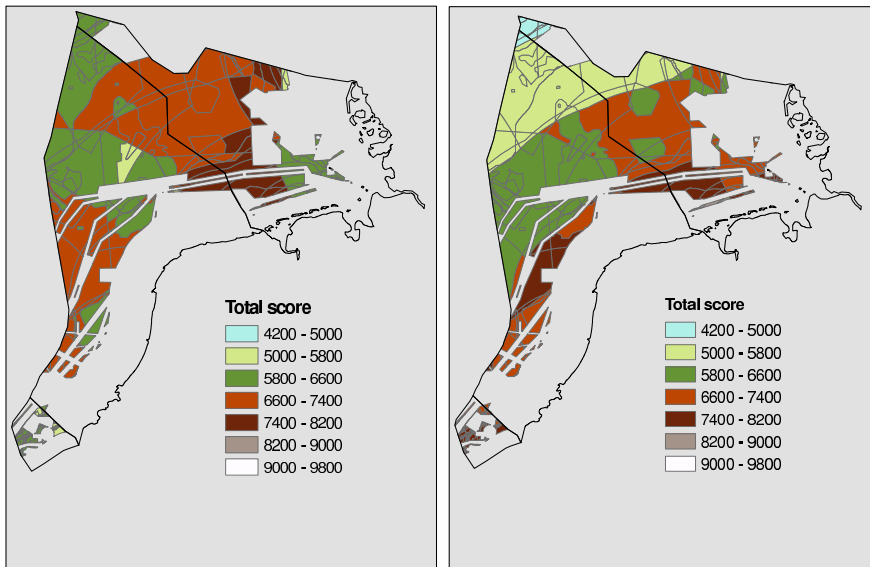


Figure 3.15: Total score for a weight of the distance to the grid of 10 (left) and 50 (right)

Near shore regions which were not attractive in the basic scenario, a.o. on the

DCS, become more suitable, when the weight equals 50 (Figure 3.15 - right). The locations which are situated far from shore are completely non-attractive in this case. Weights between 10 and 50 have been considered in [15].

Again the ratio between the factor *produced power* and the sum of the factors *distance to the shore*, *grid and harbour*, *extreme wave conditions* and *bimonthly variation of the available wave power* determines whether location further from shore or closer to shore are preferred. When this ratio is smaller than approximately 0.7 - 0.75 (when the weight of *distance to the grid* is higher than 20) locations near shore are preferred. Varying the weights of the factors *distance to the shore* and *harbour* results in the same effect as discussed in this section.

### 3.3.3 Importance of factor *extreme wave conditions*

A variation in weight from 0 to 30 is finally considered for the factor *extreme wave conditions* (Figure 3.16).

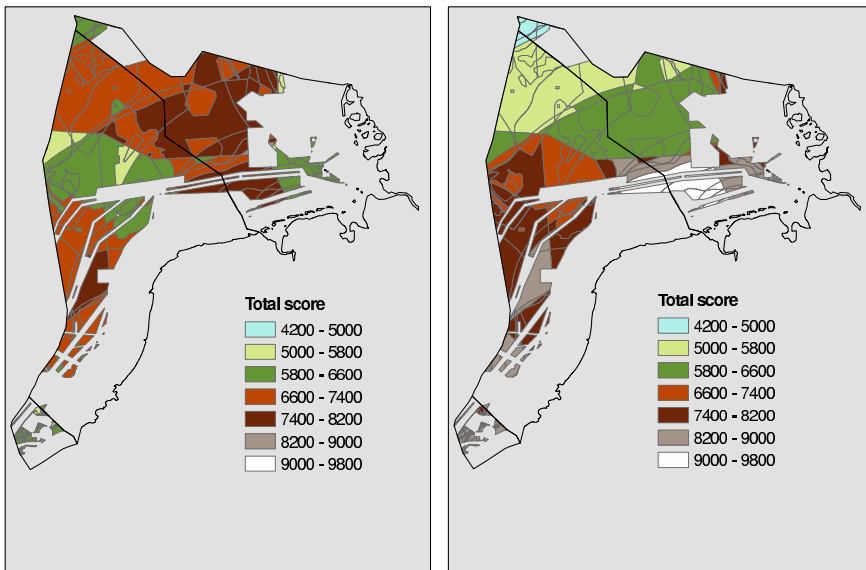


Figure 3.16: Total score for a weight of extreme wave conditions of 0 (left) and 30 (right)

More values between 0 and 30 are considered in [15]. When the weight equals 0 more dark brown areas on the DCS and GCS are observed compared to the basic scenario, but the furthest locations are still not suitable. An increase of the weight from 0 to 30 results in white areas with a maximum score of 9 791, located near shore on the GCS. Furthermore, more location on the BCS and DCS become attractive for wave power conversion compared to the GCS.

In general the ratio between the weight of the factor *produced power* and the sum of the weights of the factors *distance to shore*, *grid and harbour*, *extreme wave conditions* and *bimonthly variation of the available wave power* determines whether areas near shore or offshore are preferred. A ratio smaller than 0.7 - 0.75 [15] gives preference to the deployment of a farm of WECs closer to shore.

When studying Figure 3.12 till Figure 3.16, it is observed that a near shore area on the GCS and its continuation on the DCS has a relatively high score in all cases (dark brown, gray or white). The feasibility of a farm of Pelamis WECs in this area will be studied in chapter 10.

### 3.3.4 Installation in 12-mile zone

A possible relaxation of one or more restrictions may identify even better locations for wave power conversion [5]. The impact of the possibility to install WECs within the 12-mile zone is shown in Figure 3.17. It is observed that some locations near shore on the German Continental Shelf are very attractive for the installation of a farm of Pelamis WECs (gray).

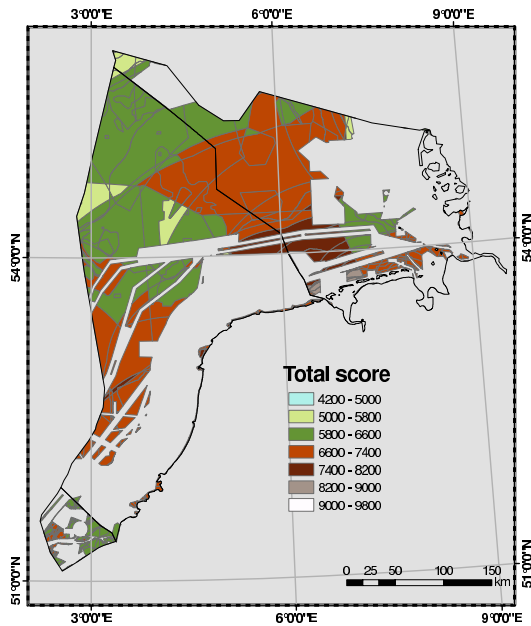


Figure 3.17: Total score with installation within the 12-mile zone

### 3.4 Accuracy of the geo-spatial multi-criteria decision analysis

The choice of a location to deploy a farm of wave energy converters in the North Sea is complicated. A GIS-based multi-criteria decision analysis gives a first indication of potential locations for wave power conversion. In future, additional factors such as visual impact and tide could be easily taken into account in the analysis. Further, more advanced expertise in wave energy will allow a better estimation of the applied weights. Recently (September 2008) a farm of 3 Pelamis WECs is installed in Portugal. The experience gained with the installation and operation of this farm will allow a more accurate estimation of the relative weights of the factors considered in the MCDA.

One should note that the accuracy of the outcome of the GIS analysis depends on the accuracy of source data. Errors in one layer will have propagated through the analysis and may cause larger inaccuracies in the output map, when combined with errors from other layers. Consequently the resulting maps are less accurate than the least accurate layer used in the analysis.

### 3.5 Conclusions

In this chapter a geo-spatial multi-criteria decision analysis has been performed to identify possible locations for the deployment of a farm of Pelamis WECs in the southern part of the North Sea. The methodology and the considered constraints and factors have been described in detail. In general, accessible areas with a relatively high energetic wave climate and situated rather close to the shore are preferred. A near shore area on the German Continental Shelf is most suitable for the installation of a farm of Pelamis WECs. The best location on the Dutch Continental Shelf is located near shore and borders on the German Continental Shelf. Allowing wave power conversion in the 12 mile zone results in even better locations for the installation of a farm of Pelamis WECs on the GCS.

In the multi-criteria decision analysis several factors are weighted according to their relevance. The attribution of a weight to each factor is a difficult and contentious task. Therefore a sensitivity analysis of the weights of the factors has been performed. It is mainly the ratio between the weight of the factor *produced power* and the sum of the weights of the factors *distance to shore, grid and harbour, extreme wave conditions* and *bimonthly variation of available wave power* that determines the location of suitable areas for the exploitation of a farm of Pelamis WECs. A ratio smaller than 0.7-0.75 gives preference to near shore locations.

In future, a more accurate estimation of the weights of the considered factors will be possible with practical experience from the first farms of WECs.

## References

- [1] J. Malczewski. *GIS-based multicriteria decision analysis: a survey of the literature*. International Journal of Geographical Information Science, 20:703–726, 2006.
- [2] S.M.J. Baban and T. Parry. *Developing and applying a GIS-assisted approach to locating wind farms in the UK*. Renewable Energy, 24:59–71, 2001.
- [3] H.S. Hansen. *GIS-based multi-criteria analysis of wind farm development*. In Proceedings of the 10<sup>th</sup> Scandinavian Research Conference on Geographical Information Science, Stockholm, Sweden, 2005.
- [4] A. Nobre, M. Pacheco, R. Jorge, M.F.P. Lopes, and L.M.C. Gato. *Geo-spatial multi-criteria analysis for wave energy conversion system deployment*. Renewable Energy, 34:97–111, 2009.
- [5] R. Prest, T. Daniell, and B. Ostendorf. *Using GIS to evaluate the impact of exclusion zones on the connection cost of wave energy to the electricity grid*. Energy Policy, 35:4516–4528, 2007.
- [6] F. Van Hulle, S. Le Bot, Y. Cabooter, J. Soens, V. Van Lancker, S. Deleu, J. P. Henriët, G. Palmers, L. Dewilde, J. Driesen, P. Van Roy, and R. Belmans. *Optimal offshore wind energy development in Belgium*. Technical report, Scientific support plan for a sustainable development policy, 2004.
- [7] F. Maes. *The international legal framework for marine spatial planning*. Marine Policy, 32:797–810, 2008.
- [8] M.T. Pontes, A.M. Sempreviva, R. Barthelmie, G. Giebel, P. Costa, and A. Sood. *Integrating Offshore Wind and Wave Resource Assessment*. In Proceedings of the 7<sup>th</sup> European Wave and Tidal Energy Conference (EWTEC), Porto, Portugal, 2007.
- [9] M. Previsic. *System Level Design, Performance and Costs for San Francisco California Pelamis Offshore Wave Power Plant - E2I EPRI Global-006A-SF*. Technical report, EPRI, 2004.
- [10] *Pelamis WEC - Conclusion of primary R&D - ETSU V/06/00181/REP*. Technical report, OPD.
- [11] A.M. Cornett. *A global wave energy resource assessment*. In Proceedings of the 18<sup>th</sup> International Offshore and Polar Engineering Conference (ISOPE), Vancouver, Canada, 2008.

- [12] P.M. Connor. *Wave Energy: Going down the Tube?* In Proceedings of the 7<sup>th</sup> European Wave and Tidal Energy Conference (EWTEC), Porto, Portugal, 2007.
- [13] T.L. Saaty. *A scaling method for priorities in hierarchical structures*. J. Math. Psychol., 15:234–281, 1977.
- [14] J. Ronald Eastman. *IDRISI Guide to GIS and Image Processing*. Technical report, Clark University, USA, 2006.
- [15] I. Ydens and V. Meirschaert. *Onderzoek naar een economische exploitatie van het golfenergiepotentieel in de Noordzee m.b.v. ArcGIS*. Master's thesis, Ghent University, 2008.

## **Part II**

# **Production of a farm of wave energy converters**





# 4

## Wave farm modelling

### 4.1 Introduction

In a second part of this PhD research the possible power production of a farm of WECs in the North Sea is estimated. In particular the impact of the farm layout on the power production is assessed. The wave climate and corresponding wave power resource in the North Sea have been studied in chapter 2. In order to estimate the overall wave power absorption of a farm in the North Sea, the interaction between the WECs need to be considered. Several methods to model a farm of WECs have been developed.

In this chapter a concise overview of these methods, is given. Especially the applicability of wave propagation models for wave farm modelling is discussed. Furthermore, the possibility to model a farm of WECs in the mild-slope wave propagation model MILDwave, used in this dissertation, is explained. The preference for this wave propagation model is briefly supported. A general description of MILDwave can be found in chapter 5. The power production of a farm of WECs studied in MILDwave, is described in chapters 6, 7 and 8.

### 4.2 State of the art in wave farm modelling

A lot of research has been carried out on the hydrodynamic behaviour of WECs based on the oscillation principle (first category) in an array. The hydrodynamic problem of wave power absorption is usually studied as a combination of two

simpler problems: the diffraction problem (scattered incident wave field due to the presence of the WEC) and the radiation problem (wave field generated by the body or water column oscillations).

An overview of theoretical methods used to calculate the hydrodynamic interaction of oscillating bodies in arrays is given in [1]:

- (i) The point-absorber method where the scattered waves are neglected under the assumption that the device dimension is much smaller than the wave length [2–4].
- (ii) The plane wave approximation where all scattered and radiated waves are approximated as plane waves under the assumption that the device spacing is many wave lengths [5–7].
- (iii) The multiple scattering method which accounts accurately for all hydrodynamic interactions [8–10].

A theoretical study concerning an infinite periodic array of identical oscillating water columns can be found in [11].

Recently, with the improvement of computer technology, Boundary Element Methods based on potential flow (e.g. WAMIT [12]) have intensively been used to study the hydrodynamic interaction of multiple oscillating bodies in an array (a.o. [13], [14] and [15]). Still the required simulation time is increasing rapidly with the number of bodies considered in the arrays and the dimensions of the domain.

The before mentioned studies all concentrate on maximizing the absorbed power of an array of oscillating bodies or oscillating water columns. As a change in wave height behind a large farm may affect other activities in the oceans (chapter 3), the knowledge of the wake of a single WEC and the wave height reduction in the lee of a farm is as important in the design of a farm of WECs. The study of the latter aspects requires a large computational domain which makes the discussed Boundary Element Methods less convenient. Recently the coastal impact of a farm of WECs has been studied in numerical wave propagation models. Millar et al. [16] have used the spectral wave propagation model, SWAN [17], to study the change of the wave climate caused by the installation of a farm of WECs 20 km off the north coast of Cornwall, UK. In Venugopal et al. [18] an array of five bottom mounted, fixed WECs has been modelled in a nonlinear Boussinesq wave model (MIKE 21). In the latter models the WEC is simplified as a porous structure which is able to extract a predefined amount of wave power. This way the incoming waves are partly reflected, diffracted, transmitted and absorbed by the

WEC. This simplification is only applicable to the second category of WECs, i.e. WECs based on the overtopping principle, as absorption of power is not caused by generation of waves. Nevertheless, Mendes et al. [19] have investigated the near shore wave climate, when multiple farms of Pelamis WECs (first category) are installed in the Portuguese Pilot zone, in a linear mild-slope wave propagation model REFDIF [20]. The Portuguese Pilot zone is a sea trial facility (320 km<sup>2</sup>) 5 to 20 km off the northwest Portuguese coast. This study has been extended by Le Crom et al. [21], which used SWAN instead of REFDIF. Also Vidal et al. [22] have studied the coastal impact of a farm of WECs of the first category (PowerBuoys) in a mild-slope equation model. Radiated waves from the motions of the WECs were neglected in these studies.

## 4.3 Discussion on the applicability of wave propagation models for wave farm modelling

### 4.3.1 Implementation of a farm of WECs in wave propagation models

Wave propagation models are usually classified in two types, i.e. phase-averaged spectral models and phase-resolving time domain models. Spectral models describe the evolution of the wave energy spectrum (wave action equation) while time domain models calculate the sea surface as a function of time (conservation of mass and momentum equations).

**Spectral models** (e.g. SWAN) take into account all relevant wave generation and dissipation processes over large spatial domains. A phase-decoupled refraction-diffraction approximation has been implemented [23] in SWAN to account for diffraction, as the wave action equation is based on refraction principles only. In Ilic et al. [24] the wave diffraction feature in SWAN has been studied using laboratory and field data. They observed a more accurate estimation of the wave heights in the lee of the obstacle with increasing frequency and directional spreading. On the other hand in Enet et al. [25] results in SWAN have been compared with analytical results for the wave height and wave direction in the lee of a semi-infinite breakwater in water of constant depth. They concluded that the results with diffraction feature in SWAN were considerably better than the results without diffraction for a decreasing directional spreading.

Millar et al. [16] have used the phase-averaged model SWAN to implement an array of WECs as a 4 km long partially transmitting obstacle, with energy transmission of respectively 0 %, 40 %, 70 % and 90 % of the incident wave energy. The significant wave height  $H_s$  and mean wave period  $T_m$  in the lee of the obstacle have been calculated on a grid with 200 m spatial resolution for a number

of reference sea states (for varying  $H_s$ ,  $T_m$  and mean wave direction). Millar et al. [16] found that the magnitude of wave height change was varying with reference sea state, level of energy transmission and location. For the most realistic wave energy transmission levels, ranging from 70 % to 90 % of the incident wave energy, the resulting average significant wave height change at the shoreline is rather small, decreasing from respectively 1.5 % to 0.5 %, while the maximum significant wave height change is respectively 6.7 % and 2.3 %. When swell waves are dominating (limited directional spreading) an increased wave height change is expected, since wind waves with a directional spreading of  $30^\circ$  had been considered in the latter study.

In Smith et al. [26], the previous study of Millar et al. [16] has been extended and generalised. A grid of 210 km by 400 km with a resolution of 500 m has been considered to study the wave height change over 200 km along the central axis behind the partially transmitting obstacle. Various parameters that impact on the onshore wave climate have been studied: the length of the obstacle perpendicular to the incoming wave (3 km, 6 km, 9 km, 12 km and 15 km), the distance of the obstacle from the shoreline, the level of wave energy transmission through the obstacle (0 %, 40 %, 70 % and 90 % of the incident wave energy) and the directional spreading of the local wave climate ( $10^\circ$ ,  $15^\circ$ ,  $20^\circ$  and  $30^\circ$ ). Smith et al. [26] observed an increasing wave height reduction in the lee of the obstacle with decreasing directional spreading. Farms of WECs are not likely to be installed 210 km off the coast, as the cost of a farm is increasing with increasing distance from shore (chapter 10). Therefore a smaller domain can be considered when studying a farm of WECs.

The spectral model SWAN has some restrictions which need to be considered. First, when swell waves are dominating the impact on the coastal wave climate is the highest. In that case the performance of the diffraction feature in SWAN is less accurate [24]. Secondly, the dimensions of the obstacle are limited by the spatial grid resolution (500 m in [26]). The recommended values for spatial resolution in SWAN are 50 m up till 1000 m [17]. To overcome the latter restrictions time domain models have been used.

**Time domain models** may be categorized into models based on (i) the linear mild-slope and (ii) the nonlinear Boussinesq equations. The mild-slope equations describe the transformation of linear water waves when propagating from deep to shallow water while the Boussinesq equations (e.g. MIKE 21) predict the propagation of nonlinear waves with high accuracy, especially in shallow water, but are computationally very demanding [27].

In Mendes et al. [19] the wave height (regular waves) and wave direction on the 10 m water depth contour behind 2 configurations of farms of Pelamis WECs, both with a total installed capacity of 202.5 MW and a total length of 16 km, have

been assessed in the **mild-slope model** REFDIF. Each farm has been modelled as an energy dissipating area in the computational domain with a grid spacing varying from 20 m till 40 m. For both configurations the maximum observed wave height change is less than 15 %. The maximum length of the coast affected by the farms is 25 km, while a wave height change higher than approximately 12 % is observed along only 0.6 km of coast. This study has been extended in [21]. Le Crom et al. [21] have used the spectral wave propagation model SWAN instead of the time-domain model REFDIF. The wave height decrease on the 10 m water depth contour behind five different configurations of several farms has been studied for irregular short-crested waves. A grid resolution of 25 m till 175 m has been used. An average and maximum wave height decrease of 10 % and 11.8 % are observed. Furthermore a comparison with REFDIF results reveals a less important but broader coastal impact of the installed farms in SWAN. This is mainly due to the consideration of directional spreading of the incident waves in SWAN.

In Vidal et al. [22] an overall wave height transmission coefficient of a farm of PowerBuoys has been calculated ( $= 0.96$ ) to study the coastal impact in a mild-slope wave propagation model. A negligible coastal impact of the farm is observed.

In Venugopal et al. [18] five bottom mounted, fixed WECs have been implemented as individual porous structures with a prescribed degree of porosity in a nonlinear **Boussinesq wave model** (MIKE 21). The changes in the wave pattern around the array have been studied on a grid with 10 m resolution for different levels of porosity while considering uni-directional irregular waves with significant wave height of 4 m and peak wave period of 10 s.

### 4.3.2 Shortcomings

The modelling approach of Millar et al. [16] and Smith et al. [26] has two major limitations which result in a rough estimate of the wave height reduction behind a farm:

- First by simplifying a farm to one transmitting obstacle, the redistribution of wave energy around the WECs in the farm due to (i) an alternation of full (gaps between the WECs) and partial transmission (through the WECs), (ii) diffraction, and (iii) radiation (floating WECs), is not taken into account.
- Secondly, one transmitting obstacle causes a proportional decrease of energy for all frequencies in the spectrum [26], while the efficiency of a WEC will vary across the spectrum.

The first limitation also applies for the method used in Mendes et al. and Vidal et al. [19, 22] while in Le Crom et al. [21] each Pelamis WEC is modelled

individually without considering reflection and radiation. Furthermore, each WEC in the farm has the same frequency-independent transmission coefficient in Le Crom et al. [21].

In the study of Venugopal et al. [18] reflection and transmission are coupled through the degree of porosity of the structure, which makes the adaptation to the incident wave climate of a WEC in a farm impossible.

### 4.3.3 Mild-slope wave propagation model MILDwave

To overcome the shortcomings of the approach in the mentioned studies a specific technique is developed in this PhD dissertation to simulate the absorbing effect of the WEC more accurately using a mild slope equation model. Based on the first derivation of the elliptic mild-slope wave equation by Berkhoff [28], the parabolic model [29] and the hyperbolic model [30] have been developed to study the propagation of monochromatic waves in larger coastal areas. In the parabolic model wave reflection and diffraction in the direction of wave propagation are neglected. Time-dependent mild-slope equations have been developed to study the transformation of random waves with a narrow frequency band. Radder and Dingemans [31] have derived a canonical form of the time-dependent mild-slope equations based on the Hamiltonian theory of surface waves, taking into account the mild-slope assumption  $\frac{|\nabla h|}{kh} \ll 1$ , where  $\nabla$  is the horizontal gradient operator,  $h$  the water depth and  $k$  the wave number. Booij [32] proved that the equations were only valid for a bed steepness up to 1/3. Suh et al. [33] extended the latter model to study wave propagation on a rapidly varying impermeable bathymetry by considering higher-order bottom effect terms proportional to the square of bottom slope and to the bottom curvature. A detailed review of the evolution of the mild-slope equations can be found in [34]. More recently a mild-slope equation model has been developed to study wave propagation over porous bottoms [35]. The reflection and transmission characteristics for submerged and emerged porous and impermeable structures have been investigated for regular [36] and random [37] waves. It sounds promising to use their approach for the application of wave power conversion.

The mild-slope equations of Radder and Dingemans [31] without the extension of Suh et al. [33] are the basic equations in the phase-resolving model MILDwave, used in the current study. Wave transformation processes such as refraction, shoaling, reflection, transmission and diffraction are simulated intrinsically in MILDwave. The mild-slope wave propagation model MILDwave, developed by Troch [38], has previously been used, e.g. to study diffraction patterns in a harbour [39]. As farms of WECs will be installed in relatively deep water to capture as much wave power as possible, the extension of Suh et al. [33] and additional terms to simulate bottom friction, currents and wave breaking are

considered unimportant. Furthermore, no wave regeneration by wind is considered as the wake effects are the largest when no wind is present (worst case). This relatively simple linear model provides a fast solution for the application of wave power conversion. WECs are modelled as individual absorbing structures with a frequency dependent absorption. A sponge layer technique is developed in order to model several combinations of amounts of reflection, transmission and consequently absorption (chapter 6), thus avoiding the coupling between reflection and transmission as seen in Venugopal et al. [18]. Moreover, a method to account for radiation by WECs of the first category is worked out as well (chapter 8).

Compared to SWAN, smaller grid sizes are required in MILDwave which makes detailed geometrical modelling of a farm of WECs possible. Compared to nonlinear Boussinesq models, a lower spatial and temporal resolution is required which results in a fast solution.

## 4.4 Conclusions

In this chapter a literature review of wave farm modelling has been given. In the past most studies concentrated on maximising the power absorption of WECs based on the oscillating principle. Research on wake effects (wave height decrease) in the lee of a farm of WECs started only a few years ago and is currently gaining more interest.

A thorough overview of available studies on the wave height decrease behind a farm of WECs has been presented in this chapter. Several wave propagation models have been used to study these effects. The applicability of these wave propagation models for the study of wake effects has been discussed in detail. Finally, the advantages of wave farm modelling in the mild-slope wave propagation model MILDwave, used in this PhD dissertation, have been specified.

## References

- [1] S.A. Mavrakos and P. McIver. *Comparison of methods for computing hydrodynamic characteristics of arrays of wave power devices*. Applied Ocean Research, 19:283–291, 1997.
- [2] K. Budal. *Theory of absorption of wave power by a system of interacting bodies*. Journal of Ship Research, 21:248–253, 1977.
- [3] D.V. Evans. *Some analytic results for two- and three-dimensional wave-energy absorbers*. In B. M. Count, editor, Power from Sea Waves, pages 213–249. Academic Press, 1980.
- [4] J. Falnes. *Radiation impedance matrix and optimum power absorption for interacting oscillators in surface waves*. Applied Ocean Research, 2:75–80, 1980.
- [5] M.J. Simon. *Multiple scattering in arrays of axisymmetric wave-energy devices. A matrix method using the plane-wave approximation*. Journal of Fluid Mechanics, 120:1–25, 1982.
- [6] P. McIver. *Wave forces on arrays of floating bodies*. Journal of Engineering mathematics, 18:273–285, 1984.
- [7] P. McIver. *Some hydrodynamic aspects of arrays of wave-energy devices*. Applied Ocean Research, 16:61–69, 1994.
- [8] S.A. Mavrakos. *Hydrodynamic coefficients for groups of interacting vertical axisymmetric bodies*. Ocean Engineering, 18:485–515, 1991.
- [9] S.A. Mavrakos and P. Koumoutsakos. *Hydrodynamic interactions among vertical axisymmetric bodies restrained in waves*. Applied Ocean Research, 9:128–140, 1987.
- [10] S.A. Mavrakos and A. Kalofonos. *Power absorption by arrays of interacting vertical axisymmetric wave-energy devices*. Journal of Offshore Mechanics and Arctic Engineering, 119:244–249, 1997.
- [11] A.F. de O. Falcão. *Wave power absorption by a periodic linear array of oscillating water columns*. Ocean Engineering, 29:1163–1186, 2002.
- [12] WAMIT User Manual [online]. Available from: <http://www.wamit.com/manual.htm>, [Accessed January 2009].
- [13] P.A.P. Justino and A.H. Clément. *Hydrodynamic performance for small arrays of submerged spheres*. In Proceedings of the 5<sup>th</sup> European Wave and Tidal Energy Conference (EWTEC), Cork, Ireland, pages 266–273, 2003.



- [14] P. Ricci, J.-B. Saulnier, and A.F. de O. Falcão. *Point-absorber arrays: a configuration study of the Portuguese West-Coast*. In Proceedings of the 7<sup>th</sup> European Wave and Tidal Energy Conference (EWTEC), Porto, Portugal, 2007.
- [15] G. De Backer, M. Vantorre, C. Beels, J. De Rouck, and P. Frigaard. *Performance of closely spaced point absorbers with constrained floater motion*. In Proceedings of the 8<sup>th</sup> European Wave and Tidal Energy Conference (EWTEC), Uppsala, Sweden, 2009.
- [16] D.L. Millar, H.C.M. Smith, and D.E. Reeve. *Modelling analysis of the sensitivity of shoreline change to a wave farm*. *Ocean Engineering*, 34:884–901, 2006.
- [17] N. Booij, I.J.G. Haagsma, L.H. Holthuijsen, A.T.M.M. Kieftenburg, R.C. Ris, A.J. van der Westhuysen, and M. Zijlema. *SWAN cycle III version 40.41 User Manual [online]*. Available from: <http://fluidmechanics.tudelft.nl/swan/default.htm>, [Accessed 7 April 2005], 2004.
- [18] V. Venugopal and G.H. Smith. *Wave climate investigation for an array of wave power devices*. In Proceedings of the 7<sup>th</sup> European Wave and Tidal Energy Conference (EWTEC), Porto, Portugal, 2007.
- [19] L. Mendes, A. Palha, J.F. Conceição, A. Brito-Melo, and A.J.N.A. Sarmiento. *Analysis of the Impact of a Pilot Zone for Wave Energy Conversion Offshore Portugal*. In Proceedings of the 18<sup>th</sup> International Offshore and Polar Engineering Conference (ISOPE), Vancouver, Canada, 2008.
- [20] R.A. Dalrymple and J.T. Kirby. *REF/DIF 1 Version 2.3 Documentation manual. Combined refraction/diffraction model. CARC Report n° 91-2*. University of Delaware, 1991.
- [21] I. Le crom, A. Brito-Melo, and A.J.N.A. Sarmiento. *Maritime Portuguese Pilot Zone for Wave Energy Conversion: Modelling Analysis of the Impact on Surfing Conditions*. In Proceedings of the 2<sup>nd</sup> International Conference on Ocean Energy (ICOE), Brest, France, 2008.
- [22] C. Vidal, F.J. Méndez, G. Díaz, and R. Legaz. *Impact of Santoña WEC installation on the littoral processes*. In Proceedings of the 7<sup>th</sup> European Wave and Tidal Energy Conference (EWTEC), Porto, Portugal, 2007.
- [23] L.H. Holthuijsen, A. Herman, and N. Booij. *Phase-decoupled refraction-diffraction for spectral wave models*. *Coastal Engineering*, 49:291–305, 2003.

- [24] S. Ilic, A.J. van der Westhuysen, J.A. Roelvink, and A.J. Chadwick. *Multidirectional wave transformation around detached breakwaters*. Coastal Engineering, 54:775–789, 2007.
- [25] F. Enet, A. Nahon, G. van Vledder, and D. Hurdle. *Evaluation of diffraction behind a semi-infinite breakwater in the SWAN wave model*. In Proceedings of the 9<sup>th</sup> International Workshop on Wave Hindcasting and Forecasting, 2006.
- [26] H.C.M. Smith, D.L. Millar, and D.E. Reeve. *Generalisation of wave farm impact assessment on inshore wave climate*. In Proceedings of the 7<sup>th</sup> European Wave and Tidal Energy Conference (EWTEC), Porto, Portugal, 2007.
- [27] G. Kim, C. Lee, and K.-D. Suh. *Internal generation of waves: Delta source function method and source term addition method*. Ocean Engineering, 34:2251–2264, 2007.
- [28] J.C.W. Berkhoff. *Computation of combined refraction-diffraction*. In Proc. of 13<sup>th</sup> Coastal Eng. Conf., Vancouver, 1:471–490, 1972.
- [29] A.C. Radder. *On the parabolic equation method for water-wave propagation*. Journal of Fluid Mechanics, 95:159–176, 1979.
- [30] G.J.M. Copeland. *A practical alternative to the mild-slope wave equation*. Coastal Engineering, 9:125–149, 1985.
- [31] A.C. Radder and M.W. Dingemans. *Canonical equations for almost periodic, weakly nonlinear gravity waves*. Wave Motion, 7:473–485, 1985.
- [32] N. Booij. *A note on the accuracy of the mild-slope equation*. Coastal Engineering, 7:191–203, 1983.
- [33] K.D. Suh, C. Lee, and W.S. Park. *Time-dependent equations for wave propagation on rapidly varying topography*. Coastal Engineering, 32:91–117, 1997.
- [34] M.W. Dingemans. *Water wave propagation over uneven bottoms*. In P. L. F. Liu, editor, Series on Ocean Engineering, volume 13. World Scientific, 1997.
- [35] R. Silva, P. Salles, and A. Palacio. *Linear waves propagating over a rapidly varying finite porous bed*. Coastal Engineering, 44:239–260, 2002.
- [36] R. Silva, E. Mendoza, and M.A. Losada. *Modelling linear wave transformation induced by dissipative structures - Regular waves*. Ocean Engineering, 33:2150–2173, 2006.

- 
- [37] R. Silva, M.A. Losada, and P. Salles. *Modelling linear wave transformation induced by dissipative structures - Random waves*. *Ocean Engineering*, 33:2174–2194, 2006.
- [38] P. Troch. *A numerical model for propagation and transformation of linear water waves*. Department of Civil Engineering, Ghent University, 1998.
- [39] J. Geeraerts, L. De Doncker, P. Troch, J. De Rouck, L. Van Damme, and T. Verwaest. *Numerical simulation of wave penetration in the planned harbour of Oostende. A comparison between numerical models*. In *Proceedings 13<sup>th</sup> International Harbour Congress. Engineering, Environment and Safety*, Antwerpen, Belgium, pages 363–370, 2003.



# 5

## Mild-slope wave propagation model MILDwave

### 5.1 Introduction

This chapter gives a general description of the mild-slope wave propagation model MILDwave. This model is used in this PhD dissertation to study the power production of a farm of WECs (chapters 6, 7 and 8). The preference for this model has been discussed in chapter 4. The basic equations for wave generation and wave propagation (mild-slope equations) in MILDwave and the finite differences scheme to solve these mild-slope equations are presented in a first part of this chapter.

In a second part the technique for wave generation, together with absorbing domain boundaries, is extended. In the past only head-on waves were generated in MILDwave while in this PhD research waves with varying wave propagation angles are considered. Therefore methods for wave generation on multiple wave generation lines and on an arc are implemented. Furthermore, wave generation on a circle is foreseen as well to simulate radiated waves generated by WECs of the first category. The implementation of these wave generation configurations requires an adaptation of the existing absorbing domain boundaries to prevent disturbances in the simulation domain. In this chapter these new wave generation configurations and adapted absorbing boundaries are validated with simple test cases and analytical solutions.

The simulation of the wave transformation processes shoaling, refraction,

reflection, diffraction and wave breaking, in MILDwave have previously been validated. MILDwave results have been compared to analytical solutions, calculations with SimWave [1] (commercial software package based on the non-linear time dependent Boussinesq equations) and experimental data.

In [2, 3] the shoaling coefficient on a uniform slope has been calculated in MILDwave. By comparing the obtained shoaling coefficient with the analytical formula from linear wave theory, it is observed that MILDwave simulates the phenomenon shoaling very accurately.

By simulating wave penetration in the harbour of Oostende, the combined effects of wave refraction, shoaling, reflection, diffraction and wave breaking have been studied. The implementation of wave breaking in MILDwave, based on the Battjes-Janssen model [4], has been described in [5]. Wave breaking on a linear slope and on a bar-trough profile has been validated through physical model tests in the wave flumes of the Department of Civil Engineering (Ghent University) and through simulations in SimWave. The wave breaking module in MILDwave works very well for irregular waves [5]. The disturbed wave heights in the inner and outer port of Oostende have been calculated in the numerical models SimWave and MILDwave. A good agreement between both models is observed in deep water [3, 6] while some deviations in shallow water occur [7]. A further validation of the wave breaking module in MILDwave is necessary. The comparison between both models in the inner harbour depends strongly on the reflection coefficient assigned to the quay walls. Prototype measurements are necessary to obtain a realistic estimation of those reflection coefficients.

When modelling WECs in MILDwave deep water (uniform water depth) is assumed. Consequently the wave transformation processes refraction, shoaling and wave breaking do not occur. The incident wave power is partly absorbed and partly redistributed through the physical processes wave reflection, transmission, diffraction and wave power absorption. The first three processes are simulated intrinsically in MILDwave and are validated at the end of this chapter. The last process is discussed in chapters 6 (WECs of the second category) and 8 (WECs of the first category). First a simple theoretical case of reflection from (and transmission through) a vertical, surface-piercing wall is studied in MILDwave. Further, Wiegel diagrams [8] are used to validate the diffraction pattern in the lee of a semi-infinite breakwater.

## 5.2 Mild-slope equations of Radder and Dingemans

The depth-integrated mild-slope equations of Radder and Dingemans (1985) [9], which describe the transformation of linear irregular waves with a narrow frequency band over a mildly varying bathymetry (bed steepness up to  $1/3$  [10]), are given in equations (5.1) and (5.2):

$$\frac{\partial \eta}{\partial t} = B\varphi - \nabla \cdot (A\nabla\varphi) \quad (5.1)$$

$$\frac{\partial \varphi}{\partial t} = -g\eta \quad (5.2)$$

where  $\eta$  and  $\varphi$  are respectively the surface elevation and velocity potential at the still water level,  $\nabla$  is the horizontal gradient operator,  $t$  is the time,  $g$  is the gravitational acceleration and where the value of  $B$  and  $A$  are calculated using equations (5.3) and (5.4):

$$B = \frac{\bar{\omega}^2 - \bar{k}^2 \bar{C} \bar{C}_g}{g} \quad (5.3)$$

$$A = \frac{\bar{C} \bar{C}_g}{g} \quad (5.4)$$

with the phase velocity  $\bar{C}$  and the group velocity  $\bar{C}_g$  for a wave with carrier wave number  $\bar{k}$  ( $= \frac{2\pi}{\bar{L}}$ ), carrier angular frequency  $\bar{\omega}$  ( $= 2\pi\bar{f}$ ), carrier wave length  $\bar{L}$  and carrier frequency  $\bar{f}$ . Overbar ( $\bar{\quad}$ ) denotes that the wave characteristic is calculated for the carrier frequency. The derivation of these equations can be found in appendix D.

A finite difference scheme (Figure 5.1), as described in [11], is used to discretize and solve equations (5.1) and (5.2). It consists of a two-step space-centered, time-staggered computational grid [12].

The domain is divided in grid cells (uniform grid) with dimensions  $\Delta x$  and  $\Delta y$  and central differences are used for spatial as well as time derivatives. Both  $\eta$  and  $\varphi$  are calculated in the centre of each grid cell at different time levels,  $(n + \frac{1}{2}) \Delta t$  and  $(n + 1) \Delta t$ , respectively, with the discretized equations (5.5) and (5.6).

$$\begin{aligned} \eta_{i,j}^{n+\frac{1}{2}} &\simeq \eta_{i,j}^{n-\frac{1}{2}} + B_{i,j} \varphi_{i,j}^n \Delta t \\ &\quad - \frac{A_{i+1,j} - A_{i-1,j}}{2\Delta x} \frac{\varphi_{i+1,j}^n - \varphi_{i-1,j}^n}{2\Delta x} \Delta t \\ &\quad - A_{i,j} \frac{\varphi_{i-1,j}^n - 2\varphi_{i,j}^n + \varphi_{i+1,j}^n}{(\Delta x)^2} \Delta t \\ &\quad - \frac{A_{i,j+1} - A_{i,j-1}}{2\Delta y} \frac{\varphi_{i,j+1}^n - \varphi_{i,j-1}^n}{2\Delta y} \Delta t \\ &\quad - A_{i,j} \frac{\varphi_{i,j-1}^n - 2\varphi_{i,j}^n + \varphi_{i,j+1}^n}{(\Delta y)^2} \Delta t \end{aligned} \quad (5.5)$$

$$\varphi_{i,j}^{n+1} \simeq \varphi_{i,j}^n - g\eta_{i,j}^{n+\frac{1}{2}} \Delta t \quad (5.6)$$

with  $A$  and  $B$  given by equation (5.3) and equation (5.4). Lower index  $i,j$  signifies the spatial grid cell at position  $i\Delta x$  and  $j\Delta y$  and upper index  $n$  signifies the time step  $n\Delta t$ .

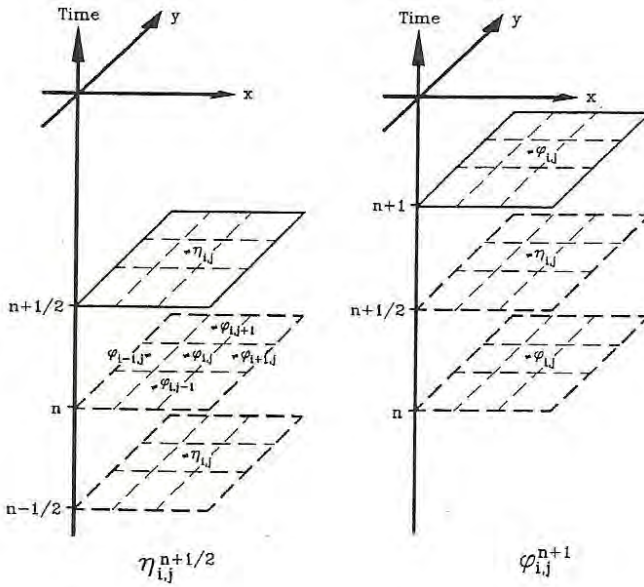


Figure 5.1: Finite difference scheme (computational space-centered, time-staggered grid) [12]

The grid spacing  $\Delta x = \Delta y$  is chosen so that  $\frac{L}{20} \leq \Delta x = \Delta y \leq \frac{L}{10}$  ( $L =$  shortest wave length (maximum frequency) for irregular waves) and the time step meets the Courant-Friedrichs-Lewy criterion<sup>1</sup>,  $\Delta t \leq \frac{\Delta x}{C}$  where  $C$  is the (maximum) phase velocity, to guarantee a stable and consistent result.

Wave generation (section 5.3) starts from quiescent water conditions at  $t = 0$ . Each time step, first  $\eta_{i,j}^{n+\frac{1}{2}}$  and then  $\varphi_{i,j}^{n+1}$  is calculated by equation (5.5) and equation (5.6), respectively, in the centre of each grid cell. Consequently waves are gradually propagating across the domain.

### 5.3 Wave generation

To calculate the wave field in a predefined domain, waves need to be generated at the offshore boundary and subsequently propagate into the simulation domain.

<sup>1</sup>The timestep  $\Delta t$  must be chosen so small that the displacement of the wave front in a time interval does not exceed the grid size  $\Delta x$ .



Outgoing waves should travel through the domain boundaries without any numerical disturbances, as if they are open boundaries. Hence, the outgoing waves must be absorbed at these open boundaries. Otherwise, reflected waves from the domain boundaries may influence the wave pattern in the simulation domain. Furthermore, waves reflected from structures in the simulation domain should pass through the wave generation boundary without being re-reflected. To avoid reflection from the domain boundaries and re-reflection at the offshore wave generation boundary, internal wave generation techniques<sup>2</sup> in combination with absorbing so-called sponge layers at the open boundaries have been used. The method of internal wave generation is presented in this section, while the numerical sponge layers are discussed in section 5.4.

### 5.3.1 Regular waves

#### 5.3.1.1 Wave generation on one or two wave generation lines

In MILDwave waves are generated at the offshore boundary by using the source term addition method, i.e. by adding an additional surface elevation  $\eta^*$  to the calculated value on a wave generation line for each time step.

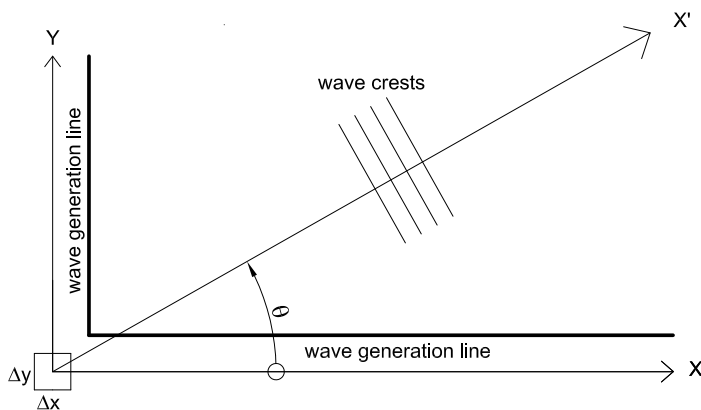


Figure 5.2: Definition sketch of wave generation

To generate a regular incident wave, with phase velocity  $C$  and wave elevation

<sup>2</sup>Two different internal wave generation techniques have been developed separately: (i) the source term addition method and (ii) the source function method. In the source term addition method, the values of the water surface elevation, representing the change of water volume by the target wave elevation, are added to the calculated values in the wave generation cells. In the source function method, an appropriate source function is added to the model equations. The source function is obtained by equating the calculated wave elevation and the target wave elevation. Both techniques modify the calculated surface elevation in wave generation grid cells. Kim et al. [13] derived the Delta source function and showed that the Delta source function method was equal to the source term addition method.

$\eta_i$  that propagates at an angle  $\theta$  ( $0^\circ \leq \theta \leq 90^\circ$ ) from the x-axis, a set-up as shown in Figure 5.2 is needed. Two wave generation lines are implemented in the horizontally two-dimensional domain; i.e. one parallel with the x-axis and one parallel with the y-axis [14]. The wave elevation  $\eta_i$  is given in equation (5.7).

$$\begin{aligned}\eta_i &= a \sin(kx' - \omega t + \phi) \\ &= a \sin(k \cos\theta x + k \sin\theta y - \omega t + \phi)\end{aligned}\quad (5.7)$$

with the wave amplitude  $a$  and the phase shift  $\phi$ . The phase velocity along the x-axis, respectively y-axis, equals  $C \cos\theta$  and  $C \sin\theta$  [15].

The volume flux per time step  $\Delta t$ , across the wave generation line parallel to the y-axis, equals  $\eta_i C \cos\theta \Delta y \Delta t$  in both the positive and negative x-direction. Since a wave generation cell covers an area  $\Delta x \Delta y$ , the additional surface elevation  $\eta^*$  on the wave generation line parallel with the y-axis, is given in equation (5.8).

$$\eta^* = 2\eta_i \frac{C \Delta t}{\Delta x} \cos\theta \quad (5.8)$$

The additional surface elevation  $\eta^*$  on a wave generation line, parallel with the x-axis, is derived in a similar way and given in equation (5.9).

$$\eta^* = 2\eta_i \frac{C \Delta t}{\Delta y} \sin\theta \quad (5.9)$$

The coefficient 2 is included because the generated waves propagate in two opposite directions from the wave generation line. When  $\theta = 90^\circ$  and  $0^\circ$  (head-on) waves are only generated on the x-axis and y-axis, respectively. A slow start of wave generation is obtained by multiplying the wave generation by  $\tanh\left(\frac{0.5t}{T}\right)$  [16], with the wave period  $T$ .

The source term addition method, using the phase velocity  $C$  for the transport of water mass, was first used by Larsen and Dancy [15] for the Boussinesq equations for short-wave simulations in shallow water. For the mild-slope equations of Radder and Dingemans, the so-called energy velocity  $C_e$  instead of the phase velocity  $C$  should be used [14]. The mass transport gives only correct results in shallow water, where the phase velocity  $C$  equals the energy velocity  $C_e$ . For regular waves the energy velocity equals the group velocity. The energy velocity  $C_e$  is derived in [14] with the geometric optics approach (equation (5.10)). The generation of irregular waves, by using the energy velocity instead of the group velocity, has been extensively studied in [3].

$$C_e = \bar{C}_g \frac{\bar{\omega}}{\omega} \sqrt{1 + \frac{\bar{C}}{\bar{C}_g} \left( \left( \frac{\omega}{\bar{\omega}} \right)^2 - 1 \right)} \quad (5.10)$$

The additional surface elevation  $\eta^*$  on a wave generation line, parallel with the y-axis and x-axis, to generate waves with wave direction  $\theta$  in deep and shallow water is given by equations (5.11) and (5.12).

$$\eta^* = 2\eta_i \frac{C_e \Delta t}{\Delta x} \cos\theta \quad (5.11)$$

$$\eta^* = 2\eta_i \frac{C_e \Delta t}{\Delta y} \sin\theta \quad (5.12)$$

To validate the wave generation on two wave generation lines, a simple test case is worked out. The computational domain consists of an inner domain of 1 000 m x 1 000 m and fully absorbing sponge layers at the boundaries (Figure 5.3).

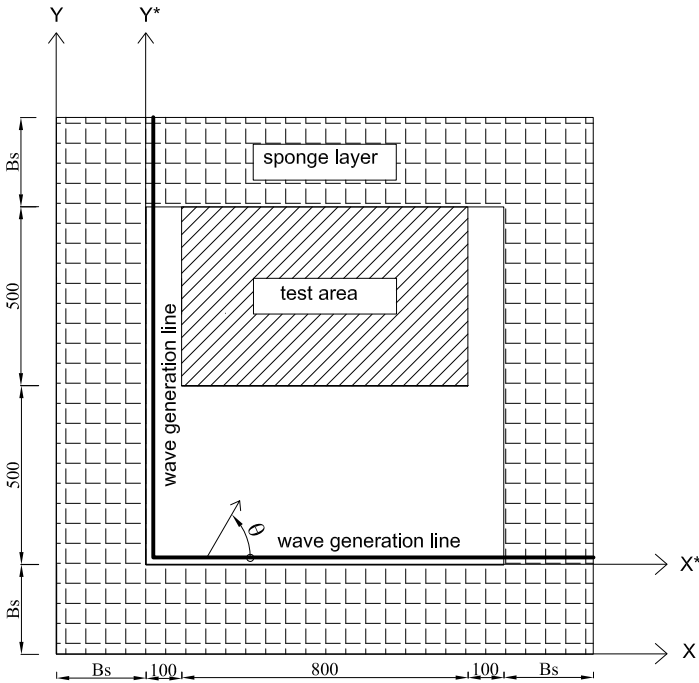


Figure 5.3: Definition sketch of simulation domain with two wave generation lines in plan view

Regular waves with a wave height  $H_i = 1$  m, wave period  $T = 5.2$  s and wave direction  $\theta = 60^\circ$  are generated on two wave generation lines in a constant water depth of 70 m. The instantaneous surface elevations at  $t = 100 T$  are shown in Figure 5.4. At the intersection of the wave generation lines wave diffraction occurs, as seen in [14]. Consequently the wave elevations are varying at that location between - 0.59 m and 0.59 m and not between - 0.5 m and 0.5 m, as expected. Note that the absorption function  $S_3$  is used in the sponge layers. The sponge layers will be discussed in section 5.4. Generating waves on two wave generation lines and an arc reduces the observed diffraction [17].

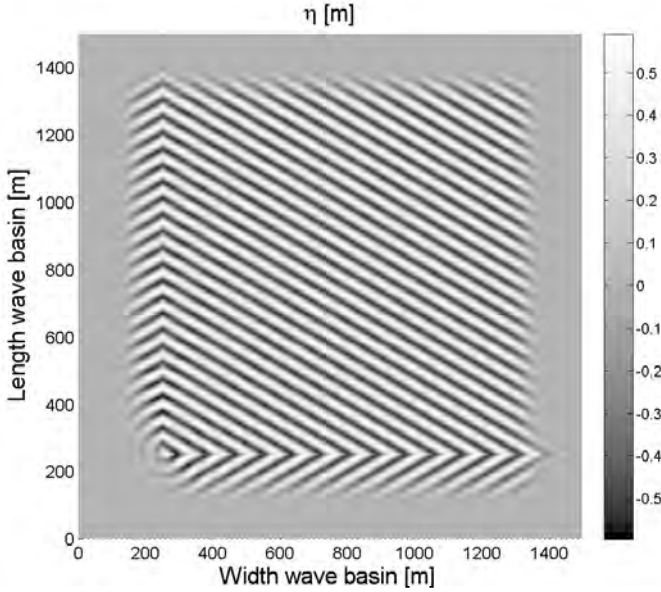


Figure 5.4: Calculated surface elevations on  $t = 100 T$  in MILDwave for regular waves with  $H_i = 1$  m,  $T = 5.2$  s and  $\theta = 60^\circ$  generated along two wave generation lines (absorption function  $S_3$  in sponge layers)

### 5.3.1.2 Wave generation on an arc and two wave generation lines

Recently, Lee and Yoon [17] developed a method for internally generating multi-directional waves on an arc in a rectangular grid system using the source term addition method. In [17] several wave generation lay-outs have been studied. Two wave generation lines with a wave generation arc gave the most accurate results (Figure 5.5).

The grid cell nearest to the arc is used as a wave generation cell. The method explained in section 5.3.1.3 is used to define these grid cells. Depending on the angle of the wave generation arc with the x-axis, respectively y-axis (Figure 5.6), the additional surface elevation is given by:

$$\eta^* = \begin{cases} 2\eta_i \frac{C_e \Delta t}{\Delta x} \frac{(-\cos(\epsilon+\theta))}{\cos\epsilon} & \text{case 1} \\ 2\eta_i \frac{C_e \Delta t}{\Delta y} \frac{(-\sin(\epsilon-\theta))}{\cos\epsilon} & \text{case 2} \\ 2\eta_i \frac{C_e \Delta t}{\Delta y} \frac{\sin(\epsilon+\theta)}{\cos\epsilon} & \text{case 3} \\ 2\eta_i \frac{C_e \Delta t}{\Delta x} \frac{\cos(\epsilon-\theta)}{\cos\epsilon} & \text{case 4} \end{cases} \quad (5.13)$$

with  $\epsilon$  the angle between the line normal to the wave generation curve and the x-axis for case 1 and 4, respectively y-axis for case 2 and 3.  $\epsilon$  is indicated on

Figure 5.6. In case 1 the energy of the incident waves propagating normally to the curve will reach the nearest two opposite cells at a distance of  $\Delta x \cos \epsilon$ .

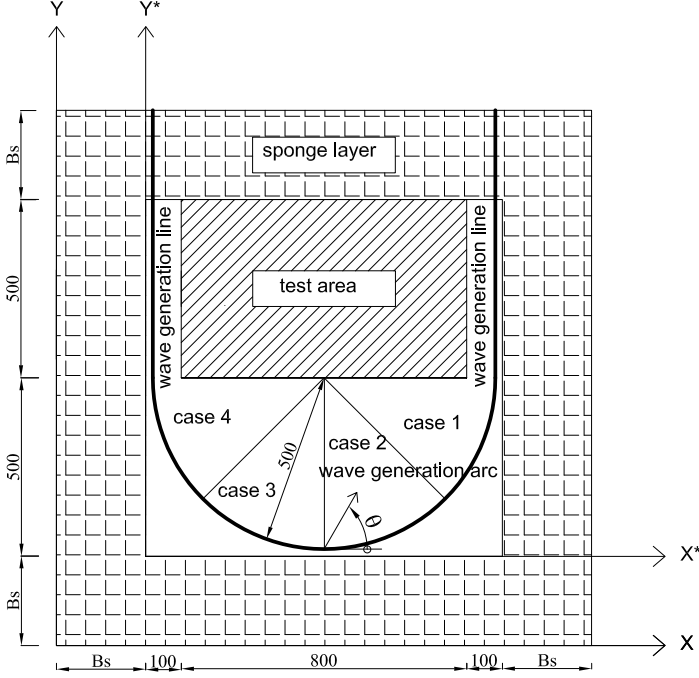


Figure 5.5: Definition sketch of simulation domain with two wave generation lines and a wave generation arc in plan view

On the left and respectively the right wave generation line, the additional surface elevation is given by equation (5.11) and equation (5.14):

$$\eta^* = 2\eta_i \frac{C_e \Delta t}{\Delta x} (-\cos\theta) \quad (5.14)$$

When the wave direction is not pointing to the inner domain on a part of the wave generation arc or on one of the wave generation lines, no waves are generated in those cells. For example when  $\theta = 45^\circ$  no waves are generated on the right generation line and on the first part of the arc (case 1).

The validation test case for wave generation on two wave generation lines is repeated here for wave generation on two wave generation lines and an arc. The surface elevations on  $t = 100 T$  for regular waves with  $H_i = 1$  m,  $T = 5.2$  s and  $\theta = 60^\circ$  generated on a wave generation arc and two wave generation lines in a water depth of 70 m are shown in Figure 5.7.

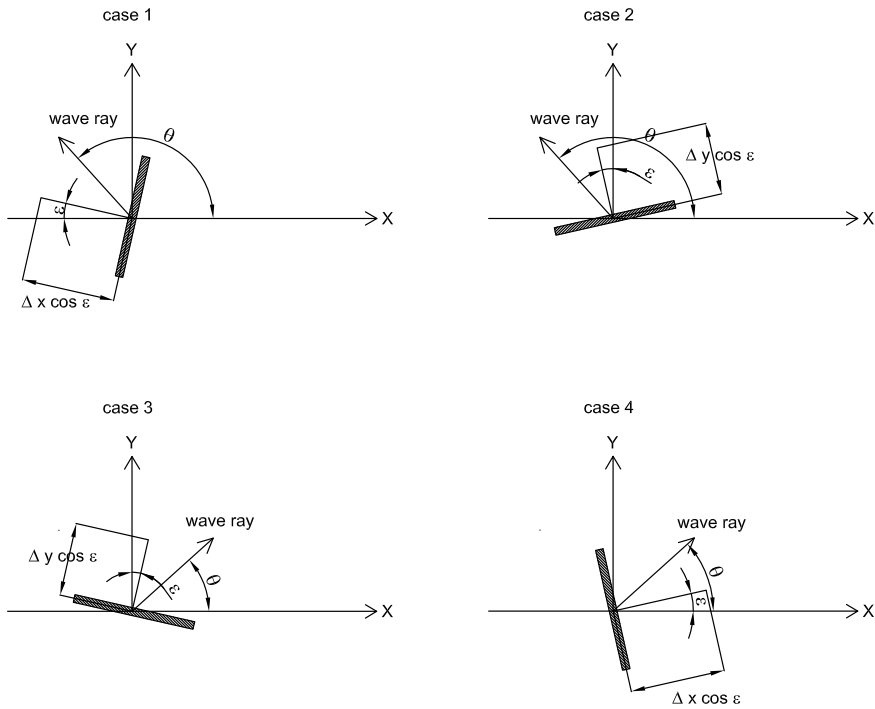


Figure 5.6: Definition sketch of wave generation on a wave generation arc in plan view

In Figure 5.7 the maximum and minimum wave elevation agree slightly better with the expected values of 0.5 m and -0.5 m, respectively.

Both wave generation lay-outs have been compared in more detail by measuring the amplitudes of the water surface elevation in a test area of 800 m x 500 m, as indicated on Figure 5.3 and Figure 5.5, and calculating the absolute error  $e_{ab}$  as:

$$e_{ab} = \frac{|a_{me} - a_{tar}|}{a_{tar}} \tag{5.15}$$

where  $a_{me}$  and  $a_{tar}$  are the measured and target amplitudes of the water surface elevations, respectively. The spatially mean value of  $e_{ab}$  is determined by averaging the values of  $e_{ab}$  in the test area. Figure 5.8 shows the spatially average value of  $e_{ab}$  for both wave generation lay-outs and for different wave angles  $\theta$ .

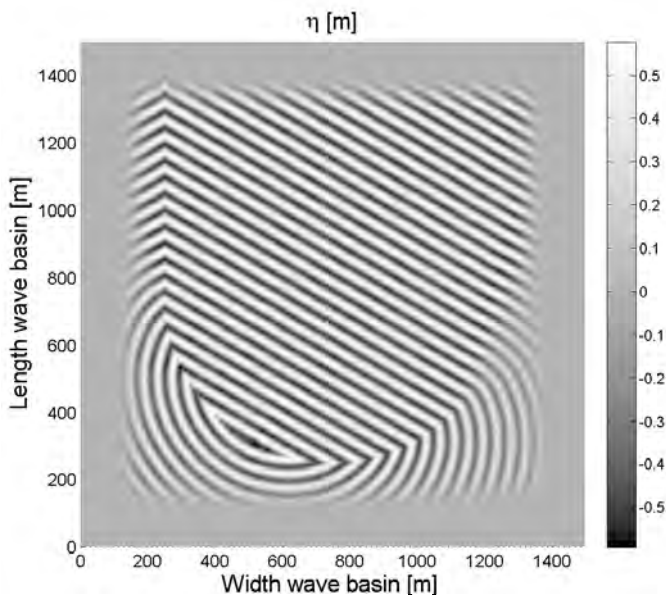


Figure 5.7: Calculated surface elevations on  $t = 100 T$  in MILDwave for regular waves with  $H_i = 1$  m,  $T = 5.2$  s and  $\theta = 60^\circ$  generated on two wave generation lines and a wave generation arc

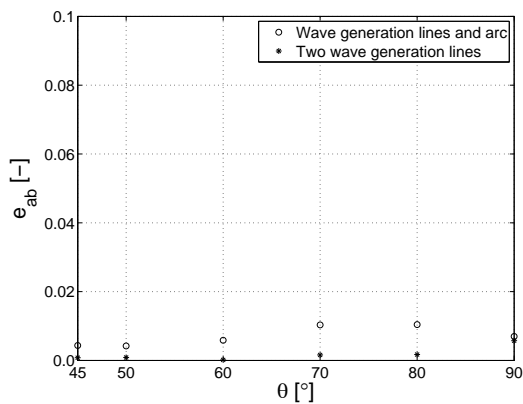


Figure 5.8: Spatially average absolute error  $e_{ab}$  for regular waves with  $H_i = 1$  m,  $T = 5.2$  s and  $45^\circ \leq \theta < 90^\circ$  generated on two wave generation lines or on two wave generation lines and a wave generation arc

For both wave generation lay-outs the spatially averaged absolute error is very small. Moreover, the difference between both wave generation lay-outs is negligible (smaller than 1 %). The maximum value of  $e_{ab}$  is shown in Figure 5.9.

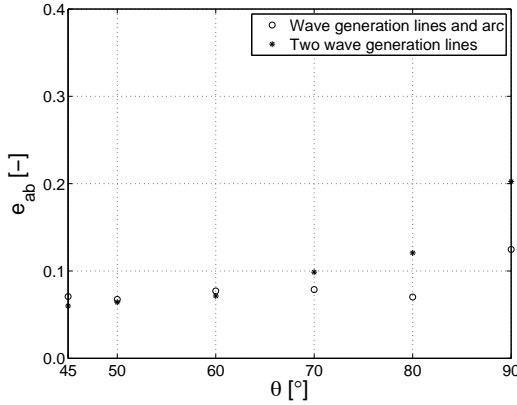


Figure 5.9: Maximum absolute error  $e_{ab}$  for regular waves with  $H_i = 1$  m,  $T = 5.2$  s and  $45^\circ \leq \theta < 90^\circ$  generated on two wave generation lines or on two wave generation lines and a wave generation arc

As seen in [14] the maximum absolute error is smaller for smaller wave direction angles. Wave generation on two wave generation lines yields a larger maximum  $e_{ab}$  when  $\theta > 60^\circ$ . When  $\theta$  equals  $90^\circ$  the maximum absolute error is approximately 7 % higher compared to wave generation on two wave generation lines and an arc. In general, for all wave directions, generating waves on two wave generation lines yields comparable or larger errors compared to a wave generation arc and two wave generation lines. Consequently the latter wave generation set-up is preferred to generate regular waves with varying wave directions.

### 5.3.1.3 Wave generation on a circle

When studying WECs of the first category, waves are generated by the body or water column oscillations. To model these radiated waves in MILDwave, waves need to be generated on a circle. To generate waves on a circle with centre  $(x_c, y_c)$  and radius  $r_c$  in a rectangular grid, the circle needs to be approximated by a discrete number of grid cells (Figure 5.10). The x- and y-co-ordinates of these grid cells are given by equations (5.16) and (5.17) for  $i \in [1, \frac{2\pi}{\Delta b}]$ :

$$x = \text{floor}(x_c + r_c \cos(i\Delta b)) \quad (5.16)$$

$$y = \text{floor}(y_c + r_c \sin(i\Delta b)) \quad (5.17)$$



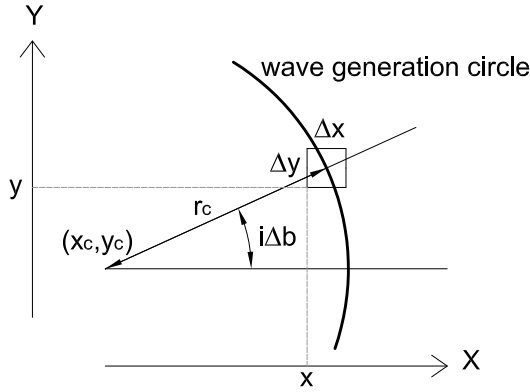


Figure 5.10: Definition sketch of wave generation on a circle

The angle interval  $\Delta b$  can be approximated by  $\arctan\left(\frac{\Delta y}{r_c}\right)$ . The additional surface elevation  $\eta^*$  is given by equation (5.18).

$$\eta^* = 2\eta_i \frac{C_e \Delta t}{\Delta x} \quad (5.18)$$

with  $\eta_i = a \sin(-\omega t)$ .

Each grid cell on the wave generation circle is an individual wave generation source, which is affected by its neighbouring wave generation sources. To minimize the disturbances in the wave generation, an absorbing sponge layer is implemented in the inner part of the wave generation circle.

The wave generation on a circle is validated with the principle of conservation of energy. Regular waves with  $H_i = 2$  m and  $T = 5$  s are generated on a wave generation circle with radius = 50 m in the centre of the simulation domain in a water depth of 100 m. Absorbing sponge layers are implemented at the domain boundaries to prevent reflection inside the domain. The wave power on a circle with radius  $r_c \geq 50$  m is equal to the wave power on the wave generation circle (conservation of energy), as no energy sources or energy sinks are present between both circles. The conservation of energy is expressed in equation (5.19). The derivation of the equation for the wave power per meter of wave crest  $p$  (W/m) can be found in appendix B. By multiplying the wave power  $p$  with the perimeter, the total wave power (W) on the circle is obtained.

$$\frac{1}{8} \rho g H_i^2 C_g 2\pi 50 = \frac{1}{8} \rho g H_{r_c}^2 C_g 2\pi r_c \quad (5.19)$$

with  $H_{r_c}$  the wave height on a circle with radius  $r_c \geq 50$  m. Equation (5.19) leads to equation (5.20) with the target wave height  $H_i = 2$  m.

$$\frac{H_{r_c}}{H_i} = \frac{\sqrt{50}}{\sqrt{r_c}} \quad (5.20)$$

The ratio  $\frac{H_{rc}}{H_i}$ , obtained from calculations using MILDwave and calculated with equation (5.20) along the radial section when  $i\Delta b = 2\pi$  is given in Figure 5.11.

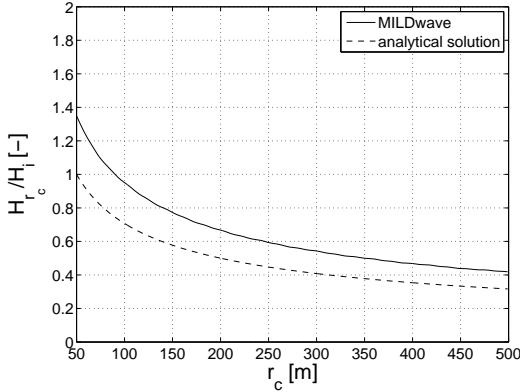


Figure 5.11: Ratio  $\frac{H_{rc}}{H_i}$  along the radial section when  $i\Delta b = 2\pi$  in the simulation domain for regular wave generation on a circle with  $r_c = 50$  m and  $\Delta b = 1.15$

As expected, the ratio decreases when  $r_c$  increases. When  $r_c = 50$  m the ratio should equal 1 (equation (5.20)). It is observed that the ratio obtained with calculations in MILDwave is too high. Too much energy is generated on the wave generation circle by using the approximated value of  $\Delta b$  ( $\arctan\left(\frac{\Delta y}{r_c}\right)$ ), due to mutual influences of the wave generation sources on the wave generation circle. Therefore an iterative approach<sup>3</sup> has been used to define the value of  $\Delta b$  in order to obtain the ratio  $\frac{H_{rc}}{H_i}$  as calculated using equation (5.20) [18]. For  $r_c = 50$  m,  $\Delta b$  equals 1.5.

The surface elevations on  $t = 100 T$  are given in Figure 5.12 for regular waves with  $H_i = 2$  m and  $T = 5$  s generated on a circle with radius = 50 m and  $\Delta b = 1.5$ . Note that the sponge layers are not shown in Figure 5.12.<sup>4</sup> It is clear that the surface elevations decrease further away from the wave generation circle.

The comparison of the calculated ratio  $\frac{H_{rc}}{H_i}$  against the analytical solution (equation (5.20)) along a radial section is given in Figure 5.13. When  $\Delta b$  is determined with an iterative approach, the results in MILDwave and the analytical results agree very well.

<sup>3</sup>One could state that the angle  $\epsilon$  should be considered in the denominator of equation (5.18), by analogy with equation (5.13). When  $i\Delta b = 2\pi$ ,  $\epsilon = 0^\circ$ . In Figure 5.11 this radial section ( $i\Delta b = 2\pi$ ) is shown. It is observed that too much energy is generated. Consequently  $\Delta b$  has been calculated through an iterative approach.  $\epsilon$  is incorporated in  $\Delta b$ , determined with this iterative approach, when waves are generated on a circle.

<sup>4</sup>When the sponge layers are not shown, the co-ordinates are given in the  $x^*y^*$  co-ordinate system (Figures 5.3 and 5.5) instead of the  $xy$  co-ordinate system.

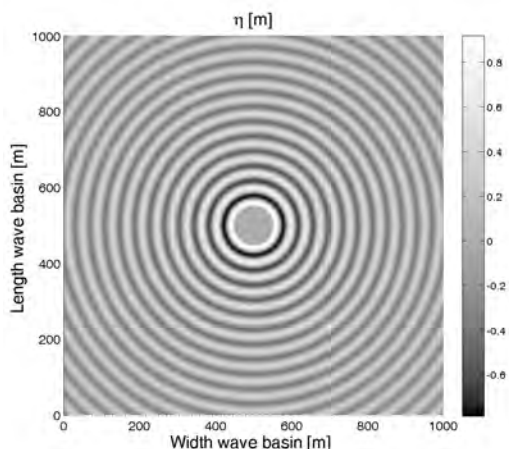


Figure 5.12: Calculated surface elevations on  $t = 100 T$  in MILDwave for waves generated on a wave generation circle with  $r_c = 50$  m and  $\Delta b = 1.5$

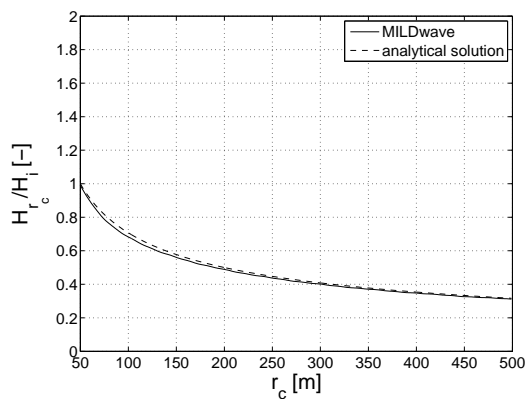


Figure 5.13: Ratio  $\frac{H_{r_c}}{H_i}$  along a radial section in the simulation domain for regular wave generation on a circle with  $r_c = 50$  m and  $\Delta b = 1.5$

The resulting value of  $\Delta b$  as a function of the radius of the wave generation circle is shown in Figure 5.14. A non-linear regression (power law) has been applied through the data.

The determination coefficient  $R^2$  equals 0.9974, which confirms that the regression line (equation (5.21)) approximates the data points very well.

$$\Delta b = 157.09 r_c^{-1.21} \quad (5.21)$$

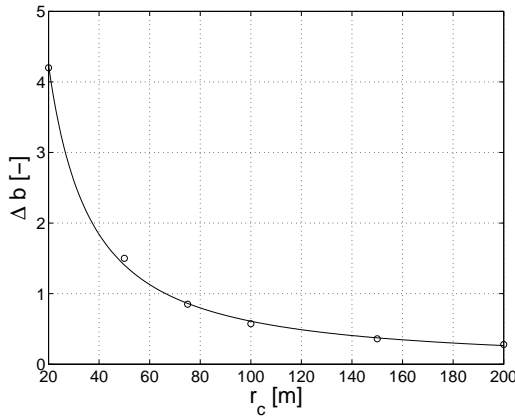


Figure 5.14:  $\Delta b$  as a function of the radius of the wave generation circle

### 5.3.2 Irregular waves

It has been proven that the model of Radder and Dingemans can be used to simulate the transformation of uni- and multi-directional random waves (also called irregular long-crested and short-crested waves) [14]. For the generation of random waves, the peak frequency will be used as a carrier frequency in equations (5.3) and (5.4) as the peak frequency is usually lower than the weight-averaged frequency and as the dispersion relation of the model of Radder and Dingemans is more accurate in the high frequency range [14, 19]. For uni-directional irregular waves the wave elevation  $\eta_i$  is given in equation (5.22) by using a single summation model:

$$\eta_i = \sum_{n=1}^N \sqrt{2S(f_n)\Delta f} \sin(k_n x \cos\theta + k_n y \sin\theta - \omega_n t + \phi_n) \quad (5.22)$$

with the angular frequency  $\omega_n = 2\pi f_n = 2\pi(n-1)\Delta f + 2\pi f_{min}$ , the frequency interval  $\Delta f = \frac{f_{max} - f_{min}}{N-1}$  and the random phase  $\phi_n$ . A parameterized JONSWAP spectrum (equation (2.4)) is used as an input frequency spectrum  $S(f_n)$  [20].

Short-crested wave generation has also been implemented with a single summation model [21]. In the latter model each wave component has a unique frequency while several wave components are travelling in the same direction.

The wave elevation  $\eta_i$  can be expressed by equation (5.23) with the single summation model:

$$\eta_i = \sum_{n=1}^N \sum_{m=1}^M \sqrt{2S(f_{nm}, \theta_m) M \Delta f \Delta \theta} \cdot \sin(k_{nm} x \cos \theta_m + k_{nm} y \sin \theta_m - \omega_{nm} t + \phi_{nm}) \quad (5.23)$$

with the angular frequency  $\omega_{nm} = 2\pi f_{nm} = 2\pi [M(n-1) + m] \Delta f + 2\pi f_{min}$ , the frequency interval  $\Delta f = \frac{f_{max} - f_{min}}{(NM) - 1}$ , the wave propagation angle  $\theta_m = (m-1) \Delta \theta + \theta_0 - \theta_{max}$ , the angle interval  $\Delta \theta = \frac{2\theta_{max}}{M-1}$ , the mean wave angle  $\theta_0$ , the random phase  $\phi_{nm}$  and the two-dimensional energy spectrum  $S(f_{nm}, \theta_m)$ .

Short-crested waves are described by a two-dimensional energy spectrum or directional wave spectrum  $S(f_{nm}, \theta_m)$  which represents the distribution of wave energy over various wave frequencies and directions (Figure 5.15).

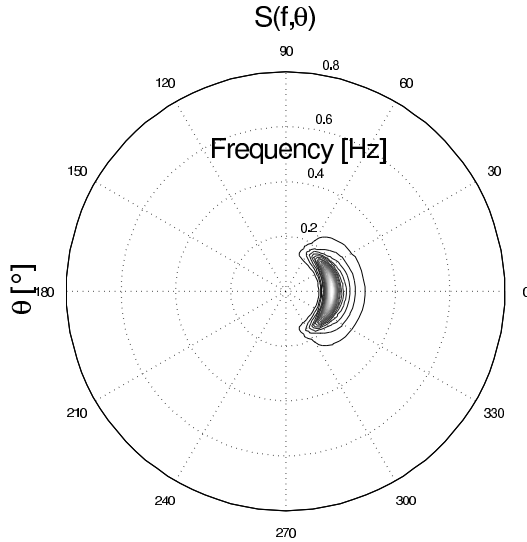


Figure 5.15: Two-dimensional energy spectrum  $S(f, \theta)$  ( $T_p = 6$  s,  $\theta_0 = 0^\circ$  and  $s_{max} = 10$ )

The two-dimensional energy spectrum  $S(f_{nm}, \theta_m)$  is generally expressed as the product of the one-dimensional frequency spectrum  $S(f_{nm})$  and the directional spreading function  $D(f_{nm}, \theta_m)$  at each frequency (equation (5.24)).

$$S(f_{nm}, \theta_m) = S(f_{nm}) D(f_{nm}, \theta_m) \quad (5.24)$$

The directional spreading function  $D(f_{nm}, \theta_m)$  is the non-negative, normalized cross section through the two-dimensional energy spectrum at a given frequency:

$$\int_{-\pi}^{\pi} D(f_{nm}, \theta_m) d\theta = 1 \quad (5.25)$$

Many parametrical models are available to represent the wave directional spreading [22–25]. The cosine power  $2s$  model (equation (5.26)), originally proposed by Longuet-Higgins et al. [24], is widely used.

$$D(f_{nm}, \theta_m) = \frac{2^{2s-1} \Gamma^2(s+1)}{\pi \Gamma(2s+1)} \cos^{2s} \left( \frac{\theta_m - \theta_0}{2} \right) \quad (5.26)$$

for  $\theta_0 - \pi \leq \theta_m \leq \theta_0 + \pi$ . The directional spreading parameter  $s$  gives the degree of directional energy concentration. For wind seas (like the North sea), the spectrum is rather broad and the value of  $s$  is rather low (Figure 5.16).

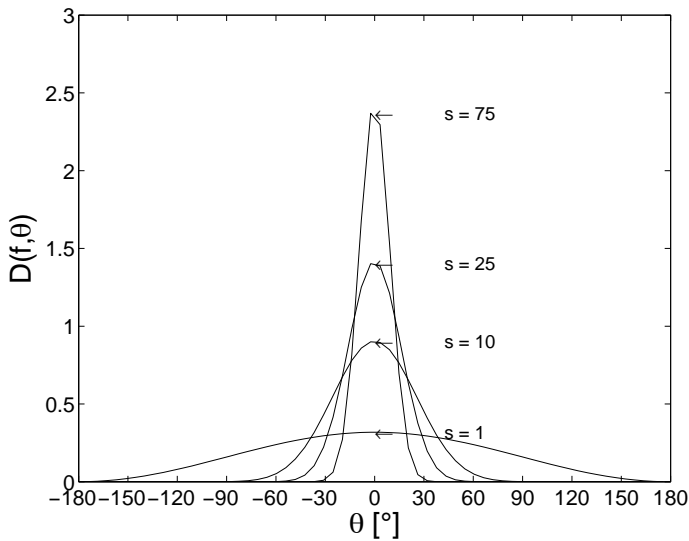


Figure 5.16: The directional spreading function  $D(f, \theta)$ , with  $\theta_0 = 0^\circ$ , for several values of the directional spreading parameter  $s$

The parameter  $s$  is related to the frequency by equation (5.27) [26]:

$$s = \begin{cases} (f_{nm}/f_p)^{5} s_{max} & : f_{nm} \leq f_p \\ (f_{nm}/f_p)^{-2.5} s_{max} & : f_{nm} \geq f_p \end{cases} \quad (5.27)$$

An example is given in Figure 5.17.

The parameter  $s_{max}$  is the maximum value of the spreading parameter. Fixed values for  $s_{max}$  are given in equation (5.28) for wind and swell waves [26]:

$$s_{max} = \begin{cases} 10 & : \text{ wind waves} \\ 25 & : \text{ swell with short decay distance} \\ 75 & : \text{ swell with long decay distance} \end{cases} \quad (5.28)$$

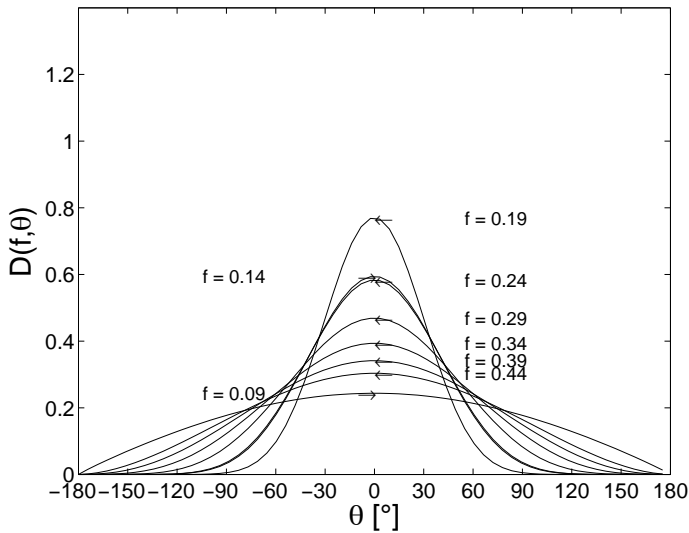


Figure 5.17: The directional spreading function  $D(f, \theta)$ , with  $\theta_0 = 0^\circ$  and  $s_{max} = 10$ , for several values of the frequency  $f$

The relation between the directional spreading parameter  $s$  and the standard deviation  $\sigma_\theta$ , which is called the directional width, is given by equation (5.29) [27].

$$\sigma_\theta = \sqrt{\frac{2}{s+1}} \quad (5.29)$$

To generate short-crested waves (SCW) with  $\theta_0 = 90^\circ$  the set-up in Figure 5.3 cannot be applied as some wave components have a wave angle  $\theta_m > 90^\circ$ . Three wave generation lines (Figure 5.18) or two wave generation lines and an arc (Figure 5.5) can be used to generate SCW with  $\theta_0 = 90^\circ$ .

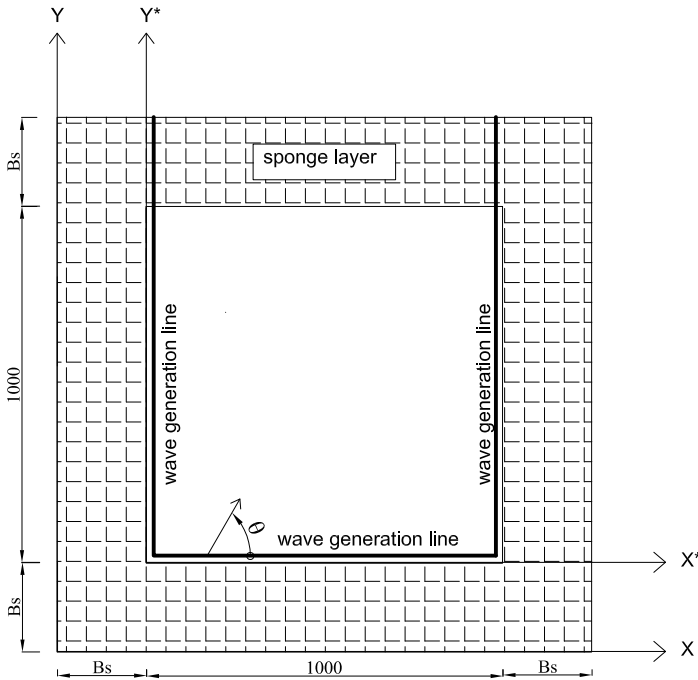


Figure 5.18: Definition sketch of simulation domain with three wave generation lines in plan view

The additional surface elevation on the right wave generation line is given by equation (5.14) for a single wave component. Both wave generation lay-outs are compared by generating irregular short-crested waves with  $H_s = 1$  m,  $T_p = 5.2$  s,  $\theta_0 = 90^\circ$  and  $s_{max} = 10$  and 75 in each lay-out in a water depth of 70 m. The length of the sponge layers at the domain boundaries is doubled compared to the test case with regular waves to prevent any reflection from the domain boundaries inside the simulation domain.

The surface elevations on  $t = 1\,000 T$  are shown in Figure 5.19 for short-crested waves with  $s_{max} = 75$  and 10, generated on three wave generation lines. Figure 5.20 shows the resulting surface elevations for two wave generation lines and an arc.

At the both ends of the horizontal wave generation line, in the set-up with three wave generation lines, a circular wave is generated which disturbs the wave pattern in the simulation domain. These circular waves can be observed better for  $s_{max} = 75$  (Figure 5.19(a)), compared to  $s_{max} = 10$  (Figure 5.19(b)). By generating waves on two wave generation lines and an arc the latter effect is prevented.



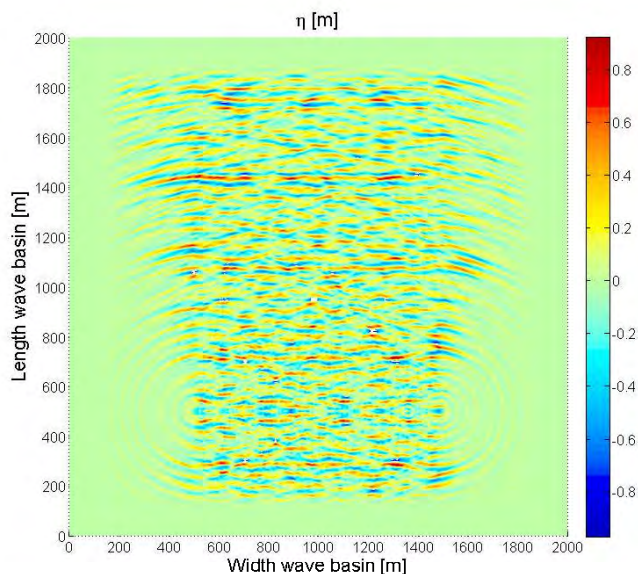
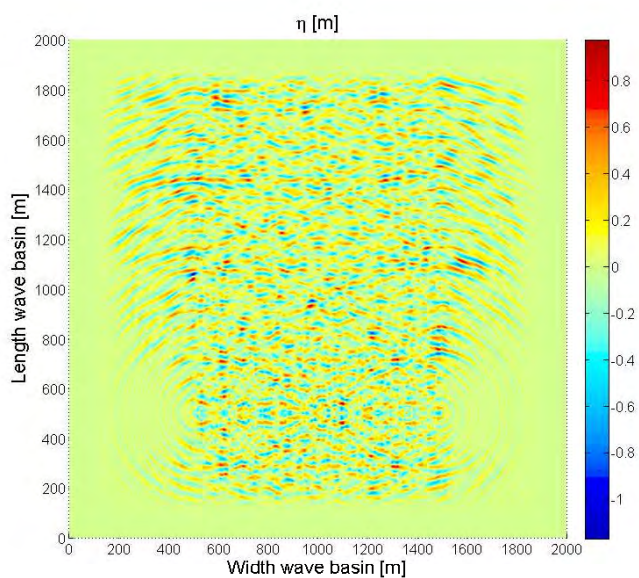
(a)  $s_{max} = 75$  - 3 generation lines(b)  $s_{max} = 10$  - 3 generation lines

Figure 5.19: Calculated surface elevations on  $t = 1000 T$  for irregular short-crested waves with  $H_s = 1$  m,  $T_p = 5.2$  s,  $\theta_0 = 90^\circ$  and (a)  $s_{max} = 75$  and (b)  $s_{max} = 10$  on three wave generation lines

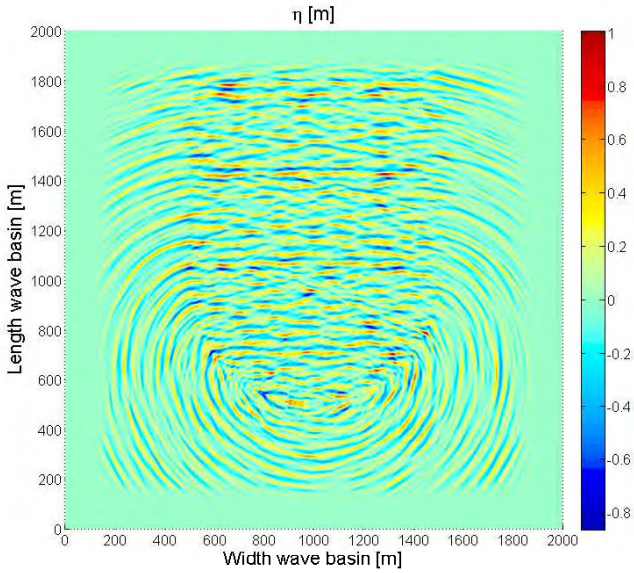
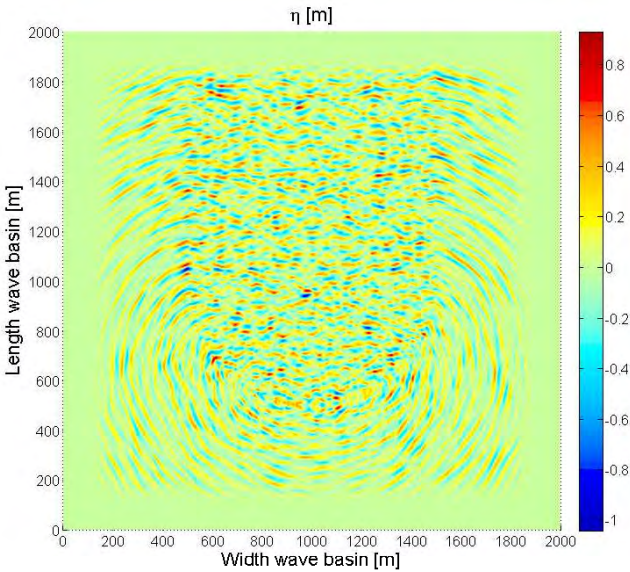
(a)  $s_{max} = 75$  - 2 generation lines + arc(b)  $s_{max} = 10$  - 2 generation lines + arc

Figure 5.20: Calculated surface elevations on  $t = 1\,000 T$  for irregular short-crested waves with  $H_s = 1\text{ m}$ ,  $T_p = 5.2\text{ s}$ ,  $\theta_0 = 90^\circ$  and (a)  $s_{max} = 75$  and (b)  $s_{max} = 10$  on two wave generation lines and an arc

To see whether these circular waves have a large impact on the generated waves, the directional wave spectrum has been measured by a group of 7 wave gauges in the centre of the simulation domain. These wave gauges have been placed in a modified CERC 5 configuration based on the recommendations of Esteva [28] and Fernandes et al. [29]. Directional spectra have been estimated by use of the software package WaveLab (Aalborg University), which is based on the Bayesian Directional Spectrum Estimation Method [30]. The surface elevations at the wave gauges have been sampled with a frequency of 20 Hz during 9 000 s, resulting in a total of 180 000 samples. The measured time series has been divided into subseries with a duration of 102.4 s corresponding to a spectral resolution of  $\Delta f = 0.00976$  Hz. A taper window and an overlap of 20 % have been used for smoother and statistically more significant spectral estimates. The frequency range was confined between  $0.75\bar{f}$  en  $2\bar{f}$ . The directional resolution was chosen to  $5^\circ$  corresponding to 72 directions. The measured frequency spectra are compared with the target spectra in Figure 5.22 for both wave generation lay-outs and for a maximum value of the spreading parameter of 75 and 10.

For  $s_{max} = 75$  very good agreement is observed between both frequency spectra. For  $s_{max} = 10$  some energy is dissipated near the peak frequency and in the tail of the spectrum (larger frequencies). In general, no significant difference between both lay-outs is observed. The two-dimensional energy spectrum for  $s_{max} = 75$  and 10 is shown in Figure 5.21. As the differences between the directional wave spectra for both wave generation lay-outs are negligible, only the directional spectra for wave generation on two wave generation lines and an arc are given.

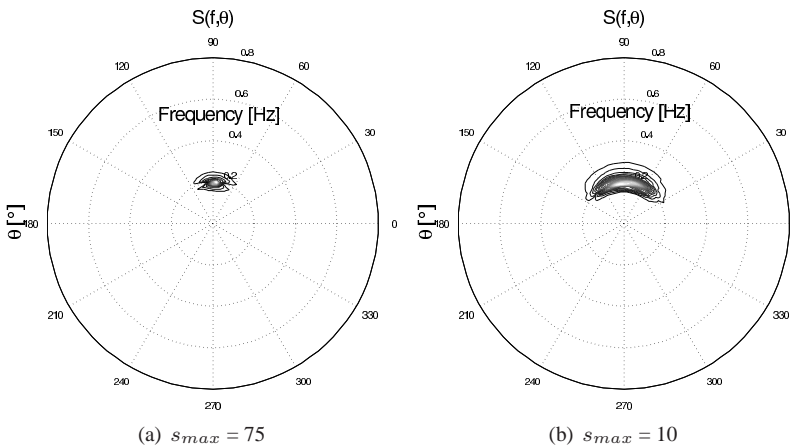


Figure 5.21: Measured directional wave spectra for irregular short-crested waves with  $H_s = 1$  m,  $T_p = 5.2$  s,  $\theta_0 = 90^\circ$  and (a)  $s_{max} = 75$  and (b)  $s_{max} = 10$  on two wave generation lines and an arc

The mean wave angle equals  $90^\circ$  for both directional wave spectra. Furthermore a larger directional spreading is observed in the spectrum for  $s_{max} = 10$ , as expected.

The differences between short-crested wave generation on three wave generation lines and on two wave generation lines and an arc are negligible. For regular waves the lay-out with two wave generation lines and an arc performs better compared to two wave generation lines. Consequently the lay-out with two wave generation lines and an arc is used in this PhD dissertation for the generation of regular and irregular long-crested waves (LCW) with  $0^\circ < \theta < 90^\circ$  and for the generation of short-crested waves. To generate regular and irregular long-crested head-on waves ( $\theta = 0^\circ$  or  $\theta = 90^\circ$ ), a single wave generation line is used.

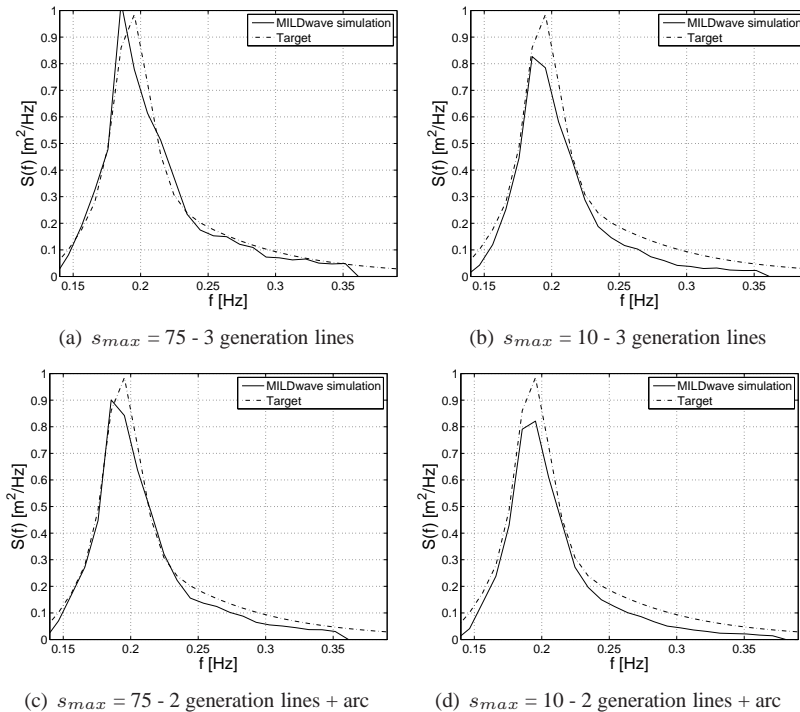


Figure 5.22: Comparison between the frequency spectrum calculated in MILDwave and the target frequency spectrum for irregular short-crested waves with  $H_s = 1$  m,  $T_p = 5.2$  s,  $\theta_0 = 90^\circ$  and (a)  $s_{max} = 75$  generated on three wave generation lines, (b)  $s_{max} = 10$  generated on three wave generation lines, (c)  $s_{max} = 75$  generated on two wave generation lines and an arc and (d)  $s_{max} = 10$  generated on two wave generation lines and an arc

## 5.4 Domain boundaries

### 5.4.1 Head-on waves

Absorbing boundary conditions are achieved using the sponge layer method [11, 15]. A sponge layer with length  $B_s$  is placed against the edges of the wave basin (Figures 5.3, 5.5 and 5.18). In MILDwave the numerical absorption of the waves is obtained by multiplying the calculated surface elevations on each new time step with an absorption function  $S(b)$  that has the value 1 at the start of the sponge layer and smoothly decreases till the value 0 at the end. Two absorption functions  $S_1(b)$  and  $S_2(b)$  have been proposed in [2]:

$$S_1(b) = \sqrt{1 - \left(\frac{b}{B_s}\right)^2} \quad (5.30)$$

$$S_2(b) = \frac{1}{2} \left(1 + \cos\left(\pi \frac{b}{B_s}\right)\right) \quad (5.31)$$

with the length of the sponge layer  $B_s$  and the distance from the outside boundary  $b$ , both expressed in number of grid cells.

The absorption functions  $S_1(b)$  and  $S_2(b)$  are shown in Figure 5.23.<sup>5</sup>

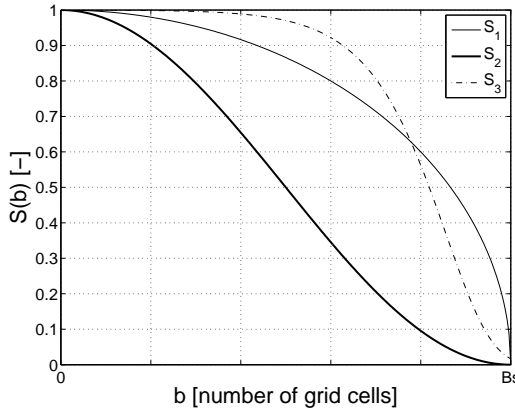


Figure 5.23: Absorption functions  $S(b)$  through the sponge layer with length  $B_s$

In [14] numerical absorption in the sponge layer is achieved by including a dissipation term in equation (5.2). Consequently equation (5.2) was modified as equation (5.32).

$$\frac{\partial \varphi}{\partial t} = -g\eta - \bar{\omega} D_s \varphi \quad (5.32)$$

<sup>5</sup>The absorption function  $S_3(b)$  is discussed in section 5.4.2.

The damping coefficient  $D_s$  is given by equation (5.33) [14] and shown in Figure 5.24.

$$D_s = \begin{cases} 0 & \text{outside sponge layer} \\ \frac{\exp(b/B_s)-1}{\exp(1)-1} & \text{inside sponge layer} \end{cases} \quad (5.33)$$

This method has also been implemented in MILDwave.

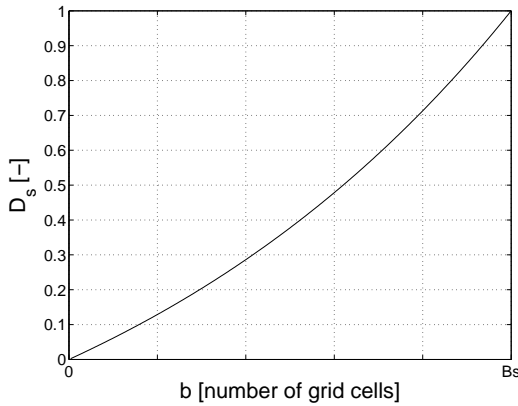


Figure 5.24: Damping coefficient  $D_s$  through the sponge layer with length  $B_s$

In general a length  $B_s$  of  $3L$  for regular waves and  $2.5L_{max}$  for irregular waves [14], where  $L_{max}$  is the maximum wave length resulting from the cut-off incident frequency spectrum, is sufficient.

To test the performance of the sponge layers, regular waves with  $H_i = 1$  m and  $T = 5.2$  s are generated in the centre of a numerical wave flume (Figure 5.25) during 1 000 s. The water depth equals 30 m. At both ends of the wave flume absorbing sponge layers with a length of  $3L$  are implemented. At each side of the wave generation line, an array of three wave gauges is installed to measure the incident wave height  $H_i$  and the reflected wave height  $H_r$ . The distances between the wave gauges are derived by Mansard and Funke in order to perform a reflection analysis [31]. The time series at the wave gauges are sampled with a frequency of 10 Hz. The reflection coefficient  $K_r = \frac{H_r}{H_i}$  when using absorption functions  $S_1$  and  $S_2$  or a damping coefficient  $D_s$  is given in Table 5.1.

Table 5.1: Reflection coefficient  $K_r$  for several types of sponge layers

Sponge layer	$K_r$ [-]
Absorption function $S_1$	0.01
Absorption function $S_2$	0.03
Absorption function $S_3$	0.02
Damping coefficient $D_s$	0.02

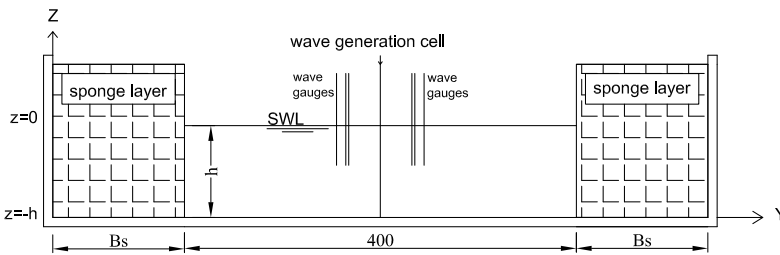


Figure 5.25: Side view of numerical wave flume

From Table 5.1 it is clear that all types of sponge layers result in a negligible amount of reflection in the wave flume, when the width of the sponge layer equals  $3L$  (regular waves).

#### 5.4.2 Waves with $0^\circ < \theta < 90^\circ$

When waves are not propagating perpendicular to the wave generation line, absorbing sponge layers need to be installed at the right and left boundaries of the simulation domain as well (Figures 5.3, 5.5 and 5.18). Otherwise too much reflection on the side boundaries would occur.

The instantaneous surface elevations at  $t = 100 T$ , when regular waves with  $H_i = 1$  m,  $T = 5.2$  s and  $\theta = 60^\circ$  are generated on two wave generation lines in a constant water depth of 70 m (test case as described in section 5.3.1.1) are shown in Figure 5.26. The absorption function  $S_1$  is implemented to absorb the out-going waves at the domain boundaries. Some reflection at the domain boundaries occurs as small disturbances of the surface elevations are observed (the wave elevations vary between -0.61 m and 0.61 m). By implementing the absorption function  $S_2$  or by including the damping coefficient  $D_s$  the same unwanted reflection is observed.



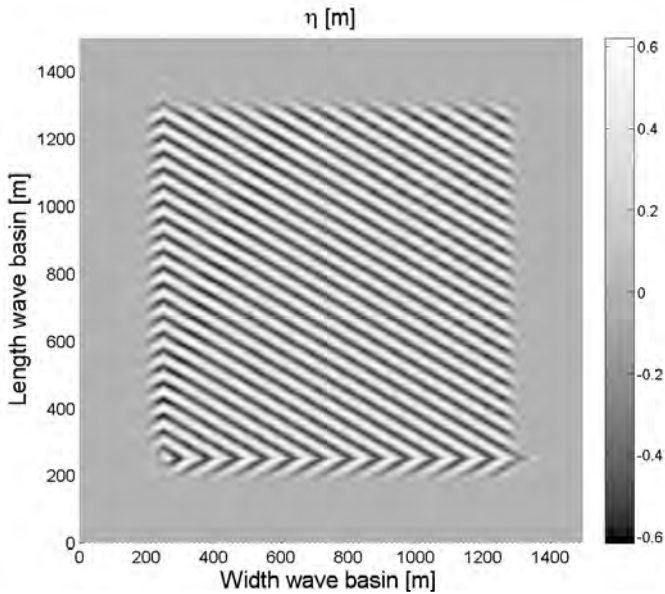


Figure 5.26: Calculated surface elevations on  $t = 100 T$  in MILDwave for regular waves with  $H_i = 1$  m,  $T = 5.2$  s and  $\theta = 60^\circ$  generated along two wave generation lines (absorption function  $S_1$  in sponge layers)

Furthermore, these sponge layers at the side boundaries absorb too much energy from the simulation domain. In Figure 5.27(a) the calculated disturbance coefficient  $K_d$  is given in an inner domain of 1 000 m x 500 m for regular waves with  $H_i = 1$  m,  $T = 5.2$  s and  $\theta = 90^\circ$ , generated on a wave generation line parallel with the x-axis in a water depth of 30 m. The disturbance coefficient  $K_d \left( = \frac{H_d}{H_i} \right)$  is the ratio between the numerically calculated disturbed wave height  $H_d$  in the domain and the numerically calculated incident wave height at the wave generation boundary  $H_i$ .

It is expected that  $K_d$  equals 1.0 in the whole inner domain, as no structure is implemented in the domain. The negative effect of the side sponge layers on  $K_d$  in the inner domain is clearly visible in Figure 5.27(a). Note that the sponge layers are not shown in Figure 5.27. This effect occurs for each type of sponge layer. When no side sponge layers are installed, the latter effect disappears (Figure 5.27(b)). When  $0^\circ < \theta < 90^\circ$  removing the side sponge layers is not possible as the generated wave pattern would be disturbed by reflection from the side boundaries.



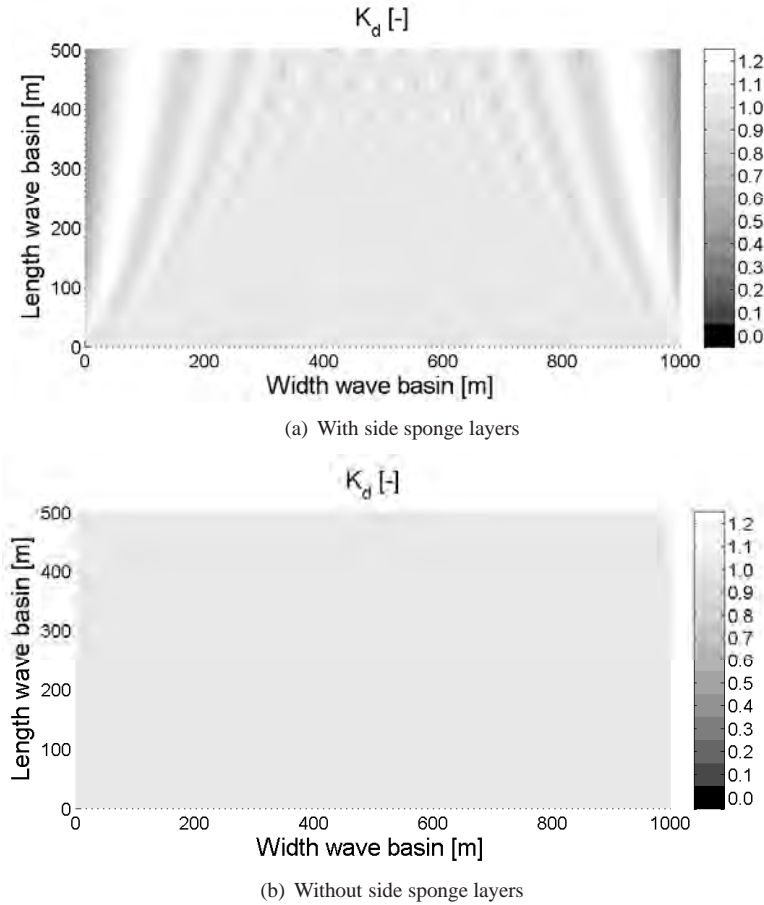


Figure 5.27: Calculated disturbance coefficient  $K_d$  for regular LCW with  $H_i = 1$  m,  $T = 5.2$  s and  $\theta = 90^\circ$  in a domain (1 000 m x 500 m) (a) with and (b) without side sponge layers

To avoid the negative effect of the side sponge layers, the wave generation has been adapted. At both ends of the wave generation line in the inner domain, along a length of  $3L$ , the additional surface elevation  $\eta^*$  is multiplied with an absorption function  $S(b)$  that decreases from the value 1 till the value 0 at the boundary with the side sponge layer, on each new time step.  $\eta^*$  equals 0 inside the side sponge layers. In Figure 5.28  $\eta^*$  has been multiplied with  $S_1$  over a length of  $3L$  at both ends of the wave generation lines.

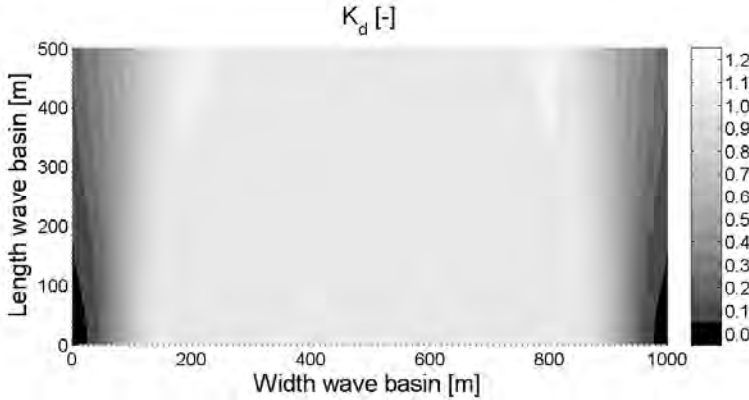


Figure 5.28: Calculated disturbance coefficient  $K_d$  for regular LCW with  $H_i = 1$  m,  $T = 5.2$  s and  $\theta = 90^\circ$  in a domain (1 000 m x 500 m) with side sponge layers and with adapted wave generation

The boundaries of the inner domain are disturbed by the decreasing values of  $\eta^*$ , which makes the useful simulation domain smaller. On the other hand the central part of the domain is not affected anymore by the side sponge layers (compared to Figure 5.27(a)).

To avoid this adapted wave generation and the negative effects from the side sponge layers, another absorption function  $S_3(b)$  has been designed, based on the absorption function in Larsen and Dancy [15], developed for a model based on the non-linear Boussinesq equations [18].  $S_3(b)$  equals approximately 1 over a longer distance in the beginning of the sponge layer (Figure 5.23).

The function  $S_3(b)$  is defined by:

$$S_3(b) = \frac{1}{\exp\left(\left(\mu^{-(B_s-b)} - \mu^{-B_s}\right) \ln a_n\right)} \quad (5.34)$$

The coefficients  $\mu$  and  $a_n$  depend on the length of the sponge layer  $B_s$  [18]. For regular waves with  $H_i = 1$  m and  $T = 5.2$  s generated in the centre of a wave flume (Figure 5.25) the reflection coefficient  $K_r$  equals 2 % for  $\mu = 1.04$  and  $a_n = 60$ . The reflection coefficient when using  $S_3$  in the sponge layer is of the same order of magnitude as when using the absorption functions  $S_1$  or  $S_2$  or when using the damping coefficient  $D_s$  (Table 5.1). Furthermore negative effects of the side sponge layers are avoided (Figure 5.29). Only at the end of the inner domain a small deviation is seen. The longer the wave basin, the larger side sponge layers are needed ( $B_s > 3L$ ). Also the reflection from the side boundaries when waves are not propagating perpendicular to the domain boundaries is much smaller, when comparing Figure 5.26 (absorption function  $S_1$ ) and Figure 5.4 (absorption function  $S_3$ ).

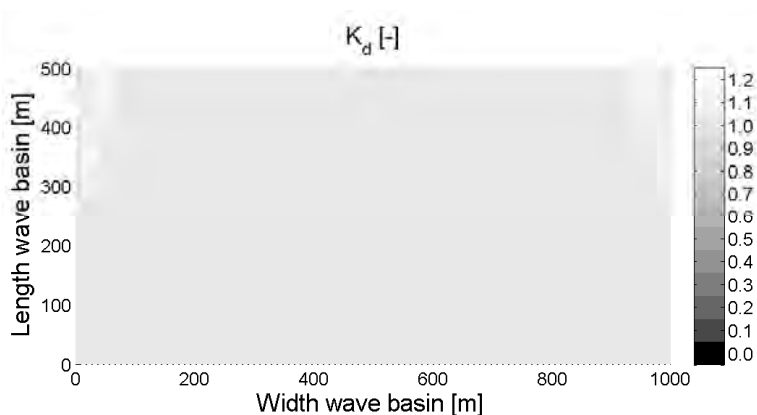


Figure 5.29: Calculated disturbance coefficient  $K_d$  for regular LCW with  $H_i = 1$  m,  $T = 5.2$  s and  $\theta = 90^\circ$  in a domain (1 000 m x 500 m) with the absorption function  $S_3$  in the side sponge layers

In this PhD work the absorption function  $S_3$  with  $\mu = 1.04$  and  $a_n = 60$  has been used in all simulations.

## 5.5 Code development

The existing source code of the mild-slope equation model MILDwave [3] has been further developed, extended and validated in this PhD research. The extension of the wave generation technique, together with the absorbing domain boundaries, has been described in the previous sections. The validation of the model is presented in the following sections and in chapter 6. The implementation of wave power absorption in MILDwave is discussed in chapters 6 and 8. Finally a preprocessor has been developed to facilitate the preparation of the required input for MILDwave. The practical use of the mild-slope equation model MILDwave together with the resulting flow chart of the calculations in MILDwave is given in appendix E.

## 5.6 Reflection on a vertical, surface-piercing wall

With the described wave generation and propagation the interaction of waves with predefined structures (reflection, transmission and diffraction) can be studied in MILDwave. The reflection on a vertical, impermeable and permeable, surface-piercing wall is validated with a simple test case in this section. In section 5.7 the diffraction around the tip of a semi-infinite breakwater is calculated in MILDwave and compared with analytical results.

### 5.6.1 Reflection on a vertical, impermeable, rigid surface-piercing wall

A vertical, impermeable wall with a length of 36 m has been implemented in a numerical wave flume (Figure 5.30).

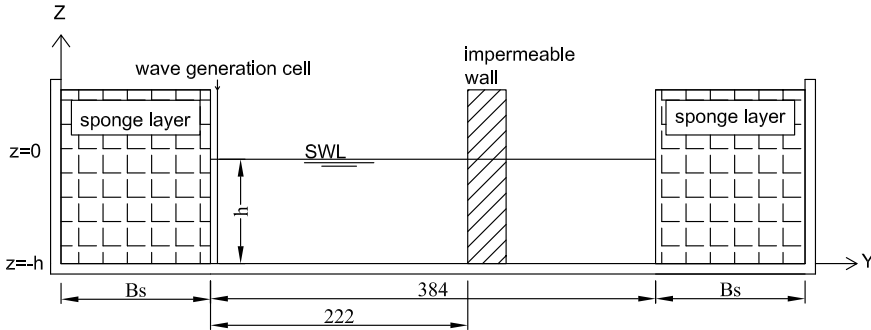


Figure 5.30: Side view of numerical wave flume - dimensions in m

The computational domain consists of an inner domain of 384 m and a sponge layer in the beginning and at the end. Regular waves with an incident wave height  $H_i = 1$  m and wave period  $T = 5.2$  s are generated in a constant water depth of 30 m. Figure 5.31 shows the surface elevations between  $t = 100 T$  and  $t = 101 T$  with an interval of  $1/13 T$ , in the inner domain. Note that the sponge layers are not shown.

A standing wave with an anti-node next to the impermeable wall is observed, as expected [32]. An anti-node of a standing wave is a point of the surface profile, where the water particle oscillates with an amplitude equal to the incident wave height. The horizontal particle velocity is equal to zero in these points. To obtain no horizontal particle velocity, the gradient of  $\varphi$  must be zero at the intersection of the water and the impermeable wall [11, 17]. Consequently the value of  $\varphi$  in the first obstacle cell in MILDwave is set equal to the value of  $\varphi$  in the water cell next to the obstacle, to prevent water flow towards the obstacle.

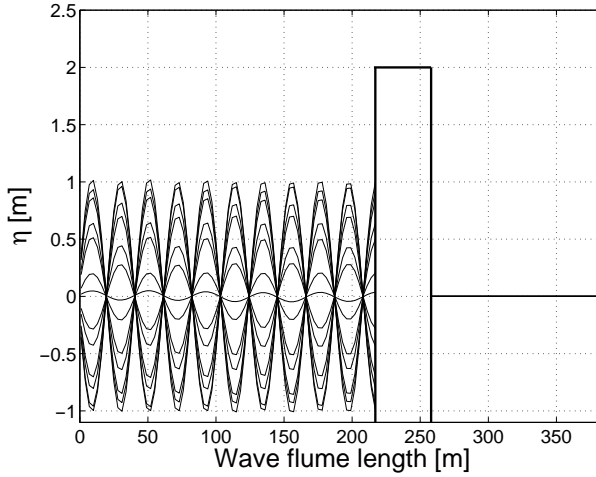


Figure 5.31: Surface elevations during one wave period (time step of  $1/13 T$ ) in a wave flume with a vertical, impermeable, rigid surface-piercing wall

## 5.6.2 Reflection on a vertical, permeable, surface-piercing wall

Further a partial reflecting and transmitting wall has been tested in the numerical wave flume, given in Figure 5.30. The partial reflecting obstacle has been modelled as an array of cells that have been assigned a given degree of absorption using the sponge layer technique. An absorption coefficient  $S = 0.95$  is attached to each cell of the structure. Each new time step, the calculated surface elevation is multiplied with this absorption coefficient. The surface elevations between  $100 T$  and  $101 T$ , with an interval of  $1/13 T$ , are shown on Figure 5.32.

The surface elevation  $\eta$  in front of the obstacle is given by:

$$\begin{aligned} \eta &= \eta_i + \eta_r \\ &= (a_i + a_r) \sin(k(y^* + B_s)) \cos(\omega t) \\ &\quad - (a_i - a_r) \cos(k(y^* + B_s)) \sin(\omega t) \end{aligned} \quad (5.35)$$

with  $\eta_i = a_i \sin(k(y^* + B_s) - \omega t)$  the incident surface elevation and  $\eta_r = a_r \sin(k(y^* + B_s) + \omega t)$  the reflected surface elevation. The largest amplitude  $a_{max} = a_i + a_r$  occurs at  $y^* + B_s = L/4 + rL/2$  ( $r = \text{integer}$ ), while the smallest amplitude  $a_{min} = a_i - a_r$  is observed at  $y^* + B_s = 0 + rL/2$ . In this example large sponge layers in the beginning and at the end of the wave flume are used to prevent any reflection inside the simulation domain. Therefore  $B_s$  equals  $6.25 L$ .  $a_i$  and  $a_r$  can be determined with equations (5.36) and (5.37) [33].

$$a_i = \frac{1}{2} (a_{max} + a_{min}) \quad (5.36)$$

$$a_r = \frac{1}{2} (a_{max} - a_{min}) \quad (5.37)$$

Finally the reflection coefficient on the permeable wall is derived by the ratio  $\frac{a_r}{a_i} = \frac{a_{max} + a_{min}}{a_{max} - a_{min}}$ . The values of  $a_{max}$  and  $a_{min}$  are measured on Figure 5.32 and equal 1.22 m and 0.82 m, respectively. The reflection coefficient is equal to 19 %, which is also obtained when measuring the waves in front of the wall with an array of three wave gauges and performing a reflection analysis.

Behind the obstacle an almost perfect progressive wave with an amplitude of 0.10 m is observed. Reflection on the absorbing sponge layer at the end of the wave flume is negligible ( $\pm 1\%$ ).

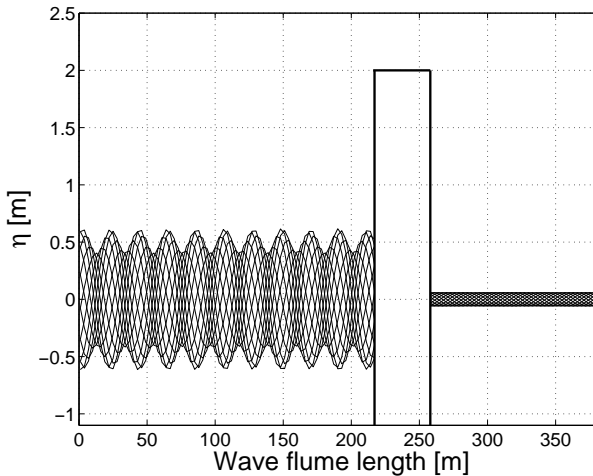


Figure 5.32: Surface elevations during one wave period (time step of  $1/13 T$ ) in a wave flume with a vertical, permeable, surface-piercing wall

## 5.7 Wave diffraction around the tip of a semi-infinite breakwater

A semi-infinite breakwater has been modelled in MILDwave as a totally reflective obstacle. Regular waves with an incident wave height  $H_i = 1$  m and a wave period  $T = 5.2$  s have been generated on a line, at a distance of  $3 L$  up wave of the breakwater, in a domain of constant water depth ( $= 30$  m). The incident waves propagate perpendicular to the breakwater ( $\theta = 90^\circ$ ). The inner domain has a width of  $20 L$  and a length of  $10 L$  behind the breakwater. Absorbing sponge layers have been placed around the inner domain to prevent reflection inside the simulation domain. The computational domain is shown in Figure 5.33.

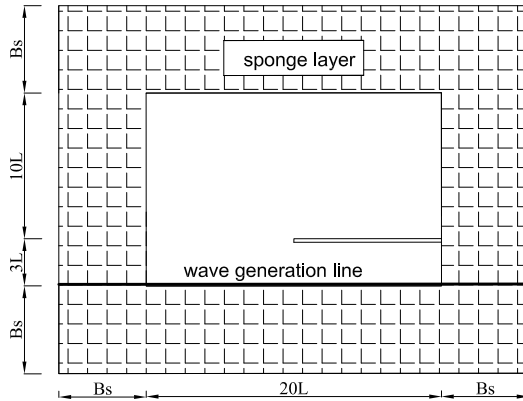


Figure 5.33: Plan view of computational domain for diffraction around a semi-infinite breakwater

The diffraction coefficient, defined as the ratio between the diffracted wave height in the lee of the breakwater and the incident wave height at the breakwater tip, calculated in MILDwave is compared to the diffraction coefficient, denoted by  $K'$ , given in the diagram of Wiegel [8] in Figure 5.34.

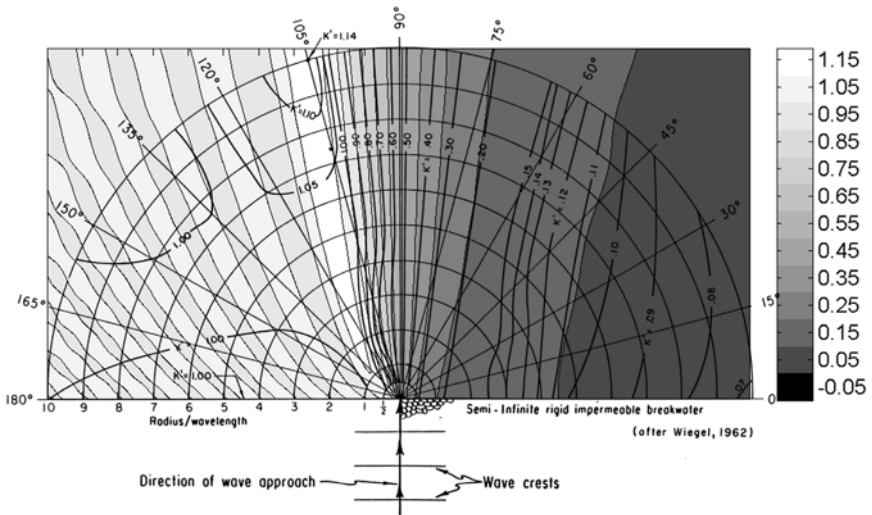


Figure 5.34: Comparison between diffraction coefficients in the lee of a semi-infinite breakwater, calculated in MILDwave and given in the diffraction diagram of Wiegel [8]

The diffraction theory for a semi-infinite breakwater was developed by Penny

and Price [34]. They showed that the solution of Sommerfeld for diffraction of light passing the edge of a semi-infinite screen, also applies to the diffraction of linear surface waves that propagate past the end of a semi-infinite thin, vertical-faced, rigid, impermeable barrier. Wiegel [35] has compiled the analytical results from Penny and Price as diffraction diagrams [8]. Figure 5.34 shows a very good agreement between the analytical and numerical results in the lee of the breakwater. Next to the breakwater, a larger zone with  $K' \geq 1.10$  is observed in MILDwave compared to the analytical results. In the left part of the figure, the contours in the numerical results and in the diffraction diagram differ, while their values vary in both cases between 0.9 and 1.1. The disturbance coefficients smaller than 0.2 are shown in more detail in Figure 5.35.

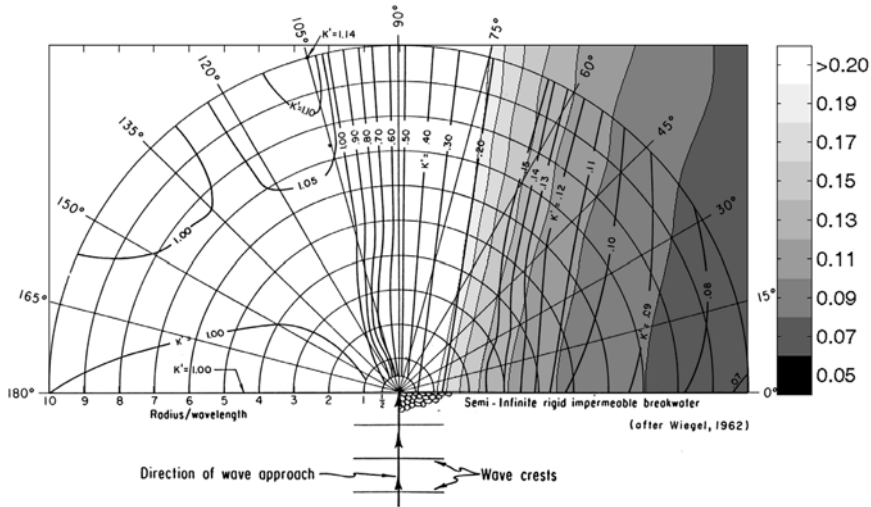


Figure 5.35: Detailed comparison between diffraction coefficients smaller than 0.2 in the lee of a semi-infinite breakwater, calculated in MILDwave and given in the diffraction diagram of Wiegel [8]

In general a good agreement is found. The contours in MILDwave correspond better with the contours in the diffraction diagram for higher values of  $K'$ .

## 5.8 Conclusions

In this chapter the wave generation and propagation in the mild-slope equation model MILDwave have been presented. In the past, only regular and irregular long-crested head-on waves were generated in MILDwave with the source term addition method. In this chapter this internal wave generation technique has been



extended to generate regular and irregular long-crested waves with varying wave angles and irregular short-crested waves. Generating regular long-crested waves with  $0^\circ < \theta < 90^\circ$  on two wave generation lines and an arc results in the most accurate wave pattern in the simulation domain. This wave generation set-up is also used to generate irregular long-crested waves with  $0^\circ < \theta < 90^\circ$  and short-crested waves in this PhD dissertation. Long-crested head-on waves are generated on a single wave generation line. Furthermore, wave generation on a circle has been implemented to simulate waves radiated by WECs of the first category. This wave generation set-up has been validated by using the principle of conservation of energy.

When waves are not propagating along the x-axis or y-axis, absorbing side sponge layers, together with absorbing sponge layers in the beginning and at the end of the simulation domain, are needed to prevent reflection from the domain boundaries. The common types of absorbing sponge layers absorb too much energy from the simulation domain when installed at the side boundaries. Moreover, still some reflection from the side boundaries is observed. Therefore a new absorption function has been developed. This absorption function overcomes this unwanted energy absorption and diminishes wave reflection inside the simulation domain.

The wave transformation processes wave reflection, transmission, diffraction and power absorption are very important when modelling a WEC in MILDwave. The first three processes are simulated intrinsically in MILDwave and have been validated at the end of this chapter with two test cases; reflection from (and transmission through) a vertical, surface-piercing wall and diffraction around the tip of a semi-infinite breakwater. As expected, a standing wave in front of an impermeable wall is obtained, while a partial reflected wave in front of a permeable wall is observed. In general, a good agreement with the diffraction diagram of Wiegel is seen.

## References

- [1] A. Sinha and G. Wei. *Simwave, a Boussinesq model wave simulator*. Technical report, 1998.
- [2] L. De Doncker. *Numeriek model voor de voortplanting van watergolven in de kustzone: validatie en toepassing*. Master's thesis, Ghent University, 2002.
- [3] R. Caspeele. *Generatie van onregelmatige lang- en kortkruinige golven in een numeriek model voor golfvoortplanting: implementatie, validatie en toepassing*. Master's thesis, Ghent University, 2006.
- [4] J.A. Battjes and J.P.F.M. Janssen. *Energy loss and set-up due to breaking of random waves*. In Proceedings of 16<sup>th</sup> Conference on Coastal Engineering, ASCE, New York, pages 569–587, 1978.
- [5] V. Gruwez. *Implementatie en validatie van golfbreking in het numeriek golfvoortplantingsmodel MILDwave*. Master's thesis, Ghent University, 2008.
- [6] J. Geeraerts, L. De Doncker, P. Troch, J. De Rouck, L. Van Damme, and T. Verwaest. *Numerical simulation of wave penetration in the planned harbour of Oostende - a comparison between numerical models*. In Proceedings of 13<sup>th</sup> International Harbour Congress, Antwerpen, Belgium, pages 363–370, 2003.
- [7] D. Vanneste, V. Stratigaki, and P. Troch. *Design of Oostende Harbour: Numerical simulation of wave propagation. Wave Conditions at Zeeheldenplein*. Technical report, Ghent University, 2008.
- [8] U.S. Army Corps of Engineers. *Shore Protection Manual, Volume I*, 1984.
- [9] A.C. Radder and M.W. Dingemans. *Canonical equations for almost periodic, weakly nonlinear gravity waves*. Wave Motion, 7:473–485, 1985.
- [10] N. Booij. *A note on the accuracy of the mild-slope equation*. Coastal Engineering, 7:191–203, 1983.
- [11] M. Brorsen and J. Helm-Petersen. *On the reflection of short-crested waves in numerical models*. In Proceedings of the 26<sup>th</sup> International Conference on Coastal Engineering, Copenhagen, Denmark, pages 394–407, 1998.
- [12] S. Andersen and T. Klindt. *Random wave propagation-based on the mild-slope equation*. Master's thesis, Department of Civil Engineering, Aalborg University, 1994.

- [13] G. Kim, C. Lee, and K.-D. Suh. *Internal generation of waves: Delta source function method and source term addition method*. Ocean Engineering, 34:2251–2264, 2007.
- [14] C. Lee and K.D. Suh. *Internal generation of waves for time-dependent mild-slope equations*. Coastal Engineering, 34:35–57, 1998.
- [15] J. Larsen and H. Dancy. *Open boundaries in short wave simulations - a new approach*. Coastal Engineering, 7:285–297, 1983.
- [16] K.D. Suh, C. Lee, Y.-H. Park, and T.H. Lee. *Experimental verification of horizontal two-dimensional modified mild-slope equation model*. Coastal Engineering, 44:1–12, 2001.
- [17] C. Lee and S.B. Yoon. *Internal generation of waves on an arc in a rectangular grid system*. Coastal Engineering, 54:357–368, 2007.
- [18] S. Pecqueur. *Het effect van radiatie bij de numerieke modellering van golfenergieconversie in een park lay-out op het Belgisch Continentaal Plat m.b.v. MILDwave*. Master's thesis, Ghent University, 2008.
- [19] C. Lee, G. Kim, and K.-D. Suh. *Extended mild-slope equation for random waves*. Coastal Engineering, 48:277–287, 2003.
- [20] Z. Liu and P. Frigaard. *Random Seas*. Technical report, Hydraulics and Coastal Engineering Laboratory, Aalborg University, 1997.
- [21] M.D. Miles. *A note on directional random wave synthesis by the single-summation method*. XXIII Congress, IAHR, Canada, C:243–250, 1989.
- [22] W.J. Pierson, G. Neuman, and R.W. James. *Practical methods for observing and forecasting ocean waves by means of wave spectra and statistics*, Pub. No. 603. US Naval Hydrographic Office, 1955.
- [23] L.J. Cote, O. Davis, W. Markes, R.J. McGough, E. Mehr, W.J. Pierson, J.F. Ropek, G. Stephenson, and R.C. Vetter. *The directional spectrum of a wind generated sea as determined from data obtained by the Stereo Wave Observation Project*. Meteor. Pap., 2:6, New York University, College of Engineering, 1960.
- [24] M.S. Longuet-Higgins, D.E. Cartwright, and N.D. Smith. *Observations of the directional spectrum of sea waves using motions of a floating buoy*. In Ocean Wave Spectra, pages 111–136. Prentice Hall, New York, 1963.
- [25] M.A. Donelan, J. Hamilton, and W.H. Hui. *Directional spectra of wind generated waves*. Philosophical Transactions of the Royal Society of London, Series A, 315:509–562, 1985.

- [26] Y. Goda and Y. Suzuki. *Computation of refraction and diffraction of sea waves with Mitsuyasu's directional spectrum*. Tech. Note of Port and Harbour Res. Inst., 230, 1975.
- [27] A.J. Kuik, G. Vledder, and L.H. Holthuijsen. *A method for the routine analysis of pitch and roll buoy wave data*. Journal of Physical Oceanography, 18:1020–1034, 1988.
- [28] D. Esteva. *Wave direction computations with three gage arrays*. In Proceedings of the 15<sup>th</sup> Coastal Engineering Conference, Honolulu, Hawaii, pages 349–367, 1976.
- [29] A.A. Fernandes, Y.V.B. Sarma, and H.B. Menon. *Directional spectrum of ocean waves from array measurements using phase/time/path difference methods*. Ocean Engineering, 27:345–363, 2000.
- [30] N. Hashimoto and K. Kobune. *Directional spectrum estimation from a Bayesian approach*. In Proceedings of the 21<sup>st</sup> International Conference on Coastal Engineering, Malaga, Spain, pages 62–76, 1988.
- [31] E.P.D. Mansard and E.R. Funke. *The measurement of incident and reflected spectra using a least squares method*. In Proceedings of the 17<sup>th</sup> International Conference on Coastal Engineering, volume 1, pages 154–172, 1980.
- [32] U.S. Army Corps of Engineers. *Coastal Engineering Manual (CEM) - Part II: Coastal Hydrodynamics - Chapter II-7: Harbor Hydrodynamics*, 2002.
- [33] J.W. Kamphuis. *Introduction to coastal engineering and management*. In Advanced Series on Ocean Engineering, volume 10. World Scientific, 2000.
- [34] W.G. Penny and A.T. Price. *The diffraction theory of sea waves by breakwaters, and the shelter afforded by breakwaters*. Philosophical Transactions of the Royal Society of London, Series A, 244:236–253, 1952.
- [35] R.L. Wiegel. *Diffraction of waves by semi-inifinite breakwater*. Journal, Hydraulics Division, American Society of Civil Engineers, 88:27–44, 1962.

# 6

## A farm of wave energy converters in MILDwave

### 6.1 Introduction

In a first part of this chapter a technique (sponge layer technique) is developed to implement a single and multiple WECs based on the overtopping principle in the time-dependent mild-slope equation model MILDwave (chapter 5). Each combination of reflection and transmission characteristics, and consequently absorption characteristics, can be modelled for all individual WECs in a farm according to the methodology presented in this chapter. The WEC implementation and its limitations are discussed in detail through a sensitivity analysis. The sponge layer technique, as described in this chapter, is extended in chapter 8 to implement a WEC of the first category.

In a second part of this chapter the developed approach is used to study the wave height reduction (wake effect) behind a single hypothetical WEC and a farm of hypothetical WECs of the overtopping type. The considered hypothetical WEC has the same working as a prototype WEC of the overtopping type and is for simplicity square. First the wake behind an isolated hypothetical WEC is investigated for uni- and multi-directional waves. Further, a farm of nine hypothetical WECs is implemented in MILDwave. The overall wave power absorption is studied for two farm lay-outs, i.e. an aligned grid and a staggered grid and for varying lateral and longitudinal spacing. The performance of each WEC in the farm is adapted to its incident wave power. The evolved technique

to study a farm in MILDwave is compared to a simplified technique, where a farm is modelled as one transmitting obstacle, used in [1–4] (see chapter 4 - section 4.3). Finally the power absorption of a farm of hypothetical WECs installed in a staggered grid on the Belgian Continental Shelf is assessed. In chapter 7, the methodology developed in this chapter is applied to a prototype WEC of the second category; the Wave Dragon WEC.

In a third part the implementation of wave power absorption in MILDwave is validated. When a WEC of the overtopping type is implemented in MILDwave the incident wave power is partly absorbed and partly redistributed around the WEC. The wave transformation processes reflection, transmission and diffraction have been validated with two simple test cases in chapter 5. In this chapter these physical processes are validated together with wave power absorption through experimental tests. First, the wave pattern around a complete reflective and an absorbing obstacle (WEC) is determined. Further, a farm of three absorbing obstacles is tested. At the end of this chapter a method is developed to calculate the power absorption of a WEC in a two-dimensional domain in MILDwave.

## 6.2 Implementation of wave power absorption in MILDwave

A WEC is a fixed or moored (rigidly or slack) structure that is able to extract wave power by its specific design. The amount of power produced by the WEC, as a function of the incident wave climate, is generally determined through a numerical or physical model of the WEC and summarized in a power matrix. In this section a technique is described to simulate WECs based on the overtopping principle which capture the water volume of overtopped waves in a basin above sea level and consequently absorb a part of the incident wave power comparable to a porous structure. Incident waves are partly reflected from the WEC, are partly overtopped in the basin and consequently absorbed and partly transmitted under and around the structure. Therefore, a WEC is only absorbing a specific amount of the incident wave power available over the width of the device. The degree of absorption, as a function of the incident wave climate, can be derived based on a power matrix from the WEC developer<sup>1</sup>. Also, the amount of reflection from the structure can be specified by the developer. In most cases the amount of reflection will be rather small as a WEC is designed to absorb wave power and to reduce energy losses by reflection and transmission.

---

<sup>1</sup>The produced power is the electrical power generated by the WEC. Transmission losses and losses due to planned and unplanned maintenance are not taken into account, unless explicitly mentioned. The produced power or electrical power generated by the WEC equals the absorbed power multiplied with a reduction factor to account for conversion losses (a.o. losses in generator).

A WEC is implemented in MILDwave as an array of cells (covering the spatial extensions of the WEC) that have been assigned a given degree of absorption using the sponge layer technique (Figure 6.1). Absorption functions  $S(x)$  or  $S(y)$  define the absorption coefficient  $S$  attached to each cell of the WEC in x-direction, respectively y-direction. By changing the values of the absorption coefficients or the number of absorbing cells, the degree of reflection and transmission and consequently absorption of the porous structure can be changed.

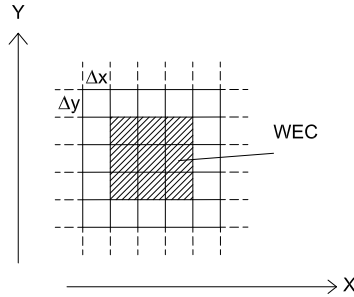


Figure 6.1: Definition sketch of a WEC implemented as an array of cells

When assuming a constant absorption coefficient  $S$  for all cells of the WEC, the amount of reflection, transmission and absorption are coupled, as seen in Venugopal et al. [5]. To avoid this coupling, different absorption functions  $S(y)$  are designed to tune the degree of absorption (and consequently transmission) for a fixed amount of reflection from the WEC as specified by the developer (section 6.2.3).

### 6.2.1 Numerical set-up

To tune the reflection, transmission and consequently absorption characteristics of a WEC a structure composed of a series of absorbing cells has been implemented in a numerical test flume (Figure 6.2). The structure has a length equal to the length of the WEC and a width equal to the wave flume width.

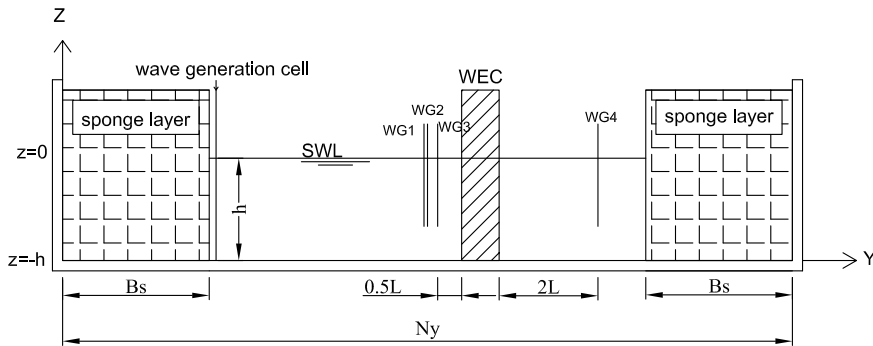


Figure 6.2: Definition sketch of numerical test flume - cross section

To determine the amount of reflection from and transmission through the absorbing structure, four wave gauges (WG) are placed in the numerical wave flume (Figure 6.2).

Three wave gauges are installed half a wave length in front of the structure to determine the incident and reflected wave with a reflection analysis. One wave gauge is placed two wave lengths behind the WEC to measure the transmitted wave. The time series at the wave gauges are sampled with a frequency of 10 Hz.

In all tests, a uniform deep water depth  $h$  is used. To obtain a steady state wave field, waves are generated during 3 000 s with a time step  $\Delta t = 0.1$  s. Waves with a peak period of approximately 5.2 s ( $T_p = 1.1 T_e$  [6]) and a significant wave height of approximately 1 m have a high frequency of occurrence in the southern North Sea (Tables 2.6, 2.10 and 2.11) and are considered as an input for the simulations.

The wave conditions (regular (reg) or irregular (irreg) waves, wave period  $T$  or peak wave period  $T_p$  and number of frequencies  $N$ ) and numerical test conditions (water depth  $h$ , grid spacing  $\Delta x$  and the number of grid cells along the length of the computational domain  $N_y$ ) are given for five test cases in Table 6.1.

Table 6.1: Wave conditions and numerical test conditions for five test cases in a wave flume

Test	Type of wave	$T$ or $T_p$ [s]	$h$ [m]	$\Delta x$ [m]	$N_y$ [-]	$N$ [-]
A	reg	5.2	30	3	214	1
B	reg	5.2	30	3	226	1
C	reg	6.5	70	3	427	1
D	reg	7.8	70	3	843	1
E	irreg	5.2	70	1	1 678	50

To study the impact of the wave period, two test cases with a higher wave



period (Test case C and D) have been selected. In all tests waves with a wave height of 1 m have been generated as the reflection coefficient  $K_r = \frac{H_r}{H_i}$ , the transmission coefficient  $K_t = \frac{H_t}{H_i}$ , where  $H_t$  is the transmitted wave height, and consequently the amount of absorption are independent of the incident wave height.

Two parameters can be varied to tune the WEC for a given wave climate; the value of the absorption coefficients (sections 6.2.2 and 6.2.3) and the number of absorbing cells (section 6.2.4).

## 6.2.2 Influence of the value of the absorption coefficient on the absorption characteristics

A WEC with a length of 36 m and with a constant absorption coefficient  $S(x)=S(y)=S$  along its length has been implemented in the wave flume (Figure 6.3).

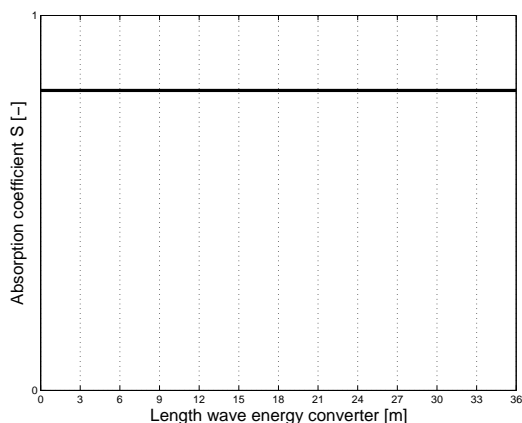


Figure 6.3: Model of WEC with a constant absorption coefficient  $S$  along its length

To study the absorbing effect of the WEC the absorption coefficient  $S$  has been assigned values from 0, increasing with 0.1 up till 1. The ratio of the measured wave amplitude  $\eta_i$  to the target wave amplitude  $a = \frac{H_t}{2}$ ,  $\frac{|\eta_i|}{a}$ , the reflection coefficient  $K_r$  and the transmission coefficient  $K_t$  are shown in Figure 6.4 as a function of the value used for  $S$  for test case A.

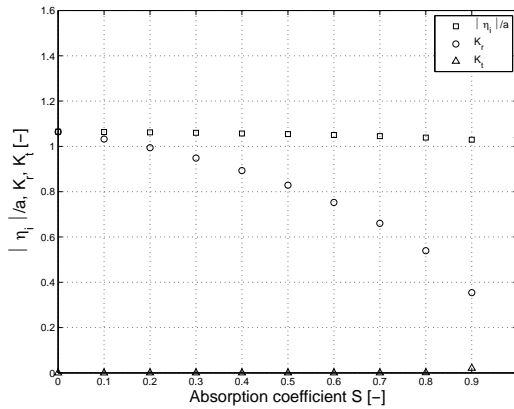


Figure 6.4: Dimensionless measured wave amplitude  $\frac{|\eta_i|}{a}$ , reflection coefficient  $K_r$  and transmission coefficient  $K_t$  for a WEC of 36 m with a constant absorption coefficient  $S$ , ranging from 0 to 1, for test case A

The measured wave amplitude  $\eta_i$  is slightly higher than the target amplitude  $a$  due to small oscillations as seen in [7, 8]. When  $S = 0$ , respectively 1, all incident wave power is reflected, respectively transmitted (Figure 6.4). A structure with a value of  $S$  equal to 0 represents a fully reflective structure. Cells with  $S$  equal to 1 are water cells. When the absorption coefficient is varying between 0 and 1, the incident wave is partly reflected, absorbed and transmitted. Figure 6.5 is showing  $\frac{|\eta_i|}{a}$ ,  $K_r$  and  $K_t$  in more detail for values of  $S$  between 0.8 and 1.

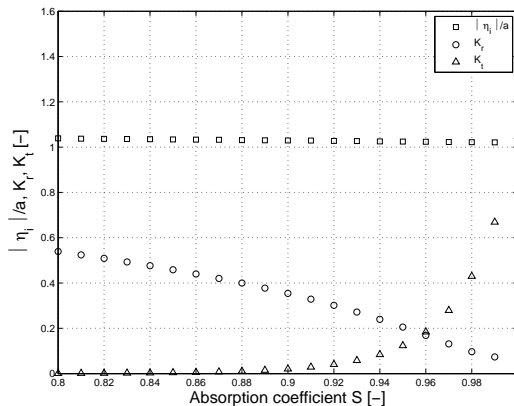


Figure 6.5: Dimensionless measured wave amplitude  $\frac{|\eta_i|}{a}$ , reflection coefficient  $K_r$  and transmission coefficient  $K_t$  for a WEC of 36 m with a constant absorption coefficient  $S$ , ranging from 0.8 to 1, for test case A

$K_t$  varies from quasi 0 to 1 for  $S$  between 0.8 and 1. For a WEC of 36 m

length, absorption coefficients need to vary between 0.9 and 1 when the WEC is not reflecting and absorbing all wave power.

The degree of absorbed power  $\frac{P_a}{P_i}$  in deep water is calculated with (conservation of energy):

$$\frac{P_a}{P_i} = 1 - K_r^2 - K_t^2 \quad (6.1)$$

with  $P_a$  the wave power absorbed by the WEC (W) and  $P_i$  the incident wave power over the width of the wave flume (W).<sup>2</sup>

Figure 6.6 gives the degree of power absorption as a function of the value used for  $S$ .

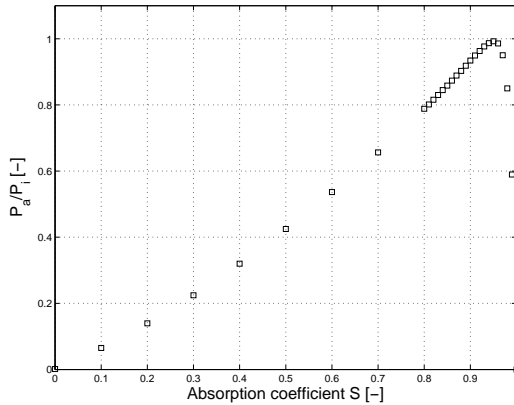


Figure 6.6: Dimensionless absorbed wave power,  $\frac{P_a}{P_i}$ , for a WEC of 36 m with a constant absorption coefficient  $S$ , ranging from 0 to 1, for test case A

As Figure 6.6 shows, each level of absorption can be modelled, but each level of absorption is coupled with a specific amount of reflection and transmission (as seen on Figure 6.4). It is possible that the amount of absorption coupled with the appropriate absorption coefficient to obtain the reflection coefficient given by the developer of the device, is not the actual degree of absorption of the device. This is the case if we consider for instance a WEC of 36 m length with a reflection coefficient of 0.1 and which is absorbing 80 % of the incident wave power. On the one hand, to obtain a reflection coefficient of 0.1, the WEC should consist of cells with an absorption coefficient of 0.98 (Figure 6.5) while on the other hand an absorption coefficient of 0.8 (Figure 6.6) is needed to obtain the required amount of absorbed power. To overcome this coupling several shapes of the absorption function  $S(y)$  have been designed. Note that the considered amount of absorption of 80 % is only used to illustrate the developed methodology. In practice the

<sup>2</sup> $P$  denotes the wave power (W) while  $p$  represents the wave power per meter of wave crest (W/m).

maximum observed amount of absorption of WECs of the overtopping type equals approximately 60 % [9, 10].

### 6.2.3 Uncoupling of reflection and transmission

The uncoupling of reflection and absorption is obtained by changing the shape of the absorption function  $S(y)$  through the WEC (when the direction of wave propagation =  $y$ -direction). As an example a WEC with a reflection coefficient of 0.35 (which means that 12 % of the incident wave power is reflected) and a degree of absorption of respectively 78 %, 86 % and 87 % for test case A has been modelled. Therefore three different curves of the absorption coefficient through the WEC,  $S_1(y)$ ,  $S_2(y)$  and  $S_3(y)$ , have been considered as shown in Figure 6.7.

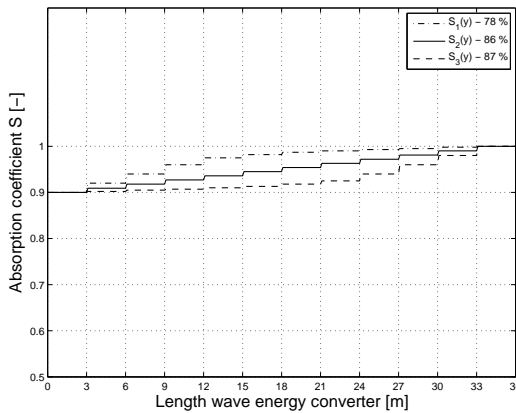


Figure 6.7: Change in absorption coefficient  $S$  through the WEC resulting in a degree of absorption of respectively 78 % for  $S_1(y)$ , 86 % for  $S_2(y)$  and 87 % for  $S_3(y)$

As  $K_t$  is only affected when  $S$  is varying between approximately 0.9 and 1 (Figure 6.5), the three chosen curves of the absorption coefficient vary between 0.9 and 1. The effect on  $K_r$  of the three different curves is minimal (Figure 6.8). The value of  $K_r$  is equal to the value of  $K_r$  for  $S = 0.9$  in Figure 6.5.  $K_r$  is only influenced by the value of  $S$  in the edge cells of the WEC. On the other hand  $K_t$  is clearly affected by the variation of  $S$  through the WEC (Figure 6.8). When using  $S_2(y)$  and  $S_3(y)$  almost no wave power is transmitted. On the other hand when  $S_1(y)$  is implemented,  $K_t$  is approximately 15 times higher than  $K_t$  for  $S = 0.9$  in Figure 6.5.

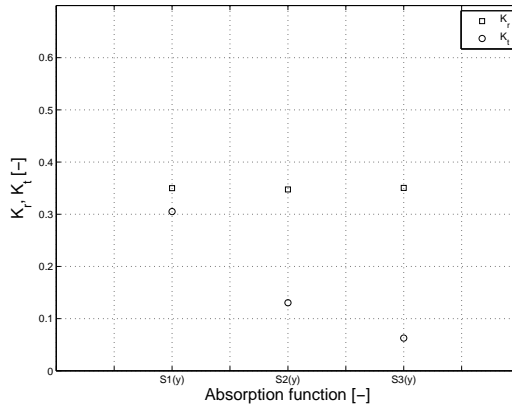


Figure 6.8: Reflection coefficient  $K_r$  and transmission coefficient  $K_t$  for three different shapes of the absorption function  $S(y)$ , as defined in Figure 6.7, for test case A

By changing the shape of the absorption function  $S(y)$  through the structure, the amount of transmission and consequently absorption is made independent of the amount of reflection. This way the degree of absorption (and consequently transmission) of the WEC, derived from the power matrix of the WEC, can be tuned for a fixed amount of reflection from the WEC as specified by the developer. So far only a WEC with a fixed length of 36 m has been considered. In a next paragraph the length of the WEC will be varied while the absorption coefficient is kept constant along its length (Figure 6.3).

## 6.2.4 Influence of the length of the WEC on the absorption characteristics

In Figures 6.9 and 6.10 the reflection, respectively transmission coefficient is given for a WEC with constant absorption coefficient  $S = 0.9$  and  $S = 0.98$  as a function of its length for test case B. After approximately 15 m the reflection coefficient is constant (Figure 6.9). Furthermore, the variation in the first 15 m is rather small ( $\leq 0.1 H_i$ ). For a higher absorption coefficient a longer obstacle is needed to reduce the amount of transmission (Figure 6.10) and consequently to obtain a higher level of absorption, as the variation of the reflection coefficient along its length is rather small (Figure 6.9).

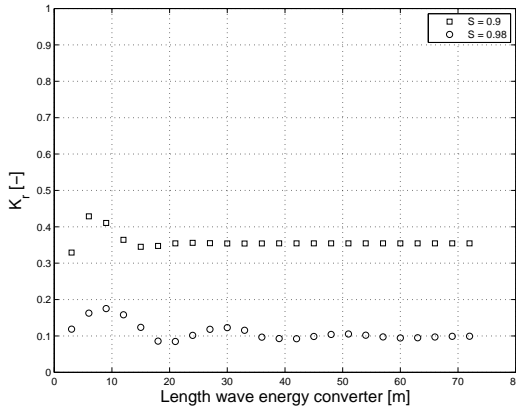


Figure 6.9: Reflection coefficient  $K_r$  for WECs with a constant absorption coefficient  $S = 0.9$  and  $S = 0.98$  and increasing length for test case B

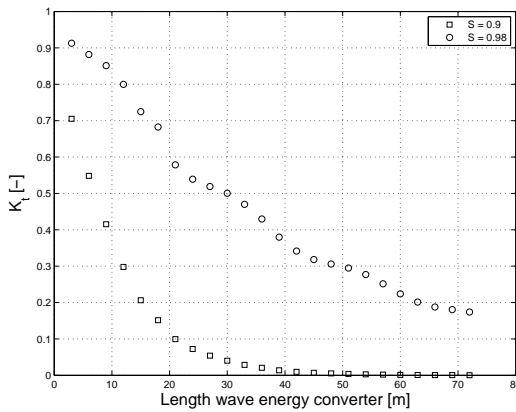


Figure 6.10: Transmission coefficient  $K_t$  for WECs with a constant absorption coefficient  $S = 0.9$  and  $S = 0.98$  and increasing length for test case B

Figure 6.11 shows the reflection coefficient as a function of the absorption coefficient  $S$  for a WEC with a length of respectively 3 m, 18 m and 36 m for regular waves with  $H_i = 1$  m and  $T = 5.2$  s (test case B). As expected  $K_r$  is equal for the three structures, as only the edge cells determine the amount of reflection. Figure 6.12 shows the dimensionless absorbed wave power as a function of the absorption coefficient  $S$  for a structure of 3 m, 18 m and 36 m for test case B. The maximum amount of absorbed wave power of the implemented WEC is depending on the dimensions of the WEC.

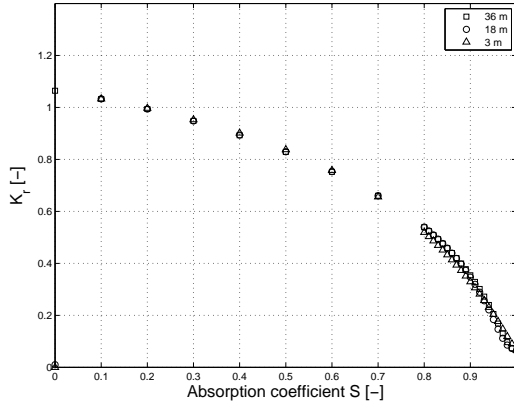


Figure 6.11: Reflection coefficient  $K_r$  for WECs with a constant absorption coefficient  $S$ , ranging from 0 to 1, and length of respectively 3 m, 18 m and 36 m for test case B

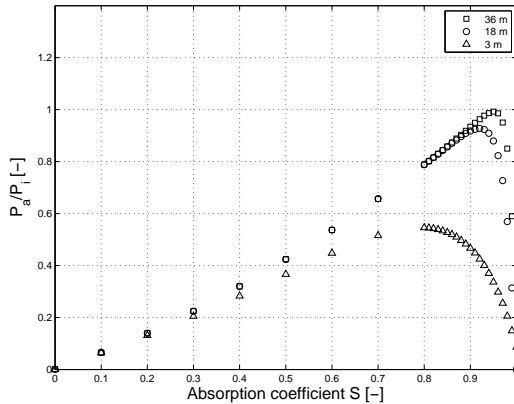


Figure 6.12: Dimensionless absorbed wave power,  $\frac{P_a}{P_i}$ , for WECs with a constant absorption coefficient  $S$ , ranging from 0 to 1, and length of respectively 3 m, 18 m and 36 m for test case B

When modelling a rather small WEC (smaller than approximately 18 m) an absorption of 100 % cannot be obtained, even not with the technique of uncoupling the reflection and transmission as the number of cells to vary the absorption coefficient is rather small. Each level of absorption can be modelled when the WEC is sufficiently long ( $\geq 18$  m). In general WECs based on the overtopping principle have sufficiently large dimensions to model each level of absorption.

The dimensionless absorbed wave power for a structure with a length of 3 m (1 cell) as shown on Figure 6.12 indicates that a cell always has a specific intrinsic absorption. An absorption coefficient of 0.8 implies an intrinsic absorption of 55 %

for regular waves with  $T = 5.2$  s. A smaller absorption cannot be obtained when implementing a WEC where the edge cell has an absorption coefficient equal to 0.8. An absorption coefficient equal to 0.8 corresponds to a reflection coefficient equal to 0.5 (Figure 6.11), which means that 25 % of the incident wave power is reflected. As WECs are designed to absorb as much wave power as possible and to minimize energy losses (e.g. by partly reflecting the incident wave) an absorption coefficient higher than 0.8 will be necessary to reduce the amount of reflection (Figure 6.11). Moreover a higher absorption coefficient results in a smaller intrinsic absorption (Figure 6.12). All levels of power absorption higher than the intrinsic absorption can be obtained under the condition that the WEC has a sufficient length to reach an absorption equal to 100 %. As a consequence the range of possible levels of power absorption increases with increasing absorption coefficient.

To summarise, for a sufficiently large WEC ( $\geq 18$  m for  $T = 5.2$  s or  $\frac{\text{length of WEC}}{L} \geq 0.4$ ) and a small amount of reflection, all levels of absorption, except very small absorption levels (smaller than the intrinsic absorption of the edge cells) which are not desirable in the current application, can be obtained.

## 6.2.5 Frequency dependent absorption

In a real situation the power absorption of a WEC will vary along the frequencies in the wave spectrum. A WEC will be tuned for a specific frequency range and cannot capture all the wave power of all frequency components. Therefore the influence of the wave period on the amount of absorbed wave power will be studied first. Further the change of the incident wave spectrum due to the absorbing effect of the WEC in the wave flume is studied. Finally, a WEC with a frequency dependent absorption as specified by the developer has been implemented in MILDwave.

### 6.2.5.1 Influence of the wave period on the absorption characteristics

In the previous sections only regular long-crested waves with wave period  $T = 5.2$  s have been generated. Two additional regular wave tests (C and D in Table 6.1) with respectively  $T = 6.5$  s and  $T = 7.8$  s are performed to analyse the frequency dependency of the absorption technique. The resulting reflection and transmission coefficients for different lengths of a WEC using a constant absorption coefficient  $S = 0.9$  are given in Figure 6.13 and Figure 6.14 for test cases B, C and D.

The amounts of reflection and transmission are increasing with increasing wave period. Moreover the increase of  $K_t$  is higher compared to the increase of  $K_r$ . Figure 6.14 indicates that for a larger wave period a longer WEC is needed to reduce the amount of transmission. One can clearly see that a transmission coefficient of 0.1 is obtained for a wave period  $T = 5.2$  s and  $T = 7.8$  s when the WEC has a length of respectively 20 m and 36 m. When calculating the amounts of



reflection and transmission as a function of the dimensionless length of the WEC ( $=\frac{\text{length of WEC}}{L}$ ), an increase in amount of reflection for increasing wave period still occurs, while on the other hand the amount of transmission is decreasing with increasing wave period.

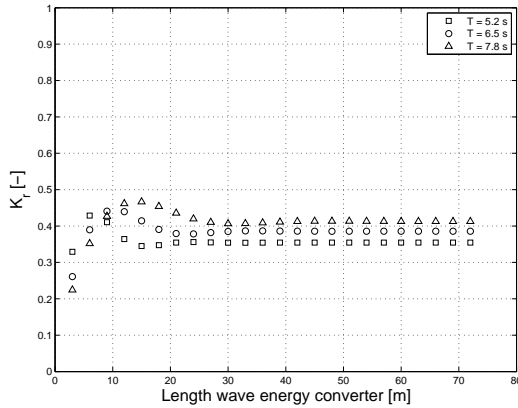


Figure 6.13: Reflection coefficient  $K_r$  for WECs with a constant absorption coefficient  $S = 0.9$  and increasing length for regular waves with wave periods of respectively 5.2 s, 6.5 s and 7.8 s

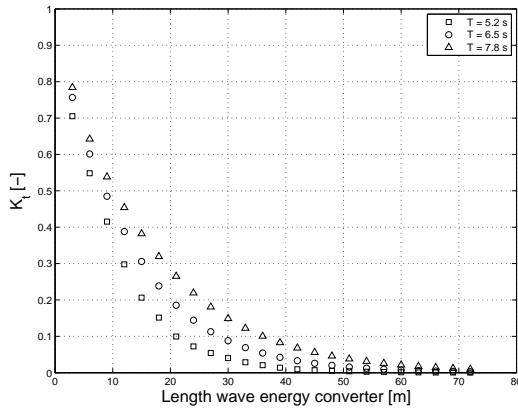


Figure 6.14: Transmission coefficient  $K_t$  for WECs with a constant absorption coefficient  $S = 0.9$  and increasing length for regular waves with incident wave periods of respectively 5.2 s, 6.5 s and 7.8 s

Further the dimensionless absorbed wave power is shown for a WEC with a fixed length of 36 m as a function of the absorption coefficient (Figure 6.15) for regular waves with respectively  $T = 5.2$  s, 6.5 s and 7.8 s.

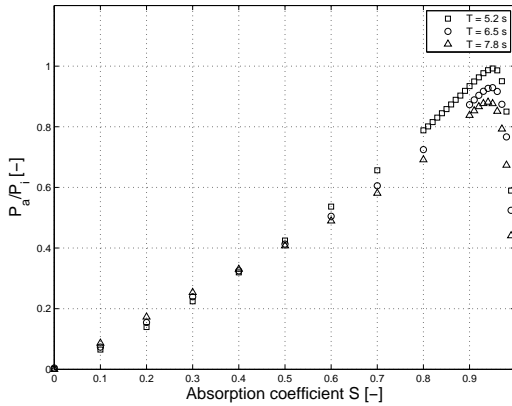


Figure 6.15: Dimensionless absorbed power,  $\frac{P_a}{P_i}$ , for WECs with a constant absorption coefficient  $S$ , ranging from 0 to 1 and a length of 36 m for regular waves with incident wave periods of respectively 5.2 s, 6.5 s and 7.8 s

As expected the amount of absorbed wave power is decreasing with increasing wave period as the amount of reflection and transmission increase with increasing wave period (Figure 6.13 and Figure 6.14). The impact of the wave period is increasing with increasing value of  $S$  (Figure 6.15).

Not only the value of the absorption coefficient and the length of the WEC affect the amount of absorption, but also the wave period. Consequently a tuning of the amount of reflection and absorption is needed for each wave climate.

### 6.2.5.2 Intrinsic frequency dependent absorption in MILDwave

As the amount of reflection from and the amount of transmission through a WEC depends on the incident wave period (Figure 6.13 and Figure 6.14), the change of the incident wave spectrum due to the energy absorbing effect of a wave energy converter in the wave flume is studied.

A WEC with a length of 36 m and a constant absorption coefficient  $S = 0.98$  has been tested in the wave flume (Figure 6.2) using irregular waves with  $H_s = 1$  m,  $T_p = 5.2$  s (Test case E). The frequency range was confined between  $0.75\bar{f}$  en  $2\bar{f}$  which covers 94 % of the total energy. Consequently the target significant wave height was reduced to 0.97 m.

The surface elevations at the wave gauges were recorded from 200 s to 3 000 s with a sampling interval of 0.1 s (total number of samples equal to 28 000). The estimation of the wave spectrum was based on subseries having a duration of 204.8 s corresponding to a spectral resolution of  $\Delta f = 0.00488$  Hz. Again a taper window and an overlap of 20 % have been used. Figure 6.16 shows the measured incident wave spectrum  $S_i(f)$  and transmitted wave spectrum  $S_t(f)$  in

front of and behind the WEC respectively. Furthermore the reflection coefficient,  $K_r(f) = \sqrt{\frac{S_r(f)}{S_i(f)}}$ , with  $S_r(f)$  the reflected wave spectrum, and the transmission coefficient  $K_t(f) = \sqrt{\frac{S_t(f)}{S_i(f)}}$  are given as a function of frequency.

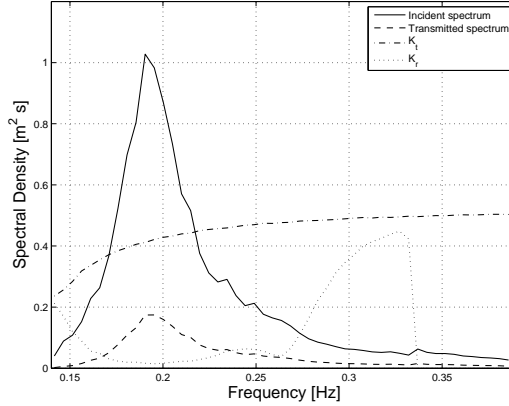


Figure 6.16: Comparison of frequency spectrum ( $\gamma = 3.3$ ) in front of and behind the WEC with a constant absorption coefficient  $S = 0.98$  and a length of 36 m for test case E

Surprisingly the transmission coefficient is slightly increasing with increasing frequency. A power absorption of 80 % ( $\frac{H_{s,i}^2 - H_{s,r}^2 - H_{s,t}^2}{H_{s,i}^2}$  where  $H_{s,i}$ ,  $H_{s,r}$ ,  $H_{s,t}$  are respectively the significant incident, reflected and transmitted wave height) is obtained which differs only slightly from the absorption of 85 % obtained for a regular wave with  $H_i = 1$  m and  $T = 5.2$  s (Figure 6.6). The small difference is caused by the nearly proportionally decrease of energy for all frequencies and consequently relatively small differences in amount of absorption for the different frequencies (Figure 6.17). Furthermore the overall reflection coefficient  $K_r = \frac{H_{s,r}}{H_{s,i}}$  and overall transmission coefficient  $K_t = \frac{H_{s,t}}{H_{s,i}}$  have approximately the same value as  $K_r$  and  $K_t$  for a regular wave with  $H_i = 1$  m and  $T = 5.2$  s. In a real situation the decrease of energy along the different frequencies of the spectrum will vary according to the amount of power absorption of the WEC for the frequency components in the spectrum as specified by the WEC developer.

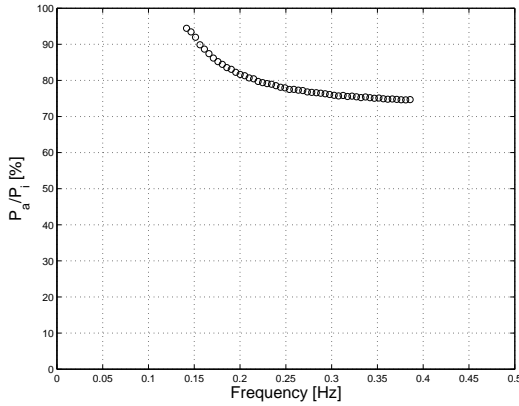


Figure 6.17: Dimensionless absorbed wave power by a WEC with a constant absorption coefficient  $S = 0.98$  and a length of 36 m for test case E

**6.2.5.3 Frequency dependent absorption as specified by the developer**

A typical example of the variation of the absorption of a WEC as a function of wave frequency is shown in Figure 6.18. In this section a WEC of 36 m and incident irregular long-crested waves with  $H_s = 1$  m and  $T_p = 5.2$  s have been considered. The corresponding overall absorption equals 37 % (= the total absorbed wave power in kW/m for all frequencies divided by the wave power in the incident wave).

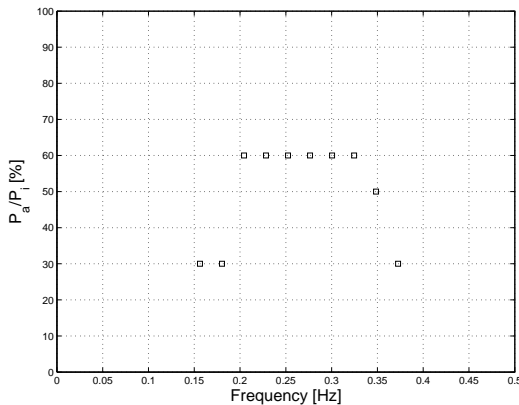


Figure 6.18: Dimensionless absorbed wave power of a WEC for ten wave frequencies as specified by the developer

For each frequency component and corresponding wave height  $H$  ( $H = \sqrt{8S(f)\Delta f}$ ) and absorption as specified in Figure 6.18, the transmitted wave

height  $H_t$  is determined based on equation (6.1).  $K_r$  is assumed smaller than 0.1 so that the amount of reflected wave power can be neglected. The resulting transmitted wave spectrum is shown in Figure 6.19.

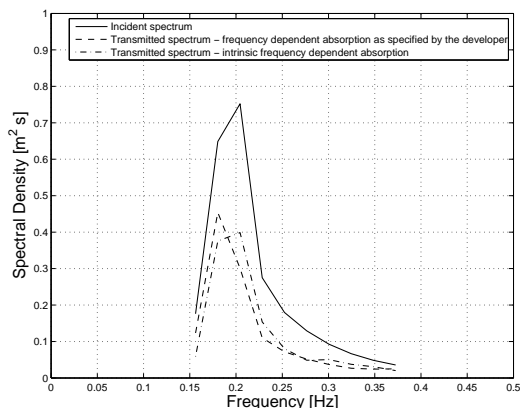


Figure 6.19: Comparison of transmitted frequency spectrum for a WEC with a frequency dependent absorption specified by the developer and with an intrinsic frequency dependent absorption

Further the transmitted wave spectrum has been measured in the wave flume (Figure 6.2) behind a WEC of 36 m with an absorption of 37 % for incident irregular long-crested waves with  $H_s = 1$  m and  $T_p = 5.2$  s.

In Figure 6.19 a comparison is made between the transmitted wave spectrum behind the WEC with an overall absorption of 37 % with a frequency dependent absorption as specified by the developer on the one hand and an intrinsic frequency dependent absorption as seen in the previous section on the other hand.

Both transmitted wave spectra correspond to a significant wave height of 0.77 m as the overall absorption is equal, but the transmitted wave spectra differ. The wake behind a WEC, where the frequency dependent absorption is specified by the developer, should be studied for each frequency component separately as the amount of absorption of the WEC in its lee will depend on the remaining energy in the considered frequency components. The latter remark also counts for wave direction dependent WECs. The wake should then not only be calculated for each frequency component but also for each wave direction.

## 6.3 Application of wave power absorption in MILD-wave

### 6.3.1 Wake behind a single hypothetical WEC

It is clear that the energy absorbing effect of a WEC reduces the wave height at its leeside. The amount of the reduction depends on the geometry (length and width) and the amount of absorption (absorption coefficient) of the WEC and on the incident wave climate. As an example the wake behind a hypothetical WEC of the overtopping type is studied in this section for four sea states with  $H_s = 1$  m and  $T_p = 5.2$  s or 7.8 s (Table 6.2). Irregular long-crested and short-crested waves are generated during respectively 3 500 s and 10 000 s with a time step of 0.05 s.

Table 6.2: Sea states

Test	$T_p$ [s]	$s_{max}$ [-]	$N$ [-]	$M$ [-]
F	5.2	-	50	-
G	7.8	-	50	-
H	5.2	75	20	11
I	5.2	10	20	11

The considered hypothetical WEC has the same working principle as a prototype WEC of the overtopping type and has for simplicity a square plan view shape (36 m x 36 m). The WEC is assumed to be fixed. The hypothetical WEC has a prespecified capture ratio of 45 % and a prespecified overall reflection coefficient of 0.14, for a sea state with  $H_s = 1$  m and  $T_p = 5.2$  s or 7.8 s. The capture ratio is defined as the ratio between the absorbed power and the wave power incident on a wave-front width equal to the width of the WEC.

Capture ratios between 10 % and 60 % for a floating WEC with multi level reservoirs have been experimentally (scale 1:45) obtained in the deep water 3D wave tank at Aalborg University [10]. In Tedd et al. [9] overtopping measurements between October 2004 and January 2005 on the 1:4.5 prototype Wave Dragon WEC at Nissum Bredning have been analysed. Capture ratios from a few per cent up to 60 per cent were observed. The assumed capture ratio of 45 % for the hypothetical WEC in this study represents the higher capture ratios which deserve most attention as they cause the largest wave height decrease. In chapter 7 a Wave Dragon WEC is implemented in MILDwave. The amount of the reflection on the ramp is determined by assuming that all energy below the bottom of the reservoir is transmitted. The ratio between the transmitted wave power and the wave power incident on a wave-front width equal to the width of the WEC varies between 2 %

and 42 %. In this study a ratio of 55 % is considered for the hypothetical WEC, as the amount of reflected wave power is negligible (overall reflection coefficient of 0.14).

The amounts of reflection and absorption of the hypothetical WEC are tuned in a wave flume with a width of 36 m. The edge cells of the WEC have been assigned an absorption coefficient with a value of 0.975 to obtain the correct amount of reflection (Figure 6.5) while the absorption coefficient increases up till the value 1 through the WEC to get a sufficient high transmission and consequently to obtain a capture ratio of 45 % for  $T_p = 5.2$  s. As the values of  $K_r$  and  $K_t$  are equal for regular and irregular long-crested waves (section 6.2.5.2) Figure 6.5 could be used. Without the technique of uncoupling the reflection and transmission, only an absorption of 90 % would have been possible with an overall reflection coefficient of 0.14, as seen in Figure 6.6. The intrinsic frequency dependent absorption in MILDwave is used as an example. As explained in section 6.2.5.3 the frequency dependent absorption of the WEC as specified by the developer can be easily taken into account.

The values of the absorption coefficient through the WEC have been tuned separately for each peak wave period to obtain a capture ratio of 45 %, since the absorption is frequency dependent. Depending on the type of WEC, the capture ratio can vary with mean incident wave direction. Only head-on waves are considered in this study.

The disturbance coefficients  $K_d$  in a wave basin with a single WEC for long-crested waves (head-on,  $\theta = 90^\circ$ ) with a peak wave period of respectively 5.2 s and 7.8 s (test cases F and G) are shown in Figures 6.20 and 6.21. The disturbance coefficient  $K_d \left( = \frac{H_{s,d}}{H_{s,i}} \right)$  is the ratio between the numerically calculated disturbed significant wave height  $H_{s,d}$  and the numerically calculated incident significant wave height at the wave generation boundary  $H_{s,i}$ . On these figures only the useful domain without sponge layers is shown. These long-crested waves are generated on a wave generation line parallel with the x-axis. The length and the width of useful domain are equal to respectively  $15L$  and  $10L$  where  $L = 100$  m (deep water wave length for  $T_p = 7.8$  s) for all test cases.

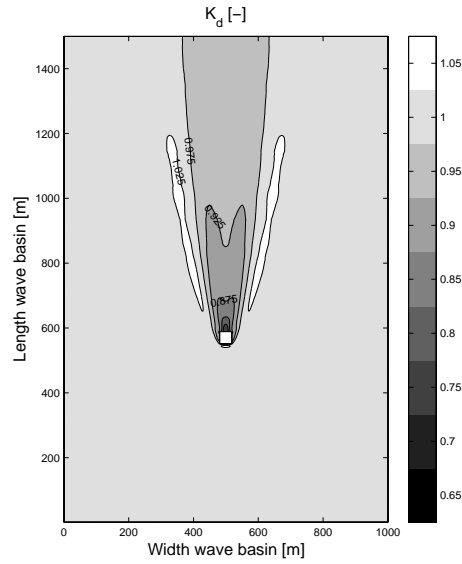


Figure 6.20: Calculated disturbance coefficient  $K_d$  in a wave basin with a single WEC (capture ratio of 45 %) for irregular long-crested waves (head-on) with  $T_p = 5.2$  s (test case F)

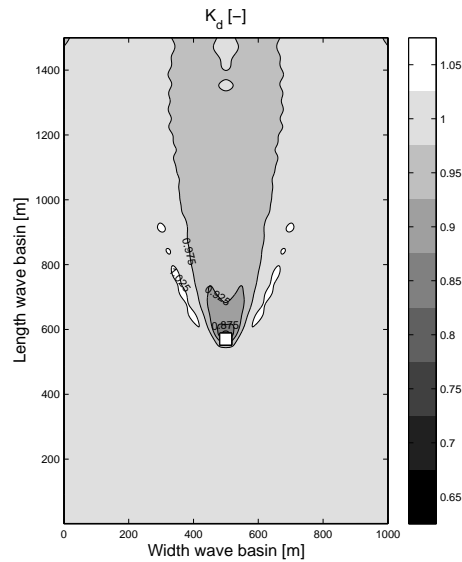


Figure 6.21: Calculated disturbance coefficient  $K_d$  in a wave basin with a single WEC (capture ratio of 45 %) for irregular long-crested waves (head-on) with  $T_p = 7.8$  s (test case G)



The position of the WEC is indicated by a white square. The WEC consists of concentric squares with values for the absorption coefficient increasing from 0.975 up to 1 ( $T_p = 5.2$  s). This concentric lay-out may have a minimal impact on the capture ratio of 45 %, as defined in the wave flume, due to edge effects. It will be shown in section 6.4.3 that this impact is negligible.

A small wave height increase at the edges of the wake due to diffraction is observed for both wave periods. The wave height decrease behind the WEC is smaller for a peak wave period of 7.8 s, approximately 0.175 m, compared to 0.225 m for a peak wave period of 5.2 s. Furthermore, the shadow zone is wider for a higher wave period. This result indicates that the peak wave length will influence the optimal pattern of a farm where a WEC should avoid the centre of the wake location of a neighbouring WEC. If swell waves are dominating, the peak wave period with the highest frequency of occurrence should be taken into account when designing the optimal pattern of a farm.

On the other hand, if wind waves are dominating, the shadow zone will be smaller and less visibly dependent on the directional spreading of the short-crested waves.

The disturbance coefficients around a single WEC are calculated for short-crested waves with a mean wave direction of  $90^\circ$  (Figure 6.22 and Figure 6.23) where the directional width is increasing from approximately  $9^\circ$  ( $s_{max} = 75$ ) up to  $24^\circ$  ( $s_{max} = 10$ ) for the peak period (as we assume a frequency dependent spreading parameter (equation (5.27))). To generate short-crested waves a set-up as shown in Figure 5.5 has been used which results in a useful domain indicated with black lines on Figures 6.22 and 6.23.

In the case of short-crested waves a wake is still observed, as the waves need to travel some distance before the effects of redistribution, caused by the directional spreading of the waves and wave diffraction around the WEC, are apparent. In Figure 6.22 a long shadow zone occurs behind the WEC, comparable with the one observed in Figure 6.20, as the directional spreading is still quite small (swell waves). In Figure 6.23 the shadow zone is shorter due to a faster redistribution behind the WEC from waves with wave angle between approximately  $90^\circ \mp 24^\circ$ .

It is clear that redistribution behind a device depends on the peak period and directional spreading of the incident wave climate. The higher the peak period and the higher the directional spreading, the faster waves are redistributed behind the WEC. The smaller the directional spreading the longer the shadow zone becomes. Therefore in the next paragraph, when studying the power absorption of a farm, only irregular long-crested waves have been considered as those waves cause the largest wake behind the WEC and consequently the largest impact on the neighbouring WECs in the farm. As a consequence, the calculated amount of absorbed power will be conservative.

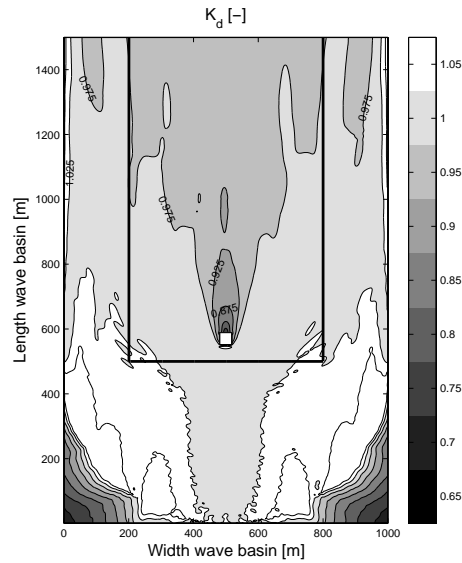


Figure 6.22: Calculated disturbance coefficient  $K_d$  in a wave basin with a single WEC (capture ratio of 45 %) for irregular short-crested waves with  $T_p = 5.2$  s,  $\theta_0 = 90^\circ$  and  $s_{max} = 75$  (test case H) - The useful domain is indicated with black lines

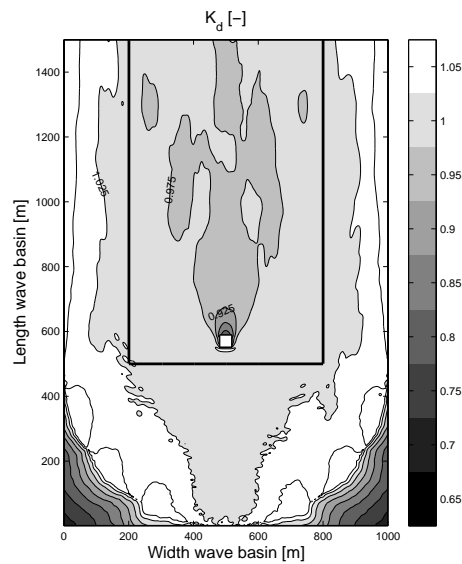


Figure 6.23: Calculated disturbance coefficient  $K_d$  in a wave basin with a single WEC (capture ratio of 45 %) for irregular short-crested waves with  $T_p = 5.2$  s,  $\theta_0 = 90^\circ$  and  $s_{max} = 10$  (test case I) - The useful domain is indicated with black lines

### 6.3.2 Wave power absorption of a farm of hypothetical WECs

The understanding of the impact of one WEC on the wave climate is very crucial in determining the capture ratio of its neighbouring WECs in a farm. Since a single WEC is reducing the incident wave height in its lee, the capture ratio of a WEC installed in its lee will decrease or increase depending on the magnitude of the wave height reduction. The latter reduction is determined by the dimensions and capture ratios of the surrounding WECs, by the incident wave climate and by the in-between distance of the WECs in the farm. The dimensions of a WEC define the diffracted wave pattern around the WEC, while the magnitude of wave height reduction in the diffracted wave pattern is depending on its capture ratio. The incident wave climate determines the redistribution of wave energy behind the WEC. The higher the distance between the WECs the more energy is travelling inside the farm. Furthermore, the distance between the WECs in a row and the in-between distance of the rows will determine the total impact of the farm on the wave climate and on the surrounding users of the sea. A minimal distance equal to twice the WEC dimension is needed to remove a damaged WEC from the farm.

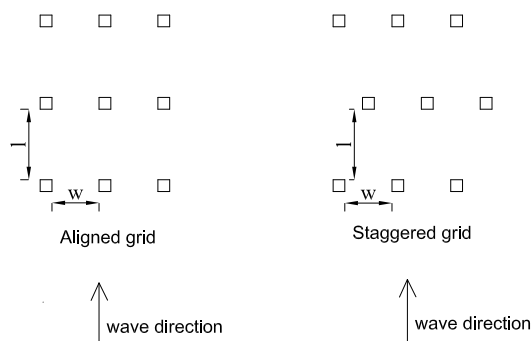


Figure 6.24: Aligned and staggered grid lay-out

In this section the influence of the lateral and longitudinal spacing, respectively  $w$  and  $l$ , on the amount of absorbed wave power is studied for incident irregular long-crested waves with  $H_s = 1$  m and  $T_p = 5.2$  s (test case F). Two different lay-outs (Figure 6.24) with nine hypothetical WECs, as defined in the previous sections, have been compared; a lay-out with 3 identical rows (an aligned grid), where the WECs are placed right behind each other and a lay-out where the first and third row are identical, but where the second row is shifted (a staggered grid). The length and the width of the wave basin defined in Figure 6.20 and Figure 6.21 have been extended to obtain a sufficiently large domain to generate long-crested head-on waves with a peak wave period of 5.2 s. A hypothetical

power matrix for irregular long-crested incident waves with  $T_p = 5.2$  s as shown in Figure 6.25 has been used as an example. The power matrix in this section is showing the ratio between the absorbed wave power and the incident wave power and not the electrical power output. This means that losses in turbines, generator, ... are ignored. The capture ratio has been plotted for significant wave heights between 0.45 m and 1 m. No variation with wave period has been considered as only irregular long-crested waves with  $H_s = 1$  m and  $T_p = 5.2$  s have been generated. Each capture ratio (Figure 6.25) has been tuned in a wave flume as explained before. The overall reflection coefficient  $K_r$  was assumed smaller than 0.15 in all cases. In that case the resulting amount of reflected wave power was smaller than 2 % of the incident wave power. Due to the technique of uncoupling reflection and transmission, it was possible to keep the reflection small for each defined capture ratio and tune the amount of transmission and consequently the amount of absorption. The latter uncoupling was needed to implement a procedure of adaptive absorption (adapting the capture ratio of each WEC in the farm to its incident wave height without changing the amount of reflection) to simulate a farm.

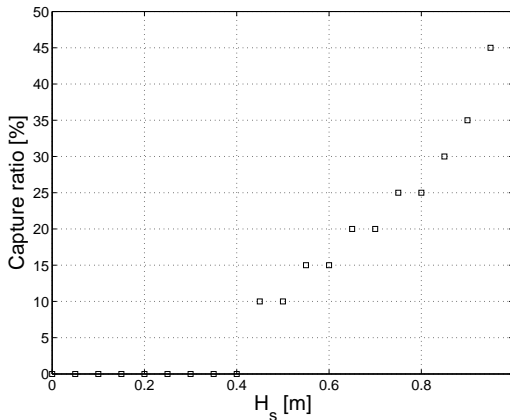


Figure 6.25: Capture ratio as a function of significant wave height  $H_s$

In a first step, only 3 WECs, with an in-between distance  $w$  of respectively  $2D_h$ ,  $4D_h$  and  $6D_h$  with  $D_h =$  width of the WEC, in the first row with the same capture ratio as an isolated WEC (45 %) have been installed. The capture ratio of the WECs that will be installed in the second row, with  $l$  respectively  $2D_h$ ,  $4D_h$ ,  $6D_h$  and  $20D_h$ , is derived by measuring the wave height on the positions of the WECs and by using Figure 6.25. In a second step, WECs in the two first rows are installed in the wave basin and the wave height is measured on the positions of the WECs in the third array. The average wave height on the WEC positions has been

used to define its capture ratio. The dimensionless calculated disturbed significant wave heights  $K_d$  in a wave basin with only the first row of WECs installed, is given in Figure 6.26 for test case F. Again, only the useful domain without sponge layers is shown and the positions of the WECs are indicated by white squares.

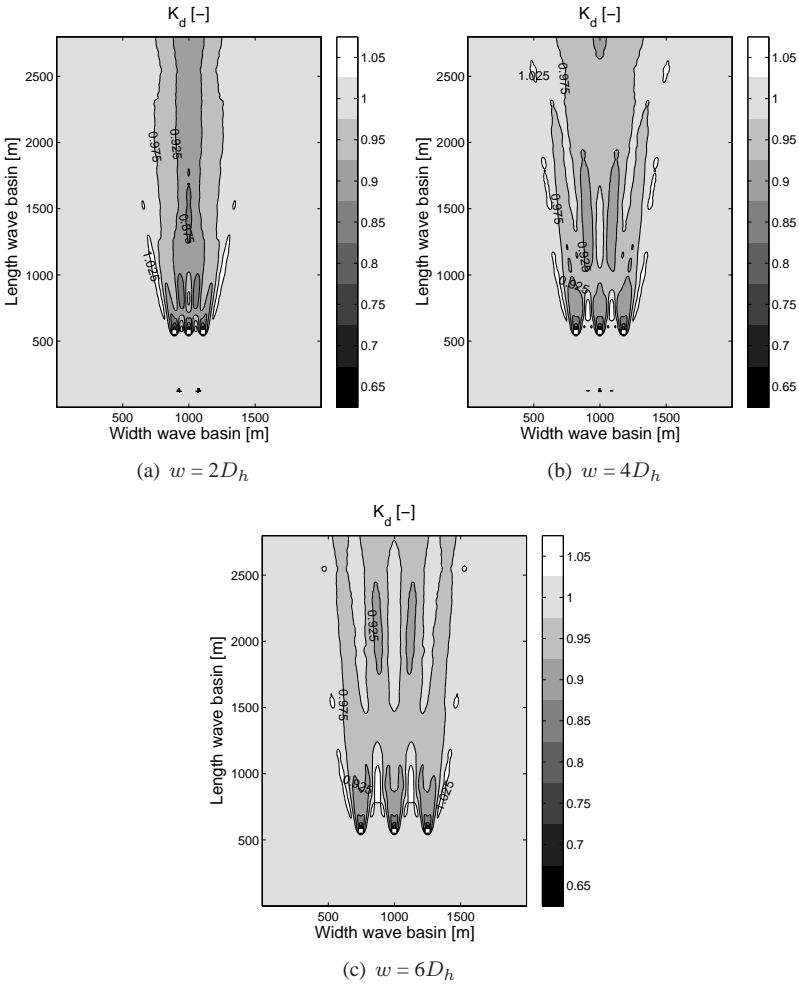


Figure 6.26: Calculated disturbance coefficient  $K_d$  in a wave basin with three hypothetical WECs with an in-between distance of respectively (a)  $2D_h$ , (b)  $4D_h$ , (c)  $6D_h$  with  $D_h = 36$  m for irregular long-crested waves (head-on) with  $T_p = 5.2$  s

The higher the in-between distance the more energy is travelling between the WECs. The closer the WECs in the first row are installed, the faster the interaction

between the individual wakes in the lee of that row.

The dimensionless calculated disturbed significant wave heights  $H_{s,d}$  for both lay-outs (aligned grid and staggered grid) are given in Figure 6.27 for test case F and a lateral and longitudinal spacing of  $2D_h$ . For both lay-outs waves are simulated during 3 500 s (time step 0.05 s) in a domain of 3 400 cells (width) x 3 500 cells (length) which resulted in a computational time of 24 hours (Intel Core 2 CPU @ 2.40 GHz - 3 GB RAM).

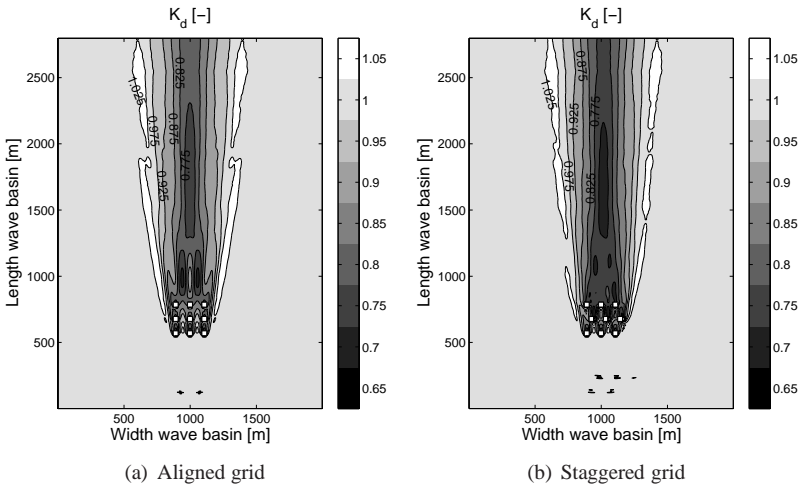


Figure 6.27: Calculated disturbance coefficient  $K_d$  in a wave basin with 9 hypothetical WECs with an in-between distance of  $2D_h$  with  $D_h = 36$  m for irregular long-crested waves (head-on) with  $T_p = 5.2$  s.

The wave height in front of the second and third row is much higher for the staggered grid, which resulted in a higher capture ratio for the WECs in those rows (capture ratio of respectively 45 % and 35 % for the second and third row) compared to the aligned grid (capture ratio of 30 % for the second and third row).

Both lay-outs are compared in more detail in Figure 6.28 and Figure 6.29 with a lateral section right behind the farm on  $y^* = 805$  m, and respectively a longitudinal section behind the farm on  $x^* = 1\,000$  m shown for both lay-outs.

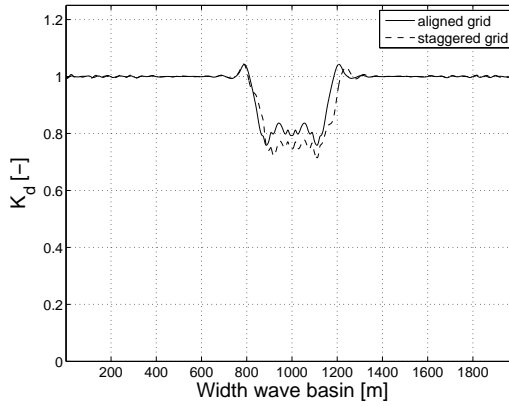


Figure 6.28: Calculated disturbance coefficient  $K_d$  in a lateral section at  $y^* = 805$  m for an aligned and a staggered grid with a lateral and longitudinal spacing of  $2D_h$  (Figure 6.27)

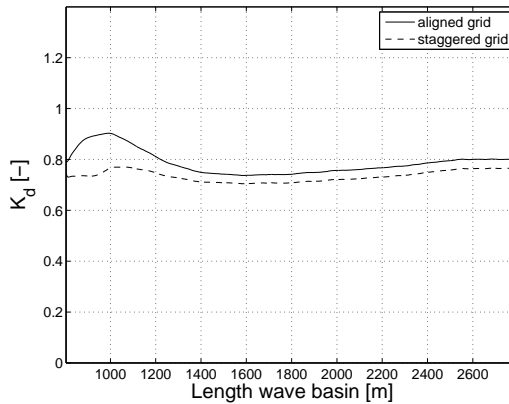


Figure 6.29: Calculated disturbance coefficient  $K_d$  in a longitudinal section at  $x^* = 1000$  m behind an aligned grid and a staggered grid with a lateral and longitudinal spacing of  $2D_h$  (Figure 6.27).

The wave height is lower (higher wave height reduction) behind the staggered grid compared with the aligned grid due to the higher capture ratio of the WECs in the second and third row. When a constant capture ratio (no adaptive absorption) would be assumed for all WECs in the farm, the difference between both lay-outs would be very small.

In Figure 6.28 the cross section is symmetric for the aligned grid, as the lay-out is symmetric as well. The wake behind both lay-outs is gradually filled up behind

the farm (Figure 6.29).

The amount of absorbed power of an aligned and a staggered grid with varying in-between distances is calculated in the next sections for irregular long-crested waves with  $H_s = 1$  m and  $T_p = 5.2$  s (test case F). The results are conservative as the considered incident waves are rather small and no directional spreading of the incident waves has been considered.

### 6.3.2.1 Aligned grid

Table 6.3(a) shows the loss of the amount of absorbed power of the farm compared to a theoretical farm of nine independent WECs, for the considered in-between distances. The theoretical farm is absorbing 9 times  $P_s$ , the power absorbed by a single WEC (capture ratio of 45 %). The loss of the amount of absorbed power is expressed in a multiple of  $P_s$ . It is expected that the absorbed power loss decreases with increasing in-between distances. However, interaction between the wakes results in some deviations. The small wave height increase at the edges of the wake, observed in Figure 6.20 and Figure 6.21, can partly compensate the wave height decrease behind a row of WECs (positive interaction of the wakes).

Table 6.3: Loss of power [multiple of  $P_s$ ]

(a) Aligned grid				(b) Staggered grid			
$l \setminus w$	$2D_h$	$4D_h$	$6D_h$	$l \setminus w$	$2D_h$	$4D_h$	$6D_h$
$2D_h$	3.02	3.11	3.11	$2D_h$	1.29	0.23	1.11
$4D_h$	2.14	2.64	2.64	$4D_h$	2.15	0	0.41
$6D_h$	1.70	2.11	2.18	$6D_h$	2.86	0.08	0
$20D_h$	2.58	0.92	0.70	$20D_h$	2.37	2.27	0.47

When  $w = 4D_h$  or  $6D_h$  the power loss is comparable. For example, for a lateral spacing  $w$  of  $2D_h$  and a longitudinal spacing  $l$  of  $4D_h$ ,  $6D_h$  positive interaction of the individual wakes occurs. Consequently, a smaller loss of power occurs compared to an aligned grid with  $w = 2D_h$  and  $l = 20D_h$ . The highest power loss ( $3.11P_s$ ) is seen for  $w = 4D_h$  or  $6D_h$ , and  $l = 2D_h$ . In those cases the WECs in the second and third row have a capture ratio of 30 %. When  $w = 6D_h$  and  $l = 20D_h$  only  $0.70P_s$  of power is lost. In that case all WECs in the farm have a capture ratio of 45 %.

Not only the total absorbed power of the farm is important. The absorbed power per  $\text{km}^2$  should be studied as well, as there may be space limitations for installing a farm of WECs. The smaller the in-between distances the higher the absorbed power per  $\text{km}^2$  (Table 6.4(a)). When calculating the absorbed power per



$\text{km}^2$  an area with half of the lateral spacing, respectively, longitudinal spacing has been added at the right and left end of the farm, respectively, in front of and behind the farm.

Table 6.4: Power absorption [ $\text{kW}/\text{km}^2$ ]

(a) Aligned grid				(b) Staggered grid			
$l \setminus w$	$2D_h$	$4D_h$	$6D_h$	$l \setminus w$	$2D_h$	$4D_h$	$6D_h$
$2D_h$	2 143	1 266	904	$2D_h$	2 761	1 886	1 212
$4D_h$	1 475	820	587	$4D_h$	1 472	1 162	792
$6D_h$	1 120	635	449	$6D_h$	943	822	597
$20D_h$	328	248	182	$20D_h$	340	207	187

The difference between loss of power for a lateral spacing of  $4D_h$  and  $6D_h$  is rather small. A lateral spacing of  $4D_h$  is preferred in comparison to  $6D_h$  as the power per  $\text{km}^2$  is higher.

### 6.3.2.2 Staggered grid

In general, a staggered grid results in a smaller loss of power compared with an aligned grid (Table 6.3(b)). Again the wave height increase at the edges of the individual wake results in some cases in positive interactions between the wakes. Consequently, the power loss is not always decreasing with increasing in-between distance.

Lay-outs with  $w = 4D_h$  and  $l = 2D_h$ ,  $4D_h$  and  $6D_h$ , respectively, and with  $w = 6D_h$  and  $l = 4D_h$ ,  $6D_h$  and  $20D_h$ , respectively, have the highest power absorption. Consequently, a lateral spacing of  $2D_h$  is not preferred. Again, a lateral distance of  $4D_h$  is preferable to  $6D_h$ , when calculating the absorbed power per  $\text{km}^2$  (Table 6.4(b)). Furthermore, a smaller longitudinal distance results in a higher power absorption per  $\text{km}^2$ . To select the best lay-out the cost per produced kWh should be considered as well. The latter aspect will be studied in chapter 9. In the next section the method to study a farm of WECs developed in this PhD work is compared to a simplified method, where a farm is modelled as a single transmitting obstacle.

### 6.3.2.3 Simplified method to estimate the wave power absorption of a farm

In most studies [1–4] a simplified method, where a farm is considered as one transmitting obstacle, is used to estimate the power absorption of a farm, as discussed in chapter 4. This simplified method takes only the overall absorption,

transmission and reflection into account while the redistribution of wave energy around the WECs in the farm due to (i) an alternation of full (gaps between the WECs) and partial transmission (WECs), (ii) diffraction, and (iii) radiation (floating WECs), is not taken into account. In this section this simplified method is used to study the power absorption of a farm of 9 WECs, as considered in the previous sections. For irregular long-crested waves (head-on) with  $H_s = 1$  m and  $T_p = 5.2$  s the wave power  $p$  equals 2.32 kW/m in deep water (appendix B). When  $w = 4D_h$ , the available wave power for one WEC in the row equals  $2.32 \cdot 5D_h = 417.6$  kW, with  $5D_h$  the width of the hypothetical WEC with half of the lateral spacing at both sides. The hypothetical WEC has a capture ratio of 45 %. Consequently the amount of absorbed power equals  $0.45 \cdot 2.32D_h = 37.6$  kW. Dividing the amount of absorbed power by the available wave power for one WEC in the row leads to an overall absorption of 9 %. Hence, an overall energy transmission of 91 % is obtained.

The available wave power for a farm with 9 hypothetical WECs with  $w = 4D_h$  equals  $2.32 \cdot 15D_h = 1\,252.8$  kW, with  $15D_h$  the width of the farm with half of the lateral spacing at both sides. Behind three rows only  $1\,252.8 \cdot (1-0.09)^3 = 944.1$  kW is left. Consequently 308.7 kW is absorbed. This amount of absorption corresponds with a loss of power of  $0.79 P_s$  compared to a theoretical farm with 9 independent WECs. This simplified method does not take the longitudinal distance  $l$ , the lay-out (staggered grid or aligned grid) and a varying capture ratio into account. When studying the results from the method developed in this chapter for  $w = 4D_h$  (Table 6.3) it is seen that the power loss varies between  $0 P_s$  and  $3.11 P_s$  for irregular long-crested waves. In [11] this simplified method has been used in an economic assessment. The author wants to underline that the use of this simplified method may result in an underestimation or overestimation of the absorbed power (up to 40 %). To conclude, it is very important to calculate the wake effects for the occurring sea states and wave directions on the location of the farm and to estimate the power absorption of the considered lay-out before performing an economic assessment.

So far only long-crested waves with  $H_s = 1$  m,  $T_p = 5.2$  s and  $\theta = 90^\circ$  have been considered. In practice, various sea states ( $H_s$  and  $T_p$ ) occur on the location of the farm (chapter 2). Furthermore, not all waves are coming from the same direction. Ultimately, ocean waves contain a low (swell waves) or high (wind waves) directional spreading. The impact of these aspects on the power absorbed by a farm is discussed in the next three sections. From the previous study a staggered grid lay-out with a lateral and longitudinal spacing of  $4D_h$  seems a good lay-out. This lay-out is considered in the following.

### 6.3.2.4 Impact of wave height and period

In this section, the wake behind nine WECs installed in a staggered grid with  $w = 4D_h$  and  $l = 4D_h$  is studied for sea states with a high frequency of occurrence at Westhinder (Belgian Continental Shelf - Table 2.3). Only the sea states with peak wave periods with a frequency of occurrence higher than 10 % are considered. For  $H_s$  varying between 0.25 m and 4.25 m, a variation of the capture ratio proportional to the variation in Figure 6.25 for irregular long-crested waves with  $H_s = 1$  m and  $T_p = 5.2$  s has been assumed. The same variation of the capture ratio has been considered for  $T_p = 3.9$  s, 6.5 s and 7.8 s (or  $T_m = 3$  s, 5 s and 6 s).

The wake behind this farm is shown in Figure 6.30 for  $T_p = 3.9$  s, 5.2 s, 6.5 s and 7.8 s. For irregular long-crested waves with  $T_p = 5.2$  s, 6.5 s and 7.8 s all WECs have a capture ratio of 45 %. For  $T_p = 3.9$  s the capture ratio of the left device on the third row decreases to 35 %. All other devices have a capture ratio of 45 %. The absorbed power per  $\text{km}^2$  is given in Table 6.5 for each sea state. Note that the significant wave height  $H_s$  and peak wave period  $T_p$  in Table 6.5 represent a  $H_s$ -interval and a  $T_p$ -interval. For example  $H_s = 1.25$  m corresponds to  $H_s$ -values between 1 m and 1.5 m.

Table 6.5: Power absorption [ $\text{kW}/\text{km}^2$ ]

$H_s$ [m]	$T_p$ [s]	3.9	5.2	6.5	7.8
0.25		52	73	90	103
0.75		466	654	812	931
1.25		1 294	1 816	2 255	2 587
1.75		-	3 560	4 420	5 070
2.25		-	5 884	7 306	8 382
2.75		-	-	10 914	12 521
3.25		-	-	15 243	17 488
3.75		-	-	-	23 283
4.25		-	-	-	29 905

The average yearly absorbed power equals 1 853  $\text{kW}/\text{km}^2$  (by multiplying the absorbed power in each sea state (Table 6.5) with its frequency of occurrence (Table 2.3) and summing up these results). The average yearly absorbed power is higher (approximately 60 %) than the absorbed power in long-crested waves with  $H_s = 1$  m and  $T_p = 5.2$  s (= 1 162  $\text{kW}/\text{km}^2$  - Table 6.4). So far only irregular long-crested waves (head-on) have been considered. In the next section the power absorption of the farm for several wave directions will be studied.

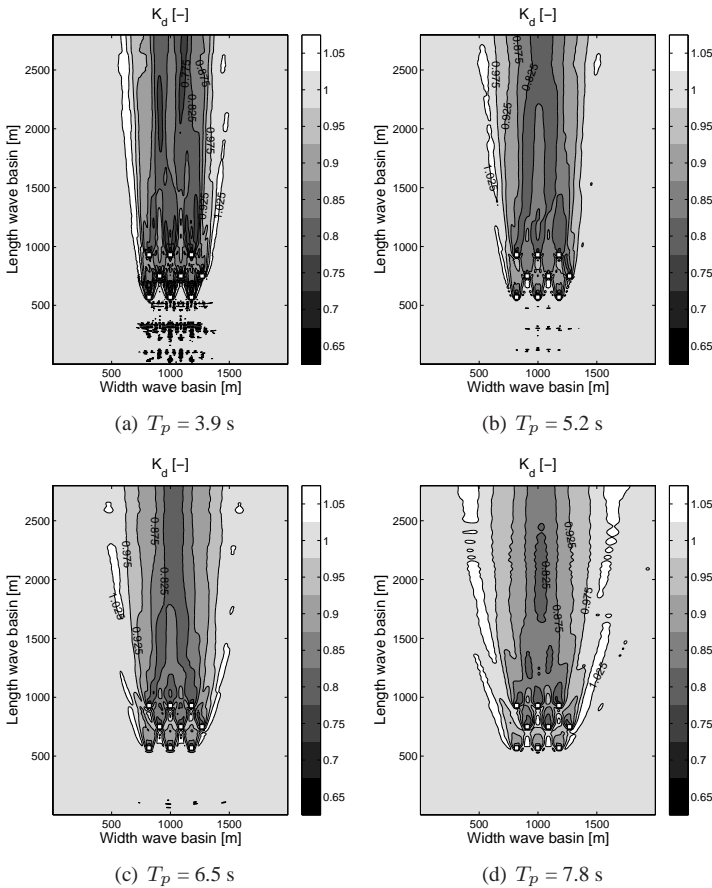


Figure 6.30: Calculated disturbance coefficient  $K_d$  in a wave basin with 9 WECs in a staggered grid with  $w = l = 4D_h$ , with  $D_h = 36$  m, for irregular long-crested (head-on) waves with (a)  $T_p = 3.9$  s, (b)  $T_p = 5.2$  s, (c)  $T_p = 6.5$  s, (d)  $T_p = 7.8$  s

### 6.3.2.5 Impact of wave direction

Sometimes the capture ratio of a WEC changes with varying wave direction (wave direction dependent WECs). When the WEC can turn towards the mean wave direction, the WEC is direction independent. For simplicity it is assumed that the hypothetical WEC can rotate  $\pm 180^\circ$ . Consequently the capture ratio of the hypothetical WEC is not changing with wave direction. On the other hand the location of the wake will turn when the wave direction is changing. Some WECs may be situated in the lee of neighbouring WECs which are not influenced by the wake of neighbouring WECs for head-on waves. As a consequence the power absorption of the farm will change. To determine the influence of the incident

wave direction on the power absorption, a farm of 10 WECs in a staggered grid with a lateral and longitudinal spacing of  $4D_h$  has been considered as shown in Figure 6.31. One WEC has been added in the farm compared to the previous sections to obtain a symmetrical lay-out.

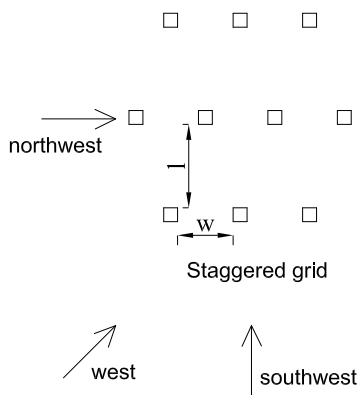


Figure 6.31: Farm of 10 WECs directed to the prevailing wave direction

A farm of WECs will be orientated towards the wave direction which contributes the most to the yearly average available wave power. On the Belgian Continental Shelf the southwest direction contains the largest part of the yearly average available wave power (Figure 2.8). Therefore the farm will be directed towards the southwest. The considered farm with 10 WECs is absorbing  $658 \text{ kW/km}^2$  when irregular long-crested waves with  $H_s = 0.75 \text{ m}$  and  $T_p = 5.2 \text{ s}$  are propagating from the southwest and northeast (Figure 6.30(b) where the additional WEC has the same power absorption as the last WEC in the second row). To calculate the absorbed power when waves are coming from the west, north, east or south respectively northwest, southeast the farm has been rotated over  $45^\circ$  and  $90^\circ$ . The resulting calculated disturbance coefficients are shown in Figure 6.32(a) and Figure 6.32(b).

When waves are coming from the west, north, east or south respectively northwest, southeast the farm is absorbing  $540 \text{ kW/km}^2$  and  $448 \text{ kW/km}^2$ . The frequency of occurrence of the considered wave sectors is given in Table 6.6. Note that 16 wave sectors had been considered on the Belgian Continental Shelf in chapter 2, while in Table 6.6 only 8 wave sectors are given. Half of the frequency of occurrence of the intermediate wave sectors has been added to its neighbouring sectors.

By multiplying the absorbed power per  $\text{km}^2$  for each wave direction with its frequency of occurrence and summing up the results, the average power absorption per  $\text{km}^2$  for the considered sea state ( $H_s = 0.75 \text{ m}$  and  $T_p = 5.2 \text{ s}$ ) is obtained. On

average  $588 \text{ kW/km}^2$  is absorbed. The absorption is approximately 10 % lower compared to the situation when only head-on waves ( $658 \text{ kW/km}^2$ ) are considered.

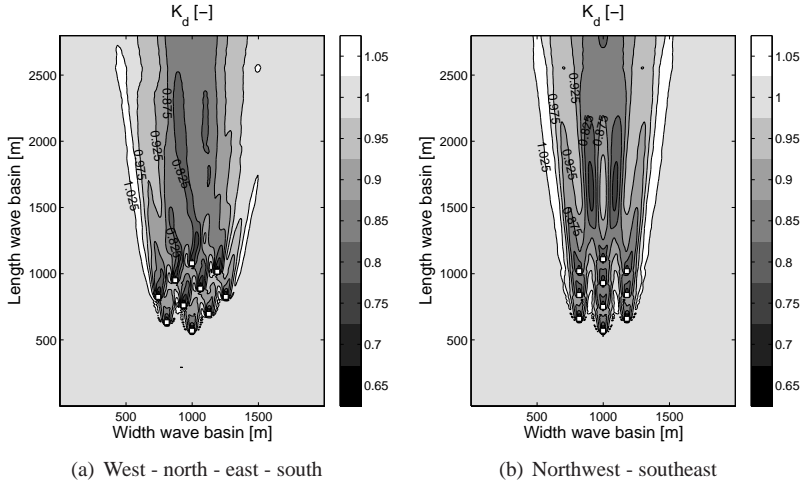


Figure 6.32: Calculated disturbance coefficient  $K_d$  in a wave basin with 10 WECs in a staggered grid with  $w = l = 4D_h$ , with  $D_h = 36 \text{ m}$ , for irregular long-crested (head-on) waves with  $T_p = 5.2 \text{ s}$  coming from the (a) west, north, east, south and (b) northwest and southeast

Table 6.6: Power absorption [ $\text{kW/km}^2$ ]

Wave sector	Frequency of occurrence [%]	Absorption per $\text{km}^2$ [ $\text{kW/km}^2$ ]
N	9.07	540
NE	12.11	658
E	9.76	540
SE	7.76	448
S	12.41	540
SW	25.92	658
W	13.74	540
NW	8.91	448

### 6.3.2.6 Impact of directional spreading

Finally the impact of the directional spreading on the wave power absorption is studied. It is expected that the power absorption will increase in a short-crested sea as a faster redistribution behind the farm occurs (Figures 6.22 and 6.23). The

wake behind 9 hypothetical WECs installed in a staggered grid with  $l = w = 4D_h$  for short-crested waves with  $H_s = 1$  m,  $T_p = 5.2$  s,  $\theta_0 = 90^\circ$  and  $s_{max} = 10$  has been compared with the wake for irregular long-crested waves with  $H_s = 1$  m and  $T_p = 5.2$  s, as studied in Figure 6.30(b). Both wakes are shown in Figure 6.33. The useful domain for short-crested waves is indicated with black lines. The black lines next to the wake for long-crested waves mark the same domain. A value of 10 for  $s_{max}$  is representative for a location on the Belgian Continental Shelf.

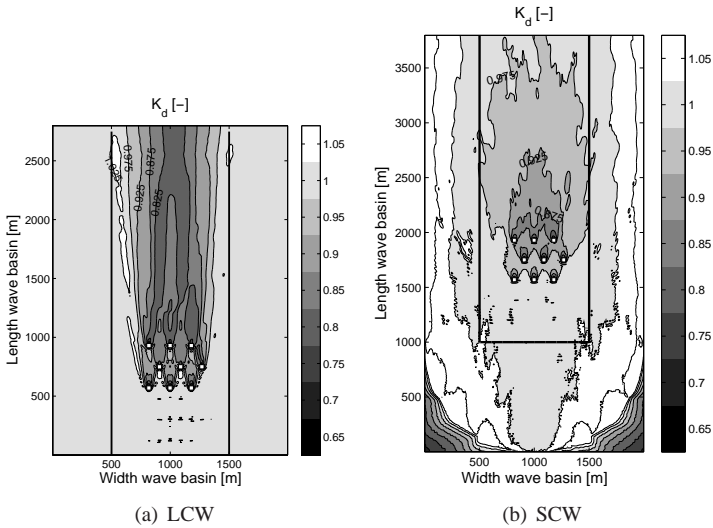


Figure 6.33: Calculated disturbance coefficient  $K_d$  in a wave basin with 9 WECs with  $w = 4D_h$  and  $l = 4D_h$ , with  $D_h = 36$  m, for (a) irregular long-crested (identical to Figure 6.30(b)) and (b) short-crested head-on waves with  $H_s = 1$  m and  $T_p = 5.2$  s

For short-crested waves a faster redistribution of waves behind the farm is observed. On the other hand, less energy is travelling between the WECs. The remaining wave height in the wake for short-crested waves is less variable compared to irregular long-crested waves. For irregular long-crested waves a wave height increase occurs at the edges of the wake (Figures 6.20 and 6.21). This wave height increase causes the high variability of the remaining wave height behind the farm. The wave height on the second row (staggered grid) is comparable for both wave conditions. The wave height increase at the edges of the wake for irregular long-crested waves causes a higher wave height on the locations of the WECs in a third row, compared to short-crested waves. Therefore WECs in a third row have a capture ratio of respectively 45 % and 35 % for irregular long-crested and short-crested waves. All devices in the first and second row have a capture ratio of 45 % for both wave conditions. It is clear that information about the directionality of

the waves is important when planning a farm of WECs. For irregular long-crested waves with  $T_p = 5.2$  s and  $H_s = 1$  m, 1 162 kW/km<sup>2</sup> is absorbed (Table 6.4). For short-crested waves the absorption decreases by 175 kW/km<sup>2</sup>. The difference in power absorption is approximately 15 %. A higher power absorption for long-crested waves is observed due to the wave height increase at the edges of the individual wakes. Furthermore, more energy is travelling in-between the WECs for irregular long-crested waves.

To conclude, by taking more sea states into account, a higher power absorption (60 %) is observed (section 6.3.2.4), while the power absorption decreases with 10 % and 15 % when taking the variation of the mean wave direction (section 6.3.2.5) and directional spreading (section 6.3.2.6) into account. In general, the values calculated for irregular long-crested waves with  $H_s = 1$  m and  $T_p = 5.2$  s (Table 6.4) are a conservative representation of the average yearly power absorption at Westhinder.

As an example, the yearly average power absorption of a farm of 10 hypothetical WECs in a staggered grid with  $w = l = 4D_h$  (Figure 6.31), installed at Westhinder has been studied. Short-crested waves with  $s_{max} = 10$  have been considered. For each wave direction the power absorption per km<sup>2</sup> for all sea states (short-crested waves with  $s_{max} = 10$ ) has been calculated. The results are summarized in Tables 6.7, 6.8 and 6.9. The absorption for short-crested waves with  $H_s = 0.75$  m and  $T_p = 5.2$  s is comparable with the absorption for long-crested waves (Table 6.6) for the wave sectors north, east, south, west. For the wave sectors southwest and northeast the power absorption in short-crested waves is lower, while for the sectors southeast and northwest the power absorption in short-crested waves is higher.

Table 6.7: Power absorption [kW/km<sup>2</sup>] for the wave sectors southwest and northeast

$H_s$ [m]	$T_p$ [s]	3.9	5.2	6.5	7.8
0.25		45	62	76	91
0.75		401	562	683	823
1.25		1 114	1 561	1 897	2 286
1.75		2 183	3 060	3 718	4 481
2.25		3 608	5 059	6 146	7 408
2.75		5 390	7 557	9 182	11 066
3.25		7 528	10 555	12 824	15 456
3.75		10 022	14 053	17 074	20 577
4.25		12 873	18 050	21 930	26 430



Table 6.8: Power absorption [ $\text{kW}/\text{km}^2$ ] for the wave sectors west, north, east, south

$H_s$ [m]	$T_p$ [s]	3.9	5.2	6.5	7.8
0.25		45	60	75	90
0.75		404	538	673	807
1.25		1 121	1 494	1 868	2 241
1.75		2 196	2 928	3 660	4 392
2.25		3 631	4 841	6 051	7 262
2.75		5 423	7 231	9 039	10 847
3.25		7 575	10 100	12 625	15 150
3.75		10 085	13 446	16 808	20 169
4.25		12 953	17 271	21 589	25 907

Table 6.9: Power absorption [ $\text{kW}/\text{km}^2$ ] for the wave sectors northwest and southeast

$H_s$ [m]	$T_p$ [s]	3.9	5.2	6.5	7.8
0.25		42	56	70	84
0.75		377	502	628	753
1.25		1 046	1 395	1 744	2 093
1.75		2 051	2 734	3 418	4 101
2.25		3 389	4 519	5 649	6 779
2.75		5 063	6 751	8 439	10 127
3.25		7 072	9 429	11 786	14 144
3.75		9 416	12 554	15 693	18 831
4.25		12 094	16 125	20 156	24 188

The power absorption for each sea state and wave direction has been multiplied with its frequency of occurrence (scatter diagrams provided by the Flemish Ministry of Transport and Public Works - Agency for Maritime and Coastal Services - Coastal Division). The overall yearly power absorption of a farm of 10 WECs installed in a staggered grid with  $w = l = 4D_h$  installed at Westhinder (Belgian Continental Shelf) equals  $1\,545 \text{ kW}/\text{km}^2$ . Note that conversion and transmission losses are not taken into account.

## 6.4 Validation of wave power absorption in MILD-wave

The technique to implement wave power absorption in MILDwave (sponge layer technique) is validated in this section with physical experiments (section 6.4.2). The wave pattern around a single and multiple absorbing obstacles is studied in a numerical and physical wave flume. Before studying absorbing obstacles, a fully reflective obstacle (without power absorption) has been numerically and physically modelled (section 6.4.1). These physical tests are used to validate the wave transformation processes reflection, transmission and diffraction. When testing the absorbing obstacle, power absorption is investigated together with these wave transformation processes. Finally, in section 6.4.3 a method is developed to calculate the power absorbed by a WEC in a numerical wave basin in MILDwave.

### 6.4.1 Wave pattern around a fully reflective obstacle

#### 6.4.1.1 Physical test set-up

The reflection from and diffraction around a fully reflective obstacle with a limited draft has been studied in the wave flume (70 m (l) x 4 m (w) x 1.4 m (h)) of Flanders Hydraulics Research in Borgerhout (Belgium). At the end of this wave flume other test models were installed. Consequently absorbing material was placed in front of these models to absorb the incoming waves and to prevent reflection. The remaining useful length (between wave paddle and absorbing material) of the wave flume equals 35.7 m. A plan view of the wave flume is given in Figure 6.34. Waves are generated with a hydraulic piston-type wave paddle.

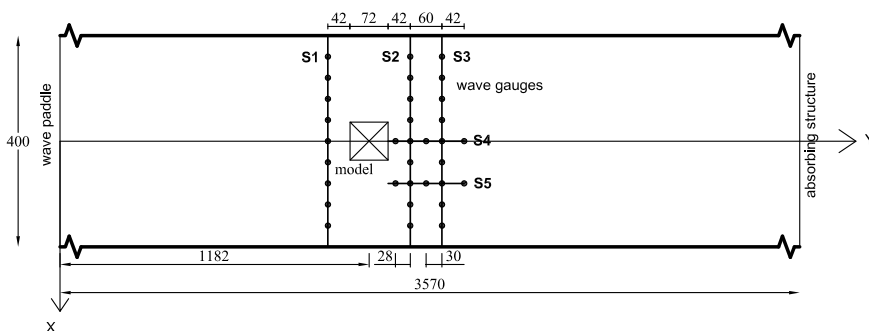


Figure 6.34: Plan view of wave flume at Flanders Hydraulics Research - dimensions in cm

A square fully reflective obstacle with a width and length of 0.72 m and a height of 0.30 m was installed on a distance of 11.82 m from the wave paddle

(Figure 6.34). The model corresponds to a prototype of 36 m (w) x 36 m (l) x 15 m (h) on scale 1/50. The obstacle consists of a frame with square aluminium profiles. The sides of the frame are covered with watertight wooden planks and the joints are sealed with silicone. Figure 6.35 shows the fully reflective obstacle. The model was fixed to wooden beams installed crosswise over the wave flume (Figure 6.45). The draft of the obstacle equals 0.15 m.

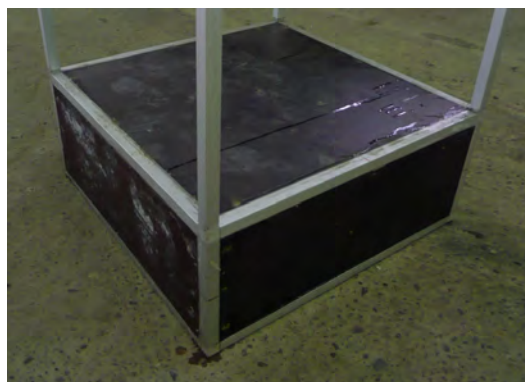


Figure 6.35: A fully reflective obstacle (36 m (w) x 36 m (l) x 15 m (h) on scale 1/50)

Wave elevations were measured with parallel-wire resistance-type wave gauges on three lateral and two longitudinal sections (S1, S2, S3, S4 and S5) as indicated on Figure 6.34. As only 6 wave gauges were available, each wave condition was repeated 6 times to obtain measurements on each location as indicated on Figure 6.34. Waves were measured during 50 s at a sampling rate of 40 Hz resulting in 2 000 data for each wave gauge. The wave height averaged over the sampling duration excluding the first waves, as these are not fully developed yet, is used to determine the reflection and diffraction pattern around the obstacle. Waves were not measured longer than 50 s as there was no active absorption system to absorb reflected waves on the wave paddle. The reflection from the absorbing material at the end of the wave flume was smaller than 15 % [12], resulting in a negligible amount of reflected wave energy ( $\leq 2\%$ ).

The undisturbed incident wave height was measured by seven wave gauges, spaced 50 cm apart, on a lateral section 14.52 m from the wave paddle, when the model was not installed in the wave flume. The measured undisturbed wave height is shown on Figure 6.36 for a target regular wave with a wave period  $T = 0.919$  s and a wave height  $H_i = 0.10$  m (model values). Note that the x-co-ordinate is divided by the width of the model  $W_m$ . The average measured wave height along the lateral section is indicated by the black line.

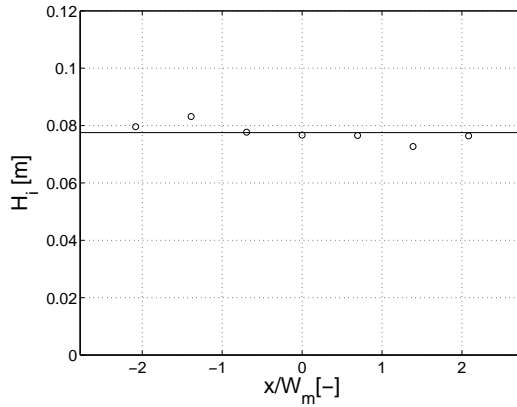


Figure 6.36: Undisturbed incident wave height along the width of the wave flume for a target regular wave with  $H_i = 0.10$  m and  $T = 0.919$  s

The measured wave height  $H_i$  is approximately 20 % smaller than the target wave height, due to mechanical losses, friction losses, ... Note the asymmetry due to a cross wave typical for a wave flume with a larger width. This cross wave was intensified by the small asymmetric reflection from the absorption material at the end of the wave flume, as the absorption material was not aligned perfectly perpendicular to the side walls of the wave flume. Similar measurements were made for a target  $T = 1.103$  s and 1.202 s and target  $H_i = 0.10$  m. An average wave height of 0.0774 m, 0.0822 m and 0.0824 m was measured for target  $T = 0.919$  s, 1.103 s and 1.202 s, respectively. On the other hand, the measured wave period agrees very well with the target values. The latter measured wave heights are used for normalization and as an input for the numerical model. All experimental tests were carried out in a constant water depth  $h = 1.00$  m (deep water conditions). An overview of the tests is given in Table 6.10.

Table 6.10: Overview of tests in the wave flume of Flanders Hydraulics Research in Borgerhout (Belgium)

Test N°	$H_i$ [m]		$T$ [s]		$h$ [m]	
	model	prototype	model	prototype	model	prototype
1	0.10	5	0.919	6.5	1	50
2	0.10	5	1.103	7.8	1	50
3	0.10	5	1.202	8.5	1	50

### 6.4.1.2 Numerical test set-up

The numerical wave flume is shown in Figure 6.37. In MILDwave prototype dimensions (using a scaling of 1/50) have been considered. The distance between the wave generation line and the sponge layer at the end of the wave flume is 1 785 m and corresponds to the useful length of the physical wave flume on scale 1/50. In the beginning and at the end of the numerical wave flume sponge layers are installed to prevent reflection. The side walls are fully reflective, as the physical wave flume walls are made of concrete. As these reflective walls are present in the physical and numerical set-up, a comparison between the experimental measurements and numerical calculations can be made. The fully reflective obstacle has been implemented in MILDwave as an array of cells with a length and a width of 36 m and an absorption coefficient equal to 0. Note that the equations in MILDwave are depth integrated. Consequently the obstacle in MILDwave has no limited draft.

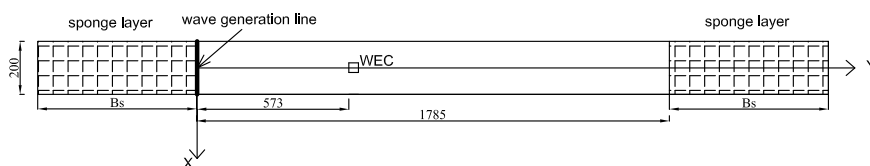
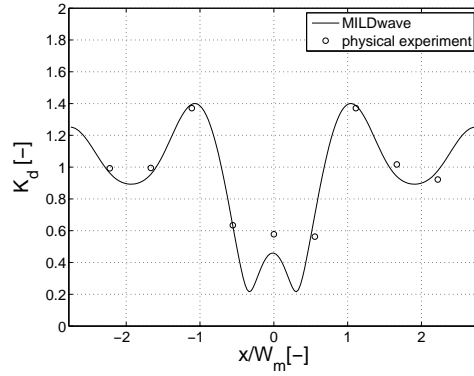


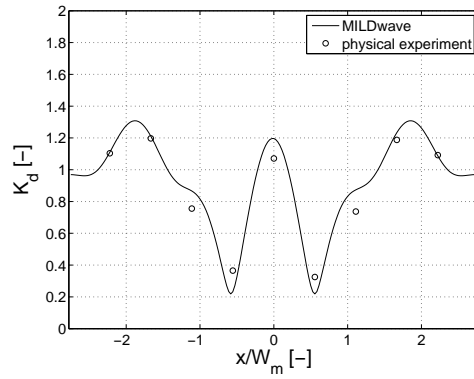
Figure 6.37: Plan view of wave flume - dimensions in m

### 6.4.1.3 Comparison between experimental measurements and numerical results

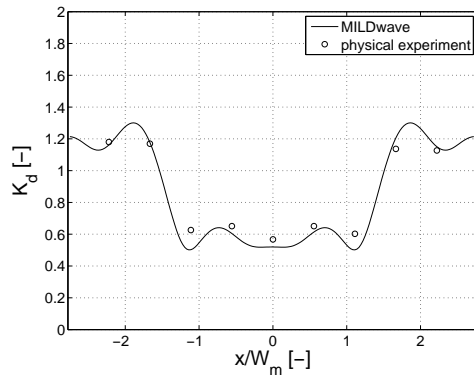
The disturbance coefficient  $K_d$ , derived from the experimental data and calculated from the numerical model results, along three lateral sections S1, S2 and S3, as shown on Figure 6.34, are given in Figure 6.38, Figure 6.39 and Figure 6.40 for target regular incident waves with  $H_i = 5$  m and  $T = 6.5$  s, 7.8 s and 8.5 s (prototype), respectively. The numerical result is indicated with a solid line while the experimental measurements are given with a circle. For the comparison of both values of  $K_d$ , waves are only generated during 354 s ( $50 \text{ s} \cdot \sqrt{50}$ ) in MILDwave, as the waves were measured during 50 s in the physical wave flume on scale 1/50.



(a) Lateral section S1

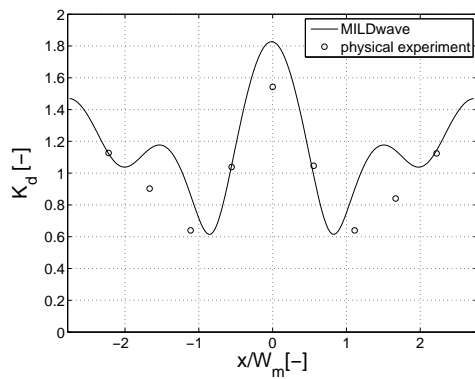


(b) Lateral section S2

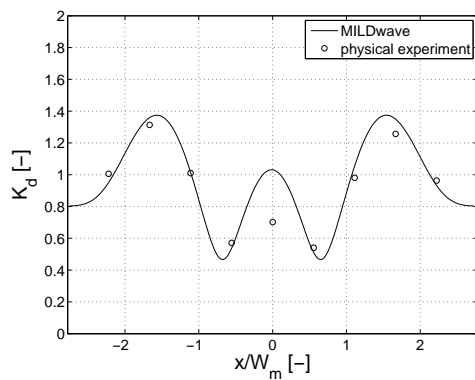


(c) Lateral section S3

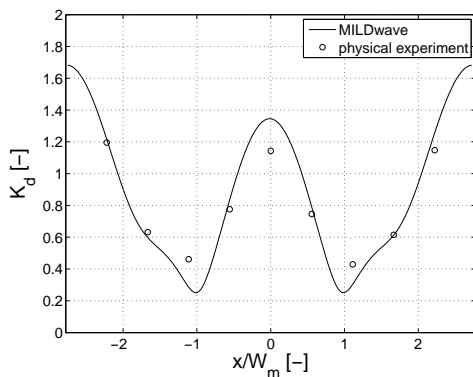
Figure 6.38: Comparison of numerical model results with experimental data in lateral sections (a) S1, (b) S2 and (c) S3, respectively, for target regular waves with  $H_i = 5$  m and  $T = 6.5$  s



(a) Lateral section S1

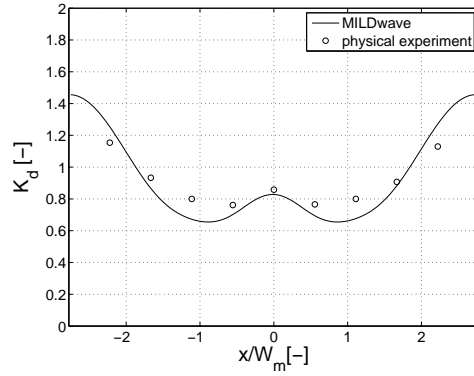


(b) Lateral section S2

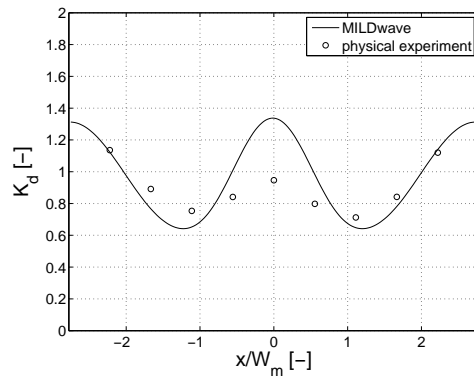


(c) Lateral section S3

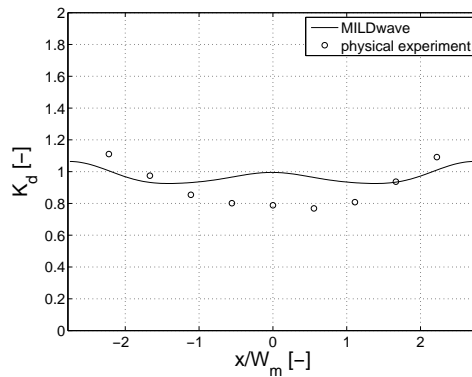
Figure 6.39: Comparison of numerical model results with experimental data in lateral sections (a) S1, (b) S2 and (c) S3, respectively, for target regular waves with  $H_i = 5$  m and  $T = 7.8$  s



(a) Lateral section S1



(b) Lateral section S2



(c) Lateral section S3

Figure 6.40: Comparison of numerical model results with experimental data in lateral sections (a) S1, (b) S2 and (c) S3, respectively, for target regular waves with  $H_i = 5$  m and  $T = 8.5$  s



In general, for target  $T = 6.5$  s a very good agreement is observed between the numerical results and the experimental data. The largest deviations occur in the centre of the domain. The data behind the obstacle (sections S2 and S3) agree very well for target  $T = 7.8$  s, except for the values in the centre of the domain. Section S1 shows a higher reflection in the numerical model. Furthermore, the two smaller peaks next to the central peak in section S1, calculated in MILDwave, are not measured in the physical model. For target  $T = 8.5$  s larger deviations between the numerical results and experimental data occur. In front of the model and behind the model, experimental data are slightly higher, respectively, smaller compared to the numerical results. The reason for this deviation is not very clear. An explanation may be that, in general, in a physical wave flume, more friction occurs for larger wave periods. This friction can cause the higher wave height decrease in the physical model. In sections S1 and S2 the waves in the physical model seem more attenuated compared to the numerical results.

Further, the experimental data and numerical results are compared on two longitudinal sections S4 (Figure 6.41) and S5 (Figure 6.42). These sections start immediately behind the fully reflective obstacle (Figure 6.34).

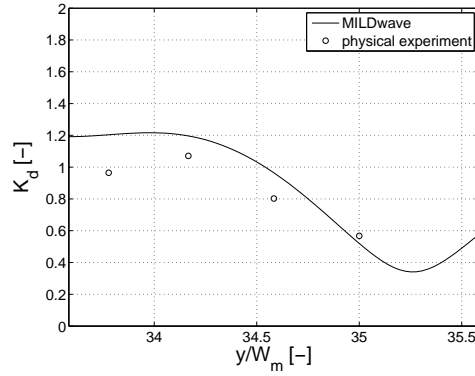
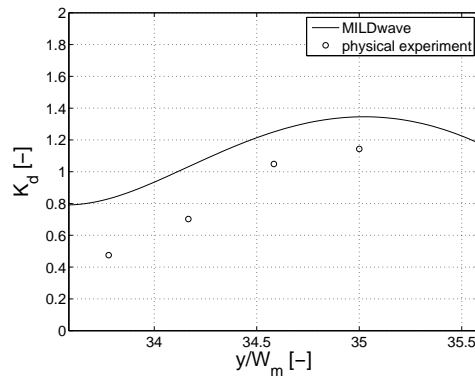
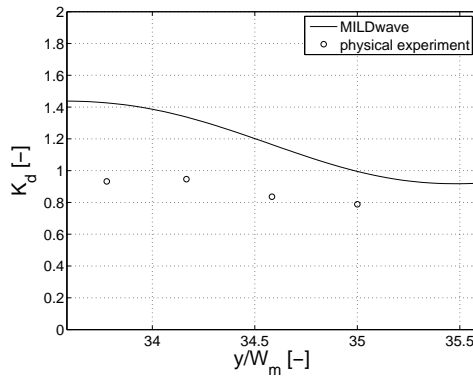
(a)  $T = 6.5$  s(b)  $T = 7.8$  s(c)  $T = 8.5$  s

Figure 6.41: Comparison of numerical model results with experimental data in longitudinal section S4 for target regular waves with  $H_i = 5$  m and  $T =$  (a) 6.5 s, (b) 7.8 s and (c) 8.5 s

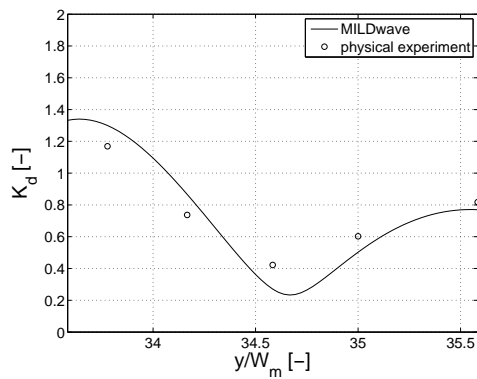
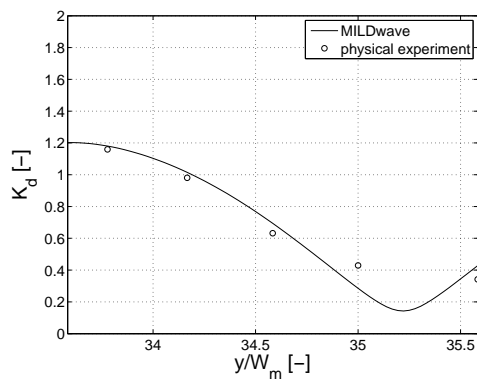
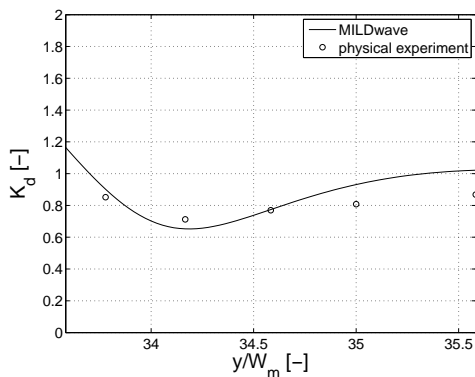
(a)  $T = 6.5$  s(b)  $T = 7.8$  s(c)  $T = 8.5$  s

Figure 6.42: Comparison of numerical model results with experimental data in longitudinal section S5 for target regular waves with  $H_i = 5$  m and  $T =$  (a) 6.5 s, (b) 7.8 s and (c) 8.5 s

The agreement on section S5 is very good, while more deviations occur on section S4. As seen on the lateral sections as well, larger differences occur in the centre of the domain (section S4). The differences are the highest immediately behind the obstacle and fade away further away from the obstacle. The larger the wave period the slower these differences disappear.

In general, the experimental data and the numerical results agree very well. Deviations occur mainly in the centre of the wave flume due to the limited draft of the obstacle in the physical wave flume, which is not modelled in MILDwave. This effect could be reduced by tuning the reflective obstacle in the numerical model. This tuning is applied to an absorbing obstacle and is explained in section 6.4.2.1.

The average value of the experimental measurements on each section is compared to the average of the numerical values, on the same positions as the experimental results, in Table 6.11.

*Table 6.11: Average of calculated disturbance coefficient  $K_d$  on three lateral sections S1, S2 and S3 in the (a) experimental and (b) numerical test set-up for target regular waves with  $H_i = 5$  m and  $T = 6.5$  s, 7.8 s and 8.5 s*

(a) Experimental set-up				(b) Numerical set-up			
$T$ [s]	S1	S2	S3	$T$ [s]	S1	S2	S3
6.5	0.94	0.87	0.86	6.5	0.93	0.89	0.85
7.8	0.99	0.93	0.79	7.8	1.11	0.95	0.80
8.5	0.90	0.89	0.90	8.5	0.86	0.93	0.95

The difference between the averages are within the interval [-5 % ,+5 %] except for the reflection from the model (section S1) for target  $T = 7.8$  s. It is expected that the average values on section S2 and S3 are the same, as no energy is reflected or absorbed behind section S2. For target  $T = 6.5$  s and 8.5 s this expectation is confirmed. For target  $T = 7.8$  s a large difference between the average on section S2 and section S3 is observed. When all values along the section in MILDwave are used an average of 0.88 is obtained on section S3, which differs 7 % from the average value on section S2. This difference can be caused by reflection from the wave flume walls.

A higher average of  $K_d$  behind the obstacle is observed for the larger wave periods, as the reflection from the obstacle decreases with increasing wave period.

The standard deviation of the wave elevations measured by the wave gauges is on average 1 mm [12]. In the following all experimental tests have been executed twice to obtain a higher accuracy (standard deviation of wave elevations less than

1 mm). The averaged wave height at each wave gauge has been used for the comparison with the numerical results.

## 6.4.2 Wave pattern around a single and multiple absorbing obstacles

In order to verify the implementation of wave power absorption in MILDwave, the hydraulic experiment of section 6.4.1 is adapted. Surface wave propagation through and around an absorbing obstacle (a WEC) with the same dimensions as the fully reflective obstacle is studied in this section.

### 6.4.2.1 Tuning of physical and numerical obstacle

A WEC is interacting with the incident waves. The incident wave power is partly absorbed by the WEC. The other part is reflected from, transmitted under and diffracted around the WEC. A scale model (1/50) of a WEC, which is absorbing a specific amount of wave power, was designed in the wave flume of the Department of Civil Engineering (Ghent University). The dimensions of the wave flume are 30 m in length, 1 m in width and 1.2 m in height. A piston-type wave paddle is used to generate waves. One of the wave flume's side walls is partially made of glass to facilitate visual observations.

The absorbing obstacle consists of an aluminium frame (1.00 m (w) x 0.72 m (l) x 0.30 m (h)) with three layers of synthetic material (Japanese filter mats) in the beginning and at the end of the frame (Figure 6.43) to absorb a specific amount of energy. Japanese filter mats absorb the incident waves without causing turbulence [12].

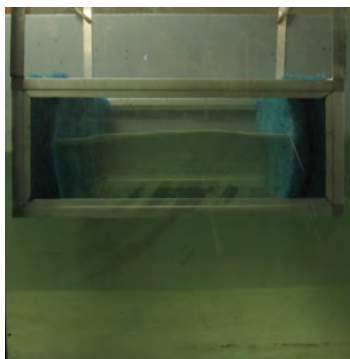


Figure 6.43: Side view of absorbing obstacle (50 m (w) x 36 m (l) x 15 m (h) on scale 1/50) in the wave flume of the Department of Civil Engineering (Ghent University)

The absorbing obstacle has a draft of 0.15 m. In the wave flume of the

Department of Civil Engineering the width of the WEC was extended to obtain a width equal to the width of the wave flume to prevent reflection on the side walls of the flume. This way the amount of absorption of the Japanese filter mats could be determined without boundary effects. A gravel beach was installed at the end of the flume to reduce wave reflection inside the flume.

The amount of power absorbed by the WEC was derived using equation (6.1) (conservation of energy). For the determination of the reflection and transmission coefficient, two arrays of 3 parallel-wire resistance-type wave gauges were placed in front of and behind the model in the wave flume (Figure 6.44). The first array was installed two wave lengths in front of the structure to measure the incident wave height  $H_i$  and the reflected wave height  $H_r$ . The transmitted wave height  $H_t$  was determined by the second array of wave gauges, installed one wave length behind the WEC. Note that also behind the WEC a reflection analysis was performed to separate the transmitted wave and the wave, reflected on the gravel beach at the end of the flume. Two wave gauges were installed in front of the wave paddle to control the active absorption, and consequently to prevent reflection from the wave paddle.

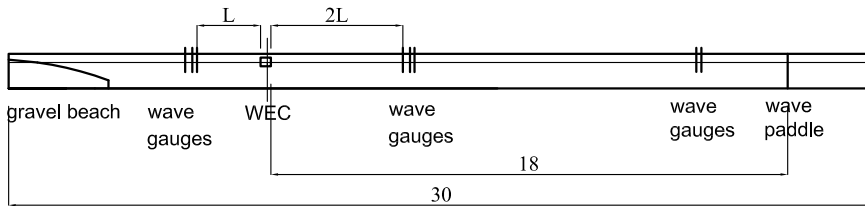


Figure 6.44: Side view of the wave flume (30 m (l) x 1 m (w) x 1.2 m (h)) of the Department of Civil Engineering (Ghent University) - dimensions in m

The reflection coefficient  $K_r$ , transmission coefficient  $K_t$  and the ratio  $\frac{P_a}{P_i}$  is given in Table 6.12 for target regular waves with  $T = 0.919$  s, 1.103 s and 1.202 s (model values). The target incident wave height is 0.10 m during the three tests. All tests were performed in a water depth of 0.75 m. The reflection coefficient decreases for longer waves, while the transmission coefficient and the absorption increase. All tests were repeated in a water depth of 0.85 m. The influence of the water depth on  $K_r$ ,  $K_t$  and  $P_a/P_i$  is negligible [13].

A WEC with the same reflection, transmission and absorption characteristics, as given in Table 6.12, has been implemented in a numerical wave flume in MILDwave by using the sponge layer technique. The length of the numerical wave flume corresponds to the useful length (distance between wave paddle and gravel beach) of the physical wave flume on scale 1/50. Absorbing sponge layers are added in the beginning and at the end of the numerical wave flume to prevent

Table 6.12: Reflection, transmission and absorption characteristics of a WEC as shown on Figure 6.43

Test N°	$H_i$ [m]		$T$ [s]		$h$ [m]		$K_r$ [-]	$K_t$ [-]	$P_a/P_i$ [%]
	model	prototype	model	prototype	model	prototype			
1	0.10	5	0.919	6.5	0.75	37.5	0.2	0.22	91
2	0.10	5	1.103	7.8	0.75	37.5	0.14	0.46	77
3	0.10	5	1.202	8.5	0.75	37.5	0.12	0.53	70

reflection inside the simulation domain. By using the sponge layer technique the reflection, transmission and absorption characteristics of the WEC have been tuned with experimental model results (Table 6.12). By tuning the WEC in the numerical model, the limited draft is taken into account.

#### 6.4.2.2 A single absorbing obstacle

The wave height near a single WEC with a limited width (0.72 m x 0.72 m x 0.30 m) and a draft of 0.15 m has been determined in the wave flume of Flanders Hydraulics Research as shown on Figure 6.45.

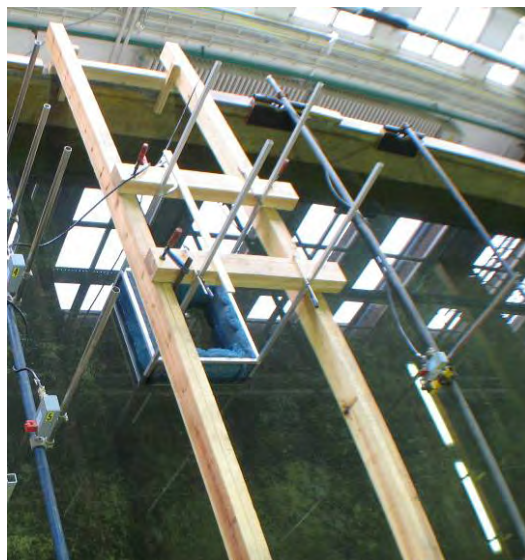


Figure 6.45: Plan view of the WEC (36 m (w) x 36 m (l) x 15 m (h) on scale 1/50) in the wave flume of Flanders Hydraulics Research

Three layers of synthetic material were placed at the four sides of the aluminium frame (Figure 6.46). By limiting the width of the model, not only reflection from and absorption by the WEC but also diffraction around the WEC can be studied. The model has the same position as the fully reflective model (section 6.4.1). The wave elevations were measured on the same locations. Again a constant water depth of 1 m was used during the simulations. Note that the WEC has the same absorption, reflection and transmission characteristics as the model studied in the wave flume of the Coastal Engineering Department, as the water depth has no influence on  $P_a/P_i$ ,  $K_r$  and  $K_t$ .

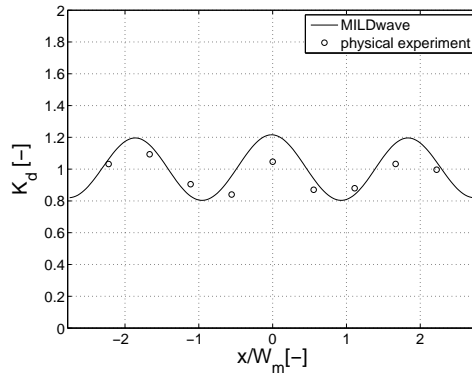
The numerical set-up is identical to the set-up used to study the fully reflective obstacle (section 6.4.1).



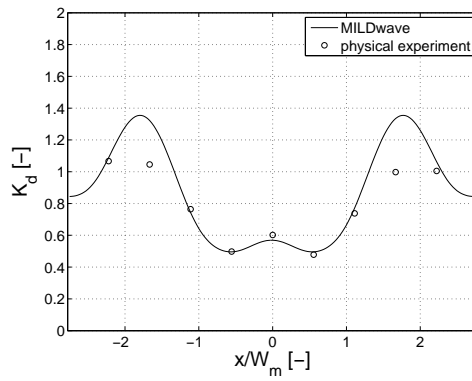
*Figure 6.46: Side view of the WEC (36 m (w) x 36 m (l) x 15 m (h) on scale 1/50) in the wave flume of Flanders Hydraulics Research*

The experimental data are compared to the numerical results on the three lateral sections S1, S2 and S3 in Figure 6.47, Figure 6.48 and Figure 6.49 for target regular waves with  $H_i = 5$  m and  $T = 6.5$  s, 7.8 s and 8.5 s (prototype), respectively.

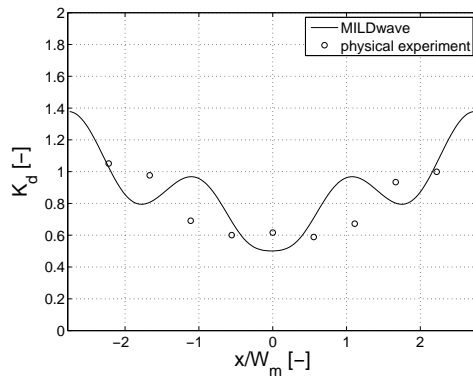




(a) Lateral section S1

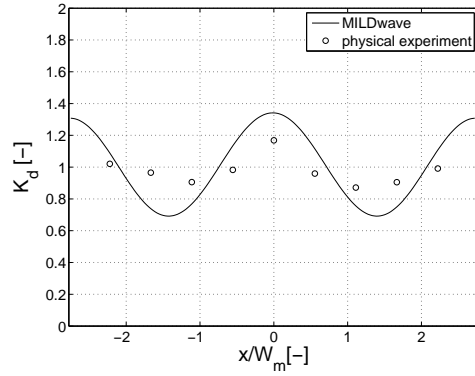


(b) Lateral section S2

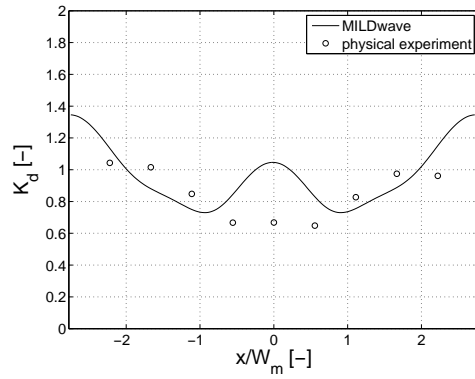


(c) Lateral section S3

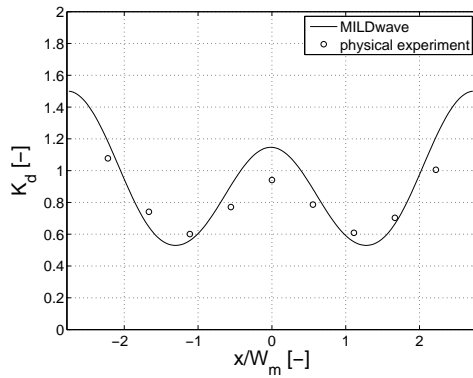
Figure 6.47: Comparison of numerical model results with experimental data in lateral sections (a) S1, (b) S2 and (c) S3, respectively, for target regular waves with  $H_i = 5$  m and  $T = 6.5$  s



(a) Lateral section S1

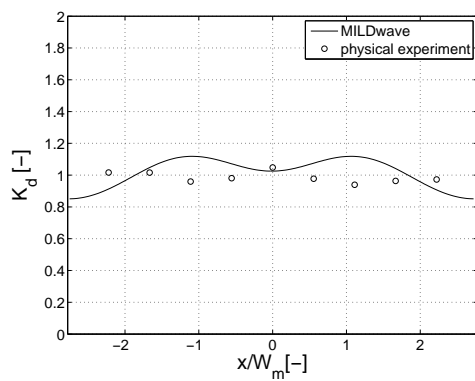


(b) Lateral section S2

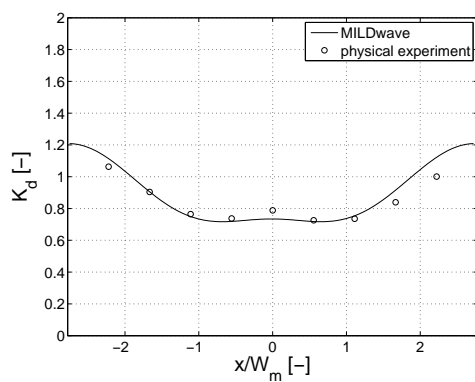


(c) Lateral section S3

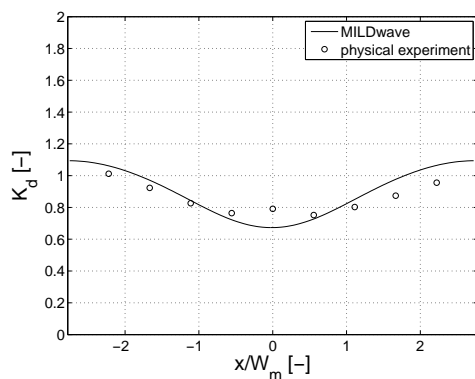
Figure 6.48: Comparison of numerical model results with experimental data in lateral sections (a) S1, (b) S2 and (c) S3, respectively, for target regular waves with  $H_i = 5$  m and  $T = 7.8$  s



(a) Lateral section S1



(b) Lateral section S2



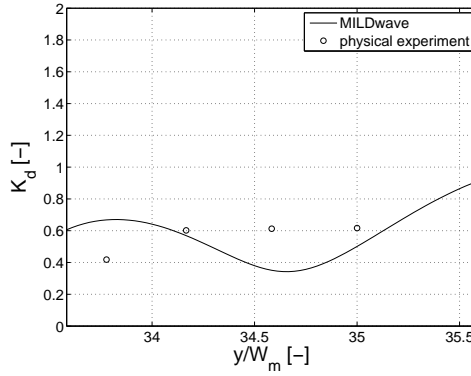
(c) Lateral section S3

Figure 6.49: Comparison of numerical model results with experimental data in lateral sections (a) S1, (b) S2 and (c) S3, respectively, for target regular waves with  $H_i = 5$  m and  $T = 8.5$  s

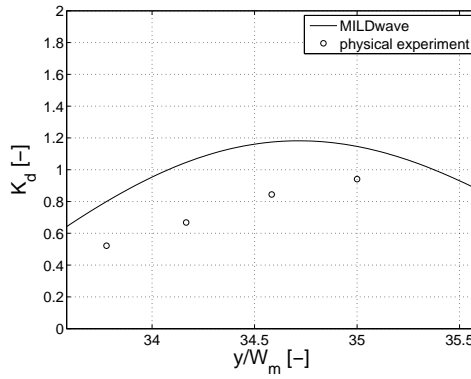
For target  $T = 6.5$  s a fairly good agreement is observed on sections S1 and S2. The physical measurements are more flattened out compared to the numerical results. On section S3 the numerical and physical results show both the decrease in wave height in the centre of the section. The two smaller peaks next to the centre of the section observed in MILDwave, are not found in the experimental results. Again the waves in the physical model seem more smoothed down. The latter effect is also observed for target  $T = 7.8$  s. Results on sections S1 and S3 have the same trend, while the trend is more marked in the numerical model. On section S2 the central peak, calculated in MILDwave, is not observed in the physical wave flume. For target  $T = 8.5$  s a good agreement is seen. Some deviations occur on sections S1 and S3 as the waves in the physical model are clearly smoothed down. It is observed that the largest deviations do not always occur in the centre of the flume as observed earlier for the fully reflective obstacle. By tuning the transmission and reflection of the model with a width equal to the wave flume width in the previous section, the limited draft of the WEC is taken into account in the numerical model.

In general variations in  $K_d$  along the cross sections are higher in the numerical model compared to the physical set-up. The smoothing down of the waves in the physical model was also observed when a fully reflective obstacle was tested (section 6.4.1). It has been assumed that the side walls of the physical wave flume are fully reflective. A slightly smaller reflection could explain the smaller difference in wave height along the cross sections in the physical wave flume. Moreover the characteristics of the synthetic material itself could cause differences in the diffraction pattern. The best agreement between the experimental and numerical results is seen for the largest wave period when the obstacle is less felt by the wave.

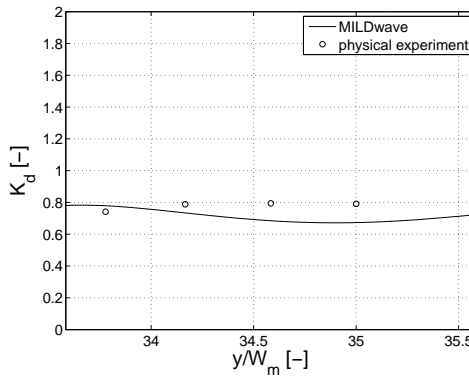
A comparison between the physical and numerical results for the three wave periods on the longitudinal sections S4 and S5 is given in Figure 6.50 and Figure 6.51, respectively.



(a)  $T = 6.5$  s



(b)  $T = 7.8$  s



(c)  $T = 8.5$  s

Figure 6.50: Comparison of numerical model results with experimental data in longitudinal section S4 for target regular waves with  $H_i = 5$  m and  $T =$  (a) 6.5 s, (b) 7.8 s and (c) 8.5 s

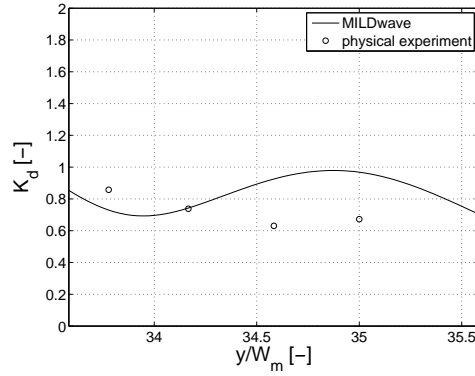
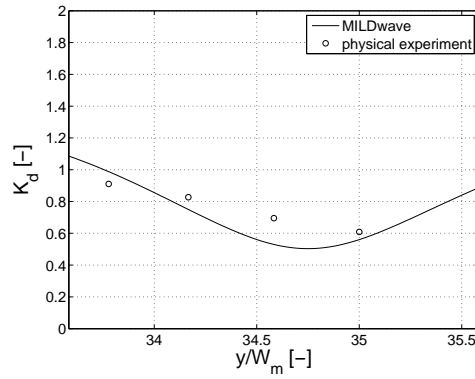
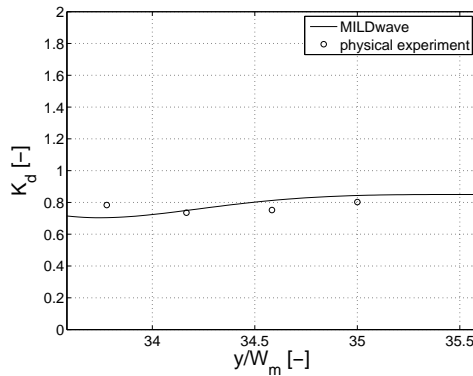
(a)  $T = 6.5$  s(b)  $T = 7.8$  s(c)  $T = 8.5$  s

Figure 6.51: Comparison of numerical model results with experimental data in longitudinal section S5 for target regular waves with  $H_i = 5$  m and  $T =$  (a) 6.5 s, (b) 7.8 s and (c) 8.5 s

The largest deviations are not always seen in section S4, behind the WEC, as the numerical model has been tuned. For target  $T = 6.5$  s large differences are seen in section S5, as observed in section S3 (Figure 6.47(c)).

Table 6.13 shows that the average of the experimental measurements is systematically lower than the average of the numerical results on the positions of the wave gauges along each cross section. The largest difference, 10 %, is seen along section S2 for target  $T = 6.5$  s.

Table 6.13: Average of calculated disturbance coefficient  $K_d$  on three lateral sections S1, S2 and S3 in the (a) experimental and (b) numerical test set-up for target regular waves with  $H_i = 5$  m and  $T = 6.5$  s, 7.8 s and 8.5 s

(a) Experimental set-up				(b) Numerical set-up			
$T$ [s]	S1	S2	S3	$T$ [s]	S1	S2	S3
6.5	0.97	0.80	0.79	6.5	1.02	0.88	0.83
7.8	0.97	0.85	0.80	7.8	0.97	0.91	0.85
8.5	0.99	0.84	0.86	8.5	1.02	0.85	0.86

The averages on sections S2 and S3 differ 7 % at maximum. Note that these averages are only based on 9 measurements along the cross sections. More measurements can result in less deviations between sections S2 and S3. Furthermore some energy can be lost due to friction, when waves are travelling from section S2 to section S3 in the physical wave flume.

The highest absorption and reflection was derived for the smallest wave period (Table 6.12), which explains the smallest average values of  $K_d$  for target  $T = 6.5$  s on sections S2 and S3 in Table 6.13. The differences in absorption and reflection for target  $T = 7.8$  s and 8.5 s were rather small (Table 6.12). Consequently, it can not be concluded from Table 6.13 whether the highest absorption occurs for target  $T = 7.8$  s or  $T = 8.5$  s.

### 6.4.2.3 A farm of absorbing obstacles

Finally the wave height near a small farm of three WECs has been studied through physical model tests in the wave flume of Flanders Hydraulics Research and numerical simulations in MILDwave. A plan view of the farm and the wave gauges is given in Figure 6.52. The first two models were installed 9.66 m from the wave paddle, against the walls of the wave flume to prevent disturbances from those wave flume walls in front of the third model. The third model was installed on the

same location as a single WEC. The longitudinal distance between the first two models and the third model equals 2 times the length of the model (= 1.44 m), as this distance is the required minimal distance to remove a damaged WEC from a farm. A plan view of the physical test set-up in the wave flume of Flanders Hydraulics Research is given in Figure 6.53. Wave elevations were measured on two additional cross sections (S6 and S7). Furthermore the longitudinal sections S4 and S5 were extended.

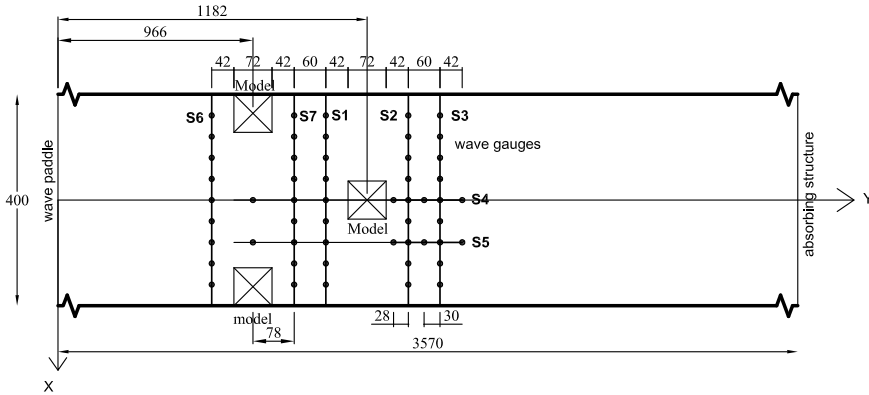


Figure 6.52: Plan view of wave flume at Flanders Hydraulics Research with 3 absorbing WECs - dimensions in cm



Figure 6.53: Plan view of a farm of 3 absorbing WECs (36 m (w) x 36 m (l) x 15 m (h) on scale 1/50) in the wave flume of Flanders Hydraulics Research

A comparison between the physical and numerical model results along the



cross sections, as indicated on Figure 6.52, is given in Figure 6.54, Figure 6.55 and Figure 6.56 for target regular waves with  $H_i = 5$  m and  $T = 6.5$  s, 7.8 s and 8.5 s, respectively.

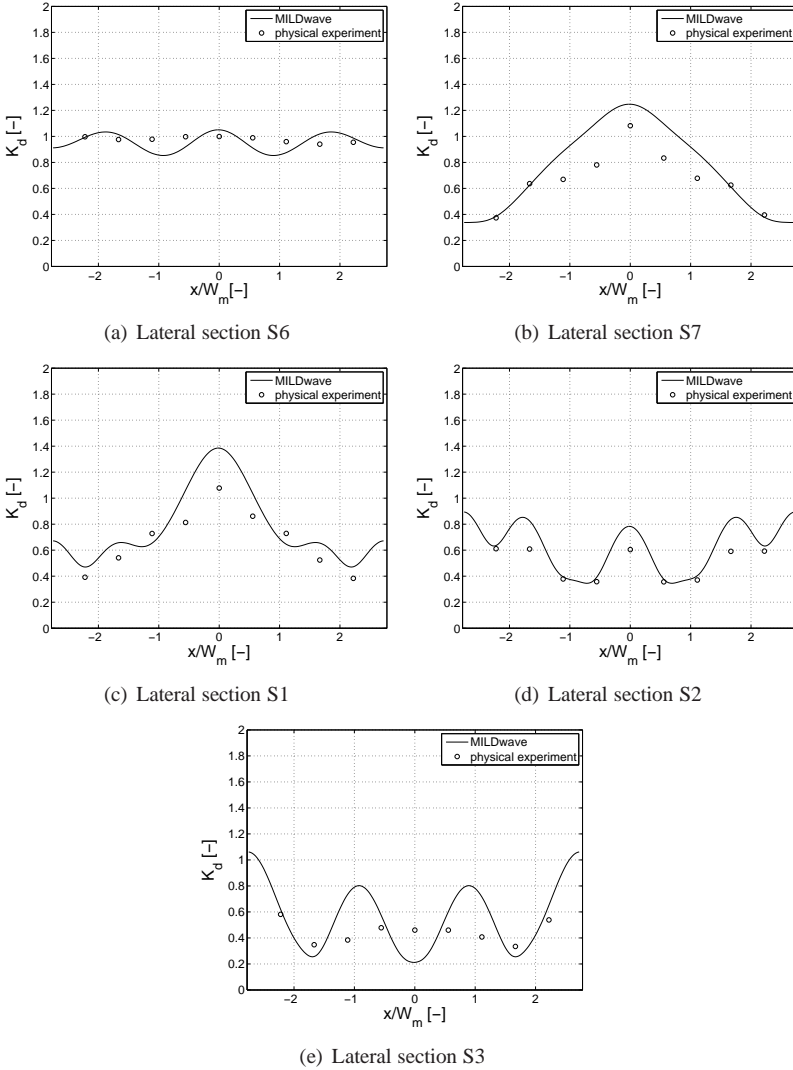


Figure 6.54: Comparison of numerical model results with experimental data in lateral sections (a) S6, (b) S7, (c) S1, (d) S2 and (e) S3, respectively, for target regular waves with  $H_i = 5$  m and  $T = 6.5$  s

As expected from the observations for a single WEC, the results agree the best for target  $T = 8.5$  s. For target  $T = 6.5$  s and 7.8 s again a less pronounced trend

is observed in the physical model compared to MILDwave. Larger deviations are seen in sections S2 and S3 compared to S7 and S1. Sections S2 and S3 are more disturbed by reflections from the side walls, as they are located further away from the first two models. On sections S7 and S1 an energy concentration in the centre of the section is observed, caused by diffraction around the first two models.

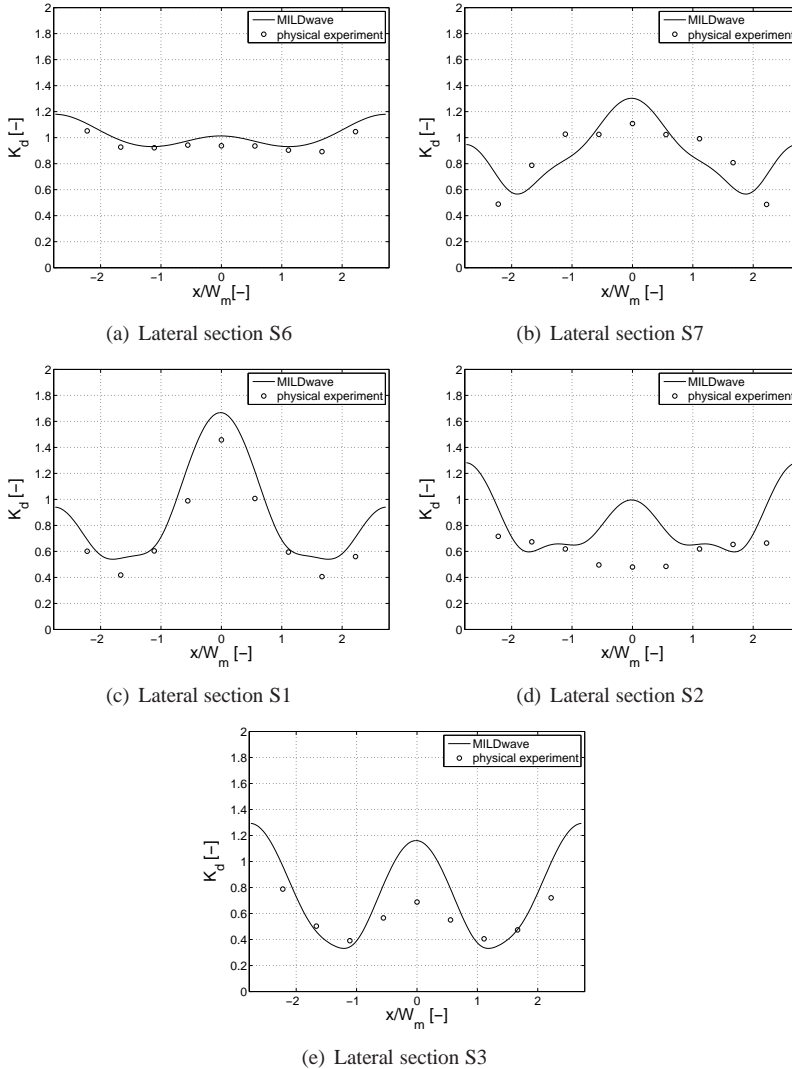


Figure 6.55: Comparison of numerical model results with experimental data in lateral sections (a) S6, (b) S7, (c) S1, (d) S2 and (e) S3, respectively, for target regular waves with  $H_i = 5$  m and  $T = 7.8$  s

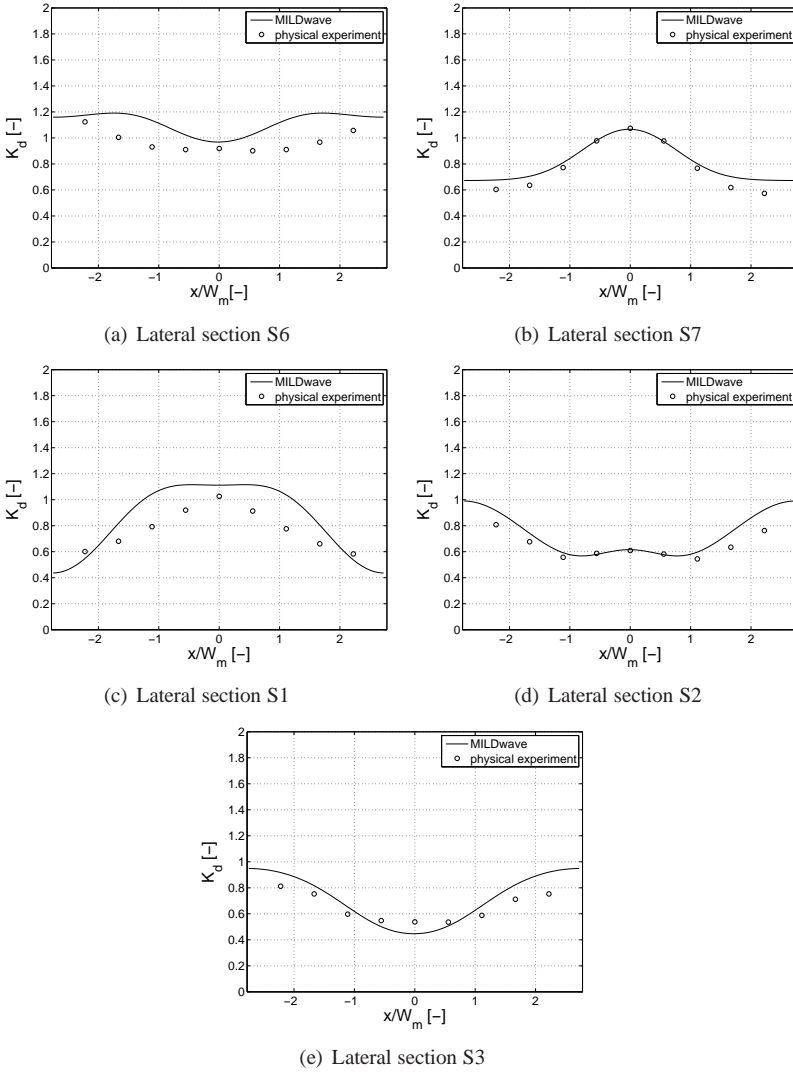


Figure 6.56: Comparison of numerical model results with experimental data in lateral sections (a) S6, (b) S7, (c) S1, (d) S2 and (e) S3, respectively, for target regular waves with  $H_i = 5$  m and  $T = 8.5$  s

The longitudinal sections S4 and S5 are given in Figure 6.57 and Figure 6.58. These sections start from the beginning of the first two models (Figure 6.52). The location of the third WEC is indicated by two vertical lines on Figure 6.57. For target  $T = 7.8$  s, results in section S5 agree better than results in section S4.

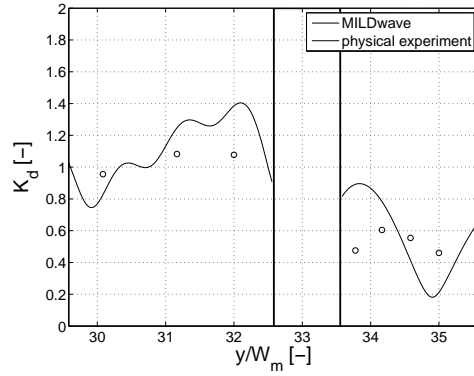
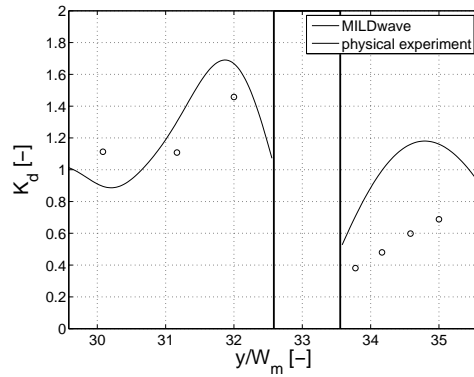
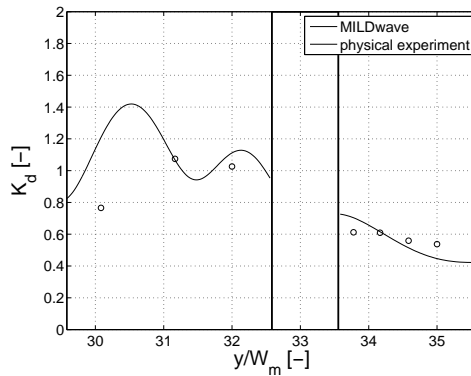
(a)  $T = 6.5$  s(b)  $T = 7.8$  s(c)  $T = 8.5$  s

Figure 6.57: Comparison of numerical model results with experimental data in longitudinal section S4 for target regular waves with  $H_i = 5$  m and  $T =$  (a) 6.5 s, (b) 7.8 s and (c) 8.5 s

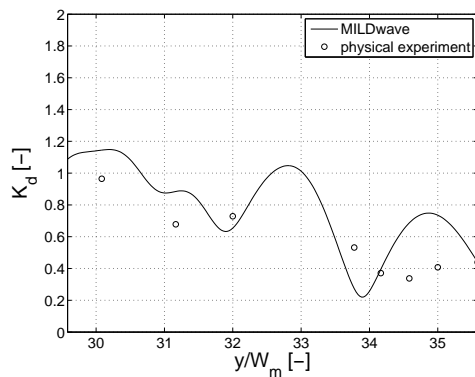
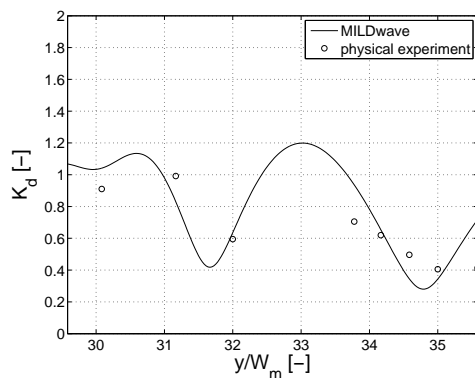
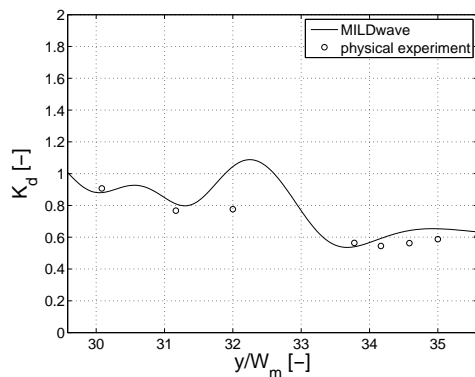
(a)  $T = 6.5$  s(b)  $T = 7.8$  s(c)  $T = 8.5$  s

Figure 6.58: Comparison of numerical model results with experimental data in longitudinal section S5 for target regular waves with  $H_i = 5$  m and  $T =$  (a) 6.5 s, (b) 7.8 s and (c) 8.5 s

In general the average values of the numerical results, on the locations of the wave gauges along each lateral section, are higher than the average values of the experimental measurements (Table 6.14). The difference increases up to 20 % compared to 10 % for a single WEC. For target  $T = 7.8$  s the difference on section S2 is even larger (27 %).

Table 6.14: Average of calculated disturbance coefficient  $K_d$  on five lateral sections S6, S7, S1, S2 and S3 in the (a) experimental and (b) numerical test set-up for target regular waves with  $H_i = 5$  m and  $T = 6.5$  s, 7.8 s and 8.5 s

(a) Experimental set-up						(b) Numerical set-up					
$T$ [s]	S6	S7	S1	S2	S3	$T$ [s]	S6	S7	S1	S2	S3
6.5	0.98	0.68	0.67	0.50	0.44	6.5	0.96	0.80	0.78	0.59	0.52
7.8	0.95	0.86	0.73	0.60	0.57	7.8	0.99	0.85	0.87	0.76	0.69
8.5	0.97	0.78	0.77	0.64	0.65	8.5	1.10	0.81	0.90	0.69	0.68

The average values in cross sections S2 and S3 are always lower than the averages of sections S7 and S1, since energy is absorbed by the third WEC. Furthermore the values for target  $T = 6.5$  s on sections S7, S1, S2 and S3 are smaller compared to the averages for target  $T = 7.8$  s and 8.5 s, as the reflection and absorption are the highest for target  $T = 6.5$  s (Table 6.12). The average of  $K_d$  on sections S2 and S3, behind three WECs, is smaller than the average on sections S2 and S3 behind a single WEC (Table 6.13), as expected.

A plan view of the disturbance coefficients in the numerical wave flume is given in Figure 6.59 for target regular waves with  $H_i = 5$  m and  $T = 6.5$  s, 7.8 s and 8.5 s, respectively. Waves are generated during 1 000 s to obtain a stationary regime. For all wave periods an energy concentration in front of the third WEC is seen.

The influence of the wave flume walls is considerable as seen in Figure 6.60(a). In Figure 6.60 the fully reflective obstacle (section 6.4.1) is implemented in the wave flume. Reflection on the wave flume walls is caused by diffraction around the implemented model with limited width. Consequently the wave height behind the obstacle is disturbed by the presence of the fully reflective walls of the wave flume and is not representative for the wake that will occur when these walls are not present. In Figure 6.60(b) a wider wave flume (width = 1 000 m) has been considered. A large wave height decrease immediately behind the obstacle and a gradual refill further behind the obstacle is observed. Still some influence of the fully reflective boundaries is seen. Absorbing sponge layers at the side walls of

the wave basin are needed to prevent these reflections (Figure 6.60(c)).

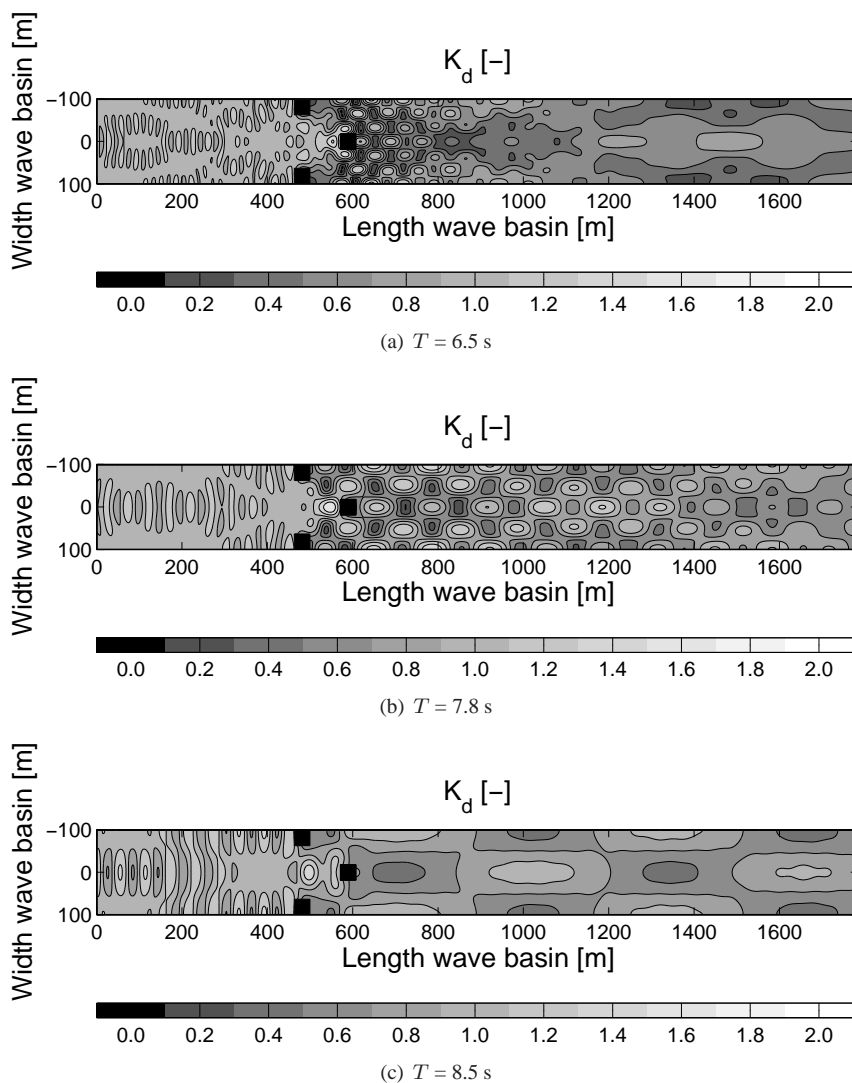
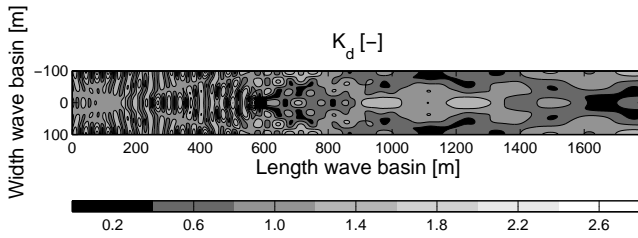
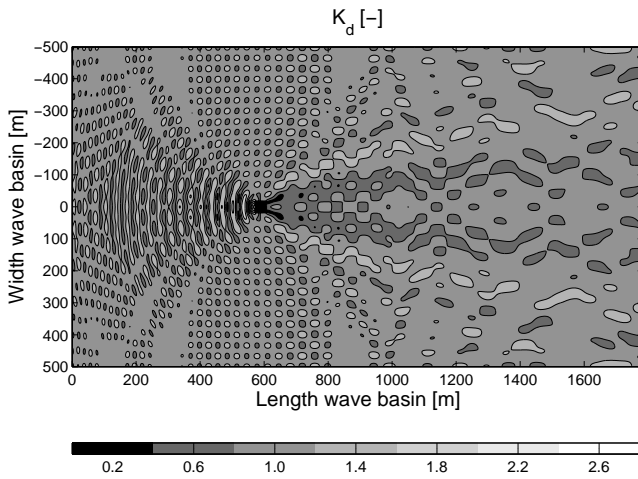


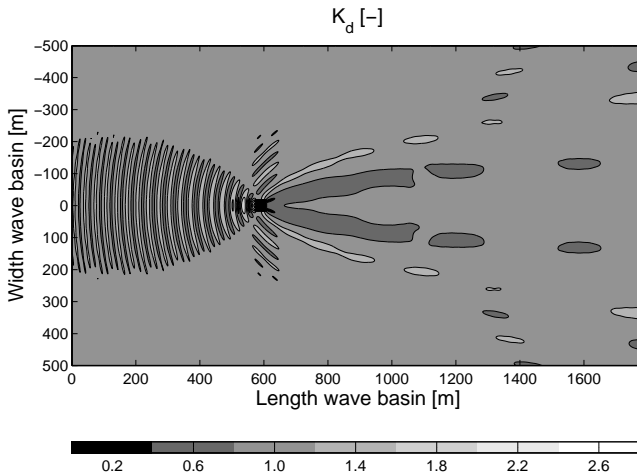
Figure 6.59: Plan view of calculated disturbance coefficient  $K_d$  in the numerical wave flume with three absorbing obstacles for target regular waves with  $H_i = 5$  m and  $T =$  (a) 6.5 s, (b) 7.8 s and (c) 8.5 s



(a) Wave flume width = 200 m



(b) Wave flume width = 1 000 m



(c) Wave flume width = 1 000 m, sponge layer at left and right boundary

Figure 6.60: Plan view of calculated disturbance coefficient  $K_d$  in a numerical wave flume (with a fully reflective obstacle) with a width = (a) 200 m, (b) 1 000 m and (c) absorbing sponge layers at the side boundaries of the domain, for target regular waves with  $H_i = 5$  m and  $T = 6.5$  s



### 6.4.3 Calculation of wave power absorption in MILDwave

As the validation of the wave power absorption through experimental tests was not straightforward due to the limited width of the wave flume (reflective walls), a method for the calculation of the amount of absorbed wave power by a WEC in a numerical wave basin in MILDwave is developed in this section. In a first step the vector field of the wave power is derived by using the velocity potential and the wave elevation across the simulation domain in MILDwave. Then, the flux of the wave power through a closed surface is calculated by using Gauss' divergence theorem. A validation of the developed method is given using simple test cases.

In MILDwave the velocity potential is given by equation (B.1):

$$\Phi(x, y, z, t) = f(z, h) \varphi(x, y, t) \quad (\text{B.1})$$

Consequently, the fluid particle velocity in x- and y-direction,  $v_x$  and  $v_y$ , can be written as:

$$v_x = \frac{\partial \Phi}{\partial x} = \frac{\partial \varphi}{\partial x} f(z, h) \quad (\text{6.2})$$

$$v_y = \frac{\partial \Phi}{\partial y} = \frac{\partial \varphi}{\partial y} f(z, h) \quad (\text{B.3})$$

The wave power vector  $\mathbf{p}$  is given in equation (6.3). The derivation is similar to appendix B but is repeated here for convenience.<sup>3</sup>

$$\mathbf{p} = \int_{-h}^0 \overline{\wp_{dyn} \mathbf{v}} dz \quad (\text{6.3})$$

with  $\mathbf{v}$  the velocity vector of the fluid and  $\wp_{dyn}$  the dynamic pressure given by equation (B.6). The overbar denotes time average.

$$\wp_{dyn} = \rho g \eta f(z, h) \quad (\text{B.6})$$

Using equations (6.2), (B.3), (6.3) and (B.6) the vector field of the wave power can be calculated using equations (6.4) and (6.5) for the wave power components in x- and y-direction, respectively. The time integration is carried out over a number of wave periods.

$$p_x = \rho g \frac{1}{2k} D(kh) \frac{1}{t} \int_0^t \eta \frac{\partial \varphi}{\partial x} dt \quad (\text{6.4})$$

$$p_y = \rho g \frac{1}{2k} D(kh) \frac{1}{t} \int_0^t \eta \frac{\partial \varphi}{\partial y} dt \quad (\text{6.5})$$

---

<sup>3</sup> $p$  represents the wave power in the direction of wave propagation (per meter of wave crest) while  $\mathbf{p}$  denotes the wave power vector (per meter of wave crest).

with  $D(kh)$  equal to [14]:

$$D(kh) = 2k \int_{-h}^0 (f(z, h))^2 dz = 2k \int_{-h}^0 \left( \frac{\cosh(k(z+h))}{\cosh(kh)} \right)^2 dz \quad (\text{B.8})$$

For deep water  $D(kh)$  equals 1.

Finally by using Gauss' divergence theorem the flux through an enclosed surface  $S$  is calculated with equation (6.6).

$$\int_S \mathbf{p} \cdot \mathbf{n} dS = \int \int \nabla \cdot \mathbf{p} dA \quad (6.6)$$

with  $\mathbf{n}$  the unit normal and  $A$  the domain contained inside the closed surface of integration  $S$ .  $\mathbf{p}$  is the vector field of the wave power, which is two-dimensional (depth integrated). The divergence of the vector field of the wave power measures the magnitude of the generated or absorbed amount of wave power in a given region.

First, three test cases (generation of head-on waves, generation source inside the domain, generation of waves with  $\theta = 45^\circ$  and  $80^\circ$ ) are considered to validate the developed method. Further, the method is used to validate the sponge layer technique, which simulates wave power absorption by a WEC.

#### 6.4.3.1 Test case 1: generation of head-on waves

Regular waves with  $H_i = 2$  m and  $T = 5$  s are generated on a wave generation line parallel with the x-axis in a constant water depth of 100 m. These waves are propagating along the y-axis across an inner domain of 300 m (width) x 500 m (length). At the beginning and at the end of the domain absorbing sponge layers are placed. As the waves are travelling along the y-axis, the wave power in x-direction is zero. The wave power in y-direction is calculated across the domain using equation (6.5) in MILDwave (Figure 6.61(a)):  $p_y$ , spatially averaged over the simulation domain, equals 19.7 kW/m. Note that the absorbing sponge layers are not shown in Figure 6.61(a).

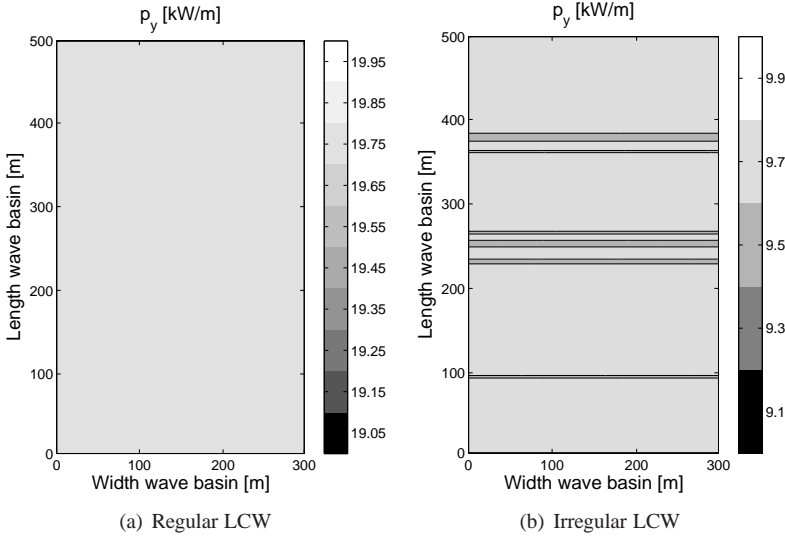


Figure 6.61: Plan view of wave power  $p_y$  in a numerical wave basin for (a) regular long-crested waves with  $H_i = 2$  m and  $T = 5$  s and for (b) irregular long-crested waves with  $H_s = 2$  m and  $T_p = 5$  s

For regular waves in deep water, the energy-flux given in equation (6.5) simplifies to equation (B.12). The derivation of equation (B.12) is given in appendix B.<sup>4</sup>

$$p_y^{(*)} = \frac{1}{2} \rho g a^2 C_g \quad (\text{B.12})$$

$p_y^{(*)}$  equals 19.8 kW/m when using the calculated value of  $a$  spatially averaged over the simulation domain. As expected,  $p_y^{(*)}$  is equal to  $p_y$  (difference  $\leq 1\%$ ).

The same test has been repeated with irregular long-crested waves with  $H_s = 2$  m and  $T_p = 5$  s. The resulting wave power in y-direction is shown in Figure 6.61(b).  $p_y$ , spatially averaged over the simulation domain, equals 9.7 kW/m for these waves (equation (6.5)). Note that the small variation in  $p_y$  corresponds with a difference in  $H_s$  of 1 cm.

In deep water the energy flux is given by equation (B.18) for irregular long-crested waves (appendix B).

$$p_y^{(*)} = \frac{\rho g^2}{64\pi} H_s^2 T_e \quad (\text{B.18})$$

<sup>4</sup>(\*) indicates that the wave power has been derived using the calculated spatially averaged amplitude  $a$  (regular waves) or significant wave height  $H_s$  (irregular waves) in MILDwave.

$p_y^{(*)}$  is approximately 10 % smaller than  $p_y$ . As expected, the wave power determined with equation (6.5) in MILDwave corresponds well with the simplified equations (equations (B.12) and (B.18) for deep water.

#### 6.4.3.2 Test case 2: wave generation source in the centre of the simulation domain

In a second example regular waves with  $H_i = 2$  m and  $T = 4$  s are generated on a wave generation circle with  $r_c = 20$  m located in the centre of the inner domain (500 m x 500 m). The calculated wave power in x- and y-direction is shown on Figure 6.62(a) and Figure 6.62(b).

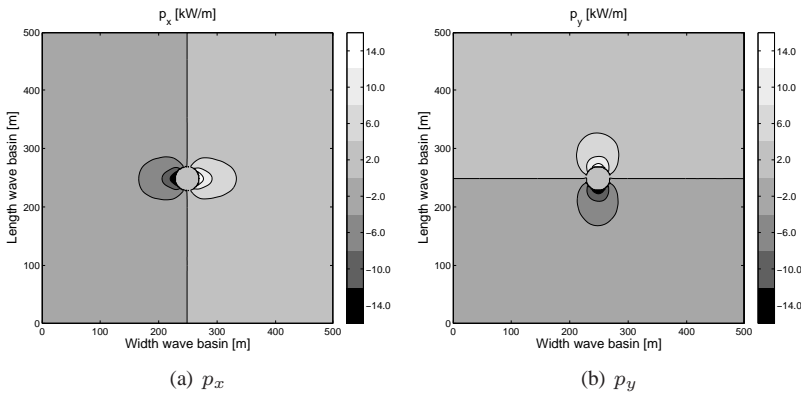


Figure 6.62: Plan view of wave power (a)  $p_x$  and (b)  $p_y$  in a numerical wave basin for regular long-crested waves with  $H_i = 2$  m and  $T = 4$  s

The wave power in y-direction is equal to the wave power in x-direction. The wave power in x- and y-direction inside the wave generation circle are set to 0. The flux through a circle with  $r_c = 150$  m in the centre of the domain equals  $1.925 \cdot 10^6$  W (equation (6.6)). A positive flux corresponds with a net power propagating from the inner part of the circle through the circle contour. The flux through a circle with  $r_c = 100$  m and 200 m and through a square with side  $z = 150$  m and 200 m, all in the centre of the domain are given in Table 6.15. It is clear that the choice of the enclosed surface has no influence on the flux.

Table 6.15: Wave power generated by a source inside an enclosed surface - regular waves

Enclosed surface [—]	Radius $r_c$ or Side $z$ [m]	Wave power $P$ [MW]
circle	100	1.9254
circle	200	1.9250
square	150	1.9254
square	200	1.9252

The generated wave power  $P^{(*)}$  (W) can also be calculated by multiplying the wave power  $p$  per meter of wave crest (appendix B) with the perimeter of the circular surface (equation (6.7)).

$$P^{(*)} = \frac{1}{2} \rho g a^2 C_g 2\pi r \quad (6.7)$$

Applying equation (6.7) results in  $1.948 \cdot 10^6$  W, when the spatially averaged value of  $a$  calculated in MILDwave on a circle with  $r_c = 150$  m is used. The latter value differs less than 2 % from the value calculated with equation (6.6).

Further, irregular long-crested waves with  $H_s = 2$  m and  $T_p = 4$  s are generated on the same wave generation circle. The flux through different enclosed surfaces is given in Table 6.16. Differences between the enclosed surfaces are a bit higher compared to regular waves, but are still smaller than 1 %.

Table 6.16: Wave power generated by a source inside an enclosed surface - irregular waves

Enclosed surface [—]	Radius $r_c$ or Side $z$ [m]	Wave power $P$ [MW]
circle	150	0.7393
circle	200	0.7393
square	100	0.7374
square	150	0.7393
square	200	0.7388

For irregular waves in deep water the power through a circular enclosed surface can be calculated with equation (6.8) (multiplying the wave power  $p$  (appendix B) with the perimeter of the circular surface).

$$P^{(*)} = \frac{\rho g^2}{64\pi} H_s^2 T_e 2\pi r \quad (6.8)$$

For a circle with  $r_c = 150$  m equation (6.8) yields 0.6825 MW and is approximately 10 % lower than  $P$ .

### 6.4.3.3 Test case 3: generation of waves with $\theta = 45^\circ$ and $80^\circ$

Regular waves with  $H_i = 1$  m,  $T = 5.2$  s and  $\theta = 45^\circ$  and  $80^\circ$  are generated in a water depth of 70 m in a wave basin as shown on Figure 5.5. The wave power in x- and y-direction, calculated in MILDwave (equations (6.4) and (6.5)) and derived with equations (6.9) and (6.10), are given in Table 6.17.

$$p_x^{(*)} = \frac{1}{2} \rho g a^2 C_g \cos \theta \quad (6.9)$$

$$p_y^{(*)} = \frac{1}{2} \rho g a^2 C_g \sin \theta \quad (6.10)$$

Table 6.17: Wave power in x- and y-direction generated by regular waves with  $H_i = 1$  m,  $T = 5.2$  s and  $\theta = 45^\circ$  and  $80^\circ$ , determined in MILDwave and with equations (6.9) and (6.10)

$\theta$ [°]	MILDwave		Equations (6.9) and (6.10)	
	$p_x$ [kW/m]	$p_y$ [kW/m]	$p_x^{(*)}$ [kW/m]	$p_y^{(*)}$ [kW/m]
45	3.60	3.59	3.60	3.60
80	0.82	4.65	0.79	4.46

When  $\theta = 45^\circ$  the wave power in x- and y-direction are almost identical and correspond well with the wave power calculated with equations (6.9) and (6.10). Only a small amount of wave power is propagating in the x-direction when  $\theta = 80^\circ$ . For  $\theta = 80^\circ$  the wave power in x- and y-direction, calculated in MILDwave, differ 5 % from the wave power determined with equations (6.9) and (6.10).

The energy flux through a square in the middle of the domain is expected to equal 0 kW as no energy is generated or absorbed inside the square. Depending on the dimensions of the considered square the divergence varies between 0.20 and 0.50 kW for  $\theta = 45^\circ$  and between 0.09 and 0.80 kW for  $\theta = 80^\circ$ . One should note that the accuracy decreases when waves are propagation nearly perpendicular to the wave generation line. For example the accuracy decreases till [-5 kW,+5 kW] when  $\theta = 89^\circ$ .

From test cases 1, 2 and 3 it is clear that wave power absorption or generation inside a simulation domain can be determined by calculating the divergence of the vector field of the wave power. Consequently the developed method has been used to determine the amount of power absorbed by a hypothetical WEC in MILDwave.

### 6.4.3.4 Validation of wave power absorption of a hypothetical WEC

First the power distribution around a fully reflective obstacle is studied. Then, the amount of absorbed power by the hypothetical WEC, defined in section 6.3, is validated by calculating the divergence of the vector field of the wave power around the hypothetical WEC.

#### *Fully reflective obstacle*

A complete reflective obstacle with a width of 106 m and a length of 45 m is implemented in a wave basin in MILDwave. The power in x- and y-direction in the simulation domain, when irregular long-crested waves with  $H_s = 1$  m and  $T_p = 5.6$  s are generated on a wave generation line parallel with the x-axis in a water depth of 200 m, are shown in Figure 6.63.

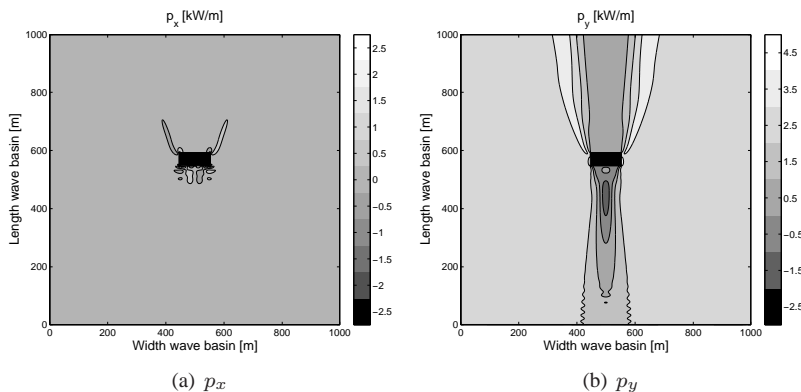


Figure 6.63: Plan view of wave power (a)  $p_x$  and (b)  $p_y$  in a numerical wave basin with a fully reflective obstacle (indicated in black) for irregular long-crested waves with  $H_s = 1$  m and  $T_p = 5.6$  s

When the obstacle would not be implemented in the basin,  $p_x^{(*)}$  and  $p_y^{(*)}$  would equal 0 and 2.5 kW/m (equation (B.18)). From Figure 6.63(a) it is seen that  $p_x = 0$  kW/m in the largest part of the domain. Near the obstacle some wave power is propagating in the x-direction due to reflection from and diffraction around the obstacle. The wave power field in the x-direction is symmetric around a vertical axis through the centre of the obstacle. Most wave power is propagating in the y-direction (Figure 6.63(b)). At the left and the right side of the obstacle  $p_y$  equals approximately 2.5 kW/m. In these zones  $p_y$  is not disturbed by the obstacle. Immediately behind the obstacle a decrease of  $p_y$  (wake) is observed, while at the edges of the wake an increase in wave power occurs. Reflection from the obstacle causes negative values of  $p_y$  in front of the obstacle. The flux through

a square around the obstacle varies between  $-5$  kW and  $+2$  kW, depending on the dimensions of the square. No wave power is generated or absorbed by the complete reflective obstacle.

### *Hypothetical WEC*

In this section the hypothetical WEC, as defined in section 6.3, is used as an example.

This hypothetical WEC is implemented in a wave basin, as shown on Figure 6.64. The WEC is indicated in black. The wave power in x- and y-direction are given in Figure 6.64 for irregular long-crested waves with  $H_s = 1$  m and  $T_p = 5.2$  s. Again most wave power is propagating in y-direction, as head-on waves with a power of  $2.3$  kW/m (equation (B.18)) are generated. The flux through a square around the hypothetical WEC, varies between  $-34$  kW (capture ratio =  $41\%$ ) and  $-48$  kW (capture ratio =  $58\%$ ) for several dimensions of the square. A negative flux corresponds to wave power absorption. On average a capture ratio of  $45\%$  is found. This capture ratio is identical to the capture ratio, tuned with the sponge layer technique in the wave flume. It can be concluded that the sponge layer technique is a good method to implement a WEC of the overtopping type in MILDwave.

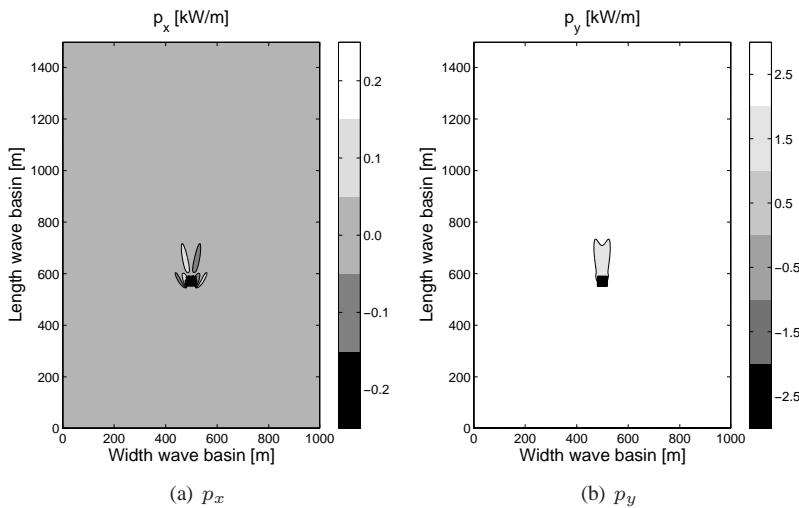


Figure 6.64: Plan view of wave power (a)  $p_x$  and (b)  $p_y$  in a numerical wave basin with a hypothetical WEC (indicated in black) for irregular long-crested waves with  $H_s = 1$  m and  $T_p = 5.2$  s

Further the wave power absorption of the hypothetical WEC in a short-crested



sea with  $H_s = 1$  m,  $T_p = 5.2$  s,  $\theta_0 = 90^\circ$  and  $s_{max} = 10$  is studied. Figure 6.65 shows the wave power in x- and y-direction. Note that only the useful domain is shown<sup>5</sup>. The wave power in x-direction is slightly higher compared to long-crested waves (Figure 6.64(a)), while the wave power in y-direction is a little smaller (Figure 6.64(b)). This is caused by the directional spreading of the generated waves. The flux through a square around the hypothetical WEC equals -36 kW and is identical for various dimensions of the square. A capture ratio of 43 % is obtained for a hypothetical WEC in a short-crested sea, which is almost identical to the tuned capture ratio of 45 %.

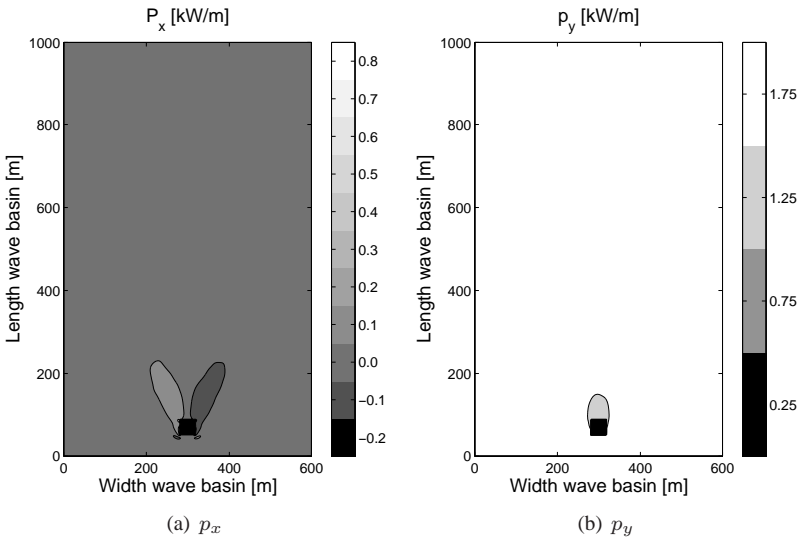


Figure 6.65: Plan view of wave power (a)  $p_x$  and (b)  $p_y$  in a numerical wave basin with a hypothetical WEC (indicated in black) for irregular short-crested waves with  $H_s = 1$  m,  $T_p = 5.2$  s,  $\theta_0 = 90^\circ$  and  $s_{max} = 10$

Finally the wave power in x- and y-direction for irregular long-crested waves with  $H_s = 1$  m and  $T_p = 5.2$  s inside a wave basin with a farm of 6 hypothetical WECs, installed in an aligned grid, are shown in Figure 6.66. The WECs in the first row have a capture ratio of 45 % while the capture ratio of the WECs in the second row equals 35 %. In total 202 kW is absorbed. The flux through a square around the farm varies between -210 kW and -220 kW, which is 5 and 10 % higher than the expected amount of power absorption (202 kW).

<sup>5</sup>The useful domain was indicated with black lines on Figures 6.22 and 6.23.

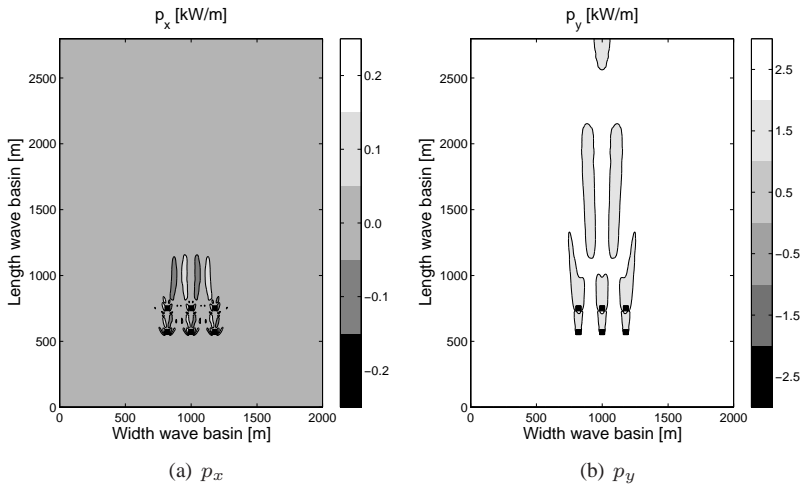


Figure 6.66: Plan view of wave power (a)  $p_x$  and (b)  $p_y$  in a numerical wave basin with 6 hypothetical WECs (indicated in black) for irregular long-crested waves with  $H_s = 1$  m and  $T_p = 5.2$  s

By calculating the divergence of the vector field of the wave power it is found that the sponge layer technique is a good method to study wake effects in the lee of farm of WECs.

## 6.5 Conclusions

In this chapter the implementation of a single WEC and a farm of WECs based on the overtopping principle in the time-dependent mild-slope equation model MILDwave has been presented. A WEC is composed of an array of absorbing cells, with the same spatial dimensions of the WEC, that have been assigned a specific absorption coefficient to obtain the amounts of reflection and absorption as specified by the developer of the WEC. The possibilities and constraints of the latter approach have been discussed.

When the WEC has a constant absorption coefficient equal to 0, the WEC is fully reflective. Cells with an absorption coefficient of 1 correspond to water cells. All values of the absorption coefficient between 0 and 1 result in a combination of reflection, absorption and transmission, depending on the dimensions of the WEC. The reflection and transmission coefficient are respectively decreasing and increasing with increasing value of the absorption coefficient. Further the amount of transmission is decreasing with increasing length of the WEC, while the amount of reflection is approximately constant. By changing the shape of the absorption

function through the WEC (in the direction of mean wave propagation), the amounts of reflection and absorption are uncoupled. As the amount of power absorption depends on the incident wave period, the WEC needs to be tuned for each wave climate. For a WEC with sufficiently large dimensions ( $\geq 18$  m for  $T = 5.2$  s or  $\frac{\text{length of WEC}}{L} \geq 0.4$ ), which is generally the case for WECs based on the overtopping principle, and a small amount of reflection (minimal loss of energy), each combination of reflection and absorption can be modelled, except small levels of absorption which are in contradiction with the concept of a WEC (absorbing as much wave power as possible).

The wake effects behind a single hypothetical WEC and multiple hypothetical WECs of the overtopping type have been studied in MILDwave.

The dimensions and the magnitude of the wake depend on the WEC specifications and on the incident wave climate. The wake increases with decreasing wave period and decreasing directional spreading.

The power absorption of two lay-outs with nine hypothetical WECs, an aligned and a staggered grid, with increasing lateral ( $2D_h$ ,  $4D_h$  and  $6D_h$  with  $D_h$  = device width) and longitudinal ( $2D_h$ ,  $4D_h$ ,  $6D_h$  and  $20D_h$ ) spacing, has been calculated for irregular long-crested waves with  $H_s = 1$  m and  $T_p = 5.2$  s. The capture ratio of each WEC in the farm has been adapted to its surrounding wave climate. In general, a staggered grid results in a higher power absorption. A lateral distance of  $4D_h$  is preferred in comparison to  $2D_h$ , as the amount of absorbed power is higher, and in comparison to  $6D_h$ , as the amount of absorbed power per  $\text{km}^2$  is higher. A smaller longitudinal distance results in a higher amount of absorbed power per  $\text{km}^2$  as well. The final in-between distances should result in the smallest cost per produced kWh.

The developed technique to study a farm of WECs has been compared to a simplified method, where a farm is modelled as a single transmitting obstacle. The simplified method may result in a high overestimation or underestimation of the economic resource (up to 40 %). A more detailed estimation of the power absorption of the considered lay-out with the method developed in this PhD manuscript is required for an economic assessment. Finally, the power absorption of a farm of hypothetical WECs installed in a staggered grid with a lateral and longitudinal spacing of  $4D_h$  at Westhinder has been estimated. In general, the results obtained for irregular long-crested waves with  $H_s = 1$  m and  $T_p = 5.2$  s are a conservative representation of the average yearly power absorption at Westhinder.

The simulation of wave power absorption in MILDwave (sponge layer technique) has been experimentally validated. First, reflection from, transmission under and diffraction around a fully reflective obstacle has been studied. Immediately behind the obstacle the largest deviations between the numerical and experimental results are observed as the limited draft of the obstacle had not been modelled

in MILDwave. The average value of numerical and experimental values of the disturbance coefficient  $K_d$  on several lateral and longitudinal sections near the obstacle agree well. In general differences are within  $\pm 5\%$ .

Further, the wave pattern around an absorbing obstacle has been assessed. The obstacle in MILDwave has been tuned to obtain the same reflection, absorption and transmission characteristics as the physical model. Consequently the limited draft of the physical model is taken into account. In general, it is seen that the results in MILDwave are more attenuated compared to the experimental measurements. The average value of  $K_d$  on lateral and longitudinal sections near the obstacle is systematic lower in the physical model compared to the numerical model (10 % at maximum). When testing a farm of three absorbing obstacles, the differences between the numerical and experimental average values of  $K_d$  increase up to 20 %.

A wave flume with a limited width is not most suitable to study wave power absorption by an obstacle with a width smaller than the wave flume width, as the wave pattern is disturbed by reflection on the side walls of the wave flume. Therefore a method has been developed to calculate the power absorbed by a WEC in a two dimensional domain in MILDwave. The wave power flux through enclosed surfaces around the WEC has been calculated with Gauss' divergence theorem. The method has been validated with several test cases to prove its reliability. Using the developed method it is illustrated that the sponge layer technique is a good tool to study wake effects behind WECs of the overtopping type.

## References

- [1] D.L. Millar, H.C.M. Smith, and D.E. Reeve. *Modelling analysis of the sensitivity of shoreline change to a wave farm*. Ocean Engineering, 34:884–901, 2006.
- [2] H.C.M. Smith, D.L. Millar, and D.E. Reeve. *Generalisation of wave farm impact assessment on inshore wave climate*. In Proceedings of the 7<sup>th</sup> European Wave and Tidal Energy Conference (EWTEC), Porto, Portugal, 2007.
- [3] L. Mendes, A. Palha, J.F. Conceição, A. Brito-Melo, and A.J.N.A. Sarmiento. *Analysis of the Impact of a Pilot Zone for Wave Energy Conversion Offshore Portugal*. In Proceedings of the 18<sup>th</sup> International Offshore and Polar Engineering Conference (ISOPE), Vancouver, British Columbia, Canada, 2008.
- [4] C. Vidal, F.J. Méndez, G. Díaz, and R. Legaz. *Impact of Santoña WEC installation on the littoral processes*. In Proceedings of the 7<sup>th</sup> European Wave and Tidal Energy Conference (EWTEC), Porto, Portugal, 2007.
- [5] V. Venugopal and G.H. Smith. *Wave climate investigation for an array of wave power devices*. In Proceedings of the 7<sup>th</sup> European Wave and Tidal Energy Conference (EWTEC), Porto, Portugal, 2007.
- [6] L.H. Holthuijsen. *Waves in oceanic and coastal waters*. Cambridge University Press, 2007.
- [7] J. Larsen and H. Dancy. *Open boundaries in short wave simulations - a new approach*. Coastal Engineering, 7:285–297, 1983.
- [8] C. Lee, Y.-S. Cho, and K. Yum. *Internal generation of waves for extended Boussinesq equations*. Coastal Engineering, 42:155–162, 2001.
- [9] J. Tedd, J.P. Kofoed, W. Knapp, E. Friis-Madsen, and H.C. Sørensen. *Wave Dragon prototype wave power production*. In Proceedings of the World Renewable Energy Congress - IX, Florence, Italy, 2006.
- [10] J.P. Kofoed. *Wave overtopping of marine structures - utilization of wave energy*. PhD thesis, Hydraulics and Coastal Engineering Laboratory, Department of Civil Engineering, Aalborg University, 2002.
- [11] R.D. Murray. *Economic wave energy resource assessment methodology & European assessment*. Master's thesis, University of Strathclyde, Glasgow, 2004.

- [12] C. Desimpelaere. *Fysisch onderzoek naar de modellering van 1 golfenergieconvector m.b.t. absorptie, diffractie, reflectie, ...* Master's thesis, Ghent University, 2007.
- [13] J. François and H. Van de Castele. *Experimentele validatie van golf-energieconvertoren in park lay-out in het numerieke golfvoortplantingsmodel MILDwave*. Master's thesis, Ghent University, 2008.
- [14] J. Falnes. *Ocean Waves and Oscillating Systems: linear interactions including wave-energy extraction*. Cambridge University Press, 2002.

# 7

## Power absorption of a farm of Wave Dragon wave energy converters

### 7.1 Introduction

The methodology to model a single WEC and a farm of WECs of the overtopping type (second category) in the linear mild-slope wave propagation model MILD-wave has been developed in chapter 6. The generic approach described in chapter 6 is applied to the Wave Dragon WEC (WD-WEC) in this chapter and is extended in chapter 8 to implement a WEC of the first category (the FO<sup>3</sup> WEC).

The WD-WEC is a floating offshore converter of the second category which consists of two main structural elements (Figure 7.1):

- Two **wave reflectors** to focus the incoming waves towards a double curved ramp;
- A **main body** where the focussed waves run up the curved ramp, overtop in a water reservoir above mean sea level and consequently have an increased potential energy compared to the surrounding sea. The reservoir contains a set of low head hydro turbines to convert the created potential energy into electricity when the water in the reservoir drains back to the sea through the turbines.

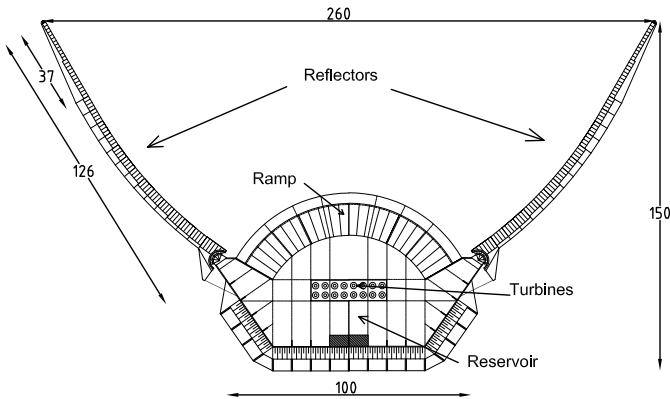


Figure 7.1: Main structural elements of a WD-WEC in plan view (copyright Wave Dragon) - dimensions in m

The wave reflectors and the main body (ramp and reservoir with turbines) are simulated as porous structures, exhibiting the same reflection, respectively absorption characteristics as the prototype WD-WEC, using the sponge layer technique. A detailed description of the implementation of the WD-WEC in MILDwave is given in this chapter. Further the wake effects in the lee of a single WD-WEC and five WD-WECs in a staggered grid (3 WECs in the first row and 2 WECs in the second row) are studied for uni- and multi-directional waves. The total power absorption and wave height reduction behind the farm of five WD-WECs are calculated for various lateral and longitudinal spacing in order to select an optimal farm lay-out.

## 7.2 Implementation of a Wave Dragon WEC in MILDwave

In this chapter a WD-WEC with a rated power of 4 MW, in a typical wave climate of the northern part of the North Sea (Location Ekofisk (Table 2.9) - 24 kW/m), is studied. The dimensions of the 4 MW WD-WEC are shown in Figure 7.1. Characteristic sea states in the northern part of the North Sea [1] for significant wave heights between 0.5 and 5.5 m and their related wave power (assuming a parameterized JONSWAP spectrum with  $\gamma = 3.3$  and deep water) and frequency of occurrence are given in Table 7.1. Note that the significant wave height  $H_s$  in Table 7.1 represents a  $H_s$ -interval. For example 43 % of the time, waves with  $H_s$  between 0.5 m and 1.5 m occur ( $H_s = 1$  m). Only 5 wave situations have been considered. During the rest of the year (frequency of occurrence = 10 %), wave heights are mainly smaller than 0.5 m and sometimes larger than 5.5 m.



These situations are neglected in the following, as they contribute only marginally to the total power production over a year. The mean wave power  $\bar{p}$  of the 5 considered wave situations (equation (2.5)) is approximately 17 kW/m. Waves with a significant wave height  $H_s = 1$  m and peak wave period  $T_p = 5.6$  s have the highest frequency of occurrence (43 %).

Table 7.1: Wave situations in the northern part of the North Sea (Location Ekofisk (Table 2.8): distance to shore = 300 km, water depth = 71 m [1])

Wave situation	$H_s$ [m]	$T_p$ [s]	Wave power $p$ [kW/m]	Frequency of occurrence (FO) [%]
1	1	5.6	2.5	43
2	2	7.0	12.4	25
3	3	8.4	33.5	12
4	4	9.8	69.6	6
5	5	11.2	124.2	4

A WD-WEC installed in sea, interacts with the incoming waves. The incident waves are partly overtopping in the reservoir and are consequently absorbed. The other part is reflected from the WEC, diffracted around the structure and even transmitted under the WEC. Therefore the WD-WEC is only absorbing a fraction of the incident wave power available over the width of the device.

The WD-WEC consists of 2 main structural elements with a different functioning (Figure 7.2): (i) **wave reflectors** (subscript R) which reflect part of the incident wave power<sup>1</sup>  $p_i$  towards the main body  $p_{R,r}$  and (ii) a **main body** (subscript B) which is absorbing as much wave power as possible  $P_{cs,B,a}$ . The wave reflectors partly reflect the incident wave power  $p_i$  to increase the available wave power in front of the main body  $P_{cs,R,i}$ . They do not absorb wave power. The remaining incident wave power (i.e. not reflected part) is transmitted under the wave reflectors  $p_{R,t}$ . The increased wave power in front of the main body  $P_{cs,R,i}$  is not completely absorbed by the main body, but is partly lost by transmission under the main body  $P_{cs,B,t}$  and by reflection from the curved ramp  $P_{cs,B,r}$ .<sup>2</sup>

Therefore the implementation of a WD-WEC in MILDwave is carried out in two phases: implementation of (i) wave reflectors and (ii) main body. Definition sketches of all relevant physical processes are given in Figure 7.2 and Figure 7.3. The used subscript abbreviations are explained in Figure 7.2 and Figure 7.3.

<sup>1</sup>For a single WD-WEC or for the first row of WD-WECs in a farm  $p_i = p$  given in Table 7.1.

<sup>2</sup> $P$  denotes the wave power (W) while  $p$  represents the wave power per meter of wave crest (W/m).

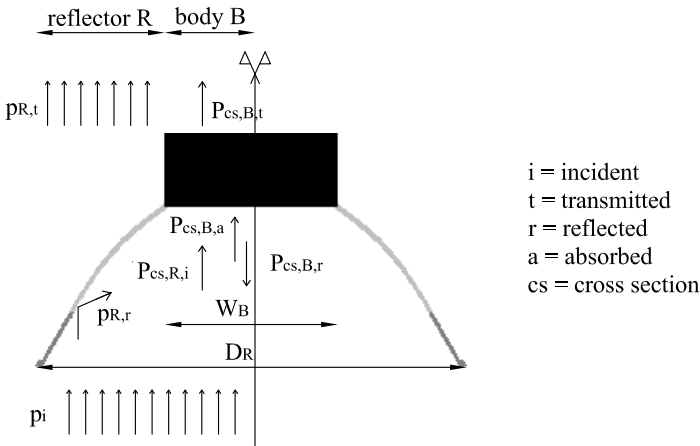


Figure 7.2: Definition sketch of reflection from, transmission under and absorption by the WD-WEC - plan view

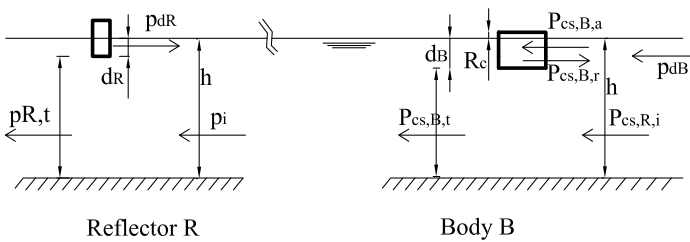


Figure 7.3: Definition sketch of (i) reflection from and transmission under the wave reflector and (ii) reflection from, transmission under and absorption by the main body - cross section

### 7.2.1 Implementation of the wave reflectors

The initial design of the wave reflectors has been evaluated by Nielsen and Kofoed [2] in a time-dependent mild-slope equation model. In Kramer et al. [3] the geometry of the wave reflectors of the WD-WEC is optimized by using a 3D boundary element method based on potential flow. This method is validated through physical experiments in the 3D wave basin at Aalborg University (scale 1/50). The efficiency of each design of the wave reflectors,  $\eta_R^{tar}$ , has been calculated using equation (7.1).

$$\eta_R^{tar} = \frac{P_{cs,R,i}}{P_{cs,i}} \tag{7.1}$$

with  $P_{cs,R,i}$  the total wave power available in the cross section between the two reflectors (with width  $W_B$ ) when the wave reflectors are present, as indicated

with a bold line on Figure 7.4, and  $P_{cs,i}$  the total wave power of the undisturbed incident wave in the same cross section when no reflectors are present in the wave field. No other parts than the wave reflectors were present in the wave field.

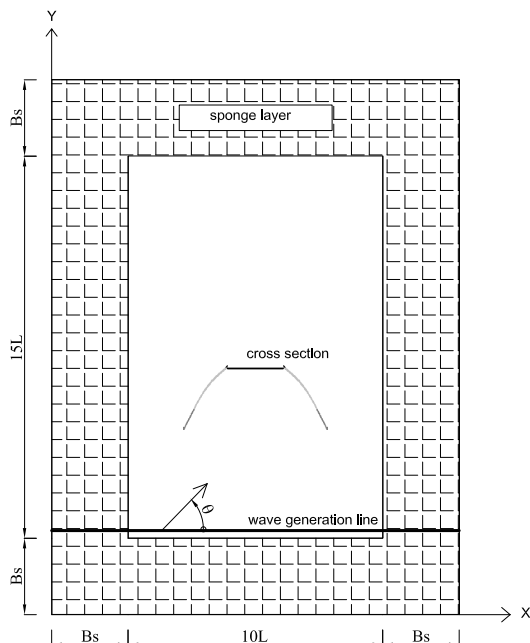


Figure 7.4: Definition sketch of wave basin with wave reflectors in plan view for generation of uni-directional waves

The resulting efficiencies  $\eta_R^{tar}$  [3] for the wave situations applied in this chapter and for the reflector lay-out shown in Figure 7.4, are given in Table 7.2.

Table 7.2: Efficiency of wave reflectors for wave situations in the northern part of the North Sea [3]

$H_s$ [m]	$T_p$ [s]	$\eta_R^{tar}$ [%]
1	5.6	185
2	7.0	145
3	8.4	124
4	9.8	120
5	11.2	115

These target efficiencies are used during the implementation of the wave

reflectors in MILDwave. The yearly averaged efficiency<sup>3</sup> of the wave reflectors in a northern North Sea wave climate is approximately 140 %. The efficiency increases for waves with a higher frequency. In general, waves with a higher wave frequency have a smaller wave height. Consequently the smaller incident significant wave heights are sufficiently increased by the wave reflectors to make wave overtopping possible. It is clear that the wave reflectors increase the frequency bandwidth of the WD-WEC.

The draft of the wave reflectors  $d_R$  varies along the length of the wave reflector. The draft decreases from approximately 8 m over a length of 89 m near the main body (indicated in light grey on Figure 7.2) to 6 m at the tip of the reflector over a length of 37 m (indicated in dark grey on Figure 7.2). As a consequence the transmission increases towards the tip of the reflector. As the equations in MILDwave are depth integrated, the difference in draft is taken into account through the absorption coefficients of the cells of the reflectors. The absorption coefficient at the tips should be closer to 1 (larger amount of transmission) compared to the coefficient near the main body (Figure 6.5). The amounts of transmitted wave power under both parts of the wave reflector (with a draft  $d_R$  equal to 6 m and 8 m respectively)  $p_{R,t}$  are derived by assuming that all wave power below the draft of the wave reflector is transmitted (Figure 7.3). The ratio between the time averaged (over one period) amount of energy flux integrated from the draft of the reflector up to the surface,  $p_{d_R}$ , and the time averaged amount of incident energy flux integrated from the seabed up to the surface or incident wave power,  $p_i$ , is given by equation (7.2) [4]:

$$\lambda_{d_R} = \frac{p_{d_R}}{p_i} = 1 - \frac{\sinh\left(2kh\left(1 - \frac{d_R}{h}\right)\right) + 2kh\left(1 - \frac{d_R}{h}\right)}{\sinh(2kh) + 2kh} \quad (7.2)$$

Consequently the amount of transmitted wave power under the wave reflectors is equal to  $p_{R,t} = p_i - p_{d_R} = p_i\left(1 - \frac{p_{d_R}}{p_i}\right) = p_i(1 - \lambda_{d_R})$ . The ratio between the transmitted wave power under the wave reflectors and the incident wave power  $\frac{p_{R,t}}{p_i} = (1 - \lambda_{d_R})$  increases with increasing wave period and decreasing draft, as shown on Figure 7.5.

In MILDwave the wave reflectors are assumed to be fixed, which is rather conservative, as small movements of the wave reflectors will increase the amount of transmission, which will blur the shadow zone in the lee of the WD-WEC. By using the efficiency of the wave reflectors (Table 7.2) and the amounts of transmission under the wave reflectors (Figure 7.5), the reflectors are modelled in MILDwave using the sponge layer technique. The wave reflectors (without main body) are implemented in a numerical wave basin as shown in Figure 7.4.

The values of the absorption coefficients of the cells of the wave reflectors, to obtain the target efficiency in the cross section (Table 7.2), are determined through

<sup>3</sup>Multiplying  $\eta_R^{tar}$  (Table 7.2) with its FO (Table 7.1) and summing up the results.

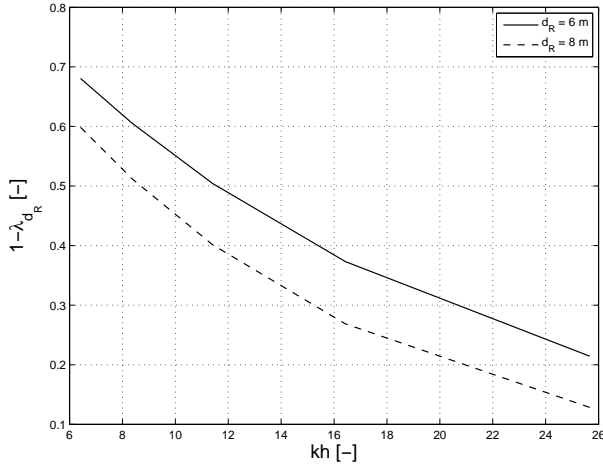


Figure 7.5: Ratio between transmitted wave power under the wave reflector  $p_{R,t}$  and incident wave power  $p_i$  as a function of  $kh$  for a reflector draft  $d_R = 6$  m and  $d_R = 8$  m

an iterative approach. The total wave power available in the cross section between the wave reflectors when the reflectors are present, as indicated on Figure 7.4 with  $W_B = 100$  m,  $P_{cs,R,i}$ , is calculated by summation of the wave power in each cell (appendix B) of that section (with cell size  $\Delta x = 1$  m):

$$P_{cs,R,i} = \sum_{k=1}^{100} \frac{\rho g^2}{64\pi} H_{s,k}^2 T_{e,k} \quad (7.3)$$

where  $\rho$  is the density of sea water and  $T_e$  the energy period (equation 2.3).

Finally the total wave power in the cross section between the wave reflectors  $P_{cs,R,i}$  is divided by the wave power in the undisturbed wave in the same section  $P_{cs,i} = W_B p_i$ , with  $W_B = 100$  m and  $p_i$  given in Table 7.1, to obtain the efficiency of the wave reflectors in the numerical model  $\eta_R^{num}$ .

The target efficiency  $\eta_R^{tar}$  is obtained with several combinations of absorption coefficients. To select the best combination the amount of transmitted wave power below the wave reflectors  $p_{R,t}$  is determined. Therefore both parts of the wave reflectors, with a draft of respectively 6 m and 8 m, have been implemented in a wave flume as shown in Figure 7.6. Wave propagation next to the reflector parts is prevented by the side walls of the wave basin.

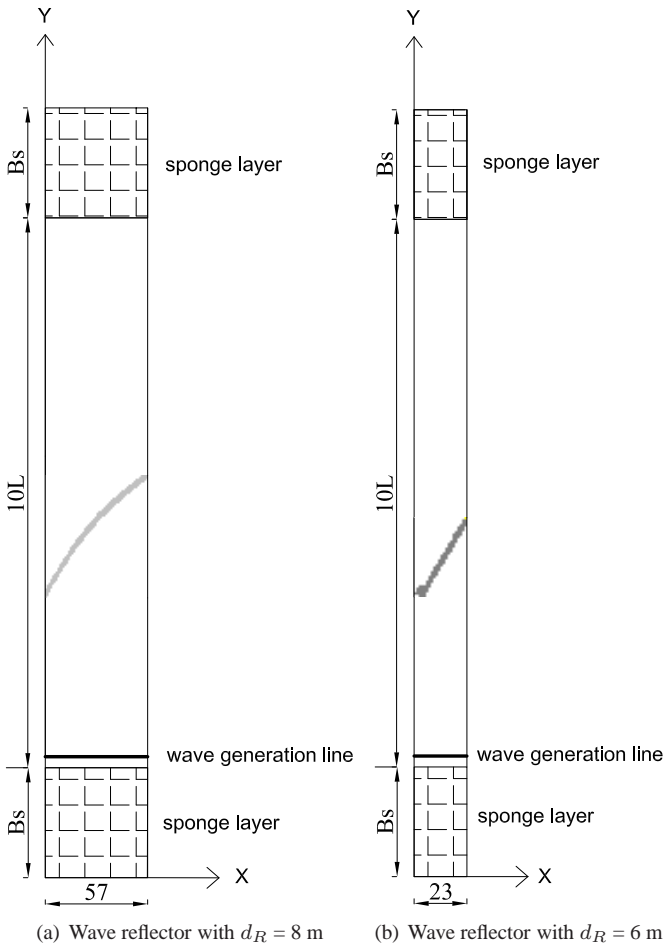


Figure 7.6: Definition sketch of a numerical wave flume with wave reflector parts with draft (a)  $d_R = 8$  m and (b)  $d_R = 6$  m - dimensions in m

By measuring the wave heights behind the wave reflector parts, the amounts of transmission under both reflector parts are determined. The combination of absorption coefficients which result in an accuracy of 5 % on the amounts of transmission (Figure 7.5) is selected. The absorption coefficients increase with increasing wave period, as the amount of reflection decreases (Table 7.2) and the amount of transmission increases (Figure 7.5).

## 7.2.2 Implementation of the main body

The main body converts potential energy into electricity by capturing the water volume of overtopped waves in a reservoir above mean sea level from which the water passes back to the sea through low head hydro turbines which drive permanent magnet generators. Consequently the main body absorbs a specific amount of wave power,  $P_{cs,B,a}$ , which can be determined with equation (7.4) [4]:

$$P_{cs,B,a} = qR_c g \rho W_B \quad (7.4)$$

with the crest freeboard  $R_c$ , the overtopping rate  $q$  and the width of the ramp  $W_B$ , which is equal to 100 m.

Based on previous simulations the optimal relative floating level,  $\frac{R_c}{H_s}$ , is approximately 0.7-0.8 for electrical power generation [5]. In this chapter the absorbed wave power (defined as the power of the water flow overtopping the ramp) is studied instead of the electrical power. To optimize the concept of the WD-WEC for maximum power absorption it seems reasonable to use a lower value of  $\frac{R_c}{H_s}$ . A value of 0.5 has been used to estimate the absorbed power.

The overtopping rate  $q$ , modified by  $\lambda_{dB}$ , is given by equation (7.5) [5]:

$$q = q_N \lambda_{dB} \sqrt{gH_s^3} \quad (7.5)$$

where  $q_N$  is the non-dimensional overtopping rate [5]:

$$q_N = 0.4 \exp^{-3.2 \frac{R_c}{H_s}} \quad (7.6)$$

Not all wave power in the cross section  $P_{cs,R,i}$  is absorbed by the main body. Again it is assumed that all wave power below the draft of the main body  $d_B$  is transmitted (Figure 7.3). The transmitted wave power under the main body  $P_{cs,B,t}$  is given by  $P_{cs,B,t} = P_{cs,R,i} - P_{d_B} = P_{cs,R,i} \left(1 - \frac{P_{d_B}}{P_{cs,R,i}}\right) = \eta_R^{tar} P_{cs,i} (1 - \lambda_{dB})$ . The remaining wave power  $P_{cs,B,r}$  is reflected. The calculated ratios between the absorbed wave power  $P_{cs,B,a}$ , respectively the transmitted wave power  $P_{cs,B,t}$  and the wave power in front of the main body  $P_{cs,R,i}$  are given in Table 7.3. These ratios have been used to implement the main body in MILDwave with the sponge layer technique.

Table 7.3: Dimensionless amounts of absorbed wave power,  $P_{cs,B,a}$ , and transmitted wave power under the main body,  $P_{cs,B,t}$ , for wave situations in the northern North Sea

$H_s$ [m]	$T_p$ [s]	$\frac{P_{cs,B,a}}{P_{cs,R,i}}$ [-]	$\frac{P_{cs,B,t}}{P_{cs,R,i}} = 1 - \lambda_{dB}$ [-]
1	5.6	0.28	0.02
2	7.0	0.36	0.09
3	8.4	0.38	0.19
4	9.8	0.33	0.31
5	11.2	0.29	0.42

In MILDwave the shape of the main body in plan view has been simplified to a rectangular body with a width  $W_B$  equal to the distance between the wave reflectors in the cross section ( $W_B = 100$  m) and a length equal to the length of the reservoir (= 45 m), as indicated on Figure 7.7.

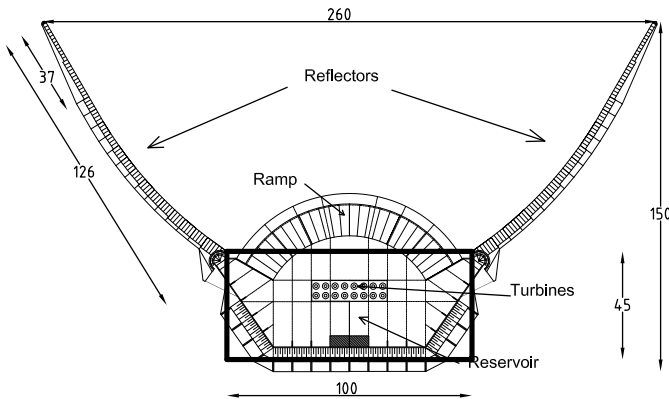


Figure 7.7: Simplification of the main body of a WD-WEC - dimensions in m

The main body has been tuned in a numerical wave flume with a width equal to the width of the rectangular body  $W_B$  as explained in chapter 6. The test set-up is shown in Figure 7.8.

The main body has been divided into 15 strips, each with a different value of  $S$ . The values of the absorption coefficients of the cells of the main body, to obtain the desired amounts of absorption and transmission (Table 7.3), are determined through an iterative approach. The surface elevations are measured by an array of three wave gauges, installed approximately one wave length in front of the main body and one wave gauge behind the main body, to determine the amounts of reflection from and transmission through the main body. The measured time series have been divided into subseries with a duration of 204.8 s corresponding to a



spectral resolution of  $\Delta f = 0.00488$  Hz.

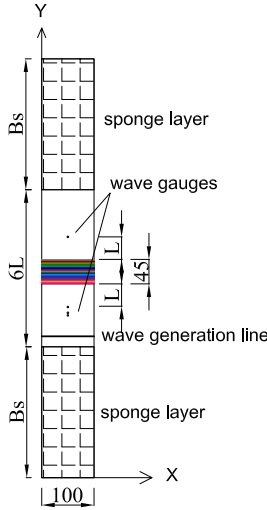


Figure 7.8: Definition sketch of a numerical wave flume with main body in plan view for generation of uni-directional waves - dimensions in m

The ratio between the absorbed wave power  $P_{cs,B,a}$  and the total wave power in the cross section  $P_{cs,R,i}$  is calculated with equation (6.1),  $\frac{P_{cs,B,a}}{P_{cs,R,i}} = \frac{P_{cs,B,a}}{\eta_R^{i,at} P_{cs,i}} = 1 - K_r^2 - K_t^2$ .

The combination of absorption coefficients  $S$  which result in an accuracy of 5 % on the amounts of absorption and transmission as given in Table 7.3, is selected. Again the absorption coefficients increase with increasing wave period.

### 7.3 Wake behind a single Wave Dragon WEC

By assembling both structural elements (reflectors and main body), which are tuned in the previous section, a WD-WEC is implemented in a wave basin in MILDwave, as shown in Figure 7.9. As the WD-WEC is floating, the WEC will move and may disturb the wave pattern. However, open air-chambers under the main body with a pressurized air system are not only adjusting the floating height, but are also reducing the movements of the WD-WEC. Furthermore its size makes the WD-WEC more stable. In [6] it is stated that the movements of the 1:4.5 prototype scale model of the WD-WEC are smaller than expected from the laboratory measurements. In this work the WD-WEC is assumed to be restrained and consequently movements are neglected. The same assumption has been made in [2].

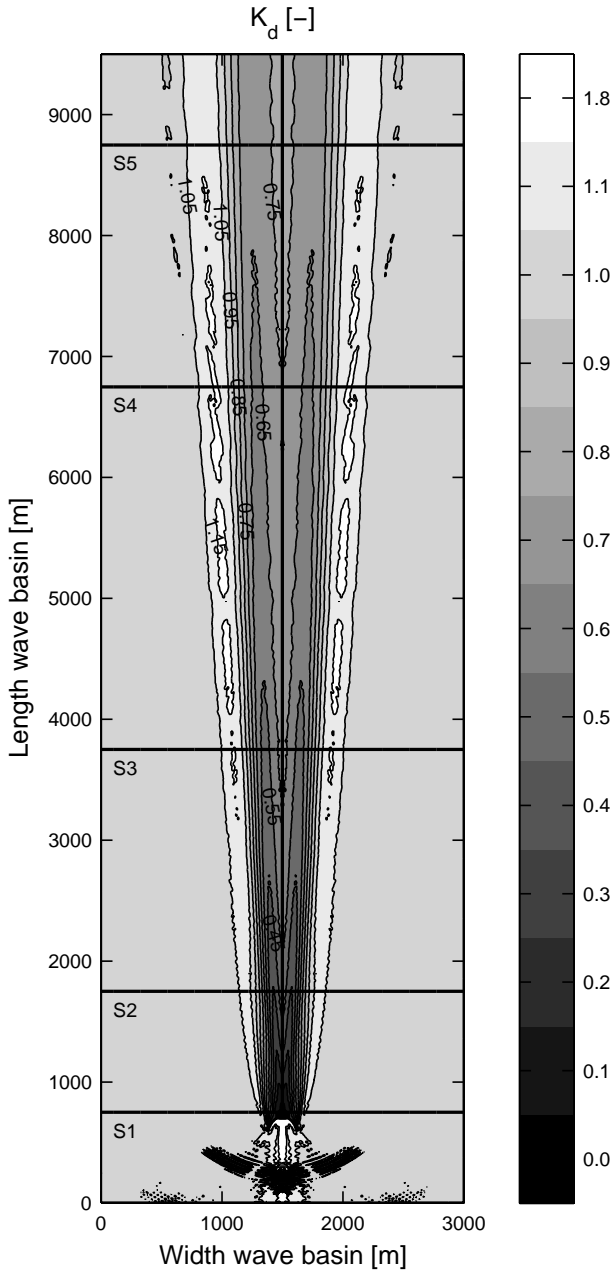


Figure 7.9: Calculated disturbance coefficient  $K_d$  in a wave basin with a single WD-WEC for irregular long-crested waves (head-on) with  $H_s = 1$  m and  $T_p = 5.6$  s

In this section the wake behind a single WD-WEC has been studied for the wave situation with the highest frequency of occurrence (Table 7.1), i.e.  $H_s = 1$  m and  $T_p = 5.6$  s. In section 7.4 the other wave situations will be considered as well. For the generation of approximately 500 irregular long-crested waves with a time step of 0.1 s and 0.05 s for  $T_p = 5.6$  s and  $T_p = 7$  s, 8.4 s, 9.8 s, 11.2 s, respectively (cell dimensions of 1 m for all wave periods) 50 frequency components are used. The number of frequency components is reduced to 20 for the generation of short-crested waves (1 000 waves). A uniform deep water depth  $h$  ( $= 200$  m) is used to avoid energy dissipation due to bottom friction and wave breaking.

The disturbance coefficients  $K_d = \left( \frac{H_{s,d}}{H_{s,i}} \right)$  in a wave basin with a single WD-WEC for long-crested (head-on) waves with a significant wave height of 1 m and a peak wave period of 5.6 s are shown in Figure 7.9. Only the useful domain without sponge layers is shown. The  $K_d$ -values near the WD-WEC are given in more detail in Figure 7.10. The WD-WEC is indicated in black.

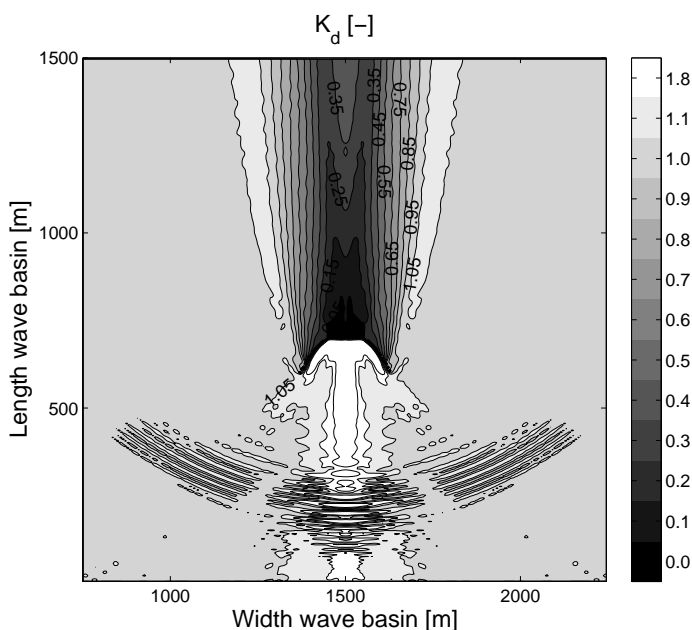


Figure 7.10: Enlargement of calculated disturbance coefficient  $K_d$  near the WD-WEC for irregular long-crested waves (head-on) with  $H_s = 1$  m and  $T_p = 5.6$  s

The disturbance coefficients in a longitudinal section at  $x^* = 1\,500$  m and in five lateral sections at respectively  $y^* = 750$  m,  $1\,750$  m,  $3\,750$  m,  $6\,750$  m and  $8\,750$  m (all sections are indicated on Figure 7.9) are shown in Figure 7.11 and Figure 7.12. Note that the longitudinal section starts right behind the WD-WEC at

$y^* = 750$  m (Figure 7.11).

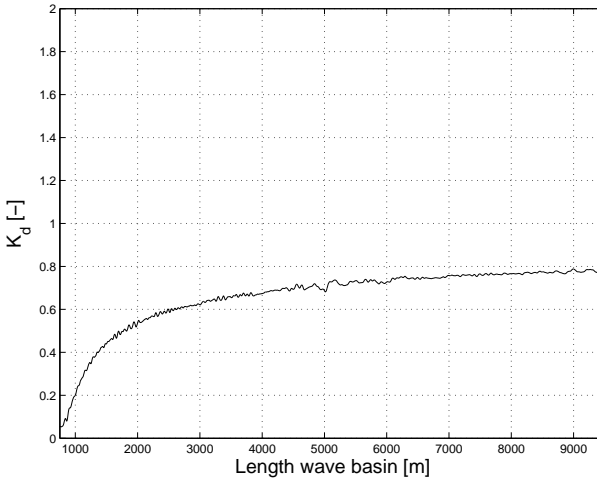


Figure 7.11: Calculated disturbance coefficient  $K_d$  in a longitudinal section at  $x^* = 1500$  m, as indicated on Figure 7.9, shown only behind the WD-WEC

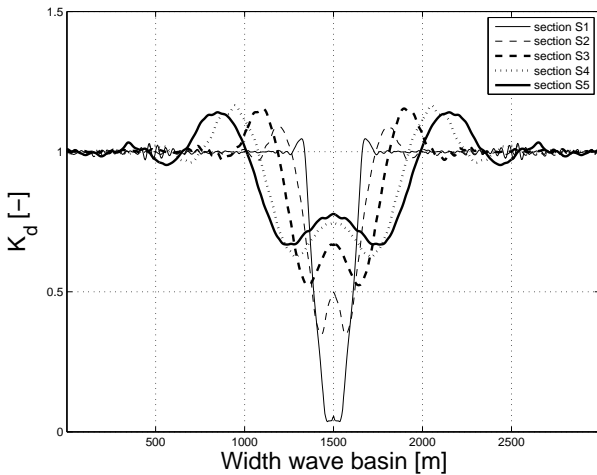


Figure 7.12: Calculated disturbance coefficient  $K_d$  in lateral sections at  $y^* = 750$  m, 1 750 m, 3 750 m, 6 750 m and 8 750 m, as indicated on Figure 7.9

Immediately behind the WD-WEC a large decrease of the disturbed significant wave height is seen, while a gradual redistribution occurs behind the WD-WEC due to diffraction around the WEC. The large wave height decrease right behind the WD-WEC does not imply that all energy is absorbed. For irregular long-

crested waves with  $H_s = 1$  m and  $T_p = 5.6$  s approximately 70 % of the wave power in front of the main body  $P_{cs,R,i}$  is reflected (28 % is absorbed and 2 % is transmitted as indicated in Table 7.3). For irregular long-crested waves with  $H_s = 1$  m and  $T_p = 5.6$  s, the WD-WEC is absorbing  $P_{cs,B,a} = 125$  kW =  $P_{s,1}$  (equation (7.4)).  $P_{s,1}$  is the absorbed power of a single WD-WEC in wave situation 1. The possible power absorbed by a second WD-WEC, installed behind the first WD-WEC between  $x^* = 1\ 370$  m and  $x^* = 1\ 630$  m, is estimated by calculating the average significant wave height in front of the second WD-WEC (Figure 7.9). This average wave height and the incident peak wave period are used to estimate the overtopping rate and consequently the absorbed power  $P_{cs,B,a}$  of the second WD-WEC with equation (7.4). It is assumed that the incident peak wave period remains unchanged in the simulation domain. When studying diffraction past the tip of a semi infinite breakwater or diffraction through a breakwater gap, a small change in peak wave period was observed [7]. A second WD-WEC installed right behind the first one at  $y^* = 1\ 750$  m,  $3\ 750$  m,  $6\ 750$  m and  $8\ 750$  m would absorb respectively only  $P_{cs,B,a} = 0.12 P_{s,1}$ ,  $0.29 P_{s,1}$ ,  $0.45 P_{s,1}$  and  $0.50 P_{s,1}$ . The average available wave power  $p_i$  in those sections is respectively 18 %, 37 %, 52 % and 57 % of the available wave power  $p = 2.5$  kW/m (Table 7.1) in front of the first WEC. A second WD-WEC, installed 8 km behind the first one, would only absorb half of the power absorbed by the first WD-WEC. For this long-crested wave situation (no directional spreading), a very large distance between the WECs is needed to have a sufficient redistribution behind the first WEC.

It is expected that this distance will be smaller for short-crested waves. Therefore the wake behind a single WD-WEC in a short-crested sea with a mean wave direction of  $90^\circ$  and a directional spreading of approximately  $9^\circ$  ( $s_{max} = 75$ ),  $16^\circ$  ( $s_{max} = 25$ ) and  $24^\circ$  ( $s_{max} = 10$ ) for the peak period of 5.6 s (equation (5.27)) is calculated. The resulting wakes are shown in Figure 7.13(b), Figure 7.13(c) and Figure 7.13(d), respectively<sup>4</sup>. Furthermore the wake for irregular long-crested waves as given in Figure 7.9 is shown in more detail ( $500$  m  $\leq x^* \leq 2\ 500$  m and  $0$  m  $\leq y^* \leq 4\ 500$  m) in Figure 7.13(a).

As expected, the wake length shortens with increasing directional spreading due to a faster redistribution behind the WEC. A wider wake is observed when short-crested waves are generated. Furthermore, the small increase in wave height, as seen at the edges of the wake in Figure 7.13(a), disappears in a short-crested sea.

---

<sup>4</sup>Note that the  $x^*y^*$  co-ordinate system in this chapter differs from the  $x^*y^*$  co-ordinate system as shown on Figure 5.5, as only the useful domain as indicated on Figures 6.22 and 6.23 is shown in the contour plots.

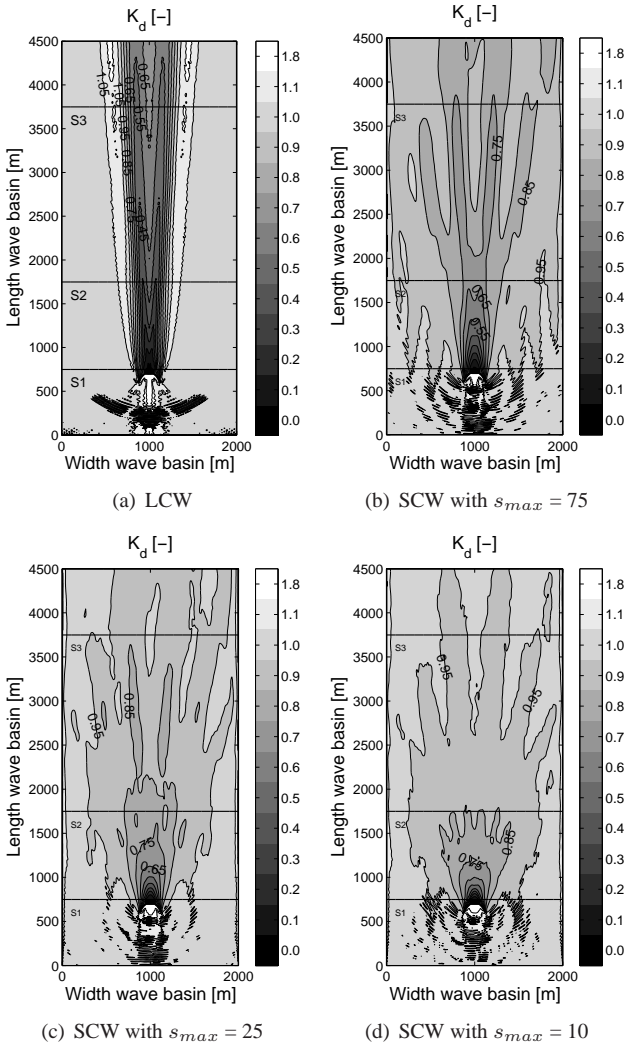


Figure 7.13: Calculated disturbance coefficient  $K_d$  in a wave basin with a single WD-WEC for irregular (a) long-crested waves (head-on) with  $T_p = 5.6$  s (identical to Figure 7.9) and short-crested waves (head-on) with  $T_p = 5.6$  s and  $s_{max} =$  (b) 75, (c) 25 and (d) 10

The length of the wake as a function of directional spreading is shown in Figure 7.14 for three  $K_d$  contours ( $K_d = 0.45, 0.55$  and  $0.65$ ). For higher values of  $K_d$  it is rather difficult to define the length of the contour as the contour is less well-defined. The wake in short-crested waves with  $s_{max} = 25$  is approximately 1.5 times longer compared to the wake in short-crested waves with  $s_{max} = 10$ . For

short-crested waves with the smallest directional spreading ( $s_{max} = 75$ ) the wake length is approximately 3 times the wake length observed in a short-crested sea with  $s_{max} = 10$ .

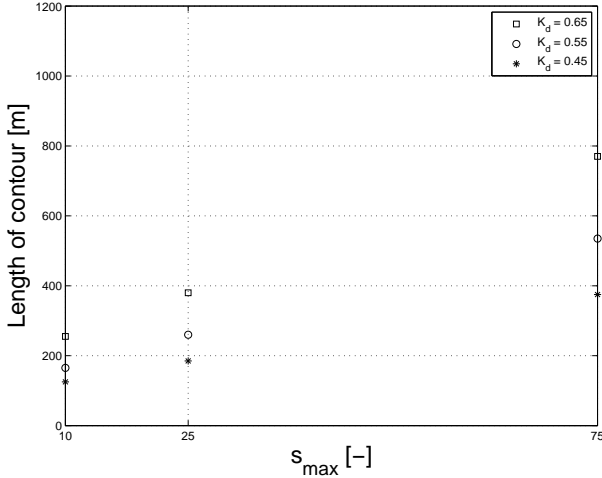


Figure 7.14: Length of wake ( $K_d$  contour = 0.45, 0.55 and 0.65) for irregular short-crested waves with  $T_p = 5.6$  s and  $s_{max} = 75, 25$  and  $10$

Three lateral sections S1, S2 and S3 behind the WD-WEC (indicated on Figure 7.13) are shown in Figure 7.15 for the same wave conditions as considered in Figure 7.13.

The wave height decrease right behind the WD-WEC at  $y^* = 750$  m is comparable for the four wave conditions. At  $y^* = 1750$  m the effects of the directional spreading are clearly present. The remaining wave height behind the WD-WEC increases with increasing directional spreading. At  $y^* = 3750$  m (3 km behind the WEC) the wave height is practically equal to the wave height in front of the WEC for short-crested waves with  $s_{max} = 10$ . A WD-WEC installed right behind the first one at  $y^* = 1750$  m and  $3750$  is absorbing  $P_{cs,B,a} = 0.41 P_{s,1}$  and  $0.68 P_{s,1}$  when  $s_{max} = 75$ ,  $P_{cs,B,a} = 0.6 P_{s,1}$  and  $0.86 P_{s,1}$  when  $s_{max} = 25$  and  $P_{cs,B,a} = 0.67 P_{s,1}$  and  $0.9 P_{s,1}$  when  $s_{max} = 10$  (equation (7.4)).

So far the potential power absorption right behind a single WD-WEC has been studied. In Figure 7.16 the potential power absorption of a second WD-WEC installed right behind the first WD-WEC (between  $x^* = 870$  m and  $x^* = 1130$  m) is compared to the potential power absorption of a second WD-WEC shifted over 260 m (WEC installed between  $x^* = 610$  m and  $x^* = 870$  m) and 520 m (WEC installed between  $x^* = 350$  m and  $x^* = 610$  m) for irregular short-crested waves with  $T_p = 5.6$  s and  $s_{max} = 75, 25$  and  $10$ .

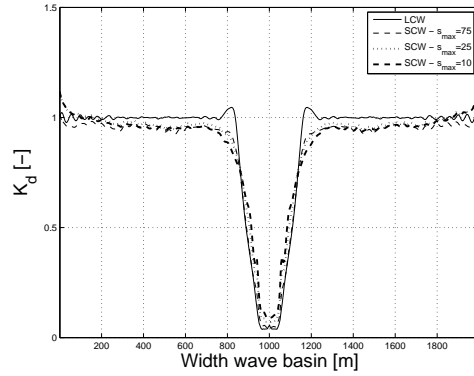
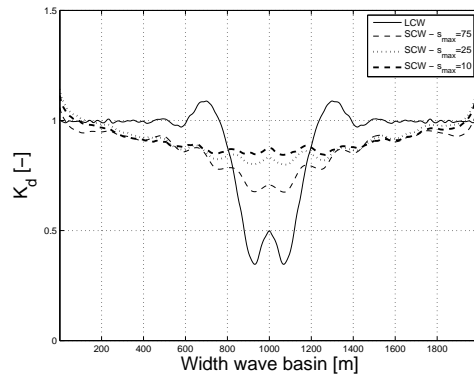
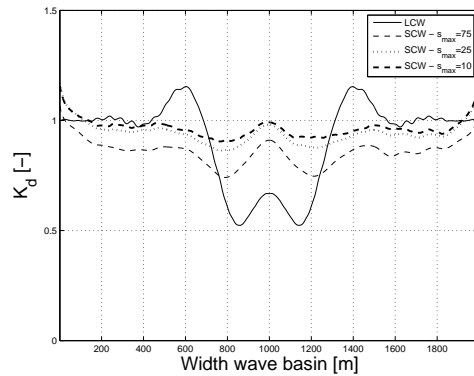
(a) Section S1 at  $y^* = 750$  m(b) Section S2 at  $y^* = 1\ 750$  m(c) Section S3 at  $y^* = 3\ 750$  m

Figure 7.15: Calculated disturbance coefficient  $K_d$  in lateral sections at  $y^* =$  (a) 750 m, (b) 1 750 m and (c) 3 750 m, as indicated on Figure 7.13, in a wave basin with a single WD-WEC for irregular long-crested waves (LCW) with  $T_p = 5.6$  s and short-crested waves (SCW) with  $T_p = 5.6$  s and  $s_{max} = 75, 25$  and 10



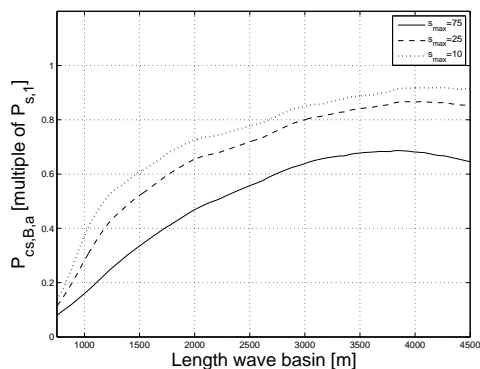
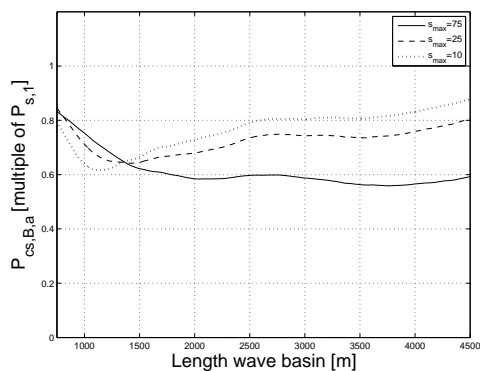
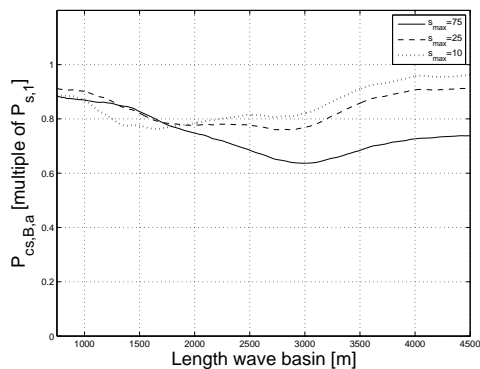
(a) WEC installed between  $x^* = 870$  m and  $x^* = 1130$  m(b) WEC installed between  $x^* = 610$  m and  $x^* = 870$  m(c) WEC installed between  $x^* = 350$  m and  $x^* = 610$  m

Figure 7.16: Power absorption of a second WD-WEC installed between (a)  $x^* = 870$  m and  $x^* = 1130$  m, (b)  $x^* = 610$  m and  $x^* = 870$  m and (c)  $x^* = 350$  m and  $x^* = 610$  m, in a wave basin with a single WD-WEC for irregular short-crested waves (SCW) with  $T_p = 5.6$  s and  $s_{max} = 75, 25$  and  $10$

Note that the potential power absorption is only given behind the first WD-WEC. The potential power absorption between  $y^* = 750$  m and  $y^* = 2\,500$  m is higher when the WEC is shifted further away from the first WEC, e.g. the potential power absorption at  $y^* = 1\,250$  m is increasing from approximately  $0.55 P_{s,1}$  for a WD-WEC installed between  $x^* = 870$  m and  $1\,130$  m to  $0.8 P_{s,1}$  for installation between  $x^* = 350$  m and  $x^* = 610$  m.

For a WD-WEC installed between  $x^* = 610$  m and  $x^* = 870$  m and between  $x^* = 350$  m and  $x^* = 610$  m, the potential power absorption is first decreasing and afterwards increasing, as there is no influence of the wake in the beginning. The initial wave height decrease is higher for  $s_{max} = 10$  as the wake is wider compared to  $s_{max} = 25$ .

To conclude, in the case of irregular long-crested waves and swell waves ( $s_{max} = 75$ ) a second WEC installed 3 km behind the first WEC is absorbing less than 70 % of the first WEC ( $0.29 P_{s,1}$  and  $0.68 P_{s,1}$ , respectively). As in practice the available space to install a farm of WECs is rather small, a WEC in a second row should not be installed right behind a WEC in the first row. Therefore, in the next section a farm of five WD-WECs, installed in a staggered grid, is studied.

## 7.4 A farm of 5 Wave Dragon WECs

The power absorption of one WD-WEC affects the available wave power for the WD-WECs in its lee. The reduction of the available wave power depends on the distances between the WD-WECs in a farm, the incident wave climate (transmission under main body and wave reflectors increases for increasing wave period and wave height) and the directional spreading of the incident waves. As a large distance between two WD-WECs installed behind each other is needed to have an acceptable absorption by the second WD-WEC, the latter WD-WEC will be shifted, resulting in a staggered grid (Figure 7.17).

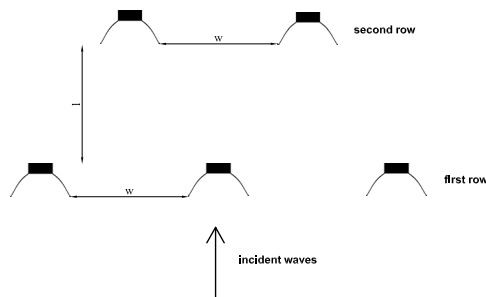


Figure 7.17: 5 WD-WECs with a lateral spacing  $w$  and a longitudinal spacing  $l$  installed in a staggered grid

The distances between the WECs in a farm should be as small as possible to reduce the use of available sea area. On the other hand a minimal lateral spacing of 260 m is needed between two adjacent WD-WECs to prevent collision<sup>5</sup> (Figure 7.18), as the rotation of the WD-WEC is assumed to be restricted to  $\pm 60^\circ$  by its anchor system [8].

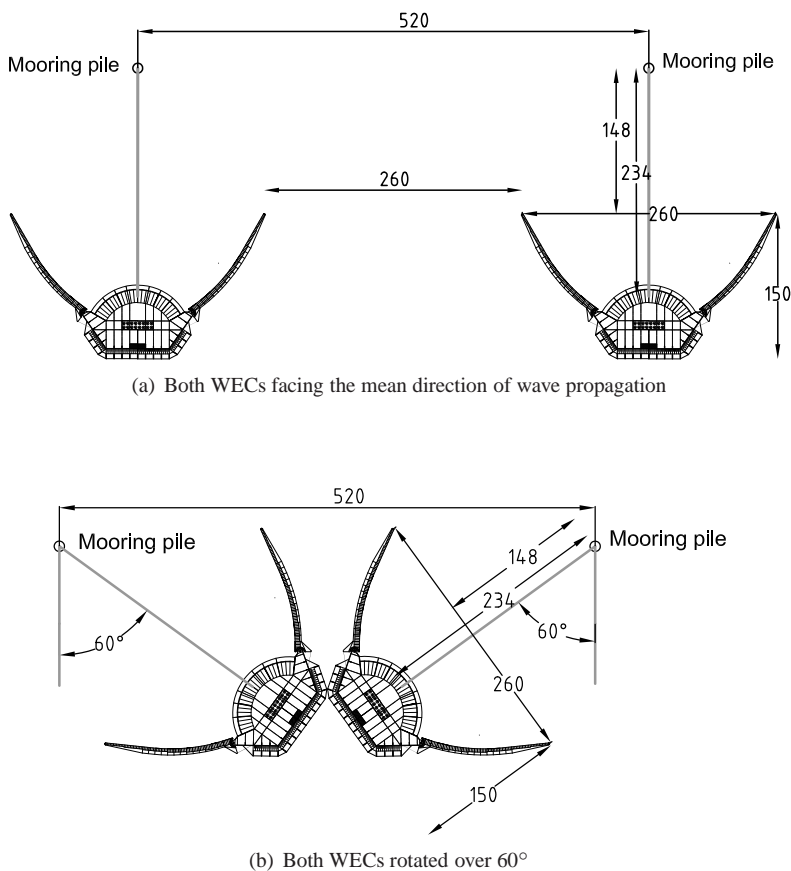


Figure 7.18: Definition sketch of minimum lateral spacing between WD-WECs - dimensions in m

In this section five WD-WECs (Figure 7.17) installed in a staggered grid with a lateral spacing of  $D_R$ ,  $2D_R$  and  $3D_R$ , with  $D_R$  the distance between the tips of the wave reflectors of a single WEC ( $= 260$  m), and varying longitudinal spacing are studied. In a first part irregular long-crested waves with  $H_s = 1$  m and  $T_p = 5.6$  s are considered (wave situation with the highest frequency of occurrence

<sup>5</sup>If one WD-WEC is fixed in its far position due to a fault and its neighbouring WEC turns to the other far position, no collision is possible.

in Table 7.1) to define an optimal lay-out for a farm of 5 WD-WECs. Further, the absorption of five WD-WECs installed in the selected farm lay-out is calculated for the remaining wave situations in the North Sea (Table 7.1). In a second part short-crested waves with  $H_s = 1$  m,  $T_p = 5.6$  s (wave situation 1) and  $s_{max} = 10$  and with  $H_s = 3$  m,  $T_p = 8.4$  s (wave situation 3) and  $s_{max} = 10$  and 75 are considered to study the impact of the wave situation and directional spreading of the wave climate on the power absorption.

### 7.4.1 Irregular long-crested waves

First only one row with 3 WD-WECs, each absorbing  $P_{cs,B,a} = 125$  kW =  $P_{s,1}$ , is installed in a wave basin as shown in Figure 7.19. The length and the width of the wave basin have been adapted for each lay-out to obtain a sufficiently large domain. The resulting calculated disturbance coefficients for an in-between distance of respectively  $D_R$ ,  $2D_R$  and  $3D_R$  are shown in Figure 7.19. Again only the useful domain without sponge layers is shown. Furthermore the positions of WD-WECs in the second row are indicated (longitudinal spacing of  $D_R$ ,  $2D_R$  and  $3D_R$ , respectively). The remaining wave height behind the first row determines the absorbed power of the WECs in the second row. On the positions of the WD-WECs in the second row the average available wave power  $p_i$  is decreased with 8 % for an in-between distance of  $D_R$  and increased with respectively 6 % and 1 % for an in-between distance of respectively  $2D_R$  and  $3D_R$  compared to the available wave power in front of the first row ( $p_i = 2.5$  kW/m). This small increase of wave power will not occur when short-crested waves are generated (section 7.4.2). The directional spreading will smooth out the latter effect. It is clear that the available wave power for the second row  $p_i$  is approximately equal to the available wave power for the first row ( $p_i = 2.5$  kW/m) for each in-between distance. A single WD-WEC in the second row will absorb respectively  $P_{cs,B,a} = 0.88P_{s,1}$ ,  $1.07P_{s,1}$  and  $P_{s,1}$ , using equation (7.4), when the WECs are installed in a staggered grid with a lateral and longitudinal spacing of respectively  $D_R$ ,  $2D_R$  and  $3D_R$ .

Further both rows are installed in a wave basin as shown in Figure 7.20. The WD-WECs in the second row have been tuned as described in section 7.2. Waves are simulated during 4 400 s (time step = 0.1 s) in a domain of 5 000 cells (width) x 8 000 cells (length) which resulted in a computational time of 64 hours (Intel Core 2 CPU @ 2.40 GHz - 3 GB RAM). The disturbance coefficients in a cross section right behind and 4 km behind the latter grids have been compared in Figure 7.21.

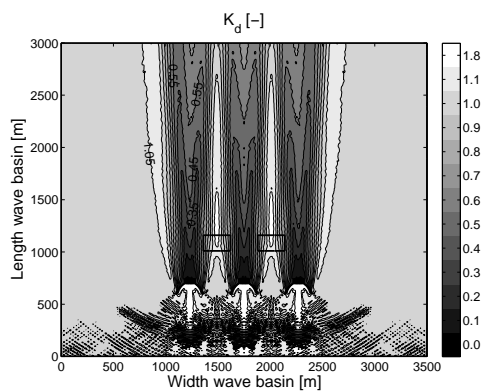
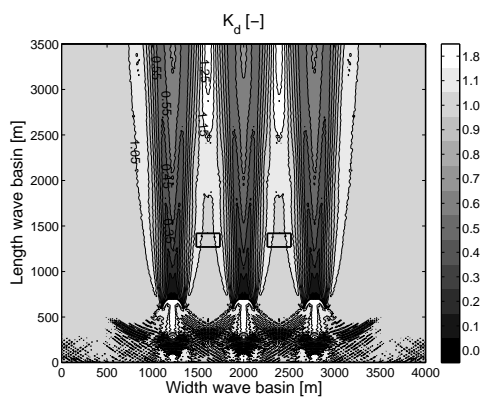
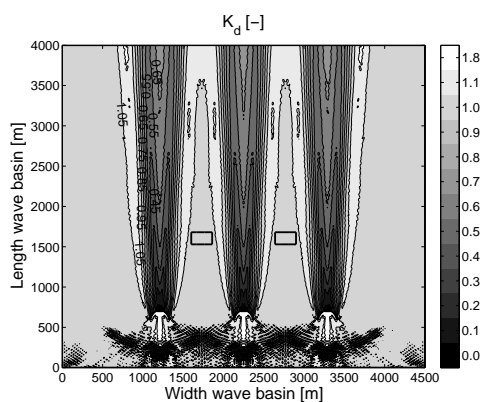
(a) In-between distance =  $D_R$ (b) In-between distance =  $2D_R$ (c) In-between distance =  $3D_R$ 

Figure 7.19: Calculated disturbance coefficient  $K_d$  in a wave basin with 3 WD-WECs with an in-between distance of respectively (a)  $D_R$ , (b)  $2D_R$  and (c)  $3D_R$ , with  $D_R = 260$  m, for irregular long-crested waves (head-on) with  $T_p = 5.6$  s

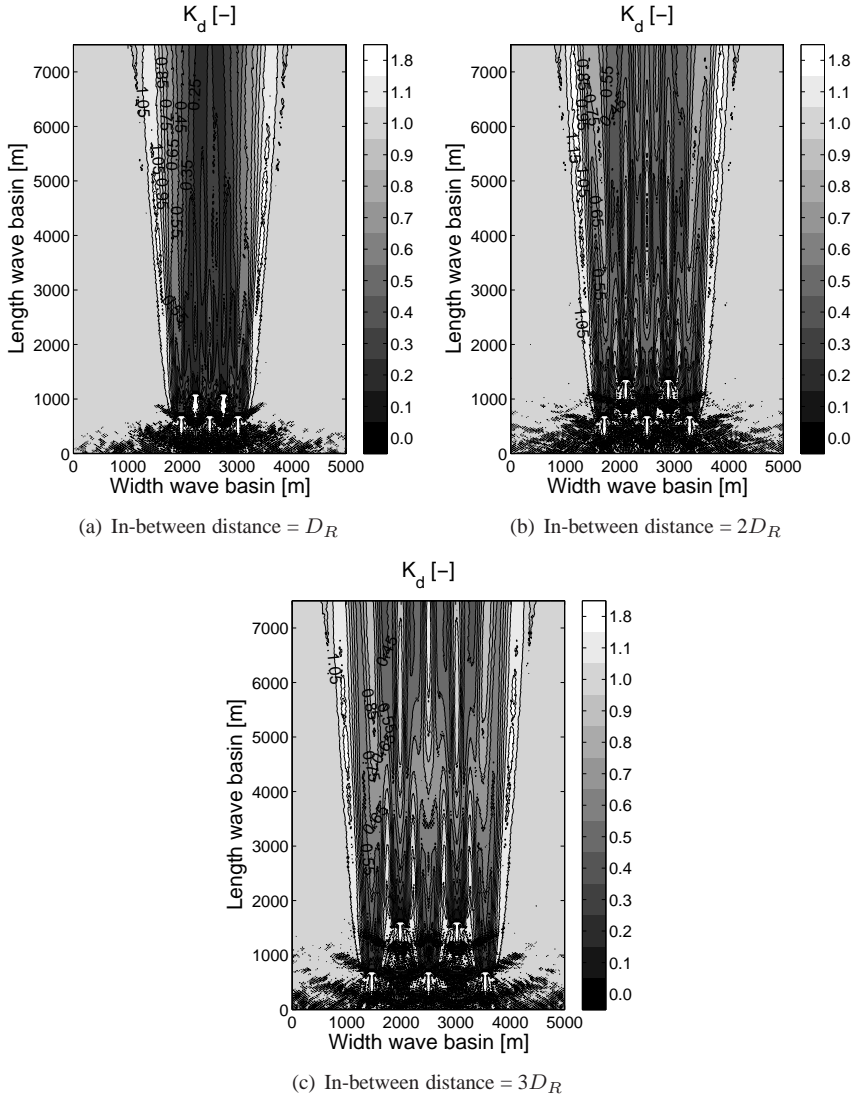
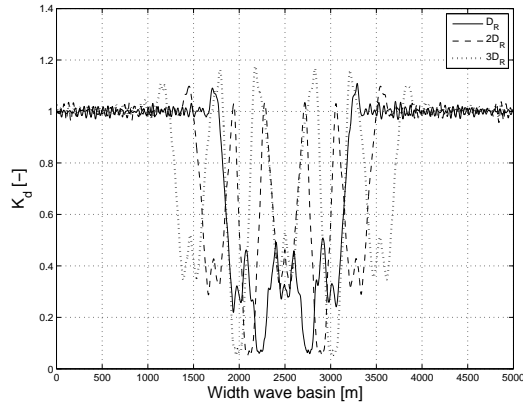


Figure 7.20: Calculated disturbance coefficient  $K_d$  in a wave basin with 5 WD-WECs with an in-between distance of respectively (a)  $D_R$ , (b)  $2D_R$  and (c)  $3D_R$ , with  $D_R = 260$  m, for irregular long-crested waves (head-on) with  $T_p = 5.6$  s

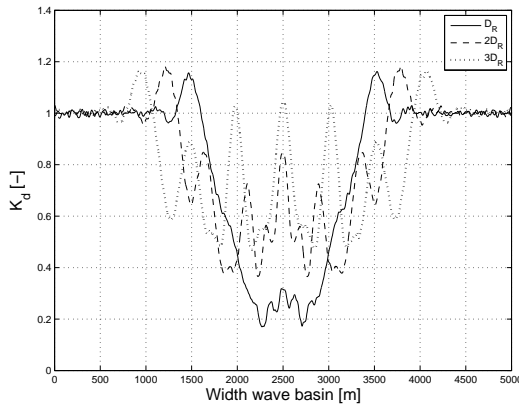
Behind each grid a large wave power decrease is observed. When the in-between distance is increasing, more wave power is propagating between the WECs in the farm (Figure 7.21(b)). The power that WECs installed in a third row (identical to the first row) would absorb, is given in Table 7.4. For all grids, the absorbed wave power of the WECs in the third row is smaller than  $0.2P_{s,1}$ . A

very large in-between distance is needed to have sufficient wave power on a third row, which is not economic.

The difference in power absorption between a lay-out of 5 WECS with an in-between distance of respectively  $D_R$ ,  $2D_R$  and  $3D_R$  is very small. The total power absorption is approximately equal to  $5P_{s,1}$ . It is clear, that the optimal lay-out consists of 2 rows, as the wave power absorption in a third row is too small. The lay-out with an in-between distance of  $2D_R$  is selected for further investigation.



(a) Section immediately behind the second row



(b) Section 4 km behind the second row

Figure 7.21: Calculated disturbance coefficient  $K_d$  in two cross sections, (a) immediately behind and (b) 4 km behind the farm lay-outs from Figure 7.20

The absorbed wave power of 5 WD-WECS, installed in a staggered grid with  $w = l = 2D_R$ , equals approximately  $5P_{s,1}$  when irregular long-crested waves with  $H_s = 1$  m and  $T_p = 5.6$  s are generated. The disturbance coefficients are calculated

Table 7.4: Absorbed wave power of WECs [multiple of  $P_{s,1}$ ] installed in a third row behind the farm with 5 WECs

	WD-WEC 1	WD-WEC 2	WD-WEC 3
In-between distance			
$D_R$	0.09	0.06	0.09
$2D_R$	0.16	0.17	0.16
$3D_R$	0.18	0.19	0.18

in a basin with only the first row of WECs installed (Figure 7.22) for the remaining irregular long-crested waves (Table 7.1) with respectively  $T_p = 7$  s, 8.4 s, 9.8 s and 11.2 s.

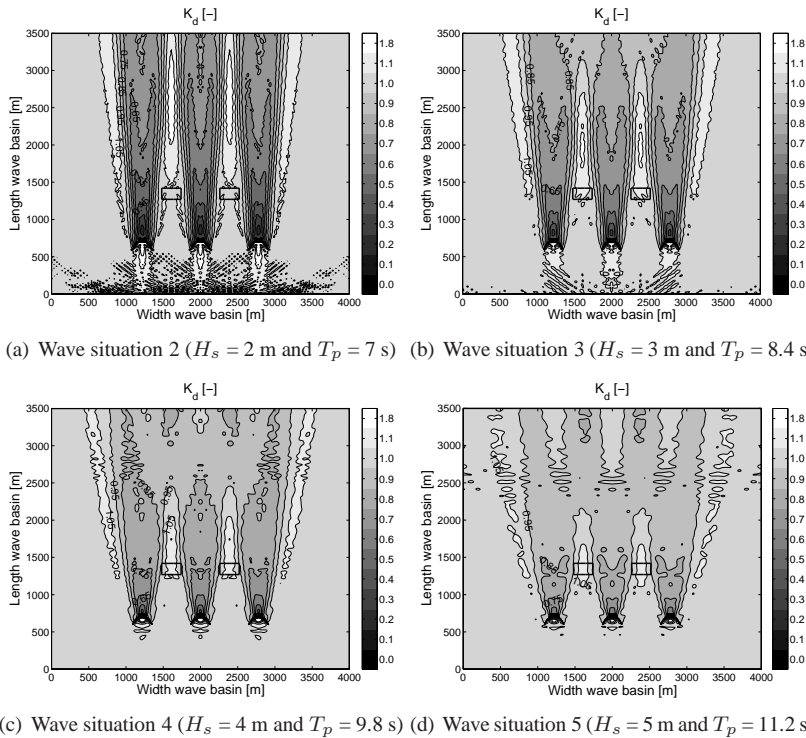


Figure 7.22: Calculated disturbance coefficient  $K_d$  in a wave basin with 3 WD-WECs with an in-between distance of  $2D_R$ , with  $D_R = 260$  m, for irregular long-crested waves (head-on) with respectively (a)  $H_s = 2$  m and  $T_p = 7$  s, (b)  $H_s = 3$  m and  $T_p = 8.4$  s, (c)  $H_s = 4$  m and  $T_p = 9.8$  s and (d)  $H_s = 5$  m and  $T_p = 11.2$  s

A wider shadow zone and a smaller wave height decrease behind each WD-



WEC is observed for higher peak periods. The smaller wave height decrease is caused by the larger transmission (Table 7.3 and Figure 7.5).

The wave power absorbed by a WD-WEC in the first, respectively second row for the different wave situations is given in Figure 7.23.

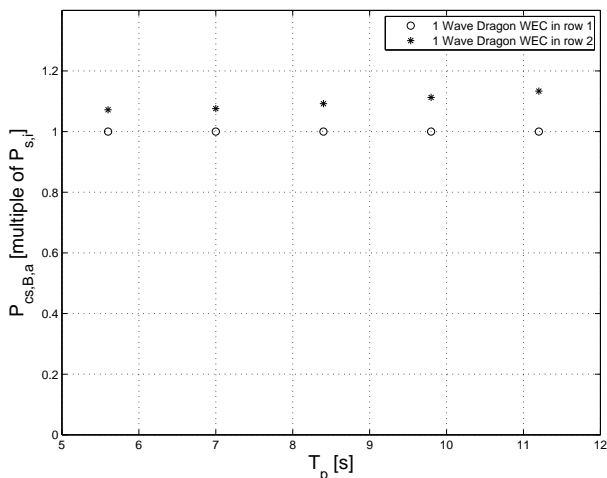


Figure 7.23: Wave power absorbed by 1 WD-WEC in the first respectively second row of the optimal farm lay-out for wave situations in the North Sea

The wave power absorption of the WD-WECs in the second row is approximately equal to the absorption of the WECs in the first row for all wave situations. Note that the slightly higher absorption of the WECs in the second row is caused by the small wave height increase at the edges of the wake of a single WD-WEC typical for irregular long-crested waves. By installing the WECs in a staggered grid with an in-between distance of  $2D_R$ , the mean wave power in front of the second row is not affected. A farm of five WD-WECs, installed in a staggered grid with an in-between distance of 520 m, will produce 5 times more than a single WD-WEC in each wave situation. The latter result can be easily extended for a wider farm consisting of two rows of WD-WECs installed in a staggered grid. WECs installed in a third row would absorb respectively approximately  $0.17P_{s,1}$  (Table 7.4),  $0.33P_{s,2}$ ,  $0.54P_{s,3}$ ,  $0.67P_{s,4}$ ,  $0.82P_{s,5}$  for  $T_p = 5.6$  s, 7 s, 8.4 s, 9.8 s and 11.2 s.  $P_{s,i}$  is the power absorbed by a single WEC in the considered wave situation  $i$  ( $i=1, 2, 3, 4$  and  $5$ ). 68 % of the time the absorption of a WEC in a third row is smaller than 50 % of the absorption of a WEC in the first two rows which makes a third row of converters not advantageously. When short-crested waves are dominating a faster redistribution was observed (Figure 7.13). Whether the installation of a third row is interesting in a short-crested sea is studied in section 7.4.2.

In this section an optimal lay-out has been selected for the wave situation with the highest frequency of occurrence. As an alternative the wave situation which contributes most to the mean wave power ( $p$  multiplied with its frequency of occurrence (Table 7.1)), which is the wave situation with  $H_s = 5$  m and  $T_p = 11.2$  s, could be considered. This approach will result in the same optimal lay-out. Note that so far only head-on waves have been studied.<sup>6</sup> In chapter 9 other mean wave directions will be considered.

## 7.4.2 Irregular short-crested waves

The wave height reduction behind a row with 3 WD-WECs with a lateral spacing of  $D_R$ ,  $2D_R$  and  $3D_R$  is shown in Figure 7.24 for wave situation 1 with a directional spreading of  $24^\circ$  ( $s_{max} = 10$ ), in Figure 7.25 for wave situation 3 with a directional spreading of  $9^\circ$  ( $s_{max} = 75$ ) and in Figure 7.26 for wave situation 3 with a directional spreading of  $24^\circ$  ( $s_{max} = 10$ ). Note that the value of the directional spreading is the value for  $T_p$  (equation 5.27). For wave situation 1 and 3 each WD-WEC is absorbing  $P_{cs,B,a} = P_{s,i}$  with  $i = 1$  and 3.

When comparing Figure 7.19 with Figure 7.24, a smaller wake is observed when short-crested waves are generated. On the other hand, less waves are propagating between the WECs. More energy is travelling in-between the WECs when the lateral spacing is increasing and the directional spreading is decreasing (Figure 7.25). The wake behind a row of WD-WECs is a little smaller and shorter for wave situation 3 (Figure 7.26) compared to wave situation 1 (Figure 7.24) as the transmission under the main body and wave reflectors is higher for wave situation 3 (Table 7.3 and Figure 7.5). Note that the differences between wave situation 1 and 3 were much higher for irregular long-crested waves (Figure 7.19 and Figure 7.22). When  $K_d = 0.85$ ,  $0.9$  and  $0.95$  the potential power absorption is  $0.66 P_{s,i}$ ,  $0.77 P_{s,i}$  and  $0.88 P_{s,i}$  (equation (7.4)), respectively. The power absorption is very fast decreasing when the wave height is decreasing. It seems more reasonable to install a second row of WD-WECs as close as possible to the first row instead of placing them further away, as even in the case with the highest energy transmission and refill behind the first row of WECs (Figure 7.26(c)) a distance of approximately 2 km is needed to have a sufficient high value of  $K_d$ .

A minimal longitudinal spacing  $l$  of 190 m (Figure 7.27), 130 m (Figure 7.28) and 0 m is needed between two adjacent WD-WECs to prevent collision when the lateral spacing is  $D_R$ ,  $2D_R$  and  $3D_R$ , respectively.

---

<sup>6</sup>For other wave directions some WD-WECs in the farm will not absorb the same amount of wave power as a single WD-WEC as they will be situated in the shadow zone of other WD-WECs (chapter 6 - section 6.3.2.5).

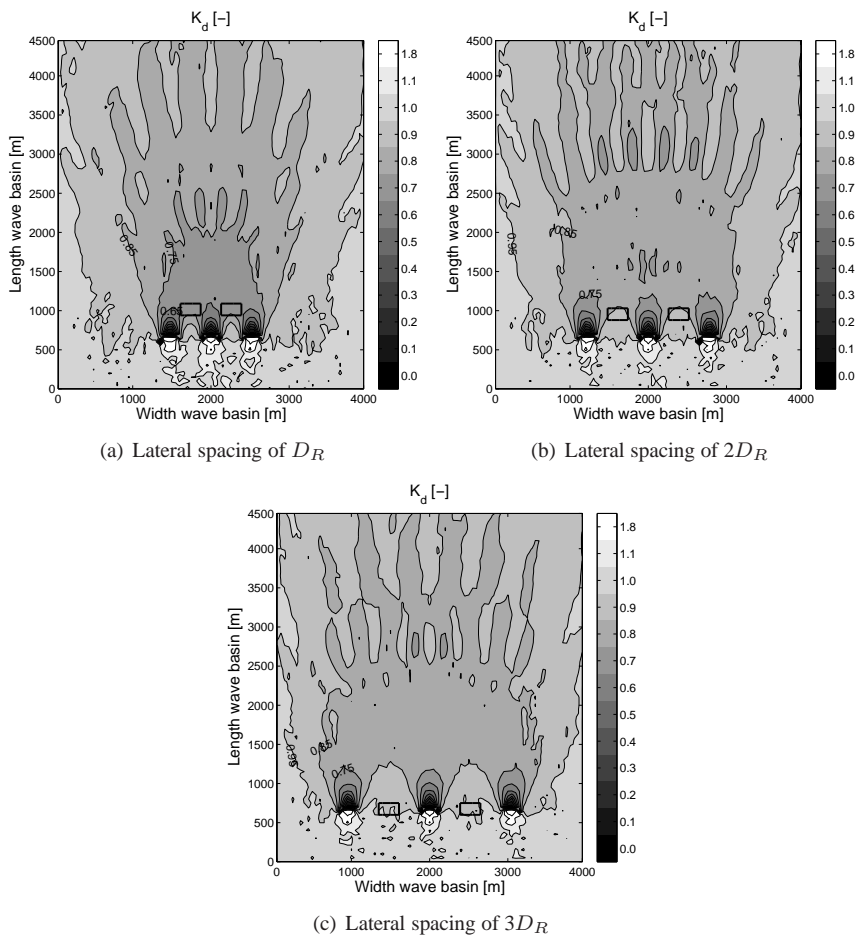


Figure 7.24: Calculated disturbance coefficient  $K_d$  in a wave basin with 3 WD-WECS with a lateral spacing of (a)  $D_R$ , (b)  $2D_R$  and (c)  $3D_R$ , for short-crested waves (SCW) with  $T_p = 5.6$  s (wave situation 1) and  $s_{max} = 10$

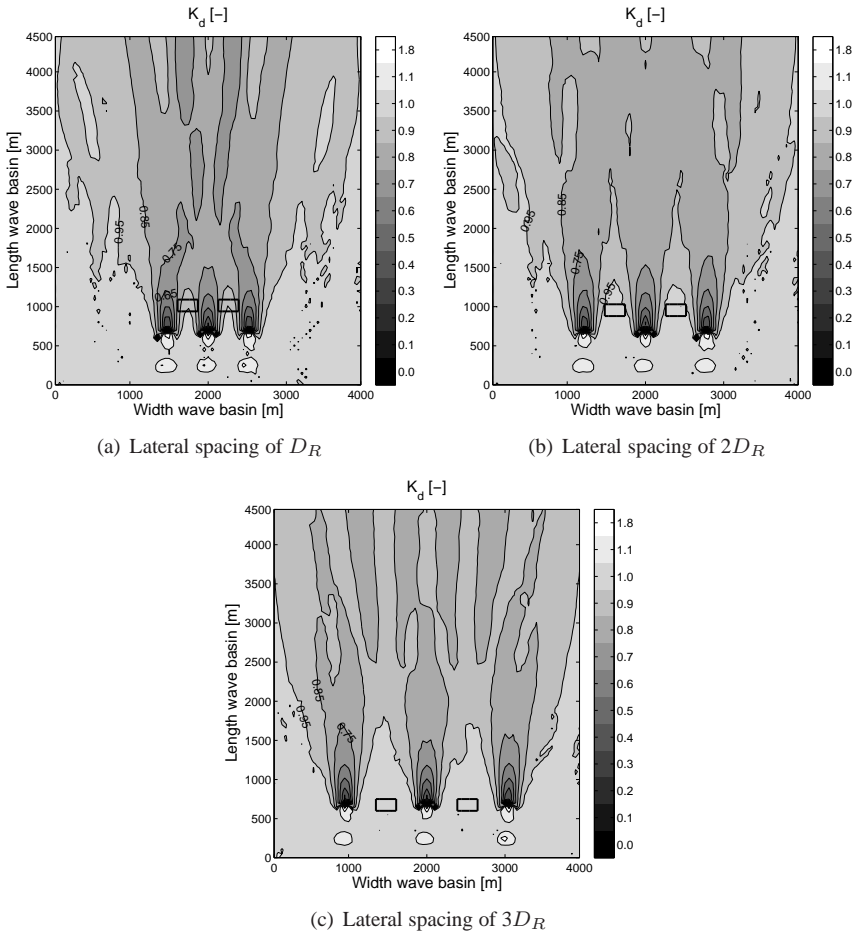


Figure 7.25: Calculated disturbance coefficient  $K_d$  in a wave basin with 3 WD-WECs with a lateral spacing of (a)  $D_R$ , (b)  $2D_R$  and (c)  $3D_R$ , for short-crested waves (SCW) with  $T_p = 8.4$  s (wave situation 3) and  $s_{max} = 75$

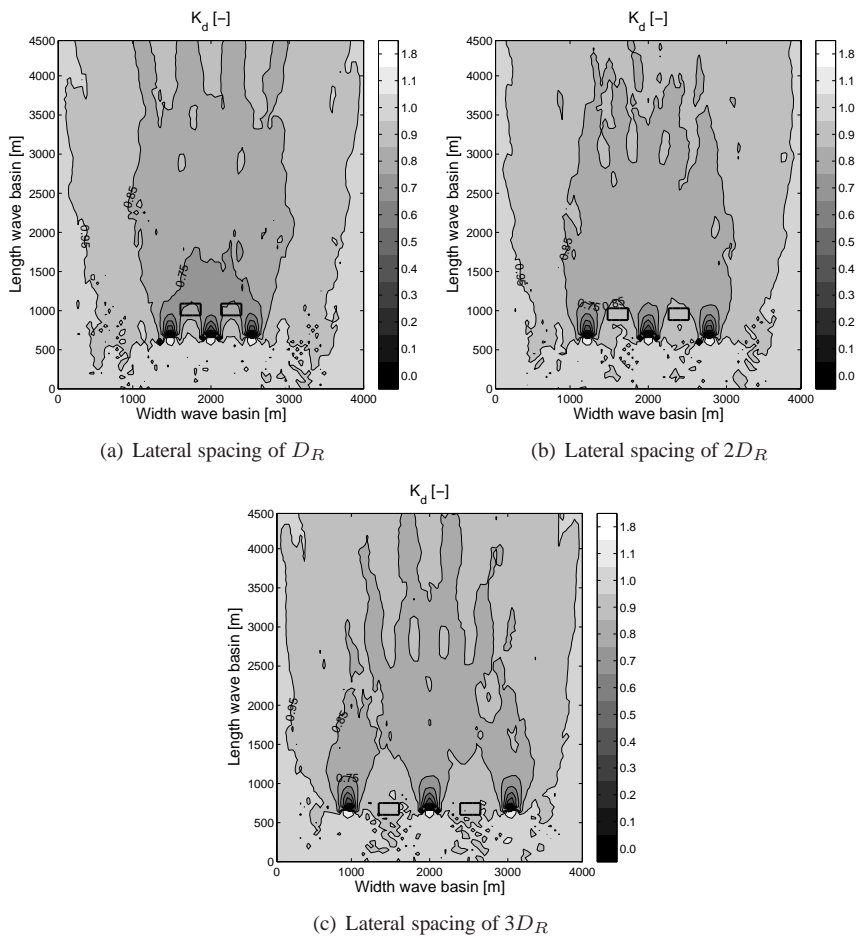
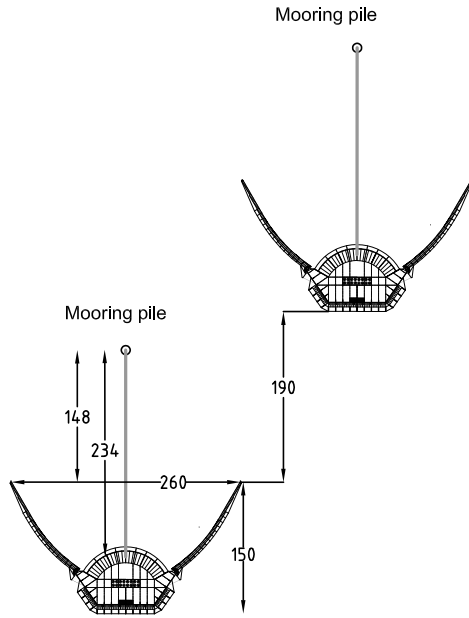
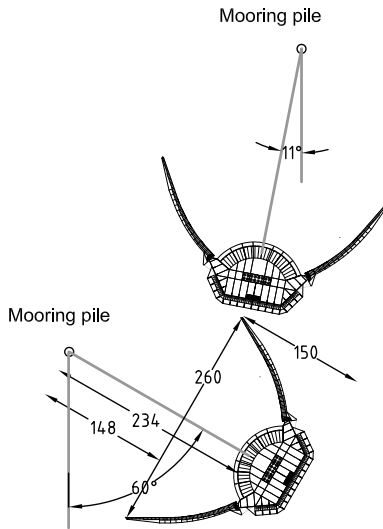


Figure 7.26: Calculated disturbance coefficient  $K_d$  in a wave basin with 3 WD-WECS with a lateral spacing of (a)  $D_R$ , (b)  $2D_R$  and (c)  $3D_R$ , for short-crested waves (SCW) with  $T_p = 8.4$  s (wave situation 3) and  $s_{max} = 10$

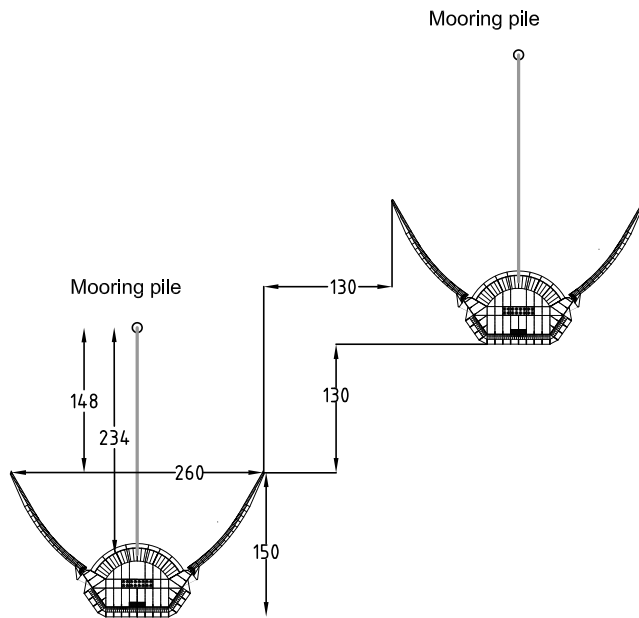


(a) Both WECs facing the mean direction of wave propagation

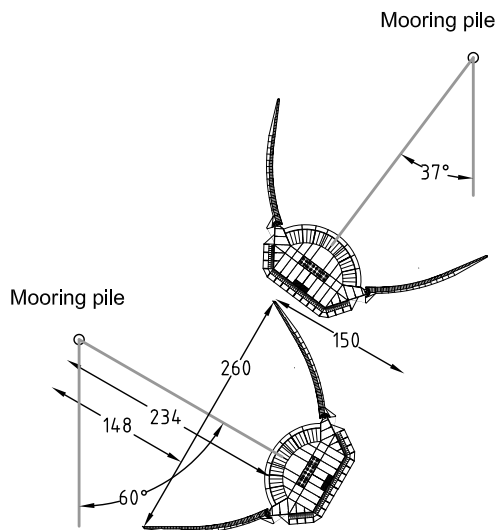


(b) First WEC rotated over 60°

Figure 7.27: Definition sketch of minimum distance between WD-WECs with lateral spacing  $D_R$  - dimensions in m



(a) Both WECS facing the mean direction of wave propagation



(b) First WEC rotated over 60°

Figure 7.28: Definition sketch of minimum distance between WD-WECS with lateral spacing  $2D_R$  - dimensions in m

The positions of WD-WECs in the second row are indicated on Figure 7.24, Figure 7.25 and Figure 7.26. The loss of the amount of absorbed power of the farm compared to the power absorption of a theoretical farm of five independent WD-WECs ( $= 5P_{s,i}$ ) is given in Table 7.5.

Table 7.5: Power absorption of a farm of 5 WD-WECs

Wave situation [—]	$w$ [multiple of $D_R$ ]	$\sigma_\theta^1$ [°]	Loss of power absorption [multiple of $P_{s,i}$ ]
1	1	24	1.09
1	2	24	0.42
1	3	24	0
3	1	9	0.46
3	2	9	0.10
3	3	9	0
3	1	24	0.88
3	2	24	0.35
3	3	24	0

<sup>1</sup> Value for  $f_p$

The power loss of a farm for wave situation 1 is a little higher compared to wave situation 3 (directional spreading of  $24^\circ$  -  $s_{max} = 10$ ). Furthermore, more energy is absorbed in a wave condition with a smaller directional spreading because more energy is travelling in-between the WECs. For a lateral spacing of  $D_R$  and a directional spreading of  $24^\circ$  ( $s_{max} = 10$ ) five WD-WECs are absorbing approximately the same as four single WD-WECs. In the latter case WD-WECs in the second row are only absorbing half of the wave power absorbed by a WD-WEC in the first row. For irregular long-crested waves it had been observed that WECs in the second row have a slightly higher power absorption compared to WECs in the first row (section 7.4.1). Not only less waves are propagating between the WECs when short-crested waves are generated, but also the wave height increase at the edges of the wake has disappeared. For a lateral spacing of  $3D_R$ , the WECs of the second row are placed in-between the WECs of the first row, resulting in a single row of five WD-WECs with a lateral spacing of  $D_R$ . Each WEC is absorbing the same amount of power as a single WEC.

Not only the amount of absorbed power is important when comparing several lay-outs, but also the use of available sea area and the cost of the cabling in the farm need to be taken into account. To make a better comparison between the considered lay-outs, the power absorption per  $\text{km}^2$  and the power absorption per km are studied. When calculating the power absorption per  $\text{km}^2$  an area with



half of the lateral spacing, respectively, longitudinal spacing has been added at the right and left end of the farm, respectively, in front of and behind the farm. By dividing the amount of absorbed power by the width of the farm (including half of the lateral spacing at both ends), the power absorption per km is obtained. The results are shown in Table 7.6. The absorption for wave situation 1 is smaller compared to wave situation 3 as the incident wave power is smaller as well (Table 7.1). Therefore the farm efficiency (= ratio between power absorption per km and incident wave power (Table 7.1)) is also calculated. The difference in farm efficiency between wave situation 1 and 3 is very small.

Table 7.6: Power absorption per  $\text{km}^2$  and per km of a farm of 5 WD-WECS

Wave situation	$w$	$\sigma_\theta^1$	Power absorption per $\text{km}^2$	Power absorption per km	Farm efficiency <sup>2</sup>
[-]	$[D_R]$	[°]	$[\text{MW}/\text{km}^2]$	$[\text{MW}/\text{km}]$	[%]
1	1	24	0.6	0.3	13
1	2	24	0.5	0.2	10
1	3	24	1.6	0.2	10
3	1	9	8.2	4.7	14
3	2	9	7.2	3.4	10
3	3	9	20.6	3.1	9
3	1	24	7.5	4.2	13
3	2	24	6.8	3.2	10
3	3	24	20.6	3.1	9

<sup>1</sup> Value for  $f_p$

<sup>2</sup> Farm efficiency = ratio between the absorbed power per km and the available wave power per km

Five WD-WECS installed in a single row with a lateral spacing of  $D_R$  results in the highest power absorption per  $\text{km}^2$ . On the other hand the absorption per km is smaller compared to a farm of five WD-WECS installed in two rows. To produce a substantial amount of wave power more than 50 WD-WECS need to be installed in a farm. When all WD-WECS are installed in a single row with a lateral spacing of  $D_R$  a width of more than 25 km is needed. Furthermore the cost of cabling inside the farm will increase (chapter 9). A farm of five WD-WECS with  $w = D_R$  and  $l = 190$  m results in a higher absorption per  $\text{km}^2$  and per km compared to a farm with  $w = 2D_R$  and  $l = 130$  m. Furthermore to install 50 WD-WECS a width of only 13 km is needed. On the other hand the power loss is twice as high compared

to a farm with  $w = 2D_R$  and  $l = 130$  m. When short-crested waves with a small directional spreading occur, the power loss is very small for a staggered grid with  $w = 2D_R$  and  $l = 130$ .

Consequently the staggered grid with  $w = 2D_R$  and  $l = 130$  m seems to be a good option when the width of the available area is small. In this case the width of a farm of 50 WD-WECs is reduced with 25 % compared to a single row of WD-WECs. When an area with a large width is available, installation of a single line of WD-WECs is preferred as this lay-out results in the highest wave power absorption. Again only head-on waves have been considered. The power absorption will decrease when other main wave directions are taken into account (chapter 9). Furthermore the cost per produced kWh should be calculated to finally determine the optimal lay-out (chapter 9).

It is clear that a single row or two rows of WD-WECs are absorbing a lot of wave power. Consequently the transmission is rather low. In all cases the wave height 3 km behind a single row of WD-WECs is at minimum 15 % lower than the wave height in front of the farm. Installing a row of WD-WECs in front of a farm of wind turbines will facilitate the maintenance of the wind turbines as the wave height is lower (chapter 9). The latter effect will even be higher when more than 1 row is installed. One should keep in mind that only two wave situations have been presented (wave situation 1 and 3). The transmission for wave situation 4 and 5 is slightly higher compared to wave situation 1 and 3. More energy will be available behind these WECs. On the other hand these wave situations do not occur very often (Table 7.1).

To install more rows behind each other on a reasonable distance, more energy should be transmitted under the wave reflectors and main body. Decreasing the rated power of the device (and consequently cost of the device) could be an option. A cost study is needed to check whether this option is feasible (chapter 9).

## 7.5 Conclusions

In this chapter the wake effects in the lee of a single WD-WEC and a farm of WD-WECs have been studied in the time-dependent mild-slope equation model MILDwave. A WD-WEC has been implemented as a porous structure with the same reflection, absorption and transmission characteristics as obtained for the prototype by using the sponge layer technique. The tuning of the WD-WEC for the northern North Sea wave climate (24 kW/m) has been described in detail for the wave reflectors and for the main body separately. By assembling the tuned wave reflectors and main body, a WD-WEC has been implemented in MILDwave.

The wake effects in the lee of a single WD-WEC have been calculated for the wave situation with the highest frequency of occurrence in a northern North Sea wave climate. For irregular long-crested head-on waves a large decrease

of wave power is observed behind the WD-WEC. The shadow zone behind the WEC is gradually filled up due to diffraction effects. The available wave power 8 km behind the WEC is only 57 % of the generated wave power ( $H_s = 1$  m and  $T_p = 5.6$  s). For short-crested waves a faster wave redistribution is observed. The available wave power 3 km behind the WEC is approximately equal to the incident wave power for short-crested waves with  $s_{max} = 10$  (and  $H_s = 1$  m,  $T_p = 5.6$  s). When installing multiple WECs in a farm, the placing of a WEC in a second row right behind a WEC in the first row should be avoided. A staggered grid lay-out is preferred.

The power absorption of a farm of five WD-WECs installed in a staggered grid (respectively three and two WD-WECs installed in a first and second row), with a lateral and longitudinal spacing of respectively  $D_R$ ,  $2D_R$  and  $3D_R$  ( $D_R$  = distance between the tips of the wave reflectors of a single WEC), has been modelled for irregular long-crested waves. The difference in power absorption between these three grids is very small and the wave height reduction behind these grids is very high. Consequently the installation of an additional row is not interesting. Five WD-WECs installed in a staggered grid with  $w = l = 2D_R$  will produce 5 times more than a single WD-WEC in a northern North Sea wave climate, as the incident wave power for the second row is not affected by the first row. Note that only head-on waves have been considered. Other wave directions are investigated in chapter 9.

When studying short-crested waves, less waves are travelling in-between the WECs compared to long-crested waves. On the other hand a shorter wake is observed. The power absorption of a farm of five Wave Dragon WECs installed in a staggered grid, with a lateral spacing of  $D_R$ ,  $2D_R$  and  $3D_R$  and a longitudinal spacing of 190 m, 130 m and 0 m, respectively, has been modelled for the wave situation with the highest frequency of occurrence ( $H_s = 1$  m and  $T_p = 5.6$  s) and a wave situation with a high contribution to the yearly power absorption ( $H_s = 3$  m and  $T_p = 8.4$  s) in the North Sea. A farm with  $w = 2D_R$  and  $l = 130$  m combines a relatively high power absorption with an acceptable farm width. The power absorption per  $\text{km}^2$  is rather low. The highest power absorption per  $\text{km}^2$  is seen for a single line of 5 WD-WECs. On the other hand a large width is needed to install this lay-out. The cost per produced kWh should be studied as well to finally determine the optimal lay-out. This aspect is discussed in chapter 9.

## References

- [1] K. Nielsen and M. Rugbjerg. *Kortlægning af bølgeenergiforhold i den danske del af Nordsøen*. Technical report, Rambøll, 1999.
- [2] A. Nielsen and J.P. Kofoed. *The Wave Dragon - evaluation of a wave energy converter*. Master's thesis, Hydraulics and Coastal Engineering Laboratory, Department of Civil Engineering, Aalborg University, 1997.
- [3] M. Kramer and P. Frigaard. *Efficient Wave Energy Amplification with Wave Reflectors*. In Proceedings of the 9<sup>th</sup> International Offshore and Polar Engineering Conference (ISOPE), Kitakyushu, Japan, 2002.
- [4] J.P. Kofoed. *Wave overtopping of marine structures - utilization of wave energy*. PhD thesis, Hydraulics and Coastal Engineering Laboratory, Department of Civil Engineering, Aalborg University, 2002.
- [5] J. Tedd, J.P. Kofoed, W. Knapp, E. Friis-Madsen, and H.C. Sørensen. *Wave Dragon prototype wave power production*. In Proceedings of the World Renewable Energy Congress - IX, Florence, Italy, 2006.
- [6] P. Frigaard, J. P. Kofoed, and M.R. Rasmussen. *Overtopping Measurements on the Wave Dragon Nissum Bredning Prototype*. In Proceedings of the 11<sup>th</sup> International Offshore and Polar Engineering Conference (ISOPE), Toulon, France, 2004.
- [7] U.S. Army Corps of Engineers. *Coastal Engineering Manual (CEM) - Part II: Coastal Hydrodynamics - Chapter II-7: Harbor Hydrodynamics*, 2002.
- [8] J. Tedd, J.P. Kofoed, E. Friis-Madsen, and L. Christensen. *Section 7.5.5 Wave Dragon*. In J. Cruz, editor, *Ocean Wave Energy, Current Status and Perspectives*, pages 371–382. Springer, 2008.

# 8

## Power absorption of a farm of FO<sup>3</sup> wave energy converters

### 8.1 Introduction

In this chapter the power absorption of 9 FO<sup>3</sup> WECs installed in a staggered or an aligned grid with varying in-between distances ( $3D$  and  $5D$ , with  $D$  = the width of the FO<sup>3</sup> WEC (deck size)) is studied in the mild-slope wave equation model MILDwave. To implement this WEC of the first category in MILDwave the sponge layer technique described and validated in chapter 6 is extended. A WEC of the first category absorbs wave power by generating a wave. Consequently its wake will differ from the wake of a WEC of the second category. Unlike the studies of Mendes et al., Le Crom et al. and Vidal et al. [1–3] radiated waves caused by the motions of the WEC are considered in the extended methodology presented in this chapter.

The dimensions of the FO<sup>3</sup> WEC, are given in Figure 8.1 [4]. The FO<sup>3</sup> WEC consists of one semi-submersed platform and 21 heaving point absorbers (egg-shaped). The platform columns and pontoons are shown on Figure 8.1. The deck size of the FO<sup>3</sup> WEC is 36 m x 36 m.

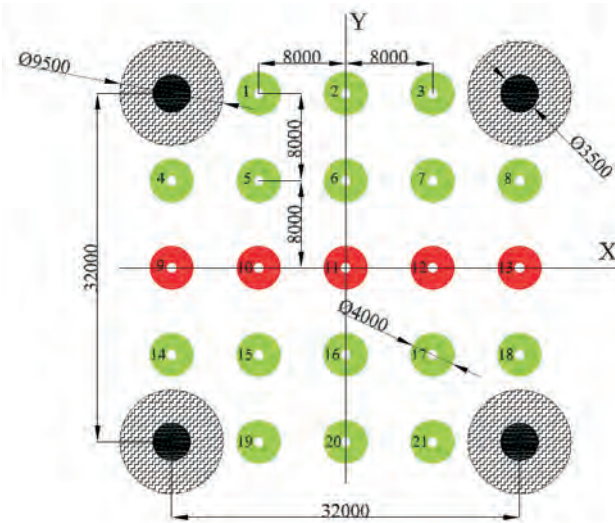


Figure 8.1: WEC Lay-out (dimension in mm) [4]

The hydrodynamic interactions between WECs of the first category in a farm are typically studied with a Boundary Element Method based on linear potential theory (e.g. WAMIT [5]). As a single  $FO^3$  WEC already consists of 22 bodies (one semi-submersed platform and 21 point absorbers) the simulation time of a farm of multiple  $FO^3$  WECs increases rapidly when using these Boundary Element Methods. Therefore a technique is developed to implement a single  $FO^3$  WEC in the wave propagation model MILDwave and to study multiple  $FO^3$  WECs in this model within a reasonable time.

When the  $FO^3$  WEC is assumed to be fixed, the incident waves are partly reflected from, diffracted around and transmitted under the WEC. In that case, no wave power is absorbed. These phenomena result in the so-called ‘scattered’ or ‘diffracted’<sup>1</sup> wave pattern. When the  $FO^3$  WEC moves the platform and the point absorbers will radiate waves. The superposition of these radiated waves is defined as the so-called ‘radiated’<sup>1</sup> wave pattern. The radiated wave patterns generated by the point absorbers in the platform and by the platform itself are not studied separately. The diffracted and radiated wave patterns around a single  $FO^3$  WEC and the amount of power absorbed by the  $FO^3$  WEC were calculated by a detailed modelling of a single  $FO^3$  WEC in the BEM package WAMIT and by assuming a realistic power take-off [4] in the equations of motion. These calculations were performed by the Norwegian University of Science and Technology (NTNU) in the EU project SEEWEC (Sustainable Economically Efficient Wave Energy Converter - contract n°: SES6-CT2005-019969). These results are discussed in section 8.2.1.

<sup>1</sup>This terminology is generally used when studying WECs of the first category (chapter 4).

Only regular waves with an incident wave direction of 90° were studied. Therefore only surge, heave and pitch motions occurred. The author refers to [4] for details on the modelling of a single FO<sup>3</sup> WEC using WAMIT.

The wave diffraction pattern generated by an FO<sup>3</sup> WEC is simulated in MILDwave using the sponge layer technique (chapter 6). In section 8.2.2 the simulation results from MILDwave are compared to the results from the validation data set on diffraction patterns (fixed FO<sup>3</sup> WEC) obtained using WAMIT.

The resulting wave radiation patterns, provided by NTNU, are used as an input to model wave power absorption in MILDwave. In MILDwave radiated waves with a wave amplitude  $a$  and phase shift  $\phi$  (as calculated in WAMIT) are generated on a circle around the FO<sup>3</sup> WEC. In section 8.2.3 the ability of MILDwave to simulate wave radiation patterns is evaluated.

Further the phase shift between the wave diffraction pattern and wave radiation pattern is determined, based on the WAMIT results, and is used to calculate the total wave pattern in MILDwave. The total wave pattern simulated in MILDwave is compared to the results obtained in WAMIT in section 8.2.4. The accuracy of the implementation of an FO<sup>3</sup> WEC in MILDwave is discussed.

Finally a farm of 9 FO<sup>3</sup> WECs is studied in MILDwave (section 8.3). Interactions between the FO<sup>3</sup> WECs in the farm are taken into account. The amount of power absorbed by 9 FO<sup>3</sup> WECs installed in several lay-outs is estimated, based on the calculated wave height in front of each FO<sup>3</sup> WEC, and an optimal lay-out is selected.

## 8.2 Implementation of an FO<sup>3</sup> WEC in MILDwave

The wave diffraction and radiation patterns generated by an FO<sup>3</sup> WEC are studied for three incident regular waves with wave amplitude  $a = 1$  m and wave period  $T$  of respectively 4, 6 and 8 s. Therefore a grid of  $20L$  (1 117 m) in y-direction and  $30L$  (1 684 m) in x-direction is defined (with  $L$ , the wave length of a regular wave with  $T = 6$  s). In WAMIT, large grid cells (9 m x 9 m) have been considered to decrease the simulation time. On the nodes of the grid, the real part and imaginary part of the wave amplitude have been calculated. An area of 10 m around the platform has not been studied, due to inaccurate results in WAMIT. In MILDwave, smaller grid cells are defined (1 m x 1 m) to obtain accurate and detailed results. In the middle of the grid cells the wave amplitude and phase shift are calculated. To compare the obtained results with WAMIT results the same area around the platform is not taken into account. Furthermore the WAMIT results are interpolated (bicubic interpolation) to make a detailed comparison of both models possible.

## 8.2.1 Results of WAMIT for a regular wave with unit wave amplitude and wave period of 6 s

### 8.2.1.1 Absorbed power

The total absorbed power by a single FO<sup>3</sup> WEC for a regular incident wave with unit wave amplitude and a wave period of 6 s is 934 kW. The total available wave power (appendix B) over the width of the FO<sup>3</sup> WEC (approximately 36 m) is 849 kW. This means that approximately 110 %<sup>2</sup> of the available wave power over the width of the FO<sup>3</sup> WEC has been absorbed.

### 8.2.1.2 Wave elevations

The wave elevation can be expressed as:

$$\eta = a \cos(\omega t + \phi) \quad (8.1)$$

with the wave amplitude  $a$  in the grid cell  $(i\Delta x, j\Delta y)$ , the angular frequency  $\omega$ , the time  $t$  and the phase shift  $\phi$  (relative to the centre of the FO<sup>3</sup> - Figure 8.1) in the grid cell  $(i\Delta x, j\Delta y)$ . Another way to describe the wave elevation is given in equation (8.2).

$$\eta = \Re(ae^{i\phi}e^{i\omega t}) = \Re(\bar{\eta}e^{i\omega t}) \quad (8.2)$$

with the complex amplitude of the wave elevation  $\bar{\eta} = ae^{i\phi} = a\cos\phi + ia\sin\phi$  at the grid cell  $(i\Delta x, j\Delta y)$ .

The wave amplitude  $a$  and the phase shift  $\phi$  can be calculated as a function of the real ( $a\cos\phi$ ) and imaginary ( $a\sin\phi$ ) parts of the wave amplitude, respectively, with equations (8.3) and (8.4).

$$a = \sqrt{(a\cos\phi)^2 + (a\sin\phi)^2} \quad (8.3)$$

$$\phi = \arctan\left(\frac{a\sin\phi}{a\cos\phi}\right) \quad (8.4)$$

The WAMIT simulations typically yield the real and imaginary parts of the wave amplitude due to diffraction, and radiation separately.

The real part of the wave amplitude ( $a\cos\phi$ ), is equal to the wave elevations  $\eta$  on  $\omega t = 0$  ( $t = 0$ ),  $2\pi$  ( $t = T$ ), ... . The WAMIT results are presented for the cases diffraction + radiation (Figure 8.2(a)), only radiation (Figure 8.2(b)) and only

---

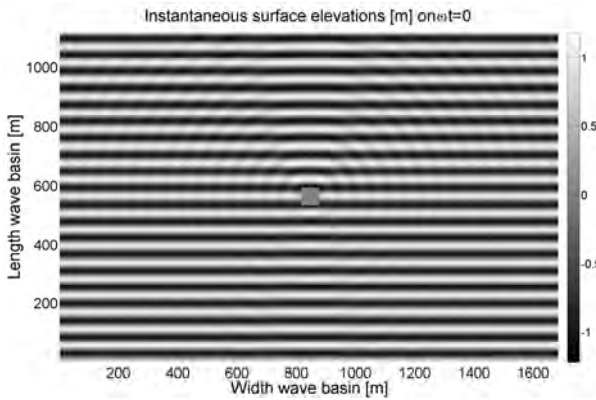
<sup>2</sup>A heaving point absorber generates circular waves which interfere with the straight incoming regular waves. The maximum energy which may be absorbed by a heaving point absorber in regular waves equals the wave energy transported by the incident wave front of width equal to the wave length divided by  $2\pi$  [6]. Consequently the wave power absorbed by the FO<sup>3</sup> WEC may be larger than the wave power available over the width of the WEC.



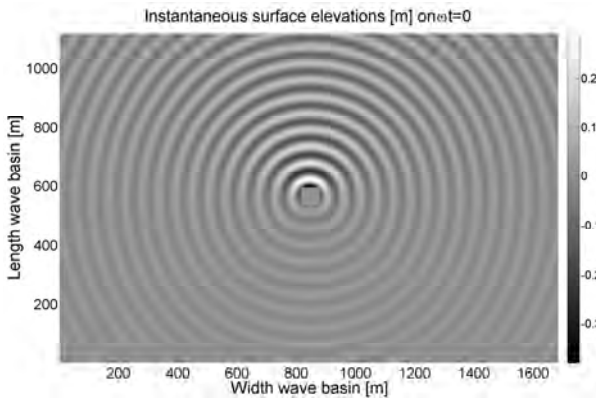
diffraction (Figure 8.2(c)) obtained from NTNU for wave conditions  $H_i = 2$  m,  $T = 6$  s.

The case only radiation includes the surface elevations due to the motions of the FO<sup>3</sup> WEC (the surface elevations due to the generated incident wave are not considered in the latter case). In the case only diffraction the motions of the floating body are not taken into account. It is clear that the wave elevations are varying between approximately -1 and +1 m (Figure 8.2(c)), which corresponds to a wave height  $H_i$  of 2 m.

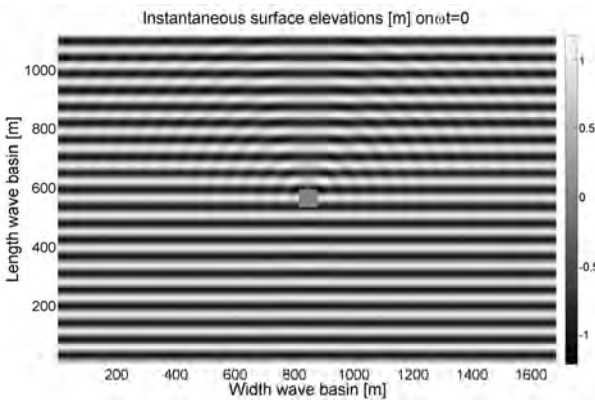
The imaginary part of the wave amplitude shows the wave elevations  $\eta$  on  $\omega t = -\pi/2$  ( $t = -T/4$ ),  $3\pi/2$  ( $t = 3T/4$ ), ... . The instantaneous surface elevations on  $\omega t = -\pi/2$  due to diffraction and radiation, only radiation and only diffraction, calculated with WAMIT for an incident wave with  $H_i = 2$  m and  $T = 6$  s, are shown in respectively Figure 8.3(a), 8.3(b) and 8.3(c).



(a) Diffraction + radiation

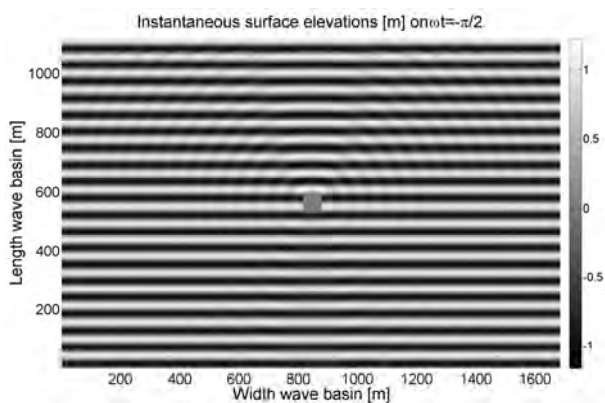


(b) Only radiation

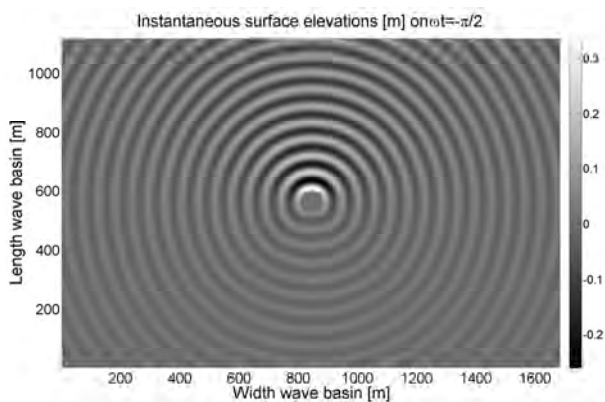


(c) Only diffraction

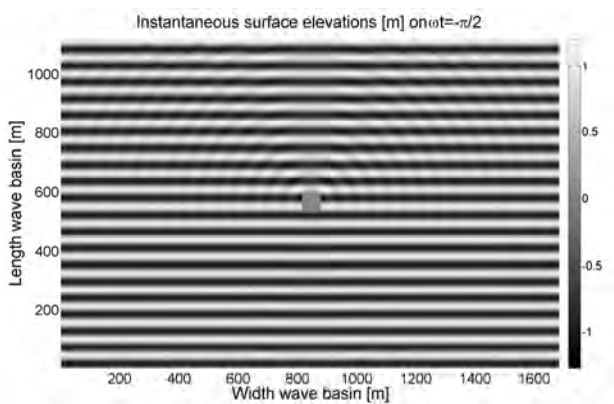
Figure 8.2: Instantaneous surface elevations on  $\omega t = 0$  calculated with WAMIT taking (a) diffraction and radiation, (b) only radiation and (c) only diffraction into account



(a) Diffraction + radiation



(b) Only radiation



(c) Only diffraction

Figure 8.3: Instantaneous surface elevations on  $\omega t = -\pi/2$  calculated with WAMIT taking (a) diffraction and radiation, (b) only radiation and (c) only diffraction into account

## 8.2.2 Wave diffraction

### 8.2.2.1 Implementation of wave diffraction in MILDwave

In this section WAMIT results are adopted and reformulated in terms of wave amplitude  $a$  and phase shift  $\phi$ , relative to the centre of the FO<sup>3</sup> WEC, instead of real and imaginary part of the wave amplitude (cf. using equations (8.3) and (8.4)). The resulting wave amplitude  $a$  and phase shift  $\phi$ , when only diffraction is considered, are shown in Figure 8.4 for a regular incident wave with a wave amplitude of 1 m and a wave period of 6 s.

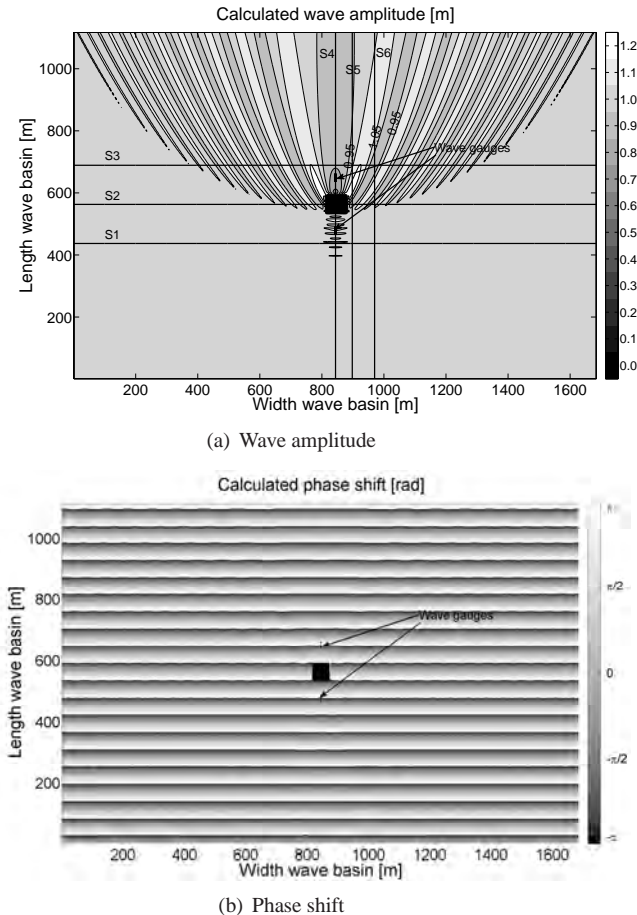


Figure 8.4: Calculated (a) wave amplitude  $a$  and (b) phase shift  $\phi$  in WAMIT

As the wave amplitude  $a$  and the phase shift  $\phi$  over the domain are known, the time series of wave elevations on a specified location in the domain have

been calculated (equation (8.1)) and consequently a reflection analysis has been performed.

A reflection analysis has been carried out using two arrays of three wave gauges. The position of the wave gauges is indicated on Figure 8.4. The first and second array of wave gauges have been placed approximately one wave length before, respectively, behind the FO<sup>3</sup> WEC. Based on the results of the reflection analysis (Table 8.1), an FO<sup>3</sup> WEC with the same amounts of reflection and transmission is modelled in MILDwave.

*Table 8.1: Reflection analysis - diffraction in WAMIT*

Wave Gauges	$H_i$ or $H_t$ [m]	$T$ [s]	$H_r$ [m]	$T$ [s]	$K_r$ [%]
1-3	2.0	6.0	0.2	6.0	7.6
4-6	1.6	6.0	0.0	6.0	1.5

In MILDwave a wave basin with the same dimensions of the domain considered in WAMIT, has been defined. The length and the width of the wave basin are extended in order to place sponge layers at the boundaries of the wave basin to prevent disturbances in the inner domain.

The diffraction pattern, generated by an FO<sup>3</sup> WEC, is modelled using the sponge layer technique. An FO<sup>3</sup> WEC is implemented as a black box of 35 cells (of 1 m) with specific sponge layer coefficients providing a comparable amount of reflection and transmission as calculated based on results in WAMIT (Table 8.1). By assuming 35 cells (35 m) instead of 36 cells (36 m), the FO<sup>3</sup> WEC can be placed in the centre of the domain (no difference in diffraction pattern of an FO<sup>3</sup> of 35 and 36 cells). The resulting wave amplitude, calculated with MILDwave, is shown on Figure 8.5. Note that the results in an area of 10 m around the platform are set to 0.

When comparing Figure 8.4(a) and Figure 8.5, the central part of the shadow zone behind the FO<sup>3</sup> WEC seems wider in MILDwave compared to WAMIT. Furthermore the peaks near the converter are smaller in MILDwave. These observations are studied in more detail by considering sections as indicated on Figure 8.4(a) and Figure 8.5.

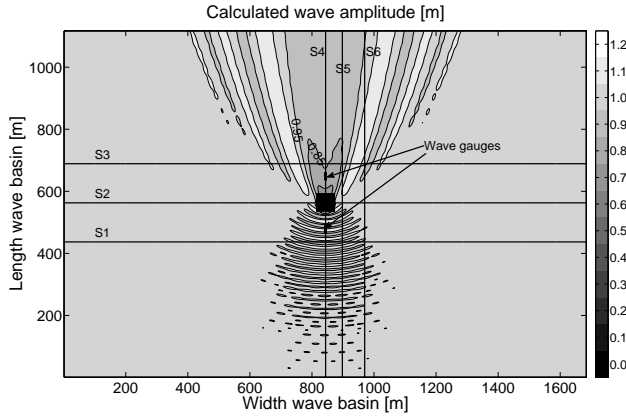


Figure 8.5: Calculated wave amplitude  $a$  in MILDwave

In a similar way as for the WAMIT results, a reflection analysis has been performed (Table 8.2). When comparing Table 8.1 and Table 8.2 an increase in reflection is observed.

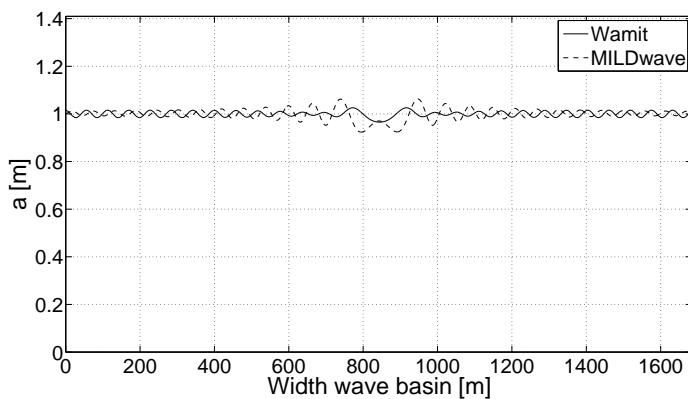
Table 8.2: Reflection analysis - diffraction in MILDwave

Wave Gauges	$H_i$ or $H_t$ [m]	$T$ [s]	$H_r$ [m]	$T$ [s]	$K_r$ [%]
1-3	2.0	6.0	0.2	6.0	11.2
4-6	1.6	6.0	0.1	7.3	4.6

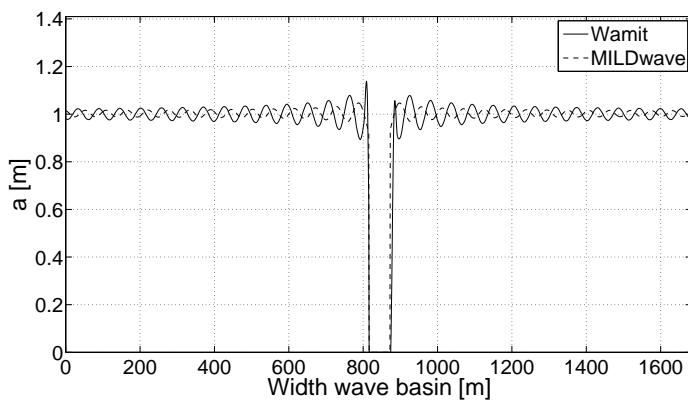
**8.2.2.2 Comparison of wave diffraction patterns generated by an FO<sup>3</sup> WEC using WAMIT and MILDwave**

To make a detailed comparison between the WAMIT and the MILDwave results, sections on a distance of 126 m from the centre of the FO<sup>3</sup> WEC (distance between two WECs in a farm will be 108 m at minimum<sup>3</sup> [7]) are studied as indicated on Figure 8.4(a) and Figure 8.5. Figure 8.6 shows a lateral section in front of (S1), through (S2) and behind (S3) the FO<sup>3</sup> WEC at respectively  $y^* = 437$  m, 563 m and 689 m. Figure 8.7 shows three longitudinal sections at  $x^* = 844$  m (S4), 898 m (S5) and 970 m (S6). In Figure 8.8 and Figure 8.9 the same sections are zoomed in.

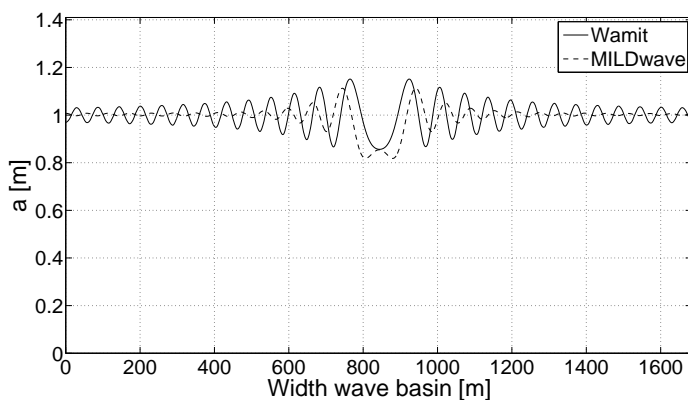
<sup>3</sup>3 times the dimension of the FO<sup>3</sup> WEC



(a) Section S1

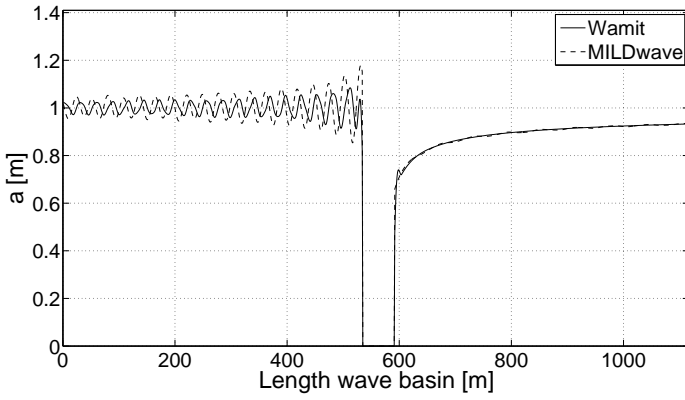


(b) Section S2

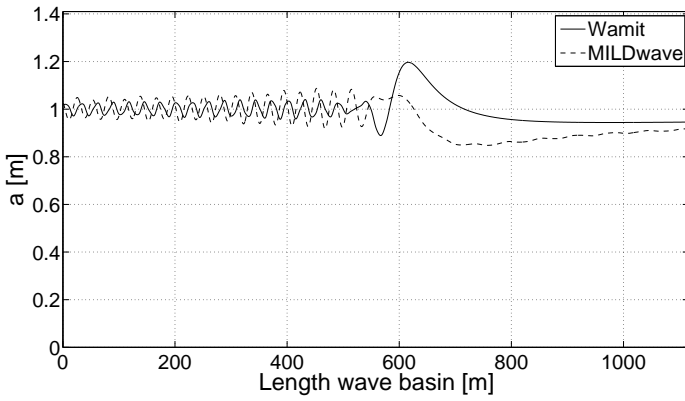


(c) Section S3

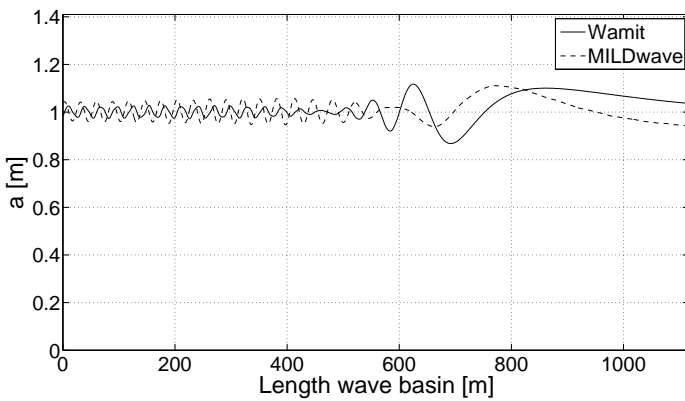
Figure 8.6: Calculated wave amplitude  $a$  in section (a) S1, (b) S2, (c) S3



(a) Section S4



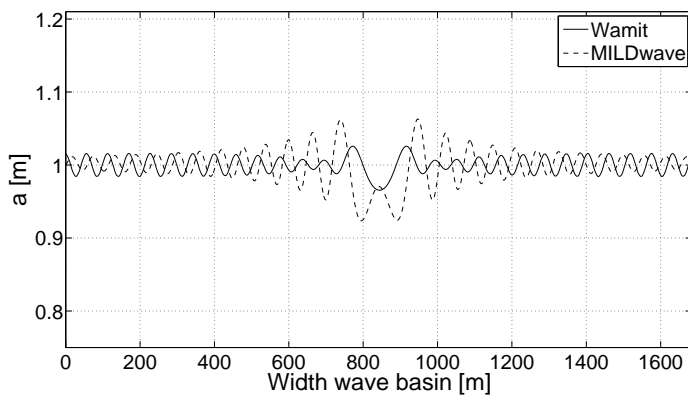
(b) Section S5



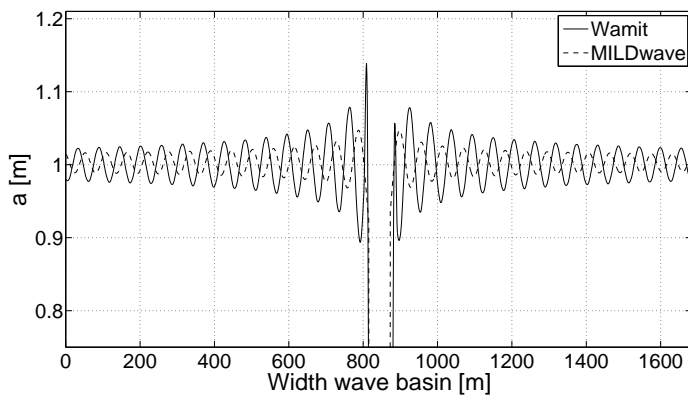
(c) Section S6

Figure 8.7: Calculated wave amplitude  $a$  in section (a) S4, (b) S5, (c) S6

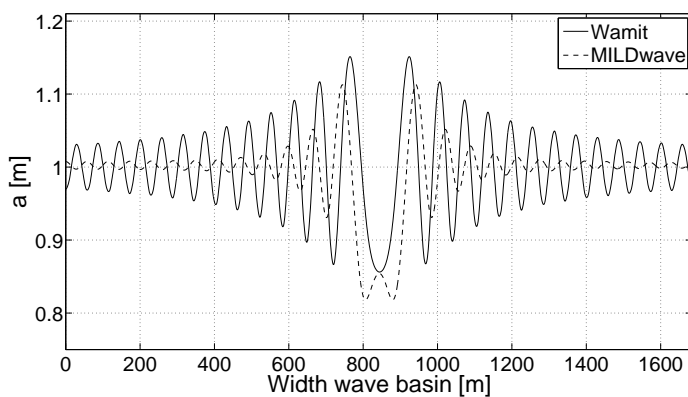




(a) Section S1

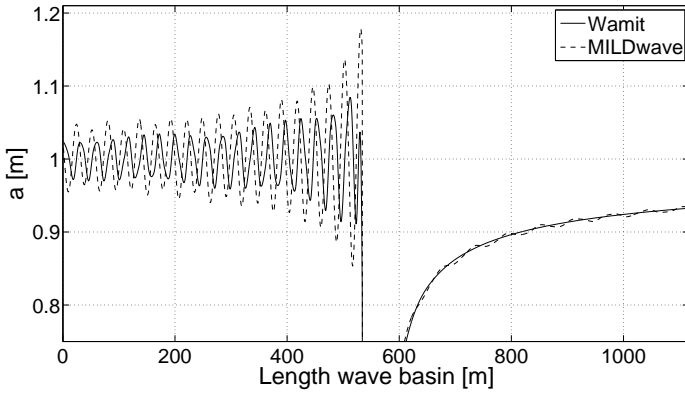


(b) Section S2

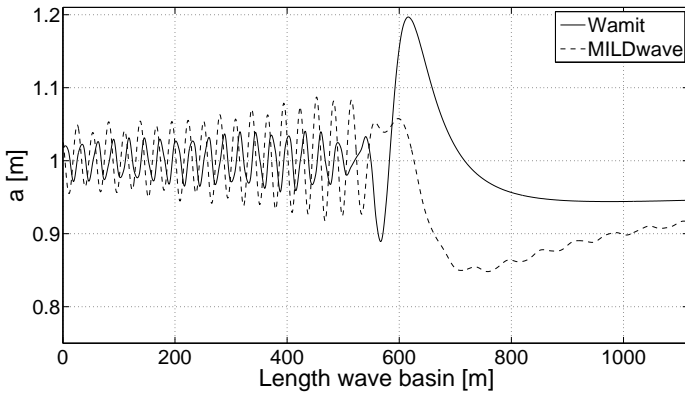


(c) Section S3

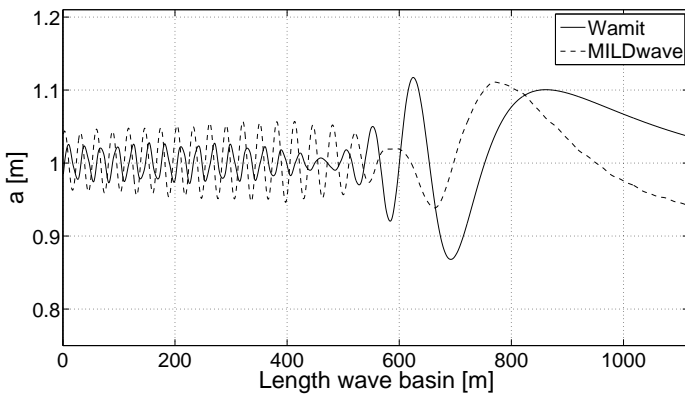
Figure 8.8: Calculated wave amplitude  $a$  (zoomed in) in section (a) S1, (b) S2, (c) S3



(a) Section S4



(b) Section S5



(c) Section S6

Figure 8.9: Calculated wave amplitude  $a$  (zoomed in) in section (a) S4, (b) S5, (c) S6

Figure 8.8(a) confirms the higher reflection observed in the MILDwave results (Table 8.2). Furthermore Figure 8.8(c) shows the wider shadow zone in MILDwave compared to WAMIT. The distance crest-to-crest between the two central peaks in WAMIT equals 159 m, in MILDwave 198 m. Figure 8.8 clearly indicates a spatial phase shift between the oscillations in WAMIT and MILDwave along the wave basin width. Figure 8.9(a) shows a very good agreement between the results in WAMIT and MILDwave along the length of the wave basin. In general good agreement between the WAMIT and MILDwave results is observed. The values in the central part of the shadow zone are exactly the same in both model results. The shadow zone in the MILDwave results is approximately 25 % wider than the shadow zone in the WAMIT results. The author wants to underline that the values in the shadow zone are more important than the width of the shadow zone, as the pattern of the shadow zone is disappearing when short-crested waves and other mean incident wave directions are considered (chapter 6).

Further the envelope of the oscillations along the width and length of the wave basin in WAMIT and MILDwave has been compared. Therefore a Hilbert transformation has been used. An area of 180 m x 180 m has been ignored when calculating the envelope. This zone has no importance when studying a farm as the minimal distance between the converters is 108 m (3 times dimension FO<sup>3</sup> WEC). Moreover by ignoring the latter zone, near-field peaks in the calculated envelope have been prevented. The resulting envelope of the WAMIT and MILDwave results are shown on Figure 8.10, respectively 8.11.

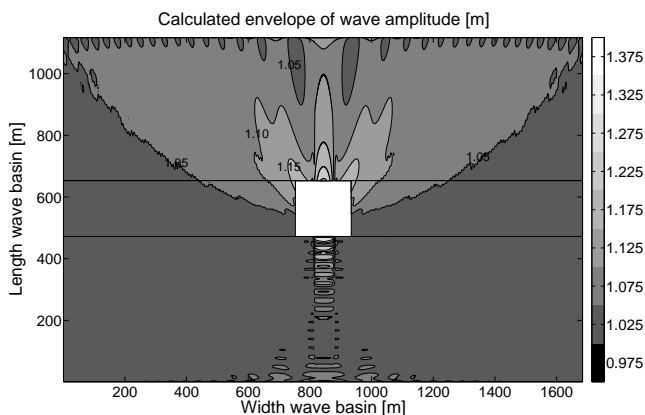


Figure 8.10: Calculated envelope of wave amplitude in WAMIT

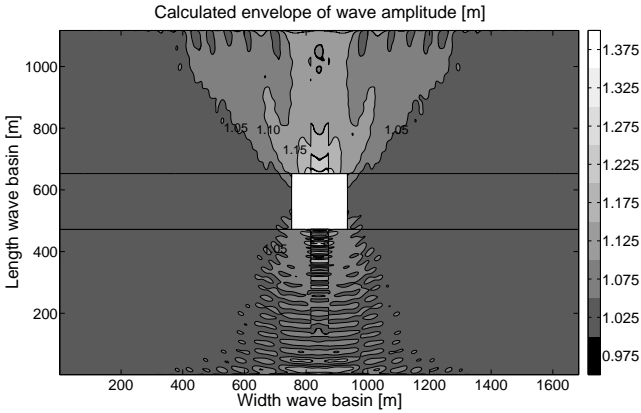


Figure 8.11: Calculated envelope of wave amplitude in MILDwave

The difference between both envelopes is shown on Figure 8.12:

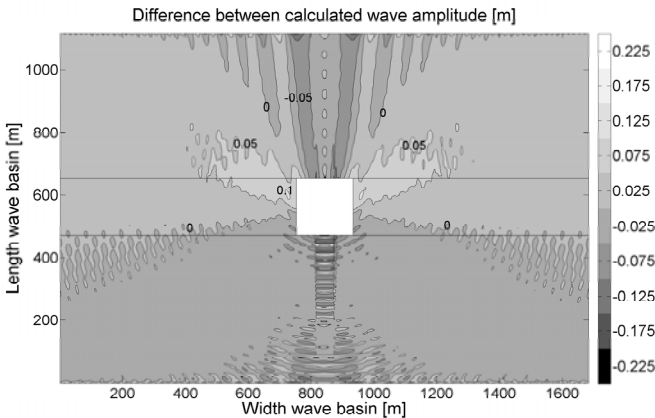


Figure 8.12: Difference between envelope of wave amplitude in WAMIT and in MILDwave

The difference between the wave amplitudes calculated from MILDwave and WAMIT is observed to be in the range of  $\pm 10\%$  in the whole domain. In the largest part of the domain the differences are reduced to the interval  $[-5\%, +5\%]$  which confirms the good agreement between the WAMIT and MILDwave results.

A difference of 5% on the wave amplitude, results in a difference of 10% on the average available wave power (proportional to wave height squared - appendix B). Therefore the wave power around a farm of WECs needs to be calculated on a sufficient distance from the outer WECs in the farm to minimize the influence of local peaks in the wave amplitude, as the latter peaks are increased

when calculating the wave power.

As it is the measured wave height that is used to determine the capture ratio of the next converter, the difference in capture ratio calculated in both models is depending on the curve of the capture ratio as a function of incident wave height.

To determine the accuracy of MILDwave, compared to WAMIT, the mean absolute error (MAE) and the root mean square error (RMSE) over the computational domain are calculated with equations (8.5) and (2.11).  $x_i$  represent the results from WAMIT,  $y_i$  the results from MILDwave and  $n$  the number of grid cells.

$$\text{MAE} = \frac{\sum_{i=1}^n |y_i - x_i|}{n} \quad (8.5)$$

$$\text{RMSE} = \sqrt{\frac{\sum_{i=1}^n (x_i - y_i)^2}{n}} \quad (2.11)$$

The MAE = 0.026 m and RMSE = 0.031 m.

Dividing the latter values through the mean value of the results in WAMIT (= 1.041 m) results in MAE = 2.34 % and RMSE = 2.99 %. In [8] it is stated that a RMSE of 3.35 % is sufficient for linear computations.

The comparison between the diffraction pattern in MILDwave and WAMIT for a regular incident wave with  $a = 1$  m and, respectively,  $T = 4$  s and 8 s, can be found in appendix F. The shadow zone in the lee of the FO<sup>3</sup> WEC is 27 % and 20 % wider in MILDwave compared to WAMIT for  $T = 4$  s and  $T = 8$  s, respectively. The differences between the wave amplitude  $a$  in WAMIT and MILDwave are slightly higher for  $T = 4$  s compared to  $T = 6$  s. Especially in small areas in front of and behind the FO<sup>3</sup> WEC higher differences occur. The differences between the wave amplitude  $a$  in WAMIT and MILDwave for  $T = 8$  s are even slightly smaller compared to the results for  $T = 6$  s. The differences are within  $\pm 10$  % in the whole domain.

## 8.2.3 Wave radiation

### 8.2.3.1 Implementation of wave radiation in MILDwave

A wave generation circle with centre  $(x_c, y_c)$  and radius  $r_c$  has been defined in the rectangular simulation grid to generate a radiated wave with amplitude  $a$  and phase shift  $\phi$  as determined in WAMIT. Wave generation on a circle has been described in chapter 5.

Waves are generated on a circle with centre equal to the centre of the FO<sup>3</sup> WEC and  $r_c = 50$  m. The wave amplitude and phase shift relative to the centre of the FO<sup>3</sup> WEC on the wave generation circle with centre equal to the centre of the FO<sup>3</sup> WEC and radius 50 m are determined from the results in WAMIT (equations (8.3) and (8.4)) and are given in Figure 8.13. A small unexpected asymmetry can be seen in the results from WAMIT.

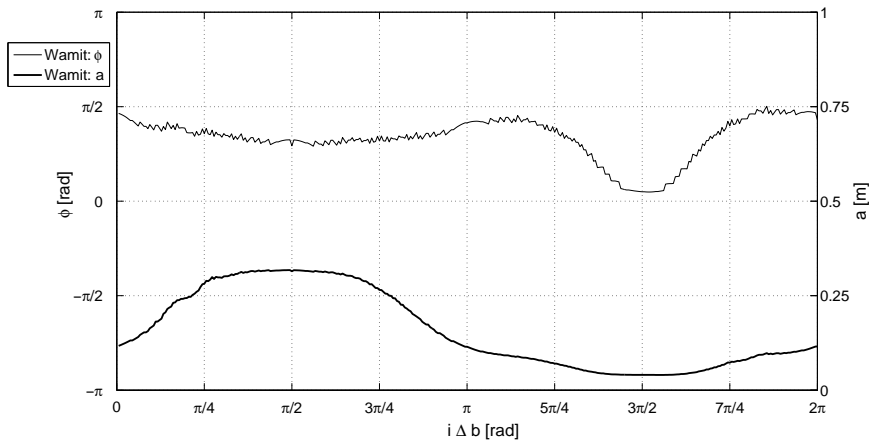
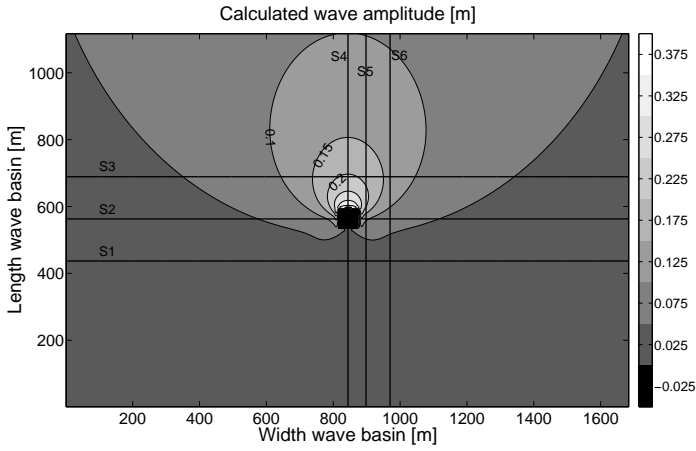
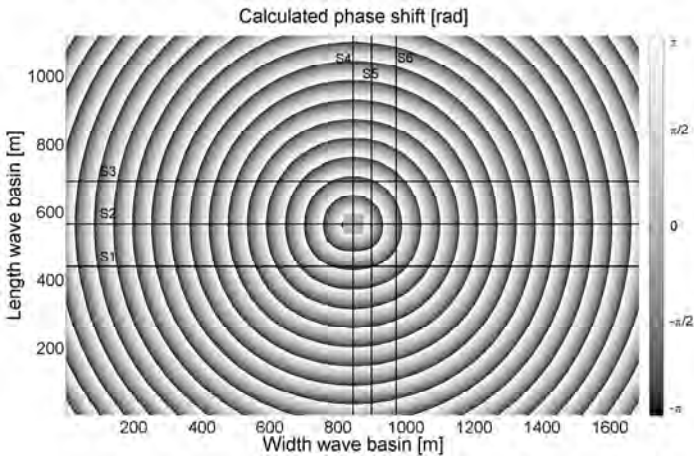


Figure 8.13: Calculated wave amplitude  $a$  and phase shift  $\phi$  on a circle with centre equal to the centre of the FO<sup>3</sup> WEC and radius = 50 m for regular incident waves with  $a = 1$  m and  $T = 6$  s

The calculated wave amplitude and phase shift relative to the centre of the FO<sup>3</sup> WEC across the whole domain in respectively WAMIT (using equations (8.3) and (8.4)) and MILDwave are shown in Figure 8.14 and Figure 8.15 for a regular incident wave with wave amplitude of 1 m and wave period of 6 s. The results in a square of 100 m x 100 m in the centre of the domain in MILDwave are set to 0 because the values within the wave generation circle ( $r_c = 50$  m) have no physical meaning.



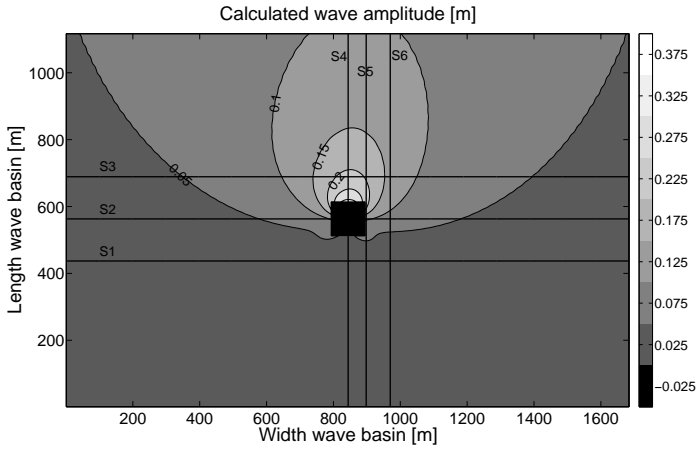
(a) Wave amplitude



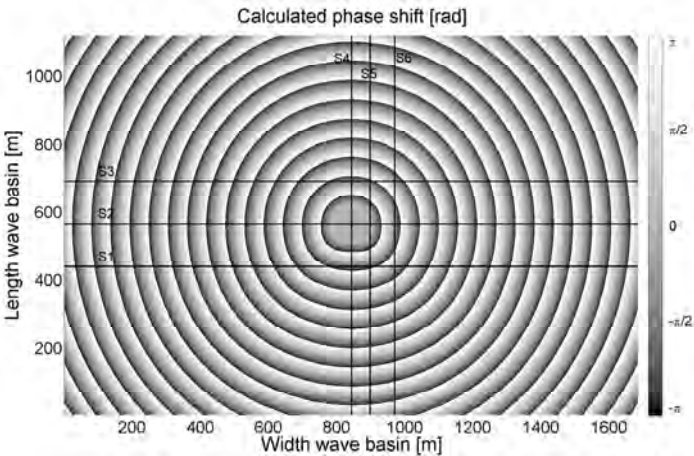
(b) Phase shift

Figure 8.14: Calculated (a) wave amplitude  $a$  and (b) phase shift  $\phi$  in WAMIT

The wave amplitude due to radiation is decreasing, further away from the converter (Figure 8.14(a)).



(a) Wave amplitude



(b) Phase shift

Figure 8.15: Calculated (a) wave amplitude  $a$  and (b) phase shift  $\phi$  in MILDwave

When comparing Figure 8.14 and Figure 8.15 the resulting wave amplitude and phase shift relative to the centre of the FO<sup>3</sup> WEC seem to be quite similar. The wave amplitudes between 0.10 m and 0.15 m occur in a larger zone in MILDwave compared to WAMIT.

The results in Figure 8.14 and Figure 8.15 are discussed in detail in the next section.



### 8.2.3.2 Comparison of wave radiation patterns generated by an FO<sup>3</sup> WEC using WAMIT and MILDwave

The calculated wave amplitude and phase shift relative to the centre of the FO<sup>3</sup> WEC in MILDwave and WAMIT are compared on two circular sections with centre equal to the centre of the FO<sup>3</sup> WEC and radius  $r_c = 70$  m and 126 m. The results are shown in Figure 8.16. Note that  $i\Delta b = \pi/2$  represents a location behind the platform.

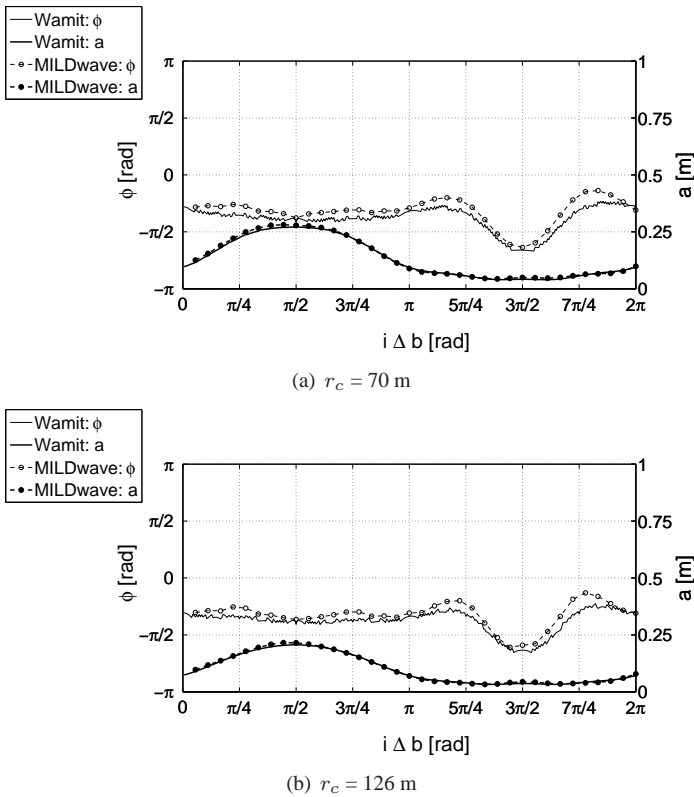


Figure 8.16: Calculated wave amplitude  $a$  and phase shift  $\phi$  on a circle with centre equal to the centre of the FO<sup>3</sup> WEC and radius  $r_c =$  (a) 70 m, (b) 126 m for regular incident waves with  $a = 1$  m and  $T = 6$  s

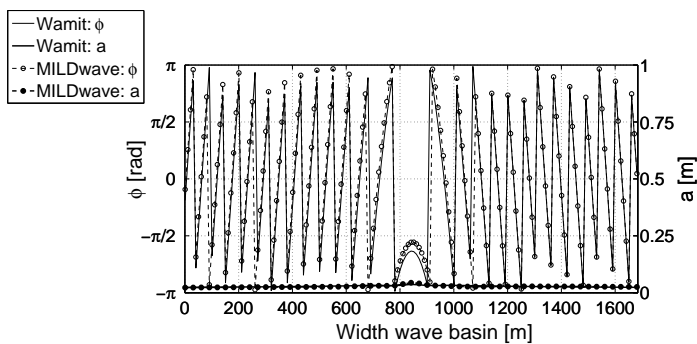
In general the results in WAMIT and MILDwave agree very well. A small phase shift between  $\phi$ , calculated in WAMIT, and  $\phi$ , calculated in MILDwave is observed. This phase shift is approximately constant along the circular section. Behind the WEC the heave motion is dominating as the phase shift is approximately constant between 0 and  $\pi$  radians. On the other hand in front of the

$FO^3$  WEC surge and pitch motions prevail.

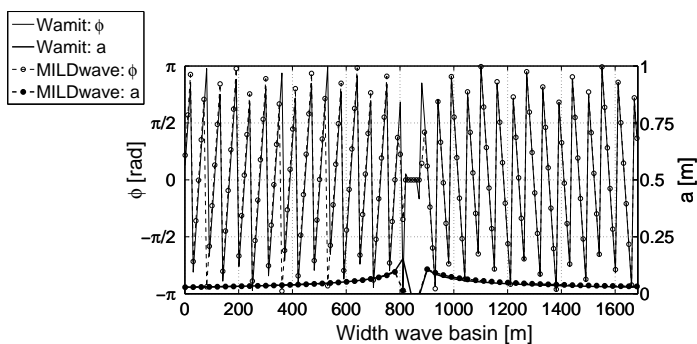
To compose the radiated and diffracted wave pattern, an additional phase shift will be imposed on the radiated wave to obtain the phase shift between the diffracted and radiated wave pattern and the overall wave pattern as calculated in WAMIT. Therefore the constant phase shift between the radiated wave in WAMIT and MILDwave along a circular section, as seen on Figure 8.16, will not influence the final results.

In Figure 8.17 and Figure 8.18 the calculated wave amplitude and phase shift in WAMIT and MILDwave are shown in, respectively, three lateral sections S1 ( $y^* = 437$  m), S2 ( $y^* = 563$  m) and S3 ( $y^* = 689$  m) and three longitudinal sections S4 ( $x^* = 844$  m), S5 ( $x^* = 898$  m) and S6 ( $x^* = 970$  m) as indicated on Figure 8.14 and Figure 8.15.

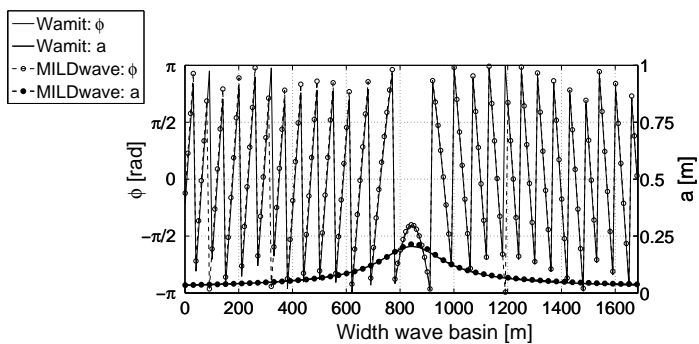
Again, in general a good agreement is seen. A small phase shift is observed in front of the  $FO^3$  WEC. Note the deviations near the platform in the sections through the platform (section S2 and section S4). As waves are radiated on a circle with  $r_c = 50$  m only the wave amplitude and phase shift outside the circle need to be studied. The values inside the circle (between 794 m and 894 m in section S2 and between 513 m and 613 m in section S4) have no physical meaning.



(a) Section S1

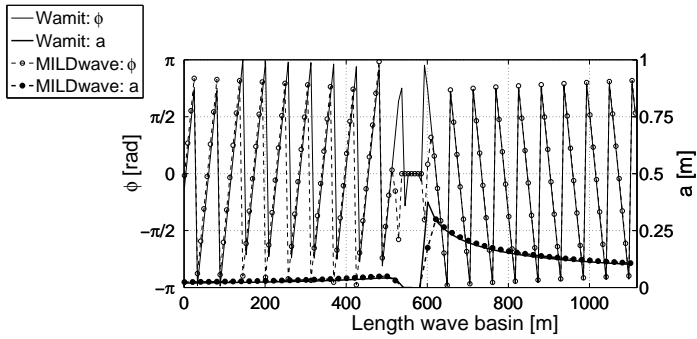


(b) Section S2

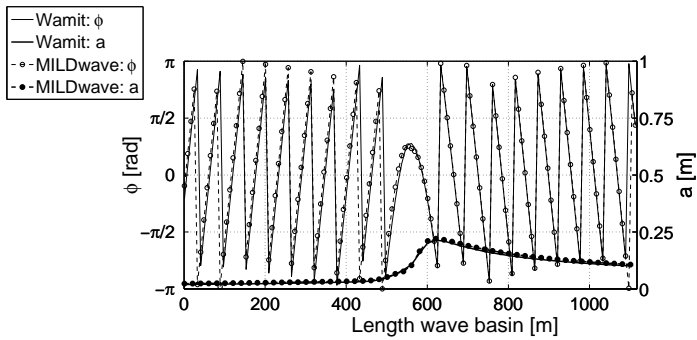


(c) Section S3

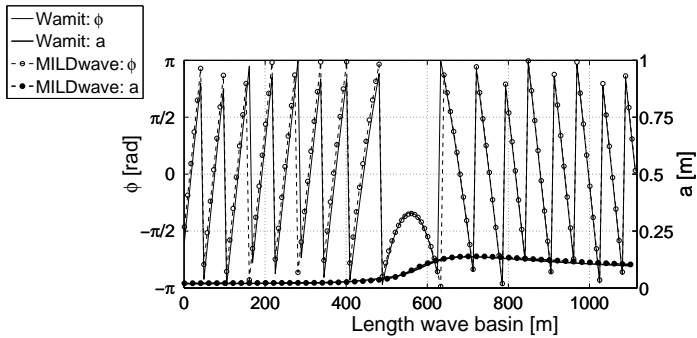
Figure 8.17: Calculated wave amplitude  $a$  and phase shift  $\phi$  in section (a) S1, (b) S2 and (c) S3 for regular incident waves with  $a = 1$  m and  $T = 6$  s



(a) Section S4



(b) Section S5



(c) Section S6

Figure 8.18: Calculated wave amplitude  $a$  and phase shift  $\phi$  in section (a) S4, (b) S5, (c) S6 for regular incident waves with  $a = 1$  m and  $T = 6$  s

The absolute difference between the wave amplitude and phase shift in WAMIT and MILDwave is shown in Figure 8.19. The results in a square of 100 m x 100 m in the centre of the domain are ignored (and set to a value of 0) as the results inside the wave generation circle with  $r_c = 50$  m have no physical meaning.

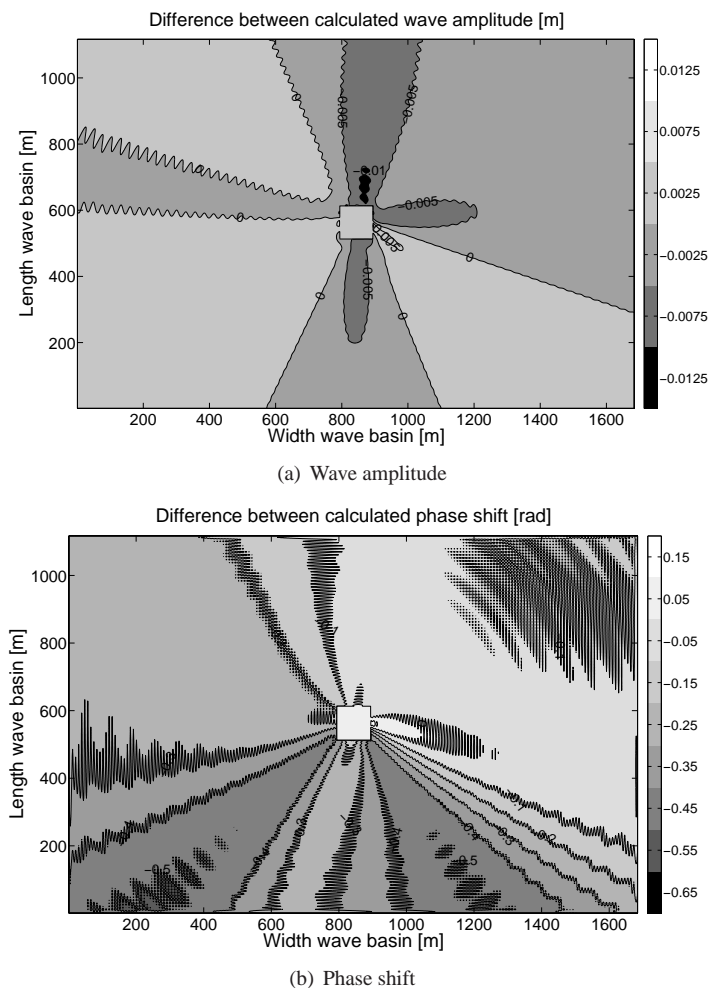


Figure 8.19: Calculated absolute difference between (a) wave amplitude  $a$  and (b) phase shift  $\phi$  in WAMIT and MILDwave

The absolute difference between the wave amplitude calculated in WAMIT and MILDwave is equal to 1.5 cm at maximum. In the largest part of the domain the absolute difference is not higher than 0.5 cm. One should keep in mind that the amplitude of the radiated wave is varying between 0 cm and 40 cm through the domain. The absolute difference in phase shift is the highest ( $0.50 \text{ rad} = 29^\circ$ ) in front of the FO<sup>3</sup> platform where the wave amplitude of the radiated wave is small. Consequently the higher difference in phase shift will not have a large impact on the resulting wave elevations.

Finally the mean absolute error and the root mean square error are calculated.

The mean absolute error and root mean square error equal 0.002 m and 0.003 m for the wave amplitude and 0.220 rad and 0.269 rad for the phase shift. When dividing the MAE and the RMSE for the wave amplitude by the mean value of the wave amplitude in WAMIT (= 0.049 m) a MAE equal to 4.07 % and a RMSE equal to 5.30 % are obtained. The latter values are slightly higher compared to the results for the diffraction pattern.

The wave radiation patterns for, respectively,  $T = 4$  s and 8 s, are studied in appendix F. For  $T = 8$  s the agreement between the WAMIT and MILDwave results is comparable to the agreement observed for  $T = 6$  s. For  $T = 4$  s a higher deviation is seen. The wave length for  $T = 4$  s (= 25 m) is smaller than the deck size (= 36 m) of the FO<sup>3</sup> WEC. Consequently the WEC experiences large pitch and surge motions which cause larger differences in phase and amplitude along the wave generation circle. Consequently a higher interaction between the individual wave generation cells on the wave generation circle is seen. A smaller grid size in MILDwave could result in a better agreement between the wave amplitude and phase shift calculated in WAMIT and MILDwave.

## 8.2.4 Diffraction and radiation

In section 8.2.2 and section 8.2.3 the diffracted and radiated wave pattern caused by an FO<sup>3</sup> WEC for a regular incident wave with  $a = 1$  m and  $T = 6$  s have been implemented in MILDwave. In this section the total wave pattern is studied. Using a superposition of the wave elevations obtained for the cases of diffraction and radiation, offers the opportunity to consider the phase shift  $\phi$  between the wave elevations due to diffraction and the wave elevations due to radiation. The resulting real and imaginary part of the wave amplitude is again reformulated in terms of wave amplitude  $a$  and phase shift  $\phi$ , relative to the centre of the FO<sup>3</sup> WEC (calculated with equations(8.3) and (8.4)). The resulting wave amplitude  $a$  when diffraction and radiation are taken into account in WAMIT is shown in Figure 8.20 for a regular incident wave with wave amplitude of 1 m and wave period of 6 s.

Again a reflection analysis is performed.

*Table 8.3: Reflection analysis - diffraction and radiation in WAMIT*

Wave Gauges	$H_i$ or $H_t$ [m]	$T$ [s]	$H_r$ [m]	$T$ [s]	$K_r$ [%]
1-3	2.0	6.0	0.2	6.0	11.7
4-6	2.1	6.0	0.0	6.0	1.2

Due to the effect of radiation there is almost no difference in wave height in front of and behind the converter (Table 8.3). There is even a small increase in

wave height. In general, the wake effect behind the FO<sup>3</sup> WEC is limited compared to the WD-WEC (chapter 7).

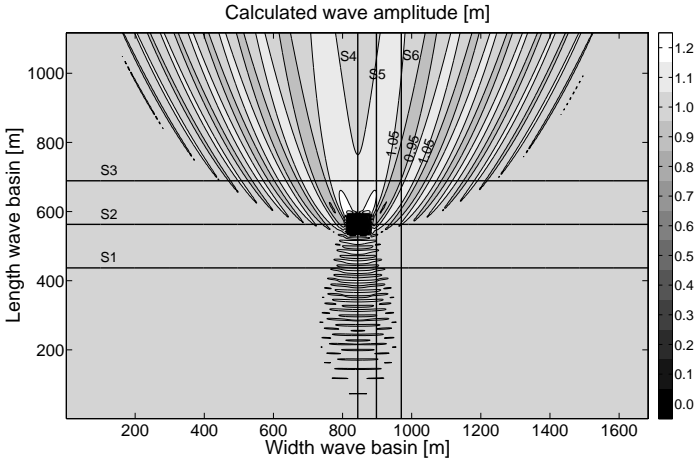


Figure 8.20: Calculated wave amplitude  $a$  in WAMIT

By determining the phase shift between the radiated and diffracted wave pattern (as calculated in WAMIT) in a longitudinal section at  $x^* = 844$  m behind the platform (Figure 8.21), the total wave pattern can be calculated in MILDwave. In this longitudinal section the radiated and diffracted wave have the same direction of wave propagation.

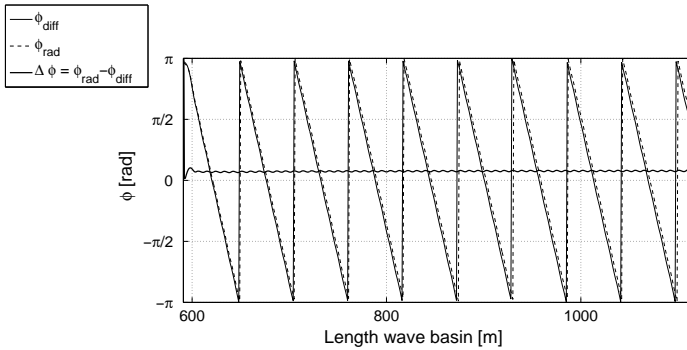


Figure 8.21: Difference between phase shift (relative to the centre of the FO<sup>3</sup> WEC) of the radiated and diffracted wave pattern

From Figure 8.21 it is seen that an additional phase shift of 0.24 rad ( $14^\circ$ ) is needed between the radiated and the diffracted wave pattern. Right behind the FO<sup>3</sup> WEC small variations in phase shift can be seen due to standing waves near

the platform (near field effects). In MILDwave each time step the diffracted and radiated wave pattern are calculated separately and afterwards the wave elevations and velocity potentials are summed up. By separating the calculation of both wave patterns the diffracted wave is not disturbed by the absorbing sponge in the wave generation circle. On the other hand the radiated wave is not disturbed by the obstacle needed for the simulation of the diffracted wave pattern. The resulting wave amplitude when diffraction and radiation are considered together in MILDwave, is shown in Figure 8.22.

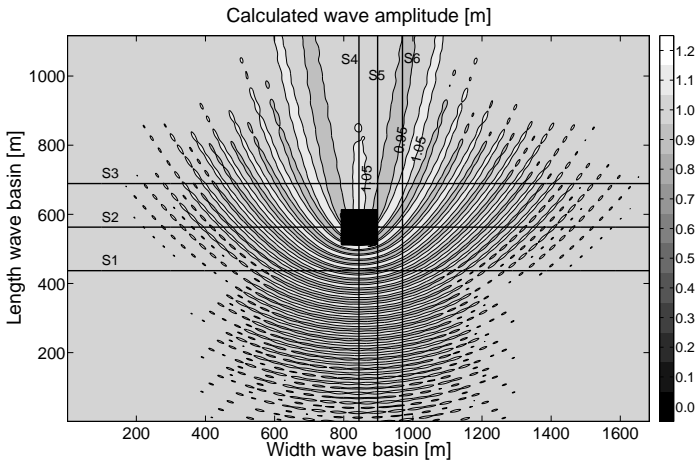


Figure 8.22: Calculated wave amplitude  $a$  in MILDwave

The resulting wave amplitude  $a$  is compared in more detail in two circular sections with centre equal to the centre of the FO<sup>3</sup> WEC and radius  $r_c = 70$  m and 126 m (Figure 8.23).



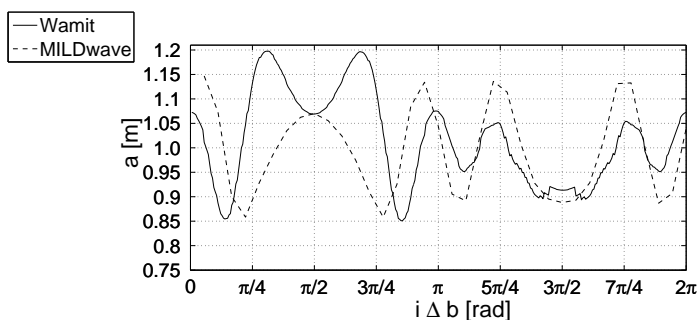
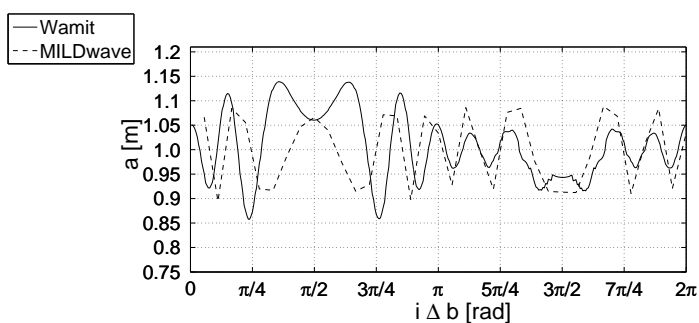
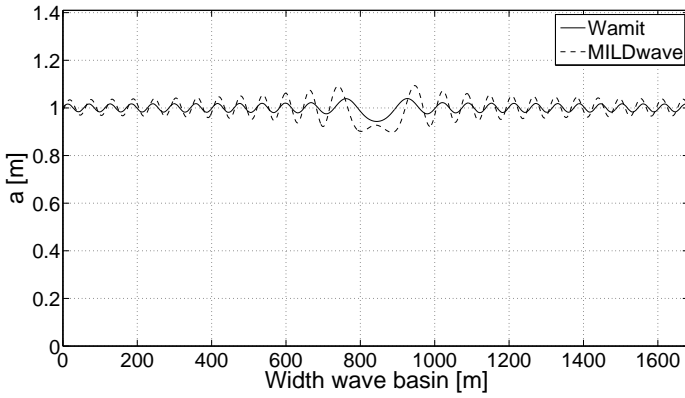
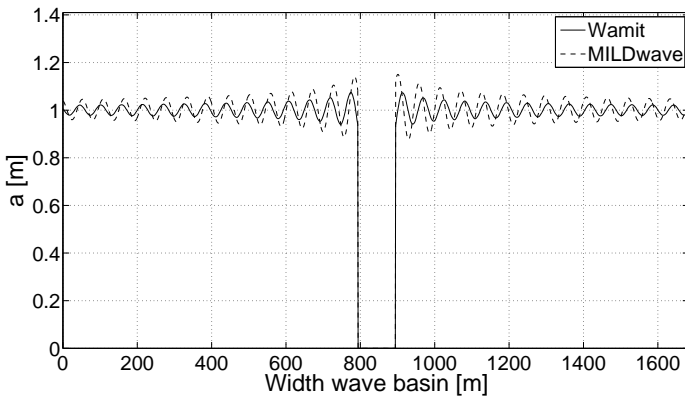
(a)  $r_c = 70$  m(b)  $r_c = 126$  m

Figure 8.23: Calculated wave amplitude  $a$  on a circle with centre equal to the centre of the FO<sup>3</sup> WEC and radius  $r_c = (a) 70$  m, (b) 126 m for regular incident waves with  $a = 1$  m and  $T = 6$  s

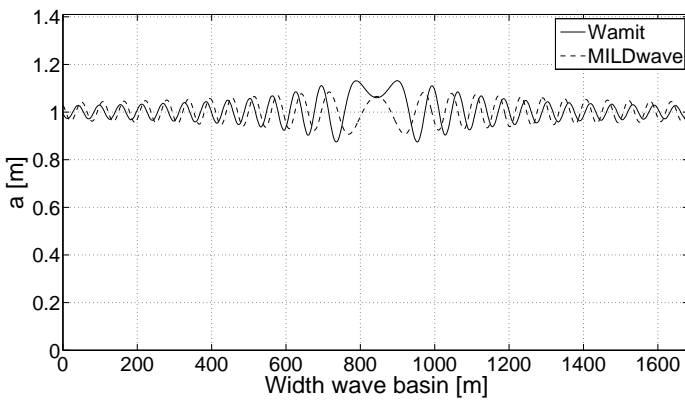
Furthermore the same lateral sections S1, S2 and S3 and longitudinal sections S4, S5 and S6 are considered as in previous sections (indicated on Figure 8.20 and Figure 8.22). Section S1, S2 and S3 are shown in Figure 8.24 and in more detail in Figure 8.26. Figure 8.25 shows section S4, S5 and S6. The same sections are given in more detail in Figure 8.27.



(a) Section S1

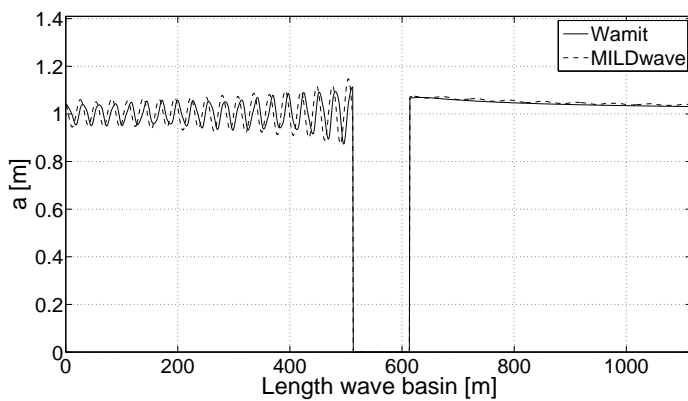


(b) Section S2

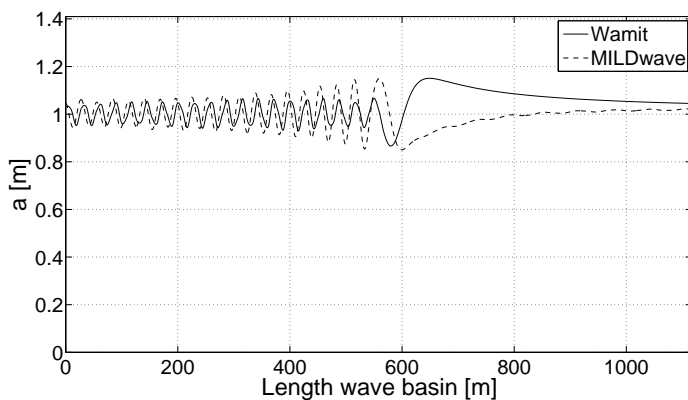


(c) Section S3

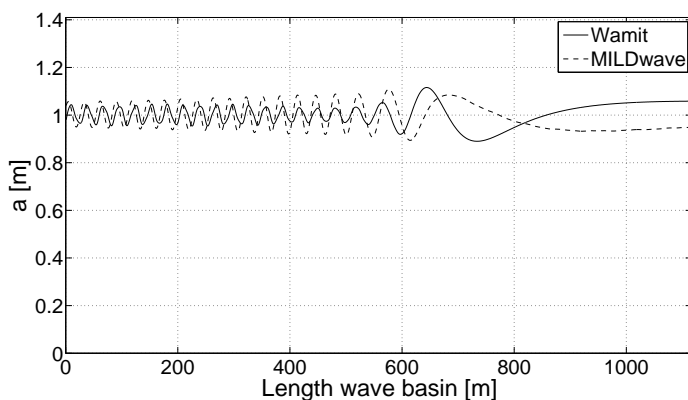
Figure 8.24: Calculated wave amplitude  $a$  in section (a) S1, (b) S2, (c) S3



(a) Section S4

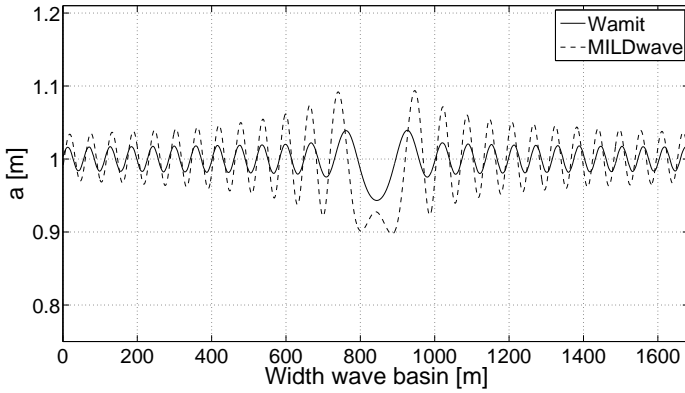


(b) Section S5

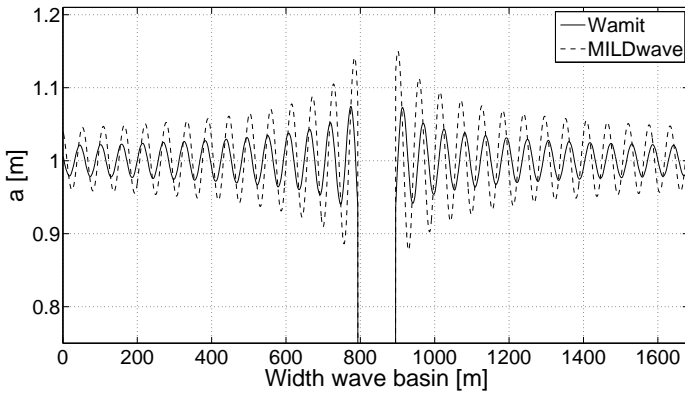


(c) Section S6

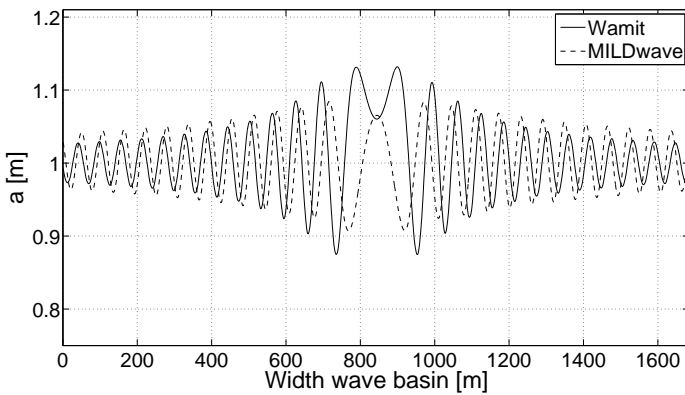
Figure 8.25: Calculated wave amplitude  $a$  in section (a) S4, (b) S5, (c) S6



(a) Section S1



(b) Section S2



(c) Section S3

Figure 8.26: Calculated wave amplitude  $a$  (zoomed in) in section (a) S1, (b) S2, (c) S3

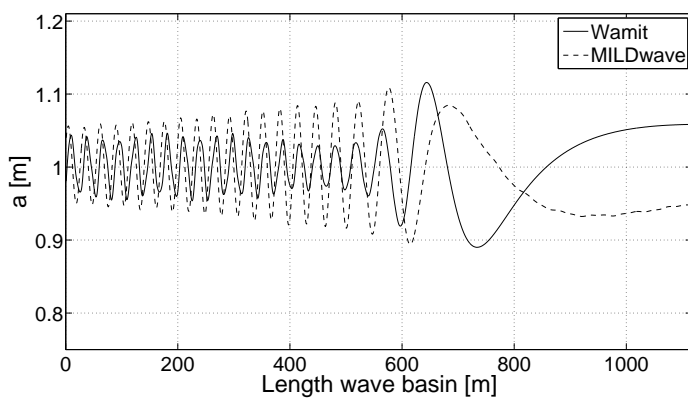
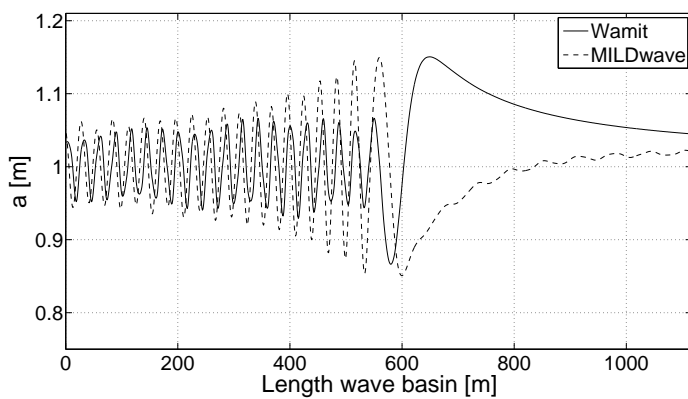
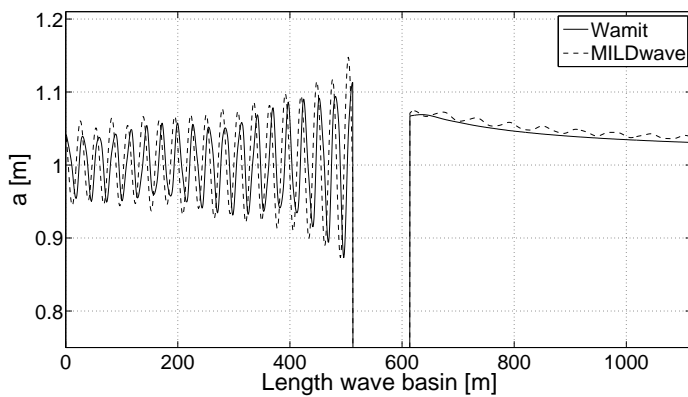


Figure 8.27: Calculated wave amplitude  $a$  (zoomed in) in section (a) S4, (b) S5, (c) S6

Figure 8.26(a) confirms the higher reflection observed in the MILDwave results. Figure 8.26 clearly indicates a spatial phase shift between the oscillations in WAMIT and MILDwave along the wave basin width. Figure 8.27(a) shows a very good agreement between the results in WAMIT and MILDwave along the length of the wave basin. The results in section S5 (Figure 8.27(b)) and S6 (Figure 8.27(c)) differ due to the spatial phase shift observed in the lateral sections S1, S2 and S3 (Figure 8.26). Furthermore, deviations between WAMIT and MILDwave as seen on the circular sections (Figure 8.23) are also due to the observed spatial phase shift.

To make a better comparison between the results in WAMIT and MILDwave the envelope of the oscillations along the width and length of the wave basin in WAMIT and MILDwave has been determined. Again an area of 180 m x 180 m has been ignored when calculating the envelope. The resulting envelopes of the WAMIT and MILDwave results are shown on Figure 8.28, respectively Figure 8.29.

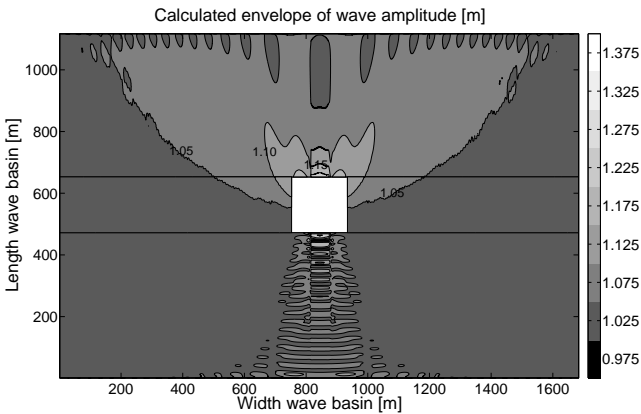


Figure 8.28: Calculated envelope in WAMIT

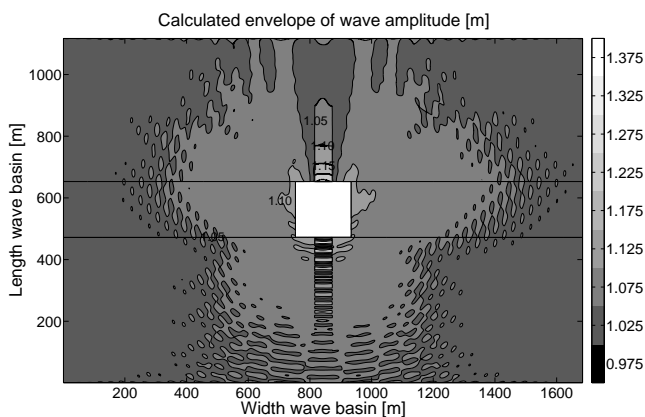


Figure 8.29: Calculated envelope in MILDwave

The difference between both envelopes is shown on Figure 8.30:

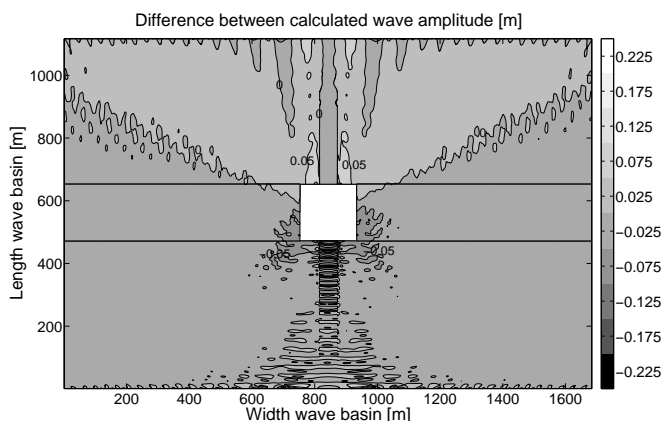


Figure 8.30: Difference between WAMIT and MILDwave

Again the differences between the wave amplitudes calculated from MILDwave and WAMIT are observed to be in the range of  $\pm 10\%$  in the whole domain. In the largest part of the domain the differences are reduced to the interval  $[-5\%, +5\%]$  which confirms the good agreement between the WAMIT and MILDwave results.

The mean absolute error over the computational domain is equal to 0.022 m and the root mean square error equals 0.026 m. Dividing the latter values to the mean value in WAMIT ( $= 1.041$  m) results in a MAE and RMSE of respectively, 2.10 % and 2.50 %. Similar results were obtained when only diffraction was

considered (section 8.2.2).

The total wave pattern for  $T = 4$  s and  $T = 8$  s is given in appendix F. The differences between  $a$  in MILDwave and WAMIT are comparable for  $T = 8$  s and a little higher for  $T = 4$  s.

### 8.3 A farm of 9 FO<sup>3</sup> WECs

After implementing a single FO<sup>3</sup> WEC in MILDwave, based on the diffraction and radiation wave patterns generated from WAMIT results, the overall power absorption of several lay-outs of FO<sup>3</sup> WECs is studied in this section. Two grid lay-outs, an aligned and a staggered grid, with varying in-between distances  $w = l$  are studied (Figure 6.24).

To study a farm of 9 FO<sup>3</sup> WECs the wave diffraction pattern (all platforms are assumed to be fixed) and the wave radiation pattern for each platform (1 platform is moving, the other 8 platforms are fixed) are calculated separately during each time step. Consequently, each time step 10 wave patterns are calculated and summed up.

The radiated wave pattern generated by each FO<sup>3</sup> WEC is determined in two steps. For simplicity the methodology is illustrated for a farm of two FO<sup>3</sup> WECs, as shown in Figure 8.31.

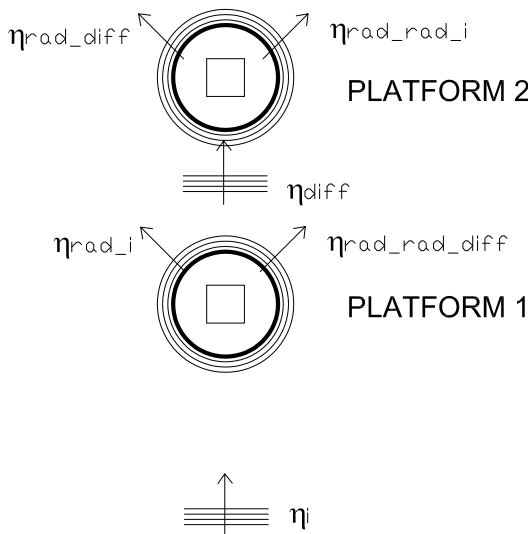


Figure 8.31: Definition sketch of interaction between two FO<sup>3</sup> WECs with an in-between distance of  $5D$

First the diffracted wave pattern caused by the incident wave in MILDwave



is calculated separately to determine the wave height in front of each FO<sup>3</sup> WEC. Further the amplitude of the radiated wave, as determined for a single FO<sup>3</sup> WEC (Figure 8.13), is multiplied with the calculated wave height in front of each platform, resulting in the primary radiated wave caused by the diffracted wave  $\eta_{rad-diff}$ . Note that in front of the first row of FO<sup>3</sup> WECs the incident wave is not diffracted yet. Consequently, the primary radiated wave of those WECs,  $\eta_{rad-i}$ , is caused by the incident wave.

In a second step the amplitude of the radiated wave of each FO<sup>3</sup> WEC ( $\eta_{rad-diff}$  or  $\eta_{rad-i}$ ) on the location of the neighbouring platform is calculated. For the neighbouring platform this radiated wave is another incident wave which causes secondary radiated waves ( $\eta_{rad-rad-i}$  or  $\eta_{rad-rad-diff}$  with  $\eta_{rad-rad-i}$ , the radiated wave in the second platform caused by the primary radiated wave  $\eta_{rad-i}$  of the first platform and with  $\eta_{rad-rad-diff}$ , the radiated wave in the first platform caused by the primary radiated wave  $\eta_{rad-diff}$  of the second platform). The amplitude of  $\eta_{rad-rad-i}$  is calculated by multiplying the amplitude of the radiated wave of a single FO<sup>3</sup> WEC, Figure 8.13, with the amplitude of  $\eta_{rad-i}$  in front of the second platform. The amplitude of  $\eta_{rad-rad-diff}$  is calculated by multiplying the amplitude of the radiated wave of a single FO<sup>3</sup> WEC, Figure 8.13, with the amplitude of  $\eta_{rad-diff}$  behind the first platform. The amplitude of these secondary radiated waves in front of the neighbouring platforms is in all cases smaller than 5 % of the incident wave. Therefore these secondary radiated waves are neglected in a first ‘engineering’ approach. As a consequence only 1 radiated wave, determined by the diffracted/incident wave height, has been generated around each FO<sup>3</sup> WEC.

For each lay-out the average total wave height (when considering the diffracted wave pattern and the nine radiated wave patterns) has been calculated in front of each FO<sup>3</sup> WEC. This wave height determines the absorption of each FO<sup>3</sup> WEC, as a single FO<sup>3</sup> WEC is absorbing 110 % ( $T = 6$  s) of the incident wave power (determined by  $H_i^2$  - appendix B) over the width of the device. A similar approach has been applied for regular incident waves with  $T = 4$  s and 8 s (appendix F).

The calculated wave amplitude  $a$  in a wave basin with nine FO<sup>3</sup> WECs installed in a staggered grid with an in-between distance of  $3D$  for a regular incident wave with  $a = 1$  m and respectively  $T = 4$  s, 6 s and 8 s is shown in Figure 8.32.

It is clear that the wave climate in and around the farm is very complicated. As the radiated wave for  $T = 8$  s has the smallest wave amplitude (Figure F.43(a)), less peaks occurs in the surrounding wave climate. For  $T = 4$  s the wake behind the FO<sup>3</sup> WEC caused by diffraction is rather narrow (Figure F.4). This phenomena causes a higher wave height in front of the WECs in the second row. Because of the relatively small in-between distance not much energy is travelling in-between

the WECs. Therefore a larger in-between distance is considered. Furthermore for  $T = 4$  s and 6 s a wave height increase is seen behind the FO<sup>3</sup> WECs. Consequently nine FO<sup>3</sup> WECs have been installed in an aligned grid as well.

The calculated wave amplitude  $a$  in a wave basin with nine FO<sup>3</sup> WECs installed in a staggered grid with an in-between distance of  $5D$  and in an aligned grid with an in-between distance of respectively  $3D$  and  $5D$  for a regular incident wave with  $a = 1$  m and  $T = 6$  s is shown in Figure 8.33.

When comparing Figure 8.32(b) and Figure 8.33(a), it is clear that there is more energy in front of the WECs in the second row for the largest in-between distance. When the WECs are installed in an aligned grid more energy is available in front of the WECs in the farm, not only in front of the second row, but also in front of the third row. In general, the wake effect behind a farm of FO<sup>3</sup> WECs is limited.

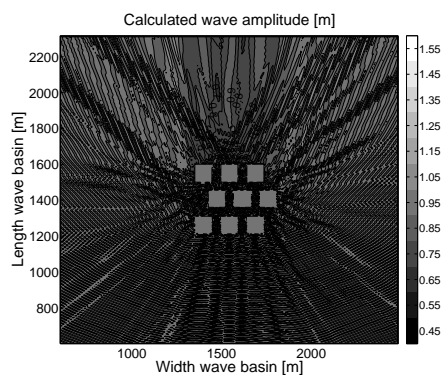
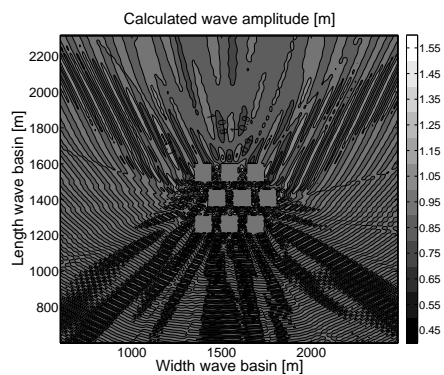
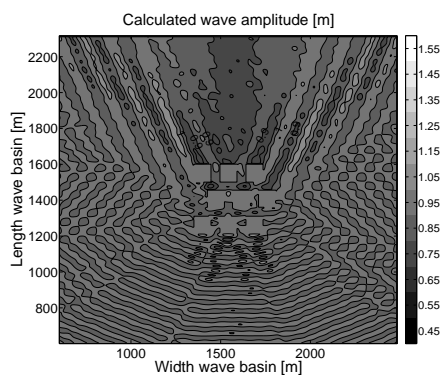
(a)  $T = 4$  s(b)  $T = 6$  s(c)  $T = 8$  s

Figure 8.32: Calculated wave amplitude  $a$  in a wave basin with nine FO<sup>3</sup> WECs installed in a staggered grid with an in-between distance of  $3D$  for a regular incident wave with  $a = 1$  m and respectively  $T =$  (a) 4 s, (b) 6 s and (b) 8 s

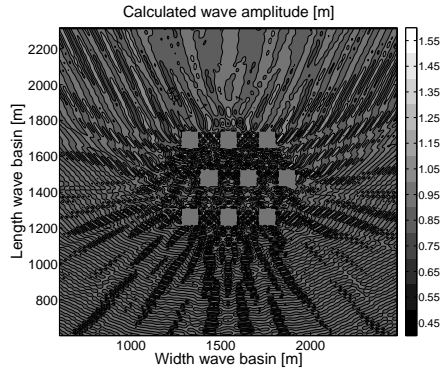
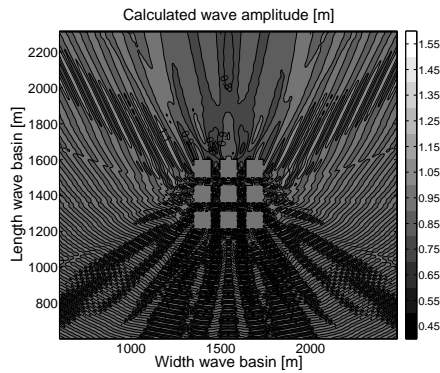
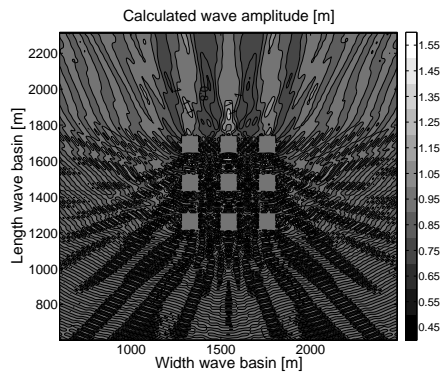
(a) Staggered grid with in-between distance =  $5D$ (b) Aligned grid with an in-between distance =  $3D$ (c) Aligned grid with an in-between distance =  $5D$ 

Figure 8.33: Calculated wave amplitude  $a$  in a wave basin with nine  $FO^3$  WECs installed in respectively (a) a staggered grid with an in-between distance of  $5D$ , (b) an aligned grid with an in-between distance of  $3D$  and (c) an aligned grid with an in-between distance of  $5D$  for a regular incident wave with  $a = 1$  m and  $T = 6$  s

The total power absorption of nine FO<sup>3</sup> WECs installed in two grids (staggered or aligned) with an in-between distance of  $3D$  or  $5D$  has been compared with the absorption of nine single FO<sup>3</sup> WECs which are not interacting. These nine single FO<sup>3</sup> WECs would absorb nine times  $P_{s,i}$ , with  $P_{s,i}$  the power absorbed by a single FO<sup>3</sup> WEC in the considered wave climate  $i$ . Furthermore the absorbed power per km<sup>2</sup> has been calculated for each lay-out. The results are given in Table 8.4.

Table 8.4: Power absorption of a farm of 9 FO<sup>3</sup> WECs for regular waves with  $H_i = 2$  m

$w = l$ [multiple of $D$ ]	Grid [—]	$T$ [s]	Difference in power absorption with nine single FO <sup>3</sup> WECs [multiple of $P_{s,i}$ ]	Power absorption per km <sup>2</sup> [MW/km <sup>2</sup> ]
3	aligned	6	0.8	49
3	staggered	6	-0.19	44
3	staggered	4	1.16	38
3	staggered	8	-0.26	20
5	aligned	6	1.4	23
5	staggered	6	0.68	22

The power absorption for  $T = 4$  s is higher compared with nine single WECs, while for  $T = 6$  s and 8 s a smaller absorption is seen. It is clear that the influence of the incident wave period is important. Consequently the lay-out should be optimized for the periods in the working range of the WEC. The power absorption increases with increasing in-between distance. An aligned grid results in a higher power absorption compared to a staggered grid, due to a wave height increase behind each FO<sup>3</sup> WEC as seen in Figure 8.27(a) for a single FO<sup>3</sup> WEC. A smaller in-between distance results in a higher absorption per km<sup>2</sup>. A detailed cost study should reveal whether an in-between distance of  $3D$  or  $5D$  is preferred.

As a comparison the power absorption has been calculated for a farm of 9 WECs with an in-between distance of  $3D$  installed in an aligned grid when the secondary waves with a wave amplitude higher than 2 % of the incident wave amplitude have been taken into account. This farm is absorbing 1.1  $P_{s,i}$  more than nine single WECs that are not interacting. Furthermore 51 MW per km<sup>2</sup> is absorbed. By taking the highest secondary waves into account 3 % more power is absorbed by the farm.

In this PhD dissertation only regular head-on waves have been considered. In future, other wave directions should be taken into account. Nevertheless it is expected that wake effects for other wave directions will be rather small as well.

## 8.4 Conclusions

In this chapter a methodology has been developed to implement a WEC of the first category. The FO<sup>3</sup> WEC has been used as an example. A validation data set on wave diffraction patterns had been generated in the numerical model WAMIT for regular waves with unit wave amplitude and wave period of respectively 4 s, 6 s and 8 s by NTNU (Norwegian Institute of Science and Technology). The diffraction patterns have been modelled in MILDwave using the sponge layer technique. The simulation results from MILDwave have been compared to the results from the validation data set obtained using WAMIT.

In general good agreement between the MILDwave and WAMIT results is observed for all wave periods. In the whole simulation domain, differences between the wave amplitudes calculated from MILDwave and WAMIT are in the range of  $\pm 10\%$  for  $T = 6$  s and  $T = 8$  s. For  $T = 4$  s a higher deviation is observed in small areas, respectively, in front of and behind, the FO<sup>3</sup> WEC. In general, a wider shadow zone behind the FO<sup>3</sup> WEC is observed in MILDwave (approximately 20 % to 27 % wider than the shadow zone in WAMIT). As in real sea conditions (short-crested waves) the pattern of the shadow zone will be disturbed, the latter difference is of minor concern.

Further a data set on wave radiation patterns, generated by the FO<sup>3</sup> WEC, had been calculated by NTNU from WAMIT results by considering a realistic power take-off for a regular wave with unit wave amplitude and wave period of respectively 4 s, 6 s and 8 s. The radiated wave patterns have been modelled in MILDwave by generating a wave with wave amplitude  $a$  and phase shift  $\phi$ , as determined from postprocessed simulation results in WAMIT, on a wave generation circle. Again a very good agreement is seen between the MILDwave and WAMIT results for  $T = 6$  s and 8 s. For  $T = 4$  s the wave length (25 m) is smaller than the deck size (36 m) of the FO<sup>3</sup> WEC. Therefore the FO<sup>3</sup> WEC experiences large pitch and surge motions which result in fast changes of  $\phi$  and  $a$  along the wave generation circle and consequently a higher interaction between the wave generation cells. A smaller grid size in MILDwave could decrease the deviation between the results in MILDwave and WAMIT for  $T = 4$  s.

Further the total wave patterns have been modelled by summing up the wave diffraction and wave radiation patterns. The phase shift between these wave patterns has been calculated from the WAMIT results. For  $T = 6$  s and 8 s, the agreement between  $a$  of the total wave pattern, calculated in WAMIT and MILDwave, is comparable to the agreement between  $a$  of the diffracted wave patterns (in the range of  $\pm 10\%$ ). For  $T = 4$  s, a large deviation (more than 10 %) is seen in front of and immediately behind the FO<sup>3</sup> WEC because of earlier deviations in  $a$  and  $\phi$  of the diffracted and radiated wave patterns.

Finally the amount of power absorbed by a farm of nine FO<sup>3</sup> WECs, installed

in a staggered or aligned grid with an in-between distance of  $3D$  or  $5D$ , has been calculated (with  $D$  = the width of the FO<sup>3</sup> WEC). By measuring the total wave height in front of each WEC in the farm, the absorption has been determined. Only primary radiated waves (radiated waves caused by the incident or diffracted wave pattern) have been considered when calculating the overall wave pattern, as the amplitude of the secondary radiated waves (radiated waves caused by primary radiated waves from neighbouring WECs) is smaller than 5 % of the incident wave amplitude in front of neighbouring WECs.

The power absorption increases with increasing in-between distance. Nine FO<sup>3</sup> WECs installed in an aligned grid absorb more than nine WECs in a staggered grid for  $T = 6$  s, due to a wave height increase behind each WEC. On the other hand, the absorption per km<sup>2</sup> increases for smaller in-between distances. In general, the wake effect behind a farm of FO<sup>3</sup> WECs is limited. Note that only regular head-on waves have been considered in this chapter.

## References

- [1] L. Mendes, A. Palha, J.F. Conceição, A. Brito-Melo, and A.J.N.A. Sarmiento. *Analysis of the Impact of a Pilot Zone for Wave Energy Conversion Offshore Portugal*. In Proceedings of the 18<sup>th</sup> International Offshore and Polar Engineering Conference (ISOPE), Vancouver, British Columbia, Canada, 2008.
- [2] I. Le crom, A. Brito-Melo, and A.J.N.A. Sarmiento. *Maritime Portuguese Pilot Zone for Wave Energy Conversion: Modelling Analysis of the Impact on Surfing Conditions*. In Proceedings of the 2<sup>nd</sup> International Conference on Ocean Energy (ICOE), Brest, France, 2008.
- [3] C. Vidal, F. J. Méndez, G. Díaz, and R. Legaz. *Impact of Santoña WEC installation on the littoral processes*. In Proceedings of the 7<sup>th</sup> European Wave and Tidal Energy Conference (EWTEC), Porto, Portugal, 2007.
- [4] R. Taghipour and T. Moan. *Efficient frequency-domain analysis of dynamic response for the multi-body wave energy converter in multi-directional waves*. In Proceedings of the 18<sup>th</sup> International Offshore and Polar Engineering Conference (ISOPE), Vancouver, Canada, 2008.
- [5] WAMIT User Manual [online]. Available from: <http://www.wamit.com/manual.htm>, [Accessed January 2009].
- [6] J. Falnes. *Ocean Waves and Oscillating Systems*. Cambridge University Press, 2002.
- [7] Z. Gao, J. Fan, and T. Moan. *Time-domain Coupled Mooring Analysis of the FO3 Wave Energy Converter (EU project SEEWEC, contract n°:SES6-CT2005-019969)*. Technical report, CeSOS, NTNU, 2009.
- [8] M.W. Dingemans. *Water wave propagation over uneven bottoms*. World Scientific, 1997.



## **Part III**

# **Cost of a farm of wave energy converters**



# 9

## Production and cost assessment of a farm of Wave Dragon wave energy converters

### 9.1 Introduction

In a third part of this PhD research the cost of a farm of WECs is discussed. The impact of the farm lay-out on the cost of a farm is studied in this chapter while in chapter 10 the influence of the location and the number of WECs on the farm investment is assessed.

In a first part of this chapter, the power production of three different farm lay-outs of WD-WECs with a rated power of 198 MW (99 WD-WECs arranged (i) in a single line, (ii) in a staggered grid and (iii) behind each other) in a near shore North Sea wave climate, is assessed in MILDwave. In a second part, an optimal (low cost) submarine cable network is designed for each lay-out by minimizing the cable cost and capitalized cost of expected constrained energy from cable losses. The cost per produced kWh is determined for each lay-out in order to select the optimal lay-out. Finally the impact of the wave height decrease behind a farm of WD-WECs on the accessibility of a farm of wind turbines installed in its lee is quantified.

## 9.2 Test conditions

In this chapter a WD-WEC, in a typical near shore North Sea wave climate (Location point 2 on the Danish Continental Shelf [1]) is studied. The mean annual available wave power on this location (Table 2.9) equals 12 kW/m (water depth  $h = 31$  m). Characteristic sea states on this location [1] for significant wave heights between 0.5 and 5.5 m and their related wave power (assuming a parameterized JONSWAP spectrum with  $\gamma = 3.3$ ) and frequency of occurrence are given in Table 9.1.<sup>1</sup>

Table 9.1: Wave situations in a near shore North Sea wave climate (Location point 2 (Table 2.8) on the Danish Continental Shelf [1])

Wave situation	$H_s$ [m]	$T_p$ [s]	Wave power $p$ [kW/m]	Frequency of occurrence (FO) [%]
1	1	5.6	2.5	48
2	2	7.0	12.4	21
3	3	8.4	33.5	10
4	4	9.8	69.6	4
5	5	11.2	124.2	1

The contribution ( $= p \text{ FO}$ ) of these 5 wave situations to the yearly average available wave power is shown in Figure 9.1. Wave situation 3 has the highest contribution to the annual average available wave power (30 %).

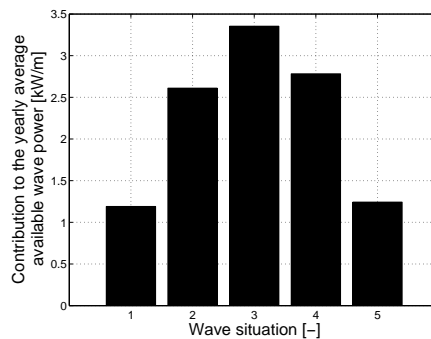


Figure 9.1: Contribution of the wave situations (Table 9.1) to the yearly average available wave power (12 kW/m)

<sup>1</sup>Wave heights smaller than 0.5 m and larger than 5.5 m (frequency of occurrence = 16 %) are neglected in the following, as they contribute only marginally to the total power production over a year.

Not all waves are coming from the same wave direction as shown in the wave rose in Figure 9.2. Each segment of the wave rose is divided into the considered  $H_s$ -intervals (Table 9.1) to indicate the contribution of high and low energetic waves. Most waves (more than 20 %) are coming from the northwest.

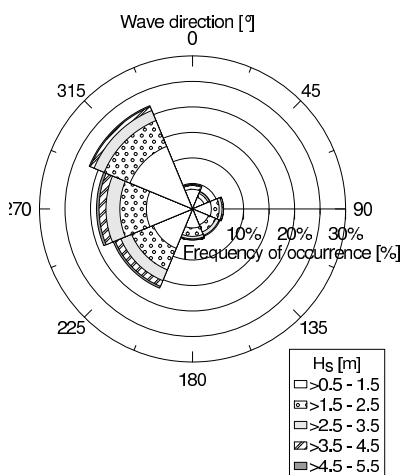


Figure 9.2: Wave rose for the near shore North Sea wave climate (12 kW/m)

The contribution of the different wave sectors to the average annual available wave power is shown in Figure 9.3. The sector west has the highest contribution.

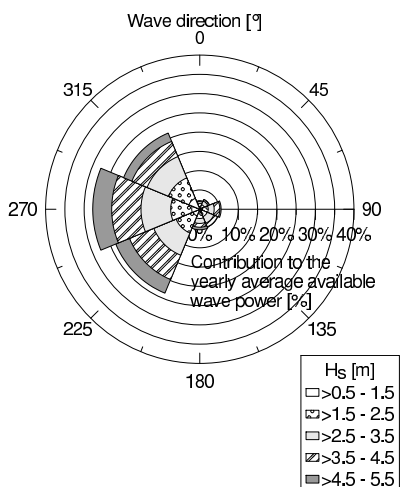


Figure 9.3: Contribution of wave sectors to the yearly average available wave power (12 kW/m)

In all simulations 20 frequency components are used to generate approximately 500 irregular short-crested waves with a time step of 0.10 s and 0.05 s for  $T_p = 5.6$  s and  $T_p = 7.0$  s, 8.4 s, 9.8 s and 11.2 s, respectively (cell dimensions of 1 m for all  $T_p$ ). A rather small directional width of  $9^\circ$  (value for  $f_p$  with  $s_{max} = 75$ ) is used, as a location near the coast is considered. The effect of the directional spreading on the wake is significant and has been analysed in chapter 7.

## 9.3 Power absorbed by a single Wave Dragon WEC

### 9.3.1 Rated power of a Wave Dragon WEC

A WD-WEC with a rated power of 4 MW is designed for a wave climate with a yearly average available wave power of 24 kW/m. The investment cost (including installation and mooring) per kW rated power of a 4 MW WD-WEC is available from Wave Dragon ApS. (Table 9.2).

Table 9.2: Investment cost of a 4 MW WD-WEC (Wave Dragon ApS.)

Wave climate [kW/m]	First device [€/kW]	After deployment of 100's [€/kW]
24	4 000	2 300

In this work, a WD-WEC is installed in a less energetic wave climate (12 kW/m). The mean annual power absorbed by a 4 MW WD-WEC in this wave climate is derived by multiplying the absorbed power in each sea state, calculated with equation (7.4), with its frequency of occurrence (Table 9.1) and summing up the results<sup>2</sup>. To obtain the electrical power, the absorbed power has been multiplied with a factor 0.7 to account for losses in turbines and generator (the overall efficiency of turbines and generators was estimated to 0.8-0.85 [2]), spilling when waves overtop and a lower head across the turbine than the crest freeboard. The ratio of the average produced electrical power to the rated power (= capacity factor) equals only 9 % for a 4 MW WD-WEC installed in the wave climate of 12 kW/m. Consequently the investment cost of the 4 MW WD-WEC per produced kWh is very high. Furthermore a farm of 4 MW WD-WECs requires large subsea cables and transformers which will increase the cost of the farm. Therefore a more realistic WD-WEC with the same structural dimensions as a 4 MW converter, but with a smaller rated power, equal to 2 MW, is considered in this chapter. The mean annual produced electrical power by the 2 MW WD-WEC is only 10 % smaller than the electrical power produced by a 4 MW WD-WEC;

<sup>2</sup>By using Table 9.1 it is assumed that the WD-WEC can absorb waves from all wave sectors.

so the capacity factor (16 %) is almost the double. Consequently a 2 MW-WEC is more suitable for the less energetic wave climate of 12 kW/m.

### 9.3.2 Wake behind a Wave Dragon WEC

In this section the wake behind a single WD-WEC with a rated power of 4 and 2 MW has been studied for wave situations in a near shore North Sea wave climate (Table 9.1).

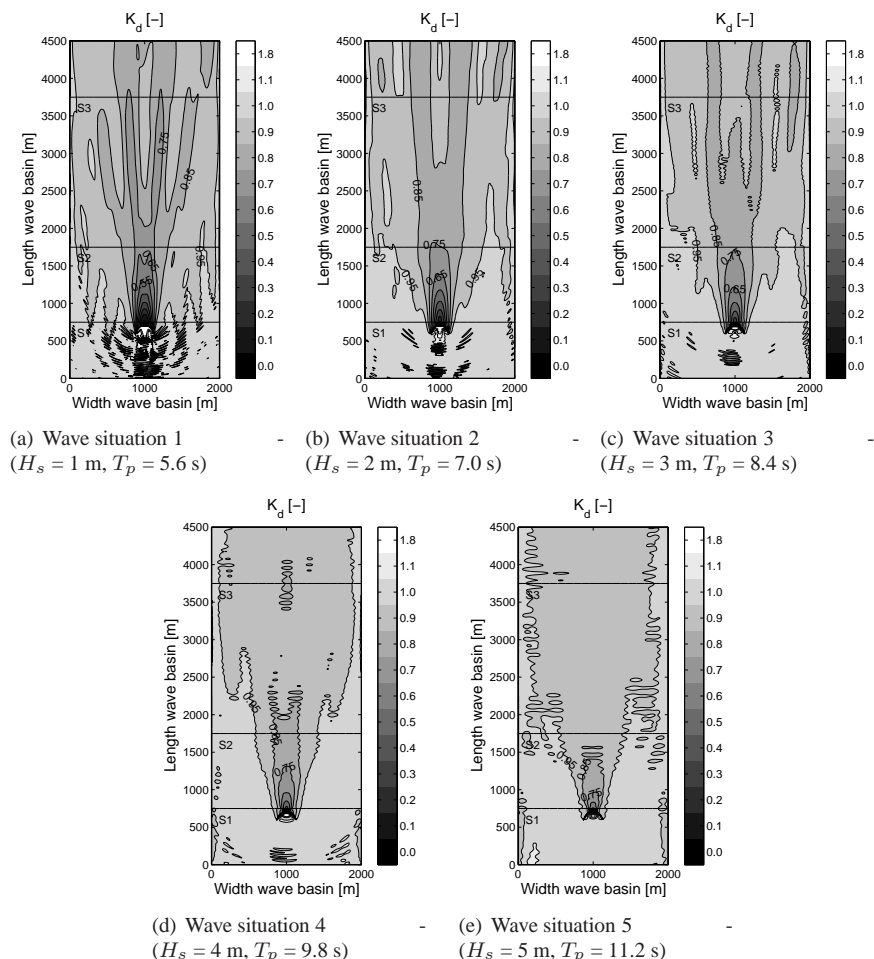


Figure 9.4: Calculated disturbance coefficient  $K_d$  in a wave basin with a single WD-WEC, with a rated power of 4 MW, for irregular short-crested waves (head-on) with  $s_{max} = 75$  and, respectively,  $H_s =$  (a) 1, (b) 2, (c) 3, (d) 4 and (e) 5 m and, respectively,  $T_p =$  (a) 5.6, (b) 7.0, (c) 8.4, (d) 9.8 and (e) 11.2 s

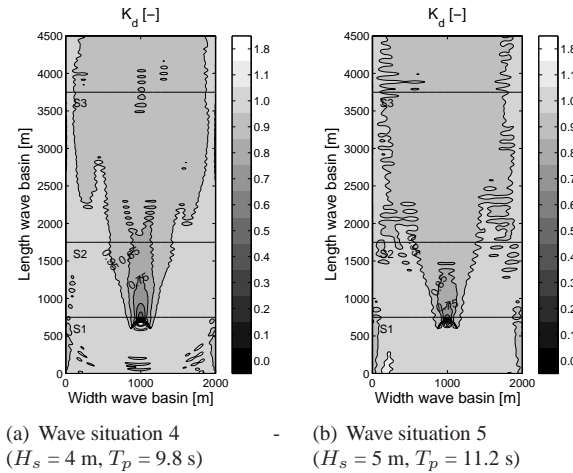


Figure 9.5: Calculated disturbance coefficient  $K_d$  in a wave basin with a single WD-WEC, with a rated power of 2 MW, for irregular short-crested waves (head-on) with  $s_{max} = 75$  and, respectively,  $H_s = (a) 4$  and  $(b) 5$  m and, respectively,  $T_p = (a) 9.8$  and  $(b) 11.2$  s

The disturbance coefficient  $K_d$  in a wave basin with a single WD-WEC (rated power of 4 MW) for short-crested (head-on) waves with  $H_s = 1, 2, 3, 4$  and  $5$  m,  $T_p = 5.6, 7.0, 8.4, 9.8$  and  $11.2$  s, respectively, and  $s_{max} = 75$  are shown in Figure 9.4. Figure 9.4(a) is identical to Figure 7.13(b), but is repeated here for convenience.

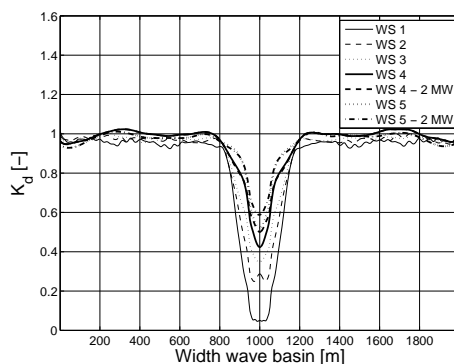
The remaining wave height behind the WD-WEC is increasing for higher significant wave heights and peak wave periods. When the rated power is limited to 2 MW, the floating level of the WD-WEC will be higher in higher waves to avoid too much wave overtopping. Consequently more energy will be transmitted under the WD-WEC. The wake behind a 2 MW WD-WEC in wave situation 4 and 5 is shown in Figure 9.5. For wave situation 1, 2 and 3 the wake behind a 4 MW WD-WEC is identical to the wake behind a 2 MW WD-WEC.

At first sight the wake seems comparable to the wake for a 4 MW WD-WEC (Figure 9.4(d) and Figure 9.4(e)). A closer look immediately behind the WD-WEC shows a slightly higher wave height for the 2 MW WD-WEC (Figure 9.5).

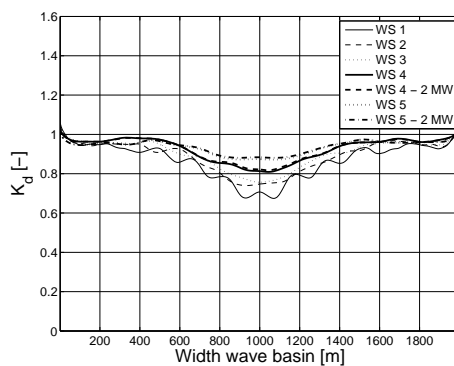
Three lateral sections S1, S2 and S3 behind the WD-WEC (indicated on Figure 9.4 and Figure 9.5) are compared in more detail in Figure 9.6 for the same wave situations and rated wave power as considered in Figure 9.4 and Figure 9.5.

The decrease in wave height behind the WD-WEC at  $y^* = 750$  m (section S1) is higher for lower wave situations. As expected, the remaining wave height is higher for a WD-WEC with a rated power of 2 MW. Furthermore, the width of the

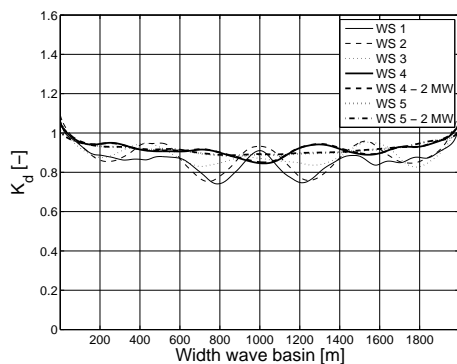




(a) Section S1 at  $y^* = 750$  m



(b) Section S2 at  $y^* = 1\ 750$  m



(c) Section S3 at  $y^* = 3\ 750$  m

Figure 9.6: Calculated disturbance coefficient  $K_d$  in lateral sections at, respectively,  $y^* =$  (a) 750 m, (b) 1 750 m and (c) 3 750 m, as indicated on Figure 9.4 and Figure 9.5, in a wave basin with a single WD-WEC for wave situations (WS) as given in Table 9.1

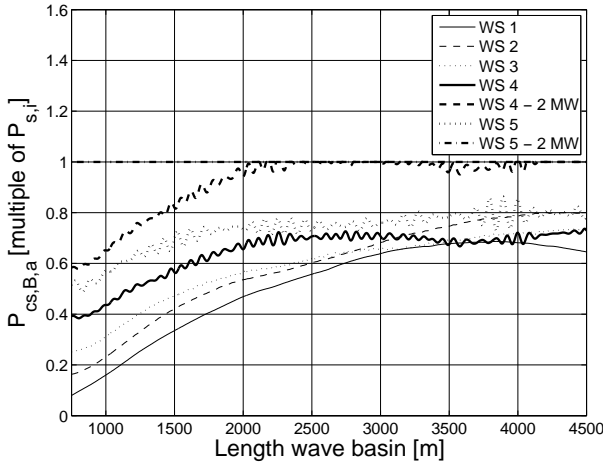


Figure 9.7: Power absorbed by a second WD-WEC installed between  $x^* = 870$  m and  $x^* = 1\,130$  m in a wave basin with a single WD-WEC for irregular short-crested (head-on) waves (SCW)

wake is small compared to Figure 9.6(b) and Figure 9.6(c). In the latter sections the effects of the directional spreading of the waves are clearly present. The wake effects are gradually spreading out (smaller decrease in wave height and wider wake). At  $y^* = 1\,750$  m (section S2) the difference between a WD-WEC with a rated power of 4 MW and 2 MW is very small and at  $y^* = 3\,750$  m (3 km behind the WEC) the difference cannot be distinguished anymore.

The possible power absorbed by a second WD-WEC, installed behind the first WD-WEC between  $x^* = 870$  m and  $x^* = 1\,130$  m, along the length of the wave basin is shown in Figure 9.7. First the average significant wave height in front of the second WD-WEC has been calculated (Figure 9.4 and 9.5). Further this average wave height and the incident peak wave period are used to estimate the overtopping rate and consequently the absorbed power  $P_{cs,B,a}$  of the second WD-WEC with equation (7.4). The possible power absorbed by a second WD-WEC is shown as a fraction of  $P_{s,i}^3$ . Note that the values on Figure 9.7 are only given behind the first WD-WEC (from  $y^* = 750$  m).

In general the possible power absorption is increasing further away from the first WD-WEC. Until approximately  $y^* = 3\,000$  m a higher wave situation results in a higher possible power absorption behind the first WD-WEC. From  $y^* = 3\,000$  m on, the power absorption for wave situation 2 is higher compared to wave situation 3 and 4. This difference can be explained when studying Figure 9.6(c). In this lateral section a central peak is observed in the wake for

<sup>3</sup> $P_{s,i}$  is the power absorbed by a single WEC in the considered wave situation  $i$  ( $i=1, 2, 3, 4$  and  $5$ ).

wave situation 2 resulting in a higher value of  $K_d$  and  $P_{cs,B,a}$  in the central part of the domain. By limiting the rated power of the WD-WEC to 2 MW, a second WD-WEC can absorb as much wave power as the first WD-WEC in wave situation 4 (from  $y^* = 2\,000$  m) and 5 (from  $y^* = 750$  m) (Figure 9.7).

As the rotation of the WD-WEC is assumed to be restricted to  $\pm 60^\circ$  by its anchor system [3], a WD-WEC can not absorb waves from all wave sectors. As most energy is coming from the sector west (Figure 9.3), a WD-WEC will be directed towards this direction to absorb as much energy as possible. The anchor system allows the WD-WEC to turn and to capture waves from the neighbouring sectors, i.e. northwest and southwest, as well. Furthermore small fractions from the sectors north and south can also be absorbed. These fractions will be neglected in the following. In Table 9.1 a weighted average frequency of occurrence of near shore North Sea wave situations is given for all wave sectors. The frequency of occurrence of these wave situations for the wave sectors southwest, west and northwest are given in Figure 9.2. It has been assumed that the wave period remains unchanged for each wave situation, as this information could not be derived from the Danish Wave Energy Atlas [1].

The power absorbed by a WD-WEC, with a rated power of 2 MW, installed in the lee of the first one (between  $x^* = 870$  m and  $x^* = 1\,130$  m) at  $y^* = 1\,750$  m and  $3\,750$  m, is given in Table 9.3 for each wave situation and wave sector. The absorbed power is again calculated with equation (7.4). The average remaining significant wave height in front of the second WD-WEC is assessed with Figure 9.4(a), 9.4(b) and 9.4(c) for wave situation 1, 2 and 3 and Figure 9.5(a) and 9.5(b) for wave situation 4 and 5. By turning these figures over  $\pm 45^\circ$  results for the sectors northwest and southwest are obtained.

Table 9.3: Absorbed power  $P_{cs,B,a}$  of a second WD-WEC installed in the lee of the first one in 5 wave situations (WS) and 3 wave sectors

Position 2 <sup>nd</sup> WEC Wave sector	$y^* = 1\,750$ m			$y^* = 3\,750$ m		
	NW	W	SW	NW	W	SW
WS 1 [multiple of $P_{s,1}$ ]	0.89	0.41	0.89	1	0.68	1
WS 2 [multiple of $P_{s,2}$ ]	0.90	0.49	0.90	1	0.78	1
WS 3 [multiple of $P_{s,3}$ ]	0.91	0.52	0.91	1	0.71	1
WS 4 [multiple of $P_{s,4}$ ]	1	0.89	1	1	0.98	1
WS 5 [multiple of $P_{s,5}$ ]	1	1	1	1	1	1
All WS ( $\bar{P}_{cs,B,a}$ ) [multiple of $P_{s,overall}$ ]	0.29	0.22	0.30	0.32	0.30	0.32
Average yearly absorbed power ( $\bar{P}_{cs,B,a}$ ) [multiple of $P_{s,overall}$ ]	0.81			0.93		

For the sectors northwest and southwest the second WD-WEC is less affected by the first WD-WEC (Table 9.3), as both WECs are rotated over  $\pm 45^\circ$ . By multiplying the frequency of occurrence of the North Sea wave situations (WS) of each of these wave sectors (Figure 9.2) with its corresponding absorbed power (Table 9.3) and summing up the results, the yearly average power absorbed by a WD-WEC is calculated (equation (9.1)).

$$\begin{aligned}\bar{P}_{cs,B,a} &= \sum_{j=1}^3 \sum_{i=1}^5 P_{cs,B,a_{i,j}} FO_{i,j} \\ &= \sum_{j=1}^3 \bar{P}_{cs,B,a_j}\end{aligned}\quad (9.1)$$

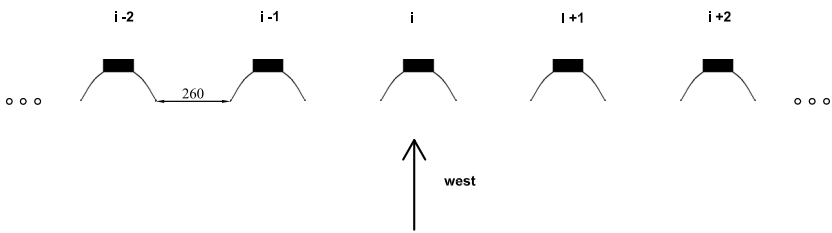
with  $P_{cs,B,a_{i,j}}$  the power absorbed by the WD-WEC in wave situation (WS)  $i$  and for wave direction or wave sector  $j$ ,  $FO_{i,j}$  the frequency of occurrence of wave situation  $i$  in wave sector  $j$  and  $\bar{P}_{cs,B,a_j}$  the average power absorbed by the WD-WEC in wave sector  $j$ .

$P_{s,overall}$  is the yearly average absorbed power of a single WD-WEC with a rated power of 2 MW. The second WD-WEC absorbs yearly on average  $\bar{P}_{cs,B,a} = 0.81 P_{s,overall}$  and  $0.93 P_{s,overall}$  for  $y^* = 1750$  m and  $y^* = 3750$  m, respectively. A second WD-WEC, installed 1 km behind the first WD-WEC, only absorbs 81 % of the power absorbed by the first WD-WEC. In a farm of wind turbines with a spacing of approximately 7 rotor diameters (which is in general smaller than 1 km) each wind turbine has a production between  $0.85 P_{overall,max}$  and  $1.0 P_{overall,max}$ , with  $P_{overall,max}$  the maximum production of a wind turbine in the farm. Installing the wind turbines in a staggered or aligned grid has almost no influence on the power production. The absorbed power of a second WD-WEC installed 1 km behind a single WD-WEC is already smaller than  $0.85 P_{s,overall}$ . Consequently a good lay-out of a farm of WD-WECs is needed to increase the absorbed power and reduce the required sea area. In the following WD-WECs with a rated power of 2 MW are considered.

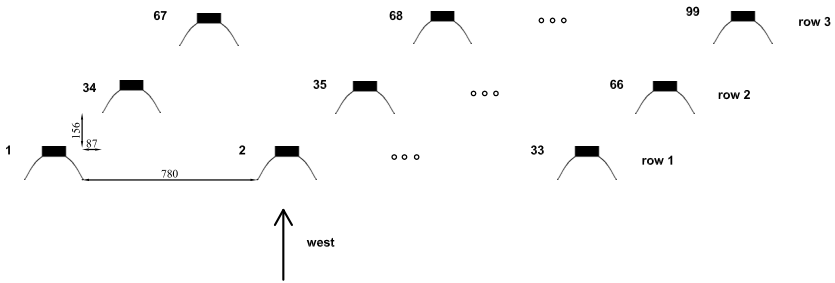
## 9.4 Production of a farm of Wave Dragon WECs

The power absorbed by a row or multiple rows of WD-WECs affect the available wave power for WD-WECs in their lee. The impact of the farm lay-out on the power absorption is studied in this section for three different grids of WD-WECs; (i) all WD-WECs installed in a single line (lay-out A), (ii) a staggered grid lay-out (lay-out B) and (iii) all WD-WECs installed behind each other (lay-out C). These three lay-outs are shown in Figure 9.8. In lay-out A and B, WD-WECs are placed as close as possible to reduce the required sea area. A minimal lateral spacing of

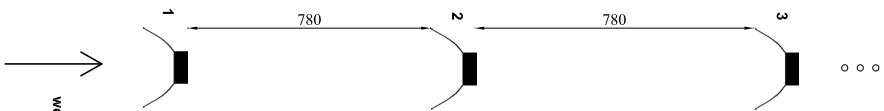
260 m is needed between two adjacent WD-WECs in lay-out A to prevent collision (Figure 7.18). A minimal longitudinal spacing of 156 m and lateral spacing of 87 m is required between two adjacent WD-WECs to prevent collision in lay-out B (Figure 9.9). In each lay-out 99 WD-WECs are installed, resulting in a rated power of 198 MW. The WD-WECs are indicated with numbers on Figure 9.8. Each farm will be positioned towards the west direction, as this wave sector has the highest contribution to the yearly average available wave power (Figure 9.3).



(a) Lay-out A: a single line of WD-WECs

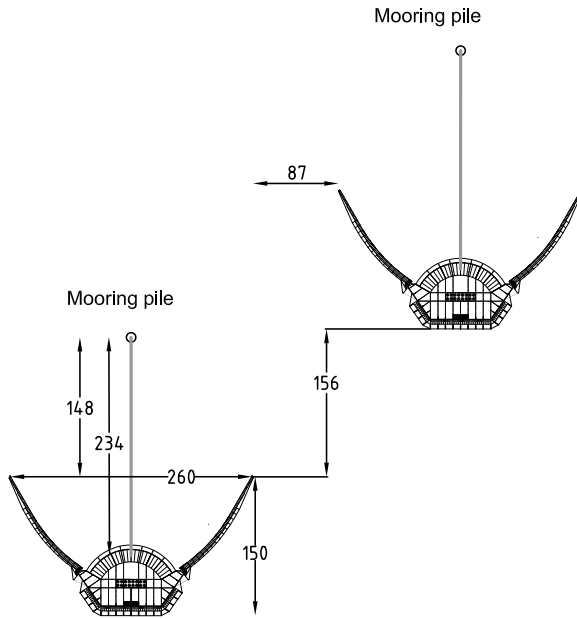


(b) Lay-out B: a staggered grid lay-out

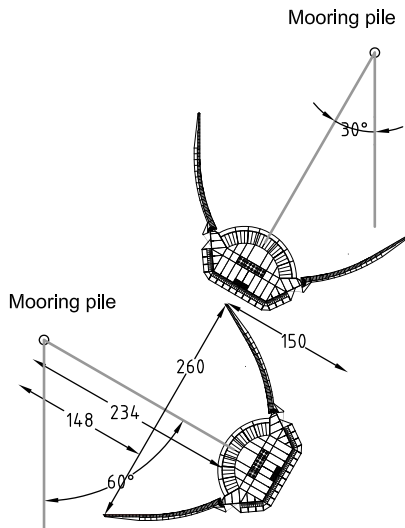


(c) Lay-out C: all WD-WECs installed behind each other

Figure 9.8: WD-WECs installed (a) in a single line (lay-out A), (b) in a staggered grid (lay-out B) and (c) behind each other (lay-out C)



(a) Both WECs facing the mean direction of wave propagation



(b) First WEC rotated over 60°

Figure 9.9: Definition sketch of minimum distance between WD-WECs in lay-out B - dimensions in m

### 9.4.1 Lay-out A: a single line of WD-WECS

The wake behind a single line of WD-WECS is shown in Figure 9.10 for the wave situation with the highest contribution to the yearly average available wave power (Figure 9.1), wave situation 3.

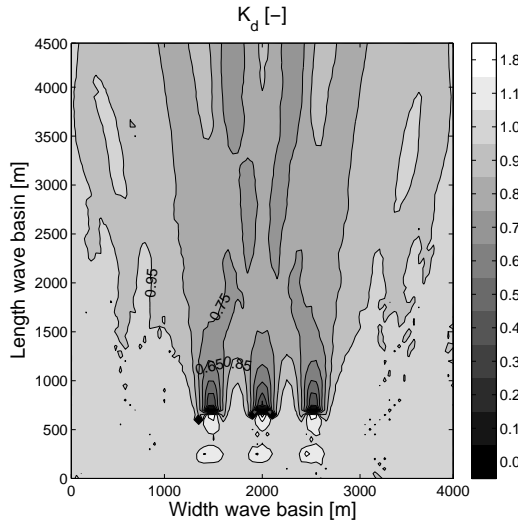


Figure 9.10: Calculated disturbance coefficient  $K_d$  in a wave basin with 3 WD-WECS with a lateral spacing of 260 m for short-crested waves (SCW) with  $H_s = 3$  m,  $T_p = 8.4$  s (wave situation 3) and  $s_{max} = 75$  coming from the sector west

When waves are coming from the sector west (Figure 9.10), each WD-WECS is absorbing the same amount of power as a single WD-WECS (Table 9.4).

For waves from the northwest, only the first WD-WECS (WD-WECS 1) has the same amount of absorption as a single WD-WECS. To determine the power absorbed by the second WD-WECS for the sector northwest Figure 9.4(a), 9.4(b) and 9.4(c) and Figure 9.5 have been turned over  $45^\circ$ . The average remaining wave height in front of the second WD-WECS has been calculated and equation (7.4) has been used to calculate  $P_{cs,B,a}$ . Each other WD-WECS in this lay-out will be affected by the edge of the wake of the previous WD-WECS for the sector northwest. The absorbed power of WD-WECS 2 to 99 is, respectively, equal to  $0.86 P_{s,1}$ ,  $0.90 P_{s,2}$ ,  $0.93 P_{s,3}$  for wave situation 1, 2 and 3. For wave situation 4 and 5 the absorbed power remains maximal.

For waves from the southwest direction the same amount of absorbed power is observed. Note that for this direction the last WD-WECS (WD-WECS 99) has a power absorption equal to the absorption of a single WD-WECS instead of the first one and that the power absorbed by the first WD-WECS, instead of the last one, is

reduced.

The yearly average absorbed power of each WD-WEC in the farm is given in Table 9.4. The yearly average absorbed power has been calculated in the same way as in Table 9.3. Each WD-WEC absorbs approximately 95 % of the power absorbed by a single WD-WEC. 5 % of wave power is lost due to small wake effects when waves are coming from the northwest or southwest. The first and last WEC have a slightly higher power absorption, as their incident wave power is not affected by the wake of another WEC when waves are coming from the northwest and southwest, respectively.

Table 9.4: Absorbed power  $P_{cs,B,a}$  of lay-out A in 5 wave situations (WS) and 3 wave sectors

Number WD-WEC Wave sector	1			2 - 98			99		
	NW	W	SW	NW	W	SW	NW	W	SW
WS 1 [multiple of $P_{s,1}$ ]	1	1	0.86	0.86	1	0.86	0.86	1	1
WS 2 [multiple of $P_{s,2}$ ]	1	1	0.90	0.90	1	0.90	0.90	1	1
WS 3 [multiple of $P_{s,3}$ ]	1	1	0.93	0.93	1	0.93	0.93	1	1
WS 4 [multiple of $P_{s,4}$ ]	1	1	1	1	1	1	1	1	1
WS 5 [multiple of $P_{s,5}$ ]	1	1	1	1	1	1	1	1	1
All WS ( $\bar{P}_{cs,B,a}$ ) [multiple of $P_{s,overall}$ ]	0.32	0.36	0.30	0.29	0.36	0.30	0.29	0.36	0.32
Average yearly absorbed power ( $\bar{P}_{cs,B,a}$ ) [multiple of $P_{s,overall}$ ]	0.98			0.95			0.97		
Average yearly absorbed power lay-out A = 94 $P_{s,overall}$									

### 9.4.2 Lay-out B: a staggered grid lay-out

The wave height reduction behind a staggered grid with 9 WD-WECs with a lateral spacing of 87 m and a longitudinal spacing of 156 m for short-crested waves with  $H_s = 3$  m,  $T_p = 8.4$  s and  $s_{max} = 75$  (wave situation 3) from the sectors west ( $\theta_0 = 90^\circ$ ), northwest ( $\theta_0 = 45^\circ$ ) and southwest ( $\theta_0 = 135^\circ$ ) is shown in Figure 9.11. Note that only 6 WD-WECs are installed for the sectors northwest and southwest. The position of the other three WD-WECs is indicated.

The amount of power absorbed by the farm is determined in two steps. In a first step, only the first row of WECs is installed in the simulation domain. In this domain, the average significant wave height in front of the WECs in the second row is calculated, to determine the absorbed power of these WECs with equation (7.4). In a second step, the first two rows of WECs are installed. The absorbed power of the WD-WECs in a third row is estimated by calculating the average significant



wave height in front of these WECs. The latter situation is shown for the sectors northwest and southwest in Figure 9.11(b) and Figure 9.11(c).

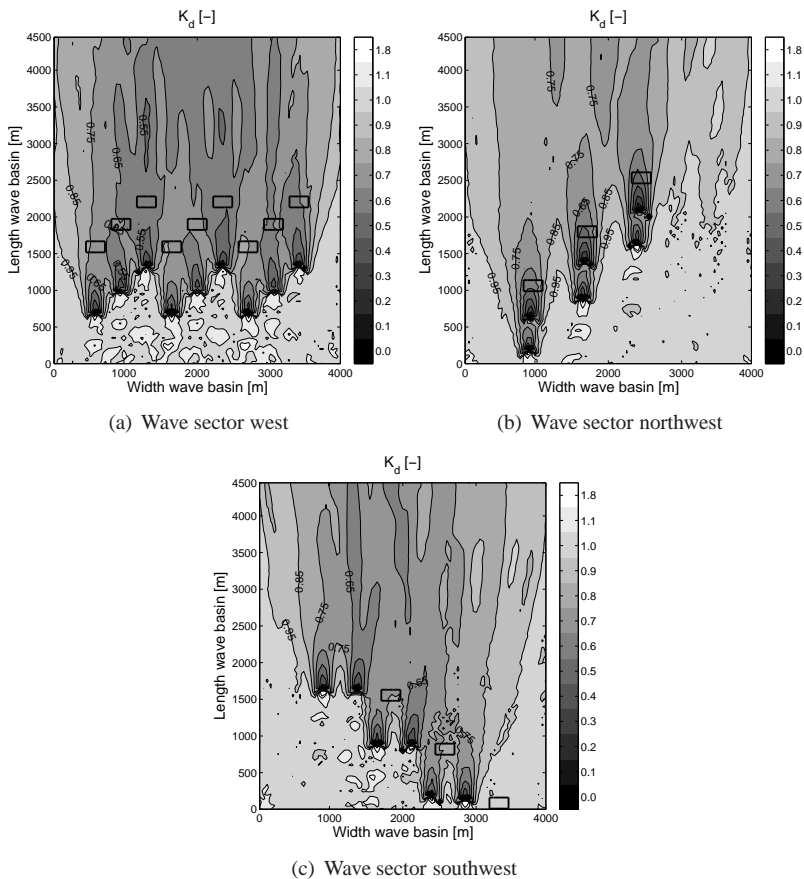


Figure 9.11: Calculated disturbance coefficient  $K_d$  in a wave basin with 9 WD-WECs with a lateral spacing of 87 m and a longitudinal spacing of 156 m for short-crested waves (SCW) with  $H_s = 3$  m,  $T_p = 8.4$  s (wave situation 3),  $s_{max} = 75$  and  $\theta_0 =$  (a)  $90^\circ$ , (b)  $45^\circ$  and (c)  $135^\circ$

The results for these 9 WECs have been extended to 99 WECs, by multiplying the absorbed power of the WEC in the middle of each row with 31. The resulting power absorbed by each WEC is given in Table 9.5<sup>4</sup>.

<sup>4</sup>The number of each WD-WEC is indicated on Figure 9.8.

Table 9.5: Absorbed power  $P_{cs,B,a}$  of lay-out B in 5 wave situations (WS) and 3 wave sectors

Row	1			2			3					
Number WD-WEC	1	2	32	33	34	35	65	66	67	68	98	99
<b>Wave sector northwest</b>												
WS 1 [multiple of $P_{s,1}$ ]	1	1	1	0.38	0.35	0.32	0.28	0.24	0.23			
WS 2 [multiple of $P_{s,2}$ ]	1	1	1	0.29	0.27	0.24	0.21	0.18	0.17			
WS 3 [multiple of $P_{s,3}$ ]	1	1	1	0.39	0.35	0.32	0.28	0.24	0.23			
WS 4 [multiple of $P_{s,4}$ ]	1	1	1	0.80	0.72	0.65	0.58	0.49	0.47			
WS 5 [multiple of $P_{s,5}$ ]	1	1	1	1	1	1	1	0.91	0.87			
All WS ( $\bar{P}_{cs,B,a}$ )	0.32	0.32	0.32	0.14	0.13	0.12	0.11	0.09	0.09			
[multiple of $P_{s,overall}$ ]												
Absorbed power sector NW = 18 $P_{s,overall}$												
<b>Wave sector west</b>												
WS 1 [multiple of $P_{s,1}$ ]	1	1	1	0.94	0.94	0.90	0.81	0.81	0.96			
WS 2 [multiple of $P_{s,2}$ ]	1	1	1	0.92	0.92	0.88	0.77	0.77	0.84			
WS 3 [multiple of $P_{s,3}$ ]	1	1	1	0.94	0.94	0.90	0.81	0.81	0.96			
WS 4 [multiple of $P_{s,4}$ ]	1	1	1	1	1	1	1	1	1			
WS 5 [multiple of $P_{s,5}$ ]	1	1	1	1	1	1	1	1	1			
All WS ( $\bar{P}_{cs,B,a}$ )	0.36	0.36	0.36	0.34	0.34	0.33	0.31	0.31	0.34			
[multiple of $P_{s,overall}$ ]												
Absorbed power sector W = 33 $P_{s,overall}$												
<b>Wave sector southwest</b>												
WS 1 [multiple of $P_{s,1}$ ]	1	1	1	0.42	0.46	1	0.48	0.52	1			
WS 2 [multiple of $P_{s,2}$ ]	1	1	1	0.40	0.44	1	0.46	0.50	1			
WS 3 [multiple of $P_{s,3}$ ]	1	1	1	0.42	0.46	1	0.49	0.53	1			
WS 4 [multiple of $P_{s,4}$ ]	1	1	1	0.65	0.71	1	0.80	0.86	1			
WS 5 [multiple of $P_{s,5}$ ]	1	1	1	0.99	1	1	1	1	1			
All WS ( $\bar{P}_{cs,B,a}$ )	0.32	0.32	0.32	0.16	0.18	0.32	0.19	0.20	0.32			
[multiple of $P_{s,overall}$ ]												
Absorbed power sector SW = 23 $P_{s,overall}$												
<b>Average yearly</b>												
absorbed power ( $\bar{P}_{cs,B,a}$ )	1	1	1	0.65	0.65	0.77	0.60	0.60	0.75			
[multiple of $P_{s,overall}$ ]												
Average yearly absorbed power lay-out B = 75 $P_{s,overall}$												

The average yearly absorbed power of the WD-WECs in the second and third row varies between 60 % and 77 % of the absorption of the WD-WECs in the first

row. This high reduction is mainly caused by large wake effects for the sectors southwest and northwest. The power absorbed by the last WEC in the second and third row is higher as their absorption is not affected by wake effects when the waves are coming from the southwest. Respectively, 31 % ( $=\frac{23}{75}$ ), 44 % ( $=\frac{33}{75}$ ) and 24 % ( $=\frac{18}{75}$ ) of the absorbed power of the farm is coming from the sector southwest, west and northwest (Table 9.5). The wake effects are the largest for the northwest sector. As the contribution from the sector west to the total power absorbed by the farm is the largest (44 %), it is investigated for the sector west whether the installation of a fourth, fifth and sixth row could be interesting. Therefore the average remaining wave height has been calculated in front of the WECs indicated with a square on Figure 9.11(a). Furthermore the remaining wave height on the fifth and sixth row has been multiplied with an additional reduction factor (equal to the reduction factor for row 2 and 3) to take the effect of the installation of a fourth and fifth row, respectively, into account. The power absorbed by WD-WECs installed in 3 additional rows has been calculated with equation (7.4) (Table 9.6).

Table 9.6: Absorbed power  $P_{cs,B,a}$  of 3 additional rows in lay-out B for 5 wave situations (WS) and 3 wave sectors

Row	4			5			6		
Position WD-WEC	L <sup>1</sup>	M <sup>2</sup>	R <sup>3</sup>	L	M	R	L	M	R
Wave sector west									
WS 1 [multiple of $P_{s,1}$ ]	0.44	0.45	0.48	0.32	0.33	0.30	0.22	0.20	0.31
WS 2 [multiple of $P_{s,2}$ ]	0.40	0.40	0.43	0.28	0.29	0.27	0.19	0.17	0.24
WS 3 [multiple of $P_{s,3}$ ]	0.44	0.45	0.48	0.32	0.34	0.31	0.22	0.21	0.31
WS 4 [multiple of $P_{s,4}$ ]	0.77	0.78	0.84	0.60	0.62	0.57	0.44	0.41	0.54
WS 5 [multiple of $P_{s,5}$ ]	1	1	1	1	1	1	0.81	0.76	0.99
All WS ( $\bar{P}_{cs,B,a}$ ) [multiple of $P_{s,overall}$ ]	0.19	0.19	0.21	0.15	0.15	0.14	0.11	0.11	0.15

<sup>1</sup> Left position

<sup>2</sup> Middle position

<sup>3</sup> Right position

Only 96 instead of 99 WD-WECs have been considered to compared lay-out B with 3 and 6 rows. The power absorbed by 96 WECs installed in a staggered grid with six rows for the sector west is decreased with 20 % compared to 96 WECs in a staggered grid of 3 rows. Placing the last three rows, 2 km behind the first three rows, instead of immediately behind these first rows (Figure 9.11(a)), results in a similar reduction. Consequently, it is not economical to install a fourth, fifth and sixth row of converters that are only absorbing approximately 50 % of the WECs in the first three rows (Table 9.5 and Table 9.6). In a farm of wind turbines a maximal reduction of approximately 15 % was seen. It is expected that the reduction for the

sectors northwest and southwest will even be higher, as the reduction behind the first three rows is higher. Whether it is economical to place WECs on the second and third row will be discussed in section 9.5.

### 9.4.3 Lay-out C: all WD-WECs installed behind each other

In a third lay-out all WD-WECs are installed behind each other. The disturbance coefficients  $K_d$  in a wave basin with two WD-WECs for short-crested (head-on) waves with a significant wave height of 3 m, a peak wave period of 8.4 s and a maximum value of the directional spreading parameter of 75 are shown in Figure 9.12. The position of a third WD-WEC is indicated as well. The longitudinal spacing between the WD-WECs equals  $3D_R$ .

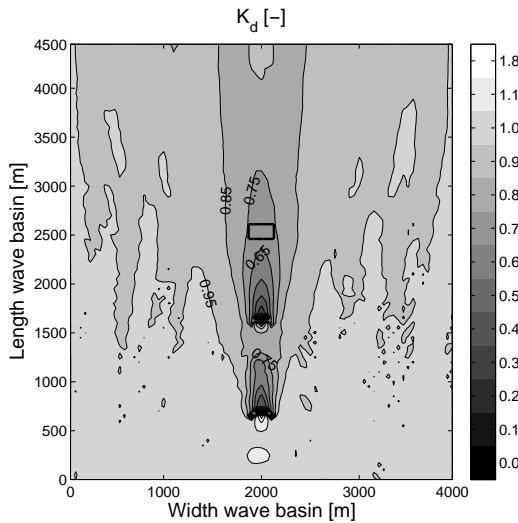
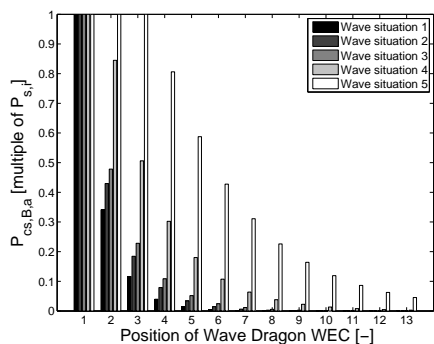
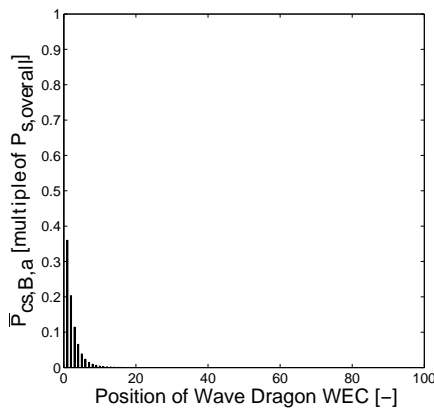


Figure 9.12: Calculated disturbance coefficient  $K_d$  in a wave basin with 2 WD-WECs with a longitudinal spacing of 780 m for short-crested waves (SCW) with  $H_s = 3$  m,  $T_p = 8.4$  s (wave situation 3),  $s_{max} = 75$  coming from the sector west

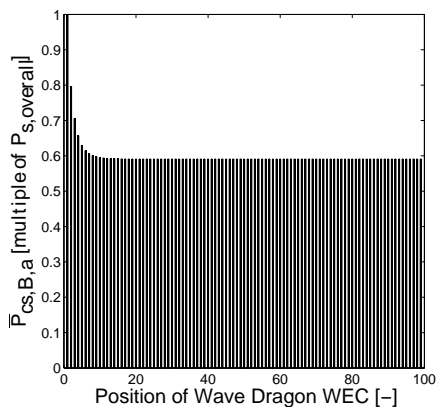
The absorbed power for the sector west is determined by calculating the average remaining wave height on the position of the second WD-WEC when only 1 WD-WEC is installed in the domain (Figure 9.4(a), 9.4(b), 9.4(c) and Figure 9.5). This way a reduction factor (ratio between remaining wave height and incident wave height) for each wave situation is obtained. To estimate the power absorbed by the following WD-WECs, the same reduction factor is each time applied to the remaining wave height. For the sector west, the 4<sup>th</sup>, 5<sup>th</sup>, 6<sup>th</sup>, 8<sup>th</sup> and 13<sup>th</sup> WD-WEC is already absorbing less than 5 % of  $P_{s,i}$  for wave situation  $i$ , as shown in Figure 9.13(a).



(a) Wave sector west - WS 1, 2, 3, 4 and 5



(b) Wave sector west - all wave situations



(c) Yearly average absorbed power - all wave sectors and all wave situations

Figure 9.13: Absorbed power of each WD-WEC in lay-out C for (a) wave sector west and each wave situation, (b) for wave sector west, considering all wave situations and (c) yearly average absorbed power of lay-out C

The average absorbed power for the sector west is shown in Figure 9.13(b). For the 8<sup>th</sup> WD-WEC the absorbed power is already smaller than 0.01  $P_{s,overall}$ . The power absorption of the following WD-WECs is negligible. As expected the power absorption for the sector west is very small. The absorbed power for the sectors northwest and southwest is equal (Table 9.7). Note that the power absorption for these sectors has been estimated in the same way as for lay-out A. For both sectors the first WEC is absorbing the same amount as a single WD-WEC. The power absorbed by the other WD-WECs is reduced with, respectively, 0.14  $P_{s,1}$ , 0.10  $P_{s,2}$  and 0.08  $P_{s,3}$  for wave situation 1, 2 and 3. This reduction is caused by the wake of the neighbouring WD-WEC. For wave situation 4 and 5 the power absorption is not reduced.

Table 9.7: Absorbed power  $P_{cs,B,a}$  of lay-out C in 5 wave situations (WS) and 3 wave sectors

Number WD-WEC	1			2 - 99		
Wave sector	NW	W	SW	NW	W	SW
WS 1 [multiple of $P_{s,1}$ ]	1	1	1	0.86	Figure 9.13(a)	0.86
WS 2 [multiple of $P_{s,2}$ ]	1	1	1	0.90	Figure 9.13(a)	0.90
WS 3 [multiple of $P_{s,3}$ ]	1	1	1	0.92	Figure 9.13(a)	0.92
WS 4 [multiple of $P_{s,4}$ ]	1	1	1	1	Figure 9.13(a)	1
WS 5 [multiple of $P_{s,5}$ ]	1	1	1	1	Figure 9.13(a)	1
All WS ( $\bar{P}_{cs,B,a}$ ) [multiple of $P_{s,overall}$ ]	0.32	0.36	0.32	0.30	Figure 9.13(b)	0.30
Average yearly absorbed power ( $\bar{P}_{cs,B,a}$ ) [multiple of $P_{s,overall}$ ]	1.00			Figure 9.13(c)		
Average yearly absorbed power lay-out C = 59 $P_{s,overall}$						

The yearly average power absorbed by each WD-WEC is given in Figure 9.13(c). The absorption of the WD-WECs is very fast decreasing until an absorption of 0.6  $P_{s,overall}$ . When the absorption is equal to 0.6  $P_{s,overall}$  there is no contribution of the sector west anymore.

The total power absorbed by this farm has been compared with the absorption of a farm where all WD-WECs are installed behind each other, but where the longitudinal spacing is respectively equal to  $4D_R$  and  $2D_R$ . The closer the WD-WECs are placed, the smaller the power absorption for the sector west. On the other hand for the sectors northwest and southwest the power absorption is approximately constant. As the contribution of the west sector to the total amount of absorbed energy is very small, the total energy absorption for an in-between distance of  $2D_R$ ,  $3D_R$  and  $4D_R$  is comparable. The difference in cost of the

subsea cables will be discussed in section 9.5.

For the sector northwest ( $\theta_0 = 45^\circ$ ) the wake of a WD-WEC has a small influence on the power absorbed by the WD-WEC in its lee. The effect of the wake of a WD-WEC on the average power absorbed by a second WD-WEC (installed in its lee) for varying mean wave directions and longitudinal spacing is shown in Figure 9.14. Note that only two WD-WECs have been considered for this comparison. For larger values of  $\theta_0$  a third WD-WEC will not only be affected by the second WD-WEC, but also by the first WD-WEC. Consequently the reduction shown in Figure 9.14 will increase for WD-WECs installed behind the second one. The remaining average wave height in front of the second WD-WEC is again determined by rotating Figure 9.4(a), 9.4(b), 9.4(c) and Figure 9.5 over  $10^\circ$  to  $45^\circ$ .

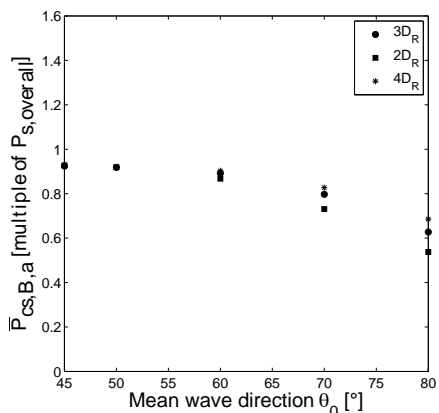


Figure 9.14: The absorbed power  $\bar{P}_{cs,B,a}$  of a second WD-WEC installed in the lee of the first one for mean wave direction varying between  $45^\circ$  and  $80^\circ$  and for a longitudinal spacing of, respectively,  $3D_R$ ,  $2D_R$  and  $4D_R$

For  $60^\circ \leq \theta_0 \leq 80^\circ$  the amount of absorbed power is increasing with increasing longitudinal spacing. When the mean wave direction differs at minimum  $30^\circ$  from the prevailing mean wave direction ( $= 90^\circ$ ), the absorbed power of a second WD-WEC is approximately 90 % of the power absorbed by the first WD-WEC, independent of the longitudinal spacing. When waves are mainly propagating in one direction, a lay-out with all WECS behind each other should be avoided.

### 9.4.4 Comparison between lay-out A, B and C

The amount of power absorbed by lay-out A, B and C as a multiple of the overall absorbed power of a single WD-WEC  $P_{s,overall}$  is given in Table 9.4, 9.5 and 9.7. Lay-out A has the highest power absorption. The absorbed power of these 99 WD-

WECs is equal to the power absorbed by approximately 94 individual WD-WECs. Lay-out C is only absorbing 60 % of the power absorbed by 99 individual WD-WECs. To calculate the electrical power produced by the farm the absorbed power is multiplied with a factor 0.7 to account for power take-off losses, spilling when waves overtop, . . . . Further, it is assumed that 5 % of the time the farm is under repair or is suffering a fault that stopped it generating [4]. Therefore the power absorption of a farm is multiplied with a factor 0.95. The yearly electrical power produced by lay-out A, B and C is shown in Table 9.8. Cable losses are not taken into account yet. These losses will be estimated in section 9.5.

*Table 9.8: Yearly average electrical power production of lay-out A, B and C (cable losses are not taken into account)*

Lay-out [-]	Yearly average electrical power production [GWh/year]
A	184.6
B	145.8
C(3D <sub>R</sub> )	116.2
C(2D <sub>R</sub> )	116.4
C(4D <sub>R</sub> )	116.3

The yearly average power produced by the farm per km<sup>2</sup> and the yearly average power production per km of each lay-out is given in Table 9.9.

*Table 9.9: Yearly average electrical power production per km and km<sup>2</sup> and farm efficiency of lay-out A, B and C (cable losses are not taken into account)*

Lay-out	Area [km <sup>2</sup> ]	Width [km]	Produced power per km <sup>2</sup> [GWh/km <sup>2</sup> /year]	Produced power per km [GWh/km/year]	Farm efficiency <sup>1</sup> [%]
A	7.72	51	23.9	3.6	5
B	31.61	35	4.6	4.2	6
C	23.94	0.26	4.9	-	-

<sup>1</sup> Farm efficiency = ratio between the mean annual produced power per km and the mean annual available wave power per km

WD-WECs installed in a single line with a lateral spacing of 260 m result in the highest power production per km<sup>2</sup>. On the other hand the production per km is



lower compared to the staggered grid lay-out. To install lay-out A a width of more than 50 km is needed. The width of lay-out B is reduced with 32 %. Lay-out C has a very high production per km as the width of the farm is only 0.26 km. This value is not realistic and is not given in Table 9.9. In the last column of Table 9.9 the farm efficiency (= ratio between the produced power per km and the available wave power per km) is shown. A comparable efficiency is obtained for lay-out A and B.

The cost of energy (€/kWh) needs to be calculated for the considered lay-outs to see whether lay-out A or B is preferable.

## 9.5 Cost of a farm of Wave Dragon WECs

The lay-out of a farm is not only affecting the power absorption. The cost of a farm of WD-WECs is also lay-out dependent. The cost of the subsea cable network changes when the lateral and longitudinal distances between the WECs or the distance from the WECs to the transformer platform vary. Also installation and operation and maintenance (O&M) costs are depending on the lay-out of the farm. In this work O&M costs are not taken into account, as no real data are available yet. The cost calculation in this PhD dissertation is only indicative in order to compare lay-outs A, B and C. A thorough cost calculation and optimization is needed when planning to install a farm of WD-WECs.

### 9.5.1 Cost of subsea cabling

When calculating the cost of the subsea cable network of a farm of WD-WECs, the knowledge and experience from the offshore wind industry has been used. The voltage of three-core submarine AC cables between the wind turbines and between the turbines and the transformer platform is in general 33 or 34 kV. As the here considered rated power of a WD-WEC (2 MW) is of the same order of magnitude as the rated power of a wind turbine, the same voltage can be used in a farm of WD-WECs. AC cables have some important disadvantages which increase when the cables are installed over long distances [5]:

- The capacitance between each phase conductor and the earth induces a charging current in the cable. As the cable must carry this current as well as the useful load current, the load carrying capability of the cable is reduced. As the capacitance is distributed along the entire length of the cable, a longer cable causes a higher charging current.
- Losses of power in the conductors which increase with increasing length of the cable.

For each lay-out there are several possibilities to connect the WD-WECs with each other (in strings - Figure 9.15(b)) and to join the different strings in clusters (Figure 9.15(b)), which are connected with the transformer platform. By changing the number of WD-WECs connected together in a string or the number of strings in a cluster, the power through the cables and consequently the diameter and the cost of the cables will change. Also the charging current in the cables and cable losses will be affected.

In general only 1, 2 or 3 cable sizes are used in a farm to (i) limit the number of spare cables, necessary in the case of a cable fault, (ii) facilitate installation as the cable laying vessel only needs to transport 1, 2 or 3 cable sizes (iii) reduce the production cost, as only 1, 2 or 3 cable sizes need to be manufactured and tested.

In this section an optimal subsea cable network is designed for lay-out A, B and C. Unit costs (without installation) of the 34 kV XLPE 3-core submarine AC cables with steel wire armour (copper conductor) with varying cross sections (between 95 mm<sup>2</sup> and 630 mm<sup>2</sup>) are provided by DONG Energy and are given in Table 9.10. The current rating  $I_{100\%}$  and charging current  $I_c$  of these cables can be found in [6].

Table 9.10: Characteristics of 34 kV XLPE 3-core AC cables

Cross section $A'$	Current rating $I_{100\%}$	Electrical resistance $R$ (equation (9.6))	Charging current $I_c$	Unit cost
[mm <sup>2</sup> /phase]	[A/phase]	[ $\Omega$ /km]	[A/km/phase]	[€/m]
95	300	0.24	0.9	107
120	340	0.19	1.0	120
150	375	0.15	1.0	133
185	420	0.12	1.1	147
240	480	0.09	1.2	167
300	530	0.07	1.3	187
400	590	0.06	1.5	233
500	655	0.04	1.6	280
630	715	0.04	1.8	313

When designing the optimal cable network not only the cost of the cable itself, but also the capitalized cost of expected energy constrained due to cable losses over the lifetime of the farm has been considered. The annual cable losses have been multiplied with the capitalized energy cost over a lifetime of 20 years, which equals €1 000 per MWh [4], to obtain the capitalized cost of the expected constrained energy. The capitalized energy cost over a lifetime of 20 years has

been derived by discounting the Cost of Energy (COE) of €100 per MWh [4] with a nominal discount rate of 10 %. The COE is described in more detail in the next section. The capitalized cost of expected energy constrained due to cable losses is 8 % to 13 % of the cable cost.

It has been assumed that the costs of the installation of the cables and WD-WECs depend only on the number of WD-WECs and not on the lay-out. Therefore these additional costs are not taken into account in the design. In practice these costs will increase for increasing distances. Furthermore capitalized costs of expected energy constrained due to outages and O&M costs have not been considered in the optimization procedure.

The optimal cable network should fulfil the following two conditions:

- The current  $I$  in each cable of the network should be smaller than the current carrying capacity of the cable (equation (9.2)) [5].

$$I < \sqrt{I_{100\%}^2 - (I_c \cdot l')^2} \quad (9.2)$$

with  $l'$ , the length of the cable. The current  $I$  in the cables is calculated with equation (9.3):

$$I = \frac{P_{\text{rated}}}{\sqrt{3} V} \quad (9.3)$$

with  $V = 34$  kV and  $P_{\text{rated}}$  the total rated power of the WD-WECs connected to the cable.

- The total cost of the cable network (cable cost itself and capitalized cost of expected energy constrained due to cable losses) should be minimal [4]. The total cost of the cable network is calculated using equation (9.4) [4].  $n$  is the total number of cables.

$$\begin{aligned} \text{Cost} = & \sum_{i=1}^n (\text{unit cost}) l'_i \\ & + \sum_{i=1}^n (\text{losses at } P_{\text{rated},i}) 8760 (\text{capitalized energy cost}) l'_i \delta \end{aligned} \quad (9.4)$$

with  $\delta$  the loss load factor. The loss load factor is the ratio between the annual average power loss and the peak power loss (= losses at 198 MW) of the farm. The losses in the cable per km for  $P_{\text{rated},i}$  are calculated by multiplying the electrical resistance with the current in the cable squared (equation (9.5)).

$$\text{Losses at } P_{\text{rated},i} = 3RI^2 \quad (9.5)$$

The electrical resistance  $R$  of each cable is given by equation (9.6):

$$R = \frac{\rho'}{A'} \quad (9.6)$$

where  $\rho'$  is the electrical resistivity ( $=2.2410^{-6} \Omega \text{ cm}$ ) of the cable. The electrical resistance of the cables is given in Table 9.10.

The optimization procedure consist of two iterations. A global iteration determines the number of WD-WECs, joined together in a string and the number of strings in a cluster, which result in a minimal cost. A subiteration determines for each option in the global iteration the optimal cable size and consequently the minimal cost. The optimization procedure results in an optimal cable network as shown in Figure 9.15(a) for lay-out A, Figure 9.15(b) for lay-out B and Figure 9.15(c) for lay-out C. Note that the cable network is only shown at one side of the transformer platform.

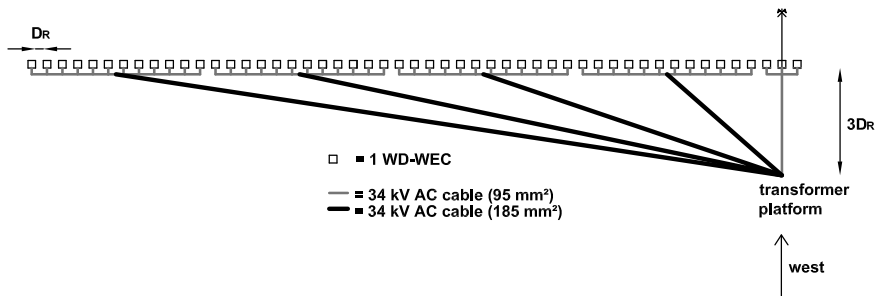
The resulting cable cost, without the capitalized cost of expected energy constrained due to cable losses, is given in Table 9.11, where  $C'$  is the cost of the cable network for lay-out A. The cable network cost for the other lay-outs is given as a fraction of  $C'$ . Details of the cable network cost for each lay-out can be found in appendix G.

Table 9.11: Relative cost of cables

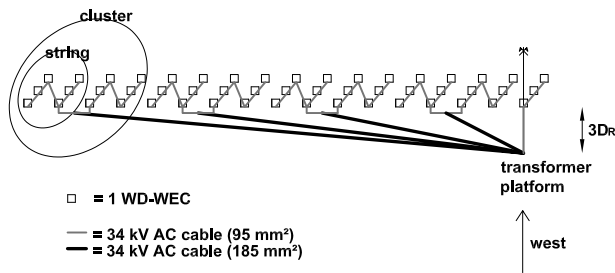
Lay-out [–]	Cost of cables [multiple of $C'$ ]
A	1
B	0.77
C ( $3D_R$ )	1.78
C ( $2D_R$ )	1.29

The cable network cost of lay-out B is 23 % smaller than the cost of the cable network of lay-out A, while the cable network cost of lay-out C (with a longitudinal spacing of  $3D_R$ ) is 78 % higher.

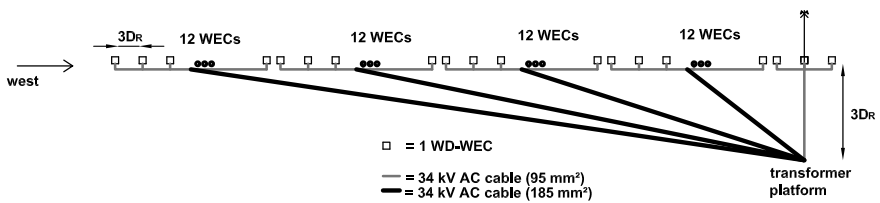
As the power production of lay-out C with a longitudinal spacing of  $2D_R$  is comparable to the power production of lay-out C with a larger longitudinal spacing (Table 9.8) the cable connection cost of lay-out C with a longitudinal spacing of  $2D_R$  has been calculated as well. The cost is 72 % ( $=\frac{1.29}{1.78}$ ) of the cost for lay-out C with a longitudinal spacing of  $3D_R$ .



(a) Lay-out A (47.6 km of 95 mm<sup>2</sup>, 106.4 km of 185 mm<sup>2</sup>)



(b) Lay-out B (50.9 km of 95 mm<sup>2</sup>, 71.1 km of 185 mm<sup>2</sup>)



(c) Lay-out C (84.5 km of 95 mm<sup>2</sup>, 189.9 km of 185 mm<sup>2</sup>)

Figure 9.15: Sketch of cable network for (a) lay-out A, (b) lay-out B and (c) lay-out C

### 9.5.2 Cost Of Energy (COE)

The Cost Of Energy (COE) is the minimum price at which energy must be sold for the energy project to break even. The COE is determined by a discounted cash flow calculation. By dividing the present value of the costs of a farm by the present value of its energy production, the COE is calculated (equation 9.7) [7]. A derivation of the COE is given in appendix H. In this chapter O&M costs, insurance costs and cost for decommissioning are not considered.

$$\begin{aligned} \text{COE} &= \frac{\text{PV}(\text{capital costs}) + \text{PV}(\text{installation costs}) + \text{PV}(\text{insurance costs})}{\text{PV}(\text{energy production})} \\ &+ \frac{\text{PV}(\text{O\&M costs}) + \text{PV}(\text{decommissioning costs})}{\text{PV}(\text{energy production})} \\ &\simeq \frac{\text{capital costs} + \text{installation costs}}{\text{PV}(\text{energy production})} \end{aligned} \quad (9.7)$$

PV indicates the present value over the service life  $n_{life}$  (20 years). The present value of the energy production is determined with equation (9.8).

$$\text{PV}(\text{energy production}) = \sum_{t=1}^{n_{life}} \frac{(\text{energy production})_t}{(1+i)^t} \quad (9.8)$$

The energy production in year  $t$  is discounted with a discount rate  $i$  (nominal discount rate of 10 %). To calculate the cost of energy of lay-out A, B and C, the investment cost of the WD-WEC (installation and mooring included) and the installation cost of the subsea cable network have been considered besides the cost of the cable network (Table 9.11).

The investment cost of a 4 MW WD-WEC (wave climate of 24 kW/m) is given in Table 9.2. By assuming that the cost of the power take-off (PTO) is  $1/4^{th}$  of the investment cost of the WD-WEC and that the cost of the PTO of the 2 MW converter is half of the PTO cost of the 4 MW converter, the investment cost of a 2 MW WD-WEC has been estimated. The cost after deployment of hundreds of WD-WECs is used in this calculation. Normally the structure of the converter should be resized as well to make the 2 MW concept more economically. One should note that the mooring cost is included in the investment cost of the WD-WEC. It is assumed that each WD-WEC is moored separately. A cost study of other mooring configurations is beyond the scope of this PhD dissertation.

It should be mentioned that the above assumption of the cost of a 2 MW-WEC is only a first rough estimate. At this moment Wave Dragon ApS. is designing a 1.5 MW WD-WEC with a width of 170 m, which is appropriate for a 12 kW/m wave climate. The investment cost per produced power of the 1.5 MW WD-WEC is expected to be lower compared to the 2 MW WD-WEC in this work.

Table 9.12: Relative total cost and relative cost of energy

Lay-out [—]	Total cost [multiple of $C'_{tot}$ ]	Cost of energy [multiple of $c'$ ]
A	1	1
B	0.99	1.23
C ( $3D_R$ )	1.02	1.63
C ( $2D_R$ )	1.01	1.58
C ( $4D_R$ )	1.03	1.65

In general submarine cables are buried in the seabed to avoid damage by fishing nets and anchors [5]. Two vessels are used to install the cables over relatively short distances:

- 1 vessel to jet. The water-jet system fluidises the seabed material to create a trench. The fluidised material falls back on the cable after the machine has passed.
- 1 cable laying vessel which is containing the cables, cable tensioning machine and a dynamic positioning system for a precise installation of the cable.

The cost for installing the cables between the WD-WECs is given by DONG Energy. The cable installation cost per WEC is approximately M€0.20, while the cost for mobilisation and demobilisation of the vessels equals approximately M€1.87. Finally the total estimated cost for the downtime for 2 vessels due to rough weather conditions during installation is equal to M€9.29 (based on an overall installation period of about 99 days). A downtime of 50 % of the installation time (experience from DONG Energy) has been considered (Table 9.1).

The resulting total cost (investment cost WD-WECs, cost of cable network (Table 9.11), installation of cables, including mobilisation, demobilisation and cost for downtime) of each lay-out is given in Table 9.12. The total cost for lay-out B and C is given as a fraction of  $C'_{tot}$ , the total cost of lay-out A. Dividing this cost by the present value of the electrical power production of the farm (equation 9.8), taking losses in the cable network into account (appendix G), results in the cost of energy. The cost of energy of lay-out B and C (Table 9.12) is again given, relative to the cost of energy of lay-out A (=  $c'$ ).

The produced power (without cable losses) of lay-out B is 21 % lower than the power production of lay-out A (Table 9.8), while the cost of the subsea cable network is 23 % smaller (Table 9.11). On the other hand the total cost of lay-out

B is only 1 % smaller than the total cost of lay-out A (Table 9.12), as the cost of the subsea cable network is relatively small compared to the investment cost of the devices. It is clear that the cost of the subsea cable network has no significant influence on the cost of energy. The cost of energy of lay-out C with a longitudinal spacing of  $2D_R$ ,  $3D_R$  and  $4D_R$  is approximately equal to € 1.6 c/kWh, as the total power production was comparable (Table 9.8). Maximizing the power production of a farm of WD-WECs is more important than minimizing the cost of the subsea cable network. Consequently lay-out A results in the smallest cost of energy (Table 9.12).

## 9.6 Wave height decrease behind a farm of Wave Dragon WECs

As the available sea area is rather scarce, it will be difficult to install a large farm (width between 35 and 51 km) of WD-WECs. When installing a limited number of WD-WECs in front of a farm of wind turbines, e.g. Horns Rev II (width and length of approximately 10 and 6 km), the rated wave power of the farm of WD-WECs will be rather low. On the other hand these WD-WECs can be connected with the transformer platform of the wind farm, which will reduce the total subsea cable cost. Furthermore these WD-WECs will reduce the wave height in their lee. A lower wave height between the wind turbines may increase the time window for accessing the wind farm. This higher accessibility will decrease the loss of energy in case of outages, as failures can be faster detected and repaired.

In this section the wave height decrease behind a single line of WD-WECs is studied. In Figure 9.10 and Figure 9.16 the wake behind a row of, respectively, 3 and 5 WD-WECs is shown.

A farm of 5 WD-WECs causes a wider and longer wake. The value of  $K_d$ , averaged over a distance equal to  $D_R$  in the middle of the wave basin (between  $x^* = 1\,870$  m and  $x^* = 2\,130$  m), behind a single line of 3 and 5 WD-WECs is shown on Figure 9.17.

From  $y^* = 1\,500$  m, the average disturbance coefficient  $K_d$  is approximately 0.8 (wave situation 3). At  $y^* = 3\,500$  m,  $K_d$  is increasing when 3 WD-WECs are installed, while  $K_d$  remains 0.8 for a single line of 5 WD-WECs. The length of the area with  $K_d$  approximately equal to 0.8 increases when the width of the farm is increasing. Five WD-WECs with a width of approximately 2 km, cause a wake of at least 3.5 km (Figure 9.17). It is expected that a single line of WD-WECs with a width of approximately 10 km (width of a farm of wind turbines) will cause a wave height decrease of 20 % (for wave situation 3) in the entire farm of wind turbines, installed behind this line of WECs. Note that the width of the line of WD-WECs should be larger than the width of the wind farm, to make sure that all



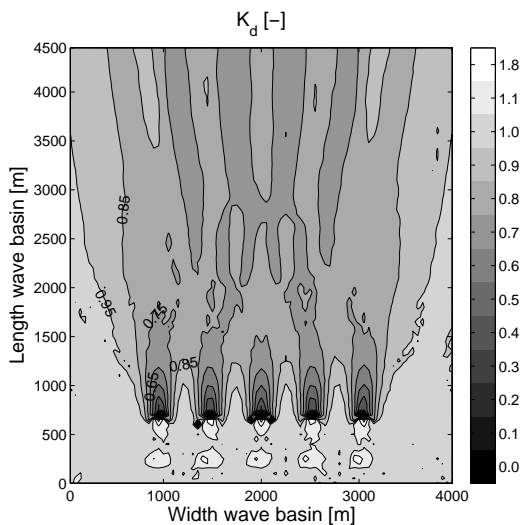


Figure 9.16: Calculated disturbance coefficient  $K_d$  in a wave basin with 5 WD-WECs with a lateral spacing of 260 m for short-crested waves (SCW) with  $H_s = 3$  m,  $T_p = 8.4$  s (wave situation 3) and  $s_{max} = 75$  coming from the west sector

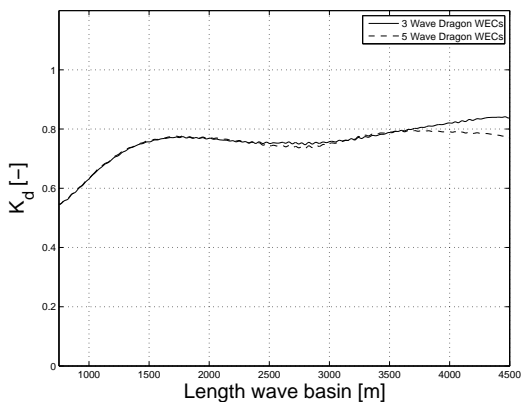


Figure 9.17: Calculated disturbance coefficient  $K_d$ , averaged between  $x^* = 1870$  m and  $x^* = 2130$  m, along the length of a wave basin with a line of 3 and 5 WD-WECs for irregular short-crested waves with  $H_s = 3$  m,  $T_p = 8.4$  s and  $s_{max} = 75$  (wave situation 3)

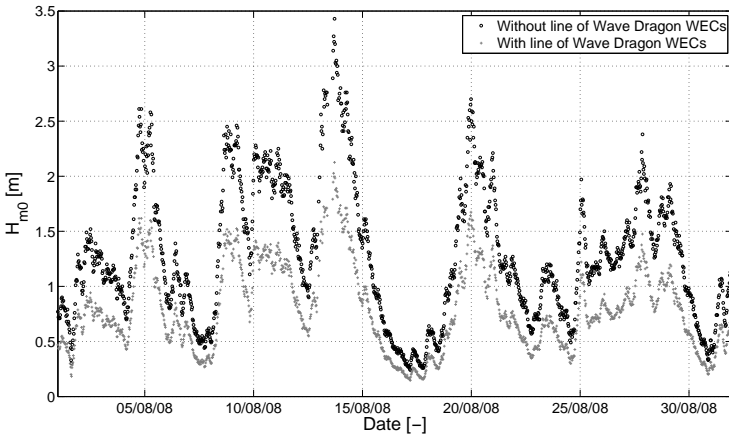


Figure 9.18: Time series of the significant wave height  $H_{m0}$  in August 2008 at Horns Rev II with and without a single line of WD-WECs in front of the wind farm

wind turbines are installed in the wake when waves are coming from the northwest and southwest. To make a detailed study of the length of the wake as a function of the farm width a longer and wider wave basin in MILDwave is needed. The values of  $K_d$  averaged between  $x^* = 1\ 870$  m and  $x^* = 2\ 130$  m at  $y^* = 4\ 000$  m are respectively 0.79, 0.8, 0.8, 0.8 and 0.86 for wave situation 1, 2, 3, 4 and 5. These values are used to estimate the accessibility of a farm of wind turbines, located in the lee of a single line of WD-WECs.

At Horns Rev II waves are measured with a Waverider buoy. The time series of the significant wave height measured between 01/08/2008 and 31/08/2008 with an interval of 30 minutes is shown in Figure 9.18. Furthermore the expected reduced significant wave height, when a single line of WD-WECs is installed in front of the wind turbines, is given in Figure 9.18 as well. The significant wave height is approximately 20 % lower by the installation of a single line of WD-WECs.

The time series of the significant wave height measured between 01/03/2008 and 28/02/2009 is provided by DONG Energy. From 12/03/2008 till 23/04/2008 and from 17/05/2008 till 23/05/2008 no data were available due to a low battery in the Waverider and a system error. In total 14 843 measurements were available. To access a farm of wind turbines the significant wave height should be smaller than 1 à 2 m during 8 hours at minimum. In Figure 9.19 the fraction of the total measurement time that maintenance was possible is shown for the situation with (lay-out A) and without the installation of a single line of WD-WECs.

The accessibility increases with 12 to 14 % by installing a single line of WD-WECs. As a comparison, the time that maintenance can be carried out when lay-

out B is installed in front of the wind farm, is calculated as well (Figure 9.19). In this case the accessibility increases even more (21 to 28 % higher). Note that only  $K_d$ , averaged between  $x^* = 1\,870$  m and  $x^* = 2\,130$  m at  $y^* = 4\,000$  m, for the west sector has been used to estimate the time series of significant wave height behind lay-out A and B, as the wave direction had not been measured during that period. For the sectors northwest and southwest the wave height decrease is even higher, as seen in section 9.4. Consequently for these sectors the average value of  $K_d$  is lower compared to the value determined for the sector west. It is expected that the accessibility would increase even more when taking a wave direction dependent value of  $K_d$  into account.

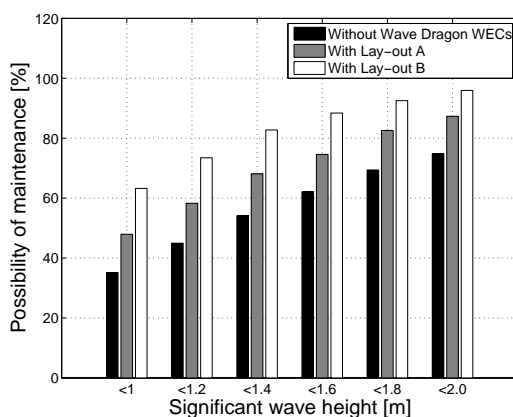


Figure 9.19: Percentage of time that maintenance is possible as a function of the maximum significant wave height that allows maintenance

So far no wave regeneration by wind is taken into account. The time series of the wind velocity, 70 m above mean sea level, between 01/03/2008 and 28/02/2009 near Horns Rev II is measured by DONG energy. There were no measurements between 02/03/2008 and 24/05/2008 due to a lightning stroke in the mast. To estimate the possible wave height increase behind a single line of WD-WECs (lay-out A) due to wind, the method of Sverdrup, Munk and Bretschneider [8, 9], adapted by Mitsuyasu [10] and Hasselman et al. [11], has been used. Based on the time series of the wind velocity, an average wind stress factor  $U_A$  [12] has been calculated for each wave situation. The wave height 10 km behind the WD-WECs can be 3 (WS 5) to 8 % (WS 1) higher than the wave height immediately behind the WD-WEC. The fraction of the total measurement time that maintenance can be carried out when a line of WD-WECs is installed in front of the farm of wind turbines, taking wave regeneration by wind (fetch length of 10 km) into account, is shown in Figure 9.20. The accessibility is approximately 9 to 11 % higher compared to the situation without WD-WECs. A small decrease (2 to 3 %) in

possible maintenance with the installation of a line of WD-WECs is observed when the impact of wind is taken into account.

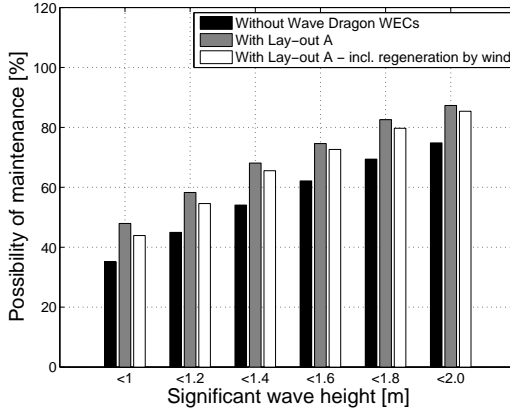


Figure 9.20: Percentage of time that maintenance is possible as a function of the maximum significant wave height that allows maintenance, when taking wave regeneration by wind into account

## 9.7 Conclusions




When designing the lay-out of a farm of WD-WECs, maximum power production should be mainly aimed at. As the investment cost of the subsea cable network in-between the WECs and between the WECs and the transformer platform is only a fraction of the total investment cost, minimizing this cost has only a small effect on the cost of energy. In this chapter three lay-outs of WD-WECs have been compared. The characteristics of the three lay-outs are summarized in Table 9.13.

Installing 99 WD-WECs (rated power of 198 MW) in a single line (lay-out A), results in a higher power production and a lower cost of energy compared to a staggered grid lay-out (lay-out B) or a lay-out where all WD-WECs are installed behind each other (lay-out C). The power production of lay-out B and C is 21 % and 37 % smaller than the power produced by lay-out A, while the cost of energy is 23 % and 63 % higher compared to lay-out A. On the other hand a wide sea area, approximately 51 km, is needed to install a single line of 99 WD-WECs.

Installing a smaller line of WD-WECs in front of a farm of wind turbines may be beneficial. On the one hand the WD-WECs can be connected to the transformer platform of the wind farm, which reduces the grid connection cost. On the other hand the WD-WECs will reduce the wave height in their lee, which makes maintenance of the wind farm easier and cheaper. The time window to access a wind farm increases with 9 to 14 % by installing a single line of WD-

WECs in front of the farm.

Table 9.13: Comparison of lay-out A, B and C

Lay-out	Area [km <sup>2</sup> ]	Width [km]	Yearly electrical power production <sup>1</sup> [GWh/year]	Total cost [C' <sub>tot</sub> ] <sup>2</sup>	Cost of energy [c'] <sup>3</sup>	Increase in access <sup>4</sup> [%]
	7.72	51	184.6	1	1	12 to 14
	31.61	35	145.8	0.99	1.23	21 to 28
	23.94	0.26	116.2	1.02	1.63	-

<sup>1</sup> Cable losses are not taken into account.

<sup>2</sup> Multiple of C'<sub>tot</sub>, total cost of lay-out A

<sup>3</sup> Multiple of c', cost of energy of lay-out A

<sup>4</sup> Increase of access of a farm of wind turbines behind the lay-out of WD-WECS, without considering regeneration by wind.

## References

- [1] K. Nielsen and M. Rugbjerg. *Kortlægning af bølgeenergiforhold i den danske del af Nordsøen*. Technical report, Rambøll, 1999.
- [2] J. Tedd, J.P. Kofoed, W. Knapp, E. Friis-Madsen, and H.C. Sørensen. *Wave Dragon prototype wave power production*. In Proceedings of the World Renewable Energy Congress - IX, Florence, Italy, 2006.
- [3] J. Tedd, J.P. Kofoed, E. Friis-Madsen, and L. Christensen. *Section 7.5.5 Wave Dragon*. In J. Cruz, editor, *Ocean Wave Energy, Current Status and Perspectives*, pages 371–382. Springer, 2008.
- [4] P. Djapic and G. Strbac. *Cost Benefit Methodology for Optimal Design of Offshore Transmission Systems*. Technical report, Centre for Sustainable Electricity and Distributed Generation, 2008.
- [5] I.M. de Alegría, J.L. Martín, I. Kortabarria, J. Andreu, and P. Ibañez. *Transmission alternatives for offshore electrical power*. *Renewable and Sustainable Energy Reviews*, 13:1027–1038, 2009.
- [6] ABB. *XLPE Submarine Cable Systems, User's guide [Online]*, Available from <http://www.abb.com>, Accessed February 2009.
- [7] Entec UK Ltd. *Cost Estimation Methodology, The Marine Energy Challenge approach to estimating the cost of energy produced by marine energy systems*. Technical report, Carbon Trust, 2006.
- [8] H.U. Sverdrup and W.H. Munk. *Wind, Sea and Swell. Theory of relations for forecasting. Pub. No. 601*. Technical report, US Navy Hydrographic Office, Washington, 1947.
- [9] C. L. Bretschneider. *Revisions in wave forecasting: deep and shallow water*. In Proceedings of the 6<sup>th</sup> conference on coastal engineering, ASCE, Council on Wave Research, pages 30–67, 1958.
- [10] H. Mitsuyasu. *On the growth of the spectrum of wind-generated waves (I)*. Technical report, Research Institute of Applied Mechanics, Kyushu University, 1968.
- [11] K. Hasselmann, T.P. Barnett, E. Bouws, H. Carlson, D.E. Cartwright, K. Enke, J.A. Ewing, H. Gienapp, D.E. Hasselmann, P. Kruseman, A. Meerburg, P. Müller, D.J. Olbers, K. Richter, W. Sell, and H. Walden. *Measurements of wind-wave growth and swell decay during the Joint North Sea Wave Project (JONSWAP)*. Technical report, Deutsches Hydrographisches Institut, 1973.

[12] U.S. Army Corps of Engineers. *Shore Protection Manual, Volume I*, 1984.





# 10

## Investment analysis

### 10.1 Introduction

In chapter 9 it is observed that the lay-out of a farm of Wave Dragon WECs has a negligible impact on the investment cost of the farm. Even when the cable network cost (without installation) is 78 % higher, the total investment cost of the farm is comparable (lay-out C versus lay-out A). On the other hand the costs of a farm are determined to a large extent by its location (chapter 3) since the grid connection, installation and Operation and Maintenance (O&M) costs depend on the distances to the grid, coast and harbour. Furthermore, the available water depth and bottom type also affect these costs. Finally the cost of a farm also depends on the number of installed WECs.

Contrary to the costs, the revenues of a farm are not only affected by the location and the number of WECs, but also by the lay-out (chapter 9). On the one hand, the location, the number of WECs and their lay-out determine the electricity production of the farm. On the other hand, the financial support (subsidies, fixed premium, ...) and electricity tariff differ from country to country and are consequently location-dependent.

In this chapter the impact of the location and the number of WECs on the farm investment is studied. Therefore five options to install a single line of Pelamis WECs in the southern North Sea are compared through an investment analysis. In option 1, 2 and 3 a single line of Pelamis WECs is installed on a site 32 km, 42 km and 67 km from shore (site 1, 2 and 3). In these options the same number

of Pelamis WECs is considered. In option 4 and 5 the maximum number of Pelamis WECs for the considered area is installed on site 2 and 3. In a first part of the investment analysis, three scenarios (worst case, base case and best case) are investigated for the five options. A second part of the investment analysis focuses on the risk of the investment for each option.

## 10.2 Sites for the deployment of a farm of Pelamis WECs

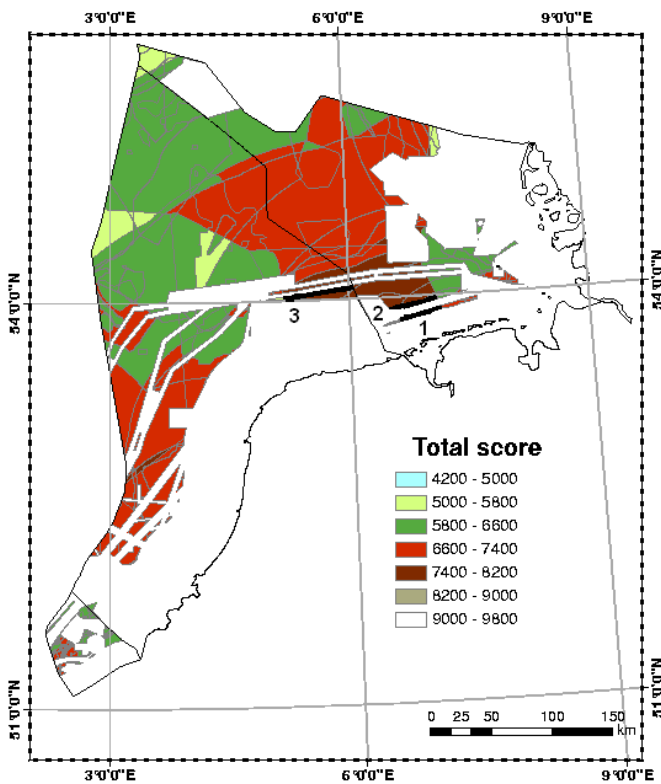


*Figure 10.1: Site 1, 2 and 3 (most suitable sites for the deployment of a farm of Pelamis WECs determined through a geo-spatial multi-criteria decision analysis in chapter 3)*

In chapter 3 a near shore area on the German Continental Shelf (GCS), near the border with the Dutch Continental Shelf (DCS), has been selected as the most suitable area for the deployment of a farm of Pelamis WECs with a multi-criteria

decision analysis. The best site on the DCS is located next to the border with the German Continental Shelf (chapter 3). Two sites in the most suitable area on the GCS, 32 km and 42 km from the coast and the best location on the DCS, 67 km from shore, are selected to install a farm of Pelamis WECs in this chapter. The three sites are shown on Figure 10.1. Characteristics of the selected sites can be found in Table 10.1.

*Table 10.1: Characteristics of the selected sites, as indicated on Figure 10.1*

	Site 1 (GCS)	Site 2 (GCS)	Site 3 (DCS)
Average annual available wave power [kW/m]	11.6	11.6	11.6
Shortest distance to coast <sup>1</sup> [km]	32	42	67
Width of area <sup>1</sup> [km]	36	40	56
Navigation routes to cross <sup>1</sup> [km]	6	12	28.5
Distance on land to grid connection <sup>1</sup> [km]	15	15	17
Max. number of Pelamis WECs in one line [-]	171	190	265
Voltage of onshore grid [kV]	220	220	110

<sup>1</sup> Calculated in [1]

All selected sites are located in the Thiessen polygon of the wave measurement buoy Fino-Borkumriff (chapter 3). Consequently, the yearly average available wave power on each location equals 11.6 kW/m (chapter 2).

In this study it is assumed that the subsea electricity cable spans the shortest distance to shore and that an onshore cable connects the subsea cable with the onshore grid. It is expected that the cable costs for site 3 will be higher, as the distance to the coast and the cable distance on land are the largest (Table 10.1). For each site, one or more navigation routes will be crossed, when installing the subsea cable. The total length of navigation routes, crossed by the offshore electricity cable has been assessed in [1] for each site and can be found in Table 10.1.

As seen in chapter 9, installing WECs in a single line results in the highest power production. Wave Dragon WECs installed in a single line have a slightly smaller power production (approximately 5 %) than individual Wave Dragon WECs due to wake effects. Note that the Wave Dragon WEC can only rotate over  $\pm 60^\circ$ . No details about the wake of a single Pelamis WEC were available for this study. As the width of the Pelamis WEC is much smaller (between 3.5 m and 4 m [2]) than the width of a Wave Dragon WEC, it is expected that the width of the wake will be smaller compared to the wake of a Wave Dragon WEC. Therefore it is assumed in this work that there will be no reduction in power production when Pelamis WECs are installed in a single line and when the rotation of the Pelamis WEC is limited to  $\pm 45^\circ$  around its tip.<sup>1</sup> Multiple lines of Pelamis WECs have

<sup>1</sup>By limiting the rotation of the Pelamis WEC, the wake behind the converter will not influence

not been considered as a good representation of the wake is needed to estimate the power production of the farm, as seen in chapter 8. In [1] the power production of multiple lines of Pelamis WECs has been assessed with the simplified method, discussed in chapter 6. The author wants to stress that the use of this method can lead to a high underestimation or overestimation of the power production.

The length of the Pelamis WEC varies between 120 m and 180 m [2]. A length of 150 m is considered in this study. As it is assumed that the Pelamis WEC can rotate  $\pm 45^\circ$  around its tip, a minimum distance between the tips of two adjacent Pelamis WECs of 212 m ( $= 2 \cdot 150 \cdot \cos(45^\circ)$ ) is needed to prevent collision. At site 1, 2 and 3, maximum 171 ( $= \frac{36\,000}{212} + 1$ ), 190 ( $= \frac{40\,000}{212} + 1$ ) and 265 ( $= \frac{56\,000}{212} + 1$ ) Pelamis WECs can be installed towards the northwest (most energetic wave direction at Fino-Borkumriff (Figure 2.17(b))) in a single line (Table 10.1).

The rated power of the Pelamis WEC is limited to 500 kW [3] because the mean annual power production of a Pelamis WEC at the considered sites is hardly affected by limiting the rated power to 500 kW (the mean annual power production of a 500 kW WEC is 4 % smaller than the mean annual power production of a 750 kW Pelamis WEC). Furthermore, the cost of a 500 kW power conversion module is smaller than for a 750 kW Pelamis WEC.

The mean annual power produced by a single 500 kW Pelamis WEC on the selected sites, taking into account the limited rotation of the Pelamis WEC, equals 89.7 kW. Note that this power production is slightly smaller than the result obtained in Figure 3.4, as a limited rotation of the Pelamis WEC and a smaller rated power (500 kW) are taken into account. The reduction in power production by limiting the rotation of the Pelamis WEC is rather small (10 %), as on the location Fino-Borkumriff almost all energy is coming from the sectors north, northwest and west (Figure 2.17(b)). The losses due to planned and unplanned maintenance are approximately 5 % [3, 4]. In [5] the total transmission losses (losses in transformer, cable, ...) vary between 6 % and 10 %. Therefore transmission losses of 8 % are considered. Consequently the resulting mean annual power generated by a single Pelamis WEC at site 1, 2 and 3 equals 78.6 kW or 688.5 MWh/year.

### 10.3 Investment analysis

In this chapter the impact of the location and the number of Pelamis WECs on the investment of a farm is studied. Therefore five options (Table 10.2) to install a farm of Pelamis WECs in a single line, are compared. Maximum 171 Pelamis WECs can be arranged in a single line orientated towards the northwest at site 1

---

another Pelamis WEC in the considered farm lay-out. Information on the wake of a Pelamis WEC is needed when allowing the Pelamis WEC to rotate  $\pm 180^\circ$  in order to estimate the power production of a Pelamis WEC installed in the lee of another one.

(Table 10.1). To study the impact of the location, without considering the influence of the number of Pelamis WECs, a single line of 171 Pelamis WECs has also been installed at site 2 and 3 (option 2 and 3). In option 4 and 5 a maximum number of Pelamis WECs in a single line is arranged on site 2 and 3. From the multi-criteria decision analysis it was observed that site 1 had a slightly better score than site 2 and site 3 (Figure 3.12). Consequently it is expected that option 1 will be the most feasible.

Table 10.2: Five options to install a single line of Pelamis WECs in the southern part of the North Sea

	Option 1	Option 2	Option 3	Option 4	Option 5
Site [-]	site 1	site 2	site 3	site 2	site 3
Number of Pelamis WECs [-]	171	171	171	190	265
Rated power [MW]	85.5	85.5	85.5	95	132.5

### 10.3.1 Bases for comparison

Several techniques are available to estimate whether an investment is economic interesting; a.o. the Net Present Value (NPV), the Internal Rate of Return (IRR) and the payback period.

The **Net Present Value (NPV)** [6] of the investment is defined as the total Present Value (PV) of a time series of cash flows and is calculated with equation (10.1).

$$\text{NPV} = -\text{CF}_o + \sum_{t=1}^{n_{life}} \frac{\text{CF}_t}{(1+i)^t} \quad (10.1)$$

The initial cash flow  $\text{CF}_o$  covers the investment costs (capital and installation costs) and the cable subsidies. The future cash flows  $\text{CF}_t$  include the revenues and costs during each year  $t$  of the project. A lifetime  $n_{life}$  of 20 years is considered in this study. To estimate the present value of future cash flows, the time value of money is taken into account. Money received today has a higher value than money received in future, as an amount of interest can be earned on the money by investing it today. Therefore future costs and revenues are discounted with a discount rate  $i$ . The NPV decreases when the discount rate  $i$  increases. In this study the hurdle rate is used as a discount rate. The hurdle rate is the minimum rate of return of a project, a company is willing to accept before starting the project. The hurdle rate also incorporates the risks associated with the project and related cash flows. A nominal (excluding inflation) hurdle rate of 8 % to 15 % has been used during the analysis [7–9].

The NPV indicates how much value an investment adds to the value of the company. The NPV is also used as a decision variable to accept ( $\text{NPV} > 0$ ) or reject ( $\text{NPV} < 0$ ) a project.

The **IRR** is defined as the discount rate that reduces the NPV to zero [6] and is calculated from equation (10.1). The IRR is an indicator of the efficiency of an investment. The IRR should be interpreted with care, e.g. a project with a higher initial investment can have a lower IRR than a project with a smaller initial investment, while the NPV at the end of the former project is the highest. Consequently, the project with the highest NPV, instead of highest IRR will be chosen, when no capital constraints are imposed. An investment is only interesting when the hurdle rate is smaller than the IRR.

The required period to recover the first cost of an investment from the net cash flow produced by that investment for an interest rate of zero, is the **payback period** without interest  $n^*$  [6].  $n^*$  satisfies equations (10.2) and (10.3).

$$\sum_{t=0}^{n^*-1} \text{CF}_t < 0 \quad (10.2)$$

$$\sum_{t=0}^{n^*} \text{CF}_t > 0 \quad (10.3)$$

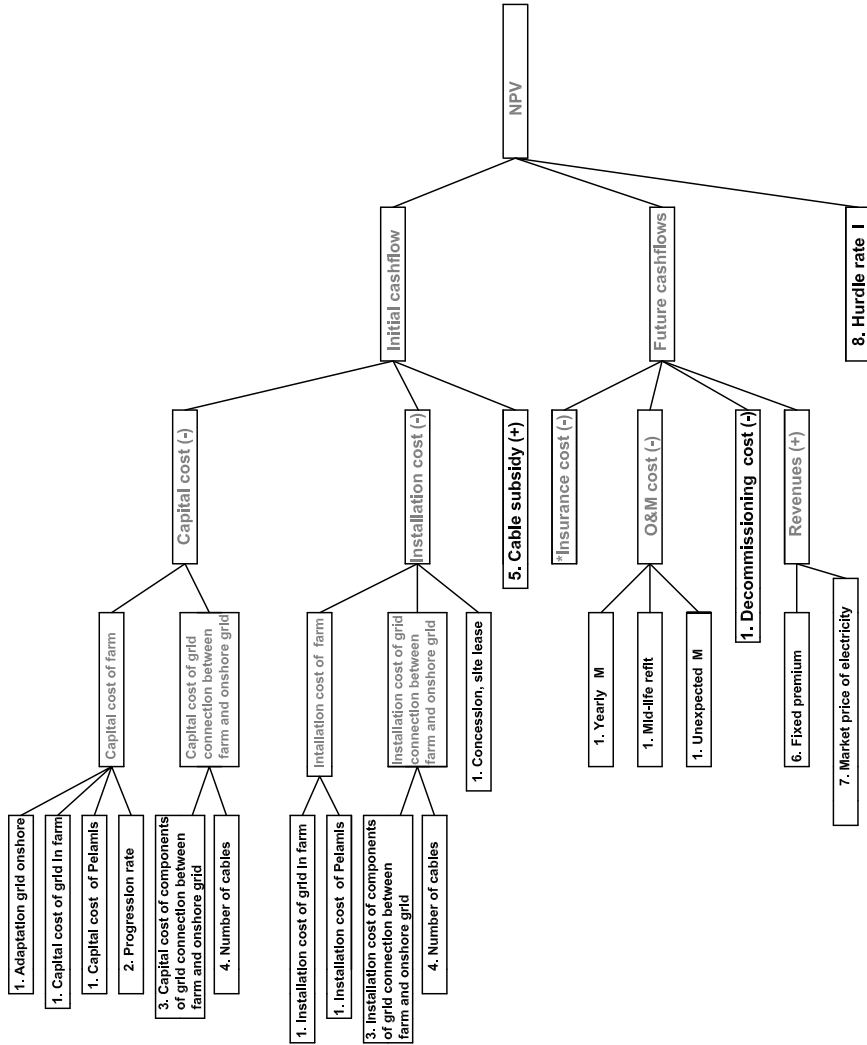
A shorter payback period is preferred. It should be noted that the payback period does not consider the time value of money. Furthermore cash flows following the payback period are not taken into account. Therefore the payback period should be calculated together with the NPV, to draw realistic conclusions.

In this investment analysis, the NPV is used as a the criterion to compare the five options.

### 10.3.2 Variables

In the investment analysis, the existence of uncertainty about the exact value of the variables that determine the NPV is recognized. Therefore a range of values (2, 3 or 4), with an estimated probability of occurrence, is considered for each variable. The variables that affect the NPV are shown in Figure 10.2. The cable subsidy and the revenues are positive cash flows (+), while the capital, installation, insurance, O&M and decommissioning costs generate negative cash flows (-). An occurrence probability (OP) of 0.8 is ascribed to the most likely value of a variable, while an OP of 0.1 or 0.2 is attributed to extreme values. The sum of the occurrence probabilities of the values of a variable is 1.0. The impact of the choice of the OP

is discussed in section 10.3.5. In this section each variable is discussed in more detail. The number of the variable is indicated on Figure 10.2.



\*No variation considered

Figure 10.2: Initial and future cash flows in an investment analysis

### 10.3.2.1 Variable 1: Capital, installation, O&M and decommissioning costs of a farm of Pelamis WECs

The cost components of a farm of Pelamis WECs have been described in two reports [3, 7]. In [7] the costs of a farm of 39 Pelamis WECs, each with a rated power of 650 kW, have been estimated by the developer of the Pelamis WEC, Ocean Power Delivery Ltd., in discussion with potential suppliers. No details concerning the farm lay-out have been provided. In [3] the costs of a farm of 213 Pelamis WECs (rated power of 500 kW), installed in three rows 28 km off the coast of San Francisco, have been assessed. The cost assessment in [3] is based on information from Ocean Power Delivery Ltd. The costs provided in [3, 7] are compounded to 2008 (reference year in this study) by considering an inflation rate of 2 %. In the following all costs are given in €2008. All costs in [3, 7], except for the cost for concession, site lease and adaptation of the grid onshore, are linearly transformed to a farm of 171, 190 and 265 Pelamis WECs. The capital, installation, O&M and decommissioning costs are given in Table 10.3 for a single Pelamis WEC, except for the cost for concession, site lease and adaptation of the grid onshore. Note that the installation costs of the cable network between the Pelamis WECs are included in the cost of the grid inside the farm. The cost of the cable network between the WECs is lay-out dependent (chapter 9) but is only a fraction of the total costs. Therefore no optimization has been performed. The capital and installation costs of the grid connection between the farm and the onshore grid are not taken into account in both studies. These costs are considered as a separate variable (variable 3) in this study and are described in section 10.3.2.3.

*Table 10.3: Estimated costs (in M€) for a single Pelamis WEC (except for costs for concession, site lease and adaptation grid onshore) based on [3, 7]*

Cost component	[7]	[3]
Capital cost of Pelamis WEC	0.78	0.86
Installation cost of Pelamis WEC	0.03	0.05
Cost of grid in farm	0.07	0.05
Yearly maintenance	0.02	0.03
Mid-life refit	0.10	0.12
Unscheduled maintenance	0.05	-
Decommissioning	0.02	-
Concession, site lease	0.80	4.63
Adaptation grid onshore	4.31	14.62

The author wants to stress that the estimation of installation and O&M costs



is very difficult as practical experience is lacking. In 2008, the first farm of 3 Pelamis WECs has been installed in Portugal. Experience from this small farm should result in more accurate estimations in near future. The installation and O&M costs depend on the distance to the harbour, the available water depth, the geology, the number of WECs, the distance between the WECs and the weather conditions. As the variation of these costs with the listed variables is unknown, a simple linear scaling is applied. Further a contradiction exists in the capital cost of the WEC. The capital cost of the device is higher in [3] compared to [7] while the device in [7] has a rated power of 650 kW, instead of 500 kW [3]. Therefore it is assumed that the costs given in [7] apply to a 500 kW device as well.

An OP of 0.8 is ascribed to the costs given in [7] in this study, as the cost calculation in [7] is more detailed and is the basis of the cost calculation in [3]. An OP of 0.2 is attributed to the costs provided in [3]. The total cost based on [3] is higher than the total cost calculated with [7]. A lower limit of the total cost has not been considered in this study as it is not likely that the first cost estimate given by the producer of the Pelamis WEC [7] will be too high.<sup>2</sup>

### 10.3.2.2 Variable 2: Progression rate

It is expected that the cost for the production of the Pelamis WEC (unit price per WEC) will diminish when the installed capacity rises [7]. Therefore the production cost of each Pelamis WEC has been estimated by taking a progression rate (PR) into account with equation (10.4). This is the so-called learning curve.

$$C'_m = C'_1 m^{\frac{\ln PR}{\ln 2}} \quad (10.4)$$

with  $C'_1$  the cost of the first Pelamis WEC and  $C'_m$  the cost of the  $m^{\text{th}}$  Pelamis WEC. For example, a PR of 85 % equates to a learning rate (LR) of 15 % ( $LR = 100 \% - PR$ ) and consequently to a 15 % reduction in cost for each doubling of the produced Pelamis WECs. A low PR represents a fast learning with a fast rate of cost reduction. When PR equals 100 % the production cost of each Pelamis WEC is equal to the production cost of the first WEC. Consequently no learning rate corresponds to  $PR = 100 \%$ .

As stated in [7], the PR of industrially processed systems varies between 0.85 and 0.95. When wave energy is considered as an immature technology a PR of 100 % should be applied. As it is not clear which value of PR is more likely, four values of PR, 85, 90, 95 and 100 %, each with an OP of 0.25 are considered in this study. The PR is only applied on the production cost of the Pelamis WEC, as no PR can be considered for the material cost. Furthermore no learning rate is taken into account for the installation cost, as experience already exists in the oil, gas

<sup>2</sup>Note that the capital cost of a 650 kW Pelamis WEC provided by the developer was already smaller than the cost of a 500 kW WEC estimated in [3].

and offshore wind industry.

### 10.3.2.3 Variable 3: Capital and installation costs of the electrical connection between farm and onshore grid

The estimation of the capital and installation costs of the cable connection between the farm and the onshore grid is based on the experience from offshore farms of wind turbines. A definition sketch of a possible offshore cable network is given in Figure 10.3.

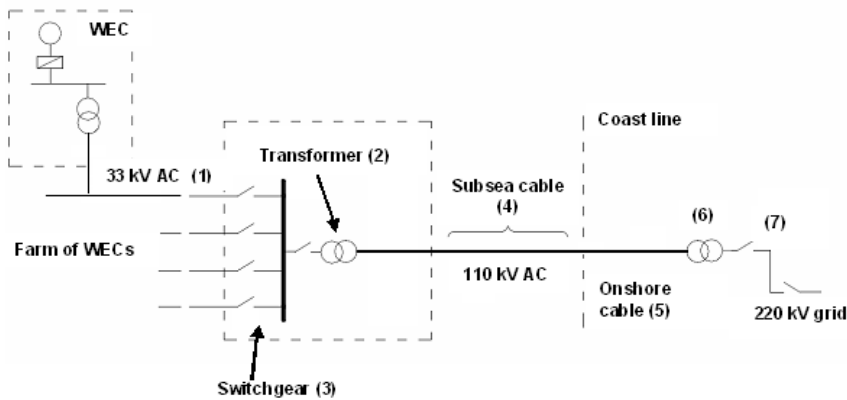


Figure 10.3: Definition sketch of electrical connection between farm and onshore grid

As seen in chapter 9, 33 kV AC cables are generally used inside the farm (1). For farms with a maximal rated power of 50 MW, these 33 kV cables are also installed between the farm and the onshore grid [1]. For larger farms, as considered here (Table 10.2), a higher voltage is needed. Consequently a transformer (2) platform, with associated switching and compensation equipment (3), to transform 33 kV to the higher voltage is installed offshore. Switchgear refers to the combination of circuit breakers to isolate electrical equipment. Typically switchgear is located on both the high voltage and the low voltage side of large power transformers. The charging current in subsea cables can be mitigated by providing reactive compensation equipment.

When the distance to the onshore grid connection is smaller than approximately 70 km, AC cables are used [1]<sup>3</sup>. AC cables apply for all options considered

<sup>3</sup>The capacitance and losses limit the technically feasible length of AC cables and can have significant impacts on the total cost of the grid connection. A HVDC (High Voltage Direct Current) transmission system has no practical transmission distance limitation [10]. In DC transmission, a

in this study. The cable between the farm and the grid connection onshore ((4)+(5)) can have the same voltage as the onshore transmission network. When the voltage in the cable differs from the onshore voltage, an onshore transformer (6) (with switchgear and reactive compensation (7)) is needed.

The voltage of the subsea cable (4) depends on three factors:

- The rated power of the farm
- The voltage of the grid connection onshore
- Cost of the electrical connection (including transformers, switchgear, ...)

The rated power of each option is given in Table 10.2 and the voltage of the onshore grid is shown in Table 10.1. Offshore subsea cable costs per km (without installation) for 132 kV and 220 kV cables are given in Table 10.4 [10]. It is assumed that the cable cost for 110 kV cables is equal to the cost for 132 kV cables as no information on the cost of 110 kV cables was available. In practice a slightly smaller cost for 110 kV cables is expected.

*Table 10.4: Unit cable costs [1, 10]*

Sea or Land	Voltage [kV]	Cost [M€/km]
Sea	132	1.5
Sea	220	1.65
Land	115	0.63

The cost of the transformer as a function of the rated power of the farm (Table 10.5) and the cost of switchgear as a function of voltage (Table 10.6) are also given in [10].

---

charging current only occurs during the instant of switching on or off, and has therefore no effect on the continuous current rating of the cable. Furthermore cable losses in DC cables are smaller compared to AC cables. When DC cables are installed two additional converter stations are required to convert AC to DC offshore and to convert DC to AC onshore. For transmission distances longer than 70 km a HVDC transmission system is cost competitive. It is expected that this distance will diminish as the cost of HVDC systems will decrease.

Table 10.5: Cost of transformer as a function of rated power [10]

Rated power [MW]	Cost [M€]
100	1.06
150	1.44

Table 10.6: Cost of switchgear as a function of voltage [10]

Voltage [kV]	Cost [M€]
33	0.058
132	0.124
220	0.183

On the DCS (site 3), 110 kV cables are selected as the voltage of the onshore grid equals 110 kV. Note that 110 kV is sufficient for the rated power of all options in this study [10]. On the GCS (site 1 and 2), the voltage of the grid connection onshore equals 220 kV. The cost of an offshore 220 kV cable (without transformer onshore) is larger than the cost of a 110 kV cable and an additional transformer (with switchgear) to transform 110 kV to 220 kV onshore. Therefore 110 kV cables are also used on the GCS. One should note that in practice, a thorough optimization is needed to select the best electrical connection between the farm and the onshore grid. A rather simple approach is used in this PhD dissertation as only limited costs were available.

On each site a platform of 300 m<sup>2</sup> with a cost of M€2.6 [1] is constructed to install all offshore equipment (transformer (2), switchgear (3), ...). The cost of an offshore transformer to transform the 33 kV to 110 kV is given in Table 10.5. It is assumed that 30 Pelamis WECs can be connected in a cluster [1]. To connect a cluster with the transformer 33 kV switchgear is needed. 110 kV switchgear is used to connect the transformer with the 110 kV subsea cable. The total cost of reactive compensation for a farm is given in [1] and equals M€2.5. Note that the cost of the 33 kV cables in the farm are included in variable 1.

The installation cost of the offshore subsea cable is given in [10] and equals M€0.1 per km. When a navigation route is crossed the cost is multiplied by 10 [1], as the cable needs to be installed in a dredged trench with a depth of at least 4 m. The cheaper technique of jetting cannot be used for this operation.

When the cable approaches land, from a water depth of approximately 5 m (required depth to use a cable laying vessel), special drilling techniques may be used to bring the cable on land. Approximately a distance of 1 km is needed. An average of the costs (including installation) specified in [1], M€3.2, is taken into account.

The cable cost per km on land (including installation) is studied in [1] and equals M€0.63/km for 115 kV cables (Table 10.4). This cost is used for the 110 kV cables in this study.

To calculate the length of the submarine and land cable, the distance to the coast and to the grid connection on land, as given in Table 10.1, are multiplied with a factor 1.25, as in practice the cable can never be installed over the shortest distance. This factor has not been applied to the width of crossed navigation routes, as the installation cost in navigation routes is very high. As in [11], it is assumed that navigation routes are crossed at an angle of 90°.

No additional O&M costs have been considered for the electrical connection between the farm and the onshore grid, as these depend on the final design. It is expected that these costs will not vary much for the considered options.

All costs related to the electrical connection between the farm and the onshore grid, given in this section, correspond to the most likely scenario (base scenario), with an OP of 0.8. No detailed cost estimates besides those provided in this section were available. Therefore the base values are multiplied with a factor 0.8 and 1.2, respectively to obtain a minimum and maximum value. This minimum and maximum value each have an OP of 0.1.

#### **10.3.2.4 Variable 4: Number of cables to shore**

The analysis in [4] suggests that the subsea cable should be designed without redundancy for wind farms up to 200 MW. In this study a single subsea cable is foreseen in the base scenario with an OP of 0.8. Providing a second subsea cable prevents total loss of electricity in case of a cable fault. Moreover, the offshore farm can be extended in future without installing an additional subsea cable. A scenario with two subsea cables has an OP of 0.2.

#### **10.3.2.5 Variable 5: Cable subsidy**

In [12] grid connection subsidies for offshore wind farms on the Belgian, Dutch, German, Danish and UK Continental Shelves are presented. For the wind farm on the Thorntonbank (BCS) a subsidy of 1/3<sup>th</sup> of the cable cost with a maximum of M€25 is provided. The farm of wind turbines Egmond aan Zee on the DCS received a state subsidy of M€27. No subsidies are foreseen for farms of wind turbines installed on the German and UK Continental Shelves. In Denmark the grid connection, except for the grid inside the farm, is paid by the grid operator.

In this study a subsidy of M€27 with an OP of 0.8 and no subsidy with an OP of 0.1 are taken into account for the site on the DCS. A subsidy equal to the capital and installation cost of the electrical connection between farm and onshore grid, has an OP of 0.1 as well. On the GCS the situation with no subsidy is more likely. Therefore an OP of 0.8 is considered for this situation on the GCS. Consequently the granting of a subsidy of M€27 has an OP of 0.1.<sup>4</sup>

### 10.3.2.6 Variable 6: Fixed premium

A fixed premium (in addition to the electricity price) guarantees return to producers of electricity from renewable energy, as the regional or national electricity utilities are obligated to buy renewable electricity at above-market rates set by the government<sup>5</sup>. On the DCS, a fixed premium of €97/MWh (on top of the actual electricity tariff) is foreseen for offshore wind energy [14]. In this study this tariff has been applied during 20 years for site 3, with an OP of 0.8. Note that in August 2006 fixed premiums were stopped for new projects on the DCS. This stop was announced as being temporary and is dependent on political priorities.

On the GCS (offshore wind farm Butendiek), a feed-in tariff of €91/MWh is foreseen during the first 12 years and €61.9 per MWh during the last 8 years [12]. The feed-in tariff is lowered after 12 years to encourage more efficient energy production. In [13] a feed-in tariff between €30/MWh and €130/MWh during the last 8 years is mentioned. In this study fixed premiums of €91/MWh during the first 12 years and €61.9 per MWh during the last 8 years are considered for the GCS, by analogy with the DCS. This situation has an OP of 0.8. Note that in practice feed-in tariffs instead of fixed premiums are foreseen on the GCS. In January 2009 new feed-in tariffs for offshore wind energy on the GCS are agreed on [15]. These new tariffs vary with distance to the coast, water depth, year of construction and year of deployment<sup>6</sup>.

In [14] the bandwidth of feed-in tariffs and fixed premiums for onshore and offshore wind power, biomass and photovoltaics in Germany, The Netherlands, Austria, Lithuania and Slovenia is given. In Germany the minimum and maximum

<sup>4</sup>Recently, the system applied in Denmark (grid connection, except for grid inside the farm, covered by the grid operator) has been approved in Germany [13]. Therefore, it would be more appropriate to assume an OP of 0.8 for this scenario and an OP of 0.1 for the scenario with no subsidy.

<sup>5</sup>Different generation-based support strategies exist [13], a.o. feed-in tariff, fixed premium and green certificates. In the case of a fixed premium, the price added to the electricity price is fixed, while in the case of a feed-in tariff (not additional to the electricity price), the total feed-in price is fixed. In the case of green certificates, a variable premium is added to the market price of electricity.

<sup>6</sup>During the first 12 years a starting feed-in tariff of €130/MWh is foreseen. For offshore wind farms installed before 1-1-2016 a bonus of €20/MWh is provided. The period of 12 years will be extended according to the distance to the coast and the water depth. The starting feed-in tariff will decrease annually by 5% for wind farms constructed after 2015. After the period of the higher starting feed-in tariff the payment goes down to the level of the base feed-in tariff. The base feed-in tariff equals €35/MWh.

feed-in tariff for photovoltaics equals €457/MWh and €624/MWh, respectively. Therefore in this study a fixed premium of €450/MWh during 20 years is assumed for both the DCS and GCS, with a small OP (0.2), to see what would be the effect if a high fixed premium (comparable to the feed-in tariff for photovoltaics) would be regulated for wave energy.<sup>7</sup>

### **10.3.2.7 Variable 7: Market price of electricity**

The market price of electricity equals approximately €70/MWh [16]. A minimum of €60/MWh (future estimate with large integration of wind [13]) and a maximum of €80/MWh (scenario with increasing prices of fossil fuels), each with an OP of 0.1, are considered in this study.

### **10.3.2.8 Variable 8: Hurdle rate**

In [7–9] the nominal hurdle rate varies between 8 % and 15 %. A nominal hurdle rate of 12 % has been used in the base scenario, with an OP of 0.8. The minimum and maximum value of the nominal hurdle rate are 8 % and 15 %, each with an OP of 0.1. Note that this variable is only considered in the sensitivity analysis.

A list of the variables with their value and OP is given in Table 10.7. Note that no variation on the insurance cost (Figure 10.2) is taken into account. The annual insurance cost is equal to 2 % [3] of the total capital and installation cost.

---

<sup>7</sup>This scenario is not likely to occur. A very high fixed premium is very effective, but not efficient. In Belgium the green certificates for photovoltaics have a minimum price of €450/MWh. This minimum price will decrease to €210/MWh in 2015 and €10/MWh in 2020.

Table 10.7: Considered values and occurrence probability (OP) for the variables that determine the NPV

N° Variable	Minimum		Base		Maximum	
	value	OP	value	OP	value	OP
1. Capital, installation, O&M and decommissioning costs of a farm of Pelamis WECs [M€]	-	-	costs in [7] <sup>1</sup>	0.8	costs in [3] <sup>1</sup>	0.2
2. Progression rate <sup>2</sup> [%]	85	0.25	90	0.25	100	0.25
3. Capital and installation costs of electrical connection between farm and onshore grid [M€]	0.8Y <sup>3</sup>	0.1	Y	0.8	1.2 Y	0.1
4. Number of cables to shore [-]	-	-	1	0.8	2	0.2
5. Cable subsidy [M€]						
GCS <sup>4</sup>	-	-	0	0.8	Y <sup>5</sup>	0.1
DCS	0	0.1	27	0.8	Y <sup>5</sup>	0.1
6. Fixed premium [€/MWh]						
GCS	-	-	91-61.9 <sup>6</sup>	0.8	450 <sup>7</sup>	0.2
DCS	-	-	97 <sup>7</sup>	0.8	450 <sup>7</sup>	0.2
7. Market price of electricity [€/MWh]	60	0.1	70	0.8	80	0.1
8. Nominal hurdle rate [%]	8	0.1	12	0.8	15	0.1

<sup>1</sup> Costs from [7] and [3] are given in section 10.3.2.1.

<sup>2</sup> An intermediate case with PR = 95 % and an OP of 0.25 has been considered as well.

<sup>3</sup> Y = the capital and installation cost of the electrical connection between farm and onshore grid as described in section 10.3.2.3.

<sup>4</sup> On the GCS an intermediate case with a cable subsidy of M€27 and an OP of 0.1 has been considered as well.

<sup>5</sup> Subsidy = the capital and installation costs of the electrical connection between farm and onshore grid

<sup>6</sup> During first 12 years €91/MWh, during the last 8 years €61.9/MWh

<sup>7</sup> During 20 years



### 10.3.3 Worst case, base case and best case scenarios

By using the values of the eight variables discussed above, three scenarios are studied:

- Worst case scenario (maximum value of costs, 2 cables to shore, hurdle rate of 12 %, minimum value of subsidy, fixed premium and market price of electricity, and a PR of 100 %)
- Base case scenario (all values with the highest OP in Table 10.7)
- Best case scenario (minimum value of costs, 1 cable to shore, hurdle rate of 12 %, maximum value of subsidy, fixed premium and market price of electricity, and a PR of 85 %)

The NPV for each scenario and each option is shown in Figure 10.4. The NPV of all options is negative in the worst and base case scenarios and positive in the best case scenario.

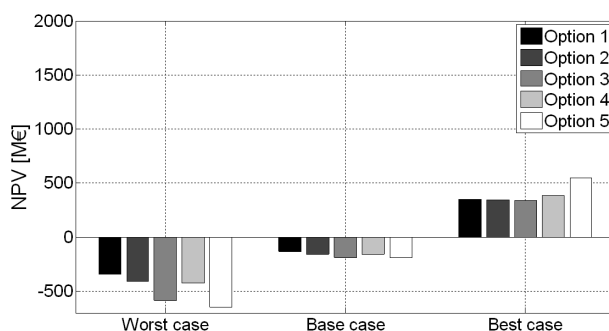


Figure 10.4: NPV of each option for three scenarios

In the worst and base case scenarios, option 1 has a slightly higher NPV. Hence in those two scenarios installing a farm of 171 Pelamis WECs on site 1 seems the best option. The NPV decreases when the site is located further from shore. On the other hand, in the best case scenario, option 5 has the highest NPV. In the best case scenario the fixed premium is very high (€450/MWh). Consequently the NPV increases very fast, when the production of the farm increases. As more Pelamis WECs are installed in option 5 compared to the other options, option 5 has the highest production and consequently the highest NPV. Furthermore the highest learning rate is considered in the best case scenario. The cost of additional Pelamis WECs in option 5 is less than 65 % of the cost of the first Pelamis WEC. This learning rate further increases the NPV.

The reader should keep in mind that the variation of installation and O&M costs with the distance to the harbour, water depth and geology is not taken into account in the analysis. It is expected that the NPV of option 3 and option 5 will be smaller due to higher installation and O&M costs, as site 3 is located further offshore. Furthermore, it is also noted that the cable subsidy and fixed premium in the base scenario is higher for site 3 (DCS). The higher cable subsidy and fixed premium partly compensate the higher cable cost of site 3.

The IRR, payback period and Cost Of Energy (COE) of each scenario is given in Table 10.8. By dividing the present value of the costs of a farm of Pelamis WECs by the present value of its energy production, the COE is calculated (equation (9.7)) [8]. A derivation of the COE is given in appendix H.

$$\text{COE} = \frac{\text{PV}(\text{capital costs}) + \text{PV}(\text{installation costs}) + \text{PV}(\text{insurance costs})}{\text{PV}(\text{energy production})} + \frac{\text{PV}(\text{O\&M costs}) + \text{PV}(\text{decommissioning costs})}{\text{PV}(\text{energy production})} \quad (9.7)$$

The COE is the minimum price at which energy must be sold for the energy project to break even when no subsidies or fixed premiums are considered.

Table 10.8: IRR, payback period and COE for three scenarios

Option	IRR [%]			Payback period [years]			COE [€/MWh]		
	Worst case	Base case	Best case	Worst case	Base case	Best case	Worst case	Base case	Best case
1	0	0	50	-	-	3	491	286	253
2	0	0	50	-	-	3	556	313	274
3	0	0	49	-	-	3	719	381	329
4	0	0	50	-	-	3	525	298	262
5	0	0	52	-	-	2	553	305	267

Only in the best case scenario a positive NPV (Figure 10.4), a high IRR and a short payback period are obtained. Even for the best case scenario the COE is rather high (between €253/MWh and €329/MWh) compared to conventional power and onshore and offshore wind power. The COE of conventional power is approximately €57/MWh [17]. Onshore wind is competitive with conventional power sources while offshore wind is more expensive by a factor 1.5 [13]. The COE for the best case scenario is 4 to 6 times higher than the COE of conventional power and 3 to 4 times higher than the COE of offshore wind power. It is clear that without subsidies the exploitation of a farm of Pelamis WECs in the southern North Sea is not feasible. Note that it is expected that the COE of conventional

power will increase if fuel price risk is taken into account. Predictions can be found in [13].

When looking only at the COE one could argue that option 5 is comparable to option 1, 2 and 4. The NPV in the worst case scenario is higher for option 1, 2 and 4, compared to option 5 (Figure 10.4), while the COE in Table 10.8 is comparable. As the production in 5 is higher, the project breaks even for a smaller COE. In the best case scenario the NPV of option 5 is higher than the NPV of the other options due to its higher production and the high fixed premium. When calculating the COE, only the higher production is taken into account. The higher production compensates the higher costs, resulting in a comparable COE for option 1, 2, 4 and 5. As option 3 has higher costs (site 3 is located 67 km from shore) and no higher production compared to option 1 and 2, the COE is the highest.

In the worst case and base case scenarios, option 1 seems to be the best one, while in the best case scenario option 5 causes the highest NPV. When studying the COE option 1, 2, 4 and 5 are comparable. Further analysis is needed to take a well supported decision. In the next section, a sensitivity analysis is performed to estimate the impact of the considered variables on the NPV.

### 10.3.4 Sensitivity analysis

To identify the variable with the largest impact on the NPV, a sensitivity analysis [18] is performed for each option. The NPV is calculated when each variable varies from its minimum till its maximum value (Table 10.7), keeping the other variables at their base value. The resulting variation of the NPV is presented in a sensitivity diagram. The sensitivity diagram for option 1 is given in Figure 10.5.

For example, variable 1 has a base and maximum value in the analysis (Table 10.7). The NPV equals M€-131 when all variables are equal to their base value. The NPV decreases to M€-178 when variable 1 is equal to its maximum value, while all other variables remain at their base value. Variable 6, the fixed premium, accounts for 50 % of the variability in option 1. The variables that cause the highest variation of the NPV are selected for further analysis: fixed premium (variable 6), cable subsidy (variable 5) and the number of cables to shore (variable 4). The variation of the NPV is comparable for variables 1, 2, 3 and 8.

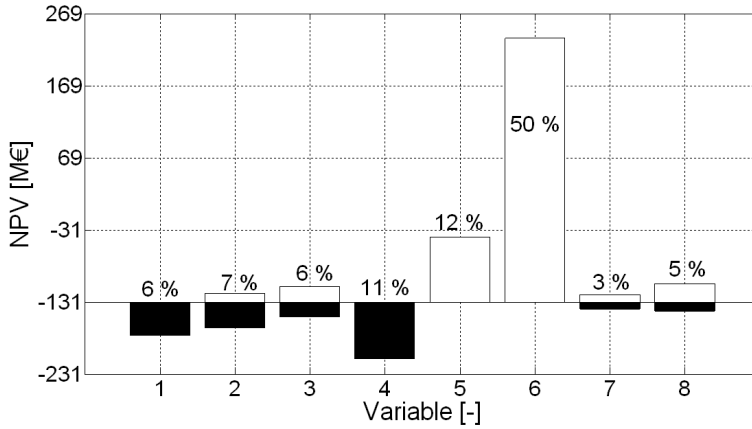


Figure 10.5: Sensitivity diagram for option 1

The sensitivity diagrams of all options are shown on a common absolute scale in Figure 10.6. The horizontal lines indicate the NPV of the base case of each option. These values do not differ a lot. When considering the possible variations of the NPV it is clear that no option stands out above the other options and no option is dominated by the other options. Consequently each option is considered in further analysis.

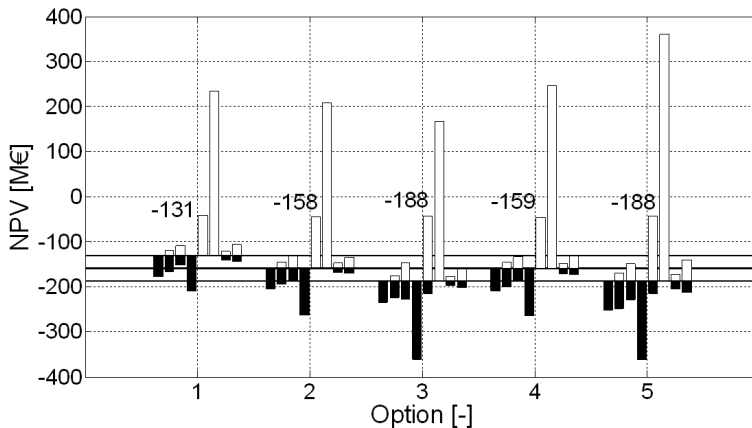


Figure 10.6: Sensitivity diagram comparing all options

For option 3, the variation of variable 3 is slightly higher than the variation of variables 1, 2 and 8 (Figure 10.6). Therefore variable 3, capital and installation

cost of electrical connection between farm and onshore grid, is selected for further analysis as well. The variation of the four selected variables account for approximately 80 % of the total variability, for each option. The uncertainty about the other variables (1,2,7 and 8) is ignored. These variables are treated as fixed at their base value.

### 10.3.5 Risk analysis

In a next step the NPV and OP of each combination of values of the remaining variables (3, 4, 5, 6), while keeping the other variables (1, 2, 7 and 8) at their base value, are calculated [18]. The cumulative probability of the NPV is shown in Figure 10.7 for the three options with the same number of Pelamis WECs, option 1, 2 and 3.

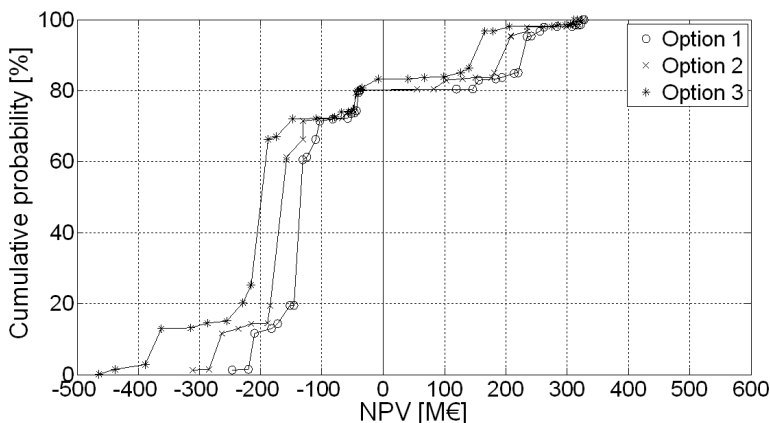


Figure 10.7: Cumulative probability of NPV for option 1, 2 and 3

For example, the chance that the NPV will be smaller than M€-250 is approximately 15 % for option 3. For option 2 and 1, the chance is smaller (12 % and 1 % respectively). The cumulative probability that the NPV will be higher than €0 equals 20 %, 20 % and 17 % for option 1, 2 and 3, respectively. The curve for option 3 is more located to the left side of the graph due to the larger distance to shore in option 3. Option 3 has always a smaller NPV and is consequently more risky. Option 1 has a slightly smaller degree of uncertainty compared to option 2 (slightly steeper curve). Furthermore the NPV of option 1 is always the highest. Consequently option 1 is preferred compared to option 2 and 3.

In Figure 10.8 a comparison between option 1, option 4 and option 5 is shown. Also for option 4 and 5 the chance of attaining a positive NPV is 20 %. Option 5 has a small chance (19 %) to obtain a higher value for the NPV compared to option 1 and 4. The chance that the NPV of option 4 is higher than option 1 is 16 %. Only

when the fixed premium is maximal, the NPV of option 4 and 5 may be higher than the NPV of option 1, as more WECs are installed in option 4 and 5. On the other hand the degree of uncertainty of option 5 is the highest. Option 1 has a slightly smaller degree of uncertainty compared to option 4. From Figure 10.7 and Figure 10.8 it can be concluded that option 1 is the best option, as was predicted by the multi-criteria decision analysis in chapter 3.

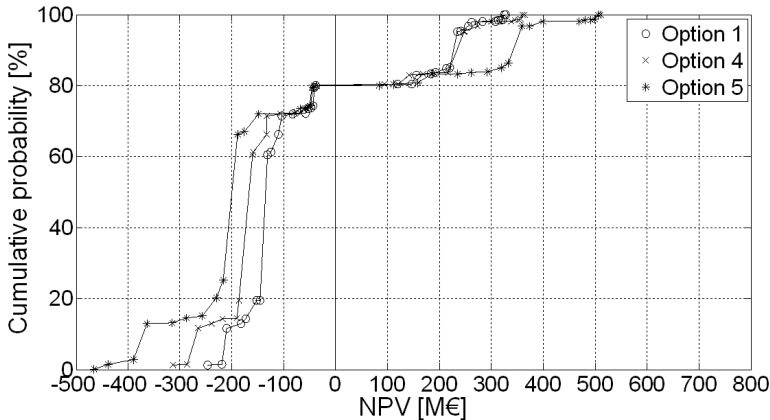


Figure 10.8: Cumulative probability of NPV for option 1, 4 and 5

The reader should remind that the OP of the maximum value of the fixed premium has a very large impact on the curves in Figures 10.7 and 10.8. This is shown in Figure 10.9 for option 1. If the OP of the base and maximum or minimum value of variable 4 and 6 is 0.6 and 0.4 instead of 0.8 and 0.2 and if the base, minimum and maximum values of variable 3 and 5 is 0.6, 0.2 and 0.2 instead of 0.8, 0.1 and 0.1 respectively, the chance to obtain a positive NPV increase to 40 %. In that case a fixed premium of €450/MWh has an OP of 0.4. The choice of a high OP for the base values (0.8) prevents a too high impact of minimum and maximum values of the variables.

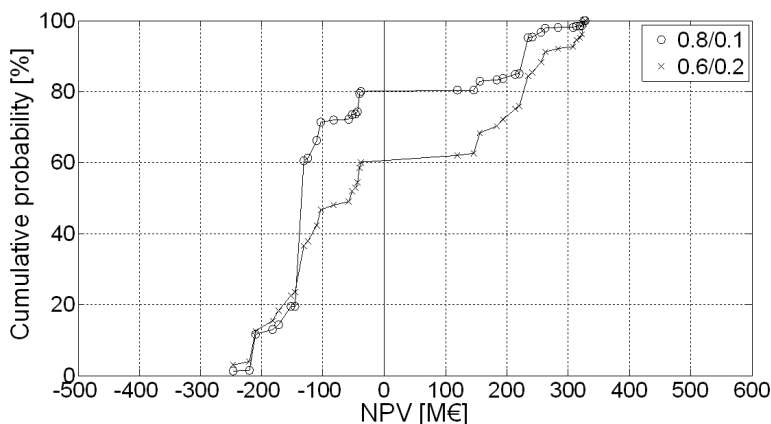


Figure 10.9: Cumulative probability of NPV for option 1 with (i) probability 0.8 for base value and 0.1 for minimum and maximum value and (ii) 0.6 for base value and 0.2 for minimum and maximum value

From the previous analysis it is clear that the value of the fixed premium has a large influence on the resulting value of the NPV. Considering more values of the fixed premium between the base and maximum value (Table 10.7) is difficult as most realistic estimates are approximately €100/MWh at maximum. From Table 10.8 it was observed that even in the best case scenario a fixed premium is needed. Consequently it is important to quantify the required fixed premium to make the exploitation of a farm of Pelamis WECs in the southern North Sea feasible. Therefore the sensitivity and risk analysis are repeated with the COE instead of the NPV as a criterion. Variables 5, 6 and 7 have no impact on the COE. Hence, only 5 variables (variable 1, 2, 3, 4 and 8) are shown in the sensitivity diagrams. The sensitivity diagram of option 1 is given in Figure 10.10. Variable 4 and 8 account for 56 % of the variability. When studying the sensitivity diagrams of the other options (Figure 10.11) it is observed that for option 3 variable 3 has a larger impact compared to variable 1 and 2. In general the impact of variable 1 and 2 is comparable. Variable 1, 3, 4 and 8 have been selected for further analysis. These variables account for 85 till 90 % of the total variability, for each option. Note that the COE of option 3 is smaller than the COE of the other options, due to the larger distance to shore and the relatively small number of WECs.

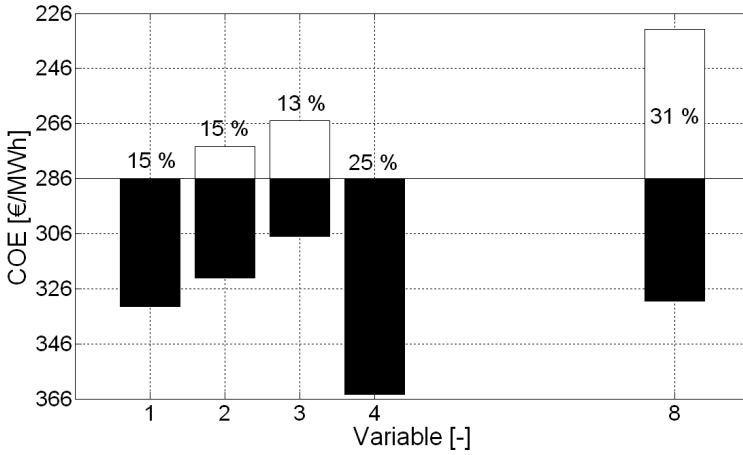


Figure 10.10: Sensitivity diagram for all options (COE)

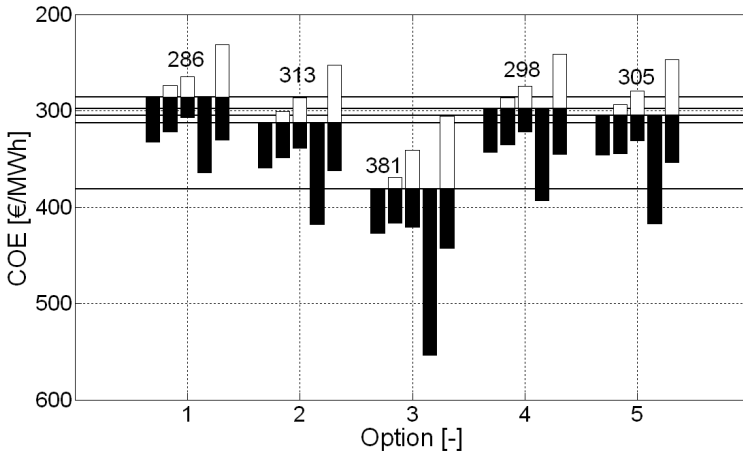


Figure 10.11: Sensitivity diagram for all options (COE)

Figure 10.12 shows the cumulative probability of the COE for the first three options. The COE decreases when the farm is located further from shore. The value of the COE of the base case (Table 10.8) has the largest probability. The chance to obtain a smaller value than the base value of the COE is only 13 % for each option. Option 1 is preferred as the COE is the smallest. If an electricity tariff of €70/MWh is considered, a fixed premium of at least €145/MWh is needed (smallest COE equals €215/MWh for option 1). Currently, fixed premiums are not



higher than €100/MWh. Larger fixed premiums or other financial incentives (a.o. a cable subsidy and tax incentives) are required to make the installation of a farm of Pelamis WECs feasible.

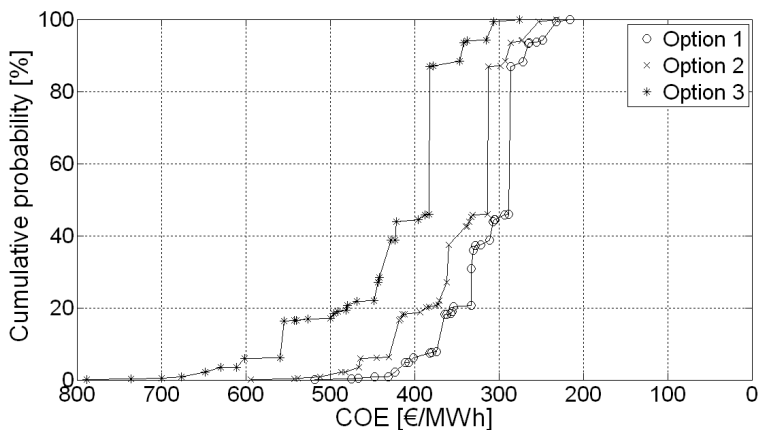


Figure 10.12: Cumulative probability of COE for option 1, 2 and 3

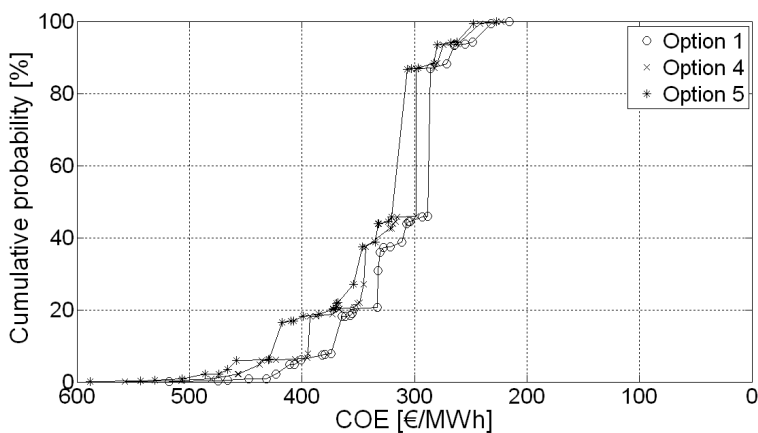


Figure 10.13: Cumulative probability of COE for option 1, 4 and 5

In Figure 10.13 option 1 is compared to option 4 and 5. Installing more WECs on site 2 and 3 reduces the COE. The COE of option 1 is still the smallest, but the difference with installing a farm on site 2 and 3 has almost completely disappeared. It seems interesting to investigate the installation of larger farms on site 2 and 3

in future research. Note that also the variation of the installation, operation and maintenance costs with the distance to shore, water depth and geology should be considered.

## 10.4 Remarks

Several, rather small, costs are not taken into account in this investment analysis: a.o. costs for Research and Development (R&D), costs for buoys to mark the farm, cost for communication and control, additional costs when subsea cables of pipelines are crossed and costs for balancing the power. Moreover, general company costs are not taken into account for the investment analysis. This means that corporate overhead (management, administration, ...) and taxes on realized benefits are not considered for the comparison in this study. When calculating the exact profit of an investment these costs should be taken into account.

## 10.5 Conclusions

In this chapter five options to install a single line of Pelamis WECs have been evaluated with an investment analysis. In option 1, 2 and 3 a constant number of Pelamis WECs (maximum number of Pelamis WECs on site 1 = 171) is installed in a single line on three sites, respectively 32 km, 42 km and 67 km offshore. In option 4 and 5 a maximum number of Pelamis WECs is arranged in a single line over the available width of site 2 (maximum 190 WECs) and 3 (maximum 265 WECs). Through this comparison the impact of the location (the distance to the coast) and the number of Pelamis WECs on the investment has been discussed.

In a first part, for each option three scenarios have been studied: (i) worst case, (ii) base case and (iii) best case. The NPV of all options is negative in the worst and base case scenarios and positive in the best case scenario. The Cost of Energy (COE) in the best case scenario is still 4 to 6 times higher than the COE of conventional power and 3 to 4 times higher than the COE of offshore wind power. Consequently subsidies are indispensable to make wave power exploitation feasible in the southern part of the North Sea. In the worst and base case scenarios option 1 has the highest NPV. In these scenarios the NPV decreases with increasing distance to shore. On the other hand, in the best case scenario, option 5 realizes the highest NPV as in this case the fixed premium is very high. Consequently the option with the highest number of Pelamis WECs (option 5) has the highest NPV. From the worst, base and best case scenarios no final conclusion on the most interesting investment can be drawn.

Therefore, in a second part, the occurrence probability of the NPV has been studied for the five options. The chance of obtaining a positive NPV is comparable for the 5 options. Option 3 is more risky compared to option 1, 2 and 4 due to its larger distance to shore. In option 5 the highest NPV is observed, but the occurrence probability of this high NPV is very small. Furthermore option 5

contains a high uncertainty. As the level of uncertainty is slightly smaller for option 1 compared to option 2 and 4, option 1 is selected as the best option to install a single line of Pelamis WECs in the southern part of the North Sea. The NPV is influenced to a large extent by the fixed premium. Installation of a single line of Pelamis WECs is not feasible without subsidies, not even for option 1. Furthermore, the current fixed premiums for offshore wind farms are in general not sufficient to make the installation of a farm of Pelamis WECs feasible. Higher fixed premiums and/or other financial incentives are required.

## References

- [1] I. Ydens and V. Meirschaert. *Onderzoek naar een economische exploitatie van het golfenergiepotentieel in de Noordzee m.b.v. ArcGIS*. Master's thesis, Ghent University, 2008.
- [2] Pelamis Wave Power Ltd. [www.pelamiswave.com](http://www.pelamiswave.com), Accessed June 2009.
- [3] M. Previsic. *System Level Design, Performance and Costs for San Francisco California Pelamis Offshore Wave Power Plant - E2I EPRI Global-006A-SF*. Technical report, EPRI, 2004.
- [4] P. Djapic and G. Strbac. *Cost Benefit Methodology for Optimal Design of Offshore Transmission Systems*. Technical report, Centre for Sustainable Electricity and Distributed Generation, 2008.
- [5] U. Henfridsson, V. Neimane, K. Strand, R. Kapper, H. Bernhoff, O. Danielsson, M. Leijon, J. Sundberg, K. Thorburn, E. Ericsson, and K. Bergman. *Wave energy potential in the Baltic Sea and the Danish part of the North Sea, with reflections on the Skagerrak*. *Renewable Energy*, 32:2069–2084, 2007.
- [6] G. J. Thuesen and W. J. Fabrycky. *Engineering Economy*. Prentice Hall, 1993.
- [7] *Pelamis WEC - Conclusion of primary R&D - ETSU V/06/00181/REP*. Technical report, OPD.
- [8] Entec UK Ltd. *Cost Estimation Methodology, The Marine Energy Challenge approach to estimating the cost of energy produced by marine energy systems*. Technical report, Carbon Trust, 2006.
- [9] W.M.J. Batten and A.S. Bahaj. *An assessment of growth scenarios and implications for ocean energy industries in Europe*. In *Proceedings of the 7<sup>th</sup> European Wave and Tidal Energy Conference (EWTEC)*, Porto, Portugal, 2007.
- [10] I.M. de Alegría, J.L. Martín, I. Kortabarria, J. Andreu, and P. Ibañez. *Transmission alternatives for offshore electrical power*. *Renewable and Sustainable Energy Reviews*, 13:1027–1038, 2009.
- [11] R. Prest, T. Daniell, and B. Ostendorf. *Using GIS to evaluate the impact of exclusion zones on the connection cost of wave energy to the electricity grid*. *Energy Policy*, 35:4516–4528, 2007.
- [12] G. Gerdes, A. Tiedemann, and S. Zeelenberg. *Case study: European offshore wind farms - a survey for the analysis of the experiences and lessons learnt by developers of offshore wind farms*. Technical report, Deutsche WindGuard GmbH, Deutsche Energie-Agentur GmbH and University of Groningen.

- 
- [13] S. Krohn, P.-E. Morthorst, and S. Awerbuch. *The Economics of Wind Energy. A report by the European Wind Energy Association*. Technical report, EWEA (European Wind Energy Association), 2009.
- [14] D.J. Swider, L. Beurskens, S. Davidson, J. Twidell, J. Pyrko, W. Prügler, H. Auer, K. Vertin, and R. Skema. *Conditions and costs for renewable electricity grid connection: Examples in Europe*. *Renewable Energy*, 33:1832–1842, 2008.
- [15] Dena Deutsche Energie-Agentur. [www.offshore-wind.de](http://www.offshore-wind.de), Accessed June 2009.
- [16] K. Lammertyn and H. Depraetere. *Getijdenenergie: een toekomst vanuit Belgisch perspectief? Onderzoek naar de technische en economische haalbaarheid*. Master's thesis, Ghent University, 2008.
- [17] B. Snyder and M.J. Kaiser. *Ecological and economic cost-benefit analysis of offshore wind energy*. *Renewable Energy*, 34:1567–1578, 2009.
- [18] R. Van Landeghem. *Making complex purchasing decisions using option analysis*. In *Proceedings of the International Purchasing, Logistics and Materials Management Conference*, Amsterdam, The Netherlands, 1986.



# 11

## General conclusions and recommendations

### 11.1 General conclusions

Wave energy has the potential to contribute significantly to our renewable energy supply. A Wave Energy Converter (WEC) converts the kinetic and/or potential energy of waves into electricity. Two main principles of wave power conversion can be distinguished: (i) Wave Energy Converters (WECs) with a body or water column that is oscillating and consequently generating a wave that interferes destructively with the incident waves and (ii) WECs that capture the overtopped waves in a basin above mean sea level and consequently absorb a part of the incident wave power.

As the rated power of a single WEC is rather small, a large number of WECs is necessary. These WECs are arranged in a geometric configuration or in a 'farm'. WECs in a farm are partly absorbing and partly redistributing the incident wave power. The presence of other WECs in the farm influence the operational behaviour of each individual WEC. Consequently the overall power production of the farm is affected. The current knowledge about the redistribution of energy inside and behind a farm of WECs is rather scarce. Both the power production and cost are dependent on the lay-out of the farm. Thus far most studies concentrate on the optimization of a single WEC, rather than optimizing a complete farm. To develop a commercial technology, the impact of arranging WECs in a farm has to be investigated as well. The optimization of the lay-out of a farm of WECs in the North Sea has been the focus of this PhD research. An optimal balance between

power production and cost of a farm of WECs has been aimed at. To that end, this work has been divided in three parts:

- The first part has been dealing with the wave power resources and the spatial planning of a farm of WECs.
- The second part has elaborated on the power production of a farm of WECs. In particular, the correlation between the farm lay-out and the power production has been studied.
- The cost of a farm of WECs has been investigated in a third part. The impact of the lay-out of a farm of WECs on its cost has been assessed. Finally an optimal lay-out, which results in the lowest cost per produced kWh, has been defined.

The main conclusions from each part are summarized in this section to provide an overall view of the outcome of the performed research.

### **11.1.1 Wave power resources and spatial planning of a farm of WECs**

Till now the **wave power resources** are mainly studied in detail for regions with a high energy density. As WECs still contend with problems regarding structural strength and mooring in a severe wave climate (i.e. survival conditions), the possibilities of wave power conversion in a milder wave climate (North Sea) have been investigated in this PhD dissertation.

Available wave data from buoy measurements and numerical wave propagation models have been gathered and analysed, resulting in the production of a map of the average annual available wave power in the North Sea. The available wave power ranges from less than 5 kW/m in the southern North Sea till more than 60 kW/m in the northern North Sea. The wave power resource on the Belgian Continental Shelf equals 4.64 kW/m at maximum. The available wave power in the northern North Sea is comparable with the one along the West European coast (40 - 70 kW/m). On the other hand, the wave power resource in the southern North Sea is rather limited as large swells from the Northern Atlantic are blocked by the UK.

An in-depth study of the wave power resource on the Belgian Continental shelf has revealed its high temporal and directional variation. Further, operational and design wave conditions have been specified. With the current knowledge and technology the Belgian Continental Shelf is a suitable area for testing scale models and WECs designed for smaller wave heights and wave periods. The mild wave climate allows testing of scale models with a 'scaled severe wave climate'. Furthermore, the relatively cheap scale model (compared to testing a prototype) can be installed without large vessels and can be easily accessed.

Not only the wave power resource but also technological requirements of the considered WEC, the costs of installation, grid connection, operation and



maintenance (O&M) and other activities in the North Sea should be considered when selecting a good location to install a farm of WECs. Therefore at the end of this part a **geo-spatial multi-criteria decision analysis** has been performed to select possible locations for the installation of a farm of Pelamis WECs in the southern North Sea. The Pelamis WEC is a semi-submerged WEC which consists of four cylindrical sections linked together by hinged joints. The rotation of these hinged joints drive a hydraulic system. The Pelamis WEC is not the most suitable WEC for the southern North Sea. Nevertheless this WEC has been used in this work as it is the only WEC of which information on the cost components of a farm is publicly available.

The results show that accessible areas with a relatively high energetic wave climate and situated rather close to shore are preferred. In the multi-criteria decision analysis several factors (e.g. distance to the electricity grid and distance to the harbour) have been weighted according to their relevance. The attribution of a weight to each factor is a difficult task. Therefore, a sensitivity analysis of the weights of the factors has been performed. It is mainly the ratio between the weight of the factor *produced power* and the sum of the weights of the factors *distances to shore, grid and harbour, extreme wave conditions* and *bimonthly variation of available wave power* that determines the location of suitable areas for the exploitation of a farm of Pelamis WECs. A ratio smaller than 0.7-0.75 gives preference to near shore locations.

### 11.1.2 Production of a farm of WECs

The power production of a farm of WECs in the North Sea has been investigated in a time-dependent mild-slope wave propagation model MILDwave, developed at Ghent University. Thus far, only head-on waves had been generated in MILDwave. As ocean waves contain a low (swell waves) or high (wind waves) directional spreading, not all wave components are propagating in the same direction. Therefore the existing wave generation technique, together with absorbing domain boundaries, has been extended and validated in this PhD dissertation.

The implementation of a farm of WECs in a numerical wave propagation model is relatively new. The applicability of wave propagation models for wave farm modelling has been thoroughly discussed in chapter 4. In some studies a farm is simplified to one transmitting obstacle. Consequently, the redistribution of wave energy around the WECs in the farm is not taken into account. In other studies the reflection from the WEC and transmission under and through the WEC are coupled through the degree of porosity assigned to the structure, which makes the adaptation of the production of the WEC to its surrounding wave climate in the farm impossible.

In this PhD dissertation a sponge layer technique has been developed to model WECs as individual obstacles with uncoupled reflection and transmission (and consequently absorption) characteristics. This technique is only applicable to WECs of the overtopping type (second category). For a WEC with sufficiently large dimensions ( $\geq 18$  m) and a small amount of reflection (minimal loss of

energy), each combination of reflection and absorption can be modelled. Only small levels of absorption which are in contradiction with the concept of a WEC (absorbing a substantial amount of wave power) cannot be obtained. As WECs of the overtopping type generally have a width and length of at least 18 m, this second category of WECs can be studied in MILDwave with the sponge layer technique.

To implement a WEC based on the oscillation principle (first category) in MILDwave the sponge layer technique has been extended. In this extension waves generated by the WEC motions (radiated waves) have been taken into account. To simulate these radiated waves in MILDwave a new wave generation lay-out, a wave generation circle, has been implemented.

In MILDwave a farm has been modelled by adapting the power absorption of each WEC to its surrounding wave climate. The power absorption of a farm of hypothetical WECs of the overtopping type obtained from MILDwave results, has been compared to the power absorption when the farm is simplified to a single transmitting obstacle. A more accurate estimation of the power absorption has been obtained with the method developed in MILDwave, as the redistribution of wave power inside the farm is taken into account. The comparison has revealed that the simplified method may result in a high overestimation or underestimation of the absorbed power (up to 40 %).

The validation of the sponge layer technique is not straightforward. The agreement between the wave pattern around a single and three absorbing obstacles, assessed both numerically and experimentally is not satisfactory. The differences in average wave height in front of and behind the test set-up increase from approximately 10 % for the single obstacle up till 20 % for the three absorbing obstacles. Reflection on the side walls of the physical wave flume with limited width (4 m) caused large disturbances of the wave pattern around the WEC (width of 0.72 m). Consequently the sponge layer technique has been validated by calculating the power absorbed by a WEC in a two dimensional domain in MILDwave. The results demonstrate that the sponge layer technique is a reliable tool to study wake effects behind WECs of the overtopping type.

This innovative sponge layer technique has been applied to a real case; the Wave Dragon WEC (WD-WEC). The WD-WEC is a floating offshore converter of the overtopping type (second category). Two wave reflectors focus the incoming waves towards a double curved ramp. The focussed wave run up the ramp and overtop in a basin above mean sea level. Power is produced when the water drains back to the sea through hydro turbines. The wave reflectors and the main body (ramp and reservoir with turbines) have been simulated as porous structures, exhibiting the same reflection, respectively absorption characteristics as the prototype WD-WEC, using the sponge layer technique. For swell waves ( $H_s = 1$  m and  $T_p = 5.6$  s) a large wake is observed behind the WD-WEC. A second WD-WEC installed 3 km behind the first WEC is absorbing less than 70 % of the first WEC. For wind waves, a faster wave redistribution and shorter wake behind the WEC is observed. A second WD-WEC installed 3 km behind the first WEC has almost the same wave power absorption as the first WEC.

Furthermore an FO<sup>3</sup> WEC (first category) has been implemented in MILD-

wave by using the extended sponge layer technique. The FO<sup>3</sup> WEC is a floating offshore converter which consists of several (12 or 21) heaving buoys placed in a floating platform. The vertical motion of the heaving buoys is converted to a rotational motion by means of a hydraulic system. In general, the wake effect behind an FO<sup>3</sup> WEC is limited compared to the WD-WEC.

The power absorption of several lay-outs of WD-WECs and FO<sup>3</sup> WECs with varying lateral and longitudinal spacing has been assessed in MILDwave. The results show that the redistribution of wave power in a farm, and consequently the production of a farm, is not only depending on the lay-out of the WECs, but also on the dimensions and absorption of the WEC, the type of WEC and the incident wave climate (wave period, wave direction and directional spreading). When installing multiple WD-WECs in a farm, the placing of a WD-WEC in a second row right behind a WD-WEC in the first row should be avoided, as a large wake behind the WEC is observed. A staggered grid lay-out is preferred. In the case of wind waves, less wave energy is propagating in-between the WD-WECs compared to long-crested waves (no directional spreading). On the other hand, a shorter, but still large wake is observed. The installation of a single line of WD-WECs results in the highest power absorption per km<sup>2</sup>. For the FO<sup>3</sup> WEC an aligned grid results in a higher power absorption.

### 11.1.3 Cost of a farm of WECs

Not only the power production but also the cost of a farm is lay-out dependent. The cost of a farm has been discussed in a third part of this PhD work. Mainly the cost of the electrical cables between the WECs in a farm is affected by the farm lay-out. The costs of installation, operation and maintenance are to a lesser degree dependent on the farm lay-out. An optimal cable network has been designed for different farm lay-outs of WD-WECs by minimizing the cost of the cable network itself and the capitalized cost of expected constrained energy from cable losses. The results indicate that the investment cost of the submarine cable network is only a fraction of the total investment cost of the farm. Consequently, minimizing the cost of the cable network has only a small effect on the cost of energy. Hence, when designing the lay-out of a farm of WD-WECs, mainly maximum power production should be aimed at. A single line of WD-WECs results in the smallest cost of energy. On the other hand this lay-out requires a wide sea area.

Installing a line of WD-WECs in front of a farm of wind turbines may be beneficial. In that case the WD-WECs may be connected to the transformer platform of the wind farm, which reduces the grid connection cost. Furthermore, the WD-WECs reduce the wave height in their lee, which makes maintenance of the farm of wind turbines easier and cheaper. Results show that the time window to access a wind farm increases with 9 to 14 % by installing a single line of WD-WECs in front of the farm of wind turbines.

Finally, an investment analysis of the deployment of a single line of Pelamis WECs in the southern North Sea has been presented. So far, cost estimates of WECs are mostly kept confidential by the WEC developers. The limited publicly

available data have been used in the investment analysis in this dissertation. The impact of the location and the number of WECs on the farm investment have been identified.

In the best case scenario the cost of energy is still 3 to 4 times higher than the cost of energy of offshore wind. Today, installation of a farm of Pelamis WECs in the southern part of the North Sea is not feasible without subsidies. Furthermore, the current fixed premiums for offshore wind farms are in general not sufficient to make the installation of a farm of Pelamis WECs feasible. Higher fixed premiums and/or other financial incentives are required.

## 11.2 Recommendations for further research

In the previous section the outcome of this PhD work has been summarized. Many aspects of a farm of WECs have been investigated in detail. However, parts of this work are worth further investigating. An overview of suggestions for future research is given below.

In the first part of this PhD dissertation the wave power resources in the North Sea have been quantified by using available wave data from buoy measurements and numerical wave propagation models on 34 locations. A more detailed spatial distribution of the wave power potential in the southern part of the North Sea has been obtained with hindcasts of the WAM-PRO model during 2003 and 2004. It would be desirable to extend this hindcast period, as the yearly variation of the available wave power is high. Furthermore, a further comparison between buoy data and data from the WAM-PRO model is recommended.

The hindcasts of the WAM-PRO model during a longer period should be used in the geo-spatial multi-criteria decision analysis instead of creating Thiessen polygons around the limited buoy locations in the southern North Sea. Finally, a more well-founded estimation of the weights used in the multi-criteria analysis is advisable, by consulting different decision groups and by using experience from the first farm of WECs, which are currently getting installed.

In a second part of this PhD work the production of a farm of WECs has been assessed in the numerical wave propagation model MILDwave. It has been shown that the developed sponge layer technique in MILDwave is a viable tool to study wave power redistribution in and around a farm and to calculate the power production of a farm. However, still a number of aspects should be addressed to make the method more reliable or to extend the developed method:

- Validation of this sponge layer technique with experiments in a physical wave flume was not easy, as the wave pattern in and around the farm was highly affected by reflections on the side walls of the wave flume. The wave pattern in and around a farm of WECs should be investigated in a large wave basin in which the farm is located further away from the side walls of the

basin to prevent disturbances from reflections on these side walls. If possible the technique should also be compared to prototype measurements in and around the first farms of WECs. It is recommended to acquire measurements of wave heights in these first farms.

- The diffraction and radiation wave patterns of the FO<sup>3</sup> WEC have only been calculated for three regular head-on waves with  $T = 4$  s, 6 s and 8 s. More calculations with the Boundary Element Method WAMIT for other wave periods and wave directions should be performed to improve the understanding of the diffraction and especially radiation wave patterns. In this respect the modelling of a single heaving buoy (or other WEC of the first category) is recommended.
- When calculating the power absorbed by a farm of FO<sup>3</sup> WECs secondary radiated waves have been neglected. A more detailed study should be carried out to gain more insight in their impact. Therefore the diffraction and radiation wave pattern around a farm of heaving buoys may be assessed in WAMIT and compared to the resulting wave pattern calculated in MILDwave. Finally, the redistribution of wave power in a farm of WECs of the first category should be studied in irregular long-crested and short-crested waves.
- In this PhD dissertation the wake behind a farm of WECs has been studied in a numerical wave basin of 5 km x 8 km at maximum. To quantify the length of the wake as a function of the farm width a longer and wider wave basin in MILDwave is needed. Furthermore, a larger domain is required to study the shoreline change caused by the installation of a farm of WECs. By application of nested grids and by use of parallelization (port to multiprocessor computer), the definition of larger domains, which consequently can include larger farms of WECs, will be possible in MILDwave. Furthermore, MILDwave will be able, in return, to produce results within shorter computational time, mostly for the more time-consuming cases of short-crested waves.
- In this work no wave regeneration by wind has been considered as the wake effects behind a farm are the largest when no wind is present (worst case). As WECs operate when waves (and mostly wind) are present, it is necessary to investigate the impact of wind regeneration on the wake behind a farm of WECs.
- Finally it may be interesting to include current fields in the mild-slope equations to study the impact of currents on the wake or the impact of the wake on wave-driven currents and near shore sediment transport.

In a third part of this PhD research the cost of a farm of WECs has been analysed. Results show that the investment cost of the submarine cable network is negligible compared to the total investment cost of the farm. In this work it has

been assumed that each WEC is moored separately. Further research should be performed to assess the impact of the farm lay-out on the mooring configuration and consequently on the cost of the mooring.

The investment analysis of a single line of Pelamis WECs in the southern North Sea has been based on assumptions and estimates. This analysis should be updated when more detailed information is available. If information on the wake of a Pelamis WEC is accessible, it could be interesting to study the installation of multiple rows of Pelamis WECs in the southern North Sea. The investment analysis should be repeated for other WECs as soon as financial data for these WECs are available.



# List of publications

## A.1 International journal publications

- C. Beels, G. De Backer, and P. Mathys. *Wave energy conversion in a sheltered sea*. *Sea Technology*, 49:21-24, 2008.
- C. Beels, P. Troch, G. De Backer, M. Vantorre, and J. De Rouck. *Numerical implementation and sensitivity analysis of a wave energy converter in a time-dependent mild-slope equation model*. Accepted for publication in *Coastal Engineering*, 2008.
- C. Beels, P. Troch, K. De Visch, J. P. Kofoed, and G. De Backer. *Application of the time-dependent mild-slope equations for the simulation of wake effects in the lee of a farm of Wave Dragon wave energy converters*. Accepted for publication in *Renewable energy*, 2009.
- C. Beels, P. Troch, J.P. Kofoed, P. Frigaard, J. Vindahl Kringelum, P. Carsten Kromann, M. Heyman Donovan, J. De Rouck and G. De Backer. *A methodology for production and cost assessment of a farm of wave energy converters*. Submitted for publication in *Renewable Energy*, 2009.
- G. De Backer, M. Vantorre, C. Beels, J. De Pré, S. Victor, J. De Rouck, C. Blommaert, and W. Van Paeppegem. *Experimental investigation of water impact on axisymmetric bodies*. Accepted for publication in *Applied Ocean Research*, 2009.
- G. De Backer, M. Vantorre, P. Frigaard, C. Beels, and J. De Rouck. *Bottom*

*slamming on heaving point absorber wave energy devices*. Submitted for publication in Journal of Marine Science and Technology, 2009.

- G. De Backer, M. Vantorre, C. Beels, J. De Rouck, and P. Frigaard. *Power absorption by closely spaced point absorbers in constrained conditions*. Submitted for publication in IET Renewable Power Generation, 2009.

## A.2 National journal publications

- G. De Backer, C. Beels, T. Mertens, and L. Victor. *Golfenergie: groene stroom uit de zeegolven*. De Grote Rede, 22:2-8, 2008.

## A.3 International conference publications

- J. Geeraerts, J. De Rouck, C. Beels, S. Gysens, and P. De Wolf. *Reduction of wave overtopping at sea dikes: stilling wave basin*. In Proceedings of the 30<sup>th</sup> International Conference on Coastal Engineering (ICCE), San Diego, USA, 2006.
- C. Beels, P. Troch, G. De Backer, J. De Rouck, T. Moan, and A. Falcão. *A model to investigate interacting wave power devices*. In Proceedings of the 1<sup>st</sup> International Conference on Ocean Energy, Bremerhaven, Germany, 2006.
- C. Beels. *A farm of interacting wave power devices*. In Proceedings of the 1<sup>st</sup> International PhD Symposium on Offshore Renewable Energy (INORE), Trondheim, Norway, 2007.
- C. Beels, J. De Rouck, H. Verhaeghe, J. Geeraerts, and G. Dumon. *Wave energy on the Belgian Continental Shelf*. In Proceedings Conf. Marine Challenges: Coastline to Deep Sea OCEANS 07 IEEE, Aberdeen, Scotland, 2007.
- G. De Backer, M. Vantorre, R. Banasiak, C. Beels, and J. De Rouck. *Numerical modelling of wave energy absorption by a floating point absorber system*. In Proceedings of the 17<sup>th</sup> International Offshore and Polar Engineering Conference (ISOPE), Lisbon, Portugal, 2007.
- C. Beels, J.C.C. Henriques, J. De Rouck, M.T. Pontes, G. De Backer, and H. Verhaeghe. *Wave energy resource in the North Sea*. In Proceedings of the 7<sup>th</sup> European Wave and Tidal Energy Conference (EWTEC), Porto, Portugal, 2007.
- G. De Backer, M. Vantorre, R. Banasiak, J. De Rouck, C. Beels, and H. Verhaeghe. *Performance of a point absorber heaving with respect to a floating platform*. In Proceedings of the 7<sup>th</sup> European Wave and Tidal Energy Conference (EWTEC), Porto, Portugal, 2007.



- G. De Backer, M. Vantorre, J. De Pré, J. De Rouck, P. Troch, C. Beels, J. Van Slycken, and P. Verleysen. *Experimental study of bottom slamming on point absorbers using drop tests*. In Proceedings of the 2<sup>nd</sup> International Conference on the Application of Physical Modelling to Port and Coastal Protection (CoastLab), Bari, Italy, 2008.
- G. De Backer, M. Vantorre, S. Victor, J. De Rouck, and C. Beels. *Investigation of vertical slamming on point absorbers*. In Proceedings of the 27<sup>th</sup> International Conference on Offshore Mechanics and Arctic Engineering (OMAE), Estoril, Portugal, 2008.
- C. Beels, V. Meirschaert, I. Ydens, P. Mathys, J. De Rouck, G. De Backer, and L. Victor. *The impact of several criteria on site selection for wave energy conversion in the North Sea*. In Proceedings of the 2<sup>nd</sup> International Conference on Ocean Energy, Brest, France, 2008.
- C. Beels, P. Troch, J. De Rouck, T. Versluys, and G. De Backer. *Numerical simulation of wake effects in the lee of a farm of wave energy converters*. In Proceedings of the 28<sup>th</sup> International Conference of Ocean, Offshore and Arctic Engineering (OMAE), Honolulu, Hawaii, 2009.
- G. De Backer, M. Vantorre, K. De Beule, C. Beels, and J. De Rouck. *Experimental investigation of the validity of linear theory to assess the behaviour of a heaving point absorber at the Belgian Continental Shelf*. In Proceedings of the 28<sup>th</sup> International Conference of Ocean, Offshore and Arctic Engineering (OMAE), Honolulu, Hawaii, 2009.
- C. Beels, P. Troch, K. De Visch, G. De Backer, J. De Rouck, and J.P. Kofoed. *Numerical simulation of wake effects in the lee of a farm of Wave Dragon wave energy converters*. In Proceedings of the 8<sup>th</sup> European Wave and Tidal Energy Conference (EWTEC), Uppsala, Sweden, 2009.
- G. De Backer, M. Vantorre, C. Beels, J. De Rouck, and P. Frigaard. *Performance of closely spaced point absorbers with constrained floater motion*. In Proceedings of the 8<sup>th</sup> European Wave and Tidal Energy Conference (EWTEC), Uppsala, Sweden, 2009.

#### A.4 National conference publications

- C. Beels, P. Troch, J. De Rouck, and M. Vantorre. *Optimal pattern of interacting wave power devices*. In Proceedings of the 7<sup>th</sup> FirW PhD Symposium, Ghent, Belgium, 2006.
- C. Beels, P. Troch, and J. De Rouck. *Optimal energy production of interacting wave power devices*. In Book of Abstracts VLIZ Young Scientists' Day, Brugge, Belgium, 2007.

- G. De Backer, C. Beels, and J. De Rouck. *Waves in the North Sea: powering our future?* In Book of Abstracts VLIZ Young Scientists' Day, Brugge, Belgium, 2008.
- C. Beels, J. De Rouck, and P. Troch. *Optimization of the lay-out of a farm of Wave Dragon wave energy converters in the North Sea.* Proceedings of the 10<sup>th</sup> FirW PhD Symposium, Ghent, Belgium, 2009.
- C. Beels, P. Troch, and J. De Rouck. *Optimization of the lay-out of a farm of Wave Dragon wave energy converters in the North Sea.* Book of Abstracts VLIZ Young Scientists' Day, Oostende, Belgium, 2009.

# B

## Wave power

### B.1 Regular waves

In linear wave theory the velocity potential  $\Phi(x, y, z, t)$  can be written as equation (B.1) by using the method of separation of variables.

$$\Phi(x, y, z, t) = f(z, h) \varphi(x, y, t) \quad (\text{B.1})$$

with  $\varphi(x, y, t)$  the velocity potential at  $z = 0$  (still water level).  $f(z, h)$  describes the vertical structure of the wave motion and is given in equation (B.2).

$$f(z, h) = \frac{\cosh(k(z + h))}{\cosh(kh)} \quad (\text{B.2})$$

For a regular wave, propagating along the y-axis, the fluid particle velocity in y-direction  $v_y$ , can be written as equation (B.3).

$$v_y = \frac{\partial \Phi}{\partial y} = \frac{\partial \varphi}{\partial y} f(z, h) \quad (\text{B.3})$$

The energy transported per unit time through an envisaged vertical strip of unit width, parallel to the wave front, or the energy-flux or wave power  $p$  (W/m) is defined in equation (B.4) [1]:

$$p = \int_{-h}^0 \overline{\varphi_{tot} v_y} dz \quad (\text{B.4})$$

where the total pressure  $\varphi_{tot}$  is the sum of the static pressure  $\varphi_{stat}$  and the dynamic pressure  $\varphi_{dyn}$ . The overbar denotes time average. Because the

time average particle velocity is zero,  $\overline{v_y} = 0$ , equation (B.4) simplifies to equation (B.5).

$$p = \int_{-h}^0 \overline{\wp_{dyn} v_y} dz \quad (\text{B.5})$$

with the water depth  $h$  and the dynamic pressure  $\wp_{dyn}$  given by equation (B.6)

$$\wp_{dyn} = \rho g \eta f(z, h) \quad (\text{B.6})$$

with the sea water density  $\rho$ , the gravitational acceleration  $g$  and the surface elevation  $\eta$ . By using equations (B.3) and (B.6) in equation (B.5) the wave power  $p$  can be written as equation (B.7). The time integration is carried out over a number of wave periods.

$$p = \rho g \frac{1}{2k} D(kh) \frac{1}{t} \int_0^t \eta \frac{\partial \phi}{\partial y} dt \quad (\text{B.7})$$

with  $D(kh)$  equal to [1]:

$$D(kh) = 2k \int_{-h}^0 (f(z, h))^2 dz = 2k \int_{-h}^0 \left( \frac{\cosh(k(z+h))}{\cosh(kh)} \right)^2 dz \quad (\text{B.8})$$

For deep water  $D(kh)$  equals 1.

For regular waves, the surface elevation  $\eta$  and the fluid particle velocity in  $y$ -direction  $v_y$  can be written as:

$$\eta = a \cos \Theta \quad (\text{B.9})$$

$$v_y = \frac{\partial \Phi}{\partial y} = \frac{agk}{\omega} \cos \Theta f(z, h) \quad (\text{B.10})$$

with the phase angle  $\Theta$ , the wave amplitude  $a$ , the wave number  $k$  and the angular frequency  $\omega$ . The energy-flux  $p$  given in equation (B.7) simplifies to equation (B.11) for regular waves.

$$p = \frac{\rho g^2 a^2}{2\omega} D(kh) \frac{1}{t} \int_0^t \cos^2 \theta dt \quad (\text{B.11})$$

By using linear frequency dispersion relation,  $\omega^2 = gk \tanh(kh)$ , the energy-flux  $p$  in deep water for regular waves is given by equation (B.12).

$$\begin{aligned} p &= \frac{1}{2} \rho g a^2 C_g \\ &= \frac{1}{8} \rho g H_i^2 C_g \end{aligned} \quad (\text{B.12})$$

with the group velocity  $C_g$  in deep water given by equation (B.13).

$$C_g = \frac{C}{2} = \frac{1}{2} \frac{g}{2\pi f} \quad (\text{B.13})$$

with the phase velocity  $C$ .

Replacing  $C_g$  in equation (B.12) leads to

$$p = \frac{1}{32\pi} \rho g^2 H_i^2 T \quad (\text{B.14})$$

with the wave period  $T = \frac{1}{f}$ . When the deep water assumption is not fulfilled, equation (B.15) should be used for the group velocity  $C_g$  [2].

$$C_g = \frac{1}{2} \left( \frac{g}{k} \tanh(kh) \right)^{\frac{1}{2}} \left( 1 + \frac{2kh}{\sinh(2kh)} \right) \quad (\text{B.15})$$

## B.2 Irregular waves

Following the linear superposition assumption, irregular waves can be described as a superposition of an infinite number of regular wave components with different wave heights  $H_i$  and frequencies  $f$ . Hence the frequency spectrum  $S(f)$  can be used to define the wave power  $p$  (equation (B.16)).

$$p = \rho g \int_0^{\infty} C_g(f, h) S(f) df \quad (\text{B.16})$$

By using equation (B.13) equation (B.16) can be written as equation (B.17) for deep water.

$$\begin{aligned} p &= \frac{\rho g^2}{4\pi} \int_0^{\infty} \frac{1}{f} S(f) df \\ &= \frac{\rho g^2}{4\pi} m_{-1} \end{aligned} \quad (\text{B.17})$$

with  $m_{-1}$  first negative spectral moment.

The energy velocity  $T_e$  is given by equation (2.3).

$$T_e = T_{m-1,0} = \frac{m_{-1}}{m_0} \quad (\text{2.3})$$

Substituting equation (2.3) in equation (B.17) and using the definition of the significant wave height  $H_s = H_{m0} = 4\sqrt{m_0}$  leads to equation (B.18).

$$\begin{aligned} p &= \frac{\rho g^2}{4\pi} m_0 T_e \\ &= \frac{\rho g^2}{64\pi} H_s^2 T_e \end{aligned} \quad (\text{B.18})$$

## References

- [1] J. Falnes. *Ocean Waves and Oscillating Systems: linear interactions including wave-energy extraction*. Cambridge University Press, 2002.
- [2] J. A. Crabb. *Synthesis of a directional wave climate*. In B. Count, editor, *Power from Sea Waves*, pages 41–74. Academic Press, 1980.



## Wave measurements at Westhinder and ZW-Akkaert from 1977 on

Scatter diagrams in [1], based on measurements between 1977 and 1986 result in an average available wave power of 5.05 kW/m at ZW-Akkaert and 4.42 kW/m at Westhinder. The resource obtained with measurements between 1990 and 2004 is comparable to the resource calculated with measurements between 1977 and 1986 at Westhinder. On the other hand, at ZW-Akkaert, a larger wave resource is observed with measurements between 1977 and 1986 compared to the resource based on measurements during 1984-2004. Therefore, the measurements between 1977 and 2008 are analysed in more detail in this appendix.

In the scatter diagrams in [1] a shift towards larger wave heights is observed, compared to the scatter diagrams used in this PhD dissertation. The shift in wave height is larger at ZW-Akkaert compared to Westhinder. Consequently it is expected that the resource, based on the scatter diagrams in [1], will be higher. A higher resource is indeed observed for ZW-Akkaert (5.05 kW/m compared to 3.64 kW/m). However, at Westhinder the resource obtained with measurements between 1990 and 2004 is comparable to the resource calculated with measurements between 1977 and 1986, while slightly larger wave heights were observed during the latter period. The yearly average  $H_s$ , calculated between 1977 and 2008 at Westhinder, is shown in Figure C.1. The average significant wave height  $H_s$  between 1977 and 1986 is slightly higher than  $H_s$  measured from 1991 on. This shift was also observed in the scatter diagrams.

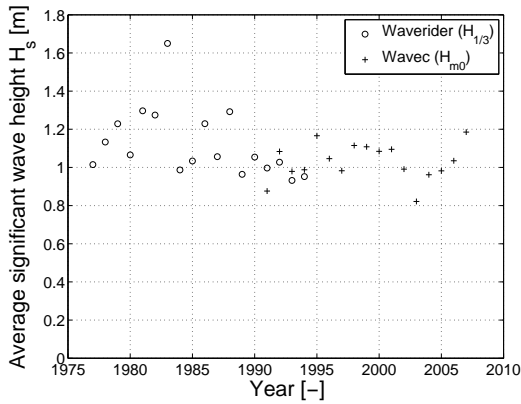


Figure C.1: Yearly variation of the average significant wave height  $H_s$  during the period 1977-2008 at Westhinder

The yearly average  $T_m$ , calculated between 1977 and 2008 at Westhinder, is shown in Figure C.2.

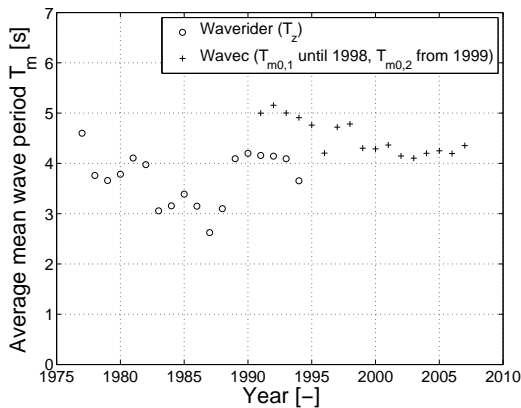


Figure C.2: Yearly variation of the average mean wave period  $T_m$  during the period 1977-2008 at Westhinder

Between 1977 and 1994 a Waverider was installed at Westhinder and  $H_s$  and  $T_m$  were calculated with a time domain analysis. From 1991 until 1994 a Wavec had been installed as well and since 1994 the Waverider had been removed. For the Wavec  $H_s$  and  $T_m$  are calculated from the energy spectrum. From 1991 until 1998  $T_m$  was calculated as  $T_{m0,1} = \frac{m_0}{m_1}$ , which was always higher than  $T_m$ , measured by a Waverider. Since 1999  $T_{m0,2}$  has been used as average wave period  $T_m$ . This period agrees well with  $T_m$ , obtained with a Waverider (Figure C.2). As a consequence the wave period between 1991 and 1998 was too high.



The smaller wave height between 1990 and 2008, compared to the period 1977-1986 is compensated by the higher mean wave period  $T_m$  between 1990 and 1998, resulting in approximately the same resource in the first and second measurement period at Westhinder.

One should note that measurements and analysis during the last 20 year occur more accurately, which can also partly explain the differences between both measurement periods. When only considering the measurements between 1999 and 2008 (when  $T_m = T_{m0,2}$ ) an average available wave power of 4.4 kW/m is obtained at Westhinder which is only 5 % lower than resource obtained with measurements between 1990 and 2008 (4.64 kW/m).

## References

- [1] Haecon. *Atlas Hydro-meteo waarnemingen voor de Vlaamse kust*. Technical report, Vlaamse Gemeenschap, Diensten van de Vlaamse executieve openbare werken en verkeer, Bestuur der waterwegen en van het zeezezen, Dienst der kust.



# D

## Mild-slope equations of Radder and Dingemans

A short derivation of the mild-slope equations of Radder and Dingemans is given in this appendix. A more detailed discussion about these equations can be found in [1].

The mild-slope equations are based on linear wave theory. In linear wave theory it is assumed that the wave height is small compared to the wave length or water depth. The linear equations for an incompressible and inviscid fluid with irrotational flow in the  $(x,y)$ -plane over an uneven bottom  $z = -h(x, y)$ , with atmospheric pressure 0 at the surface are given in equations (D.1)<sup>1</sup>, (D.2)<sup>2</sup>, (D.3)<sup>3</sup> and (D.4)<sup>4</sup>.

$$\nabla^2 \Phi + \frac{\partial^2 \Phi}{\partial z^2} = 0 \quad \text{for} \quad -h(x, y) \leq z \leq 0 \quad (\text{D.1})$$

$$\frac{\partial \Phi}{\partial z} + \nabla \Phi \cdot \nabla h = 0 \quad \text{at} \quad z = -h(x, y) \quad (\text{D.2})$$

$$\frac{\partial \Phi}{\partial z} = \frac{\partial \eta}{\partial t} \quad \text{at} \quad z = 0 \quad (\text{D.3})$$

$$\frac{\partial \Phi}{\partial t} + g\eta = 0 \quad \text{at} \quad z = 0 \quad (\text{D.4})$$

---

<sup>1</sup>Laplace equation

<sup>2</sup>Bottom boundary condition (rigid and impermeable bottom)

<sup>3</sup>Linearized kinematic boundary condition

<sup>4</sup>Linearized dynamic boundary condition

with the velocity potential  $\Phi(x, y, z, t)$ , the surface elevation  $\eta(x, y, t)$ , the horizontal gradient operator  $\nabla = \left( \frac{\partial}{\partial x}, \frac{\partial}{\partial y} \right)$ , the gravitational acceleration  $g$  and the time  $t$ . For an irrotational flow the velocity vector  $\mathbf{v}$  of the fluid can be derived from the velocity potential  $\Phi(x, y, z, t)$  with equation (D.5).

$$\mathbf{v} = \nabla\Phi \quad (\text{D.5})$$

A definition sketch in a vertical section is shown in Figure D.1. The free surface is given by  $z = \eta(x, y, t)$ . SWL indicates still water level.

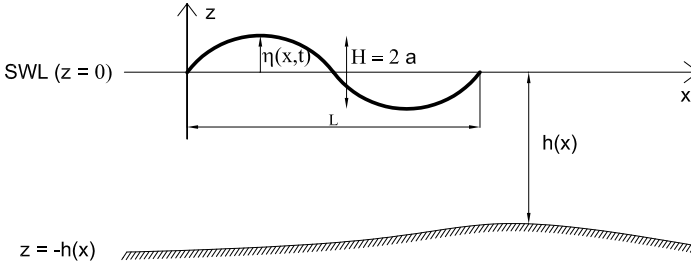


Figure D.1: Definition sketch in a vertical section

The vertical structure of the wave motion is described by  $f(z, h)$  with a weak dependency on the co-ordinates  $(x, y)$  through the water depth  $h(x, y)$ . In practice, the vertical structure for a linearized wave over a horizontal bottom is chosen (equation (B.2)). The defined structure is considered locally valid for an uneven bottom.

$$f(z, h) = \frac{\cosh(k(z + h))}{\cosh(kh)} \quad (\text{B.2})$$

Through equation (B.2)  $f(z, h)$  is dependent on the wave number  $k$ .

The velocity potential  $\Phi(x, y, z, t)$  can be written as equation (B.1) by using the method of separation of variables.

$$\Phi(x, y, z, t) = f(z, h)\varphi(x, y, t) \quad (\text{B.1})$$

with  $\varphi(x, y, t)$  the velocity potential at  $z = 0$ .

The gradient of the velocity potential is expressed by equation (D.6).

$$\nabla\Phi = f\nabla\varphi + \varphi\nabla f \quad (\text{D.6})$$

For the derivation of the mild-slope equation a variational formulation based on the Hamiltonian is used. The Hamiltonian  $\mathcal{H}$  is the total energy of the fluid and is given by equation (D.7).

$$\mathcal{H} = \int \int (E_{kin} + E_{pot}) dx dy \quad (D.7)$$

with  $E_{kin}$  the kinetic energy density and  $E_{pot}$  the potential energy density.

It has been shown that the Hamiltonian constitutes a variational principle when it is expressed in terms of the free surface elevation  $\eta$  and the value of the velocity potential at the free surface  $\Phi(x, y, \eta(x, y, t), t)$  [2–4]. For linear waves, the velocity potential at the free surface can be replaced by the velocity potential at  $z = 0$ ,  $\varphi(x, y, t)$ .

The kinetic energy density is determined by equation (D.8) (using equation (D.5)).

$$\begin{aligned} E_{kin} &= \frac{1}{2} \rho \int_{-h(x,y)}^{\eta(x,y,t)} \mathbf{v}^2 dz \\ &= \frac{1}{2} \rho \int_{-h(x,y)}^{\eta(x,y,t)} \left( (\nabla \Phi)^2 + \left( \frac{\partial \Phi}{\partial z} \right)^2 \right) dz \end{aligned} \quad (D.8)$$

with the density of sea water  $\rho$ .

The potential energy density is given by equation (D.9).

$$E_{pot} = \frac{1}{2} \rho g \eta^2 \quad (D.9)$$

Using equation (D.6), equation (D.8) can be written as equation (D.10).

$$E_{kin} = \frac{1}{2} \rho \int_{-h(x,y)}^{\eta(x,y,t)} \left( f^2 (\nabla \varphi)^2 + 2f\varphi \nabla \varphi \cdot \nabla f + \varphi^2 (\nabla f)^2 + \left( \frac{\partial f}{\partial z} \right)^2 \varphi^2 \right) dz \quad (D.10)$$

Equations (D.11) and (D.12) show that  $\nabla f$  is proportional with  $\nabla h$ .

$$\nabla f = \frac{\partial f}{\partial h} \nabla h + \frac{\partial f}{\partial k} \nabla k \quad (D.11)$$

$$\nabla k = \frac{\partial k}{\partial h} \nabla h \quad (D.12)$$

Using the mild slope assumption  $\frac{|\nabla h|}{kh} \ll 1$  which states that the depth variation over a wave length has to be small, equation (D.10) can be approximated to equation (D.13).

$$E_{kin} = \frac{1}{2} \rho \int_{-h(x,y)}^{\eta(x,y,t)} \left( f^2 (\nabla \varphi)^2 + \left( \frac{\partial f}{\partial z} \right)^2 \varphi^2 \right) dz \quad (D.13)$$

If the latter assumption is not taken into account, an extended mild-slope equation is obtained. In practice the depth variation over one wave length is maximal 1/3. By assuming linear waves, the integration limit  $z = \eta$  can be replaced by  $z = 0$  (depth integration).

Introducing  $A$  and  $B$ , given by equations (D.14) and (D.15), in equation (D.13) leads to equation (D.16).

$$A = \int_{-h}^0 f^2 dz \quad (\text{D.14})$$

$$B = \int_{-h}^0 \left( \frac{\partial f}{\partial z} \right)^2 dz \quad (\text{D.15})$$

$$E_{kin} = \frac{1}{2} \rho \left( A (\nabla \varphi)^2 + B \varphi^2 \right) \quad (\text{D.16})$$

Finally, the Hamiltonian  $\mathcal{H}$  (equation (D.7)) can be modified to equation (D.17).

$$\mathcal{H} = \int \int \frac{1}{2} \rho \left( A (\nabla \varphi)^2 + B \varphi^2 + g \eta^2 \right) dx dy \quad (\text{D.17})$$

The Hamiltonian is a functional of  $\eta$  and  $\varphi$ . By using the variational principle equation (D.18) is obtained.

$$\delta \mathcal{H} = \delta \int \int (E_{kin} + E_{pot}) dx dy = 0 \quad (\text{D.18})$$

with  $\delta$  the variational derivative. The canonical theorem states that  $\eta$  and  $\varphi$  are canonical variables, with  $\mathcal{H}(\eta, \varphi)$  as the corresponding Hamiltonian functional. The Hamiltonian satisfies the canonical equations (D.19) and (D.20).

$$\frac{\partial \eta}{\partial t} = \frac{1}{\rho} \frac{\delta \mathcal{H}}{\delta \varphi} \quad (\text{D.19})$$

$$\frac{\partial \varphi}{\partial t} = -\frac{1}{\rho} \frac{\delta \mathcal{H}}{\delta \eta} \quad (\text{D.20})$$

These two equations give the boundary conditions at the free surface (equations (D.3) and (D.4)). The Laplace equation (equation (D.1)) and the bottom boundary condition (equation (D.2)) have been used as constraints [1].

Using equation (D.17) and the definition of variational derivative, equations (D.21) and (D.22) are derived.

$$\frac{\partial \eta}{\partial t} = B \varphi - \nabla \cdot (A \nabla \varphi) \quad (\text{D.21})$$

$$\frac{\partial \varphi}{\partial t} = -g \eta \quad (\text{D.22})$$

By using equation (B.2) and the linear frequency dispersion relation,  $\omega^2 = g k \tanh(kh)$ , the equations for  $A$  and  $B$  can be written as equations (D.23) and (D.24).

$$A = \int_{-h}^0 f^2 dz = \frac{CC_g}{g} \quad (\text{D.23})$$

$$B = \int_{-h}^0 \left( \frac{\partial f}{\partial z} \right)^2 dz = \frac{\omega^2 - k^2 CC_g}{g} \quad (\text{D.24})$$

with the phase velocity  $C$ , the group velocity  $C_g$  and the angular frequency  $\omega$ .

Using these expressions for  $A$  and  $B$  in equations (D.21) and (D.22) result in equations (D.25) and (D.26).

$$\frac{\partial \eta}{\partial t} = \frac{\omega^2 - k^2 CC_g}{g} \varphi - \nabla \cdot \left( \frac{CC_g}{g} \nabla \varphi \right) \quad (\text{D.25})$$

$$\frac{\partial \varphi}{\partial t} = -g\eta \quad (\text{D.26})$$

Elimination of  $\eta$  leads to the mild slope equation of Smith and Sprinks (1975).

$$-\frac{\partial^2 \varphi}{\partial t^2} - (\omega^2 - k^2 CC_g) \varphi + \nabla \cdot (CC_g \nabla \varphi) = 0 \quad (\text{D.27})$$

If, instead of  $\eta$ , the potential  $\varphi$  is eliminated, equation (D.28) is obtained.

$$-\frac{\partial^2 \eta}{\partial t^2} - (\omega^2 - k^2 CC_g) \eta + \nabla \cdot (CC_g \nabla \eta) = 0 \quad (\text{D.28})$$

Equations (D.25), (D.26), (D.27) and (D.28) are time-dependent mild-slope equations for nearly harmonic waves. Some small modulation in  $\omega$  and  $k$  is still permitted here.

The equations are able to handle refraction, shoaling, diffraction, reflection and transmission of linear, irregular waves provided that the sea state can be described by a narrow frequency spectrum [1] with a dominant carrier frequency  $\bar{\omega}$ .

## References

- [1] M. W. Dingemans. *Water wave propagation over uneven bottoms*. World Scientific, 1997.
- [2] V.E. Zakharov. *Stability of periodic waves of finite amplitude on the surface of a deep fluid*. Journal of Appl. Mech. Techn. Phys., 2:190–194, 1968.
- [3] J. W. Miles. *On Hamilton's principle for surface waves*. Journal of Fluid Mech., 83(1):153–158, 1977.
- [4] L. J. F. Broer. *On the Hamiltonian theory of surface waves*. Appl. Sci. Res., 30:430–446, 1974.





# E

## Practical use of MILDwave

Calculations with MILDwave consists of three steps:

- Preparation of the input data with a preprocessor
- Calculation of the surface elevation  $\eta$ , the velocity potential  $\varphi$ , the disturbance coefficient  $K_d$  and the wave power per meter of wave crest in x- and y-direction  $p_x$  and  $p_y$  across the domain
- Postprocessing of the results in Matlab

### **E.1 Preprocessor**

A preprocessor has been developed to facilitate the preparation of the input for the mild-slope wave propagation model MILDwave. The software tool is an executable program developed in C++ programming language and compiled with C++ builder 6. A screen shot of the preprocessor is given in Figure E.1.

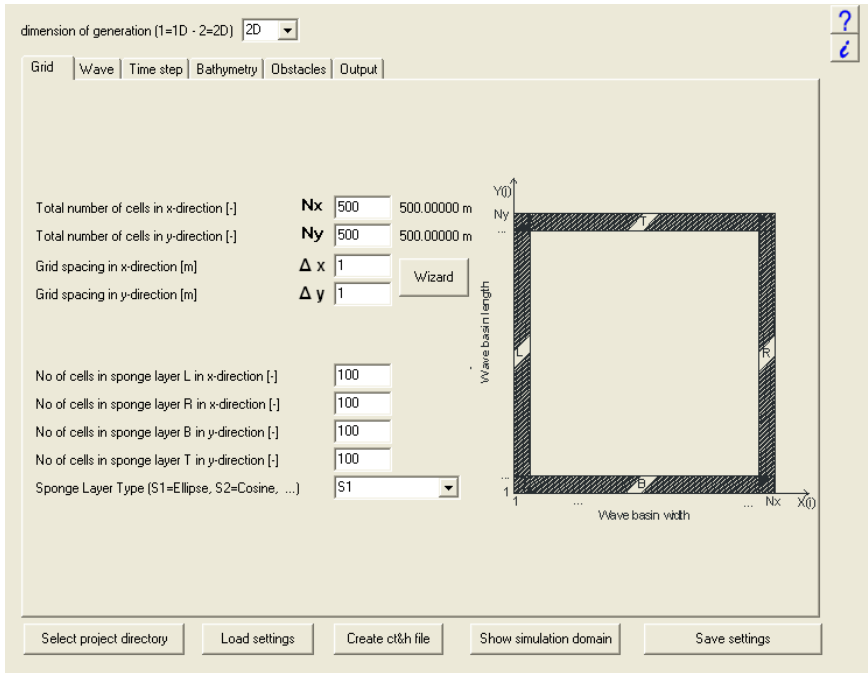
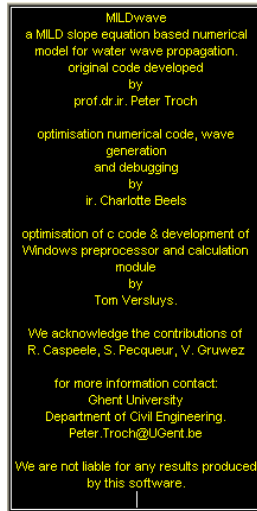


Figure E.1: First tab of the preprocessor

The input parameters are grouped in different tabs. Five buttons at the bottom of the screen allow the user to load the input settings from a previous file and to save the changed input settings<sup>1</sup>. Furthermore, a file with the type (ct file) and water depth (h file) of each cell in the domain is needed for the calculation and is prepared with the button *Create ct&h file*. The cell type specifies the absorption coefficient of each cell. Cell type 0 represents water cells (absorption coefficient 1), while cell type 1 corresponds to fully reflective cells (absorption coefficient 0). The absorption coefficient of other cell types can be defined by the user to implement obstacles in the domain. The implementation of obstacles is described in detail in chapter 6. The simulation domain (with sponge layers, wave gauges, wave generation cells, obstacle cells and water depth) is shown with the button *Show simulation domain*. At the top of the screen the dimension of the domain is defined (1D = wave flume, 2D = wave basin). In the top right corner of the screen a help function (?), which explains the input parameters for the grid, wave generation and bathymetry, is available. The info button (i) provides information about the development of MILDwave (Figure E.2). The tabs with the input settings are discussed in the next sections.

<sup>1</sup>All input and output files need to be saved in the same directory. This directory is loaded with the button *Select project directory*.



MILDwave  
a MILD slope equation based numerical  
model for water wave propagation,  
original code developed  
by  
prof.dr.ir. Peter Troch

optimisation numerical code, wave  
generation  
and debugging  
by  
ir. Charlotte Beels

optimisation of c code & development of  
Windows preprocessor and calculation  
module  
by  
Tom Versluys.

We acknowledge the contributions of  
R. Caspeele, S. Pecqueur, V. Gruwez

for more information contact:  
Ghent University  
Department of Civil Engineering,  
Peter.Troch@UGent.be

We are not liable for any results produced  
by this software.

Figure E.2: Development of the wave propagation model MILDwave

### E.1.1 Grid

In this tab (Figure E.1) the simulation domain is defined; the number of grid cells in x-direction  $N_x$ , the number of grid cells in y-direction  $N_y$ , the grid size  $\Delta x = \Delta y$ , the length of the sponge layer  $B_s$  at the top (T), bottom (B), left (L) and right (R) boundary and the absorption function used in the absorbing boundaries  $S_1$ ,  $S_2$  or  $S_3$  need to be specified. The button *Wizard* gives the recommended interval for  $\Delta x = \Delta y$ .

## E.1.2 Wave

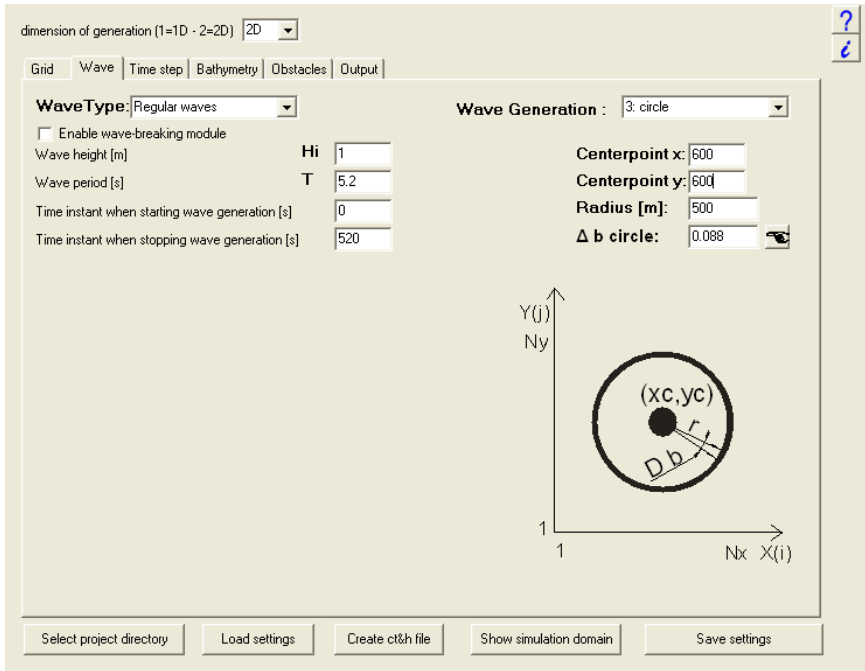


Figure E.3: Second tab of the preprocessor (regular waves)

The second tab (Figure E.3) allows the definition of the wave generation parameters. First the type of wave is specified; regular or irregular waves. It is optional to account for the physical process wave breaking during the calculations (Option *Enable wave-breaking module*).

### E.1.2.1 Regular waves

The wave parameters (wave height  $H_i$ , wave period  $T$  and wave angle  $\theta$ ) and the instant to start and stop the wave generation are defined in the left part of the screen. Note that the wave angle  $\theta$  is not shown in Figure E.3, as this parameter is not needed for the selected wave generation lay-out. A wave generation lay-out is chosen in the right part of the screen. Three lay-outs are available:

- Two wave generation lines (the location of the vertical wave generation line  $i$ -line and the location of the horizontal wave generation line  $j$ -line need to be specified.)
- Two wave generation lines and an arc (the location of the left vertical

wave generation line  $i$  – line and the centre of the arc  $(x_c, y_c)$  need to be specified.<sup>2)</sup>

- A circle (the centre of the circle  $(x_c, y_c)$ , the radius of the circle and the interval  $\Delta b$  along the circle need to be specified.<sup>3</sup> By clicking on the button next to  $\Delta b$  a recommended value for  $\Delta b$  is given.)

For each option a small definition sketch with the required parameters is shown. All options are discussed in detail in chapter 5. In Figure E.3 regular wave generation on a circle is selected.

### E.1.2.2 Irregular waves

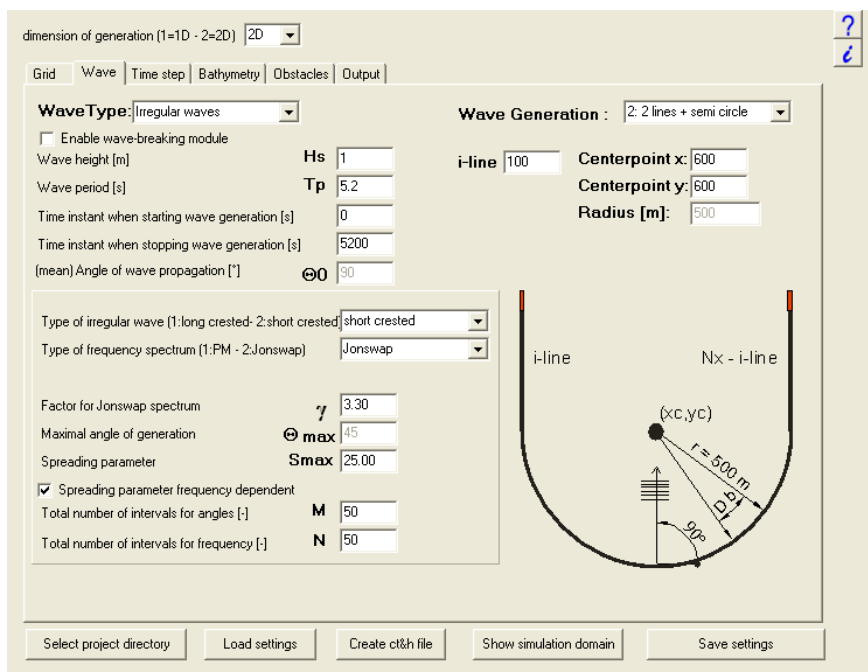


Figure E.4: Second tab of the preprocessor (irregular waves)

When irregular waves (Figure E.4) are generated, the user can select either long-crested or short-crested waves. The specified wave parameters for long-crested wave generation are; the significant wave height  $H_s$ , the peak period  $T_p$ , the wave angle  $\theta$ , the frequency spectrum  $S(f)$ , the number of frequency components  $N$

<sup>2</sup>Currently, only a wave generation arc with radius = 500 m in a grid with  $\Delta x = \Delta y = 1$  m is implemented.

<sup>3</sup>Grid size is fixed ( $\Delta x = \Delta y = 1$  m).

and the instant to start and stop the wave generation. The same wave generation lay-outs as for regular waves are available.

For short-crested waves some additional parameters are required; the spreading parameter  $s$  or the maximum value of the spreading parameter  $s_{max}$  (when the option *Spreading parameter frequency dependent* is chosen), the angle interval  $(-\theta_{max}, \theta_{max})$  and the number of angular components  $M$ . Two wave generation lay-outs are available for short-crested waves:

- Three wave generation lines (the location of the left vertical wave generation line  $i - line$  and the location of the horizontal wave generation line  $j - line$  need to be specified.)
- Two wave generation lines and an arc (the location of the left vertical wave generation line  $i - line$  and the centre of the arc  $(x_c, y_c)$  need to be specified.<sup>4</sup>)

Short-crested wave generation is only available for a mean wave angle equal to  $90^\circ$ . All wave parameters needed for irregular long-crested and short-crested wave generation are discussed in detail in chapter 5.

An example of the generation of short-crested waves on two wave generation lines and an arc is given in Figure E.4 .

---

<sup>4</sup>Currently, only a wave generation arc with radius = 500 m in a grid with  $\Delta x = \Delta y = 1$  m is implemented.

### E.1.3 Time step

The time step  $\Delta t$  and the end of the simulation (*twfin*) are specified in this tap (Figure E.5).

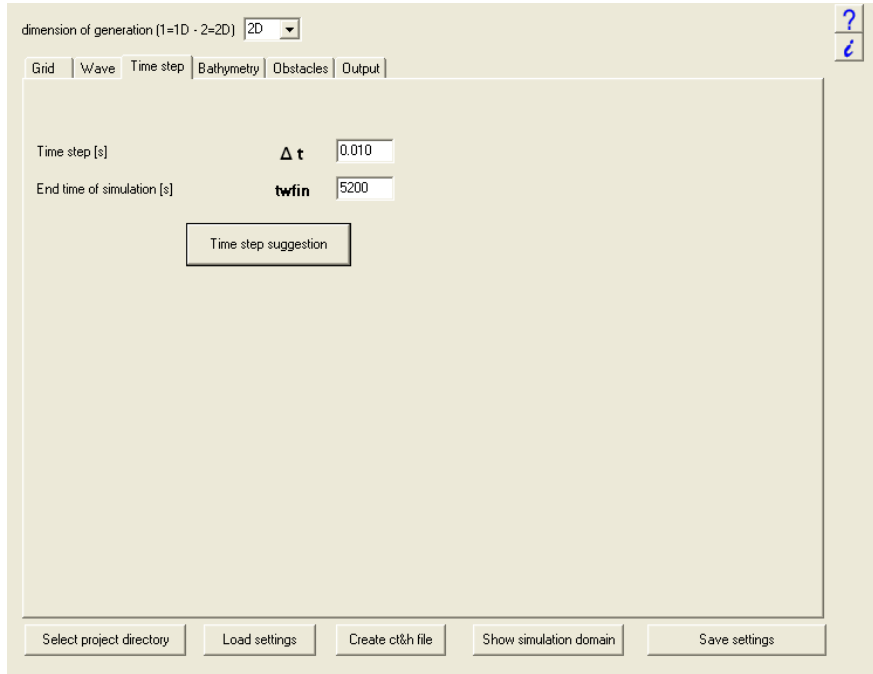


Figure E.5: Third tab of the preprocessor

The simulation time consists of a set-up time (approximately the time needed for the generated waves to propagate two times back and forth) and the actual calculation time. The button *Time step suggestion* provides an upper limit (Courant-Friedrichs-Lewy criterion) for the time step.

## E.1.4 Bathymetry

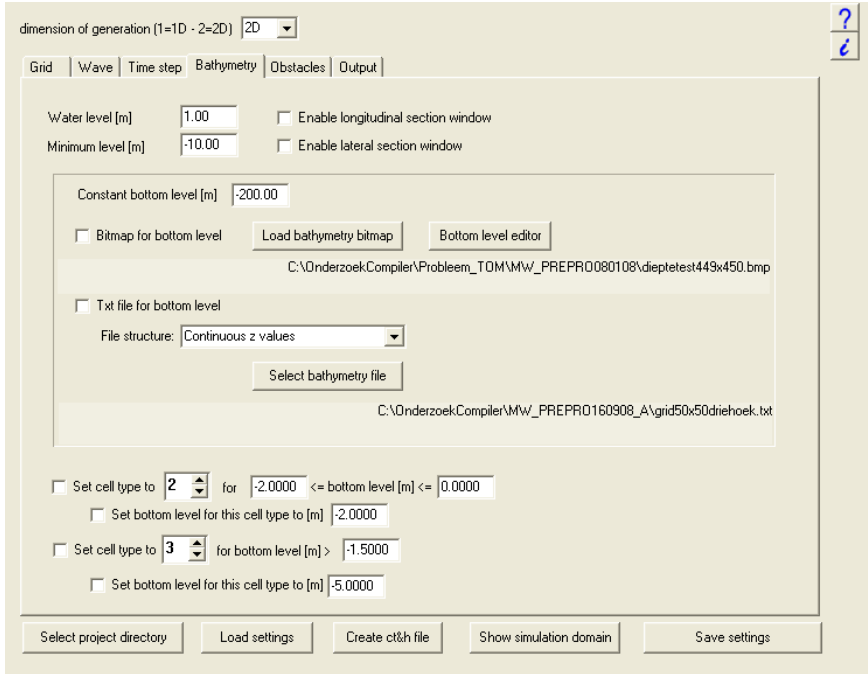


Figure E.6: Fourth tab of the preprocessor

There are three main options to specify the bathymetry in MILDwave (Figure E.6):

- Constant bathymetry
- Bathymetry specified in a text file. There are several options for the lay-out of the text file.
- Bathymetry specified in a bitmap. With the button *Depth type editor* a bottom level can be assigned to each colour in the bitmap.

The parameters water level, bottom level (or bathymetry) and minimum water depth are explained in the help function (Figure E.7). In the second and the third option, obstacles can be placed when the bottom level has a specific value. This feature is very useful to define the coastline, islands, . . .



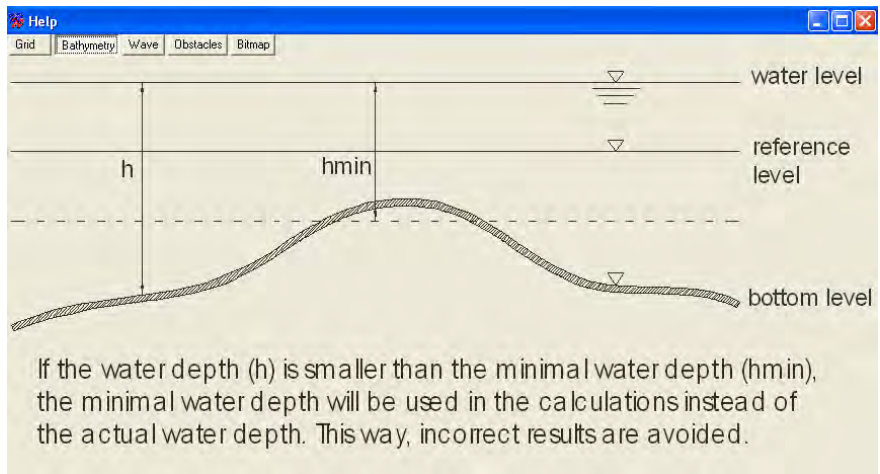


Figure E.7: Definition of the parameters water level, bottom level and minimum water depth in the help function of MILDwave

### E.1.5 Obstacles

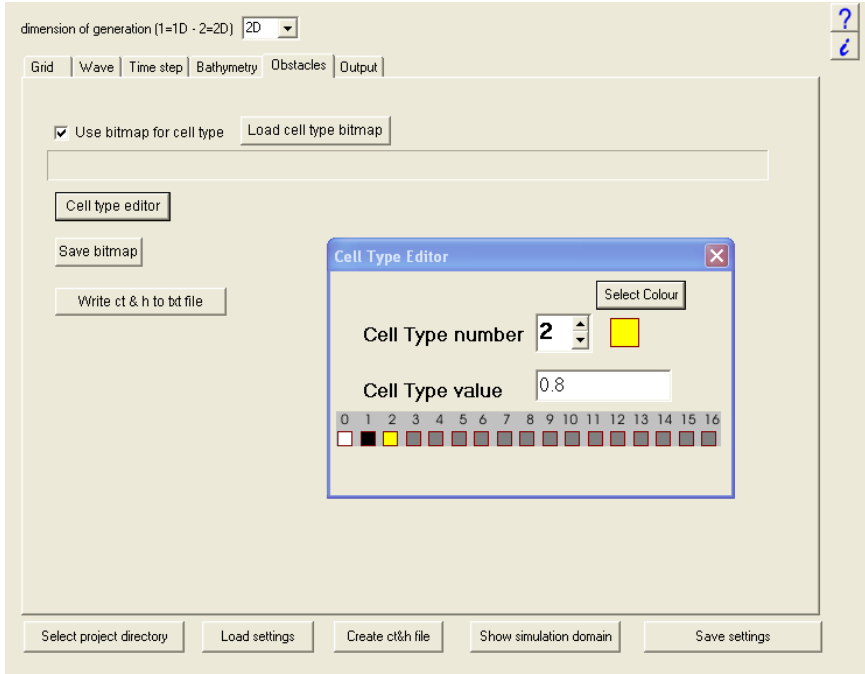


Figure E.8: Fifth tab of the preprocessor

In this tap (Figure E.8) a bitmap of the simulation domain, where the cells with the same absorption coefficient have the same colour, is loaded. With the button *Cell type editor* an absorption coefficient can be assigned to each colour in the bitmap.

## E.1.6 Output

dimension of generation (1=1D - 2=2D)

Grid | Wave | Time step | Bathymetry | Obstacles | **Output**

Use of WaveGauges

Number of WG arrays [max 100]  Reference point X[cell]:  0.00 m

Number of WG per array [max 100]  Reference point Y[cell]:  0.00 m

Angle of rotation [°]:

C:\Onderzoek\Compiler\MW\_PREPRO20090317\VPWG\_45.txt

Use of 3D output   
Time when writing 3D mesh to file [s]

Write multiple 3D measurements to file

Output of  $K_d$

Output of power-vector field

Time limit for calculation on [s]

Time limit for calculation off [s]

Density [kg/m<sup>3</sup>]

Figure E.9: Sixth tab of the preprocessor

The output tab (Figure E.9) allows the user to select the desired output parameters. Wave gauges (WGs) can be installed in the simulation domain to measure the wave elevations on predefined locations. The wave elevations in the simulation domain (3D output) can be saved on one or multiple (button *Edit multiple measurements*) instants. Furthermore, the disturbance coefficient  $K_d$  and the vector field of the wave power  $p$  can be calculated in the simulation domain and saved. The instant to start and to end the calculation of the latter parameters needs to be specified, to take only fully developed waves into account. The density of sea water equals 1 026 kg/m<sup>3</sup>.

## E.2 Calculation of $\eta$ , $\varphi$ , $K_d$ , $p_x$ and $p_y$ across the domain

The wave propagation model MILDwave is an executable program developed in C++ programming language and compiled with C++ builder 6. The calculation in MILDwave is summarized in a flow chart (Figure E.11). A screen shot of the executable MILDwave\_CALC.exe is given in Figure E.10.

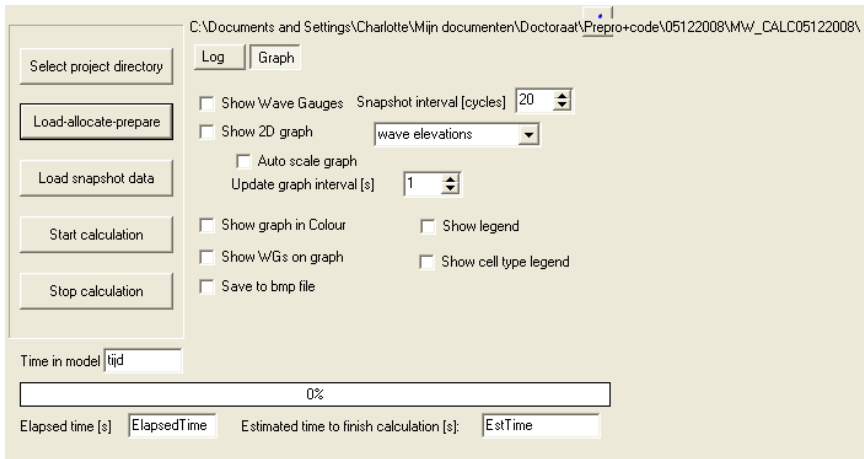


Figure E.10: Screen short of the executable MILDwave\_CALC.exe

Before starting a calculation (button *Start calculation*) the input files need to be imported and memory needs to be allocated to the variables with the button *Load-allocate-prepare*. The wave elevations calculated in MILDwave can be viewed during the calculation on the location of the wave gauges or in the complete domain (Figure E.10). These elevations can also be saved as bmp-files on predefined instants. Furthermore it is possible to save intermediate results on regular time intervals (Snapshot interval). The progress of the calculation is shown at the bottom of the screen. When a calculation stops before the end of the simulation time, these intermediate results can be used to restart the calculation (button *Load snapshot data*).

## E.3 Postprocessing of the results in Matlab

Matlab software is used to plot the generated output files.

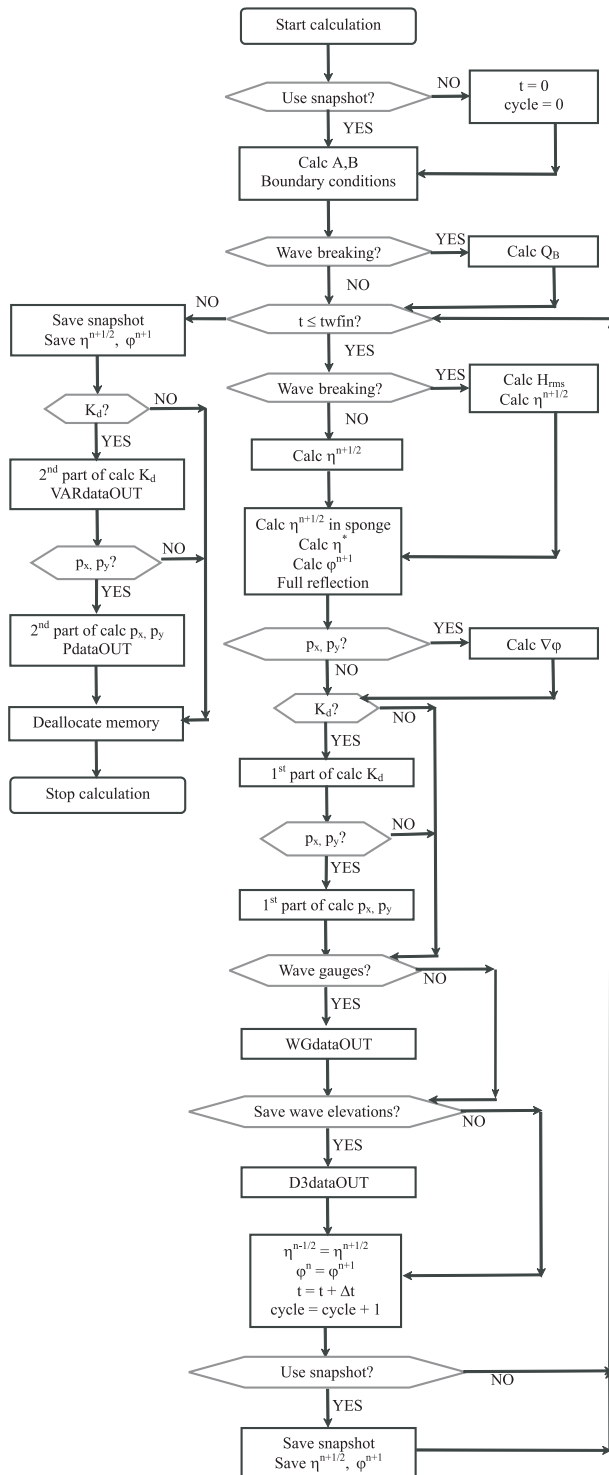


Figure E.11: Flow chart of calculation in MILDwave



# F

## Results for an FO<sup>3</sup> WEC in regular waves with $T = 4$ s and 8 s

### **F.1 Results for a regular wave with unit wave amplitude and wave period of 4 s**

#### **F.1.1 Results of WAMIT**

##### **F.1.1.1 Absorbed power**

The total absorbed power by a single FO<sup>3</sup> WEC for a regular incident wave with unit wave amplitude and a wave period of 4 s is 702 kW. The total available wave power over the width of the FO<sup>3</sup> WEC (approximately 36 m) is 566 kW. This means that approximately 124 % of the total available wave power over the width of the FO<sup>3</sup> WEC has been absorbed.

##### **F.1.1.2 Wave elevations**

##### **Real part of the wave amplitude**

The WAMIT results are presented in this paragraph for the cases diffraction + radiation (Figure F.1(a)), only radiation (Figure F.1(b)) and only diffraction (Figure F.1(c)) obtained from NTNU for wave conditions  $H_i = 2$  m,  $T = 4$  s.

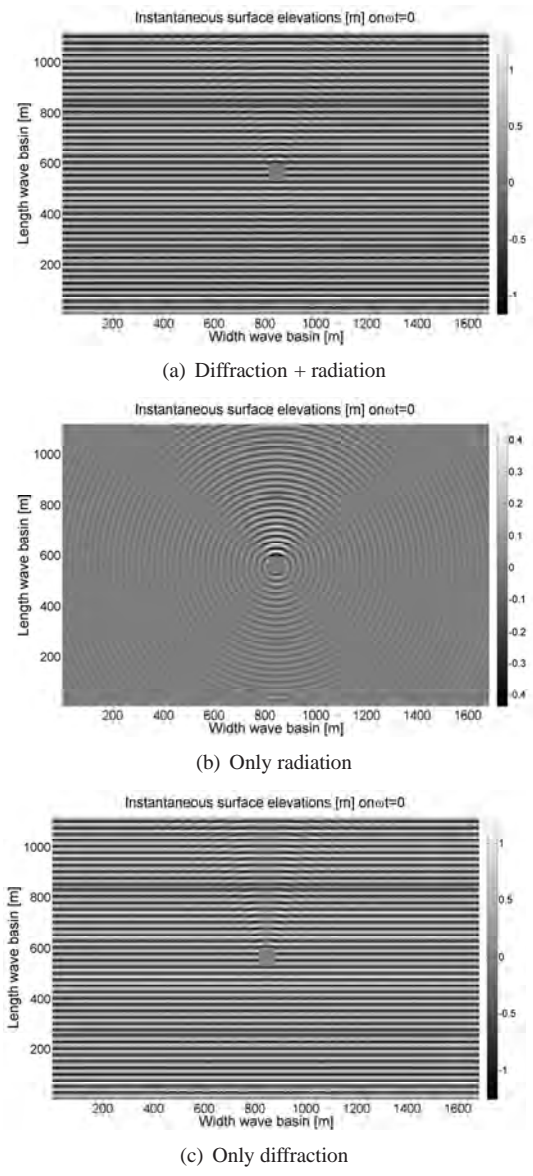
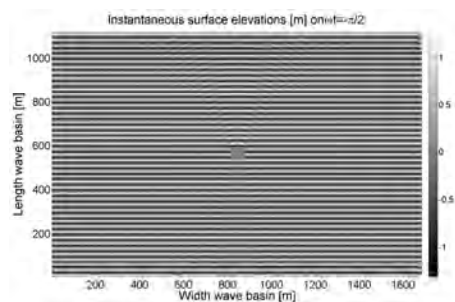


Figure F.1: Instantaneous surface elevations on  $\omega t = 0$  calculated with WAMIT taking (a) diffraction and radiation, (b) only radiation and (c) only diffraction into account

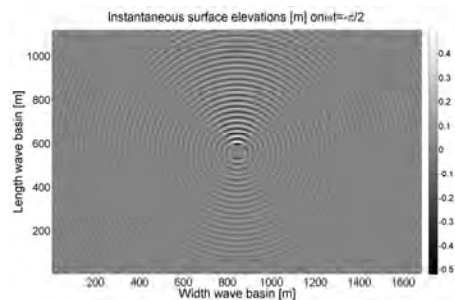


### Imaginary part of the wave amplitude

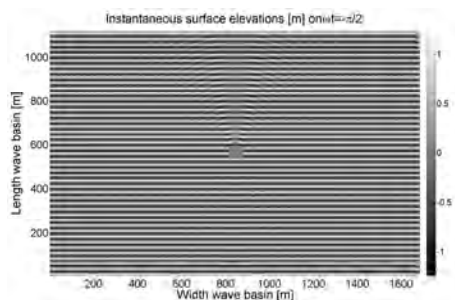
The instantaneous surface elevations on  $\omega t = -\pi/2$  due to diffraction and radiation, only radiation and only diffraction, calculated with WAMIT for an incident wave with  $H_i = 2$  m and  $T = 4$  s, are shown in respectively Figure F.2(a), F.2(b) and F.2(c).



(a) Diffraction + radiation



(b) Only radiation



(c) Only diffraction

Figure F.2: Instantaneous surface elevations on  $\omega t = -\pi/2$  calculated with WAMIT taking (a) diffraction and radiation, (b) only radiation and (c) only diffraction into account

## F.1.2 Wave diffraction

### F.1.2.1 Implementation of wave diffraction in MILDwave

In this section WAMIT results are adopted and reformulated in terms of wave amplitude  $a$  and phase shift  $\phi$ , relative to the centre of the FO<sup>3</sup> WEC, instead of real and imaginary part of the wave amplitude (cf. using equations (8.3) and (8.4)). The resulting wave amplitude  $a$  and phase shift  $\phi$  relative to the centre of the FO<sup>3</sup> WEC, when only diffraction is considered, are shown in Figure F.3 for a regular incident wave with a wave amplitude of 1 m and a wave period of 4 s.

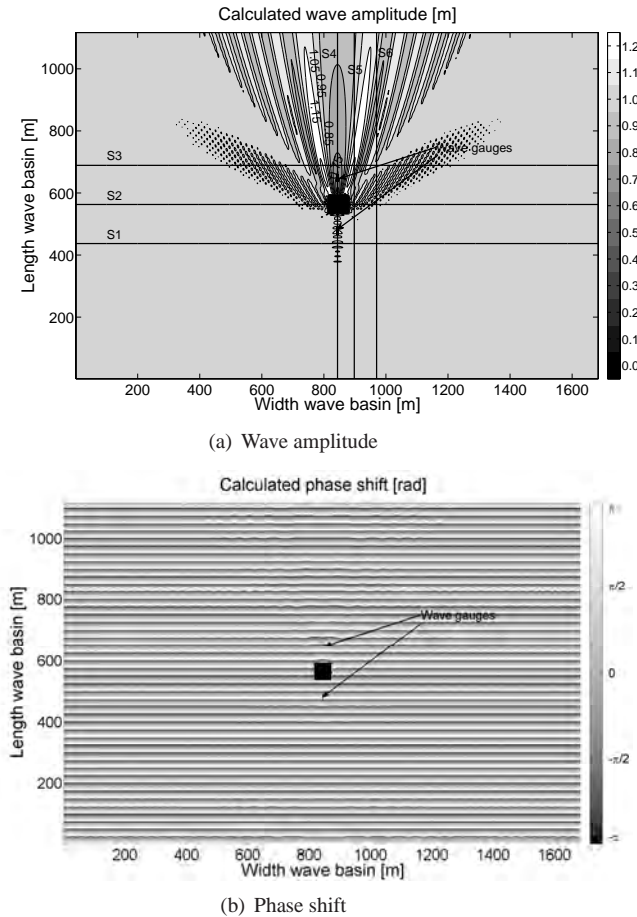


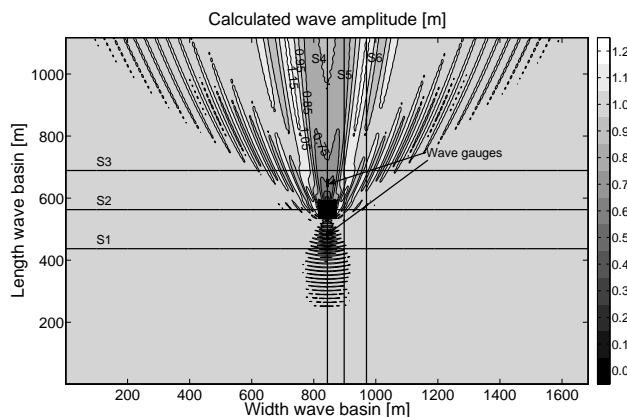
Figure F.3: Calculated (a) wave amplitude  $a$  and (b) phase shift  $\phi$  in WAMIT

The amounts of reflection and transmission have been determined by a reflection analysis (Table F.1) and have been used to implement an FO<sup>3</sup> WEC.

Table F.1: Reflection analysis - diffraction WAMIT

Wave Gauges	$H_i$ or $H_t$ [m]	$T$ [s]	$H_r$ [m]	$T$ [s]	$K_r$ [%]
1-3	1.98	4.016	0.19	4.016	9.67
4-6	1.28	4.016	0.04	4.016	3.00

The diffraction pattern, generated by an FO<sup>3</sup> WEC, is modelled using the sponge layer technique (chapter 6). The resulting wave amplitude in MILDwave is shown in Figure F.4.

Figure F.4: Calculated wave amplitude  $a$  in MILDwave

When comparing Figure F.3(a) and Figure F.4, the shadow zone behind the FO<sup>3</sup> WEC seems wider in MILDwave compared to WAMIT. Furthermore the peaks near the converter are smaller in MILDwave. These observations will be studied in more detail by considering sections as indicated on Figure F.3(a) and Figure F.4.

Again a reflection analysis is performed (Table F.2). When comparing Table F.1 and Table F.2 a good agreement between the amounts of reflection and transmission calculated in WAMIT and MILDwave is seen.

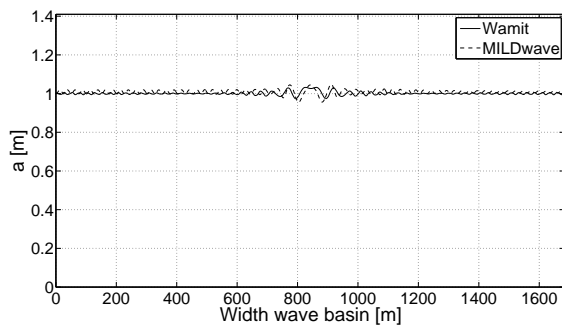
Table F.2: Reflection analysis - diffraction in MILDwave

Wave Gauges	$H_i$ or $H_t$ [m]	$T$ [s]	$H_r$ [m]	$T$ [s]	$K_r$ [%]
1-3	2.01	4.016	0.195	4.016	9.71
4-6	1.271	4.016	0.042	3.977	3.30

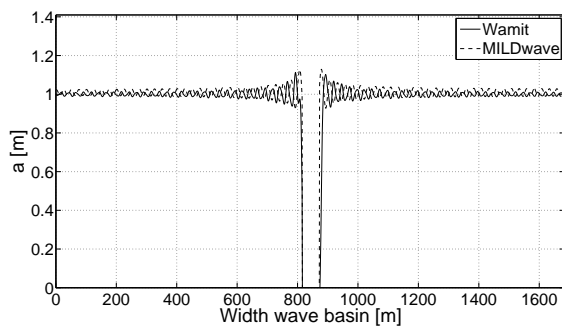
### **F.1.2.2 Comparison of wave diffraction patterns generated by an FO<sup>3</sup> WEC using WAMIT and MILDwave**

To make a detailed comparison, sections on a distance of 126 m from the centre of the FO<sup>3</sup> WEC (distance between two converters in a farm will be 108 m at minimum) will be studied as indicated on Figure F.3(a) and Figure F.4. Figure F.5 shows a lateral section in front of (S1), through (S2) and behind (S3) the FO<sup>3</sup> WEC at respectively  $y^* = 437$  m, 563 m and 689 m. Figure F.6 shows three longitudinal sections at  $x^* = 844$  m (S4), 898 m (S5) and 970 m (S6). In Figure F.7 and Figure F.8 the same sections are zoomed in.

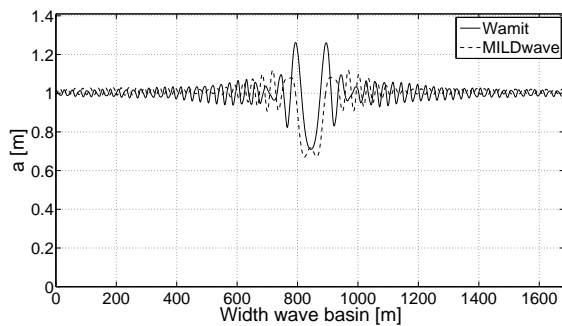
Figure F.5(c) shows the wider shadow zone in MILDwave compared to WAMIT. The distance crest-to-crest between the two central peaks in WAMIT equals 102 m, in MILDwave 130 m. Figure F.7 clearly indicates a spatial phase shift between the oscillations in WAMIT and MILDwave along the wave basin width. Figure F.8(a) shows a very good agreement between the results in WAMIT and MILDwave along the length of the wave basin. In general good agreement between the WAMIT and MILDwave results is observed. The values in the central part of the shadow zone differ less than 1 cm. The shadow zone in the MILDwave results is approximately 27 % wider than the shadow zone in the WAMIT results.



(a) Section S1

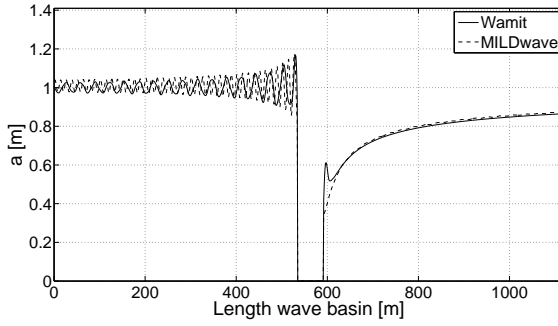


(b) Section S2

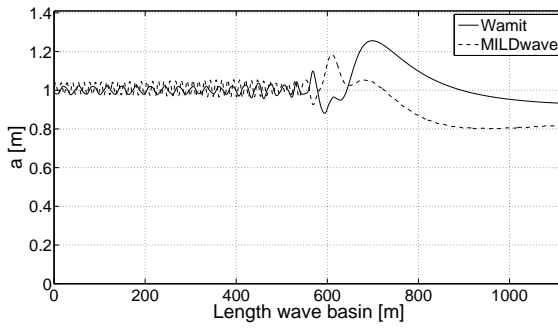


(c) Section S3

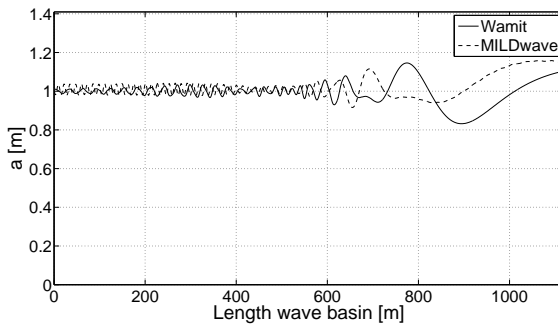
*Figure F.5: Calculated wave amplitude  $a$  in section (a) S1, (b) S2, (c) S3*



(a) Section S4

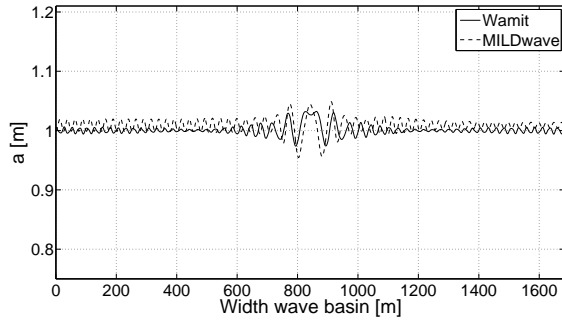


(b) Section S5

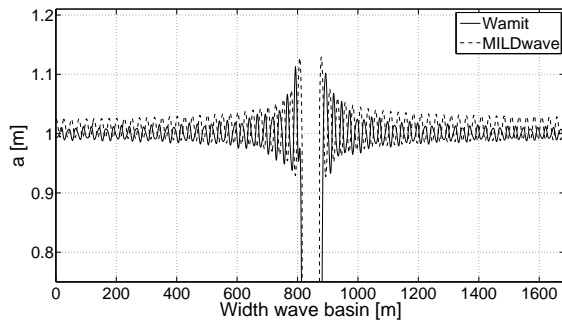


(c) Section S6

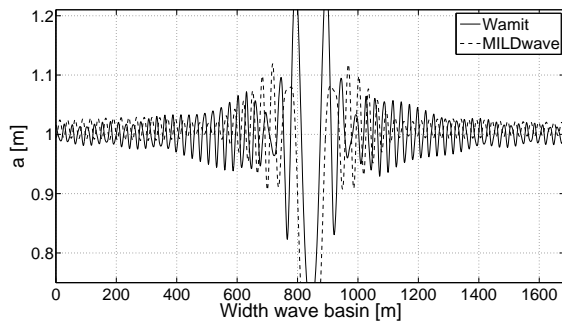
Figure F.6: Calculated wave amplitude  $a$  in section (a) S4, (b) S5, (c) S6



(a) Section S1

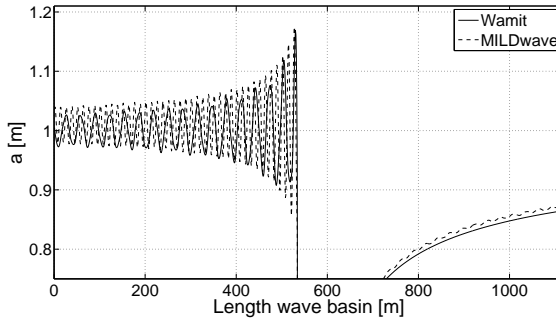


(b) Section S2

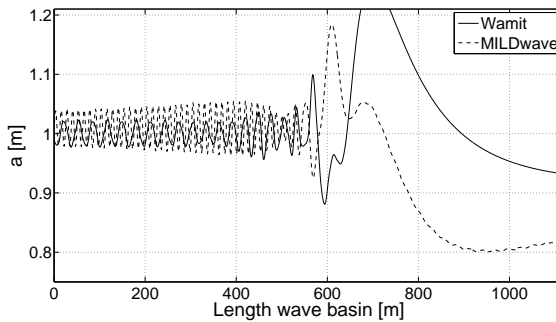


(c) Section S3

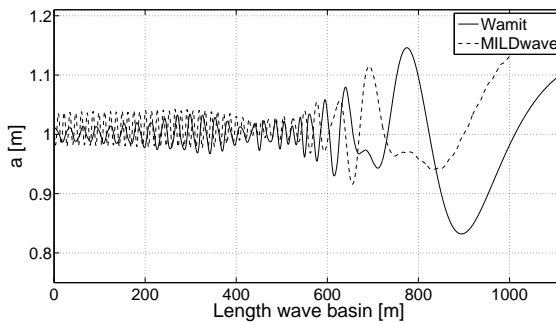
Figure F.7: Calculated wave amplitude  $a$  (zoomed in) in section (a) S1, (b) S2, (c) S3



(a) Section S4



(b) Section S5



(c) Section S6

Figure F.8: Calculated wave amplitude  $a$  (zoomed in) in section (a) S4, (b) S5, (c) S6

Further the envelope of the oscillations along the width and length of the wave basin in WAMIT and MILDwave has been compared. Therefore a Hilbert transformation has been used. An area of 180 m x 180 m has been ignored when calculating the envelope. This zone has no importance when studying a farm as the minimal distance between the converters is 108 m (3 times dimension  $FO^3$  WEC). Moreover by ignoring the latter zone, near-field peaks in the calculated envelope have been prevented. The resulting envelope of the WAMIT and MILDwave



results are shown in Figure F.9, respectively F.10.

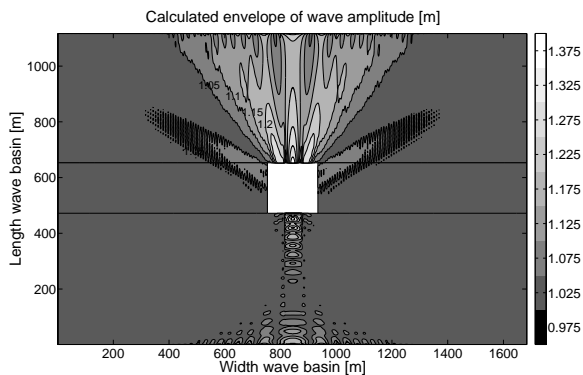


Figure F.9: Calculated envelope of wave amplitude in WAMIT

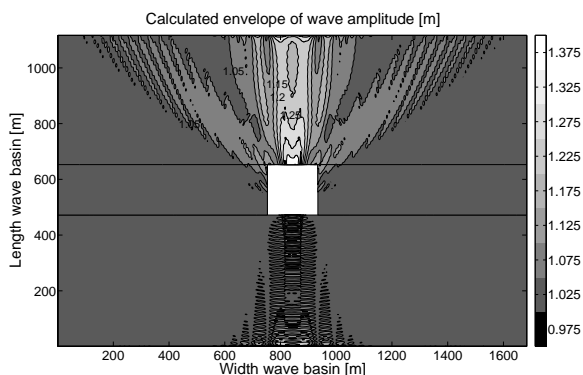


Figure F.10: Calculated envelope of wave amplitude in MILDwave

The difference between both envelopes is shown on Figure F.11. The difference between the wave amplitudes calculated from MILDwave and WAMIT is observed to be in the range of  $\pm 10\%$  in the largest part of the domain. This difference is a little higher compared with the results for  $T = 6$  s. Note the slightly higher difference in small areas in front of and behind the FO<sup>3</sup> WEC.

To determine the accuracy of MILDwave, compared to WAMIT, the mean absolute error (MAE) and the root mean square error (RMSE) over the computational domain are calculated. The MAE and RMSE equal respectively 0.020 m and 0.033 m.

Dividing the latter values through the mean value of the results in WAMIT ( $= 1.037$  m) results in MAE = 1.95 % and RMSE = 3.21 %. These values are a little higher than the results for  $T = 6$  s.

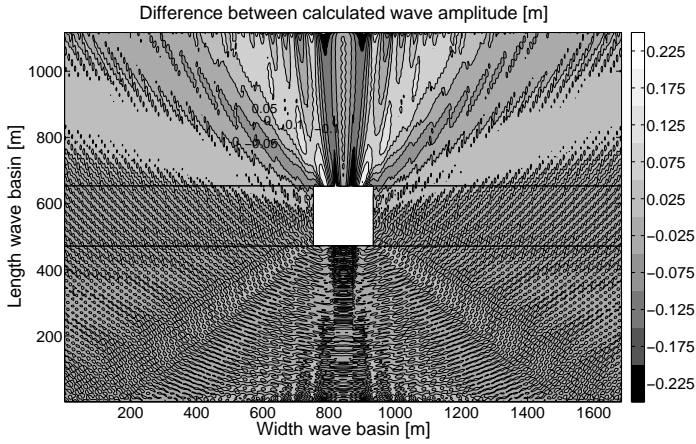


Figure F.11: Difference between envelope of wave amplitude in WAMIT and in MILDwave

### F.1.3 Wave radiation

#### F.1.3.1 Implementation of wave radiation in MILDwave

The wave amplitude and phase shift relative to the centre of the FO<sup>3</sup> WEC on the wave generation circle with centre equal to the centre of the FO<sup>3</sup> and radius 50 m are determined from the results in WAMIT (equations (8.3) and (8.4)) and are given in Figure F.12. These wave amplitude and phase shift are used to generate a radiated wave on the wave generation circle in MILDwave.

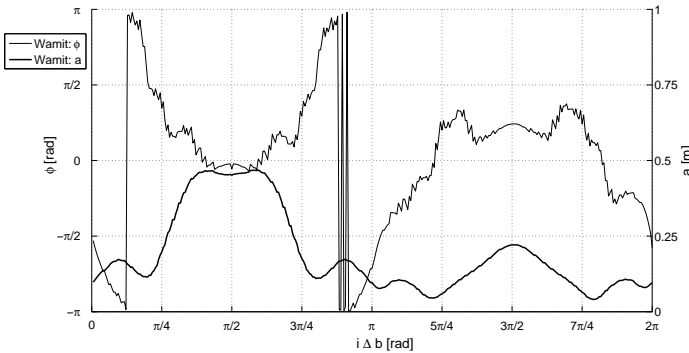
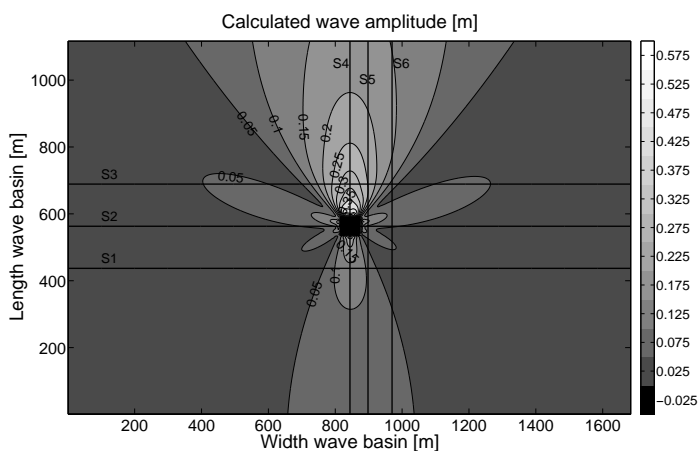


Figure F.12: Calculated wave amplitude  $a$  and phase shift  $\phi$  on a circle with centre equal to the centre of the FO<sup>3</sup> WEC and radius = 50 m for regular incident waves with  $a = 1$  m and  $T = 4$  s

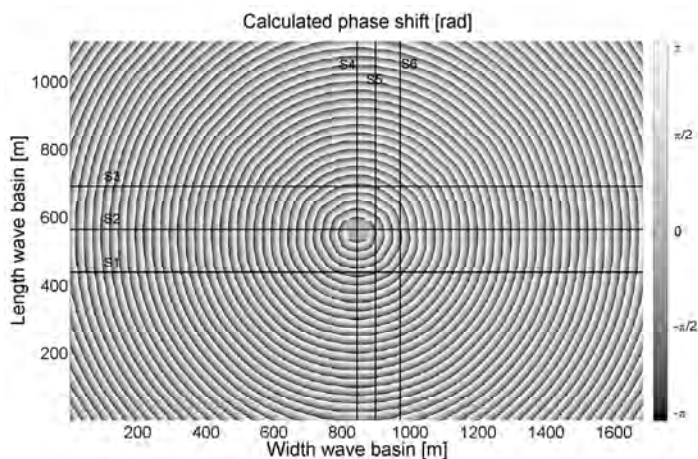
As the wave length (25 m) is smaller than the dimensions of the FO<sup>3</sup> WEC, the WEC experiences large pitch and surge motions, which result in larger differences

in phase and amplitude along the wave generation circle, compared with  $T = 6$  s (Figure 8.13).

The calculated wave amplitude and phase shift across the whole domain in respectively WAMIT (using equations (8.3) and (8.4)) and MILDwave are shown in Figure F.13 and Figure F.14 for a regular incident wave with wave amplitude of 1 m and wave period of 4 s.



(a) Wave amplitude



(b) Phase shift

Figure F.13: Calculated (a) wave amplitude  $a$  and (b) phase shift  $\phi$  in WAMIT

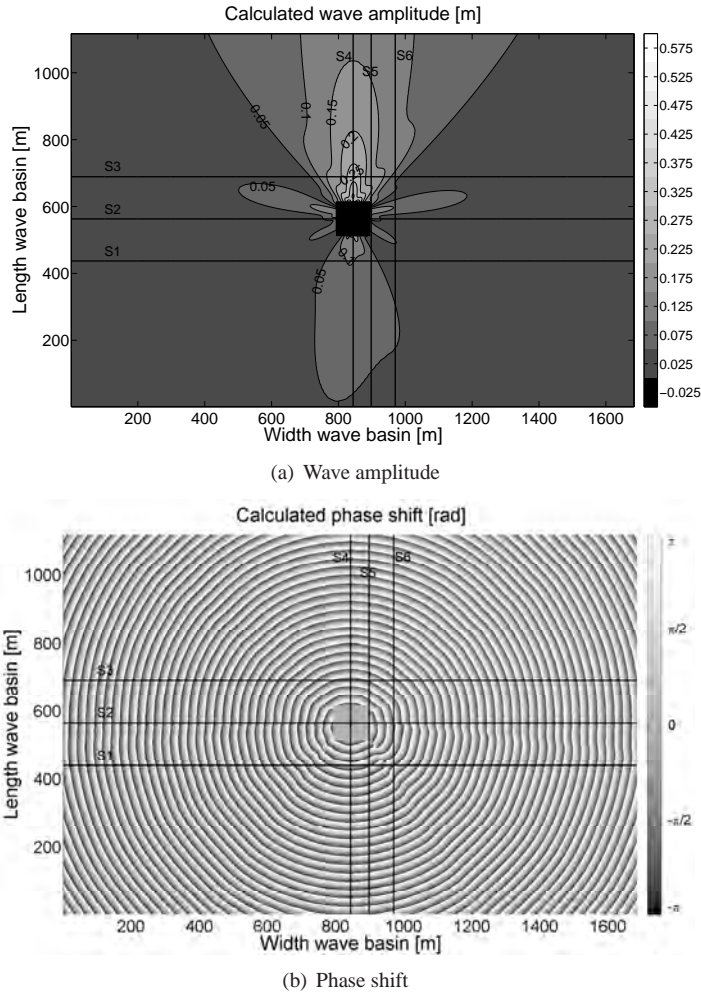


Figure F.14: Calculated (a) wave amplitude  $a$  and (b) phase shift  $\phi$  in MILDwave

The results in a square of 100 m x 100 m in the centre of the domain in MILDwave are set to 0 because the values within the wave generation circle ( $r_c = 50$  m) have no physical meaning. When comparing Figure F.13 and Figure F.14 the resulting phase shift seems to be similar. A smaller wave height, respectively, in front of and behind the FO<sup>3</sup> WEC, is observed in MILDwave.

The results in Figure F.13 and Figure F.14 are discussed in detail in the next section.

### F.1.3.2 Comparison of wave radiation patterns generated by an FO<sup>3</sup> WEC using WAMIT and MILDwave

The calculated wave amplitude and phase shift in MILDwave and WAMIT have been compared on two circular sections with centre equal to the centre of the FO<sup>3</sup> WEC and radius  $r_c = 70$  m and 126 m. The results are shown in Figure F.15. Note that  $i\Delta b = \pi/2$  represents a location behind the platform.

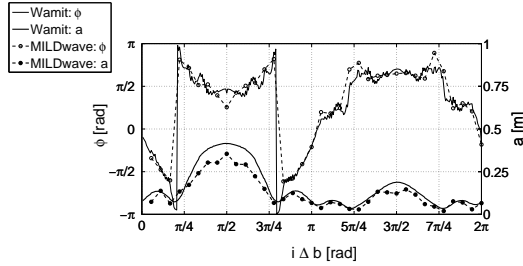
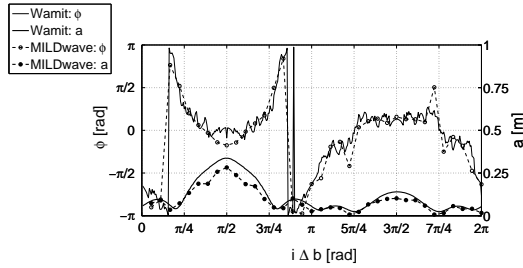
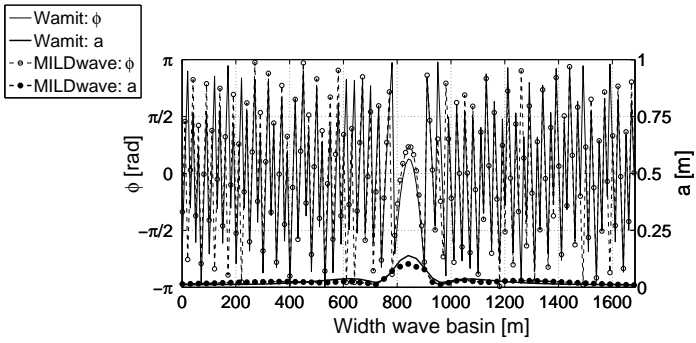
(a)  $r_c = 70$  m(b)  $r_c = 126$  m

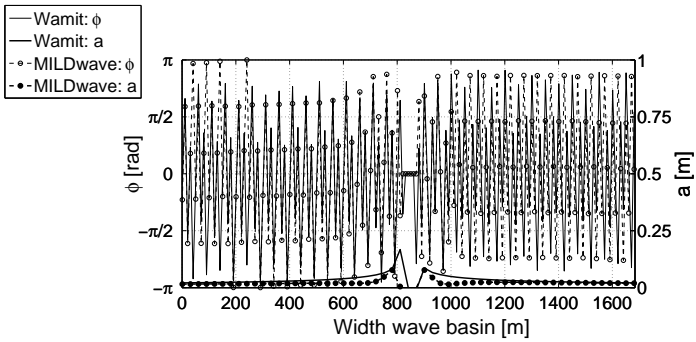
Figure F.15: Calculated wave amplitude  $a$  and phase shift  $\phi$  on a circle with centre equal to the centre of the FO<sup>3</sup> WEC and radius  $r_c =$  (a) 70 m, (b) 126 m for regular incident waves with  $a = 1$  m and  $T = 4$  s

The wave amplitude calculated in MILDwave is smaller than the amplitude calculated in WAMIT. The difference is the highest behind ( $i\Delta b = \pi/2$ ) and in front of ( $i\Delta b = 3\pi/2$ ) the FO<sup>3</sup> WEC. In general a small phase shift between  $\phi$  calculated in WAMIT and MILDwave is observed. The highest difference in phase shift occurs behind the platform ( $i\Delta b = \pi/2$ ) and when  $i\Delta b$  equals approximately  $5\pi/4$  and  $7\pi/4$ . The results in MILDwave and WAMIT agree less compared to the results for  $T = 6$  s. The higher variations in phase shift along the wave generation circle result in a higher interaction between the individual wave generation cells of the wave generation circle. The grid size in MILDwave is equal to 1 m for  $T = 4$  s and 6 s. A smaller grid size could result in more accurate results for  $T = 4$  s. In Figure F.16 and Figure F.17 the calculated wave amplitude and phase shift in WAMIT and MILDwave are shown in three lateral sections S1 ( $y^* = 437$  m), S2 ( $y^* = 563$  m) and S3 ( $y^* = 689$  m) and three longitudinal sections S4 ( $x^* = 844$  m),

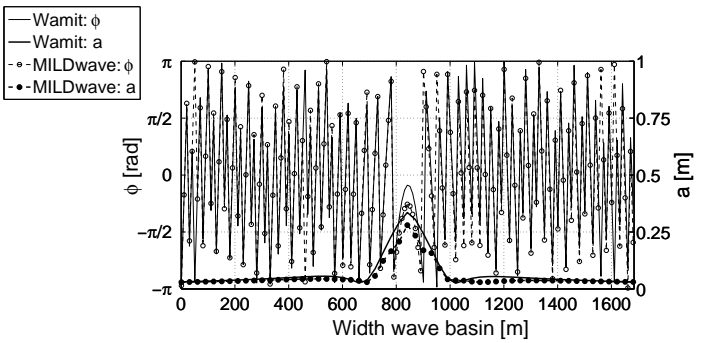
S5 ( $x^* = 898$  m) and S6 ( $x^* = 970$  m) as indicated on Figure F.13 and Figure F.14.



(a) Section S1



(b) Section S2



(c) Section S3

Figure F.16: Calculated wave amplitude  $a$  and phase shift  $\phi$  in section (a) S1, (b) S2 and (c) S3 for regular incident waves with  $a = 1$  m and  $T = 4$  s

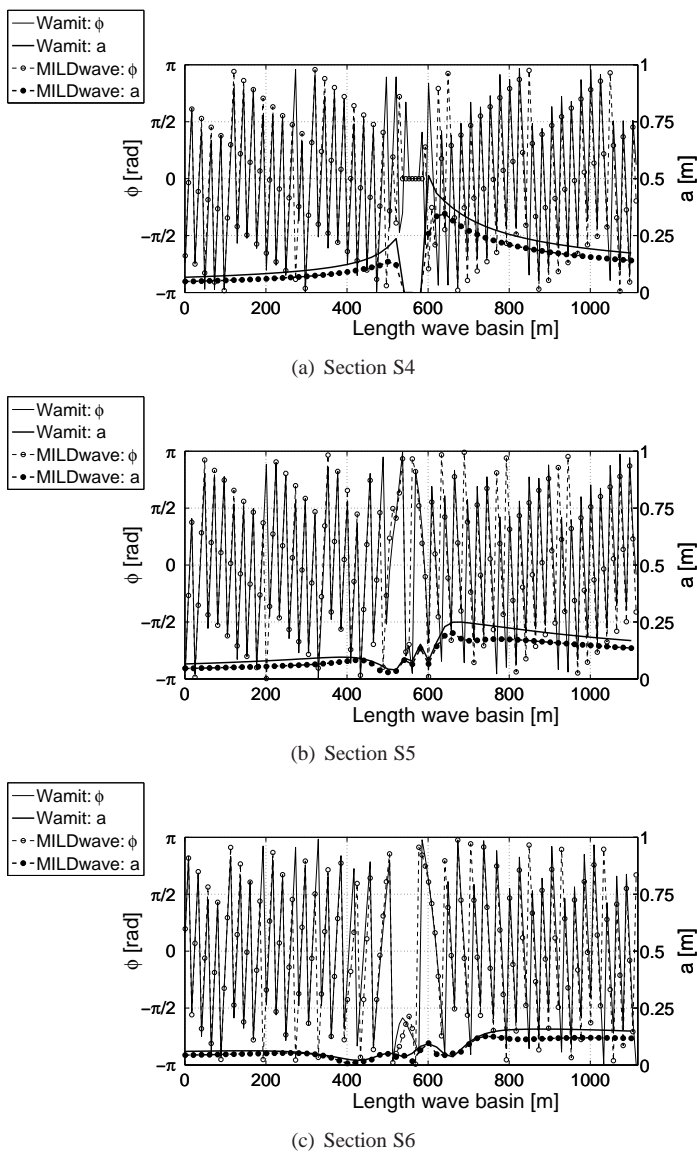


Figure F.17: Calculated wave amplitude  $a$  and phase shift  $\phi$  in section (a) S4, (b) S5, (c) S6 for regular incident waves with  $a = 1$  m and  $T = 4$  s

Again, in general a smaller wave height is seen in MILDwave compared to WAMIT, especially in front of and behind the FO<sup>3</sup> WEC (section S4). Note the deviations near the platform in the sections through the platform (section S2 and section S4). As waves are radiated on a circle with  $r_c = 50$  m only the wave amplitude and phase shift outside the circle need to be studied. The values inside

the circle (between 794 m and 894 m in section S2 and between 513 m and 613 m in section S4) have no physical meaning.

The absolute difference between the wave amplitude in WAMIT and MILDwave is shown in Figure F.18. The results in a square of 100 m x 100 m in the centre of the domain are ignored (and set to a value of 0) as the results inside the wave generation circle with  $r_c = 50$  m have no physical meaning.

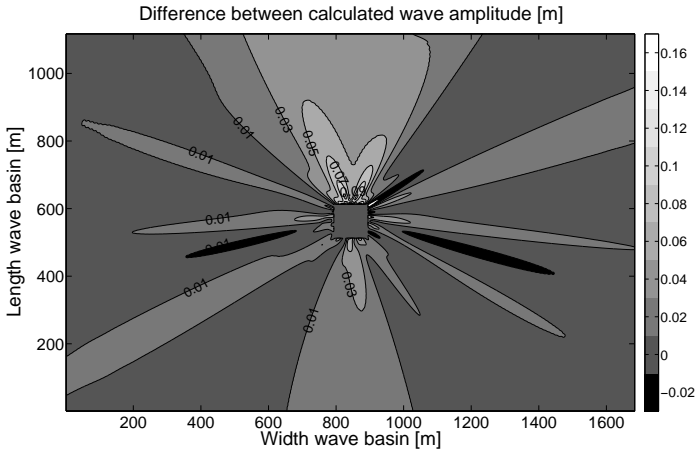


Figure F.18: Calculated absolute difference between wave amplitude  $a$  in WAMIT and MILDwave

The absolute difference between the wave amplitude calculated in WAMIT and MILDwave is equal to 10 cm at maximum. In the largest part of the domain the absolute difference is not higher than 3 cm. One should keep in mind that the amplitude of the radiated wave is varying between 0 cm and 50 cm through the domain.

Finally the mean absolute error and the root mean square error are calculated. The mean absolute error and root mean square error for the wave amplitude equal 0.011 m and 0.017 m. When dividing the MAE and the RMSE for the wave amplitude by the mean value of the wave amplitude in WAMIT ( $= 0.049$  m) a MAE equal to 23 % and a RMSE equal to 35 % are obtained. The latter values are much higher compared with the results for  $T = 6$  s and 8 s.

## F.1.4 Diffraction and radiation

The resulting wave amplitude  $a$  when diffraction and radiation are taken into account in WAMIT is shown in Figure F.19 for a regular incident wave with wave amplitude of 1 m and wave period of 4 s.



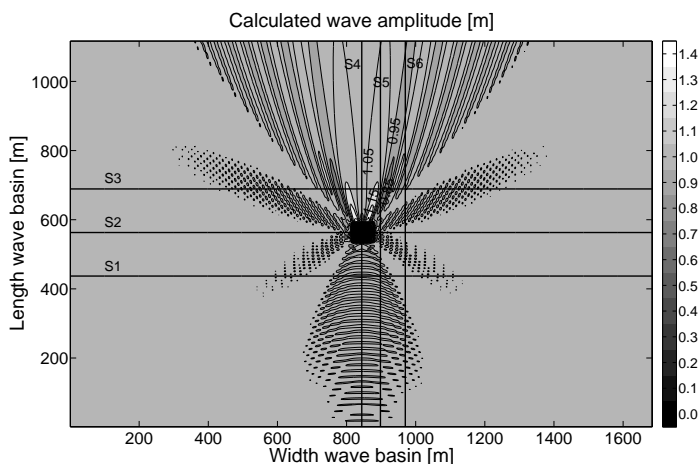


Figure F.19: Calculated wave amplitude  $a$  in WAMIT

By estimating the phase shift between the diffracted and radiated wave pattern (as calculated in WAMIT) in a longitudinal section at  $x^* = 844$  m behind the platform, the total wave pattern can be calculated in MILDwave (Figure F.20). In this longitudinal section the radiated and diffracted wave have the same direction of wave propagation.

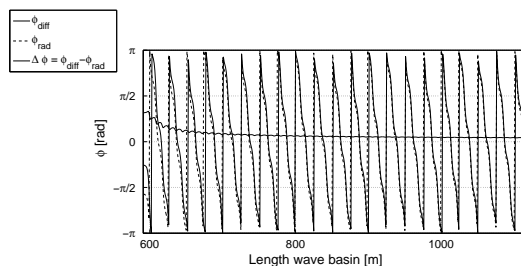


Figure F.20: Difference between phase shift (relative to the centre of the  $FO^3$  WEC) of the diffracted and radiated wave pattern

Note that the radiated wave is propagating behind the diffracted wave. For  $T = 6$  s and  $T = 8$  s the opposite is observed. From Figure F.20 it is seen that the diffracted and radiated wave are almost in phase. A small additional phase shift of  $0.08$  rad ( $4.6^\circ$ ) is needed between the diffracted and the radiated wave pattern. Near the platform a higher difference in phase is seen, due to the occurrence of standing waves. The resulting wave amplitude when diffraction and radiation are considered together in MILDwave is shown in Figure F.21.

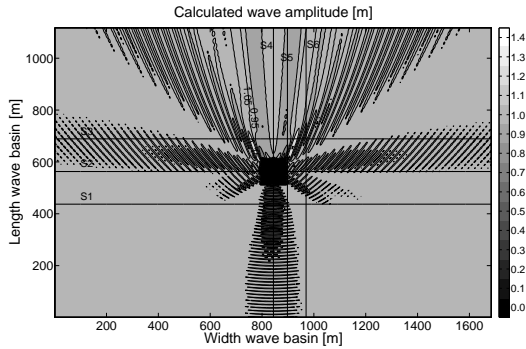


Figure F.21: Calculated wave amplitude  $a$  in MILDwave

The resulting wave amplitude  $a$  will be compared in more detail in two circular sections with centre equal to the centre of the FO<sup>3</sup> WEC and radius  $r_c = 70$  m and 126 m (Figure F.22).

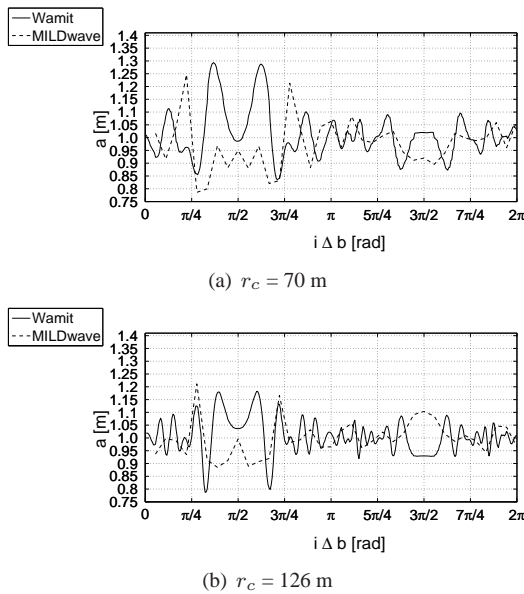
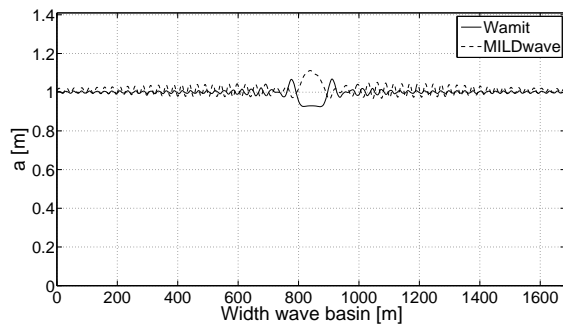


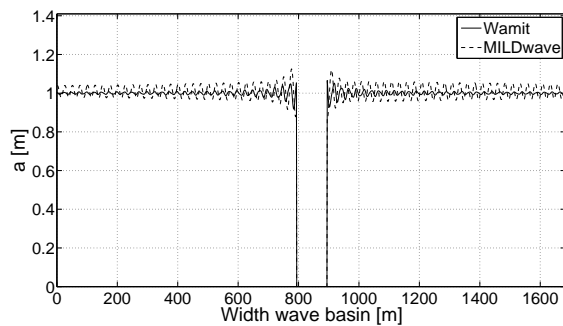
Figure F.22: Calculated wave amplitude  $a$  on a circle with centre equal to the centre of the FO<sup>3</sup> WEC and radius  $r_c = (a) 70$  m,  $(b) 126$  m for regular incident waves with  $a = 1$  m and  $T = 4$  s

Furthermore the same lateral sections S1, S2 and S3 and longitudinal sections S4, S5 and S6 are considered as in previous sections (indicated on Figure F.19 and Figure F.21). Sections S1, S2 and S3 are shown in Figure F.23 and in more detail

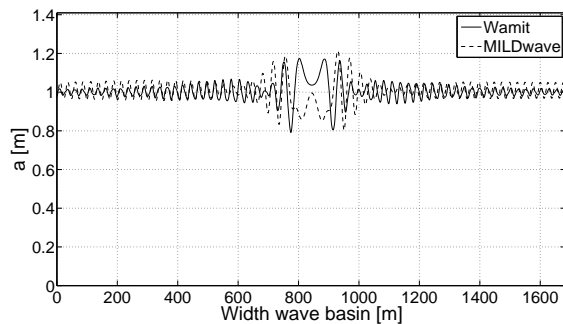
in Figure F.25. Figure F.24 shows section S4, S5 and S6. The same sections are given in more detail in Figure F.26.



(a) Section S1

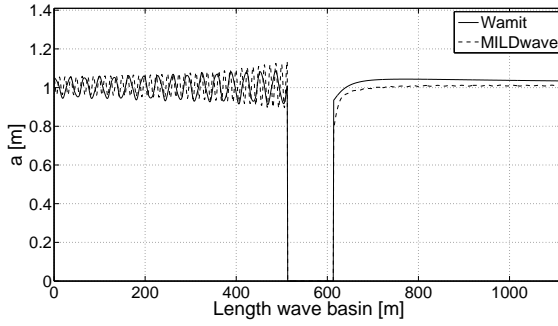


(b) Section S2

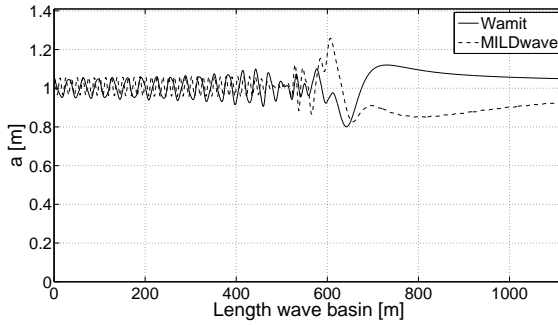


(c) Section S3

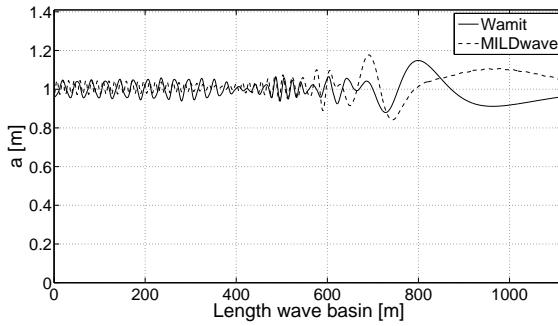
Figure F.23: Calculated wave amplitude  $a$  in section (a) S1, (b) S2, (c) S3



(a) Section S4



(b) Section S5



(c) Section S6

Figure F.24: Calculated wave amplitude  $a$  in section (a) S4, (b) S5, (c) S6

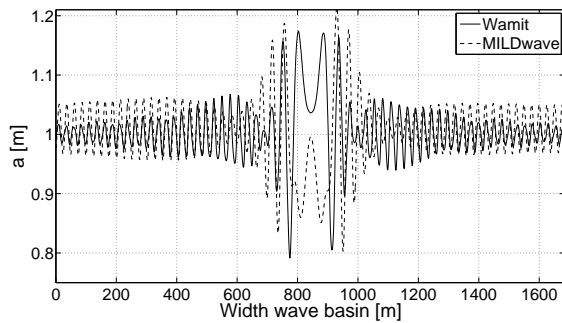
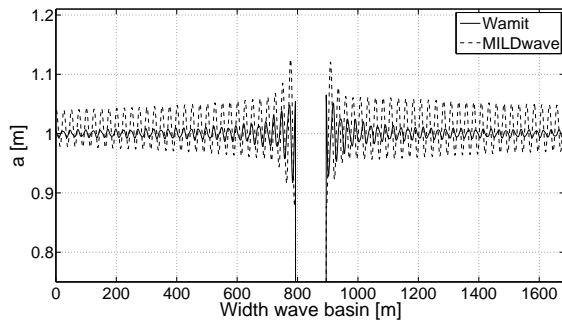
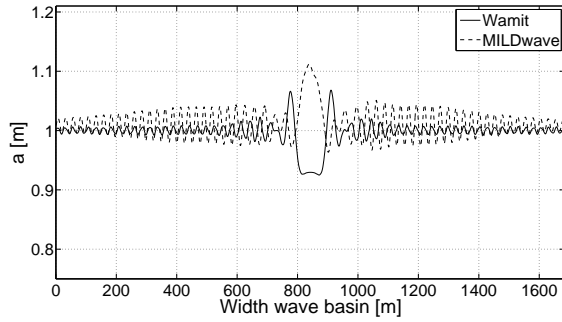
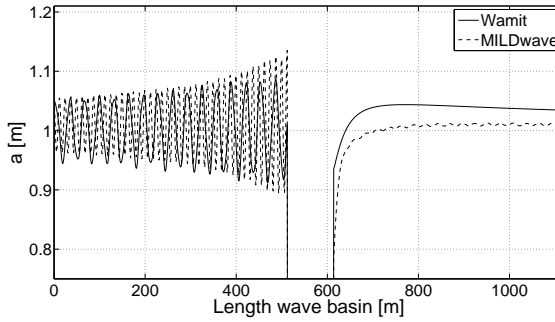
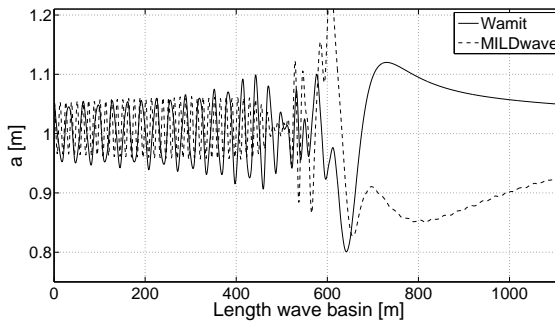


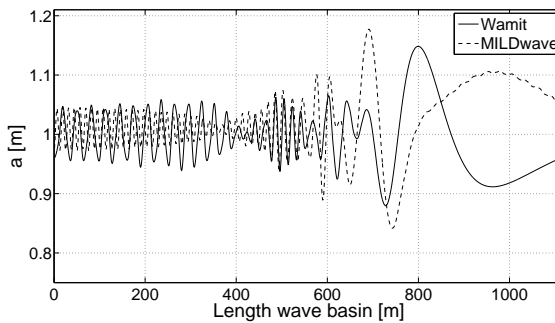
Figure F.25: Calculated wave amplitude  $a$  (zoomed in) in section (a) S1, (b) S2, (c) S3



(a) Section S4



(b) Section S5



(c) Section S6

Figure F.26: Calculated wave amplitude  $a$  (zoomed in) in section (a) S4, (b) S5, (c) S6

Figure F.25(a) and Figure F.25(c) show large deviations in wave amplitude in front of and behind the  $FO^3$  WEC through a large difference in phase shift and amplitude in the radiated wave pattern (Figure F.16(a) and Figure F.16(c)). Figure F.25 clearly indicates a spatial phase shift between the oscillations in WAMIT and MILDwave along the wave basin width. Figure F.26(a) shows a difference of approximately 5 cm between the results in WAMIT and MILDwave along the length of the wave basin. The results in section S5 (Figure F.26(b))

and S6 (Figure F.26(c)) differ due to the spatial phase shift observed in the lateral sections S1, S2 and S3 (Figure F.25). Furthermore deviations between WAMIT and MILDwave as seen on the circular sections (Figure F.22) are also due to the observed spatial phase shift.

To make a better comparison between the results in WAMIT and MILDwave the envelope of the oscillations along the width and length of the wave basin in WAMIT and MILDwave has been determined. Again an area of 180 m x 180 m has been ignored when calculating the envelope. The resulting envelope of the WAMIT and MILDwave results are shown on Figure F.27, respectively F.28.

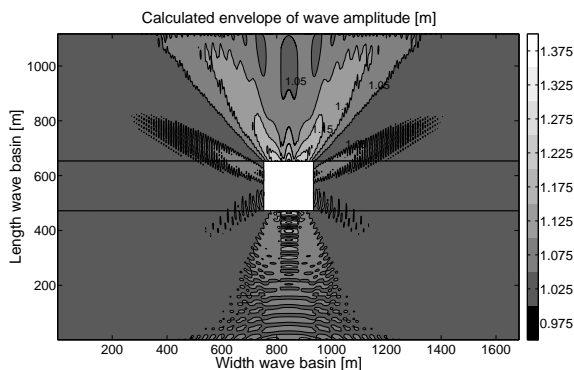


Figure F.27: Calculated envelope in WAMIT

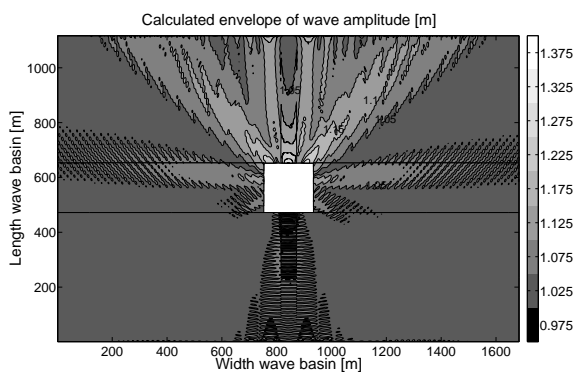


Figure F.28: Calculated envelope in MILDwave

The difference between both envelopes is shown on Figure F.29:

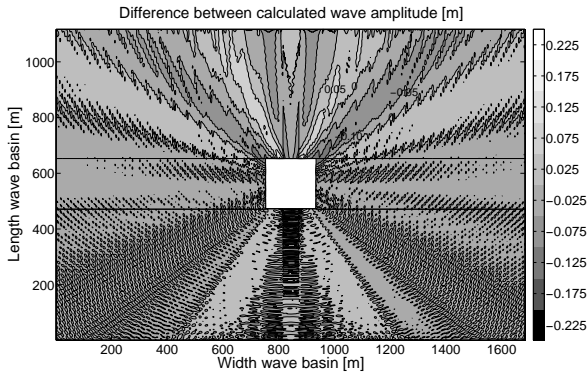


Figure F.29: Difference between WAMIT and MILDwave

The difference between the wave amplitudes calculated from MILDwave and WAMIT is observed to be in the range of  $\pm 10\%$  in the largest part of the domain. Near the  $FO^3$  WEC some larger differences occur.

The mean absolute error over the computational domain is equal to 0.023 m and the root mean square error equals 0.030 m. Dividing the latter values to the mean value in WAMIT ( $= 1.036$  m) results in a MAE and RMSE of respectively, 2.19 % and 2.90 %. The MAE and RMSE are higher compared to the results for  $T = 6$  s.

## F.2 Results for a regular wave with unit wave amplitude and wave period of 8 s

### F.2.1 Results of WAMIT

#### F.2.1.1 Absorbed power

For  $T = 8$  s and  $a = 1$  m approximately 34 % ( $= \frac{384}{1131}$ ) of the total available wave power over the width of the  $FO^3$  WEC has been absorbed.

#### F.2.1.2 Wave elevations

##### Real part of the wave amplitude

The WAMIT results are presented in this paragraph for the cases diffraction + radiation (Figure F.30(a)), only radiation (Figure F.30(b)) and only diffraction (Figure F.30(c)) obtained from NTNU for wave conditions  $H_i = 2$  m,  $T = 8$  s.



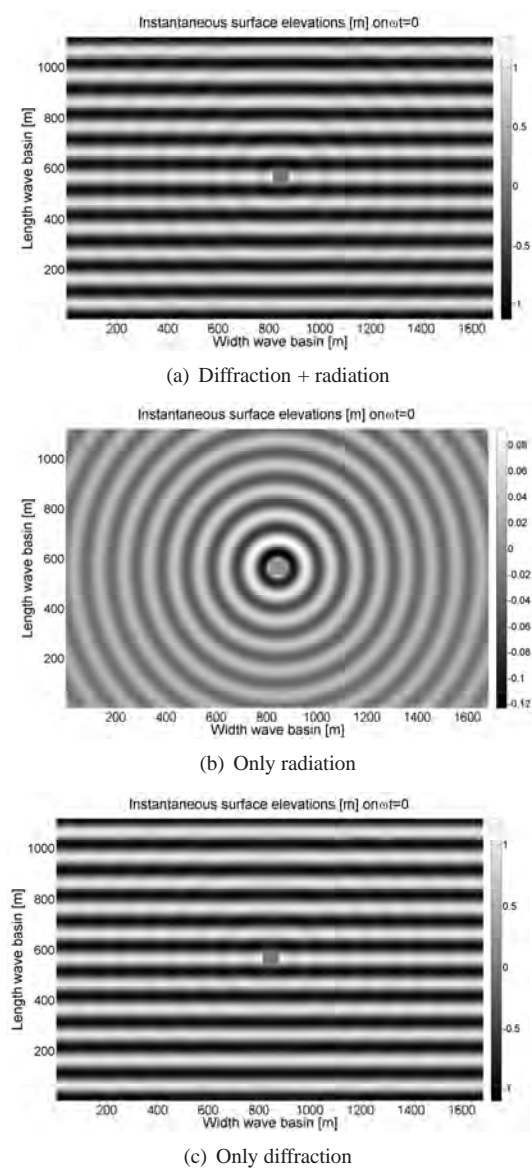


Figure F.30: Instantaneous surface elevations on  $\omega t = 0$  calculated with WAMIT taking (a) diffraction and radiation, (b) only radiation and (c) only diffraction into account

### Imaginary part of the wave amplitude

The instantaneous surface elevations on  $\omega t = -\pi/2$  due to diffraction and radiation, only radiation and only diffraction, calculated with WAMIT for an

incident wave with  $H_i = 2$  m and  $T = 8$  s, are shown in respectively Figure F.31(a), F.31(b) and F.31(c).

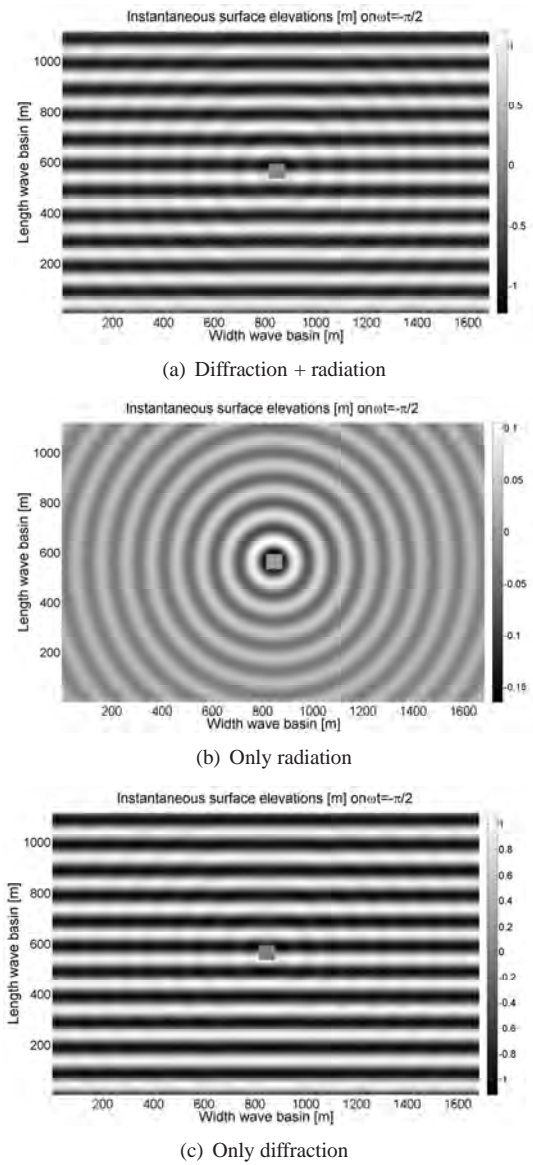


Figure F.31: Instantaneous surface elevations on  $\omega t = -\pi/2$  calculated with WAMIT taking (a) diffraction and radiation, (b) only radiation and (c) only diffraction into account

## F.2.2 Wave diffraction

### F.2.2.1 Implementation of wave diffraction in MILDwave

In this section WAMIT results are adopted and reformulated in terms of wave amplitude  $a$  and phase shift  $\phi$ , relative to the centre of the  $FO^3$  WEC, instead of real and imaginary part of the wave amplitude (cf. using equations (8.3) and (8.4)). The resulting wave amplitude  $a$  and phase shift  $\phi$  relative to the centre of the  $FO^3$  WEC, when only diffraction is considered, are shown in Figure F.32 for a regular incident wave with a wave amplitude of 1 m and a wave period of 8 s.

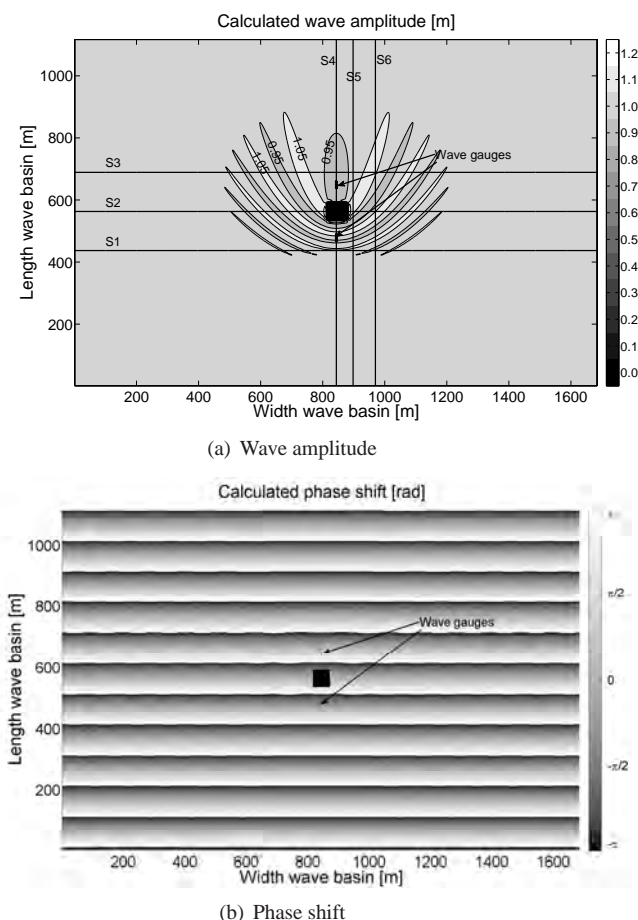


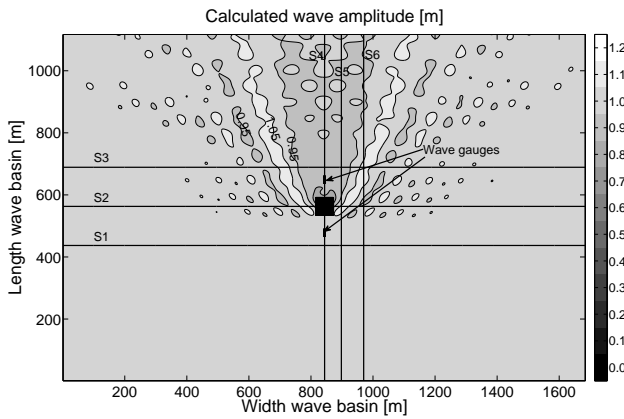
Figure F.32: Calculated (a) wave amplitude  $a$  and (b) phase shift  $\phi$  in WAMIT

The amounts of reflection and transmission have been determined by a reflection analysis (Table F.3) and have been used to implement an  $FO^3$  WEC.

Table F.3: Reflection analysis - diffraction WAMIT

Wave Gauges	$H_i$ or $H_t$ [m]	$T$ [s]	$H_r$ [m]	$T$ [s]	$K_r$ [%]
1-3	2.001	8.031	0.132	8.031	6.57
4-6	1.826	8.031	0.028	8.031	1.56

The diffraction pattern, generated by an  $FO^3$  WEC, is modelled using the sponge layer technique (chapter 6). The resulting wave amplitude in MILDwave is shown in Figure F.33.

Figure F.33: Calculated wave amplitude  $a$  in MILDwave

When comparing Figure F.32(a) and Figure F.33, the shadow zone behind the  $FO^3$  WEC seems again wider in MILDwave compared to WAMIT. This will be studied in more detail by considering sections as indicated on Figure F.32(a) and Figure F.33.

Again a reflection analysis is performed (Table F.4). When comparing Table F.3 and Table F.4 a small decrease in reflection is observed.

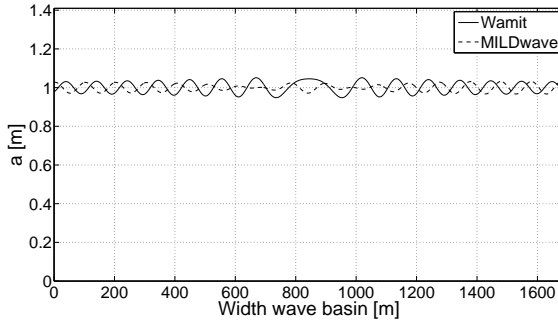
Table F.4: Reflection analysis - diffraction in MILDwave

Wave Gauges	$H_i$ or $H_t$ [m]	$T$ [s]	$H_r$ [m]	$T$ [s]	$K_r$ [%]
1-3	2.03	7.877	0.091	7.877	4.49
4-6	1.761	7.877	0.067	8.192	3.80

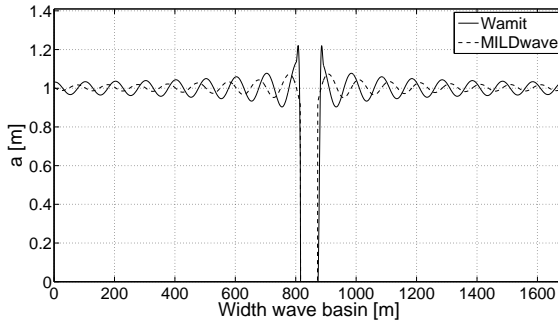
### F.2.2.2 Comparison of wave diffraction patterns generated by an FO<sup>3</sup> WEC using WAMIT and MILDwave

To make a detailed comparison, sections on a distance of 126 m from the centre of the FO<sup>3</sup> WEC (distance between two converters in a farm will be 108 m at minimum) will be studied as indicated on Figure F.32(a) and Figure F.33. Figure F.34 shows a lateral section in front of (S1), through (S2) and behind (S3) the FO<sup>3</sup> WEC at respectively  $y^* = 437$  m, 563 m and 689 m. Figure F.35 shows three longitudinal sections at  $x^* = 844$  m (S4), 898 m (S5) and 970 m (S6). In Figure F.36 and Figure F.37 the same sections are zoomed in.

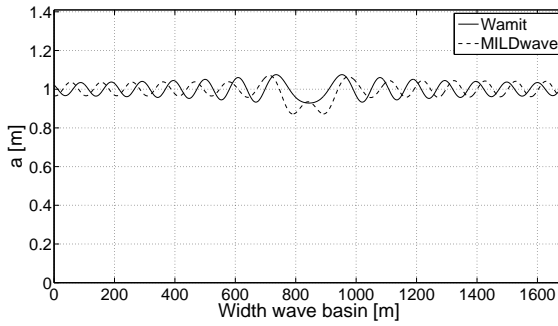
Figure F.36(a) confirms the higher reflection observed in the WAMIT results. Furthermore Figure F.36(c) shows the wider shadow zone in MILDwave compared to WAMIT. The distance crest-to-crest between the two central peaks in WAMIT equals 218 m, in MILDwave 261 m. Figure F.36 clearly indicates a spatial phase shift between the oscillations in WAMIT and MILDwave along the wave basin width. Figure F.37(a) shows a very good agreement between the results in WAMIT and MILDwave along the length of the wave basin. In general good agreement between the WAMIT and MILDwave results is observed. The values in the central part of the shadow zone in MILDwave oscillate around the value obtained in WAMIT. The shadow zone in the MILDwave results is approximately 20 % wider than the shadow zone in the WAMIT results.



(a) Section S1



(b) Section S2



(c) Section S3

Figure F.34: Calculated wave amplitude  $a$  in section (a) S1, (b) S2, (c) S3

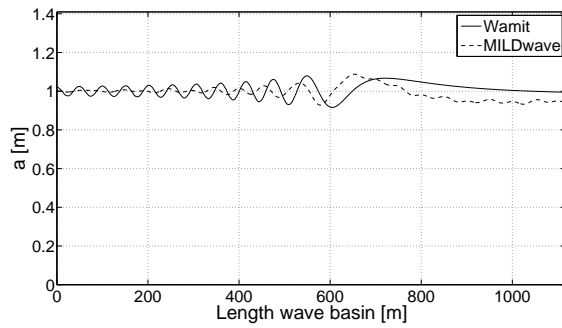
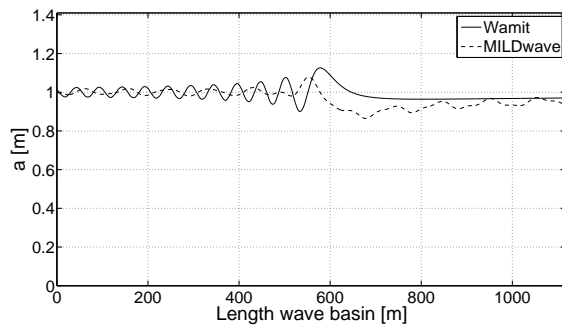
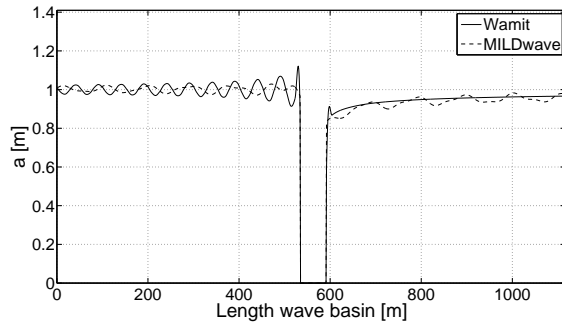
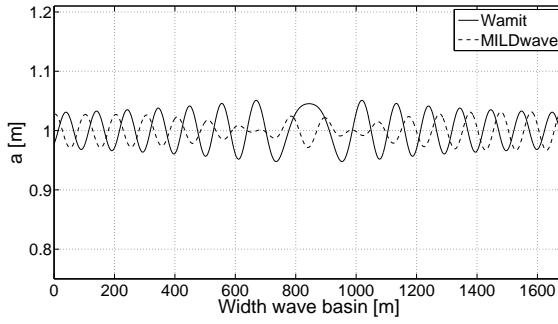
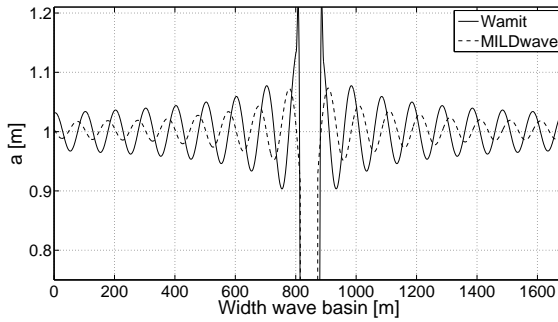


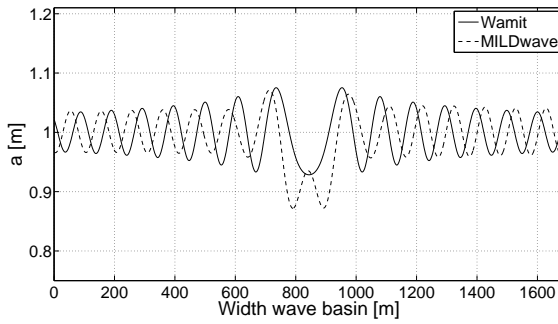
Figure F.35: Calculated wave amplitude  $a$  in section (a) S4, (b) S5, (c) S6



(a) Section S1



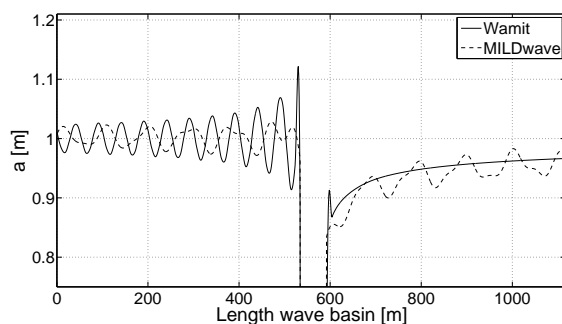
(b) Section S2



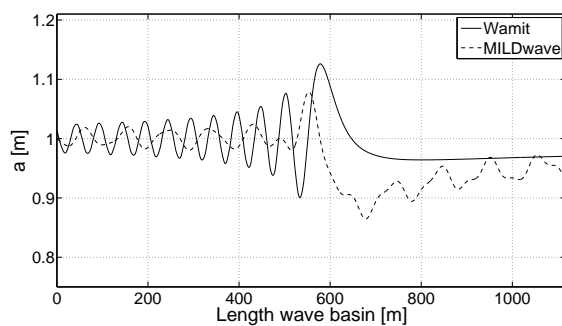
(c) Section S3

Figure F.36: Calculated wave amplitude  $a$  (zoomed in) in section (a) S1, (b) S2, (c) S3

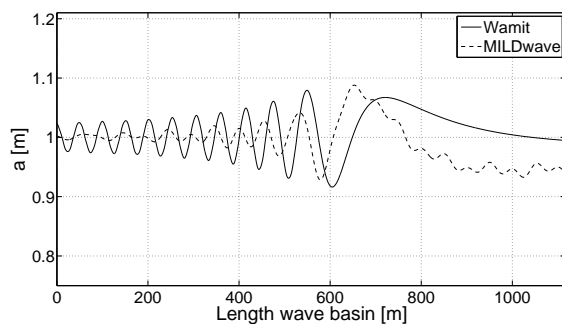




(a) Section S4



(b) Section S5



(c) Section S6

Figure F.37: Calculated wave amplitude  $a$  (zoomed in) in section (a) S4, (b) S5, (c) S6

Further the envelope of the oscillations along the width and length of the wave basin in WAMIT and MILDwave has been compared. Therefore a Hilbert transformation has been used. An area of 180 m x 180 m has been ignored when calculating the envelope. This zone has no importance when studying a farm as the minimal distance between the converters is 108 m ( $3 * \text{dimension } FO^3 \text{ WEC}$ ). Moreover by ignoring the latter zone, near-field peaks in the calculated envelope have been prevented. The resulting envelope of the WAMIT and MILDwave

results are shown on Figure F.38, respectively F.39.

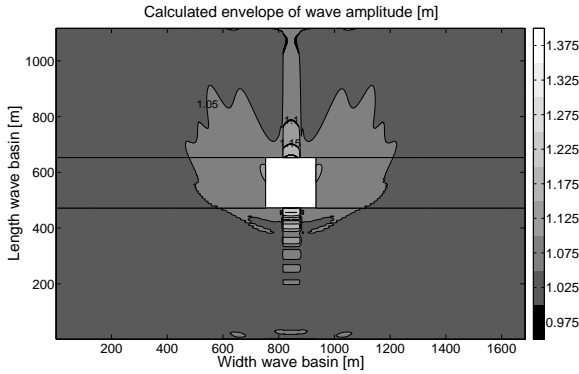


Figure F.38: Calculated envelope of wave amplitude in WAMIT

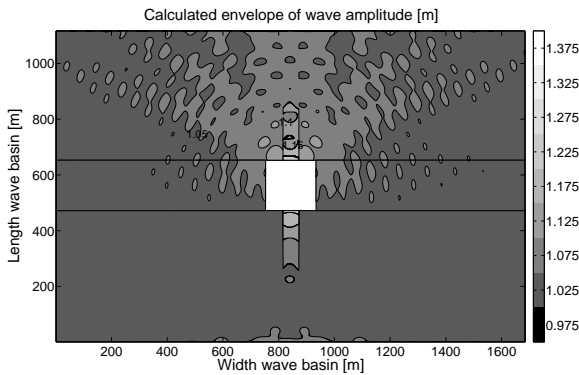


Figure F.39: Calculated envelope of wave amplitude in MILDwave

The difference between both envelopes is shown on Figure F.40. The difference between the wave amplitudes calculated from MILDwave and WAMIT is observed to be in the range of  $\pm 5\%$  in the largest part of the domain. In some very small areas a little higher difference is seen.

To determine the accuracy of MILDwave, compared to WAMIT, the mean absolute error (MAE) and the root mean square error (RMSE) over the computational domain are calculated. The MAE and RMSE equal respectively 0.015 m and 0.019 m.

Dividing the latter values through the mean value of the results in WAMIT ( $= 1.039$  m) results in  $MAE = 1.47\%$  and  $RMSE = 1.87\%$ . The MAE and RMSE are even smaller than the results obtained for  $T = 6$  s.

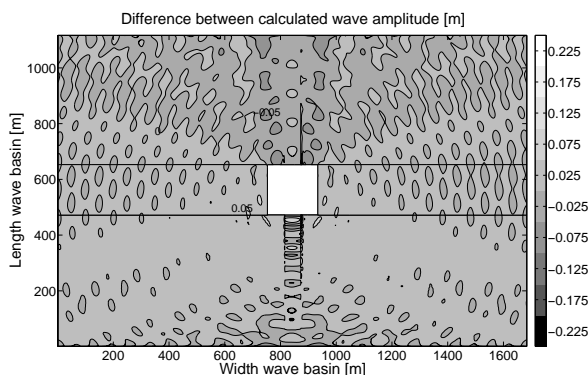


Figure F.40: Difference between envelope of wave amplitude in WAMIT and in MILDwave

## F.2.3 Wave radiation

### F.2.3.1 Implementation of wave radiation in MILDwave

The wave amplitude and phase shift relative to the centre of the  $FO^3$  WEC on the wave generation circle with centre equal to the centre of the  $FO^3$  and radius 50 m are determined from the results in WAMIT (equations (8.3) and (8.4)) and are given in Figure F.41. These wave amplitude and phase shift are used to generate the radiated wave on the wave generation circle in MILDwave.

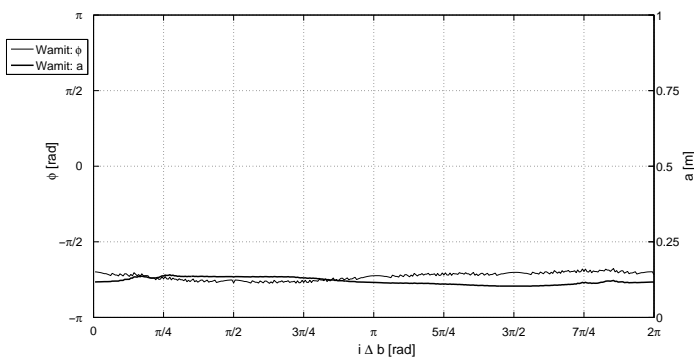


Figure F.41: Calculated wave amplitude  $a$  and phase shift  $\phi$  on a circle with centre equal to the centre of the  $FO^3$  WEC and radius = 50 m for regular incident waves with  $a = 1$  m and  $T = 8$  s

As the wave length ( $= 100$  m) is higher than the dimension of the  $FO^3$ , the heave motion is dominating. Consequently the amplitude  $a$  and phase shift  $\phi$  relative to the centre of the  $FO^3$  differ less along the circular section compared to the results for  $T = 4$  s and  $T = 6$  s.

The calculated wave amplitude and phase shift across the whole domain in respectively WAMIT (using equations (8.3) and (8.4)) and MILDwave are shown in Figure F.42 and Figure F.43 for a regular incident wave with wave amplitude of 1 m and wave period of 8 s. The results in a square of 100 m x 100 m in the centre of the domain in MILDwave are set to 0 because the values within the wave generation circle ( $r_c = 50$  m) have no physical meaning.

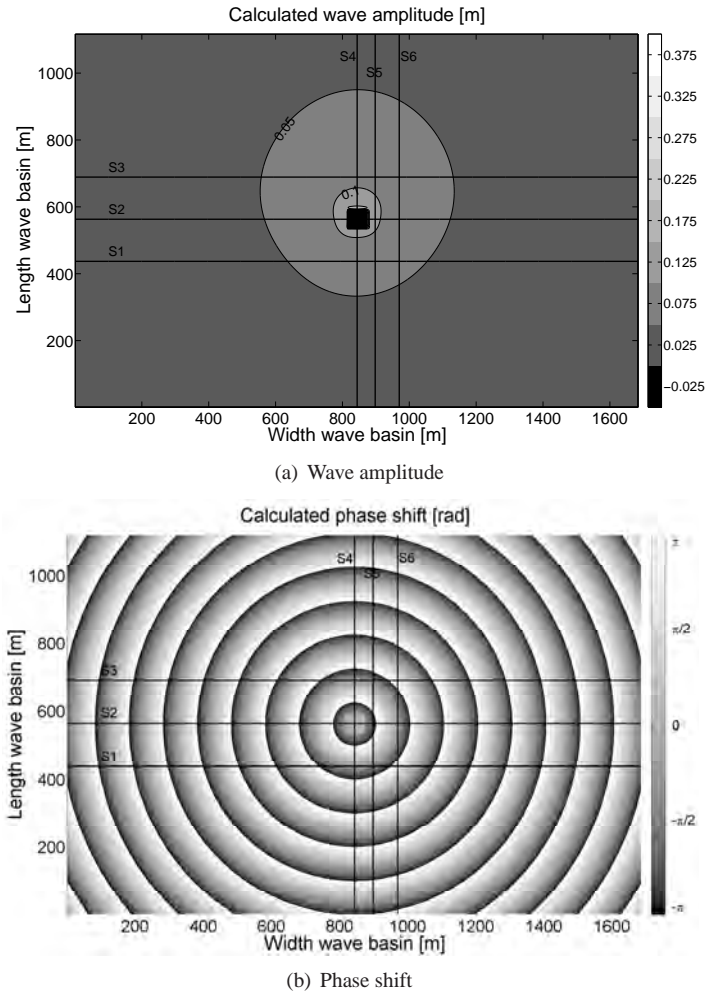
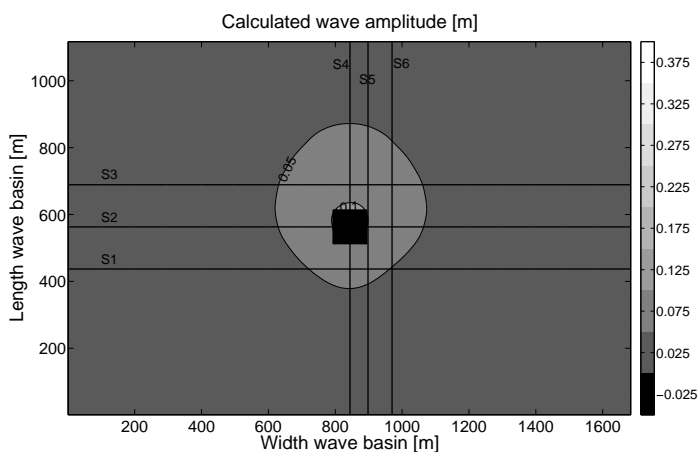
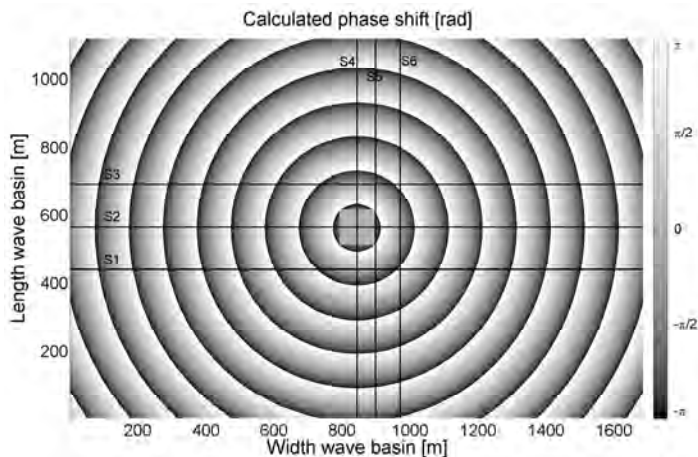


Figure F.42: Calculated (a) wave amplitude  $a$  and (b) phase shift  $\phi$  in WAMIT



(a) Wave amplitude



(b) Phase shift

Figure F.43: Calculated (a) wave amplitude  $a$  and (b) phase shift  $\phi$  in MILDwave

When comparing Figure F.42 and Figure F.43 the resulting wave amplitude and phase shift seem to be quite similar. The wave amplitudes between 0.05 m and 0.10 m occur in a larger zone in WAMIT compared to MILDwave. A slightly smaller wave height in MILDwave is observed.

The results in Figure F.42 and Figure F.43 are discussed in detail in the next section.

### F.2.3.2 Comparison of wave radiation patterns generated by an FO<sup>3</sup> WEC using WAMIT and MILDwave

The calculated wave amplitude and phase shift in MILDwave and WAMIT have been compared in two circular sections with centre equal to the centre of the FO<sup>3</sup> WEC and radius  $r_c = 70$  m and 126 m. The results are shown in Figure F.44. Note that  $i\Delta b = \pi/2$  represents a location behind the platform.

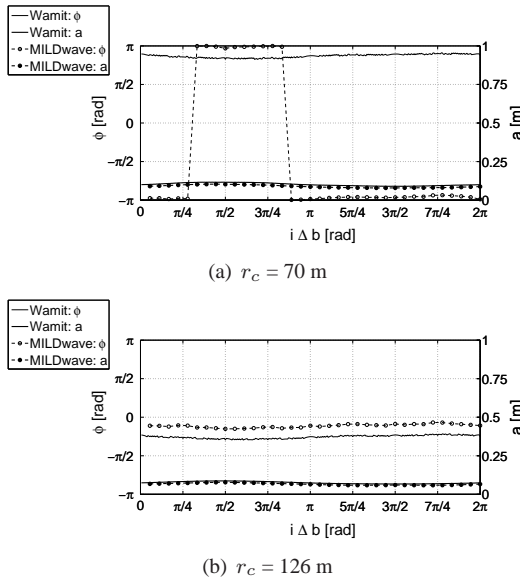
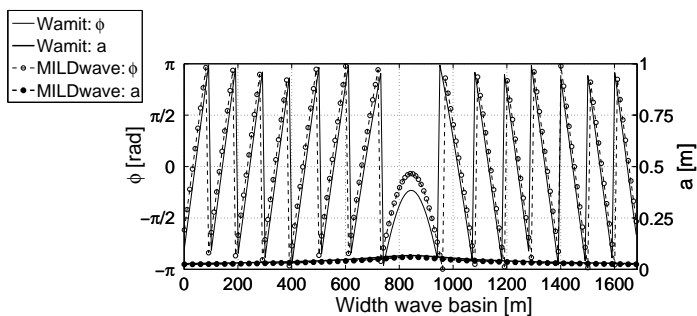


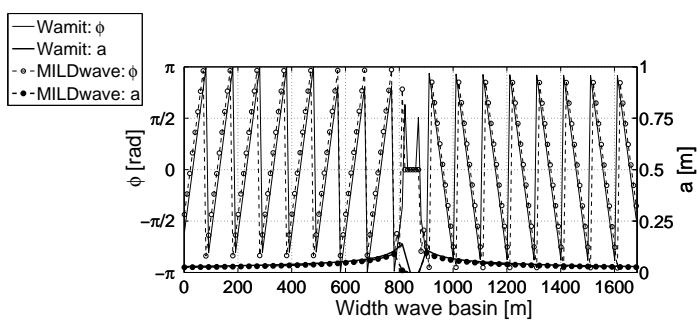
Figure F.44: Calculated wave amplitude  $a$  and phase shift  $\phi$  on a circle with centre equal to the centre of the FO<sup>3</sup> WEC and radius  $r_c =$  (a) 70 m, (b) 126 m for regular incident waves with  $a = 1$  m and  $T = 8$  s

In general the results in WAMIT and MILDwave agree very well. The wave amplitude  $a$  is a little smaller than  $a$  calculated in WAMIT. Further a phase shift between  $\phi$ , calculated in WAMIT and MILDwave, is observed. This phase shift is approximately constant along the circular section. To compose the radiated and diffracted wave, an additional phase shift will be imposed on the radiated wave to obtain the phase shift between the diffracted and radiated wave pattern and the overall wave pattern, as determined in WAMIT. Therefore the constant phase shift between the radiated wave in WAMIT and MILDwave along a circular section as seen on Figure F.44 will not influence the final results.

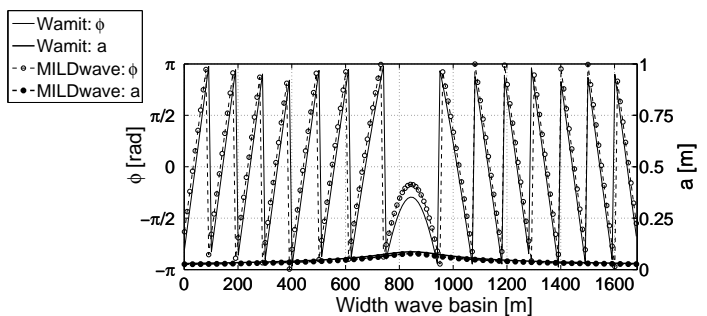
In Figure F.45 and Figure F.46 the calculated wave amplitude and phase shift in WAMIT and MILDwave are shown in, respectively, three lateral sections S1 ( $y^* = 437$  m), S2 ( $y^* = 563$  m) and S3 ( $y^* = 689$  m) and three longitudinal sections S4 ( $x^* = 844$  m), S5 ( $x^* = 898$  m) and S6 ( $x^* = 970$  m) as indicated on Figure F.42 and Figure F.43.



(a) Section S1

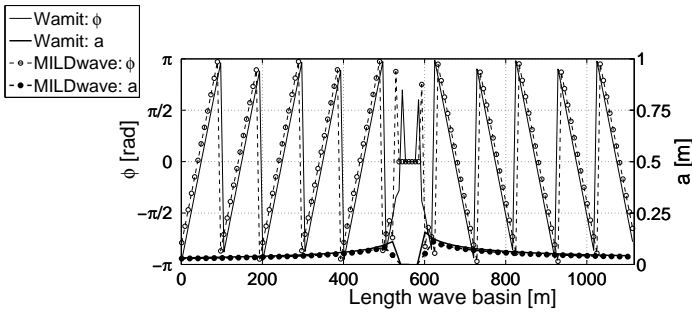


(b) Section S2

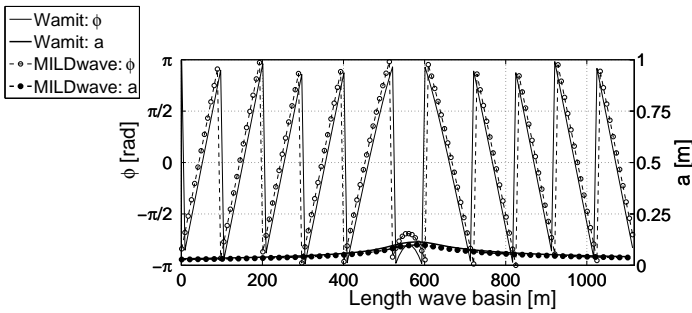


(c) Section S3

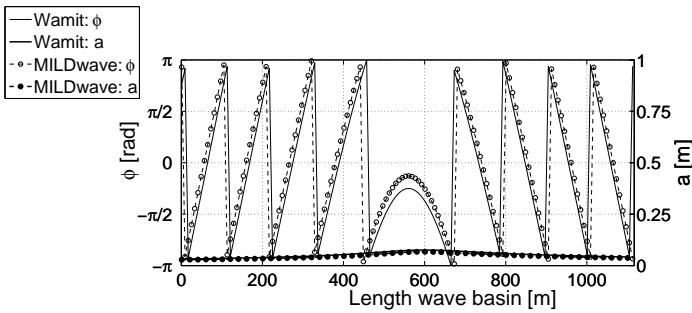
Figure F.45: Calculated wave amplitude  $a$  and phase shift  $\phi$  in section (a) S1, (b) S2 and (c) S3 for regular incident waves with  $a = 1$  m and  $T = 8$  s



(a) Section S4



(b) Section S5



(c) Section S6

Figure F.46: Calculated wave amplitude  $a$  and phase shift  $\phi$  in section (a) S4, (b) S5, (c) S6 for regular incident waves with  $a = 1$  m and  $T = 8$  s

Again, in general a good agreement is seen. Note the deviations near the platform in the sections through the platform (section S2 and section S4). As waves are radiated on a circle with  $r_c = 50$  m only the wave amplitude and phase shift outside the circle need to be studied. The values inside the circle (between 794 m and 894 m in section S2 and between 513 m and 613 m in section S4) have no physical meaning.

The absolute difference between the wave amplitude and phase shift in



WAMIT and MILDwave is shown in Figure F.47. The results in a square of 100 m x 100 m in the centre of the domain are ignored (and set to a value of 0) as the results inside the wave generation circle with  $r_c = 50$  m have no physical meaning.

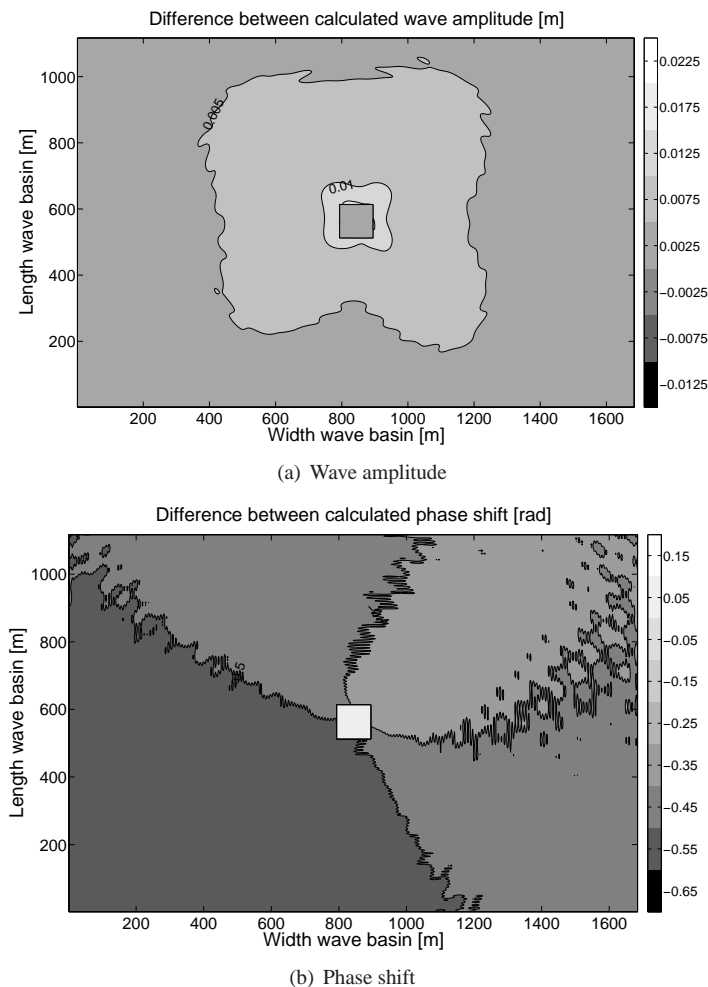


Figure F.47: Calculated absolute difference between (a) wave amplitude  $a$  and (b) phase shift  $\phi$  in WAMIT and MILDwave

The absolute difference between the wave amplitude calculated in WAMIT and MILDwave is equal to 1 cm at maximum. One should keep in mind that the amplitude of the radiated wave is varying between 0 cm and 12 cm through the domain. The absolute difference in phase shift varies between  $-0.30$  rad ( $-17^\circ$ ) and  $-0.60$  rad ( $-34^\circ$ ). As no large variation in phase shift occurs, the total wave pattern will not be influenced.

Finally the mean absolute error and the root mean square error are calculated. The mean absolute error and root mean square error equal 0.002 m and 0.003 m for the wave amplitude and 0.228 rad and 0.269 rad for the phase shift. When dividing the MAE and the RMSE for the wave amplitude by the mean value of the wave amplitude in WAMIT ( $= 0.039$  m) a MAE equal to 5.08 % and a RMSE equal to 6.60 % are obtained. The latter values are slightly higher compared to the results for  $T = 6$  s, but much smaller than the results for  $T = 4$  s.

### F.2.4 Diffraction and radiation

The resulting wave amplitude  $a$  when diffraction and radiation are taken into account in WAMIT is shown in Figure F.48 for a regular incident wave with wave amplitude of 1 m and wave period of 8 s.

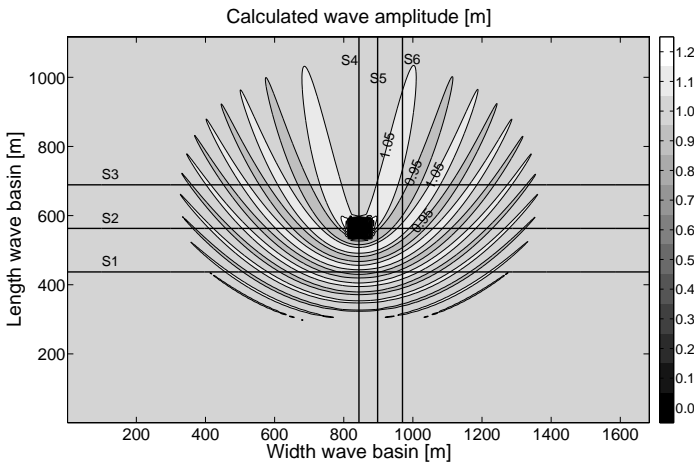


Figure F.48: Calculated wave amplitude  $a$  in WAMIT

By estimating the phase shift between the diffracted and radiated wave pattern (as calculated in WAMIT) in a longitudinal section at  $x^* = 844$  m behind the platform, the total wave pattern can be calculated in MILDwave (Figure F.49). In this longitudinal section the radiated and diffracted wave have the same direction of wave propagation. As seen for  $T = 6$  s, the diffracted wave propagates behind the radiated wave. From Figure F.49 it is seen that an additional phase shift of 0.706 rad ( $40^\circ$ ) is needed between the diffracted and the radiated wave pattern.

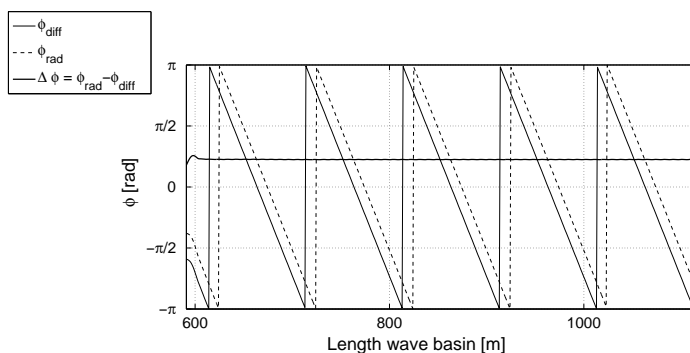


Figure F.49: Difference between phase shift (relative to the centre of the FO<sup>3</sup> WEC) of the radiated and diffracted wave pattern

The resulting wave amplitude when diffraction and radiation are considered together in MILDwave is shown in Figure F.50.

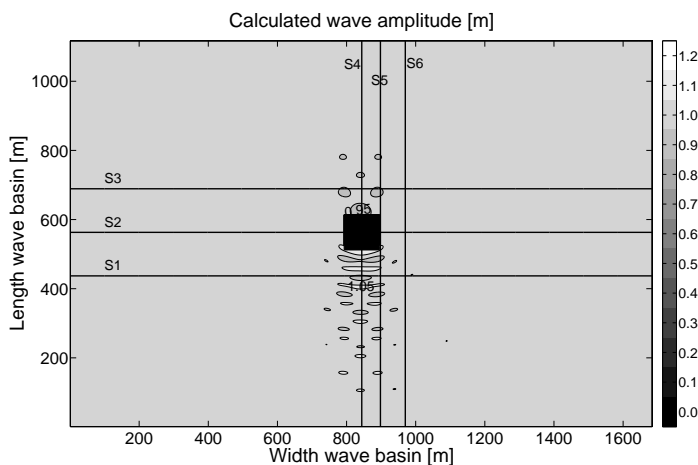


Figure F.50: Calculated wave amplitude  $a$  in MILDwave

At first sight the calculated wave amplitude is less variable in MILDwave compared to WAMIT. The resulting wave amplitude  $a$  will be compared in more detail in two circular sections with centre equal to the centre of the FO<sup>3</sup> WEC and radius  $r_c = 70$  m and 126 m (Figure F.51). Furthermore the same lateral sections S1, S2 and S3 and longitudinal sections S4, S5 and S6 are considered as in previous sections (indicated on Figure F.48 and Figure F.50). Section S1, S2 and S3 are shown in Figure F.52 and in more detail in Figure F.54. Figure F.53 shows section S4, S5 and S6. The same sections are given in more detail in Figure F.55.

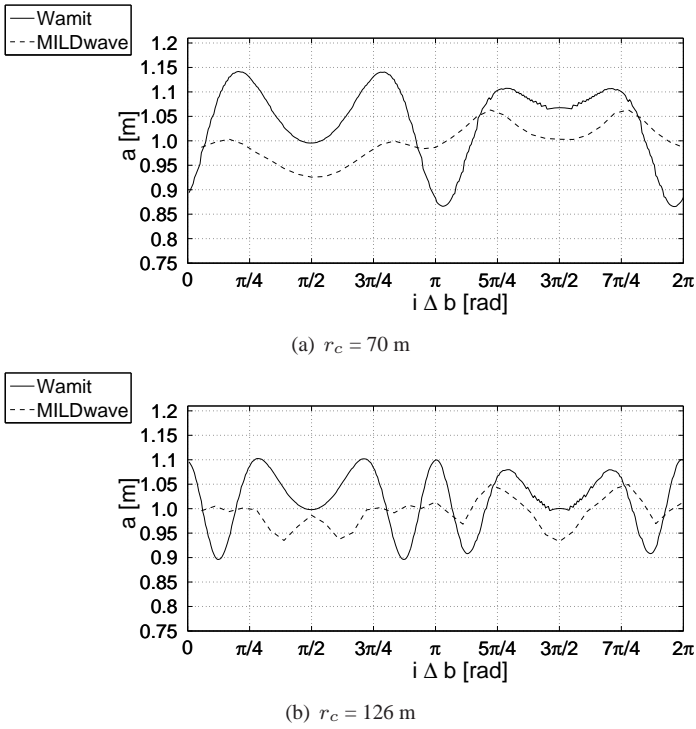


Figure F.51: Calculated wave amplitude  $a$  on a circle with centre equal to the centre of the  $FO^3$  WEC and radius  $r_c =$  (a) 70 m, (b) 126 m for regular incident waves with  $a = 1$  m and  $T = 8$  s

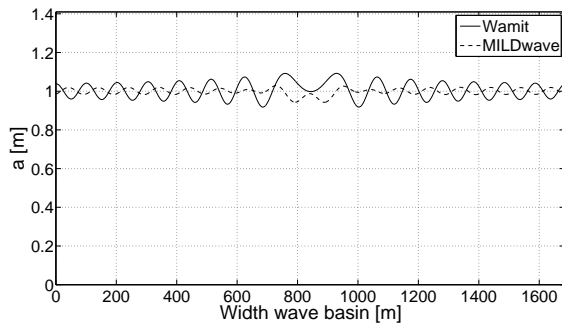
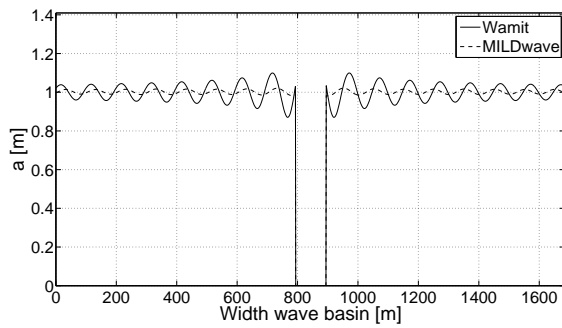
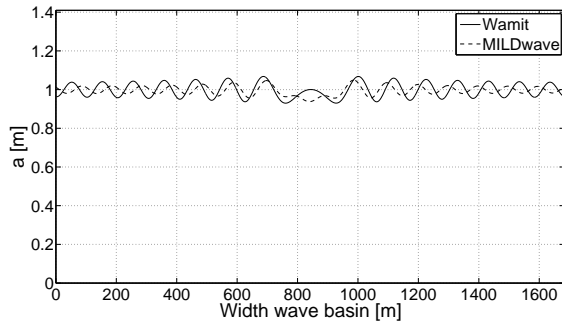
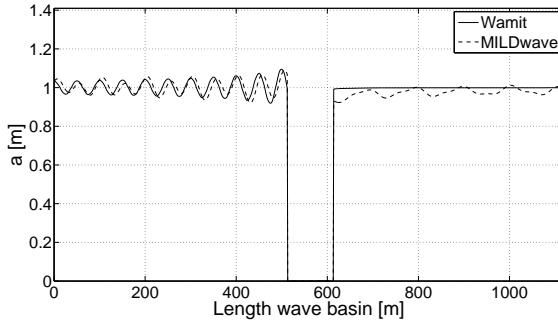
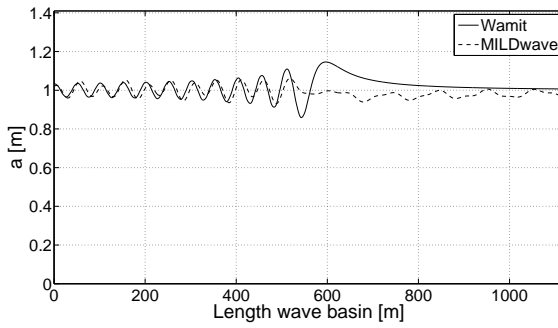


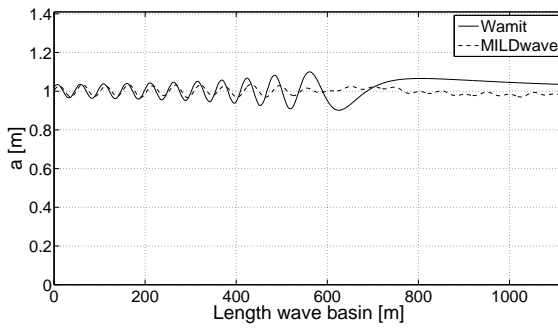
Figure F.52: Calculated wave amplitude  $a$  in section (a) S1, (b) S2, (c) S3



(a) Section S4

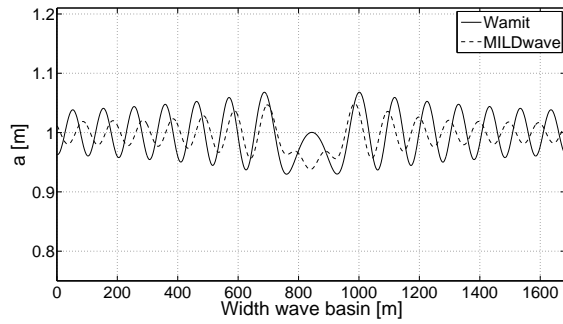


(b) Section S5

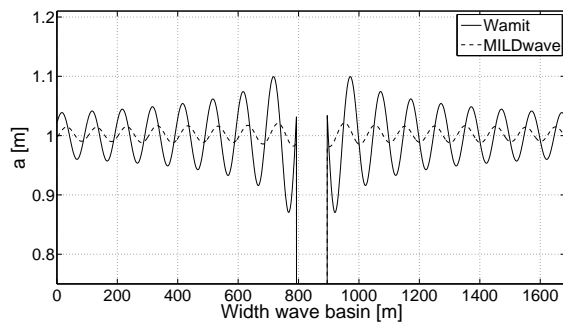


(c) Section S6

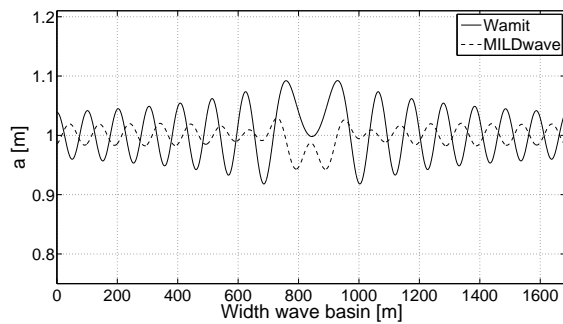
Figure F.53: Calculated wave amplitude  $a$  in section (a) S4, (b) S5, (c) S6



(a) Section S1

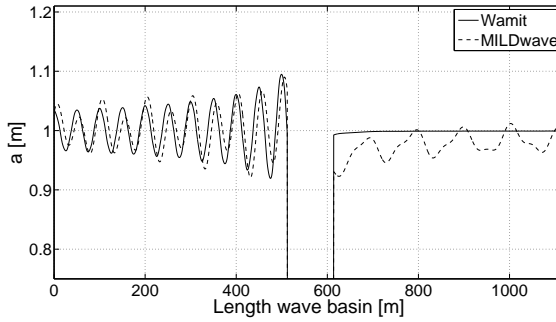


(b) Section S2

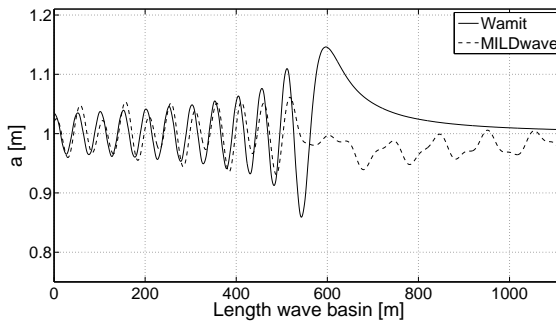


(c) Section S3

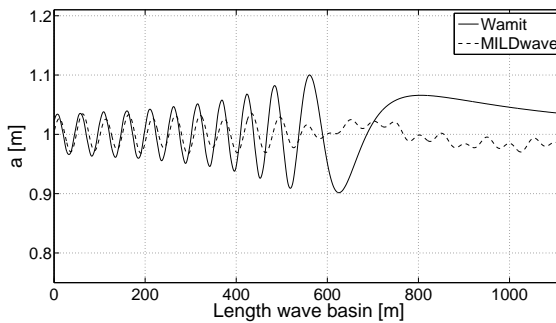
Figure F.54: Calculated wave amplitude  $a$  (zoomed in) in section (a) S1, (b) S2, (c) S3



(a) Section S4



(b) Section S5



(c) Section S6

Figure F.55: Calculated wave amplitude  $a$  (zoomed in) in section (a) S4, (b) S5, (c) S6

Figure F.54(a) confirms the higher reflection observed in the WAMIT results. Figure F.54 clearly indicates a spatial phase shift between the oscillations in WAMIT and MILDwave along the wave basin width. Figure F.55(a) shows a good agreement between the results in WAMIT and MILDwave along the length of the wave basin. The wave amplitude in MILDwave is a little smaller. The results in section S5 (Figure F.55(b)) and S6 (Figure F.55(c)) differ due to the spatial phase shift observed in the lateral sections S1, S2 and S3 (Figure F.54).



Furthermore deviations between WAMIT and MILDwave as seen on the circular sections (Figure F.51) are also due to the observed spatial phase shift.

To make a better comparison between the results in WAMIT and MILDwave the envelope of the oscillations along the width and length of the wave basin in WAMIT and MILDwave has been determined. Again an area of 180 m x 180 m has been ignored when calculating the envelope. The resulting envelope of the WAMIT and MILDwave results are shown on Figure F.56, respectively F.57.

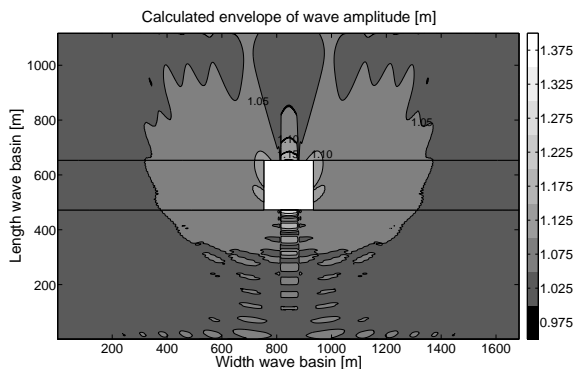


Figure F.56: Calculated envelope in WAMIT

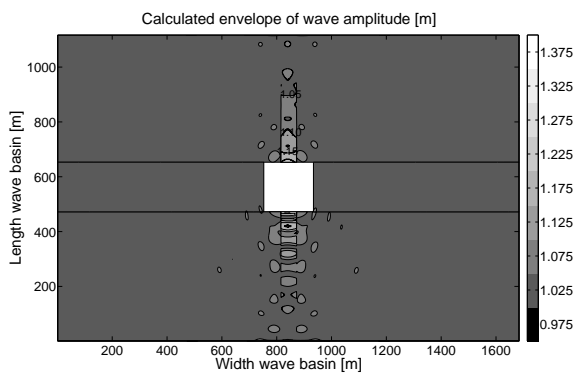


Figure F.57: Calculated envelope in MILDwave

The difference between both envelopes is shown on Figure F.58:

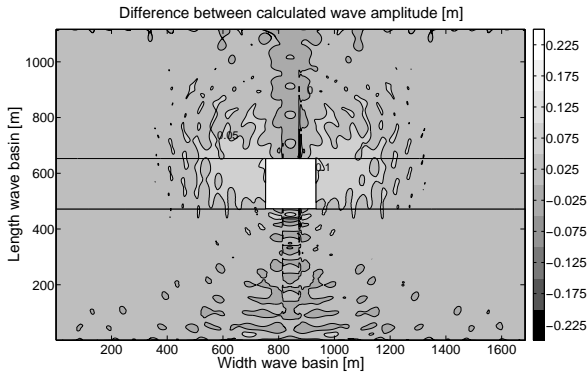


Figure F.58: Difference between WAMIT and MILDwave

The differences between the wave amplitudes calculated from MILDwave and WAMIT are observed to be in the range of  $\pm 10\%$  in the whole domain. In the largest part of the domain the differences are reduced to the interval  $[-5\%, +5\%]$  which confirms the good agreement between the WAMIT and MILDwave results.

The mean absolute error over the computational domain is equal to 0.028 m and the root mean square error equals 0.032 m. Dividing the latter values to the mean value in WAMIT ( $= 1.048$  m) results in a MAE and RMSE of respectively, 2.60 % and 3.00 %. These errors are slightly higher compared to  $T = 6$  s.

# G

## Cable network cost

### G.1 Lay-out A: a single line of WD-WECs

Table G.1: Cost lay-out A

Clusters	Cables in cluster					Cables from cluster to platform				
	$P_{\text{rated}}$ [MW]	$l'$ [km]	$A'$ [mm <sup>2</sup> ]	Annual Losses [kW]	Cost [€]	$P_{\text{rated}}$ [MW]	$l'$ [km]	$A'$ [mm <sup>2</sup> ]	Annual Losses [kW]	Cost [€]
2 strings of 6	12	5.720	95	7.7	610 133	24	22.633	185	62.2	3 319 507
2 strings of 6	12	5.720	95	7.7	610 133	24	16.399	185	45.1	2 405 187
2 strings of 6	12	5.720	95	7.7	610 133	24	10.170	185	28.0	1 491 600
2 strings of 6	12	5.720	95	7.7	610 133	24	3.977	185	11.0	583 293
1 string of 3	4	1.040	95	0.2	110 933	6	0.780	95	0.3	83 200
2 strings of 6	12	5.720	95	7.7	610 133	24	3.977	185	11.0	583 293
2 strings of 6	12	5.720	95	7.7	610 133	24	10.170	185	28.0	1 491 600
2 strings of 6	12	5.720	95	7.7	610 133	24	16.399	185	45.1	2 405 187
2 strings of 6	12	5.720	95	7.7	610 133	24	22.633	185	62.2	3 319 507

Cost cable network = €20 674 373

## G.2 Lay-out B: a staggered grid lay-out

Table G.2: Cost lay-out B

Clusters	Cables in cluster					Cables from cluster to platform				
	$P_{\text{rated}}$	$l'$	$A'$	Annual Losses	Cost	$P_{\text{rated}}$	$l'$	$A'$	Annual Losses	Cost
	[MW]	[km]	[mm <sup>2</sup> ]	[kW]	[€]	[MW]	[km]	[mm <sup>2</sup> ]	[kW]	[€]
2 strings of 6	12	6.150	95	5.8	656 000	24	15.100	185	29.0	2 214 667
2 strings of 6	12	6.150	95	5.8	656 000	24	10.948	185	21.0	1 605 707
2 strings of 6	12	6.150	95	5.8	656 000	24	6.805	185	13.1	998 067
2 strings of 6	12	6.150	95	5.8	656 000	24	2.714	185	5.2	398 053
1 string of 3	6	0.926	95	0.2	98 773	6	0.780	95	0.18	83 200
2 strings of 6	12	6.150	95	5.8	656 000	24	2.714	185	5.2	398 053
2 strings of 6	12	6.150	95	5.8	656 000	24	6.805	185	13.1	998 067
2 strings of 6	12	6.150	95	5.8	656 000	24	10.948	185	21.0	1 605 707
2 strings of 6	12	6.150	95	5.8	656 000	24	15.100	185	29.0	2 214 667

Cost cable network = €15 862 960

### G.3 Lay-out C: all WD-WECs installed behind each other

Table G.3: Cost lay-out C

Clusters	Cables in cluster					Cables from cluster to platform				
	$P_{\text{rated}}$	$l'$	$A'$	Annual Losses	Cost	$P_{\text{rated}}$	$l'$	$A'$	Annual Losses	Cost
	[MW]	[km]	[mm <sup>2</sup> ]	[kW]	[€]	[MW]	[km]	[mm <sup>2</sup> ]	[kW]	[€]
<b>Longitudinal distance = 3D<sub>R</sub></b>										
2 strings of 6	12	10.230	95	8.1	1 091 200	24	40.463	185	66.1	5 934 573
2 strings of 6	12	10.230	95	8.1	1 091 200	24	29.305	185	48.0	4 298 067
2 strings of 6	12	10.230	95	8.1	1 091 200	24	18.152	185	29.7	2 662 293
2 strings of 6	12	10.230	95	8.1	1 091 200	24	7.018	185	11.5	1 029 307
1 string of 3	4	1.860	95	0.2	198 400	6	0.780	95	0.2	83 200
2 strings of 6	12	10.230	95	8.1	1 091 200	24	7.018	185	11.5	1 029 307
2 strings of 6	12	10.230	95	8.1	1 091 200	24	18.152	185	29.7	2 662 293
2 strings of 6	12	10.230	95	8.1	1 091 200	24	29.305	185	48.0	4 298 067
2 strings of 6	12	10.230	95	8.1	1 091 200	24	40.463	185	66.1	5 934 573
Cost cable network = €36 859 680										
<b>Longitudinal distance = 2D<sub>R</sub></b>										
2 strings of 6	12	7.370	95	5.9	786 133	24	29.155	185	47.7	4 276 067
2 strings of 6	12	7.370	95	5.9	786 133	24	21.119	185	34.5	3 097 453
2 strings of 6	12	7.370	95	5.9	786 133	24	13.088	185	21.4	1 919 573
2 strings of 6	12	7.370	95	5.9	786 133	24	5.085	185	8.3	745 800
1 string of 3	4	1.340	95	0.1	142 933	6	0.780	95	0.2	83 200
2 strings of 6	12	7.370	95	5.9	786 133	24	5.085	185	8.3	745 800
2 strings of 6	12	7.370	95	5.9	786 133	24	13.088	185	21.4	1 919 573
2 strings of 6	12	7.370	95	5.9	786 133	24	21.119	185	34.5	3 097 453
2 strings of 6	12	7.370	95	5.9	786 133	24	29.155	185	47.7	4 276 067
Cost cable network = €26 592 987										
<b>Longitudinal distance = 4D<sub>R</sub></b>										
2 strings of 6	12	13.090	95	10.4	1 396 267	24	51.771	185	84.6	7 593 080
2 strings of 6	12	13.090	95	10.4	1 396 267	24	37.493	185	61.3	5 498 973
2 strings of 6	12	13.090	95	10.4	1 396 267	24	23.218	185	38.0	3 405 307
2 strings of 6	12	13.090	95	10.4	1 396 267	24	8.959	185	14.6	1 313 987
1 string of 3	4	2.380	95	0.2	253 867	6	0.780	95	0.2	83 200
2 strings of 6	12	13.090	95	10.4	1 396 267	24	8.959	185	14.6	1 313 987
2 strings of 6	12	13.090	95	10.4	1 396 267	24	23.218	185	38.0	3 405 307
2 strings of 6	12	13.090	95	10.4	1 396 267	24	37.493	185	61.3	5 798 973
2 strings of 6	12	13.090	95	10.4	1 396 267	24	51.771	185	84.6	7 593 080
Cost cable network = €47 129 893										



# H

## Cost of Energy

The Net Present Value (NPV) of the project is defined as the total present value (PV) of a time series of cash flows and is calculated using equation (10.1):

$$\text{NPV} = -\text{CF}_o + \sum_{t=1}^{n_{life}} \frac{\text{CF}_t}{(1+i)^t} \quad (10.1)$$

with  $\text{CF}_o$  the initial cash flow in the reference year,  $n_{life}$  the lifetime of the project and  $\text{CF}_t$  the future cash flows, which include the costs and revenues during each year  $t$  of the project:

$$\text{NPV} = -\text{CF}_o + \sum_{t=1}^{n_{life}} \frac{(\text{revenues} - \text{costs})_t}{(1+i)^t} \quad (H.1)$$

The Cost of Energy (COE) is the minimum price at which energy must be sold for the energy project to break even. An energy project breaks even when the NPV of the project equals zero:

$$0 = -\text{CF}_o + \sum_{t=1}^{n_{life}} \frac{\text{energy production}_t}{(1+i)^t} (\text{COE}) - \sum_{t=1}^{n_{life}} \frac{\text{costs}_t}{(1+i)^t} \quad (H.2)$$

Consequently the COE can be calculated using equation (H.3):

$$\text{COE} = \frac{\text{CF}_o + \sum_{t=1}^{n_{life}} \frac{\text{costs}_t}{(1+i)^t}}{\sum_{t=1}^{n_{life}} \frac{\text{energy production}_t}{(1+i)^t}} \quad (H.3)$$

or equation (H.4):

$$\text{COE} = \frac{\text{PV}(\text{costs})}{\text{PV}(\text{energy production})} \quad (\text{H.4})$$





